IntechOpen

Magnesium Alloys

Design, Processing and Properties

Edited by Frank Czerwinski

MAGNESIUM ALLOYS - DESIGN, PROCESSING AND PROPERTIES

Edited by **Frank Czerwinski**

Magnesium Alloys - Design, Processing and Properties
http://dx.doi.org/10.5772/560
Edited by Frank Czerwinski

Contributors

Ma Qian, Anthony Ramirez, Kaveh Meshinchi Asl, Étienne Martin, Raj Mishra, John Jonas, Katarzyna Braszczyńska-Malik, Rajeev Ahuja, Krisztina Kádas, Levente Vitos, Borje Johansson, Hualei Zhang, Aibin Ma, Jinghua Jiang, Taku Sakai, Hiromi Miura, Kunio Funami, Masafumi Noda, Andrzej Kielbus, Xiulan Ai, Gaofeng Quan, Shuisheng Xie, Mariana Kuffova, Hong Yan, Tomasz Arkadiusz Tański, Leszek A. Dobrzański, Justyna Domagała-Dubiel, Szymon Malara, Mariusz Król, František Chmelik, Milos Janecek, Zuzanka Trojanova, Zoltán Száraz, Peter Palček, Mária Chalupová, He Yang, Liang Huang, Mei Zhan, Hiroshi Noguchi, Shae K. Kim, Frank Czerwinski, Yasuo Shimizu, Pavel Lukac, Faramarz Zarandi, Stephen Yue

Notice

First published in Croatia, 2011 by INTECH d.o.o.
eBook (PDF) Published by IN TECH d.o.o.
Place and year of publication of eBook (PDF): Rijeka, 2019. IntechOpen is the global imprint of IN TECH d.o.o.
Printed in Croatia

Legal deposit, Croatia: National and University Library in Zagreb

Additional hard and PDF copies can be obtained from orders@intechopen.com

Magnesium Alloys - Design, Processing and Properties
Edited by Frank Czerwinski
p. cm.
ISBN 978-953-307-520-4
eBook (PDF) ISBN 978-953-51-4527-1

Meet the editor

Dr. Frank Czerwinski holds a Ph.D. degree in metallurgical engineering from McGill University, Montreal, Quebec, Canada and Ph.D. (Hons) and M.Sci. (Hons) degrees in materials science from the University of Mining and Metallurgy, Cracow, Poland. He has also completed post-doctoral studies at McMaster University, Hamilton, Ontario and at McGill University, Montreal, Quebec. During professional career Dr. Czerwinski was a University Professor of materials and metallurgical engineering and the faculty member. He was also Manager and Principal Scientist of numerous research projects sponsored by universities, research institutions and industry. After years of university teaching and research he joined the global industrial sector.

Contents

Preface

The global manufacturing using light metals is on the edge of substantial growth and opportunity. Among light metals of strategic importance that include titanium, aluminum and magnesium the latter one with its density of 1.74 g/cm^3 is the lightest metal, commonly used for structural purposes. In addition to low density, magnesium is recognized for its high strength to weight ratio, high electrical and thermal conductivity, vibration damping, biocompatibility, recycling potential and esthetics. Magnesium is used in the form of alloys and usually subjected to casting, rolling, extruding or forging. Further fabrication frequently involves a wide range of operations such as forming, joining, machining, heat treatment or surface engineering.

In parallel with application expansion there is also tremendous interest in magnesium research at academic and industrial levels. A number of conferences devoted to magnesium and research papers published indicate that magnesium-related activities are present at large number of universities and government institutions. Recent downturn in economy that reduced industrial research contributions shifted more responsibility to academia. There is also a shift in geography of research activities. An essential change in global location of primary magnesium production which took place in late 90s and its transfer to Asia is followed by expansion of magnesium research there.

Despite the progress, there are still challenges which limit use of magnesium. They include often not sufficient creep resistance at elevated temperatures, low formability at room temperature, poor castability of some alloys, especially those with reactive elements, general corrosion resistance or electrochemical corrosion in joints with dissimilar metals. The breakthrough in that areas would remove the presently existing application barriers.

This book was created by contributions from experts in different fields of magnesium science and technology from over 20 research centers. It offers a broad review of recent global developments in theory and practical applications of magnesium alloys. The volume covers fundamental aspects of alloy strengthening, recrystallization, details of microstructure and a unique role of grain refinement. Due to the importance of grain size, its refinement methods such as ultrasonic and multi-axial deformation are considered. The theory is linked with elements of alloy design and specific properties including fatigue and creep resistance. Several chapters are devoted to alloy processing and component manufacturing stages and cover sheet rolling, semi-solid forming, welding and joining. Finally, an opportunity of creation of metal matrix composites based on magnesium matrix is described, along with carbon nanotubes as an effective

reinforcement. At the end of each chapter there is a rich selection of references, useful for further reading.

A combination of fundamentals, advanced knowledge, theory as well as intricate technological details makes the book very useful for a broad audience of scientists and engineers from academia and industry. I anticipate this book will also attract readers from outside the magnesium field, not only to generate genuine interest but also to create new application opportunities for this promising light metal.

December 2010

Frank Czerwinski
Bolton, Ontario,
Canada

FCzerwinski@sympatico.ca

1

Hardening and Softening in Magnesium Alloys

Pavel Lukáč and Zuzanka Trojanová,
Charles University in Prague,
Czech Republic

1. Introduction

There is an increasing interest in automobile and aerospace industries for lightweight materials (alloys and metal matrix composites). Magnesium alloys with their high specific strength (the strength-to-density ratio – σ/ρ) may be used as structural materials. Over the last two decades, use of magnesium alloys has progressively grown. Different magnesium alloys have been developed and tested. Research and development of magnesium alloys have shown that they have a great potential for applications as the lightweight materials. This is because of their high specific strength, high damping capacity and good machinability. However, their applications are limited at elevated temperatures. New alloys with improved creep resistance and high strength have been developed in recent years. Among the alloys, the Mg-Al-Ca and Mg-Al-Sr alloys exhibit good creep resistance due to the presence of thermally stable phases. During plastic deformation over wide ranges of temperature and strain rate, different micro-mechanisms may play important role. It is important to estimate the mechanisms responsible for the deformation behaviour – hardening and softening – of the alloys. An analysis of deformation microstructures has shown that one should consider dislocation-based mechanisms in order to explain the deformation behaviour. The values of strength may be influenced by different hardening mechanisms.
The aim of this paper is to present the deformation behaviour of some magnesium alloys at different temperatures and to propose the mechanisms responsible for plastic deformation of the alloys.

2. Stress strain curves

A set of the true stress – true strain curves for some magnesium alloys deformed in tension or in compression at different temperatures are shown in Figs. 1-3. It can be seen that the shape of the deformation curves depends very sensitively on the testing temperature. At lower temperatures (lower than about 150 °C), the flow stress increases with strain – a high strain hardening is observed. On the other hand, at temperatures higher than 200 °C, the stress – strain curves are flat; the strain hardening rate is close to zero. It means there is a dynamic balance between hardening and softening; hardening is compensated for by recovery. Strain hardening – the change in the flow stress with strain – depends on the dislocation structure evolved with plastic deformation. An increase in the flow stress is due to dislocation storage. Dislocations stored at obstacles contribute to hardening, whereas cross slip and/or climb of dislocations contribute to softening. Dislocations after cross slip

or after climb may annihilate, the dislocation density decreases, which causes a decrease of the flow stress with strain, i.e. a decrease in the strain hardening rate. Interplay between work hardening and softening may help to account for the deformation behaviour. In the following we shall present some models describing the stress dependence of the strain hardening rate in metallic materials.

3. Strain hardening models

It is widely accepted that the resolved shear stress, τ, necessary for the dislocation motion in the slip plane can be divided into two components:

$$\tau = \tau_i + \tau^*, \tag{1}$$

where τ_i is the internal stress and $\tau^*$is the thermal component, oft called effective stress. The effective stress acts on dislocations during their thermally activated motion when they overcome short range obstacles as forest dislocations, solute atoms, etc. The internal stress component can be expressed as

$$\tau_i = \alpha_1 G b \rho_t^{1/2}, \tag{2}$$

where ρ_t is the total dislocation density, G is the shear modulus, b is the magnitude of the Burgers vector and α_1 is a constant.
The applied stress σ acting on a polycrystal is related to the resolved shear stress τ by the Taylor factor M:

$$\sigma = M\,\tau. \tag{2}$$

Then similarly σ may be also divided into the internal and effective stress components

$$\sigma = \sigma_i + \sigma^* \tag{3}$$

Stress relaxation can be considered as a method for studying the internal stress field, based on the separation of the flow stress, i. e. on the determination of the average effective internal stress $(\sigma_i)_{eff}$. For the simplicity it will be called the internal stress σ_i.
In spite of very long time investigating of polycrystals up to now, the generally accepted analytical description of the stress - strain curves does not exist. It is a consequence of the complicated nature of the stress in polycrystals, which is dependent on many structure parameters as type of crystal structure, grain size, texture, concentration and distribution of solute atoms, presence of second phase, etc. A change of the flow stress is connected with development of the material structure. This development depends on strain, temperature, strain rate, preceding history of the sample, and on other parameters. Up to now it was not detailed investigated. It is considered, for simplicity, that the plastic deformation is determined by one main structural parameter S that describes the actual structural state of the material.
The flow stress of crystalline materials σ depends on the dislocation structure and is related to the dislocation density, ρ, as

$$\sigma = \alpha_1 M G b \rho^{1/2}, \tag{4}$$

where G is the shear modulus, b is the magnitude of the Burgers vector. The relationship (4) implies that the strength of the material is determined by dislocation-dislocation interaction.

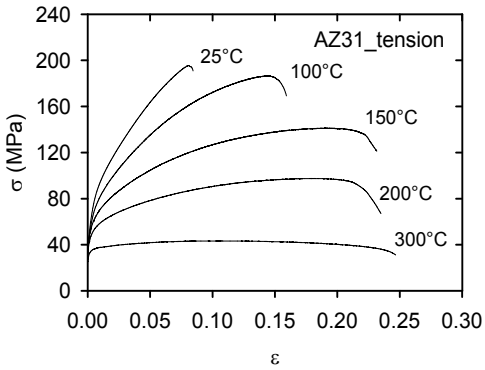

Fig. 1. Stress strain curves obtained for AZ31 gravity cast alloy at various temperatures in tension.

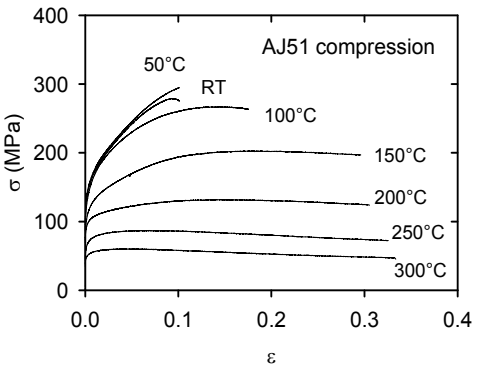

Fig. 2. Stress strain curves obtained for AJ51 squeeze cast alloy at various temperatures in compression.

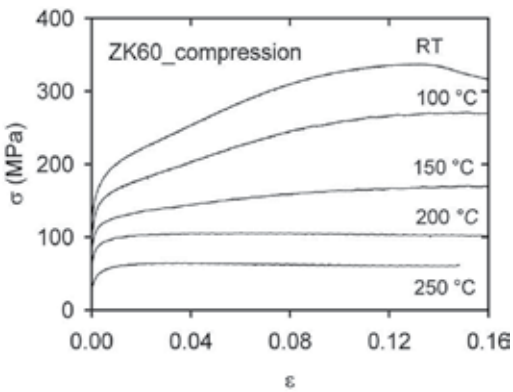

Fig. 3. Stress strain curves obtained for ZK60 alloy deformed in compression at various temperatures.

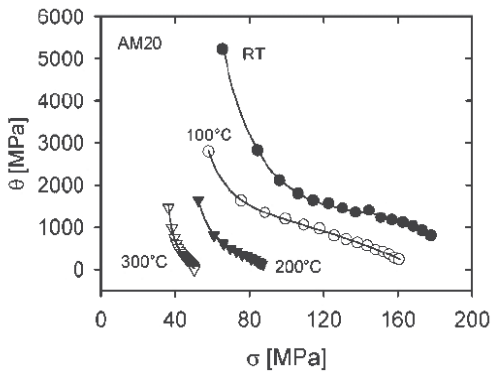

Fig. 4. Work hardening coefficient versus stress obtained for AM20 alloy deformed in tension at various temperatures.

The evolution equation describing the development of the dislocation structure with time or strain can be generally described in the following form:

$$\frac{d\rho}{d\varepsilon} = \left(\frac{d\rho}{d\varepsilon}\right)_h - \left(\frac{d\rho}{d\varepsilon}\right)_r . \tag{5}$$

The first (positive) term on the right hand accounts for the dislocation storage, while the second one represents the annihilation of dislocations; it contributes to softening.

Model of Kocks

Kocks (Kocks, 1976) has assumed that the dislocation mean free path is proportional to the average spacing between forest dislocations. He considered that an increase in the dislocation density with strain is due to dislocation storage and a decrease in the dislocation density is caused by annihilation of dislocations by cross slip.
Then, the evolution equation for the dislocation density reads:

$$\frac{d\rho}{d\varepsilon} = \kappa_f \rho^{1/2} - \frac{L_r \rho}{b}, \tag{6}$$

where L_r is the average length of the dislocation segment recovered in one recovery event (due to cross slip), κ_f is a geometrical factor based on the assumption that the mean free path Λ of the dislocation glide is proportional to the average spacing between forest dislocations ℓ_d i.e.

$$\Lambda = \beta \ell_d = \beta \rho^{-1/2}. \tag{7}$$

L_r is a function of temperature and strain rate. The stress dependence of the strain hardening rate of polycrystals (it is necessary to take into account the relationship between work hardening coefficient (rate) of single crystals and polycrystals) $\Theta = d\sigma / d\varepsilon = M^2\theta$, ($\sigma = M\tau$, $\varepsilon = \gamma / M$, $\theta = d\tau / d\gamma$).can be written.

$$\Theta = \frac{d\sigma}{d\varepsilon} = \Theta_{0K}\left(1 - \frac{\sigma}{\sigma_{SK}}\right), \tag{8}$$

where $\Theta_{0K} = \frac{\alpha_1 M^2 G b \kappa_f}{2}$ and $\sigma_{SK} = \frac{\alpha_1 M G b^2 \kappa_f}{L_r}$.

In many cases, equation (8) cannot describe the whole work hardening curve that consists of several regions with different slopes. This phenomenon is common for many materials. It should be mentioned that texture influences the hardening parameters and therefore, variation in M can be large (Cáceres & Lukáč, 2008).

Model of Estrin and Mecking

In contrary to the model of Kocks, Estrin and Mecking (Estrin & Mecking, 1984) have assumed that the mean free path of dislocations Λ is constant and it is determined by the spacing between impenetrable obstacles (grain boundaries, incoherent precipitates, dispersion particles). Finally they obtained

$$\frac{d\rho}{d\varepsilon} = \frac{1}{bs} - \frac{L_r}{b}\rho \tag{9}$$

and

$$\sigma\Theta = \Theta_{0EM}\left(1 - \frac{\sigma^2}{\sigma_{SEM}^2}\right), \tag{10}$$

where $\Theta_{0EM} = \frac{M^3(\alpha_1 G b)^2}{2sb}$, $\sigma_{SEM} = \frac{M\alpha_1 G b}{\left(sL_r\right)^{1/2}}$ and s is the particle spacing or the grain size.

Model of Malygin

Malygin (Malygin, 1990) took into account: storage of dislocations on impenetrable obstacles, storage of dislocations on forest dislocations and annihilation of dislocations due to cross slip. The evolution equation has, in this case, the following form:

$$\frac{d\rho}{d\varepsilon} = \frac{1}{bs} + \kappa_f \rho^{1/2} - \kappa_a \rho, \tag{11}$$

where s is the particle spacing or the grain size, κ_f is the coefficient of the dislocation multiplication intensity due to interaction of moving dislocations with forest dislocations and κ_a is the coefficient of the dislocation annihilation intensity due to cross slip. Finally, the equation suitable for an analysis of the experimental strain hardening rate of polycrystals is then

$$\Theta = d\sigma / d\varepsilon = \mathcal{A}/ (\sigma - \sigma_y) + \mathcal{B} - C (\sigma - \sigma_y). \quad (12)$$

Here the following substitutions were made:

$$\mathrm{A} = \frac{1}{2} M^3 \left(\alpha_1 G b\right)^2 \frac{1}{bs};\ \mathrm{B} = \frac{1}{2} M^2 \alpha_1 G b \kappa_f;\ \text{and } \mathrm{C} = \frac{1}{2} M \kappa_a .$$

The yield stress σ_y corresponds to the beginning of plastic deformation and comprises all contributions from the various hardening mechanisms.

The model of Lukáč and Balík

In many cases, the Malygin model describes the whole work hardening curve at lower temperatures where only stage II and III hardening occurs. At intermediate temperatures (about 0.3 T_m), there are deviations from the prediction of this model, which indicates the presence of some other recovery process in addition to cross slip. Lukáč and Balík (Lukáč & Balík, 1994) assumed that hardening occurs due to multiplication of dislocations at both non-dislocation obstacles and forest dislocations. As the dominant softening processes, annihilation of dislocations due to both cross slip and climb are considered. They derived the kinetic equation for single crystals in the following form:

$$\frac{d\rho}{d\gamma} = \frac{1}{bs} + \kappa_f \rho^{1/2} - \frac{cL_{CS}}{b} - \frac{D_c b^2 \psi_c}{\chi k_B T \dot{\gamma}} \tau \rho^{3/2}, \quad (13)$$

where L_{CS} is the dislocation segment length recovered by one cross slip event, c is the area concentration of the recovery sites in a slip plane, ψ_c is a fraction of the dislocations which can be annihilated by climb of dislocations with jogs, χ is a parameter which gives the relation between dislocation climb distance w (i.e. distance between storage of a dislocation and its annihilation site) and the average dislocation spacing $1/\sqrt{\rho}$ in the form $w = \chi / \sqrt{\rho}$, τ is the shear stress, γ is the shear strain, k_B is the Bolzmann constant and D_c is an abbreviation which includes the diffusion coefficient and the stacking fault energy. The stress dependence of the work hardening rate for polycrystals reads:

$$\Theta = A / (\sigma - \sigma_y) + B - C\left(\sigma - \sigma_y\right) - D\left(\sigma - \sigma_y\right)^3 . \quad (14)$$

Here the meaning of the parameters used is the following:

$$A = M^3 \left(\alpha_1 G\right)^2 \frac{b}{2s} \left(\frac{\dot{\varepsilon}}{\dot{\varepsilon}_1}\right)^{\frac{2}{n}};\ B = \frac{1}{2} M^2 \alpha_1 G n \kappa_f \left(\frac{\dot{\varepsilon}}{\dot{\varepsilon}_1}\right)^{\frac{1}{n}};\ C = M \frac{cL_{CS}}{2b\rho};\ D = \frac{1}{M^2} \frac{\psi_c D_c b}{2\chi \alpha_1 G k_B T \dot{\varepsilon}} \left(\frac{\dot{\varepsilon}}{\dot{\varepsilon}_1}\right)^{-\frac{1}{n}}$$

Here $\dot{\varepsilon}_1$ is a parameter and n is the stress exponent. It should be mention that, in the face-centred-cubic metals, the parameters A and B are independent of temperature and the parameters C and D depend on temperature.

Model of Estrin and Kubin.

In many cases, a model employing just one internal variable (the total dislocation density) is not sufficient for describing deformation histories involving rapid changes of the deformation path. Instead of using a single internal variable related to the total dislocation density ρ, Estrin and Kubin (Estrin & Kubin, 1986) considered the density of mobile dislocation ρ_m and the relatively immobile dislocation density (or the forest dislocation density) ρ_f. The evolution equations for the two populations of dislocations proposed by Estrin and Kubin can be expressed as

$$\frac{d\rho_m}{d\gamma} = -k_1\sqrt{\rho_f} - k_3\rho_m + k_4\frac{\rho_f}{\rho_m} \tag{15}$$

$$\frac{d\rho_f}{d\gamma} = k_1\sqrt{\rho_f} - k_2\rho_f + k_3\rho_m . \tag{16}$$

Here k_i are constants. It can be seen that the negative terms in Eq. (15), which represent the loss of the mobile dislocation density due to various dislocations reaction, reappear as positive terms in eq. (16). Newly formulated two variable constitutive model was solved by Estrin (Estrin, 1996) and Braasch, Estrin and Brechet (Braasch et al., 1996).

Model of Nes

Three parameters approach to the modelling of metal plasticity has been proposed by Nes & Marthinsen (Nes & Marthinsen, 2002). It is assumed in the model that at small strains (stage II) the stored dislocations are arranged in a cell structure which may be characterised by thickness *t* of cell walls; internal dislocation density ρ_b; dislocation density within cells. At large strains (stage IV), the cell walls collapse into sub-boundaries with a misorientation φ. The main features of the model can be summarised as follows:

1. The flow stress τ is done by

$$\tau = \tau_i + \alpha_1 Gb\sqrt{\rho_i} + \alpha_2 Gb/\delta , \tag{17}$$

where τ_I is the frictional stress, α_1 and α_2 are constants, and δ is the size of cells or subgrains. The frictional stress reflects short range interactions associated with the intersection of forest dislocations and dragging of jogs which can be expressed by

$$2\sinh\frac{\tau_i V_a}{k_B T} = \left(b^2\rho_m C_i \nu_D\right)^{-1}\dot{\gamma}\exp\left(\frac{U_i}{k_B T}\right), \tag{18}$$

where V_a is the activation volume, U_i is the activation energy, ρ_m is the mobile dislocation density ν_D the Debye frequency and C_i is a constant; k_B T has its usual meaning.

2. Dislocations are stored during deformation in three sites: in the cell interior, in old boundaries and/or by forming new boundaries. These processes can be described by the following equation

$$\frac{d\rho_{nb}^{+}}{d\gamma} = 2S\rho_i \frac{L}{b}, \tag{19}$$

where ρ_{nb} are dislocations stored in new boundaries, L is the mean free path of dislocations before being stored, $L=C\rho^{-1/2}$ (C is a constant), ρ is the total density of stored dislocations. S is dislocation storage parameter that can be defined using microstructural scaling C_i constants and volume fraction of cell walls f: $S=S_{sc}=S_{sc}(f, C_c, C_t, C_{cb})$, where $C_c=\delta\rho_i^{1/2}$, $C_t=t/\delta$ and $C_{cb}=\delta\rho_b^{1/2}$. Equation (19) can be expressed in the following alternative forms:

Stage II: $\frac{d\rho_i^{+}}{d\gamma} = -\frac{2\rho_i^{1/2}}{bC\left[1-f+\left(C_b/C_c\right)^2\right]^{1/2}}$

Stage III and IV: $\frac{d\delta^{-}}{d\gamma} = -\frac{2\rho_{III}SC\delta^2}{\kappa\varphi\left(\rho_{III}+\kappa\varphi/b\delta\right)^{1/2}}$

where $C_b=fC_{cb}$ and κ is a geometric constant that is equal to 2 for a regular cell structure. Based on experimental observations the sub-boundary orientation, φ, depends on δ in stage III and becomes a constant in stage IV, while S is treated as a modelling parameter.

3. Dynamic recovery is incorporated assuming two mechanisms: a) a dislocation segment in a Frank network which may migrate under a force per unit length, F, with a velocity

$$\upsilon = \upsilon_D b C_\rho^{1/2} \exp\left(-\frac{U_\rho}{kT}\right) 2\sinh\frac{Fb^2}{k_B T},$$

where $F=\alpha_3\xi_\rho Gb^2\rho_i^{1/2}$, C_ρ and α_3 are constants, U_ρ is the activation energy and ξ_ρ a dynamic stress intensity factor. The average subgrain size will increase according to

$$\frac{d\delta^{+}}{dt} = \dot{\gamma}\frac{d\delta^{+}}{dt} = \upsilon_D b C_\delta \rho^{1/2} \exp\left(-\frac{U_\delta}{k_B T}\right) 2\sinh\frac{pV_a}{k_B T},$$

where V_a is the activation volume. It should be mentioned that the models mentioned above were developed for polycrystals of face-centred-cubic metals that have more than 5 independent slip systems. On the other hand, hexagonal metals with the low symmetry do not provide 5 identical slip systems. To fulfil the von Mises criterion for polycrystal deformation, several different crystallographic slip systems have to be activated.

In magnesium and its alloys, the dominant slip mode is the basal slip with two independent modes, which is not sufficient for the satisfying the von Mises criterion. The glide of dislocation in second-order pyramidal slip systems should be considered.

Comparison with experimental results

Comparing experimental stress strain curves (for example curves introduced in Figs. 1-3) with the models of the strain hardening, the best agreement for hexagonal magnesium alloys was found for the Lukáč and Balík model (L-B model). Corresponding stress dependences of the work hardening coefficients are introduced in Fig. 4. From Fig. 4 it can be easily seen that the work hardening coefficient Θ does not decreases with the increasing stress linearly; then the Kocks model may not work. Note that the Nes model was not analysed because of missing dislocation substructure data. Parameters following from the L-B model are introduced in Table 1 (Máthis & Trojanová, 2005).

	A (MPa^2)	B (MPa)	C	D x 10^4 (MPa^{-2})	R^2	σ_y (MPa)	σ_{02} (exp) (MPa)
0.2%Zn	820 ± 178	2010 ± 20	5.4 ± 0.3	2.77 ± 0.07	0.987	57.40 ± 0.10	59
0.3%Zn	930 ± 60	1750 ± 10	0.5 ± 0.2	4.97 ± 0.05	0.988	71.48 ± 0.07	71
0.4%Zn	1940 ± 160	1910 ± 20	4.2 ± 0.3	2.30 ± 0.04	0.986	65.76 ± 0.04	70
1%Zn	1870 ± 170	1780 ± 20	2.7 ± 0.3	1.65 ± 0.06	0.97	87.28 ± 0.06	86
2%Zn	11100 ± 600	1780 ± 30	1.6 ± 0.3	1.00 ± 0.04	0.984	97.80 ± 0.20	100
3%Zn	46000 ± 6000	1360 ± 190	3e-3 ± 1.7	1.17 ± 0.28	0.988	114.70 ± 0.10	109

Table 1. Concentration dependence of the parameters of best fit for the L-B model and the calculated and measured yield stress for Mg-Zn alloys.

	A (MPa^2)	B (MPa)	C	D x 10^4 (MPa^{-2})	R^2	σ_y (MPa)	σ_{02} (exp) (MPa)
20 °C	68.700 ± 400	1532 ± 12	0	3.5 ± 0.6	0.99	78.3 ± 0.2	79
50 °C	49.200 ± 600	1471 ± 23	0	2.5 ± 0.7	0.99	61.2 ± 0.2	68
100 °C	54.800 ± 400	846 ± 15	0	4.4 ± 0.1	0.99	67.0 ± 0.7	69
150 °C	29.000 ± 100	346 ± 29	0	9.3 ± 0.1	0.99	67.0 ± 0.3	65
200 °C	4.173 ± 896	691 ± 52	14.1 ± 0.6	6.0 ± 0.3	0.97	64.2 ± 0.2	64

Table 2. Temperature dependence of the parameters of best fit to L-B-model and the calculated and measured yield stress for Mg alloy AM60.

The parameter A increases monotonically with the increasing solute content for Mg-Zn alloys in agreement with the prediction of the model, i.e. the parameter A is reciprocally proportional to the distance of impenetrable obstacles. The results suggest the increasing role of non-dislocation obstacles (e.g. solute atoms, clusters, precipitates, dispersoids) in the hardening mechanism. The parameter B remains nearly constant for all concentrations. Since this parameter is connected with the dislocation – forest dislocation interaction, this result indicates that the dislocation density in non-basal slip systems does not change with increasing solute content. There is a significant difference in parameter C, which characterizes the cross slip of screw dislocations. Cross slip takes place through prismatic slip system, and an increased activity of this slip system could enhance the ductility. In the case of Mg-Zn alloys, values of parameter C are of the order assumed by the model and

suggest the importance of cross slip in the deformation process. The concentration dependencies of this parameter (see Table 1) and ductility are in agreement, i.e. decrease with increasing concentration of Zn, thus the probability of cross slip decreases as well. It seems that 2 at.% Zn is a critical concentration; above that Zn content ceases improving the slip in prismatic slip system. It is necessary to remark that the model is able to describe drop in ductility for 0.3 at.% Zn, where the value of parameter C is small. This result supports the hypothesis of Akthar and Tegthsoonian (Akthar & Tegthsoonian, 1972), who assumed a hardening in prismatic plane for this concentration of Zn. Decreasing of parameter D with increasing solute content is most probably connected with reduced climb ability because of the high concentration of solute atoms along the dislocation line, and due to the lowering of the stacking fault energy as the solute content increases. Lowering of stacking fault energy improves the twinning activity as well. Note that the twin boundaries may be the impenetrable obstacles for dislocation motion. In materials with the strong texture (rolled sheets) when twinning is unfavourable it is necessary to consider the evolution of the dislocation substructure in both basal and non-basal slip systems, as it was shown by Balík et al. (Balík et al., 2009).

Similar analysis according to L-B model was performed for magnesium alloy AM60 deformed at various temperatures by Máthis et al. (Máthis et al., 2004a) Results are introduced in Table 2. The parameter A is not expected to depend on temperature, while Table 2 shows that the value of A drops rapidly above 150 °C. Alloy AM60 contains about 4% volume fraction of the intermetallic phase $Mg_{17}Al_{12}$, which is likely to dissolve as the temperature is increased. This will result in increased spacing between non-dislocations obstacles, which, in turn, would lower the value of the parameter A. Similarly, a decrease in the forest dislocation density (the density of dislocations in non-basal planes) can be expected at increasing temperatures. The mean free path of dislocations and therefore the storage distance will increase. The storage probability should decrease. This could cause the temperature decrease in the parameter B. The parameter C becomes >0 at 200 °C, which indicates that the cross slip becomes a significant recovery process at higher temperatures. The parameter D increases with increasing temperature, which is expected in the case of climb. Above 250 °C the model does not describe the experimental curves satisfactory; we suggest that another softening mechanism, most likely dynamic recrystallisation, may become operative.

4. Internal stress in magnesium alloys

In the stress relaxation tests, specimen is deformed to a certain stress (strain) and then allowed to relax by stopping the machine. Stress relaxation (SR) is usually analysed under an assumption that the strain rate during the SR experiments is proportional to the stress rate (the stress drops in one second). Components of the applied stress (σ_i, σ^*) can be estimated using Li's method (Li, 1967, 1981). The SR curves were fitted to a power law function in the form:

$$\sigma - \sigma_i = \left[a(m-1)\right]^{\frac{1}{1-m}} \left(t + t_0\right)^{\frac{1}{1-m}}, \tag{20}$$

where a, t_0, and m are fitting parameters.

A part of the AX41 true stress – true strain curve measured in compression at 25 °C with points indicating the stresses at which the SR tests were performed is shown in Fig. 5. Open circles and full circles depict the internal stress σ_i, and the effective stress σ^*, respectively. It is obvious that the internal stress σ_i is a substantial contribution to the applied stress σ_{ap}. Similar curves estimated at 150 °C are shown in Fig. 6. The effective stress component increases with increasing strain while the internal stress increases to the maximum and then decreases with increasing strain. Fig. 7 shows the curves obtained at 300 °C. The internal stress is lower than the effective stress and it decreases for strains higher than $\varepsilon = 0.02$. The internal stress depends on the dislocation density, i.e. $\sigma_i \propto \rho^{1/2}$. A decrease of the internal stress indicates a decrease of the dislocation density. In the case when the internal stress is approximately constant or slightly decreasing with strain, some equilibrium between multiplication and annihilation of dislocations may be considered.

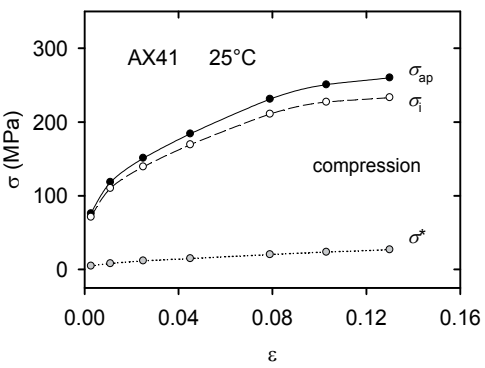

Fig. 5. A part of the true stress–true strain curve obtained for the AX41 alloy at 25 °C in compression. The points of σ_{ap} on the curve indicate the stresses at which the SR tests were performed.

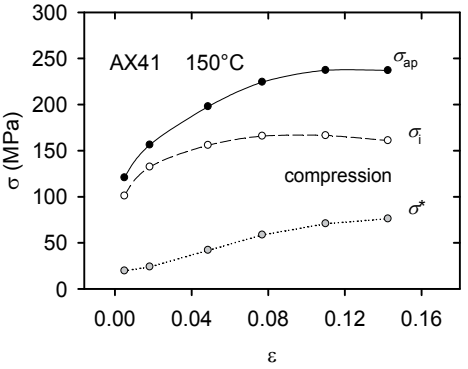

Fig. 6. A part of the true stress-true strain curve obtained for the AX41 alloy at 150 °C in compression. The points of σ_{ap} on the curve indicate the stresses at which the SR tests were performed.

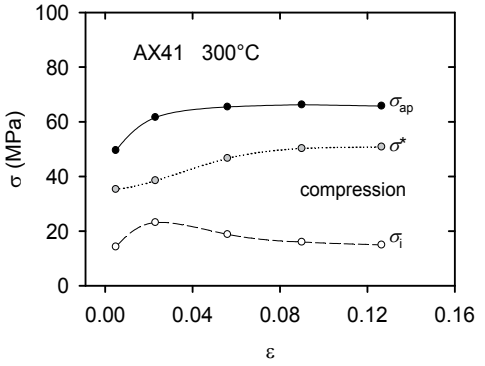

Fig. 7. Part of the stress– strain curve for AX41 alloy at 300 °C. The points of σ_{ap} on the curve indicate the stresses at which the SR tests were performed.

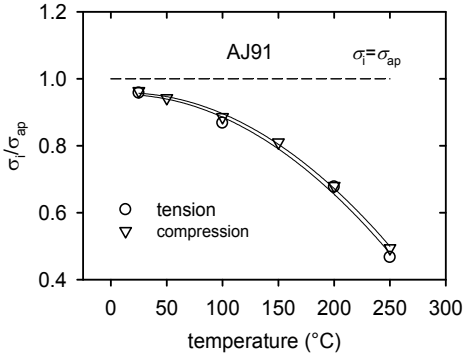

Fig. 8. Variation of the internal/applied stress ratio obtained from the first SR test with temperature estimated for the AJ91 samples.

The moving dislocations can cross slip and after cross slip they may annihilate, which causes the decrease in the dislocation density. At higher temperatures, the moving dislocations can also climb. The activity of cross slip and climb increases with increasing temperature. This means that the total dislocation density decreases with increasing temperature. The internal stress/applied stress ratio decreases significantly with increasing temperature independent of the deformation mode (the values of the ratio for compression deformation are practically the same as for tension) (see Fig. 8 where the temperature dependence of σ_i/σ_{ap} is introduced for AJ91 alloy). It is possible to estimate the internal stress also in creep experiments as it was performed by Milička et al. (Milička et al., 2007) for several magnesium alloys. They found that the internal stress σ_i reflects the creep resistance of the material. Experimental internal stresses determined in creep well correspond to those determined in SR tests under comparable testing conditions.

5. Thermally activated dislocation motion

The deformation behaviour of materials depends on temperature and strain rate. Practically in all polycrystals, the temperature and strain rate dependences of the flow stresses can be found. These dependences indicate thermally activated processes. The motion of dislocations through a crystal is affected by many kinds of obstacles. The mean velocity of dislocations is connected with the strain rate by the Orowan equation

$$\dot{\varepsilon}=(1/M)\rho_m b v \tag{21}$$

where ρ_m is the density of mobile dislocations moving at a mean velocity v. It is obvious that the stress dependence of $\dot{\varepsilon}$ is done by the stress dependence of ρ and v. At a finite temperature, the obstacles can be overcome with the help of thermal fluctuations. Therefore, the dislocations are able to move even if the force on dislocations is lower than that exerted by the obstacles; the additional energy is supplied by thermal fluctuations. The short-range thermally activated processes are important for the understanding of deformation behaviour. If a single process is controlling the rate of dislocation glide, the plastic strain rate $\dot{\varepsilon}$ can be expressed as:

$$\dot{\varepsilon}=\dot{\varepsilon}_0 \exp\left[-\frac{\Delta G(\sigma^*)}{k_B T}\right], \tag{22}$$

where $\dot{\varepsilon}_0$ is a pre-exponential factor containing the mobile dislocation density, the average area covered by the dislocations in every activation act, the Burgers vector, the vibration frequency of the average dislocation segment and a geometric factor. $\Delta G(\sigma^*)$ is the change in the Gibbs free enthalpy depending on the effective stress $\sigma^*=\sigma-\sigma_i$, T is the absolute temperature and k_B is the Boltzmann constant. The stress dependence of the free enthalpy may be expressed by a simple relation

$$\Delta G(\sigma^*) = \Delta G_0 - V\sigma^* = \Delta G_0 - V(\sigma - \sigma_i), \tag{23}$$

where ΔG_0 is the Gibbs free enthalpy necessary for overcoming a short-range obstacle without the stress and V = bdL is the activation volume where d is the obstacle width and L is the mean length of dislocation segments between obstacles. It should be mentioned that L may depend on the stress acting on dislocation segments.

The nature and the distribution of obstacles determine the activation parameters (the activation energy and the activation volume). For a given arrangement of obstacles in a material, the thermally activated process controls the temperature and strain rate dependence of the flow stress. Two methods are very often used for the estimation of the activation volume: differential constant strain rate tests and stress relaxation experiments. In differential constant strain rate tests, the specimen is deformed with a constant strain rate to a given strain (stress) and then the strain rate is suddenly changed by a known factor. The resulting change in stress is observed; an increase (decrease) in the stress is observed if the strain rate increases (decreases). The activation volume is inversely proportional to this stress change. The activation volume can be estimated from the stress relaxation tests. The stress decrease with time during the SR test can be described by the known Feltham equation (Feltham, 1963)

$$\Delta\sigma(t) = \sigma(0) - \sigma(t) = \alpha\ln(\beta t + 1)\,, \tag{24}$$

where $\sigma(0)$ is the stress at the beginning of the stress relaxation at time $t = 0$, β is a constant. The activation volume is done by:

$$\alpha = \frac{k_B T}{V}\,. \tag{25}$$

and the constant β

$$\beta = \frac{M\dot{\varepsilon}_0 V}{k_B T}\exp\left[-\frac{\Delta G_0 - V\sigma^*(0)}{k_B T}\right] = \frac{M\dot{\varepsilon}(0)}{\alpha}\,. \tag{26}$$

Values of the apparent activation volume estimated using Eq. (24) are plotted against the applied stress in Fig. 9 for AJ51 and in Fig. 10 for AZ63 alloys for several deformation temperatures. The activation volume depends on the applied stress and testing temperature. Apparent (experimental) activation volume estimated in experiments with polycrystals is proportional to the dislocation activation volume, $V_{d,}$ as $V = (1/M)V_d$. Usually, the values of activation volume are given in b^3, which allows their comparison with processes responsible for the thermally activated dislocation motion. Apparent activation volumes for AJ51 alloy estimated for four deformation temperatures in tensile (T) and compression (C) tests are plotted against the effective (thermal) stress in Fig. 11. All values appear to lie on one line, "master curve". Similar results were found for other magnesium alloys among them also for AZ63 alloy (see Fig. 12).

In order to analyse the dependences, we will assume an empirical relation between the Gibbs free enthalpy ΔG and the effective stress, σ^*, suggested by Kocks and co-workers (Kocks et al., 1975) in the following form:

$$\Delta G = \Delta G_0\left[1 - \left(\frac{\sigma^*}{\sigma_0^*}\right)^p\right]^q \tag{27}$$

where σ_0^* is the effective stress at 0 K. From (22) and (27) it follows:

$$\sigma^* = \sigma_0^*\left[1 - \left(\frac{k_B T}{\Delta G_0}\ln\frac{\dot{\varepsilon}_0}{\dot{\varepsilon}}\right)^{1/q}\right]^{1/p}, \tag{28}$$

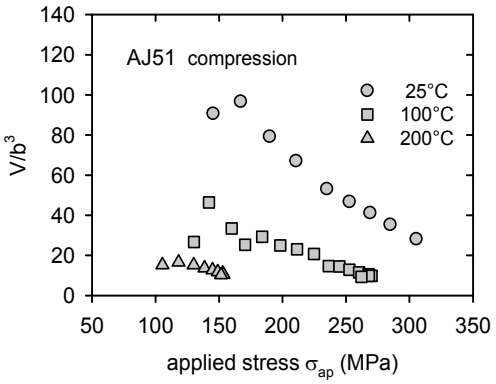

Fig. 9. Plot of the apparent activation volume (in b^3) against the applied stress σ_{ap} estimated for the AJ51 alloy in compression, at three temperatures.

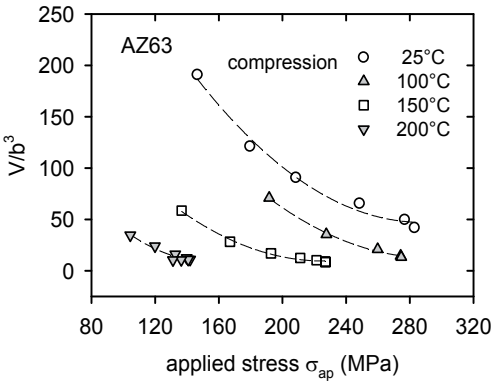

Fig. 10. Plot of the apparent activation volume (in b^3) against the applied stress σ_{ap} estimated for four deformation temperatures in compression.

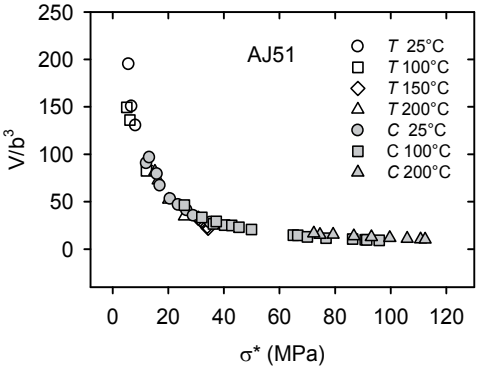

Fig. 11. Plot of the apparent activation volume (in b^3) against the thermal stress σ^* estimated for four deformation temperatures in tension (T) and compression (C) for the AJ51 alloy.

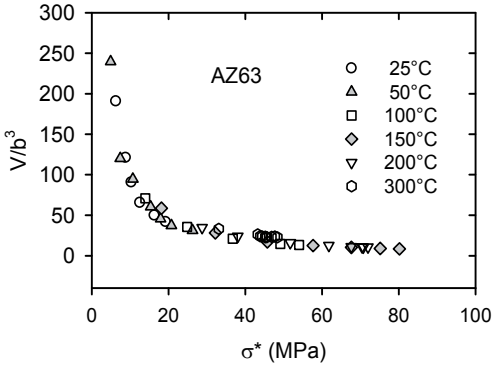

Fig. 12. Plot of the apparent activation volume (in b^3) against the thermal stress σ^* estimated for various deformation temperatures (AZ63 alloy).

where p and q in Eqs. (27) and (28) are phenomenological parameters reflecting the shape of a obstacle profile. The possible ranges of values p and q are limited by the conditions $0 < p \leq 1$ and $1 \leq q \leq 2$. Ono (Ono, 1968) and Kappor and co-workers (Kapoor et al., 2002) suggested that Eq. (28) with $p = 1/2$, $q = 3/2$ describes a barrier shape profile that fits many predicted barrier shapes. Equation (28) can be rewritten as

$$\dot{\varepsilon} = \dot{\varepsilon}_0 \exp\left[-\frac{\Delta G_0}{k_B T}\left(1 - \left(\frac{\sigma^*}{\sigma_0^*} \right)^p \right)^q \right]. \tag{29}$$

The dependence of the activation volume on the effective stress can be expressed as

$$V = k_B T \frac{\partial \ln \dot{\varepsilon} / \dot{\varepsilon}_0}{\partial \sigma^*} = \frac{\Delta G_0 pq}{\sigma_0^*} \left[1 - \left(\frac{\sigma^*}{\sigma_0^*} \right)^p \right]^{q-1} \left(\frac{\sigma^*}{\sigma_0^*} \right)^{p-1} . \quad (30)$$

The values of the activation volume should lie at the curve given by Eq. (30). The fit of the experimental values of Eq. (30) gives for the activation enthalpy ΔG_0 = 0.95 ± 0.05 eV for both alloys (AJ51 and AZ63). Similar values ΔG_0 ~ 1.00 ± 0.05 eV were estimated for all magnesium alloys studied. The values of the activation volume and the activation enthalpy may help to identify thermally activated process considering some of the common short range barriers to dislocation motion. We should consider that a rapid decrease in the internal stress with increasing temperature indicates that observed softening during deformation is connected with dynamic recovery. It is well-known that the main deformation mode in magnesium and magnesium alloys with hcp structure is basal glide system with dislocations of the Burgers vector <a> = $1/3[11\bar{2}0]$. The secondary conservative slip may be realised by the <a> dislocations on prismatic and pyramidal of the first-order. Couret and Caillard (Couret and Caillard, 1985a,b) using TEM showed that the screw dislocations with the Burgers vector of $1/3[11\bar{2}0]$ in magnesium are able to glide on prismatic planes and their mobility is much lower than the mobility of edge dislocations. They concluded that the deformation behaviour of magnesium over a wide temperature range is controlled by thermally activated glide of those screw dislocation segments. A single controlling mechanism has been identified as the Friedel-Escaig cross slip mechanism. This mechanism assumes dissociated dislocations on compact planes, like (0001), that joint together along a critical length L_{cr} producing double kinks on non-compact planes. Therefore, the activation volume is proportional to the critical length between two kinks. The activation volume of the Friedel–Escaig mechanism has a value of ~70 b^3. Prismatic slip has been also observed by Koike and Ohyama (Koike & Ohyama, 2005) in deformed AZ61 sheets. The activation of the prismatic slip and subsequent annihilation of the dislocation segments with the opposite sign are probably the main reason for the observed internal stress decrease. The double cross slip may be thermally activated process controlling the dislocation velocity. The activation of the prismatic slip of <a> dislocations and subsequent annihilation of the dislocation segments with the opposite sign may contribute to the observed internal stress decrease.

The number of independent slip systems in the basal plane is only two. Thus, the von Mises requirement for five independent deformation modes to ensure a reasonably deformability of magnesium alloy polycrystals is not fulfilled. Twinning and the activity of non-basal slip is required. From activities of non-basal slip systems, motion of dislocations with <c+a> Burgers vector in the second-order pyramidal slip systems is expected. The critical resolved shear stress (CRSS) for non-basal slip systems at room temperature is higher by about a factor 100 than the CRSS for basal slip. On the other hand, the CRSS for non-basal slip decreases rapidly with increasing temperature. It means that the activity of a non-basal slip system increases with increasing temperature. It is worth mentioning that Máthis and co-workers (Máthis et al., 2004b), who studied the evolution of different types of dislocations with temperature in Mg using X-ray diffraction, found that at higher temperatures, the fraction of <c+a> dislocations increases at a cost of <a> dislocations. The total dislocation density decreases with increasing temperature. The glide of <c+a> dislocations may affect the deformation behaviour of magnesium alloys.

The shape of the true stress – true strain curves (Figs. 1-3) indicates that the flow stress and strain hardening and softening are influenced by the testing temperature – at temperatures above about 200 °C, the strain hardening is very close to zero. From the dislocation theory point of view, this deformation behaviour may be explained assuming changes in deformation mechanisms. At temperatures below about 200 °C, strain hardening is caused by multiplication and storage of dislocations. Above about 200 °C, there is not only storage of dislocations during straining leading to hardening but also annihilation of dislocations leading to softening. The intensity of the latter is highly dependent on temperature. A dynamic balance between hardening and softening may take place at higher temperatures. The activity of non-basal slip systems has to play an important role in both hardening and recovery processes in magnesium alloys. The glide of <c+a> dislocations may be responsible for an additional work hardening because of the development of several systems of immobile or sessile dislocations. Different reactions between <a> basal dislocations and <c+a> pyramidal dislocations can occur (Lukáč, 1981; Lukáč, 1985). Glissile (glide) <c+a> dislocations can interact with <a> dislocations – immobile <c> dislocations may arise within the basal plane according to the following reaction:

$$\tfrac{1}{3}\left\langle 2\bar{1}\bar{1}3\right\rangle + \tfrac{1}{3}\left\langle \bar{2}110\right\rangle \rightarrow \left\langle 0001\right\rangle \ . \tag{31}$$

Another reaction that employs the basal <a> dislocations yields a sessile <c+a> dislocation

$$\tfrac{1}{3}\left\langle 2\bar{1}\bar{1}3\right\rangle + \tfrac{1}{3}\left\langle \bar{1}2\bar{1}0\right\rangle \rightarrow \tfrac{1}{3}\left\langle 11\bar{2}3\right\rangle \ . \tag{32}$$

Finally, a combination of two glissile <c+a> dislocations gives rise to a sessile dislocation of <a> type that lays along the intersection of the second order pyramidal planes according to the following reaction:

$$\tfrac{1}{3}\left\langle 2\bar{1}\bar{1}3\right\rangle + \tfrac{1}{3}\left\langle \bar{1}2\bar{1}\bar{3}\right\rangle \rightarrow \tfrac{1}{3}\left\langle 11\bar{2}0\right\rangle . \tag{33}$$

Different dislocation reactions may produce both sessile and glissile dislocations. Production of sessile dislocations increases the density of the forest dislocations that are obstacles for moving dislocations. Therefore, an increase in the flow stress with straining follows, which is observed in the experiment. On the other hand, screw components of <c+a> (and also <a>) dislocation may move to the parallel slip planes by double cross slip and they can annihilate – the dislocation density decreases, which leads to softening. One has to consider that twins and grain boundaries are also obstacles for moving dislocations in polycrystalline materials. Dislocation pile-ups are formed at the grain boundaries. The stress concentrations at the head of pile-ups contribute to initiations of the activity of the pyramidal slip systems. Another possible source mechanism for <c+a> dislocations was proposed by Yoo and co-workers (Yoo et al., 2001). The scenario described above can help in understanding the deformation behaviour of magnesium alloy over a wide temperature range. The increase in the elongation to failure with increasing temperature can be also explained by an increase in the activity of non-basal slip systems. At certain, sufficient, level of the flow stress, the non-basal slip becomes active. To describe the evolution of dislocations in both slip systems, it is necessary to take into account the storage and annihilation in both slip systems (basal and non-basal) and mutual interaction.

Very recently, it has been reported atomistic study of edge and screw <c+a> dislocations in magnesium (Nogaret et al. 2010). They concluded that at 300 K both screw and edge <c+a> dislocations may glide at stresses smaller than the experimentally observed.

6. Strain ageing

From the temperature dependence of the yield stress, introduced in Fig. 13 for AZ63 alloy, some local maximum between 50 and 100 °C is obvious. This maximum is a consequence of dynamic strain ageing. It is also manifested at the stress strain curve by the so called post relaxation effect. When the internal stress as well as the dislocation density are constant then the deformation process continues at the same stress as at the beginning of the SR test. On the stress - strain curve shown in Fig. 14, a stress increase after SR test is obvious. The flow stress after the stress relaxation, σ_1, is higher than the flow stress at the beginning of the relaxation. The values of $\Delta\sigma = \sigma_1 - \sigma_0$ are plotted against strain for two temperatures of 25 and 50 °C in Fig. 15. For other temperatures the post relaxation effect was not observed. From Fig. 15 it can be seen that the strain dependence of $\Delta\sigma$ has some maximum at a certain strain. Analogous maximum was found in the stress dependence of the stress increment. Similar results were found for alloys containing the rare earth in the temperature interval between 150 and 250 °C (Fig. 16) (Trojanová et al., 2005), while such effects may be observed in alloys of the AZ series slightly over room temperature (Trojanová et al., 2001).

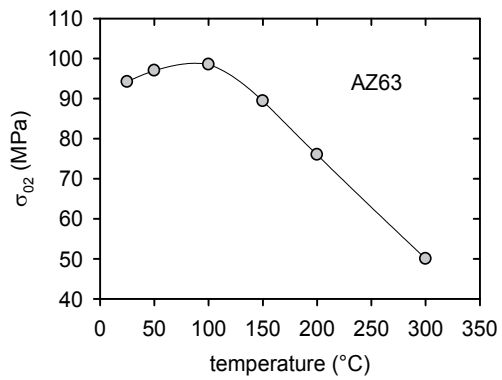

Fig. 13. Temperature dependence of the yield stress obtained for AZ63 alloy.

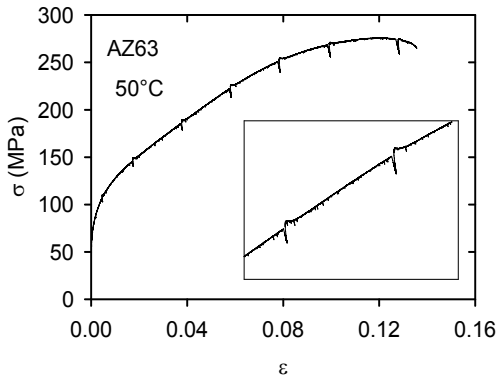

Fig. 14. The stress-strain curve obtained at 50 °C. An increase of the stress after the stress relaxation test is from the insert well visible (AZ63 alloy).

In an alloy the flow stress may be consider as a sum of two additive contributions:

$$\sigma = \sigma_f + \sigma_d \,, \tag{34}$$

with σ_f relating to a friction imposed by the solutes-dislocation interaction, σ_d relating to the dislocation–dislocation interaction. Hong (Hong, 1987, 1989) suggested that the stress σ_f could be described by the following equation:

$$\sigma_f = \alpha_1 G b \delta c \exp\left(-\frac{(T-T_0)^2}{B}\right), \tag{35}$$

where α_1 is a constant, δ is the atomic size misfit parameter, c is the solute concentration and B is the width of the distribution about the temperature T_0 where the maximum of solute-dislocation interaction force occurs. The critical dislocation velocity V_c at which the maximum force occurs can be expressed as:

$$V_c = \alpha_2 \frac{kT_0 D_0}{Gb\delta\Omega} \exp\left(-\frac{Q_D}{k_B T}\right), \tag{36}$$

where α_2 is a constant, D_0 is the diffusion constant for solute atoms, Ω is the atomic volume and Q_D is the activation energy for diffusion of solute atoms in magnesium matrix. The critical strain rate at which the maximum interaction stress occurs can be predicted using the following equation:

$$\dot{\varepsilon}_c = \rho_m b \frac{\pi(1-\nu)kT_0 D_0}{(1+\nu)Gb\delta\Omega} \exp\left(-\frac{Q_D}{k_B T}\right), \tag{37}$$

where ν is the Poisson ratio, ρ_m is the mobile dislocation density. From Eq. (35) it can be seen that the friction force due to solute atoms interaction with moving dislocations exists only in a certain temperature interval depending on solute atoms type. This friction force (stress) is added to the temperature dependence of the yield stress resulting to a local maximum in the temperature dependence of the yield stress. Such local maximum in the temperature dependence is demonstrated in Fig. 15 for AZ63 alloy and in Fig. 16 for the binary Mg-Nd alloy at 150 and 200 °C (Trojanová & Lukáč, 2010). Similar local maximum was observed in the case of ZE41 alloy (Trojanová & Lukáč, 2005), AZ91 alloy (Trojanová et al., 2001).

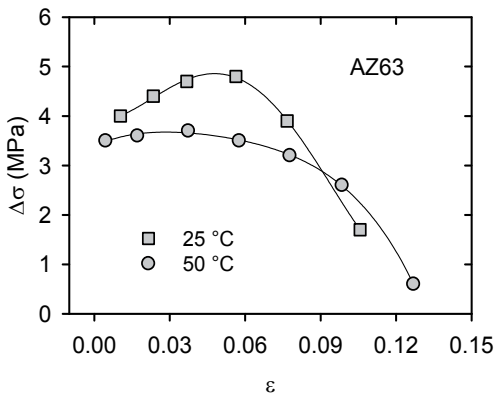

Fig. 15. The stress increase Δσ depending on the strain estimated for AZ63 alloy at 25 and 50 °C.

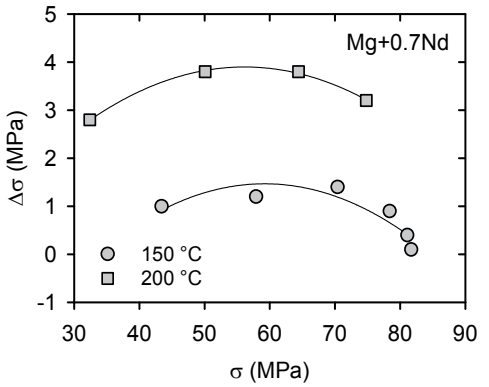

Fig. 16. The stress increase Δσ depending on the stress estimated for Mg-0.7%Nd at 150 and 200 °C.

According to Malygin (Malygin, 1986) and Rubiolo and Bozzano (Rubiolo & Bozzano, 1995) solute atoms diffuse to dislocations arrested at local obstacles for waiting time t_w. The concentration of solute atoms at dislocation lines as a function of the waiting time $c(t_w)$ is done by the following function

$$c = c_m \left[1 - \exp\left(-\frac{c_0}{c_m} \left(\alpha_n D t_w / b^2 \right) \right)^{2/(n+2)} \right], \tag{38}$$

where

$$\alpha_n = n(n+2)\pi^{(n+2)/2} \left(W_B / k_B T \right). \tag{39}$$

c_0 is the average concentration of impurities in the crystal and c_m is the limiting value of impurities on the dislocations. W_B is the binding energy of solute atoms to dislocations. The value of n depends on the details of interaction between solute atom and dislocations. The exponent in Eq. (38) p=2/(n + 2) is typically 2/3 and 1/3 for bulk and pipe diffusion, respectively (Balík & Lukáč, 1998). The stress increment $\Delta\sigma$ after SR due to solute atoms segregation may be also expressed for longer time by the following equation

$$\Delta\sigma(t,\varepsilon,T) = \Delta\sigma_m(\varepsilon,T) \{1 - \exp[-(t/t_c)^r]\}, \tag{40}$$

where $\Delta\sigma_m(\varepsilon,T)$ is the stress increment for $t \to \infty$ and it depends on the binding energy between solute atoms and dislocations. (It increases with increasing solute atom concentration and with decreasing temperature.) t_c is a characteristic time which depends on the strain as $t_c \sim \varepsilon^{-k}$. (Lubenets et al., 1986). Solute atoms locking dislocations cause the stress increase after stress relaxation, which depends on strain and on temperature. An increase in the flow stress is needed to move the dislocations after stress relaxation. It is reasonably to assume that $\Delta\sigma$ is proportional to the number of impurities on dislocation lines.

Concluding remarks

It should be noted that it is generally accepted that twinning plays an important role during plastic deformation of magnesium alloys. Twins influence also ductility in different way depending on the tensile/compression tests (Barnett, 2007a; 2007b). The effect of twins depends on the testing temperature and strain (Barnett at al., 2005). Serra and Bacon (Serra and Bacon, 2005) concluded that the motion of the twinning dislocations is thermally activated. The mobility of such dislocations increases with increasing temperature.

7. Acknowledgements

The authors dedicate this paper to Prof. RNDr. František Chmelík, CSc., on the occasion of his 50th birthday. This work received a support from the Ministry of Education, Youth and Sports of the Czech Republic by the project MSM 0021620834. This work was also supported by the Grant Agency of the Academy of Sciences of the Czech Republic under Grant IAA201120902.

8. References

Akthar, A. & Teghtsoonian, E. (1972). Substitutional solution hardening of magnesium single crystals. *Phil. Mag.*, *25*, 897-905, ISSN: 1478-6435.

Balík, J. & Lukáč, P. (1998). On the kinetics of dynamic strain ageing. *Kovove Mater.*, 36, 3-9, . ISSN: 0023-432X.

Balik, J.; Lukáč, P.; Drozd, Z. & Kužel, R. (2009). Strain hardening of AZ31 magnesium alloy. *Int. J. Mat. Res.*, 100, 322-325, ISSN: 1862-5282.

Barnett, M.R.; Davies, C.H.J. & Ma, X. (2005). An analytical constitutive law for twinning dominated flow in magnesium. Scripta Mater. 52, 627-632, ISSN: 1359-6462.

Barnett, M.R. (2007a). Twinning and the ductility of magnesium alloys. Part I: "Tension" twins. *Mater. Sci. Eng. A*, 464, 1-7, ISSN: 0921-5093.

Barnett, M.R. (2007b). Twinning and the ductility of magnesium alloys. Part II: "Contraction" twins. *Mater. Sci. Eng. A*, 464, 8-16, ISSN: 0921-5093.

Braasch, H.; Estrin, Y. & Brechet, Y. (1996). A stochastic model for dislocation density evolution. *Scripta Mater.*, 35, 279-284, ISSN: 1359-6462.

Cáceres, C.H. & Lukáč, P. (2008). Strain hardening behaviour and the Taylor factor of pure magnesium. *Phil. Mag.*, 88, 977-989, ISSN: 1478-6435.

Couret, A. & Caillard, D. (1985a). An *in situ* study of prismatic glide in magnesium – I. The rate controlling mechanism. *Acta metall.*, 33, 1447–1454, ISSN: 1359-6454.

Couret, A. & Caillard, D. (1985b). An *in situ* study of prismatic glide in magnesium – II. Microscopic activation parameters. *Acta metall.,* 33, 1455–1462, ISSN: 1359-6454.

Estrin, Y. & Mecking, H. (1984). A unified phenomenological decription of work hardening and creep based on one-parameter models. *Acta Metall.*, 32, 57-70, ISSN: 1359-6454.

Estrin, Y. & Kubin, L. (1986). Local strain hardening and nonuniformity of plastic deformation. *Acta Metall.*, 34, 2455-2464. ISSN: 1359-6454.

Estrin, Y. (1996). Dislocation-density-related constitutive modelling. In: *Unified constitutive laws of plastic deformation*. Krausz, A.S. & Krausz, K. (Eds.), 69-105, Academic Press, ISBN: 0-12-425970-7, New York.

Feltham, P. (1963). Stress relaxation in magnesium at low temperatures. *Phys. Stat. Sol.*, 3. 1340–1346, ISSN: 1862-6300.

Hong, S. I. (1987). Influence of dynamic strain aging on the creep ductility of solid solution alloys. *Mater. Sci. Eng.*, 91, 137-142, ISSN: 0921-5093.

Hong, S. I. (1989). Influence of dynamic strain aging on the transition of creep characteristics of a solid solution alloy at various temperatures. *Mater. Sci. Eng. A,* 110, 125-130, ISSN: 0921-5093.

Kapoor, R.; Wadekar, S.L. & Chakravartty, J.K. (2002). Deformation in Zr-1Nb-1Sn-0.1Fe using stress relaxation technique. *Mater. Sci. Eng. A,* 328, 324–333, ISSN: 0921-5093.

Kocks, U.F. (1976). Laws for work hardening and low-temperature creep. *J. Eng. Mater.Techn.*, 98, 76-85, ISSN (printed): 0094-4289. ISSN (electronic): 1528-8889.

Kocks, U.F.; Argon, A.S. & Ashby, M.F. (1975). Thermodynamics and kinetics of slip. *Progr. Mater. Sci.*, 19, 1–288, ISSN: 0079-6425.

Koike, J. & Ohyama, R. Mater., 53, 1963. Geometrical criterion for the activation of prismatic slip in AZ61 Mg alloy sheets deformed at room temperature. *Acta Mater.*, 53 (2005) 1963–1972, ISSN: 1359-6454.

Li, J.C.M, (1967). Dislocation dynamics in deformation and recovery *Canad. J. Appl. Phys.*, 45 493–509. ISSN : 0008-4204..

Li, J.C.M. (1981). On stress relaxation based on dislocation dynamics. *Scripta Metall.*, 15, 935-936, ISSN: 1359-6462.

Lubenets, S.V.; Startsev, V.I. & Fomenko, L.S. (1986). Strain aging kinetics in indium-based alloys. *Czech. J. Phys. B*, 36, 493-497, ISSN: 0011-4626.

Lukáč, P. (1981). Plastic deformation of hexagonal metals. *Czech. J. Phys. B*, 31, 135-141, ISSN: 0011-4626.

Lukáč P. (1985). Hardening and softening during plastic deformation of hexagonal metals. *Czech. J. Phys. B*, 35, 275-285, ISSN: 0011-4626.

Lukáč, P. & Balík, J. (1994). Kinetics of plastic deformation. *Key Engn. Mater.*, 97-98, 307-322, ISBN: 0-87849-687-4

Malygin, G.A. (1990). Dislocation density evolution equation and strain hardening of f.c.c. crystals. *Phys. Stat. Sol. (a)*. 119, 423-436, ISSN: 1862-6300.

Malygin, G.A. (1982). Impurity atmospheres and effective activation parameters of dislocation motion with special reference to Al-Mg and Zr-O alloys. *Phys. Stat. Sol. (a)*, 1982, 72, 493-501, ISSN: 1862-6300.

Máthis, K.; Trojanová, Z.; Lukáč, P.; Cáceres, C.H. & Lendvai, J. 2004a). Modeling of hardening and softening processes in Mg alloys. *J. Alloys Comp.*, 378, 176-179, ISSN**:** 0925-8388.

Máthis, K.; Nyilas, K.; Axt, A.; Dragomir-Cernatescu, I.; Ungár, T. & Lukáč, P. (2004b). The evolution of non-basal dislocations as a function of deformation temperature in pure magnesium determined by X-ray diffraction. *Acta Mater.*, 52, 2889–2894, ISSN: 1359-6454.

Máthis, K. & Trojanová, Z. (2005). Application of Lukáč-Balík model for characterization of work hardening behaviour of Mg-Zn and Mg-Al alloys. *Kovové Mater.* 43, 238-244, ISSN: 0023-432X.

Milička, K.; Trojanová, Z. & Lukáč, P. (2007). Internal stresses during creep of magnesium alloys at 523 K. *Mater. Sci. Eng. A*, 462, 215–219, ISSN: 0921-5093.

Nes, E. & Marthinsen, K. (2002). Modeling the evolution in microstructure and properties during plastic deformation of fcc-metals and alloys –an approach towards a unified model. *Mater. Sci. Eng. A*, 322, 176-193, ISSN: 0921-5093.

Nogaret, T.;Curtin, W.A.;Yasi, J.A.; Hector Jr, L.G. & Trinkle, D.R. (2010). Atomistic study of edge and screw <c+a> dislocations in magnesium. *Acta Mater.*, 58, 4332-4343, ISSN: 1359-6454.

Ono, K. (1968). Temperature dependence of dispersed barrier hardening. *J. Appl. Phys.*, 39, 1803–1806, ISSN: 0021-8979.

Rubiolo, G.H. & Bozzano, P.B (1995). Dynamic interaction of impurity atmospheres with moving dislocations during stress relaxation. *Mater. Trans. JIM*, 36, 1124-1133, ISSN: 1345-9678.

Serra, A. & Bacon, D.J. (2005). Modelling the motion of $\{11\bar{2}2\}$ twinning dislocations in the hcp metals. *Mater. Sci. Eng. A*, 400-401, 496-498, ISSN: 0921-5093.

Trojanová, Z.; Lukáč, P.; Gabor, P.; Drozd, Z. & Máthis, K. (2001). Stress relaxation in an AZ91 magnesium alloy. *Kovove Mater.*, 39, 368-378, ISSN: 0023-432X.

Trojanová, Z.; Lukáč, P.; Kainer, K.U. & Gärtnerová, V. (2005). Dynamic strain ageing in selected magnesium alloys containing rare earth elements. *Adv. Engn. Mater.*, 7, 1027-1032, ISSN: 1438-1656.

Trojanová, Z. & Lukáč, P. (2005). Compressive deformation of ZE41 magnesium alloy between 23 and 300 ^{o}C. *Kovove Mater.*, 43, 73-80, ISSN: 0023-432X.

Trojanová. Z. & Lukáč, P. (2010). Mobility of solute atoms in a Mg-Nd alloy studies by nondestructive and destructive methods. In: *Magnesium Alloys and their Applications 8*, Kainer, K.U. (Ed), 785-802, Willey-VCH, ISBN: 978-3-527-32732-4, Weinheim.

Yoo, M.H.; Agnew, S.R.; Morris, J.R. & Ho, K. (2001). Non-basal slip systems in hcp metals and alloys: source mechanisms. *Mater. Sci. Eng.* A, 321, p. 87-92. ISSN: 0921-5093.

2

Deformation Structures and Recrystallization in Magnesium Alloys

Étienne Martin[1], Raj K. Mishra[2] and John J. Jonas[1]
[1]McGill University, Montreal, QC, H3A 2B2,
[2]General Motors Research and Development Center, Warren, MI, 48090,
[1]Canada
[2]USA

1. Introduction

Magnesium, being a hexagonal close-packed metal, has limited ductility and poor formability at room temperature. These characteristics hinder the production of magnesium wrought products, which represent a mere 1% of the total annual magnesium usage (Polmear, 1995). Formability can be significantly increased when additional slip systems are thermally activated. As such, hot deformation is extensively used to produce wrought magnesium products such as sheet metal or extruded bars and tubes (Barnett, 2001). Besides ductility limitations, Mg alloys also suffer from strong mechanical anisotropy (Kleiner & Uggowitzer, 2004). Depending on the crystallographic texture, different combinations of deformation systems may be activated. Since the deformation modes available for displacements parallel to the c-axis are limited, the crystallographic orientation has a strong influence on the deformation of Mg.

In many metals, dynamic recrystallization leads to the randomization of initial textures and can therefore be of practical interest with regards to subsequent forming (Humphreys & Hatherly, 2004). According to the literature, recrystallization is not usually accompanied by sharp changes in the crystallographic texture. Yi et al. (Yi et al., 2006) have reported, for example, that the ODF (orientation distribution function) intensities in AZ31 were similar in the large deformed and small dynamically recrystallized (DRX) grains. (Nevertheless, they did observe a slight shift in the location of the main texture component.) Other investigators have reported that most of the newly recrystallised grains in Mg alloys have orientations similar to those of the matrix grains, but with slightly weaker intensities (Backx et al., 2004; del Valle et al., 2005; Jäger et al., 2006). Such recrystallization appears to promote 30^{o} <0001> rotations that preserve the basal texture or, at the very least, delay its decomposition (Gottstein & Al Samman, 2005; Beausir et al., 2007). However, these investigations were mostly performed on highly deformed samples, so that it is difficult to separate the influence of the different recrystallization and deformation mechanisms on the texture.

In magnesium, basal glide invariably leads to a basal texture (i.e. c-axis aligned with the compression axis (CA)) or perpendicular to the tensile axis (TA)). However, different twinning and slip systems can also be activated under different deformation conditions (i.e. temperature, strain rate, texture, etc.). It is well known that the deformed state has a strong influence on recrystallization, and several studies have linked the different deformation

structures found in magnesium to the recrystallization behavior (Ion et al., 1982; Galiyev et al., 2001; Myshlyaev et al., 2002). However, few have mentioned its effects on the texture, and most studies to date have focused on relatively small orientation scan areas. Thus, while these studies provide some insight, it should be noted that the number of grains and grain boundaries sampled are not statistically reliable. While presenting a more statistically relevant picture of these phenomena, this chapter aims to characterize the orientation aspects of deformation structures and to follow their evolution during recrystallization.

2. Misorientations and Rodrigues-Frank space

It is essential to note that slip and twinning take place by simple shear and not pure shear: they correspond to a displacement in the shear direction on one side of the shear plane (Kocks et al., 1998). Since the occurrence of simple shear induces rotations, it is appropriate to characterize the deformation structures in terms of the misorientations that are produced with respect to their neighborhoods. There are different ways of representing a misorientation between two given crystallographic orientations (Mason & Schuh, 2008). The angle and axis pair (ω, d) is a convenient method as it involves readily recognizable geometric quantities and enables the physical effect of the rotation to be visualized in a straightforward manner. For this purpose, the orientation matrices identifying crystallites A and B in the specimen coordinate system are labeled $\mathbf{g_A}$ and $\mathbf{g_B}$, respectively. Here, $\mathbf{g}$ defines a rotation that brings the laboratory coordinate system into coincidence with that of a crystallite. Then, the misorientation matrix M_{AB} relating two crystallites, where crystallite A is arbitrarily chosen to be the reference system, is given by (Engler & Randle, 2010):

$$M_{AB}=g_B g_A^{-1}. \tag{1}$$

This matrix defines a rotation that converts the coordinate system of the reference crystallite into that of the other crystallite. The angle-axis pair associated with M_{AB} is then defined as

$$\omega = \arccos\left(\frac{1}{2}[\mathrm{trace}(M_{AB})-1]\right) \tag{2}$$

$$[d_1,d_2,d_3] =[m_{23}-m_{32},\ m_{31}-m_{13},\ m_{12}-m_{21}] \tag{3}$$

Here $\boldsymbol{\omega}$ is the misorientation angle between crystallites A and B, d_i (i=1,2,3) are the axial components of the rotation axis d, and m_{ij} (i,j=1,2,3) are the elements of M_{AB}. Note that the minimum angle-axis pair representation is used here; it is obtained by taking the crystal symmetry into account (Engler & Randle, 2010).

The angle-axis pair can be represented in three dimensions by combining the unit vector $\mathbf{d}$ and the rotation angle $\boldsymbol{\omega}$ using the Rodrigues formula (Frank, 1988) given by:

$$R =\tan\frac{\omega}{2}[d_1,\ d_2,\ d_3] \tag{4}$$

Each misorientation can then be described by the three components (R_1,R_2,R_3) of the Rodrigues-Frank vector. When the minimum angle-axis pair representation is employed, Rodrigues-Frank space is reduced to a finite subspace called the fundamental zone, which can be further reduced by considering only 1/24 of this space (Heinz & Neumann, 1991) in the case of hexagonal materials.

3. Initial material

The present work is based on investigations that were carried out on extruded tubes of magnesium alloys AM30 and AZ31 (Martin et al., 2009; Martin et al., 2010; Martin & Jonas, 2010). The tubes from which the samples were made were extruded using porthole dies. The chemical compositions of the two materials are presented in Table 1. The most significant difference between the two alloys is their zinc (Zn) content: the amount of Zn in AM30 is considerably lower than in AZ31.

	Al	Zn	Mn	Fe	Ni	Cu
AZ31	3.1	1.05	0.54	0.0035	0.007	0.008
AM30	3.4	0.16	0.33	0.0026	0.006	0.008

Table 1. Chemical compositions of the AZ31 and AM30 alloy samples (in wt. %).

The initial grain orientations of the as-received tubes consist of two main components: one with its *c*-axis approximately parallel to the radial direction (called the RD or $\{10\bar{1}0\}<1\bar{2}10>$ component) and the other with its *c*-axis approximately parallel to the tangential direction (called the TD or $\{1\bar{2}10\}<0001>$). The above planes are normal to the extrusion direction (ED) and the directions parallel to TD.

The macrotextures of the as-received tubes are shown in Fig. 1. in the form of inverse pole figures. The volume fractions of the two components were similar in the AM30 (48 % for the TD and 39 % for the RD), while the AZ31 had a stronger TD component (65 %) compared to the RD (15 %) (Jiang et al., 2007). A fibre texture links the two components by continuous rotations around $\boldsymbol{\Phi}$ of ± 90° and $\boldsymbol{\varphi_2}$ of ± 30° starting from the TD orientation (0,0,30) and ending at the RD orientation (0,90,0) (following the Bunge notation (Bunge, 1982)).

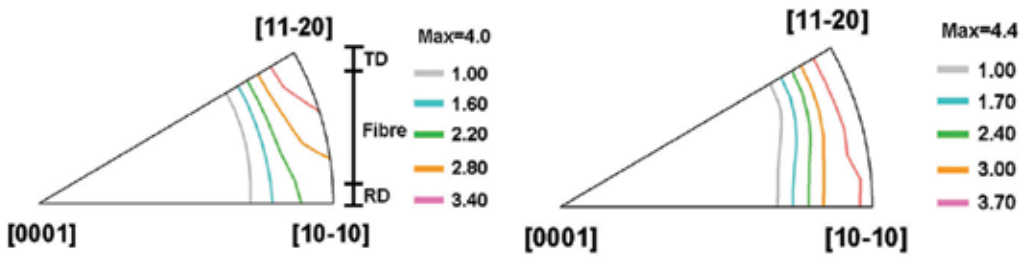

(a) (b)

Fig. 1. Inverse pole figures that display the orientation of the extrusion direction in the hexagonal crystal reference frame of the (a) AZ31 and (b) AM30.

4. Recrystallization of twins

Above the critical value of the Zener–Hollomon parameter for the activation of twinning (~ 7×10^{12} s^{-1}), the deformation of magnesium takes place by both slip and twinning (Barnett, 2003). Two types of twins are frequently reported: i.e. the $\{10\bar{1}2\}$-$<\bar{1}011>$ extension and $\{10\bar{1}1\}$-$<10\bar{1}\bar{2}>$ contraction twins. When elongation along the c-axis is accommodated by the formation of extension twins, the basal planes are reoriented by 86° around a $<1\bar{2}10>$ axis. Such boundaries are very mobile and the extension twins readily

thicken rather than generating further strain localizations (Jiang et al., 2007). Therefore, such twins are not very effective sites for the initiation of recrystallization. Extension twins are essentially activated in the early stages of deformation (when the texture is unstable[1]). As such, they do not have much influence on the final texture during thermomechanical processing, although they accelerate the formation of the deformation (stable) end texture (Godet et al., 2006; Yi et al., 2009b).

By contrast, when contraction along the c-axis is accommodated by the formation of contraction twins, the basal planes are reoriented by 56° around a $< 1\bar{2}10 >$ axis. This change facilitates glide on the basal planes and generates zones of flow localization (Jiang et al., 2006). Because of the polarity of this mechanism, these twins can be activated in grains that have stable orientations. In this way, their formation can modify the previous deformation texture. Moreover, these twins do not thicken significantly, but rather undergo extension twinning in their interiors, also referred to as double twinning (Barnett, 2007). Because of these characteristics, contraction twins can serve as effective sites for recrystallization. In this context, this section will concentrate on the occurrence of recrystallization at contraction and double twins.

In the work described below, the recrystallization of twins was investigated on magnesium samples deformed in tension along the ED. Because the tensile stress was applied along the $< 1\bar{2}10 >$ and $< 01\bar{1}0 >$ directions in the TD and RD components, respectively, or in other words, perpendicular to the c -axis, a deviator stress was induced along the c -axis that is compressive. As a result, the twins induced were of the *contraction* type and also contained double (secondary or extension) twins. In order to maximize the amount of twins generated, the samples were deformed at ambient temperature and a true strain rate of 0.1 s^{-1}. The samples were pulled to true strains 0.15, which is the maximum strain that can be achieved under these conditions. Finally, the twinned samples were annealed at 300 °C for 30 and 60 minutes. The electron backscatter diffraction technique (EBSD) was employed to follow the orientation changes that took place as the recrystallized grains formed within the twins.

4.1 Contraction and double twinning

There are 12 symmetry operations associated with hcp crystals; these lead to the existence of six equivalent contraction and six equivalent extension twin variants. In the case of double twinning, each primary (contraction) twin is associated with six different secondary (extension) twins; these are identified in Table 2. Note that the misorientation relationship associated with each double twin variant in Table 2 is expressed with respect to the *matrix* orientation. The misorientations are therefore not the ones conventionally associated with single extension twins ($< 11\bar{2}0 > 86°$). The current representation reveals that the ensemble of secondary twin variants can be divided into four groups (S^A, S^B, S^C and S^D); here variants C1 and C2 as well as D1 and D2 are subgroups of groups S^C and S^D, respectively. The members of each group are defined by rotations that are geometrically equivalent. Given that there are six different primary twin variants, the S^A and S^B groups each contain 6 variants while the S^C and S^D each contain 12.

[1] Texture stability is defined here with respect to basal glide and the imposed strain path. A crystallographic orientation is stable when the c-axis is aligned with the compression direction or is perpendicular to the tensile axis.

Double twin symmetry group	Double twin symmetry subgroup	Minimum angle-axis pair	Symmetry elements
A	N/A	$<1\bar{2}10>$ (37.5°)	6
B	N/A	$<1\bar{2}10>$ (30.1°)	6
C	C1	$<7\bar{3}\bar{4}2>$ (66.5°)	6
	C2	$<\bar{4}\bar{3}7\bar{2}>$ (66.5°)	6
D	D1	$<14\bar{7}\bar{7}3>$ (69.9°)	6
	D2	$<\bar{7}\bar{7}14\bar{3}>$ (69.9°)	6

Table 2. The four $\{10\bar{1}1\}$-$\{10\bar{1}2\}$ double twin variant groups.

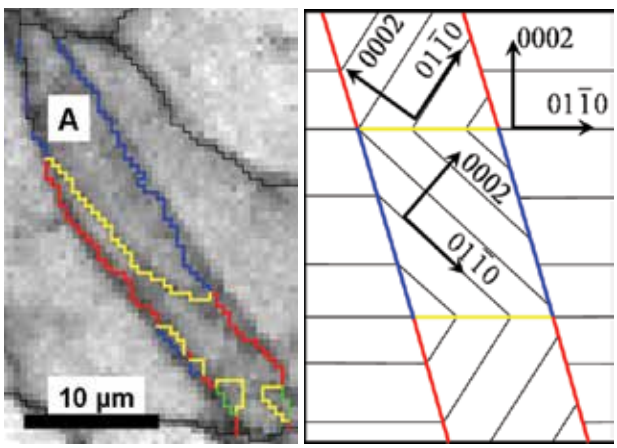

(a) (b)

Fig. 2. (a) EBSD map showing an S^A and an S^D secondary twin variants formed within a contraction twin, and (b) a schematic representation of an S^A secondary twin variant and the change of basal plane orientation. The $\{10\bar{1}1\}$ contraction twin boundaries are shown in red (56° $<1\bar{2}10>$ +/-5°), $\{10\bar{1}2\}$ extension in yellow (86° $<1\bar{2}10>$ +/-5°), the double twin boundaries associated with variant A (38° $<1\bar{2}10>$ +/-4°) in blue, and variant D (69.9° $<14\bar{7}\bar{7}3>$ +/-4°) in green. The tensile axis is vertical on this figure.

An example of secondary twins propagating within a contraction twin is displayed in Fig. 2 (a). The upper part of the primary twin has transformed into an S^A double twin while an S^D double twin has nucleated in the lower part. Since these secondary twins are *extension* twins, each double twin variant is delineated from the primary twin by an extension twin boundary (86° around $<1\bar{2}10>$). However, the boundaries that delineate the matrix and the double twin are the net result of two successive rotations and thus depend on the particular combination of the contraction and extension twin variants that is activated. The reorientation of the basal plane associated with the formation of an S^A double twin variant is illustrated in Fig. 2 (b)). The more favourable alignment of the basal slip plane (compared to the parent grain orientation) is shown, as well as the development of the secondary (extension) twin in the primary (contraction) twin interior.

4.2 Variant selection during primary and secondary twinning

A basal pole figure representation of the 6 primary twin and 36 double twin orientations that can form in a [0,0,0][2] orientated grain (in terms of Euler angles) is presented in Fig. 3. Each group of variants (S^A, S^B, S^C and S^D) is illustrated with a different symbol and a color code links each set of six secondary twin variants to its respective primary twin. The pole figure representation reveals the considerable potential for texture randomization as a single orientation may split into as many as 42 new orientations. Note that the S^A and S^B variants *decrease* the misorientation angle with respect to the matrix compared to that associated with the contraction twins. By contrast, the misorientations are *increased* when the S^C and S^D variants are activated.

The description of the variant selection associated with primary and secondary twinning is a laborious task: each grain is associated with 42 variants and each sample includes hundreds of grains. The characterization of these twins is however simplified when the *misorientations* rather than the orientations are considered. The rotation that links each twin (primary or secondary) to the parent orientation was thus measured from the EBSD scans performed on the deformed samples. The misorientations were obtained by considering the mean matrix grain and mean twin orientations. Each rotation was then applied to a perfect [0,0,0] orientation. The new orientations obtained correspond to the positions of the twins when the parent grain host is taken as the origin of the pole figure. In this way, the character of the variant selection is immediately evident when these orientations are superimposed on the ideal twin orientations in Fig. 3.

It can be seen that only four of the six possible primary twins are activated under the present strain path conditions. Such selection is associated with differences in the Schmid factors (SF's) of the variants: those selected were formed on the four systems with the highest SF's (Martin et al., 2010). Numerous secondary twins are clustered close to the four S^A and S^D locations associated with the four observed primary variants. Further selection occurs within the S^D group of variants since only four variants were detected (out of a possible eight associated with the four observed primary twin variants). By contrast, the S^B and S^C variants are almost never observed. The few twins situated close to these variants probably resulted from additional deformation-induced lattice rotations occurring within the S^A and S^D variants (Martin et al., 2010). The secondary twinning that took place was thus limited to the formation of only two of the four geometric configurations. The double twins only developed matrix misorientations of 37.5° or 69.9°. Since only four primary twins were activated, the 42 possible twin orientations were reduced to 12. Such variant selection is a major limitation to randomization of the crystallographic texture.

4.3 Recrystallization of contraction and double twins

Annealing of the twinned samples at 300 °C led to recrystallization of the twins. An example of an initial grain containing both recrystallized and unrecrystallized twins is displayed in Fig. 4. Here the local misorientation is specified by the colour as defined by the kernel average misorientation (KAM) approach. At a given point in the EBSD scan, the average misorientation of the point with respect to its immediate neighbors is calculated. The local misorientation is linked to the local lattice curvature; both these quantities are closely

[2] The reference frame is chosen so that the $< 10\bar{1}0 >$, $< \bar{1}2\bar{1}0 >$ and <0002> directions correspond to the x, y and z axes.

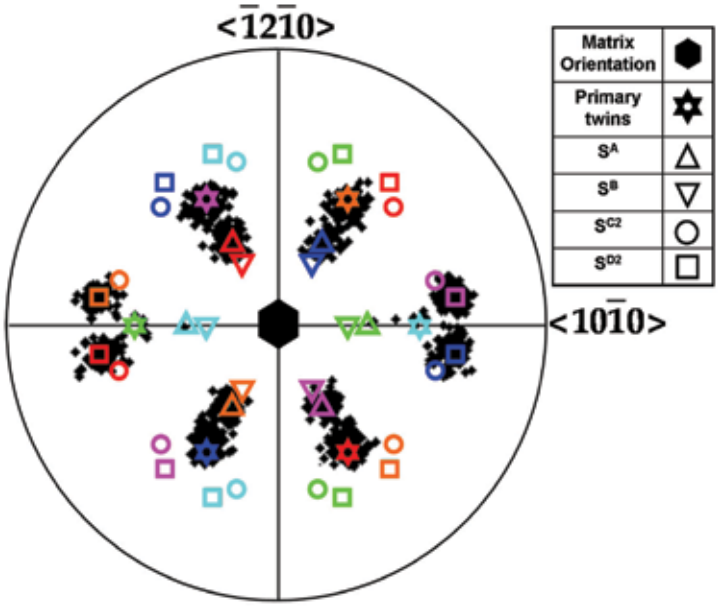

Fig. 3. {0002} pole figure of the measured primary and secondary twins (black dots) present in samples of AM30 and AZ31 deformed to 0.15 strain. The orientations were obtained by applying the rotation associated with each twin to a [0,0,0] orientation (black hexagon in the centre of the pole figure). The ideal (predicted) orientations of the six primary (colored stars) and 36 secondary twins are also displayed. The color code relates the secondary twin variants (circles, squares and triangles) to their respective primary twin variants (stars).

related to the stored energy and dislocation density. The twins have higher KAM values than the matrix grains. This is because the twins are narrow and more favorably oriented for basal slip, so that dislocation pile-up occurs more readily. Some unindexed twin networks are even revealed by their high KAM values (see the red arrows in Fig. 4). The driving forces for nucleation and growth are thus limited essentially to the neighborhoods of the twins. Indeed, the shapes of the new grains (identified with black arrows) follow those of their parent twins, so that the original coarse grains were not consumed by the recrystallizing grains even after 60 minutes of annealing. They were instead subdivided by the lamellae of the elongated new grains visible in Fig. 4. The widths of the recrystallized lamellae varied within the annealed samples. This is due to the uneven distribution of twins in the deformed samples. When twins are closely spaced, nucleus growth can occur within a larger region of stored energy leading to larger new grains (Martin et al., 2009).

The formation of a *secondary* twin produces strain incompatibilities within the parent grain (Martin et al., 2010). Such regions of strain concentration are preferred sites for nucleation. Moreover, the secondary twins and their matrix grains are not separated by special (CSL) boundaries, while the contraction twin boundaries have stable configurations and are generally considered to be immobile (Li et al., 2009). The double twin boundaries are thus more mobile and nucleation is initiated more readily in their vicinity. This interpretation is supported by Fig. 5, which shows that ~70% of the secondary twin boundaries have already lost their character after 30 minutes of annealing at 300 °C; by contrast, the contraction twins only *begin* to vanish after 30 minutes.

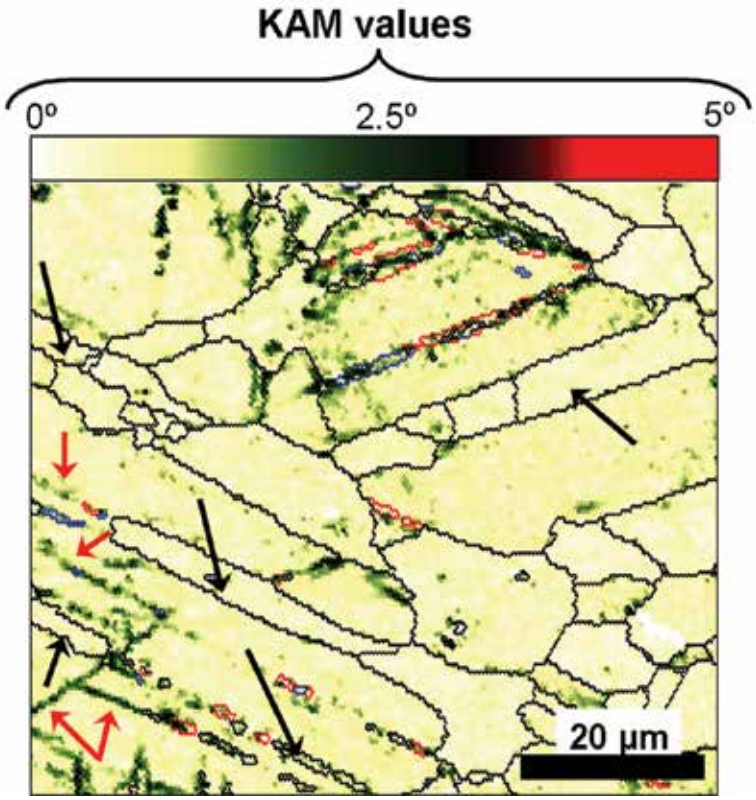

Fig. 4. EBSD map of a twinned sample annealed for 30 minutes at 300 ºC. KAM coloring is used as the background while the different types of twins are highlighted using the color scheme of Fig. 2 (a).

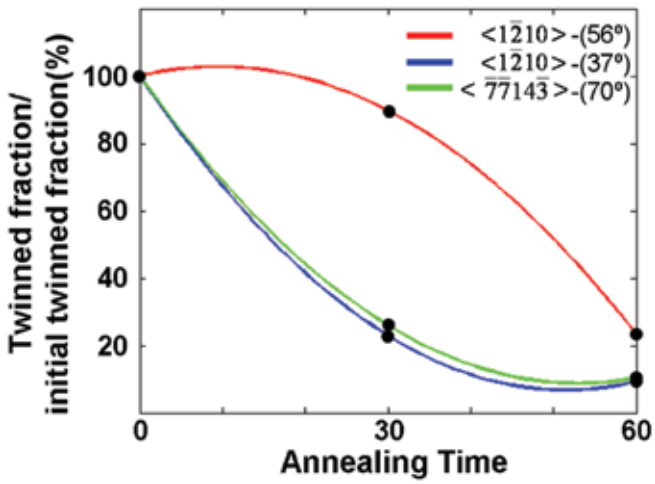

Fig. 5. Evolution of the twin boundary fractions in the magnesium AZ31 during annealing at 300 ºC.

4.4 Crystallographic orientations associated with annealing twins

From the above discussion, it can be concluded that annealing twinned samples cannot lead to significant texture changes since the un-twinned matrix grains are not consumed by growth of the twin-based nuclei. Indeed, the macrotextures of as-deformed samples and annealed ones display similar intensities, see Fig. 6. In special cases, nucleation can occur at the intersection of two S^A double twins when they share a common rotation axis (the blue and orange variants in Fig. 3, for example). Even though these nuclei grew during subsequent annealing, their new orientations are related to those of their parent grains by rotations about an axis close to the <0001> (Yi et al., 2009a). Because of this, they contribute to the persistence of the basal texture. Nevertheless, a slight shift of the major texture component is observed when the deformation texture is compared to the annealing texture, see Fig. 6. The intensity of the TD component is decreased by annealing, while that of the RD component is strengthened after 60 minutes of annealing.

The orientation changes associated with twin recrystallization are illustrated in Fig. 7. As in Fig. 3, the rotations that link recrystallized grains to their adjoining matrix grains were deduced from the EBSD data in the AZ31 and AM30. The rotations were then applied to a perfect [0,0,0] orientation (centre of the pole figure). Thus, the centre of the pole figure represents the matrix grain for each recrystallized grain. The 4 primary twin variants observed in the deformation microstructure prior to annealing (see Fig. 3) as well as the 8 (4 S^A and 4 S^D) secondary variants are superimposed here. They illustrate the 12 possible orientations within which the recrystallized grains are able to nucleate. The evolution of the recrystallized twin orientations from the as-received to the annealing material can thus be followed in Fig. 7.

Even though most of the twin boundaries lose their character during annealing, the new grains in Fig. 7 can still be associated in an approximate way with their respective parent twins. The recrystallized grains are, for the most part, restricted to two regions. In the first, recrystallization of the four S^D twin variants induces a spread around these orientations. This event corresponds exactly to the modification of the RD component observed in Fig. 6. The second group of new grains originated from the four S^A twin variants; their c-axes are rotated *towards* the matrix orientation (the centre of the pole figure in Fig. 7). The rotation axes associated with these grains are inclined with respect to the c-axis by about 30° to 60° (Martin et al., 2009). Thus, they do not correspond to the above description of nucleation at S^A double twin intersections.

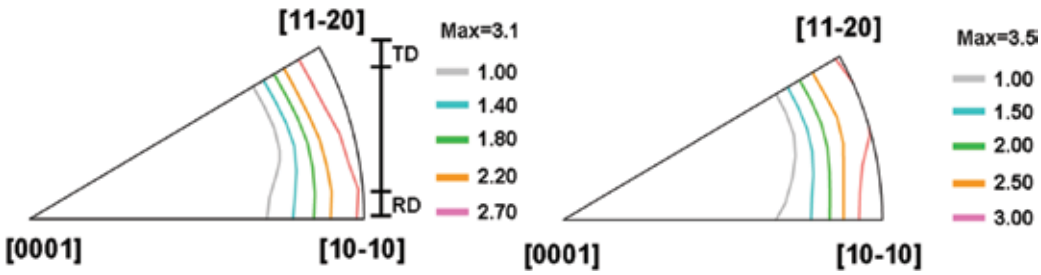

(a) (b)

Fig. 6. Inverse pole figures displaying the orientations of the extrusion direction (ED) in the hexagonal crystal reference frame of the AZ31 (a) after 15% tensile strain and (b) after 1 hour annealing at 300 °C.

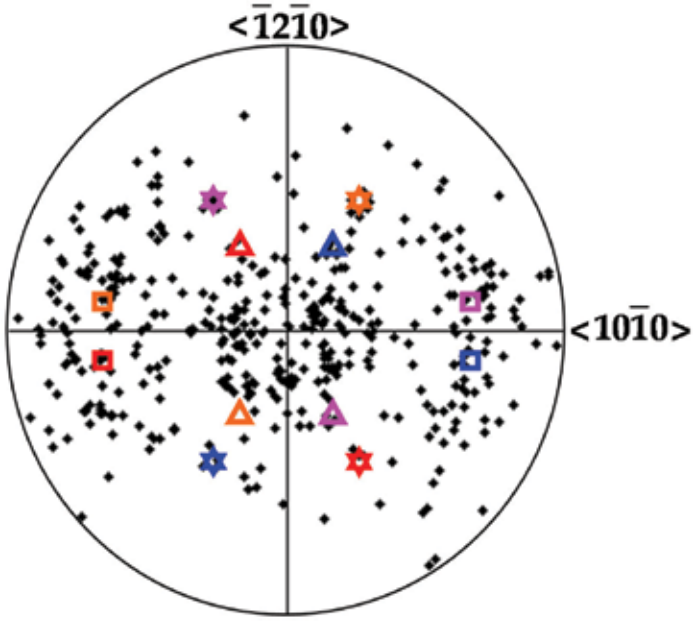

Fig. 7. Basal pole figure displaying the recrystallized grains (black dots) present in AM30 and AZ31 samples deformed to 0.15 strain and annealed for 1 hour. These orientations were deduced by employing the rotation associated with each grain with respect to the [0,0,0] orientation (center of the pole figure). The ideal (predicted) orientations of selected primary (six-pointed stars) and secondary (squares and triangles) twin variants are also plotted using the nomenclature of Fig. 3.

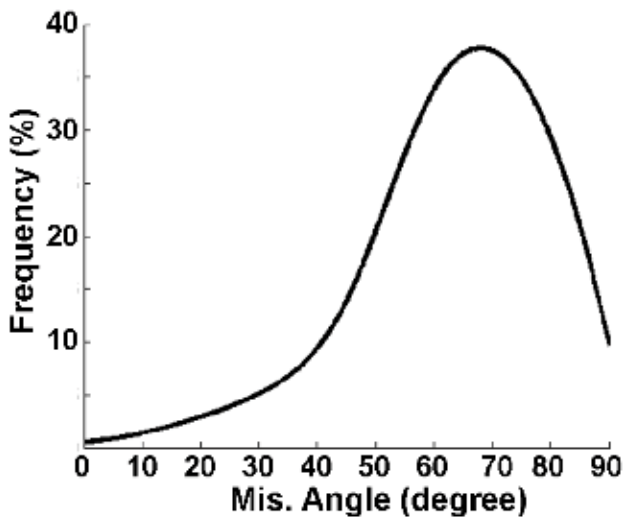

Fig. 8. Distribution of the misorientation angles between recrystallized grains and their primary twin hosts.

The misorientation distribution associated with the new grains (with respect to their primary twin hosts) is illustrated in Fig. 8. These misorientations were measured in partially recrystallized twins in the samples that were annealed for 30 minutes. The high intensity peak at ~70^{o} reveals that the orientations of the recrystallized grains are closer to those of the secondary, rather than of the primary, twins. Because the secondary twins are of the extension type, they always have misorientation angles of 86^{o} with respect to their primary twin hosts. There are few grains with orientations similar to the primary twin variants (four-pointed stars in Fig. 7); they have misorientations close to 0^{o} in Fig. 8. This is because the nucleation rate is much higher in the vicinity of the double twins while growth is facilitated within the primary twins. As a result, contraction twins are more likely to vanish during growth of the double twin nuclei rather than to provide recrystallization nuclei.

5. Continuous and discontinuous recrystallization

As the Zener-Hollomon parameter of the deformation is decreased, the ease of cross-slip increases, (Couret & Caillard, 1985) and the accumulation and rearrangement of dislocations leads to the formation of numerous low-angle boundaries (LABs). Subsequent continuous rotation of the new substructures results in a progressive increase in misorientation and in the gradual appearance of more and more high angle boundaries (HABs) (Ion et al., 1982; Galiyev et al., 2001; Tan & Tan, 2003). This process is generally referred to as continuous dynamic recrystallization (cDRX) or extended recovery. Moreover, when the activation energy of plastic flow approaches that for volume self-diffusion (~135 kJ mol^{-1} in Mg (Frost & Ashby, 1982)), the controlling deformation mechanism becomes the climb of basal dislocations (Galiyev et al., 2001; Barnett, 2003). DRX nucleation by the bulging of initial grain boundaries (also referred to as discontinuous dynamic recrystallization (dDRX)) is also frequently reported under such deformation conditions (Sitdikov & Kaibyshev, 2001; Guo et al., 2005; Martin et al., 2008).

The cDRX and dDRX mechanisms were investigated in the present magnesium alloys on samples deformed at a high temperature (350 ^{o}C) and a low strain rate (0.001 s^{-1}) in order to promote the occurrence of recovery and diffusion. The specimens were compressed rather than pulled in tension to facilitate the cooling of the samples and to preserve the deformation microstructure. Because the compressive stress was applied along the ED (i.e. the $<1\bar{2}10>$ and $<01\bar{1}0>$ directions in the TD and RD components, respectively), extensive deviator tensile stresses were induced along the c -axes. Under such conditions, extension twinning would normally be favored. However, as straining was carried out below the critical value of the Zener–Hollomon parameter for the activation of twinning (~ 7 × 10^{12} s^{-1}), i.e. at stresses below that required to activate twinning, the deformation was essentially accommodated by slip.

5.1 Microbands and kink bands

In the early stages of high temperature deformation, magnesium grains are fragmented by geometrically necessary boundaries (GNBs). These boundaries separate microbands (MBs) of material with distinctly different orientations. Examples of the MBs and GNBs present in magnesium alloy AM30 deformed to a true strain of 0.05 at 350 ^{o}C are displayed in Fig. 9(a). The boundaries are essentially straight, are oriented perpendicular to the compression axis, and traverse into the grain interior.

Such boundaries are also referred to as kink boundaries (Yang et al., 2009) as they are occasionally present in closely spaced, parallel pairs. In such cases, there is a double change

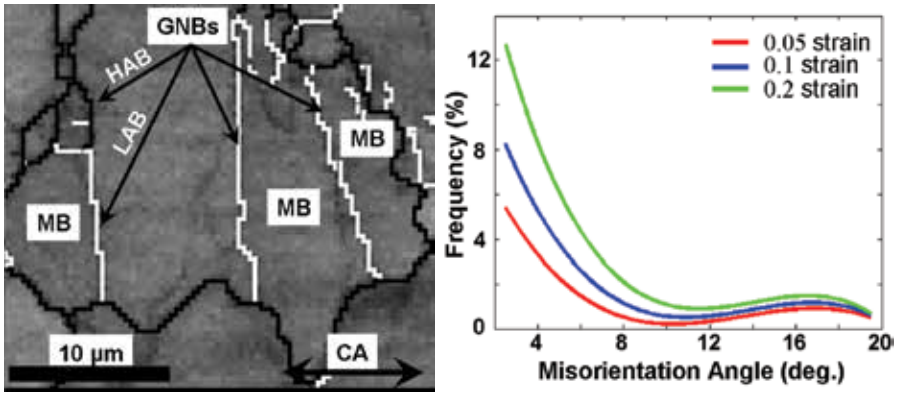

(a) (b)

Fig. 9. (a) EBSD map illustrating the geometrically necessary boundaries (highlighted by the black arrows) that delineate microbands. The low-angle boundaries ($5^o<\omega<15^o$) are shown in white and the high-angle boundaries ($\omega \geq 15^o$) in black. (b) Misorientation frequencies of the boundaries developed during the hot compression of magnesium AM30.

of orientation, which is generally self-compensating. Nevertheless, the rotation characteristics associated with the individual boundaries pertaining to these two types of bands are similar, so that the above discussion applies to kink bands (KBs) as well as MB boundaries.

The formation of MBs and KBs is attributed to the mechanism of dynamic recovery. Indeed, their concentration increases rapidly with strain, as shown indirectly in Fig. 9(b). The misorientations of the GNBs and kink boundaries increase progressively with strain. However, the rate of increase is significantly lower when the boundaries take on misorientation angles above 8^o.

The formation of MBs and KBs is depicted schematically in Fig. 10. In the present work, the planes of these bands (GNBs and kink boundaries) were essentially perpendicular to the compression axis; thus they are not crystallographic. Even though the prismatic and <c+a> slip systems are more favorably oriented for glide under the loading conditions of Fig. 10, MBs and KBs are nevertheless formed by the accumulation and rearrangement of *basal* dislocations (Martin & Jonas, 2010). Even a small inclination of the basal plane with respect to the compression axis is enough to promote basal glide because of the very low CRSS for this type of slip. In the experiments carried out to strains of 0.05 described here, the grains that contained MBs had higher Schmid factors for basal slip (SF =0.15) than the grains in which these bands were absent (SF =0.07). Moreover, according to Frank's formula (Hirth & Lothe, 1968), the polygonization of basal edge dislocations leads to rotation axes that lie in the basal plane and are thus perpendicular to the compression axis. In this way, the c-axes are gradually rotated towards the compression axis, moving the basal slip systems away from the hard slip towards the softer slip directions (Martin & Jonas, 2010).

5.2 Continuous dynamic recrystallization

During the hot deformation of magnesium, substructures ($\omega < 15^o$) gradually form in the grain interiors. The misorientation and number of such boundaries increase rapidly with strain, resulting in the in-situ evolution of new grains. The progressive increase in the boundary misorientation during deformation has been frequently reported in the literature and is referred to as continuous DRX (Kaibyshev & Sitdikov, 1996; Yang et al., 2003).

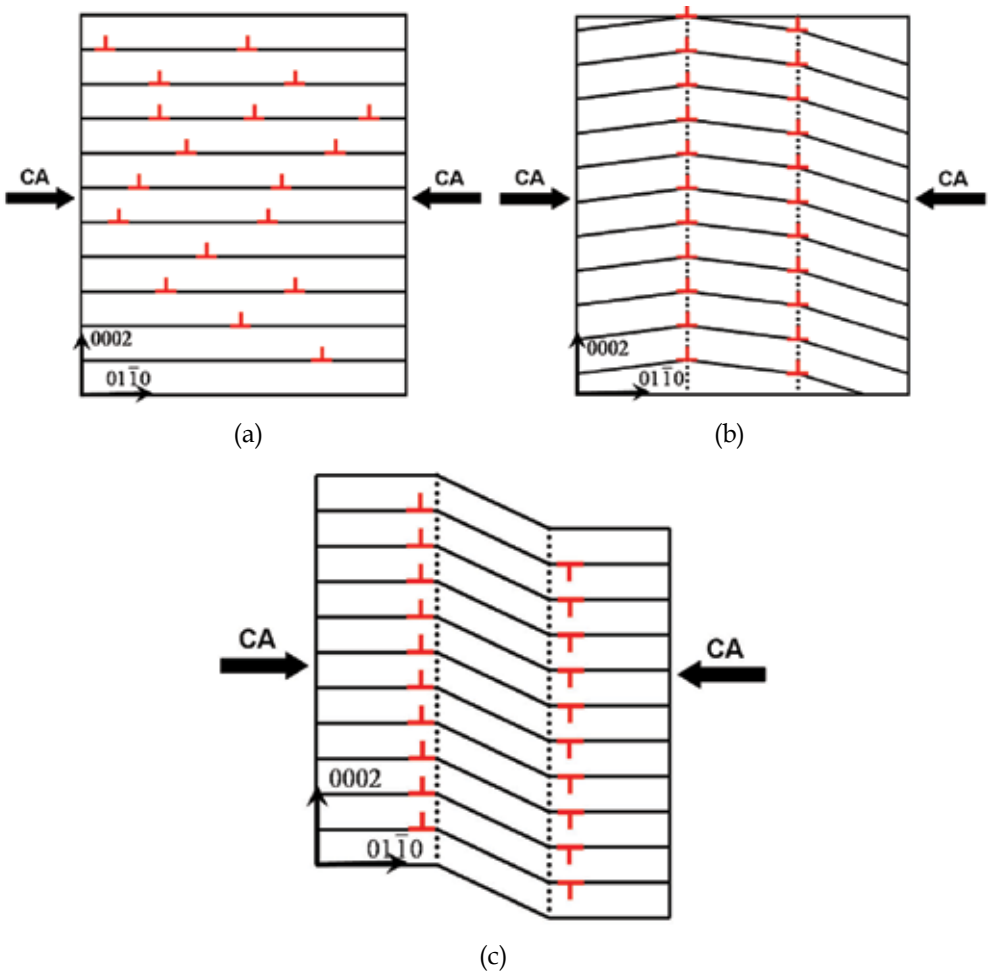

Fig. 10. A schematic representation of the formation of microbands and kink bands, their associated boundaries, and the associated changes in basal plane orientation. (a) An RD grain deformed in compression, (b) the microbands originate from the rearrangement of basal dislocations (shown in red), and (c) when two dislocation walls are composed of basal dislocations of opposite sign, the rotations are self-compensating and a kink band forms. The dotted lines correspond to the geometrically necessary boundaries and the kink boundaries in (b) and (c), respectively.

The evolution of such dislocation networks has been studied in detail. (Tan & Tan, 2003). However, TEM–based *microtexture* investigations do not generally provide statistically relevant analyses because of the very small volumes examined in a single specimen; they also require laborious specimen preparation. These limitations can be overcome by using microtexture analysis based on the EBSD technique. The very high measurement speed that can be achieved (currently more than 300 measurements per second) contributes to their effectiveness. However, the angular resolution is limited, so that the boundary rotation axes cannot be determined with accuracy when the misorientation is less than 5^{o} (Prior, 1999; Wilkinson, 2001).

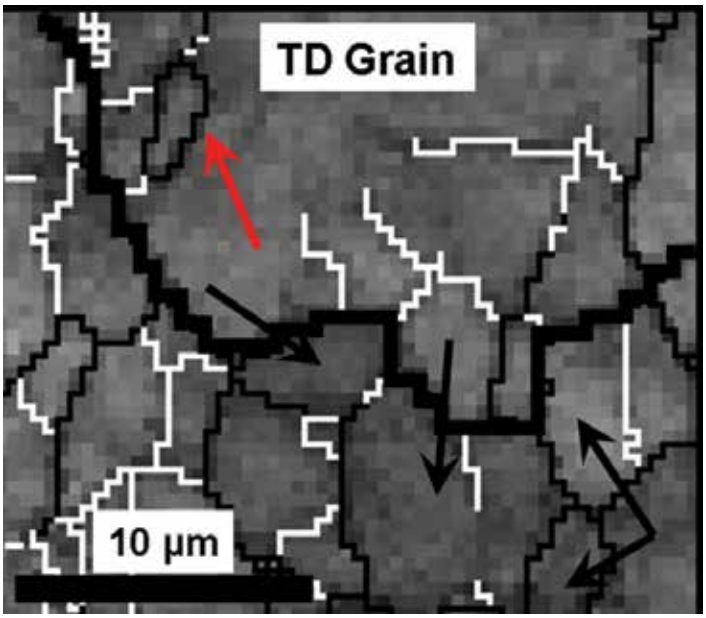

Fig. 11. EBSD map of a sample deformed to a strain of 0.2 at 350 °C. The sub-boundaries ($5^o<\omega<15^o$) are delineated by thin white lines; the new grains ($\omega \geq 15^o$) are outlined in black (see the red and black arrows). The initial grain boundary is shown as a thick black line.

The new grains that developed within the deformation substructure are illustrated in Fig. 11. These grains do not differ in size from the surrounding subgrains. They began their existence as subgrains entirely enclosed by LAB's. On becoming grains, they are enclosed by HAB's. In order to demonstrate that cDRX grains are produced by dislocation rearrangement, the c-axis orientations associated with matrix grains were compared with these of new grains. For this purpose, the angle α between the c-axis of a given crystallite and the compression axis was derived as follows:

$$\alpha = \arccos\left([\, g^{-1} <001>] \bullet <CA>\right) \tag{5}$$

Here **g** is the orientation matrix of the crystallite given by the triplet of Euler angles provided by the EBSD scan and <001> is the c-axis direction as expressed in an orthogonal reference frame. Then, the difference between the c-axis orientations of crystallites A and B with respect to the CA is obtained from:

$$\alpha_A - \alpha_B \tag{6}$$

where α_A and α_B are the angles between the c-axis and the CA associated with crystallites A and B, respectively. In this case, the A crystallite refers to the matrix, while the B crystallite refers to the microstructure feature of interest (i.e. the MB, KB, subgrain or new grain). Finally, these differences are normalized with respect to the rotation angle ω calculated from Eqs. 1 and 2 as follows:

$$\theta = \frac{\alpha_A - \alpha_B}{\omega} \tag{7}$$

According to Eq. 7, a boundary will have a θ value of one if the c-axis rotation towards the CA associated with it is equal to its misorientation angle ω. Positive values of θ describe c-axis rotations toward the CA, while negative values are associated with c-axis movements away from the CA. Finally, θ is zero under two conditions: i) if only a rotation about the c-axis is involved; and ii) if the c-axis is rotated around an axis that is parallel to CA.
Fig. 12 (a) shows that MBs and KBs are largely associated with a θ value of one, meaning that the c-axes are rotated towards the stress direction when these features are formed. This

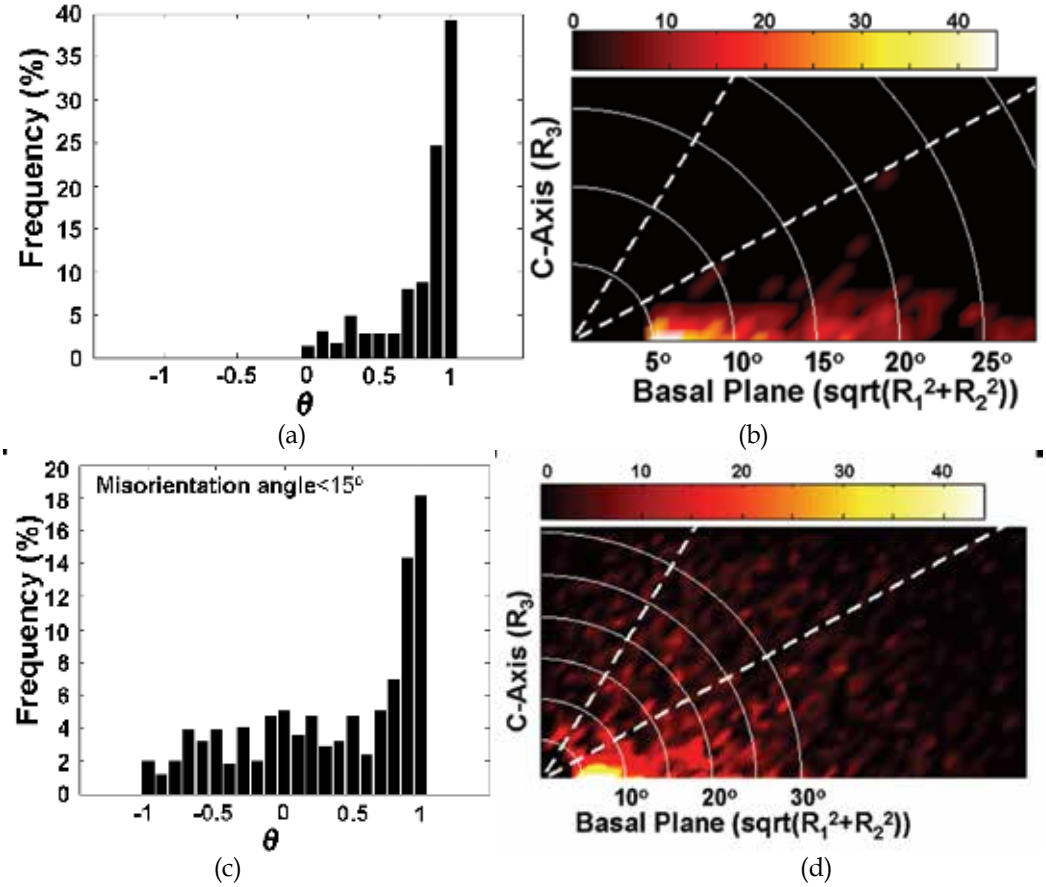

Fig. 12. c-axis displacements towards the CA direction attributable to the formation of (a) microbands and kinkbands and (c) subgrains. Side views of the reduced zones[3] displaying the rotations associated with (b) MBs and KBs and (d) new grains. The two dashed white lines represent vectors that are inclined at 30° and 60° to the c-axis and the white quarter circles identify the misorientation angles associated with the Rodrigues-Frank (RF) vectors.

[3] These side views of Rodrigues-Frank space are displayed here by plotting the R_3 (c-axis) value as a function of the projected length of the R-F vector on the basal plane ($\sqrt{R_1^2 + R_2^2}$). In this way, the inclinations of the RF vectors with respect to the c-axis are immediately evident; the lengths of the vectors are also preserved (see (Martin & Jonas (2010))).

type of rotation corresponds to the accumulation of basal dislocations. The inverse pole figures displayed in Fig. 1 show that the c-axes are initially aligned perpendicular to the compression axis. During the discussion of twinning presented above, it was stated that such a texture is unstable with respect to the compressive loading. The activation and especially the accumulation of basal dislocations thus lead invariably to rotations of the c-axes towards the contraction direction (the stable final orientation).

Further evidence is provided when the axis-angle pairs describing the MBs-KBs are considered. In Fig. 12 (b), the rotations are expressed in the form of Rodrigues-Frank vectors. Since MBs-KBs result from the progressive accumulation of basal dislocations, their rotations (Fig. 12 (b)) lie essentially in the basal plane and take on low to high angles in magnitude.

The characteristics of the rotations associated with subgrain formation are displayed in Fig. 12 (c). Here, the θ distribution is more broadly based than in Fig. 12(a), although it does exhibit a peak close to θ=1. These rotations also exhibit a strong intensity peak near 5^o (Fig. 12(d)), where the axes again lie mostly near the basal plane. The formation of subgrains thus also involves the progressive accumulation of basal dislocations. However, as the misorientation angles increase (see the range from $10^o \leq \omega \leq 20^o$ in Fig. 12(d)), the inclinations of the rotation axes with respect to the basal plane increase.

According to Frank's formula, this change is consistent with the view that prismatic and/or <c + a> dislocations are incorporated into the sub-boundaries as they gradually take on a high angle character. The activation of non-basal dislocations is required in the vicinities of the initial boundaries in order to accommodate the large plastic incompatibility stresses (Koike et al., 2003). The differences between the two distributions therefore arise because the cDRX grains considered here were formed essentially near the initial grain boundaries while the MBs-KBs developed in the grain interiors.

5.3 Discontinuous dynamic recrystallization

As the misorientation angles increase in Fig. 12(b), the RF vectors associated with the MBs and KBs remain close to the basal plane and their misorientations rarely exceed 20^o. This is because the formation of these boundaries, even those of high misorientation, continues to involve the pile-up of basal dislocations. Conversely, the differences in the distribution of the RF vectors associated with the new grains ($\omega > 20^o$) in Fig. 12(d) reveal that a second mechanism is involved in the formation of new DRX grains. In the first place, the RF vectors are more evenly distributed. Furthermore, there are many new grains with misorientation angles higher than 20^o. These two observations are inconsistent with the view that these ($\omega > 20^o$) grains were formed by cDRX.

This can be seen more clearly by examining the RF vectors that describe the initial microstructure, as illustrated in Fig. 13(a). These were measured in the as-received AM30 tubes. This distribution is somewhat similar to that associated with the new ($\omega > 20^o$) grains displayed in Fig. 12(d); in the two cases, 63% ±3% of the RF vectors are within 30^o of the basal plane, while the regions near the c-axis are clearly not favoured (8% ±1%). The similarity can be attributed to the formation of the new grains by the bulging of the pre-existing grain boundaries. In this way, their boundary misorientation characteristics reproduce those of their parent grains.

Of course the mother grains of bulged new grains cannot be identified with certainty. If bulging is initiated in a grain right above or below the plane of section, the mother grain is

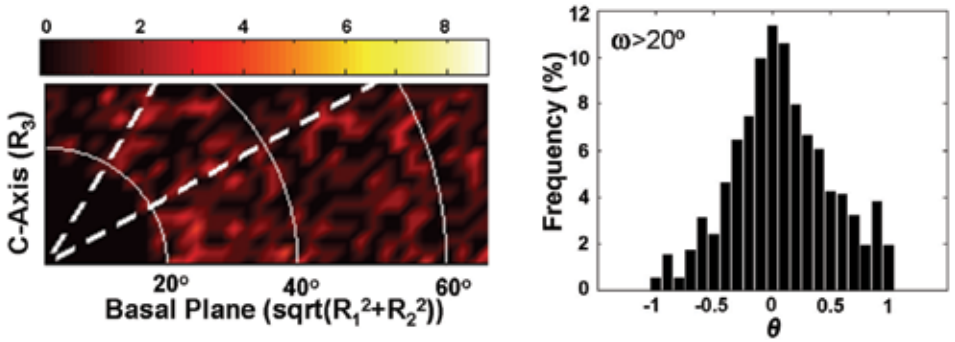

(a) (b)

Fig. 13. (a) Side view of the reduced zone displaying the misorientations associated with the initial grain boundaries. (b) c-axis displacements with respect to the CA direction attributable to the formation of new grains (delineated by HAB's).

not on the polishing plane. This is an inherent weakness of 2D metallography. In Fig. 11, the grain highlighted by the red arrow was considered to be a cDRX grain and the surrounding TD grain to be the mother grain. However, the new grain could have formed by the bulging of a grain right above or below the plane of the image, i.e. by a dDRX rather than a cDRX process. In this case, the HAB highlighted by the red arrow could have migrated from the initial grain into the TD grain. In such a case, the rotation characteristics would correspond to those of the *initial* grain boundaries rather than to those of the boundaries produced by the accumulation of basal dislocations.

A characteristic feature of the discontinuous mechanism is that the new grains have orientations that are similar to those of the old grains out of which they have grown. The boundaries of new grains have misorientation angles that generally exceeded 20°. It can be seen from Fig. 13 (b) that, in such a case, most of the c-axes rotate about axes that are approximately parallel to the compression axis (i.e. much of the distribution falls within $-0.25 < \theta < +0.25$ and is centered exactly on $\theta = 0$). In this way, the new grains have orientations close to those of the initial grains. Thus, more generally, new grains within the RD-TD fibre tend to grow within the other RD-TD fibre grains, as long as the latter are of different orientation. As a consequence, the main features of the initial RD-TD texture are retained during discontinuous dynamic recrystallization, even if the maximum intensity is somewhat reduced (Martin & Jonas, 2010).

The driving force for bulging is usually assumed to be the difference in dislocation density on opposite sides of the grain boundary. In a material with a well-recovered substructure, the low dislocation density region may be a large single subgrain (Humphreys & Hatherly, 2004). A bulge of this type, enclosed by a well defined subgrain with no detectable substructure within it, is illustrated in Fig. 14(a). Other subgrains may rotate during deformation into orientations that differ slightly from those of their parents (Martin & Jonas, 2010). Examples of bulge grains of somewhat different orientations, and therefore delineated by HABs, are displayed in Fig. 14(b).

In many metals, bulging is particularly important when deforming to low strains. In aluminum, for example, this mechanism is replaced when the rolling reduction exceeds 40% (Beck & Sperry, 1950). As the present work was restricted to low strain deformation, no conclusions can be drawn about the possible role of bulging in highly deformed magnesium alloys.

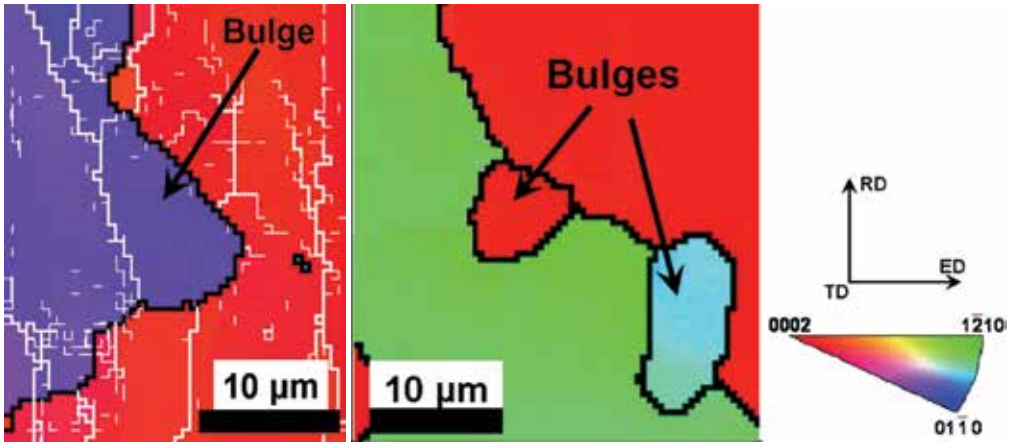

(a) (b)

Fig. 14. Inverse pole figure (IPF) maps of an AM30 sample deformed to 0.2 strain; three examples of bulge nucleation are shown. The low-angle boundaries ($2^o<\omega<15^o$) are shown in white and the high-angle boundaries ($\omega \geq 15^o$) in black. The IPF color triangle indicates the orientation of the TD axis in the hexagonal crystal reference system.

6. Conclusions

The recrystallization of magnesium is a fairly complex topic, essentially because the deformation of magnesium involves several different mechanisms. Furthermore, the subsequent occurrence of recrystallization also involves several mechanisms, which may occur simultaneously. Mesoscale (i.e. grain scale) investigations are thus especially suitable for the exploration of such phenomena. The crystallographic characterization of the recrystallization phenomena described here has led to the clarification of the contributions of the different nucleation mechanisms to texture evolution. Moreover, by considering the deformation structure within which the new grains nucleate, it has been possible to gain some insights into the nucleation mechanisms themselves. The results described above have led to the following conclusions.

1. Strong variant selection takes place during the formation of primary and secondary twins. In the first case, the primary (contraction) twin orientations that are activated depend on the processing conditions. In the present case, these were limited to four out of six possible variants. It has been shown elsewhere (Martin et al., 2010) that secondary (extension) twins that require relatively easy accommodation strains tend to form. This is why only 18 out of 36 possible secondary twin variants can be activated in the general case. These all belong to the S^A and S^D variant categories (misorientations of 37.5^o and 69.9^o, respectively, with respect to the parent grain).
2. Double twins recrystallize more rapidly than primary twins during annealing. The new grains do not generate significant rotations (texture changes), so that the new orientations remain similar to those of the secondary twins. Recrystallization of the four S^D twin variants induces a spread around these orientations. On the other hand, recrystallization of the S^A twin variants rotates the c-axes towards the parent grain orientations, so that they contribute to the persistence of the initial texture.

3. The double twin nuclei tend to grow solely within the primary twins rather than spreading into the parent grains. This is because the primary twins are favorably orientated for basal slip, so that dislocation pile-up occurs more extensively within them. The driving forces for growth are thus larger within the twin lamella than within the parent grains. In this way, the primary twins do not contribute significantly to texture change since these twins are essentially consumed during growth of the secondary twin nuclei. They do not themselves provide recrystallization (and therefore new orientation) nuclei.
4. When the deformation temperature is increased sufficiently to allow significant recovery to take place, microbands and kink bands form by the accumulation and rearrangement of *basal* dislocations. They thus contribute to the formation of the basal (stable) end texture. These bands form in the early stages of high temperature deformation and lead to the formation of new grains with relatively low misorientations with respect to the parent grains. This is considered here to involve the continuous dynamic recrystallization mechanism.
5. New grains also form in magnesium due to the migration of the pre-existing grain boundaries. This is referred to here as discontinuous DRX or dDRX. The driving force for bulging arises from dislocation density and substructure size differences across the initial boundaries. These new "bulge" grains are initially enclosed by low angle boundaries that continuously increase in misorientation to become high angle boundaries. Nevertheless, the dDRX grains can still be differentiated from the cDRX grains. The former grains have orientations that are similar to those of the initial grains out of which they have grown. The formation of the basal texture is thus somewhat retarded when dDRX is taking place. By contrast, the cDRX grains essentially rotate the c-axes towards the basal end texture.

7. References

Backx, P.; Barnett, M. R. & Kestens, L. (2004). Texture changes during uniaxial compression of Mg-3Al-1Zn. *Materials Science Forum*, 467-470, 6.

Barnett, M. R. (2001). Influence of deformation conditions and texture on the high temperature flow stress of magnesium AZ31. *Journal of Light Metals* 1, 11.

Barnett, M. R. (2003). A Taylor model based description of the proof stress of magnesium AZ31 during hot working. *Metallurgical and Materials Transactions A*, 34, 8.

Barnett, M. R. (2007). Twinning and the ductility of magnesium alloys. Part II. "Contraction" twins. *Materials Science and Engineering A*, 464, 1-2, 8.

Beausir, B.; Suwas, S.; Toth, L.; Neale, K. W. & Fundenberger, J. J. (2007). Analysis of texture evolution in magnesium during equal channel angular extrusion. *Acta Materialia*, 56, 2, 15.

Beck, P. A. & Sperry, P. R. (1950). Strain induced grain boundary migration in high purity aluminum. *Journal of Applied Physics*, 221, 2, 3.

Bunge, H. J. (1982). *Texture Analysis in Material Science*, Butterworths, London

Couret, A. & Caillard, D. (1985). An in situ study of prismatic glide in magnesium - I: the rate controlling mechanism. *Acta Metallurgica*, 33, 8, 8.

del Valle, J. A.; Pérez-Prado, M. T. & Ruano, O. A. (2005). Deformation mechanisms responsible for the high ductility in a Mg AZ31 alloy analyzed by electron backscattered diffraction. *Metallurgical and Materials Transactions A* 36A, 12.

Engler, O. & Randle, V. (2010). *Introduction to Texture Analysis: Macrotexture, Microtexture & Orientation Mapping*, Gordon and Breach Science, New York

Frank, F. C. (1988). Orientation mapping. *Metallurgical Transactions A*, 19, 3, 6.

Frost, H. J. & Ashby, M. F. (1982). *Deformation-Mechanism Maps*, Pergamon Press, Oxford

Galiyev, A.; Kaibyshev, R. & Gottstein, G. (2001). Correlation of plastic deformation and dynamic recrystallization in magnesium alloy ZK60. *Acta Materialia*, 49, 8.

Godet, S.; Jiang, L.; Luo, A. A. & Jonas, J. J. (2006). Use of Schmid factors to select extension twin variants in extruded magnesium alloy tubes. *Scripta Materialia*, 55, 11, 4.

Gottstein, G. & Al Samman, T. (2005). Texture development in pure Mg and Mg alloy AZ31. *Materials Science Forum*, 495-497, PART 1, 10.

Guo, Q.; Yan, H. G.; Zhang, H.; Chen, Z. H. & Wang, Z. F. (2005). Behavior of AZ31 magnesium alloy during compression at elevated temperature. *Materials Science and technology*, 21, 11, 6.

Heinz, A. & Neumann, P. (1991). Representation of orientation and disorientation data for cubic, hexagonal, tetragonal and orthorhombic crystals. *Acta Crystallographica*, A47, 10.

Hirth, J. P. & Lothe, J. (1968). *Theory of Dislocations*, McGraw-Hill, New York

Humphreys, F. J. & Hatherly, M. (2004). *Recrystallization and Related Annealing Phenomena*, Elsevier, Oxford

Ion, S. E.; Humphreys, F. J. & White, S. H. (1982). Dynamic recrystallisation and the development of microstructure during the high temperature deformation of magnesium. *Acta Metallurgica*, 30, 11.

Jäger, A.; Lukác, P.; Gärtnerová, V.; Haloda, J. & Dopita, M. (2006). Influence of annealing on the microstructure of commercial Mg alloy AZ31 after mechanical forming. *Materials Science and Engineering A*, 432, 1-2, 6.

Jiang, L.; Jonas, J. J.; Luo, A. A.; Sachdev, A. K. & Godet, S. (2006). Twinning-induced softening in polycrystalline AM30 Mg alloy at moderate temperatures. *Scripta Materialia*, 54, 5, 5.

Jiang, L.; Jonas, J. J.; Mishra, R. K.; Luo, A. A.; Sachdev, A. K. & Godet, S. (2007). Twinning and texture development in two Mg alloys subjected to loading along three different strain paths. *Acta Materialia*, 55, 12.

Kaibyshev, R. O. & Sitdikov, O. (1996). Bulging mechanism of dynamic recrystallization. *Proceedings of Third international conference on recrystallisation and related phenomena*.

Kleiner, S. & Uggowitzer, P. J. (2004). Mechanical anisotropy of extruded Mg–6% Al–1% Zn alloy. *Materials Science and Engineering A*, 379, 1-2, 6.

Kocks, U. F.; Tomé, C. N. & Wenk, H.-R. (1998). *Texture and Anisotropy : Preferred Orientation in Polycrystals and their Effect on Materials Properties*, Cambridge University Press, Cambridge

Koike, J.; Kobayashi, T.; Mukai, T.; Watanabe, H.; Suzuki, M.; Maruyama, K. & Higashi, K. (2003). The activity of non-basal slip systems and dynamic recovery at room temperature in fine-grained AZ31B magnesium alloys. *Acta Materialia*, 51, 6, 11.

Li, X.; Yang, P.; Wang, L.-N.; Meng, L. & Cui, F. (2009). Orientational analysis of static recrystallization at compression twins in a magnesium alloy AZ31. *Material Science and Engineering A*, 517, 10.

Martin, E.; Godet, S.; Jiang, L.; Elwazri, A.; Jacques, P. J. & Jonas, J. J. (2008). An EBSD study of the misorientations related to dynamic recrystallization in Mg AM30 deformed at high temperatures. *Proceedings of 15th International Conference on Textures of Materials*, Pittsburgh, PA, United States, American Ceramic Society, 577.

Martin, E.; Jiang, L.; Godet, S. & Jonas, J. J. (2009). The combined effect of static recrystallization and twinning on texture in magnesium alloys AM30 and AZ31. *International Journal of Materials Research*, 100, 8.

Martin, E. & Jonas, J. J. (2010). Evolution of Microstructure and Microtexture during the Hot Deformation of Mg -3% Al. *Acta Materialia. 58,12, 15*.

Martin, E.; Capolungo, L.; Jiang, L. & Jonas, J. J. (2010). Variant selection during secondary twinning in Mg–3%Al. *Acta Materialia. 58, 11, 15*.

Mason, J. K. & Schuh, C. A. (2008). Hyperspherical harmonics for the representation of crystallographic texture. *Acta materialia*, 56, 20, 15.

Myshlyaev, M. M.; McQueen, H. J.; Mwembela, A. & Konopleva, E. (2002). Twinning, dynamic recovery and recrystallization in hot worked Mg-Al-Zn alloy. *Materials Science and Engineering A*, 337, 13.

Polmear, I. J. (1995). *Light Alloys: Metallurgy of the Light Metals*, John Wiley and Sons, London

Prior, D. J. (1999). Problems in determining the misorientation axes, for small angular misorientations, using electron backscatter diffraction in the SEM. *Journal of Microscopy*, 195, 9.

Sitdikov, O. & Kaibyshev, R. (2001). Dynamic recrystallization in pure magnesium. *Materials Transactions*, 42, 6, 1928.

Tan, J. C. & Tan, M. J. (2003). Dynamic continuous recrystallization characteristics in two stage deformation of Mg-3Al-1Zn alloy sheet. *Materials Science and Engineering A*, 339, 9.

Wilkinson, A. J. (2001). A new method for determining small misorientation from electron back scatter diffraction patterns. *Scripta Materialia*, 44, 10, 7.

Yang, X.; Miura, H. & Sakai, T. (2003). Dynamic evolution of new grains in magnesium alloy AZ31 during hot deformation. *Materials Transactions*, 44, 1, 7.

Yang, X.; Ze-sheng, J.; Miura, H. & Sakai, T. (2009). Dynamic recrystallization and texture development during hot deformation of magnesium alloy AZ31. *Trans. Nonferrous Met. Soc. China*, 19, 4, 6.

Yi, S.; Schestakowb, I. & Zaefferer, S. (2009a). Twinning-related microstructural evolution during hot rolling and subsequent annealing of pure magnesium. *Materials Science and Engineering A*, 516, 7.

Yi, S.; Schestakow, I. & Zaefferer, S. & Brokmeier, H.-G. (2006). Mechanical behaviour and microstructural evolution of magnesium alloy AZ31 in tension at different temperatures. *Materials Science and Engineering A*, 424, 1-2, 7.

Yi, S. B.; Zaefferer, S. & Brokmeier, H.-G. (2009b). Twinning-related microstructural evolution during hot rolling and subsequent annealing of pure magnesium. *Materials Science & Engineering A*, 424, 1-2.

3

Mechanisms of Plastic Deformation in AZ31 Magnesium Alloy Investigated by Acoustic Emission and Electron Microscopy

Miloš Janeček and František Chmelík
Charles University Prague, Department of Physics of Materials
Czech Republic

1. Introduction

Magnesium alloys are the lightest metallic structural materials and are therefore very attractive in applications in automobile, railway and aerospace industries where the mass reduction is an important issue. However, owing to their hexagonal close-packed structure and a limited number of slip systems, Mg alloys exhibit only limited ductility and accommodation ability. Parts of these alloys for structural applications are often produced by casting with no or very limited mechanical pressing. This obviously limits the range of possible engineering applications of Mg alloys.

In the recent years, there has been a renewed interest in Mg alloy sheet products, especially in automotive applications where considerable weight savings can be made by substituting magnesium for aluminium or steel components. Mg-3Al-1Zn alloy (AZ31) is currently the most common Mg alloy used for sheet applications. Due to its poor cold rolling response it has to be rolled at elevated temperatures, which considerably increases manufacturing costs of sheet products of this alloy. Optimization of conditions of the hot rolling process is therefore a big challenge. The properties of the rolled sheet obviously depend on the initial state of the material, the temperature of plate before rolling and many other parameters. However, at present there is only a limited knowledge of this area. One of the possible ways how to improve the final properties of the rolled state is to optimize the conditions of the material preheating before rolling. Too high temperature of preheating increases the costs of the final sheet and too low temperature may result in the failure of the material during successive rolling.

Next to rolling the techniques of severe plastic deformation attracted recently the interest of researchers. Ultrafine-grained materials processed by these techniques exhibit enhanced mechanical and other physical properties and offer a wide range of possible practical applications. The properties of materials with fine grain sizes and face centred cubic lattice were extensively studied and reported in the literature. On the other hand, there is a limited knowledge of properties and microstructure evolution of materials with hexagonal structure. AZ31 alloy is a typical representative of this class of materials.

A well established method of investigating the dynamic processes taking place during plastic deformation is acoustic emission (AE). AE signals originate from transient elastic waves, which are generated within the material due to sudden localized structural changes. Typical sources of intense AE are collective dislocation movement or twinning.

The objective of this review paper is to investigate various mechanisms of plastic deformation in AZ31 magnesium alloy by AE and to correlate them with the evolution of microstructure observed by electron microscopy and electron diffraction and to asses critically the differences in the material processed by different processing routes.

2. Experimental part

2.1 Experimental material

In this chapter the properties of AZ31 (3 wt.% Al, 0.8 wt.%Zn, 0.2 wt.% Mn) alloy as a typical representative of wrought magnesium alloys are summarized. Two different processing routes, in particular

a. hot rolling,
b. severe plastic deformation,

were used to prepare the material for the investigation. Squeeze cast material was used as a reference material to compare the behaviour of wrought and cast AZ31.

The properties of the material were investigated by different experimental techniques.

Mechanical properties in tension and compression were investigated by standard screw driven Instron and Zwick machines equipped with furnaces allowing deformation up to 300°C. Fatigue behaviour was investigated both in push-pull and rotating beam tests up to the very high cycle range.

During mechanical tests (tension, compression, fatigue) AE was monitored using a sophisticated new generation AE system whose details will be described in the following part as its application to detect and understand microphysical processes occurring during plastic deformation, fatigue and fracture is one of the main topics of this paper.

Microstructure evolution and characterization was performed using various techniques of electron microscopy and electron diffraction – light, scanning and transmission electron microscopy, electron back scattered diffraction. These techniques are particularly important in the characterization of ultrafine-grained materials prepared by severe plastic deformation. X-ray diffraction was also used to investigate microstructure and texture evolution in various specimens.

2.2 Acoustic emission

2.2.1 Introduction

AE may be characterized as a manifestation of transient elastic waves arising in a material from sudden localized irreversible structure changes. Since the pioneering work of Kaiser (Kaiser, 1953), AE has been frequently used to investigate plastic deformation of materials. AE methods that were used in the past and reported in the literature both by other authors (Botten, R. et al., 2001; Vinogradov et al., 2003) and in our previous work (Richeton et al., 2006; Mathis et al., 2006), were based on evaluation of individual AE events which surpass some set threshold level. Various parameters of such events can be evaluated such as frequency of events for different thresholds, energy of events and waveforms of AE signal. Nevertheless, in many cases the effects remain hidden below the minimum threshold given by the noise level of the equipment. In such cases AE methods did not allow detecting any events and as such could not contribute to the understanding of processes in the material. In our laboratory we have developed a qualitatively new approach to the AE measurement, which in some extent eliminates the above described limitations (Král et al. 2007). The main difference from previously used methods is a continuous sampling and storage of the AE

signal from several channels as measured by the AE transducer and performing consequently a statistical analysis on a complete stored signal data. The fact that the complete signal is stored allows to i) run various successive analyses, ii) evaluate individual time moments with respect to the properties of the entire signal set, iii) use time consuming analyses that would not be possible to use in real time (during experiment).

2.2 Principles and systems of acoustic emission detection

The detection of AE is based on its physical nature, namely the elastic energy release due to some irreversible change of (micro)structure. Near the source of AE the released energy (AE event) forms the stress pulse, which propagates through the material bulk as transient elastic waves and at the surface of the material it is transformed into a certain wave mode which corresponds to the geometrical configuration and the dimensions of the specimen. The wave component perpendicular to the surface may be detected by piezoelectric transducers, which are coupled to the specimen surface either mechanically or through a waveguide. Electrical signal from the transducer (emission signal) is first preamplified and then led to the input of the measuring system, where it is amplified and analyzed.

The AE signal is either of continuous character, whereby the amplitude does not fall under a certain threshold level during relatively long period of time, or discontinuous. The former has a character of noise while the latter features pulses, distinctly separated in time, so called emission events.

In case of the continuous AE the mean quadratic value of the signal voltage and the number of hits above threshold levels are evaluated during a certain adjustable period of time. In case of discontinuous AE each emission event is evaluated independently. The following parameters are usually used to characterize individual separated events, see Fig. 1:

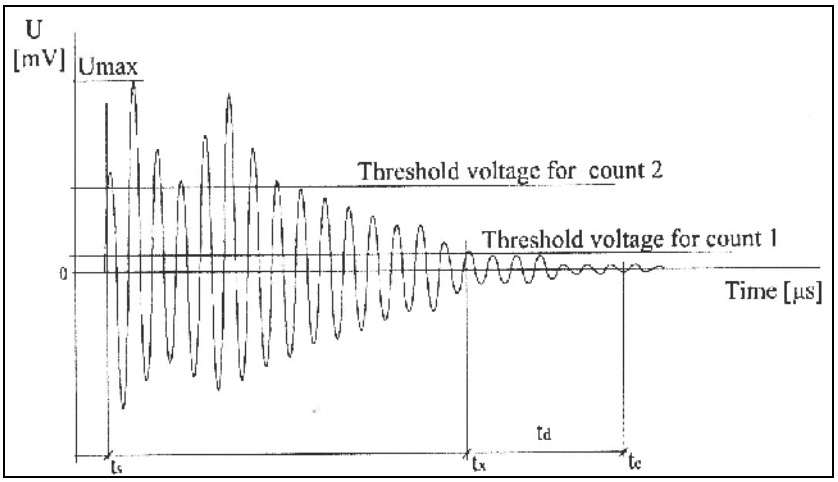

Fig. 1. The characteristics of a single AE event at the threshold level 1

- t_s is the onset of AE event when the first signal overshoot above the threshold level is detected,
- t_d is the event dead time,
- t_x is the time when the last overshoot is detected,
- t_e is the termination of the event ($t_e = t_x + t_d$),

- t_e-t_s is the duration of the event.

Two different systems of AE detection may be employed:

a) a standard generation of AE systems (we use the system DAKEL-XEDO-3 by the manufacturer DAKEL-ZD Rpety, Czech Republic). In this case the electrical signal is analyzed and evaluated in real time and the evaluated data (AE parameters) are stored. A two threshold level detection giving a simple amplitude discrimination and two AE count rates (AE1 and AE2) is used and the sampling rate of 4 MHz is used.

b) a new generation DAKEL-CONTI-4 AE system allows continuous sampling and storage of AE signal from 1 up to 4 channels with 2 MHz sampling frequency. The sampled AE signal is continuously stored on a dedicated hard disk connected to the measuring unit via a high speed interface, i.e. no data processing by the computer used to control the measuring unit takes place and high data transfer speed is ensured. The software enables both the evaluation of individual AE events in a standard way (Trojanová & Cáceres, 2007) (two-threshold-level detection recommended by an ASTM standard (ASTM, 1994) was used with the thresholds set to 1.06 and 2.10 mV) and the analysis of the complete stored spectra based on statistical method. The method of averaged frequency spectra was used. A miniaturized MICRO-06 piezoelectric transducer with 3 mm diameter and a flat response in a frequency band from 100 to 600 kHz was used. If we denote generally the registered AE signal in time t as $x(t)$ then the total energy E in some time interval can be written as

$$E = k \int x^2 (t)\, dt, \tag{1}$$

where k is a constant equal to Z^{-1}, where Z is the impedance of the experimental set-up. In the case of discrete substitution the integral in (1) is replaced by a sum and dt is replaced by f^{-1}, f being the sampling frequency, which yields

$$E = Z^{-1} f^{-1} \sum x_i^2 \tag{2}$$

By confining to relative values of energy, the factors Z^{-1} and f^{-1} in (2) are insignificant. The value of the sum must be determined and related to some unit value (typically the maximum value registered during the experiment). The sum in (2) is computed in time intervals $t_n = n \cdot 4096$ μs for 8192 samples (which corresponds to 4096 μs at the sampling frequency of 2 MHz).

The 4096 μs interval was found to be optimal with the respect to noise minimization while preserving sufficient sensitivity for detecting effects in AE signal.

The energy E_k of the k-th interval of 4096 μs may be expressed as (k is going from 0):

$$E_k = K \sum_{i=kx8192}^{(k+1)x8192} x_i^2 , \tag{3}$$

where K is a constant found from the condition $\{E_k\} = 1$. Histograms of relative energies of AE signal are then computed in 10 s time intervals, i.e. each histogram comprises 2441 energies.

3. Results and discussion

3.1 Hot rolled AZ31

Wrought magnesium alloys have a high potential for structural application due to their improved mechanical properties compared to cast components.

However, due to the hexagonal close-packed (hcp) crystallographic structure, a limited activation of slip planes at room temperature is available so the formability of the sheet is poor. Furthermore, the mechanical properties show an anisotropic behaviour (Kaiser et al. 2003). It was also found that the heat treatment condition has an influence on the extension of the anisotropic behaviour. Thus, a heat treatment of the stress-relieved sheet leads to changes in the microstructure as well as in the texture of the material and therefore results in a decrease of the orientation dependence of mechanical properties.

Basal slip is known to be the most important mechanism of plastic deformation in magnesium (Emley, 1996). However, there are only three equivalent basal slip systems in Mg, but the compatibility of deformation in polycrystals requires at least five independent slip systems. Therefore, secondary (prismatic, pyramidal) slip systems or twinning, primarily in (10.2) planes, must be activated during deformation. Furthermore, twinning in Mg can reorientate basal planes so that they become more favourable oriented for slip (Zhang et al., 2000). The activation of twinning itself depends on grain orientation (Emley, 1996).

AE, which stems from transient elastic waves, generated within a material due to sudden localised and irreversible structure changes, responds to dislocation motion and twinning (Heiple, & Carpenter, 1987) and therefore yields information on the dynamic processes involved in plastic deformation of magnesium alloys. Friesel and Carpenter (Friesel & Carpenter, 1984) investigated AE during the deformation of pure Mg and an AZ31B alloy and found a distinct correlation of the AE activity with sample orientation, purity, strain rate and the mode of testing (tension, compression).

In our previous investigation (Bohlen et al., 2004) AE was observed and analysed during plastic deformation of an AZ31 rolled sheet in an H24 temper as well as after a heat-treatment at elevated temperatures. The AE count rates showed a well-known correlation with the stress–strain curves revealing a well-defined peak close to the macroscopic yield point followed by a subsequent decrease in the AE activity.

In all cases, deformation twinning and dislocation glide were found to be the major sources of AE. AE proves therefore for a justifiable method to study dynamic processes involved in plastic deformation of magnesium and magnesium alloys.

One of the effects that can contribute to the understanding of deformation mechanisms is a spatio-temporal localization of plastic deformation (Portevin–Le Chatelier effect, hereafter PLC effect) that occurs in some alloys at suitable deformation conditions. In hexagonal alloys, an interplay of the PLC effect with twinning (non-propagative plastic instability) may be anticipated. (Caceres et al., 2002) observed recently the PLC effect in a heat-treated AZ91 alloy deformed at room temperature. However, to date no PLC effect was reported in AZ31 alloy (Tan & Tan, (2002). Therefore we employed AE to investigate unstable plastic flow in a hot-rolled AZ31 alloy under different deformation conditions.

The extruded AZ31 alloy was hot rolled at 300°C by twelve successive passes perpendicular to the extrusion direction. The thickness reduction between individual passes of rolling was kept constant. The final thickness after the reduction was 1 mm. The stripes were compact with limited cracking on both sides of the rolled stripe and had a width of 40 to 43 mm and the length of 950 to 1100 mm. Two sets of samples prepared from hot-rolled sheets, which were preheated at two different temperatures, T_{PR} (325 and 475°C) prior to individual passes of hot rolling were studied. AE study of the unstable plastic flow under different deformation conditions (temperature, strain rate) was performed. In Fig. 2, the true stress–true strain curves for the highest (200°C) and lowest test temperatures (RT) and both specimens are shown. The deformation behaviour differs significantly at both temperatures.

While at RT the flow stress increases with increasing deformation up to the fracture, at the temperature of 200°C the strain hardening region is limited to a small region of low strains only and is followed by an extended softening region for larger strains. Both the yield stress and the tensile strength decrease with increasing temperature of deformation. The ductility was found to increase significantly with increasing temperature of deformation in both specimens. At both temperatures of deformation enhanced ductility was also observed in the specimen preheated at higher temperature. The PLC effect was observed for all used strain rates both at room and elevated temperatures. Plastic deformation is accompanied by a pronounced AE activity with a maximum near the yield point. With further straining AE activity decreases significantly. However, some AE persists to fracture. Fig. 3 shows an example of a stress–strain curve correlated with the AE counts at room temperature. The stress is plotted as a solid line and the AE counts as bars.

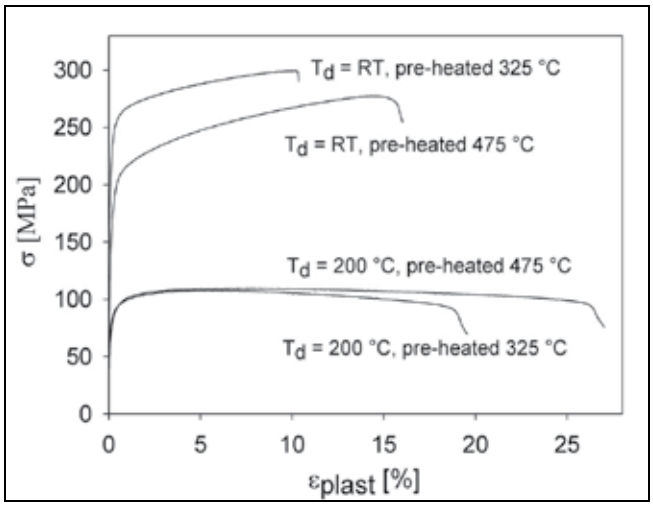

Fig. 2. Stress–strain curves for two AZ31 specimens deformed at RT and 200°C; T_d= deformation temperature.

The AE counts reveal a well-defined master curve with superimposed large bursts. The burst character of AE is clearly seen in the inset of Fig. 3, where a small portion of serrated stress–strain curve correlated with the AE counts is shown. Such an AE response is typical for the PLC effect, see, e.g. (Chmelík et al., 2002). The AE counts show a similar shape at both threshold levels, which indicates that no changes in the AE count distribution occur throughout the tests.

The shape of the AE count rate dependences does not seem to be influenced by the deformation conditions as the respective curves for all tested temperatures and strain rates have a similar shape. Therefore, only two examples of AE curves are shown, for RT in Fig. 3 and 200°C in Fig. 4. However, two differences are worth noting. Firstly, the AE activity increases with increasing temperature of preheating, and secondly, a distinct double peak at the yield point is observed at 200°C, see Fig. 4, while only a single AE peak curve was found at RT, see Fig. 3.

The microstructure of the alloy was investigated by light and transmission electron microscopy. The average grain size of the as extruded alloy is 200-300 μm. Hot rolling causes significant grain refinement. The bimodal distribution of grains was found in hot

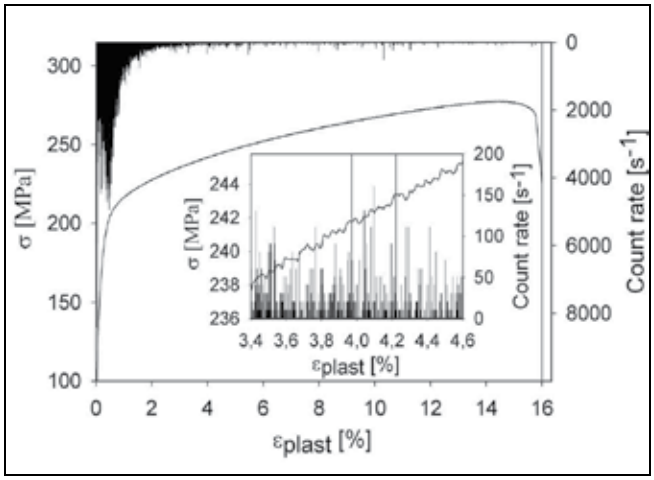

Fig. 3. A typical stress–strain curve and the corresponding AE count rates (the character of serrations and AE bursts are shown in the inset). The *y*-axis for the AE plot is on the right hand side of the graph and has an inverse polarity, i.e. the bars corresponding to AE counts are plotted from the upper border of the graph downwards.

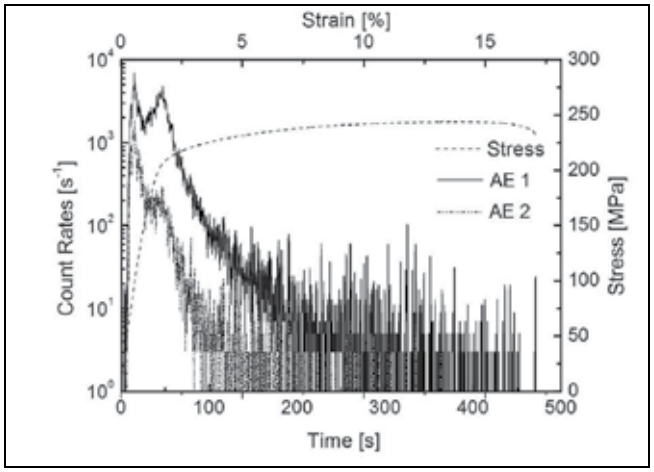

Fig. 4. The AE curve of AZ31 alloy deformed at 200°C showing a double peak at the yield point (AE 1 and AE 2 are count rates at the respective threshold levels 1 and 2, strain rate = 3.3×10^{-4} s^{-1}).

rolled sheets. The preheating temperature between individual steps of rolling influences the final grain size. The average size of the finer population of grains in the alloy preheated at 325°C and 475°C is 9 μm and 17 μm, respectively, whereas that of the bigger grains is 33 μm and 71 μm, respectively.

Fig. 5 illustrates an example of the microstructure of specimens deformed at RT and 200°C to 2.8%. Extensive twinning was found almost in all areas of the specimen implying that twinning is prevalent mechanism of deformation at low strains. Several families of almost parallel twins with high density of dislocations passing through several grains and

intersecting each other were observed (so called compound twinning (Yin et al., (2005)). Much higher number of twins was found in the specimen deformed at RT (Fig. 5a) than in that deformed at 200°C (Fig. 5b).

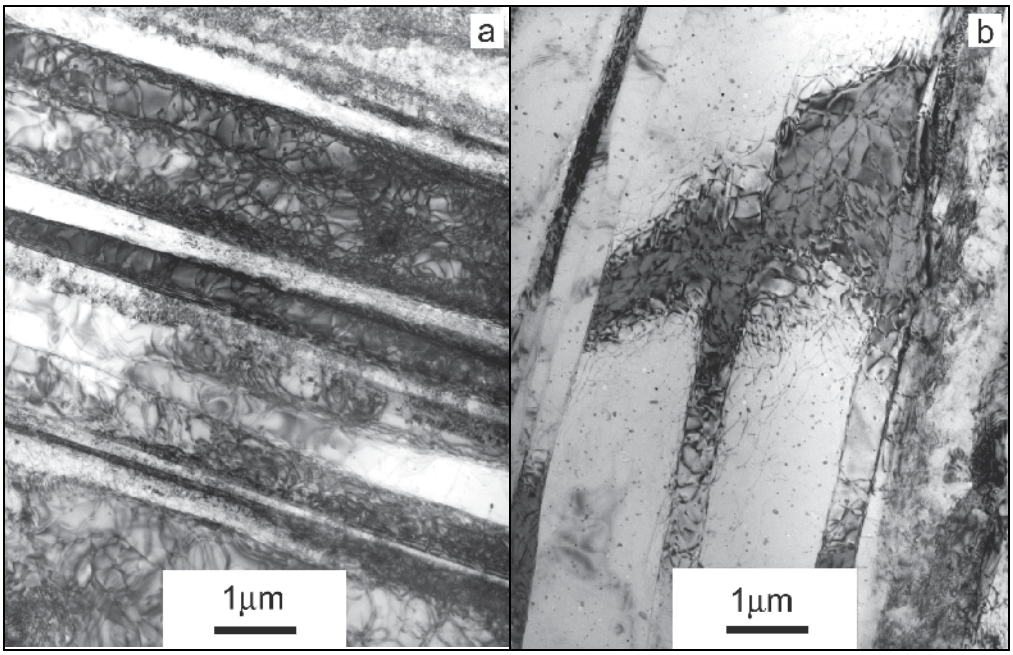

Fig. 5. Twinning in deformed AZ31 a) RT, b) 200°C (ε = 2.8%, T_{PR} = 475°C)

Serrated flow has been recently observed in an AZ91 alloy at room temperature by Corby (Corby et al, 2004). The authors discuss the possible mechanisms controlling plastic instabilities in this alloy suggesting some combined effect of both solutes - Al and Zn. The same mechanisms are probably in effect in the AZ31 alloy. Even lower concentrations of Al in AZ31 alloy as compared to AZ91 are high enough to ensure its role in the PLC effect formation. On the other hand, the concentration of Zn is the same in both alloys and therefore its enhancing effect on prismatic slip and consequently the forest dislocation formation remains unchanged in AZ31.

3.2 Ultra-fine grained AZ31

3.2.1 Mechanical properties and acoustic emission

Several techniques of severe plastic deformation were shown to result in significant grain refinement of coarse-grained polycrystals. Over recent years, equal channel angular pressing (ECAP) became one of the most popular methods of severe plastic deformation for producing bulk ultra-fine grained (UFG) metallic materials. This method leads to grain refinement due to shear deformation introduced into a work piece which is repeatedly pressed through an angular channel without changing its cross-sectional dimensions (Segal, 1995). Generally, this leads to improved mechanical properties, such as high strength and, at proper processing conditions, also to reasonable room temperature ductility (Valiev et al., 2000). At elevated temperatures, high strain rate superplastic behaviour can be achieved due to ECAP processing (Watanabe et al., 2003; Matsubara et al., 2003). Magnesium alloys with

their low density and high specific strength are of interest for many technical applications especially in the field of automotive industry. There is a strong demand to improve the mechanical properties of these materials to broaden their field of application. Depending on the targeted application, either a good combination of strength and ductility or a good superplastic formability is sought. Beneficial effects of ECAP on magnesium alloys have been demonstrated recently by many authors, e.g. (Mabuchi et al, 1997; Kim et al., 2003; Yoshida et al., 2004). Various ECAP conditions were also investigated. Grain refinement and deformation twins after ECAP processing in the temperature range of 200–250°C were observed (Kamado et al., 2000; Mukai et al, 2001; Agnew et al., 2001). Furthermore, recrystallisation was found to occur above 200°C by Kamado et al. (Kamado et al., 2000). Average grain size of 1μm after eight passes of ECAP by route B_C at 200°C was reported in (Mukai et al, 2001). Agnew (Agnew et al., 2001) conducted ECAP of AZ31 at 300°C because they experienced cracking of samples at a low temperature of 200°C. They neither found any significant grain refinement nor a change in the tensile properties at 300°C.

For ECAP processing of Mg alloys with their hcp crystal structure, elevated pressing temperatures are necessary to activate a sufficient number of slip systems (Ishikawa et al., 2005). To avoid excessive dynamic recrystallization during ECAP, the processing temperature should be chosen carefully, however.

AE from the magnesium alloy AZ31B alloy was first investigated by (Friesel & Carpenter, 1984). In their investigation dislocation glide and deformation twinning were identified as main sources of AE. Due to the lack of experimental data on AE in UFG Mg alloys we performed a detail investigation of the AE behaviour of ECAP processed AZ31 at different temperatures in compression tests and compare these results with those for the material that did not undergo the ECAP processing.

A squeeze-cast magnesium alloy AZ31 having an initial grain size of approximately 450μm was used as the initial material. The specimens after one and four passes of ECAP were used in this investigation and compared with the as squeeze-cast material. ECAP was performed at 200°C following route B_C and the pressing speed of 15 mm/min was used.

Compression tests at a strain rate of 10^{-3} s^{-1} on specimens of ECAP processed material and the reference, not pre-strained material, were performed on an Instron 4507 universal testing machine at room temperature as well as at 200°C and 300°C. The hardening behaviour for the ECAP processed and the as cast material was also evaluated from true stress versus true strain curves at different temperatures. Except for room temperature tests of the ECAP processed specimens, the strain hardening coefficient was determined up to a true strain of 0.1. As early buckling was observed in ECAP processed AZ31 in room temperature tests, only true strains up to approximately 0.02–0.03 depending on the specimen behaviour were used to determine the strain hardening coefficient.

AE was measured during compression testing. As the transducer could not withstand high temperatures, it was not possible to measure AE inside the furnace for the tests at 200°C and 300°C. Therefore, as a general setup, a waveguide was used to route the signals to the transducer that was fixed outside the furnace. After preamplification, the AE signal was analysed with the Dakel XEDO-3 AE system.

Microstructure evolution with strain due to ECAP and after the compression deformation at various temperatures was observed by TEM.

After ECAP an inhomogeneous structure was found. The typical microstructure after one pass of ECAP is presented on the TEM micrograph in Fig. 6. It is a typical heavily deformed structure with high density of homogeneously distributed dislocations, cf. Fig. 6a. Several

bands of parallel elongated subgrains passing through the whole transparent area of the thin foil were also found in the specimen, cf. Fig. 6b. With further pressing the first grains having sharp boundaries and high misorientation started to be formed. However, the grain structures were not homogeneous. Rather, a mixed structure of coarse and fine grains was observed. Figure 7 shows an example of such a zone with grains. Some grains contained no dislocations whereas in others dislocations were clearly seen. The presence of dislocations in some recrystallized grains is probably due to large strain imposed by ECAP. The average size of bigger grains was 1-3 μm, while that of smaller grains varied from 500 to 800 nm. Fine grains of 100 nm were also found in the specimen. Besides zones with clearly formed grains, which were observed in approximately 80% of the transparent areas of the specimen, the specimen contained regions of heavily deformed structure similar to that after one pass of ECAP.

Microstructure changes due to deformation are presented only for the highest temperature (300°C). TEM micrographs of both specimens (after 1 and 4 passes of ECAP) are presented in Fig. 8. In order to demonstrate the influence of temperature, all specimens were deformed to the same level of compressive strain of approximately 1%. It is clearly seen that dynamic recrystallization occurs during the compression test. However, the final microstructure is rather inhomogeneous with respect to the direction of ECAP pressing before straining. A clear influence of strain imposed by ECAP pressing is also seen. Figure 8a presents the microstructure of the specimen after 1 pass taken from the cross-section plane (X). Deformed structure with high density of heterogeneously distributed dislocations was observed in this specimen. Dislocation or cell wall formation was often observed. Only very few recrystallized grains were found in this specimen. By contrast, in the deformed specimen after 4 passes of ECAP only recrystallized grains of the average size of several micrometers

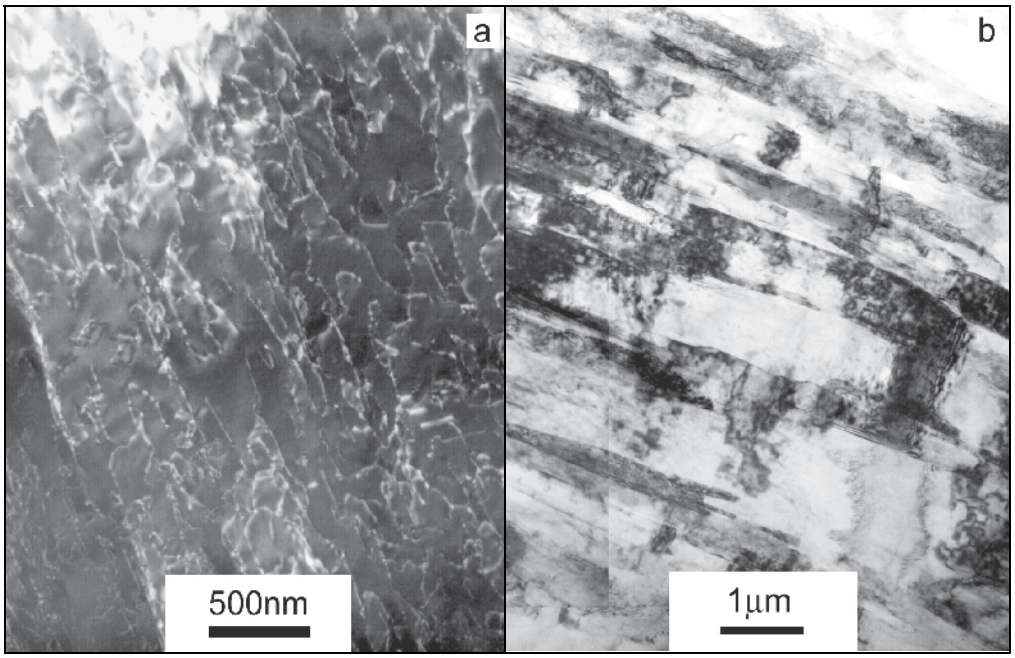

Fig. 6. The microstructure of AZ31 alloy after 1 pass of ECAP (X plane), a) dislocations – Weak beam dark field , B=[1-2.0], g=(-10.1), b) subgrains, B=[1-2.0], g=(10.0]

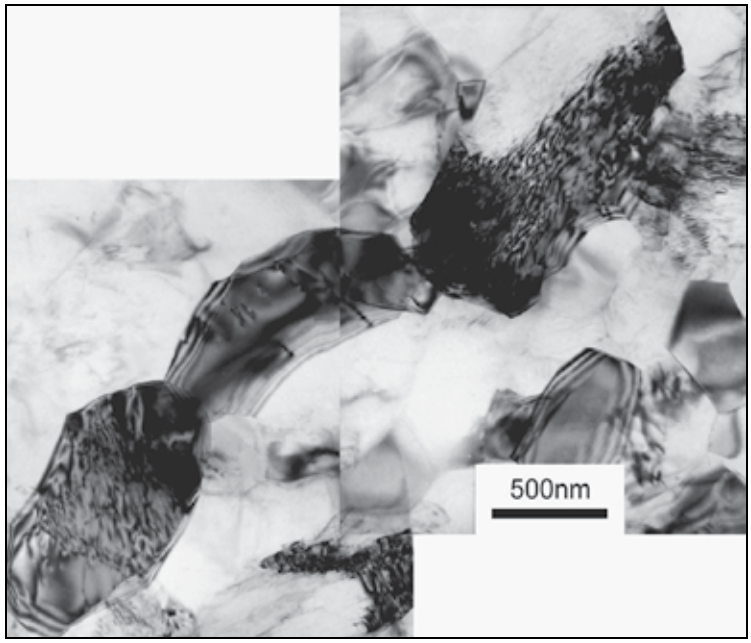

Fig. 7. TEM micrograph of the specimen after 4 passes of ECAP

were observed, as seen in Fig. 8b. The size of several grains (not shown in the micrograph) even exceeded 10 μm. Some grains contained dislocations, while others did not. The heterogeneity of the deformed structure of the specimen after 1 pass of ECAP is obvious from the micrographs in Figs. 8a and 8c. Figure 8c shows the microstructure of this specimen in the longitudinal plane (Y). The microstructure consists of recrystallized grains of the average size of approximately 1 μm with some dislocations within the grains. By contrast, no significant heterogeneity of the microstructure was found in the deformed specimen after 4 passes of ECAP. In Fig. 8d the microstructure of the deformed specimen in the longitudinal plane is shown. Fully recrystallized structure very similar to that in the cross-section plane is seen. The average size of dynamically recrystallized grains increases with increasing strain imposed by ECAP.

Mechanical properties during compression tests are presented in Fig. 9. It shows the temperature dependence of the yield stress of an as cast specimen and the specimens after 1 and 4 passes of ECAP. ECAP pressing resulted in significant increase of the yield stress as measured by compression tests. The as-received alloy (after squeeze-casting, marked 0P) deformed at room temperature (RT) had a yield stress of 65 MPa. After 1 ECAP pass the yield stress increased to 120 MPa whereas after 4 passes the yield stress reached 210 MPa, which is about three times larger than that of the as cast specimen and twice as large as that for the specimen after 1 ECAP pass. Two temperature regions were found in the as cast specimen and the specimen after one ECAP pass. In the low temperature region ($T < 200°C$) the yield stress was almost independent of the temperature or decreased only slightly with the temperature. At higher temperatures ($T>200°C$) the yield stress decreased with increasing temperature. In the specimen after 4 passes of ECAP the yield stress decreased with increasing temperature in the whole temperature region at a much higher rate and at 300°C it reached the lowest value of all three specimens tested. The

analysis of complete stress-strain curves showed that at low temperatures the alloy exhibited a limited ductility.
Enhanced ductility exceeding 40% was observed at elevated temperatures (> 200°C). Both the yield stress and the ultimate strength decreased with increasing temperature. However, only incomplete tests could have been performed on specimens after ECAP. Due to limited dimensions of the test billets (15 mm in height) the tests had to be stopped before the ultimate stress was reached (usually at the specimen height of 3-5 mm) and no data on the temperature dependence of the ultimate strength and the ductility are therefore available.
AE measurements during compression tests were performed at various temperatures and in as cast and two ECAPed specimens.
Fig. 10 shows the compression test results for squeeze-cast AZ31 at various temperatures (room temperature, 200°C and 300°C) together with the detected AE recordings. The yield strength decreases while the ductility increases with temperature, which is not surprising. The AE count rates exhibit a characteristic maximum related to the macroscopic yield point, which is followed by an AE activity with slowly decreasing count rate values. This behaviour lasts until fracture. The AE signals are very strong for all three conditions; they even rise at elevated temperatures, being strongest at 200°C. A similar observation was made by (Máthis et al., 2004) for an AM 50 alloy, where an even more pronounced effect was seen.
Fig. 11 shows the results for ECAP deformed squeeze-cast AZ31 tested in compression at room temperature. As expected, the yield strength is seen to increase significantly already after a single ECAP pass. Further increase was observed after four passes (4 P). The shape of the AE count rate versus strain curves is very similar to that for the squeeze-cast alloy (0 P). The AE activity of the single pass (1 P) specimen at room temperature is almost identical to that of the non-ECAPed AZ31 suggesting that the mechanisms responsible for AE are the same in these two conditions. This is different for the 4 P specimen, which already had a pronounced ultra-fine grained structure. The AE activity is about a factor of 10 lower than in the previous case, which indicates a significant influence of the microstructure on the AE mechanisms.
The AE behaviour of the ECAPed specimens at 200°C is presented in Fig. 12. For 1 P specimen the same effect can be seen as the one observed for the non-ECAPed specimens. The AE activity sustains up to significantly higher strains than in the case of room temperature compression. This again confirms the similarity of the AE behaviour of non-ECAPed and 1 P specimens. For the 4 P specimen only a very weak AE signal could be detected at 200°C. This indicates that a change in the deformation processes has taken place.
The compression tests at 200°C on ECAPed specimens do not show any surprising results: a significant decrease in yield strength was observed for 4 P specimen, which was less pronounced for 1 P specimen.
The AE behaviour of the ECAPed specimens at 200°C is presented in Fig. 12. For 1 P specimen the same effect can be seen as the one observed for the non-ECAPed specimens. The AE activity sustains up to significantly higher strains than in the case of room temperature compression. This again confirms the similarity of the AE behaviour of non-ECAPed and 1 P specimens. For the 4 P specimen only a very weak AE signal could be detected at 200°C. This indicates that a change in the deformation processes has taken place.

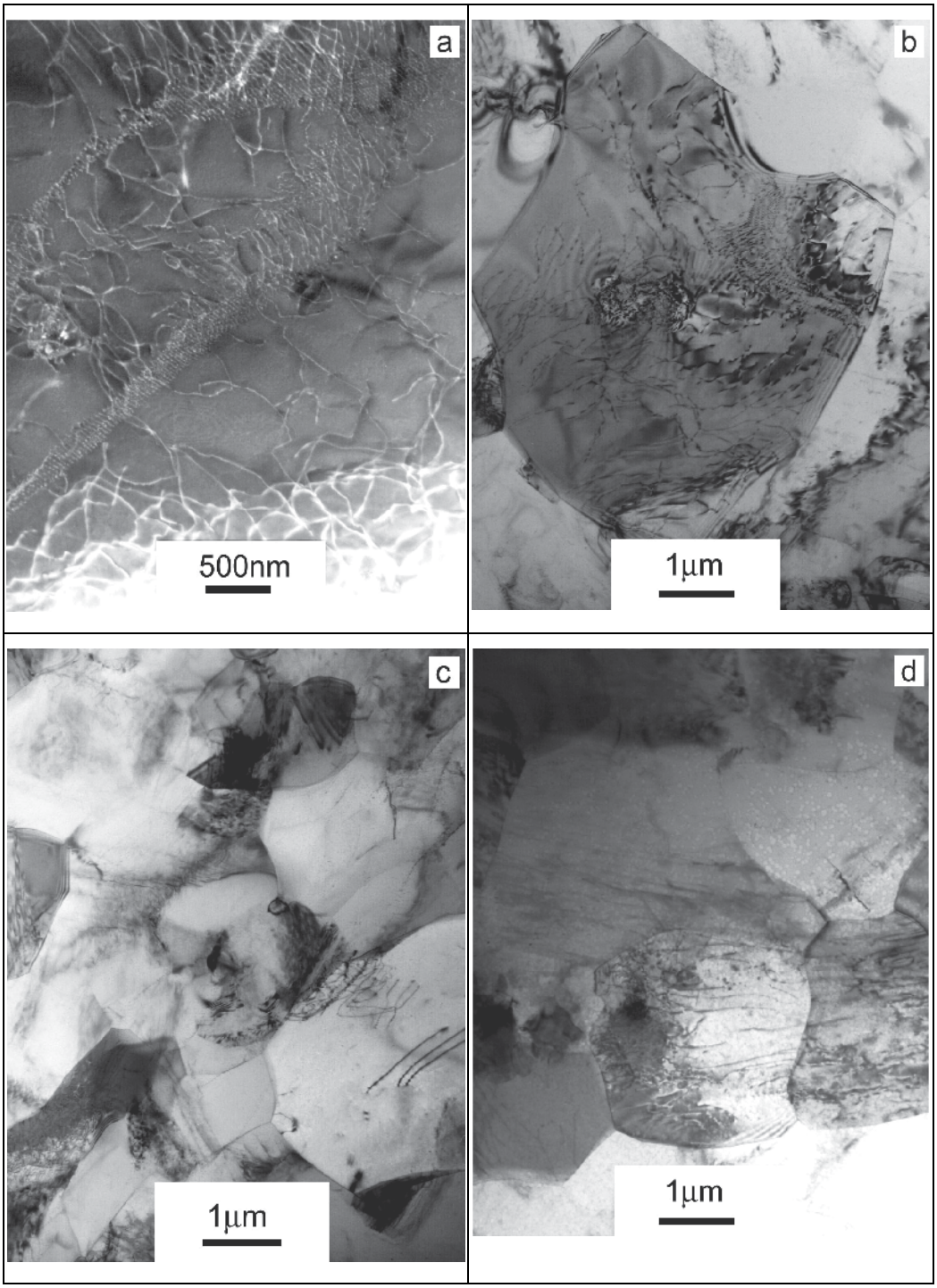

Fig. 8. The microstructure changes in the deformed specimen at 300°C, a) 1 pass, X plane, b) 4 passes, X plane, c) 1 pass, Y plane, d) 4 passes Y plane

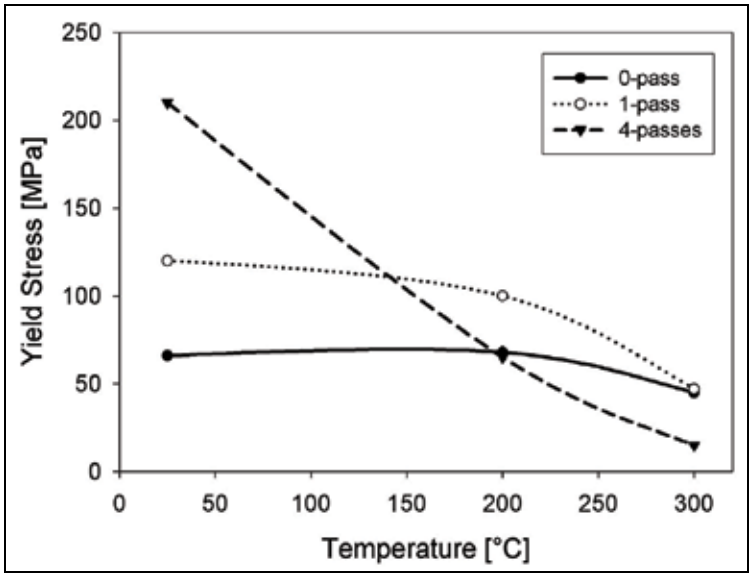

Fig. 9. The yield stress of the non-deformed AZ31 and AZ31 after ECAP at different temperatures

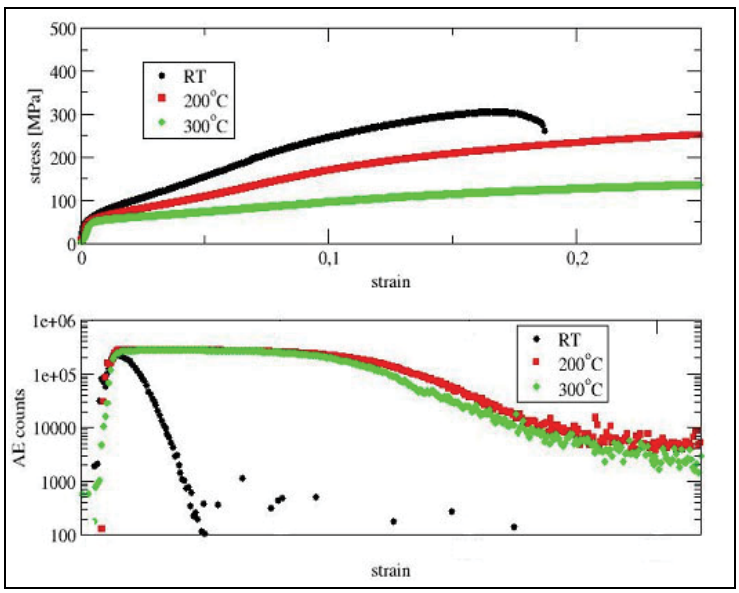

Fig. 10. Compressive true stress–true strain curves vis-à-vis AE at 3 different temperatures for as-cast AZ31. The scale of strain is the same in both figures

The compression tests at 200°C on ECAPed specimens do not show any surprising results: a significant decrease in yield strength was observed for 4 P specimen, which was less pronounced for 1 P specimen.

The AE behaviour of the ECAP processed specimens under subsequent compression at 300°C is shown in Fig. 13. For 1 P specimen, a strong decrease in AE counts was observed

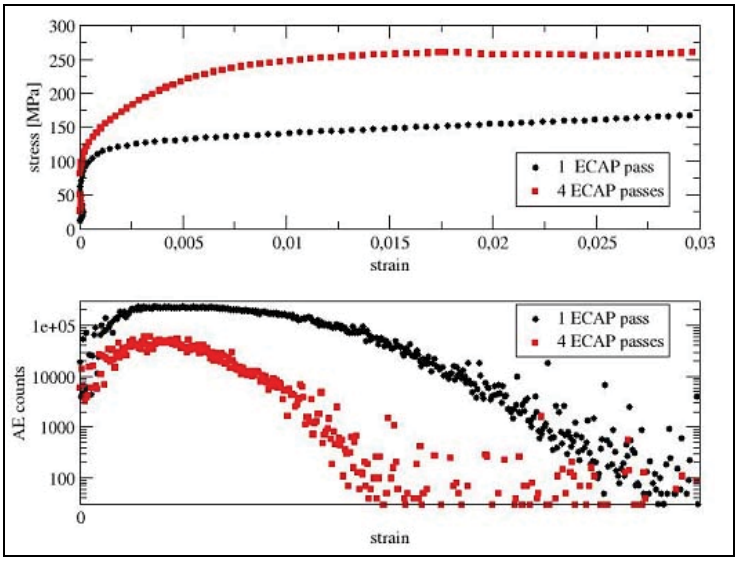

Fig. 11. Compressive true stress–true strain curves vis-à-vis AE at room temperature for ECAP processed specimens (1 and 4P). The scale of strain is the same in both figures

for larger strains, as distinct from the behaviour found for the non-ECAPed deformed material. The 4 P specimen exhibits almost no AE, which confirms the tendency already observed in compression tests at 200°C. With further increase of temperature, at 300°C, the yield strength dropped to very low values around 50MPa (1 P) and 15MPa (4 P).

AE signals correlate well with microstructure processes operating during ECAP straining and/or following compression deformation.

At room temperature compression, the AE is most likely caused by dislocation avalanches produced by dislocation slip as well as twinning (Heiple & Carpenter, 1987). The AE peak at the yield point can be attributed to massive dislocation multiplication accompanied with twinning. With increasing strain the multiplication of forest dislocations decreases the AE count rate by reducing the flight distance of moving dislocations. During deformation of the coarse grained specimens persisting twinning is commonly observed (Barnett et al., 2004). That is why the decrease of the AE activity in AZ31 is less pronounced than, e.g., in Al alloys (Heiple & Carpenter, 1987). The explanation of the observed increase of the AE count rate with increasing temperature which was also reported in other alloys (e.g., Máthis et al., 2004) is still ambiguous. One of possible interpretations of this effect is the interplay between twinning and dislocation glide under conditions of enhanced recovery. This may explain the AE behaviour observed at 200°C and 300°C. The slightly lower AE at 300°C could be a result of a less pronounced effect of twinning at this high temperature, while collective dislocation motion is still operative (Máthis et al., 2004). Starting at about 200°C dislocation motion is also activated on non-basal slip planes, which is further facilitated at 300°C (Polmear, 1992). Therefore, twinning becomes less important and, consequently, the overall AE activity is reduced.

In 1 P ECAPed specimen the AE curves were almost identical with those of the non-ECAPed material. Our TEM observations may contribute to the explanation of this behaviour. In 1P ECAPed specimen a significant portion of the original coarse grain microstructure was still

retained. Therefore the AE behaviour of 1 P specimen showed similarity with the non-ECAPed material. In 4 P specimen a new grain structure was observed by TEM. In particular, in 4 P specimen deformed at 200°C almost fully recrystallized structure with an average grain size of about 800 nm was found. The fine grain structure leads to a smaller mean free path of gliding dislocations. Moreover, it suppresses the propensity for twinning, which reduces the AE count rate (Kiesewetter & Schiller, 1976). All this can explain the generally lower AE activity observed in specimens after 4 ECAP passes.

At 200°C compression, a significantly (about one order) reduced AE activity at higher strains in 1 P ECAPed specimen as compared to the non-ECAPed specimen is probably caused by reduced contribution of collective dislocation motion and/or twinning In 4 P specimen only a very low AE signal was detected which further support the assumption of reduced dislocation motion or twinning. As the 4 P pass material has a recrystallized ultra-fine grained structure, dynamic recrystallization must have occurred during subsequent compression testing. Obviously, the recrystallization reduces the amount of twinning and collective dislocation motion (as manifested in reduced AE activity), most likely owing to elimination of stress concentration sites necessary to initiate the above processes.

At 300°C compression, the collective dislocation glide in 1 P ECAPed specimens concurs with dynamic recrystallization taking place during compression testing. TEM investigations revealed an inhomogeneous structure, which contains recrystallized grains of 1μm in diameter in one direction co-existing with a deformed microstructure containing a high density of heterogeneously distributed dislocations. No signs of twinning were seen in the TEM pictures. This is in agreement with a strongly reduced AE activity measured in these specimens. The structure of the 4 P ECAPed specimens after compression tests showed a fully recrystallized microstructure with a grain size ranging from 1 μm to 10μm. Again, owing to the initial ultra-fine grained recrystallized structure that existed prior to the compression test, no AE activity whatsoever was detected.

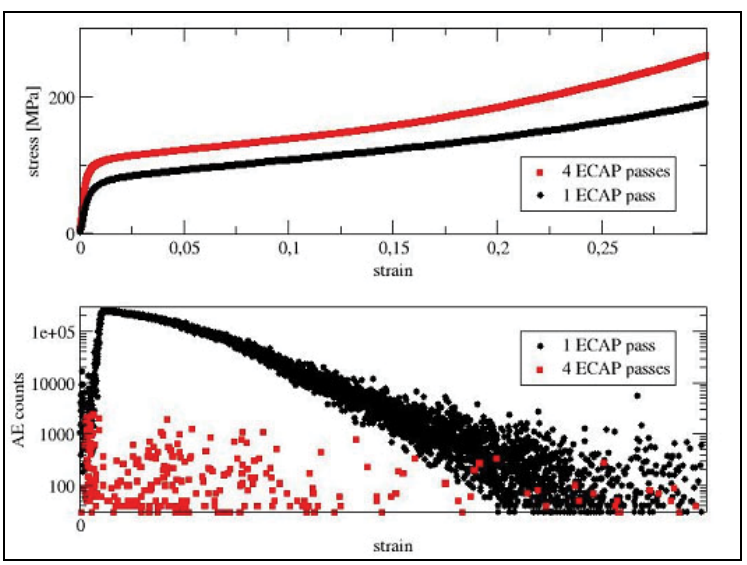

Fig. 12. Compressive true stress–true strain curves vis-à-vis AE at 200°C for ECAPed specimens. The scale of strain is the same in both figures.

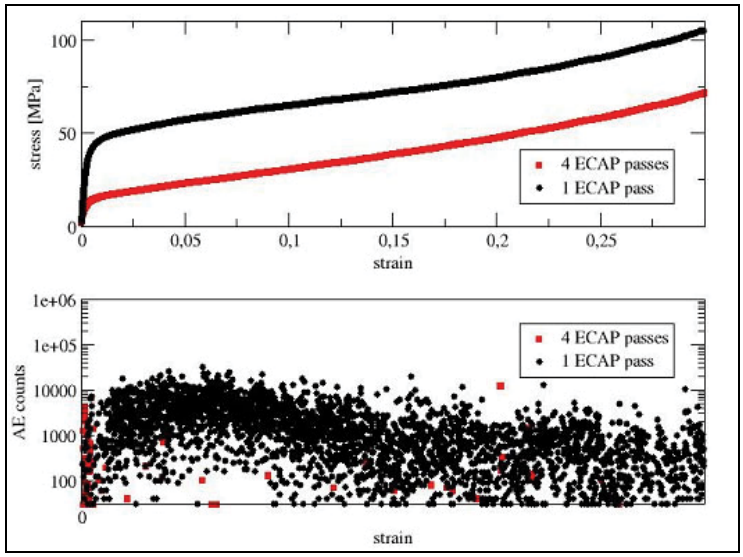

Fig. 13. Compressive true stress–true strain curves vis-à-vis AE at 300°C for ECAPed specimens. The scale of strain is the same in both figures.

3.2.2 Microstructure and texture evolution

As cast AZ31 alloy was processed by equal channel angular pressing (ECAP) at 180°C following route B_c resulting in a maximum equivalent strain of 12 (1, 2, 4, 8 and 12 passes). Prior to ECAP, the specimens were extruded at T = 350°C with extrusion ratio ER = 22. The texture of the extruded and the ECAPed samples was analyzed by the electron backscatter diffraction (EBSD). Samples for EBSD measurements were cut from ECAPed billets from the plane perpendicular to the pressing direction (plane X). EBSD scans were carried out at the mid-part of the cross-section of each billet.

The microstructure of the initial extruded bar (0P) shown in Fig. 14 consists of large grains of 50 ~ 100μm and relatively fine grains of 2 ~ 5μm around the large ones. Most grains have their crystallographic c-axis perpendicular to the extrusion direction (ED), i.e. <10-10> axes parallel to the ED, which is typically found after extrusion of Mg alloys.

Fig. 15 presents the microstructure and texture of sample after 1 ECAP pass (1P). Sample coordinate system, i.e. X–Y–Z directions, which is used for representing the textures are illustrated in Fig. 15d. As shown in Fig. 15a, the bimodal distribution of grain sizes is still observed in the 1P sample. A new texture component, which corresponds to the basal poles rotated about 40° from the initial orientation towards the pressing direction, is visible in the 1P sample, Fig. 15b. This mechanism caused by the shear strain imposed by ECAP was also reported by other authors (Estrin, 2008). However, the mentioned orientation change is observed mainly in large grains (grain size of 10 μm). Figure 15c presents the (0001) pole figure of grains smaller than 3 μm in the 1P sample. The intensity of the tilted basal poles is rather weak compared to the pole figure constructed using all grains. Moreover, the small grains (< 3 μm) with the tilted basal pole are found mainly in neighbouring areas around large grains. These results regarding distinct textures depending on the grain sizes indicate that the shear strain by the first ECAP pass is mainly accommodated within the large grains. It corresponds well to the fact that larger grains are deformed by lower energy comparing to

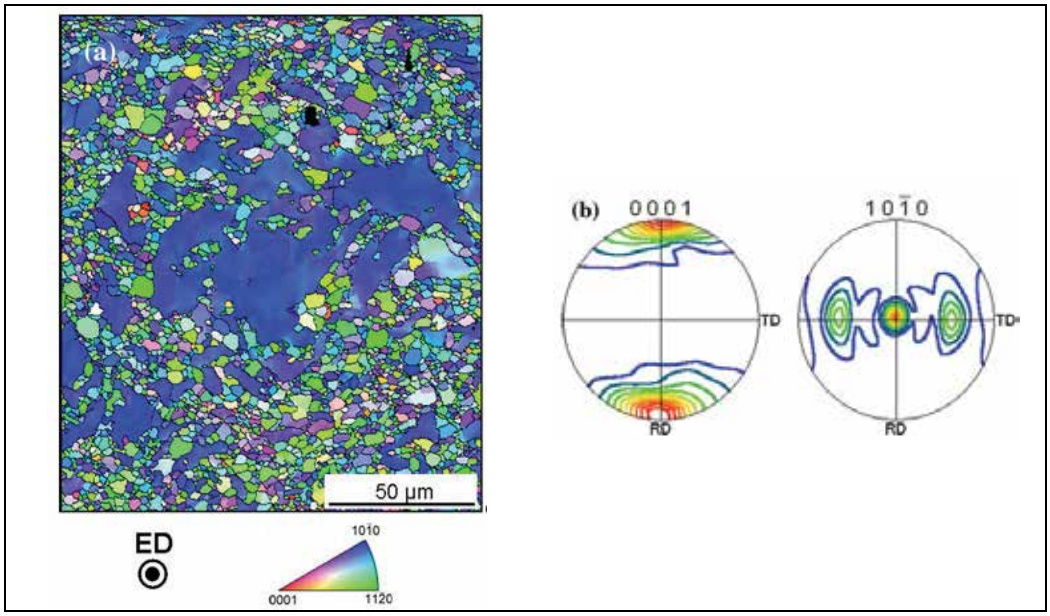

Fig. 14. (a) - EBSD orientation map, (b) - recalculated pole figures of the extruded bar (0P), measured at the cross-section transverse to the extrusion direction (contour level = 1, 2, ...10)

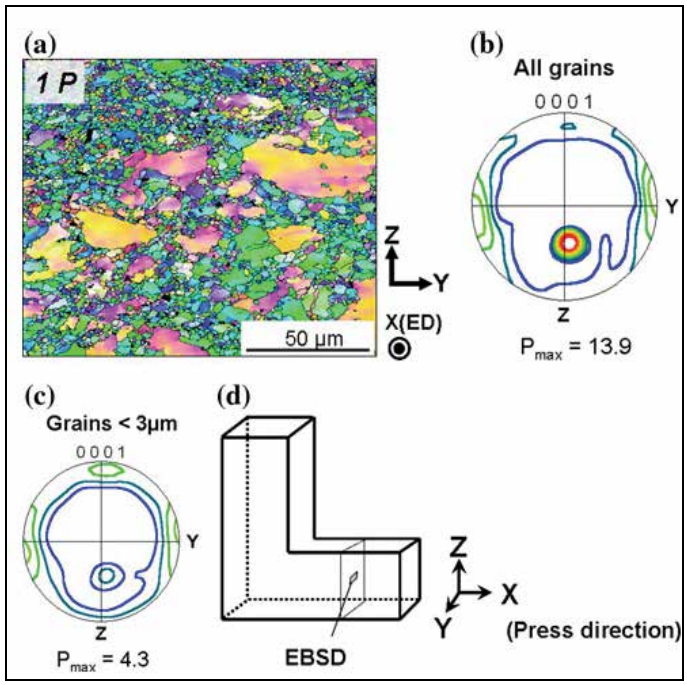

Fig. 15. (a) - EBSD orientation map of the sample after 1 ECAP pass, (b) - (0001) pole figure calculated using all grains, (c) - (0001) pole figure of grains smaller than 3 µm and (d) - the scheme of the geometry of specimens for EBSD measurements (contour level = 1, 2, … 10)

the small grains, e.g. Hall–Petch relation. The discontinuity of material flow caused by the inhomogeneous deformation seems to be compensated by the occurrence of the dynamic recrystallisation in the vicinity of grain boundaries of large grains, such that the sample could be deformed without failure. Microstructural features of the sample after 2 ECAP passes are very similar to those after 1 ECAP pass, i.e. the bimodal distribution of grain sizes and the orientation change in large grains remain almost unchanged.

The amount of large grains decreases significantly after 4 ECAP passes (4P), and their size becomes smaller when compared to the initial and the 1P samples. Moreover, fine grains were observed mainly near grain boundaries of large grains. It indicates that the refinement of large grains occurs gradually with increasing strain due to ECAP by dynamic rotation mechanism suggested by (Ion, et al., 1982). Differently to the 1P sample, the fine grains (<3 μm) have mainly the orientation of the rotated basal poles in the 4P sample, Fig. 16a. Comparing pole figures evaluated from the whole area of the EBSD measurement to that from fine grains (<3 μm) Fig. 16a and b, indicates unambiguously that the texture heterogeneity depending on the grain size disappears after 4 ECAP passes.

The 12P sample, Fig. 17, shows the homogeneous distribution of fine almost equiaxed grains, i.e. no large grains are visible. Fig. 17a shows grain agglomerates, having different colours, distributed along a diagonal line. This indicates the heterogeneity in texture depending on the

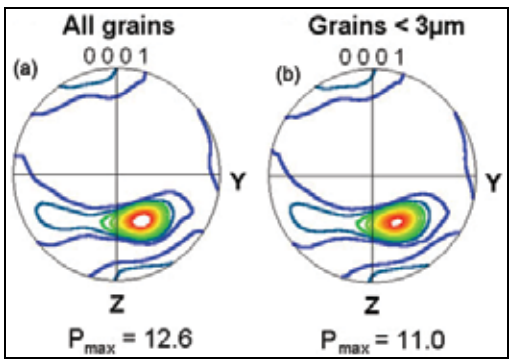

Fig. 16. (a) - (0001) pole figure of all grains and (b) - grains smaller than 3 μm (contour level = 1, 2, … 10)

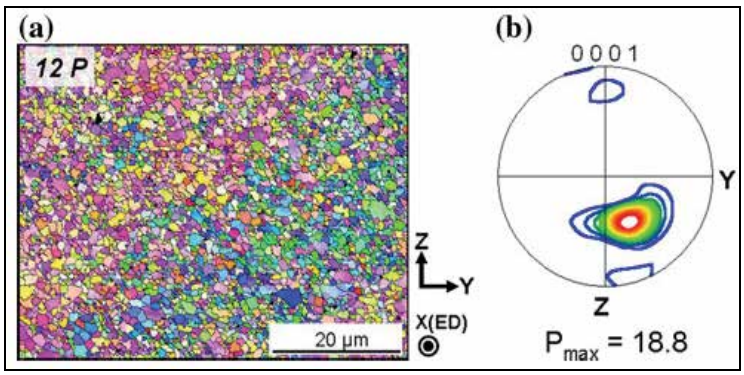

Fig. 17. (a) - EBSD orientation map and (b) - (0001) pole figure of the sample after 12 ECAP passes (contour level = 1, 2, … 15)

locations. This texture inhomogeneity can be understood as a result of non-uniform deformation along the ECAP billet after multiple passes (Agnew et al, 2005) Though the heterogeneous texture is visible, the fraction of the grains relating to the inhomogeneity is small such that the main texture component is found at the rotated basal pole, Fig. 17b.

3.3 Mechanical and fatigue properties of cast and wrought AZ31 alloy

Sufficient fatigue resistance is an important requirement on engineering materials used for components subjected to cyclic loading. The demand for improving the efficiency of automotive vehicles, particularly by weight reduction, results in tougher requirements on fatigue resistance of Mg alloys as candidate materials for automotive parts. To that end, a better knowledge of fatigue behavior and damage processes in relation to the microstructure of Mg alloys is necessary. Microstructure and mechanical properties strongly depend on the method of processing.

AZ31 alloy is often produced as a high pressure cast material, because it exhibits excellent castability. Squeeze casting (SC) consisting of two casting steps is one of the most frequently applied procedures. Wrought AZ31 alloy have had a much more limited use than the high-pressure die castings. To date, the knowledge of the fatigue behavior of wrought alloys is surprisingly limited.

Conventional AZ31 alloy was prepared by three different processing techniques: squeeze casting at 200°C employing a two step loading process, hot rolling (HR) at 370°C and 4 pass route B_C ECAP pressing of the HR material at 200°C. The microstructure of these materials was investigated by (Zúberová et al., 2007). SC alloy has a typical dendritic structure comprising large grains of 450 μm. HR material exhibited a homogeneous structure with grains in the range of 3 to 20 μm while ECAP specimen consisted of almost equiaxed grain with average size of 1 to 2 μm.

A comparison of the tensile stress-strain curves for all three materials is shown in Figure 18 and summarized in Table 1.

As expected the ductility was found to increase with grain refinement (from SC over HR to ECAP). The improved ductility of ECAP specimen with respect to HR one may be explained by texture development that occurs during ECAP (see the section 3.2.2). For Mg alloys, basal planes tend to lie parallel to the extrusion direction after extrusion, indicating that slip on the basal plane becomes difficult and the strength increases due to limited nonbasal slip activity (Kim et al, 2005). The enhancement of tensile ductility after ECAP could be a result of large strain hardening after yielding, in addition to the aforementioned texture effect.

Enhanced hardening may be attributed to the activation of two or more slip planes as a consequence of rotation of slip planes during ECAP (Kim et al, 2005).

The experimentally determined fatigue life of squeeze cast, hot-rolled, and ECAP-processed AZ31 alloy is shown in Figure 19. It can be seen that there is a strong influence of the production procedure on the fatigue properties. The SC material exhibits the lowest fatigue strength of approximately 40 MPa. HR improves the fatigue life substantially, while ECAP exhibits slightly worse fatigue behaviour. However, in the high-cycle region both HR and ECAP exhibit the same fatigue strength of 95 MPa. An increase of fatigue strength is very often related to grain size reduction. The explanation can be sought in inhibited crack initiation and in an increase of the number of barriers to early crack propagation. Smaller grains also tend to inhibit dislocation motion. Our finding that severe plastic deformation of

hot-rolled AZ31 by ECAP does not result in any improvement of fatigue life suggests that a reduction in strength associated with the texture effects (as seen for monotonic deformation (Somekawa & Mukai, 2006) may counterbalance concurrent strengthening due to grain refinement. ECAP is also known to change the character of grain boundaries which may also affect the tensile strength.

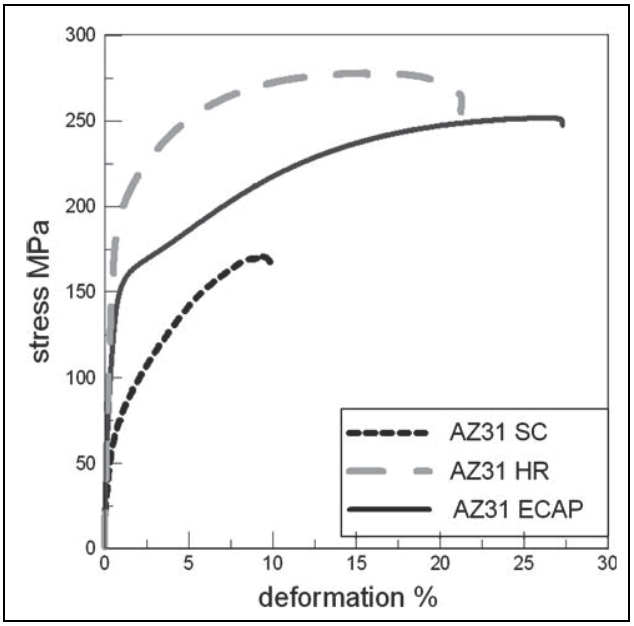

Fig. 18. Tensile curves of AZ31 alloy in SC, HR and ECAP condition

AZ31	YS (MPa)	UTS (MPa)	Ductility (%)	Endurance limit (MPa)
SC	50	170	10	40
HR	175	277	21	95
ECAP	175	251	27	95

Table 1. Tensile and fatigue properties of AZ31 alloy

4. Summary and conclusions

4.1 Hot rolled AZ31

- The ductility of hot-rolled AZ31 alloy increases significantly with the deformation temperature and with the preheating temperature.
- Serrated yielding (PLC effect) was observed in a hot-rolled AZ31 alloy at all deformation temperatures and strain rates.
- Twinning characterized by a compound mode with differently oriented twins intersecting each other is the dominant mechanism in the initial stage of deformation.

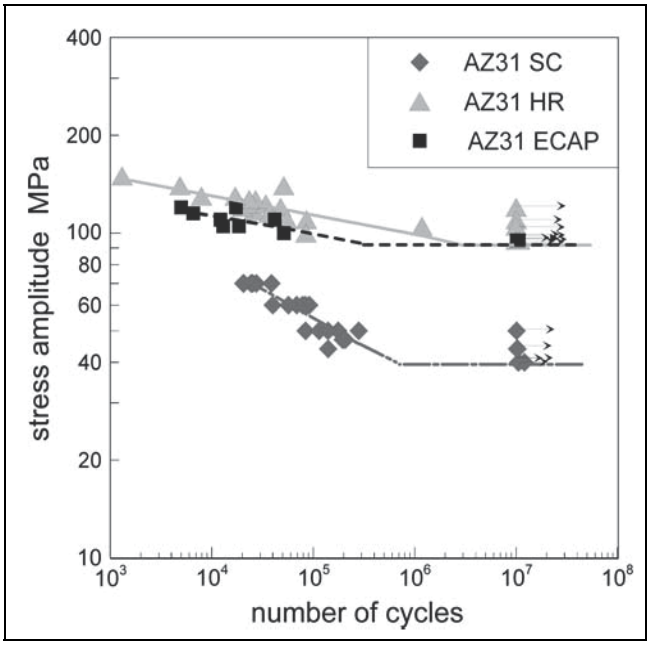

Fig. 19. Comparison of fatigue life in SC, HR and ECAP conditions

- Total AE activity is a result of interplay of different effects, mainly twinning and PLC effect. The challenge for the future is to separate the respective AE bursts.
- Strong anisotropy of mechanical properties was found in the extruded alloy. Much weaker anisotropy was found in the cast alloy. After rolling the anisotropy was smeared out.
- The temperature of 350°C seems to be the optimum preheating temperature for attaining the best mechanical properties of hot rolled sheets both from the extruded and the cast material.
- Significant strain hardening due to twinning occurs during room temperature deformation of hot-rolled specimens.
- Significant grain refinement was found after rolling. The temperature of preheating influences the final rolled structure, which tends to coarsen with increasing T.
- Numerous cracks were observed in the cast alloy after rolling due to extensive porosity.
- dynamic recrystallisation occurs during rolling. The rate of dynamic recrystallisation is enhanced by the temperature of preheating.

4.2 Ultrafine-grained AZ31 processed by ECAP

a) Mechanical properties vis-à-vis AE

- As-cast AZ31 specimens exhibited strong AE at all testing temperatures, which can be explained as a result of collective dislocation motion and twinning.
- At room temperature and 200°C, a single pass ECAP processed specimen exhibited AE behaviour similar to that of the as-cast material. This can be rationalized as a result of an inhomogeneous microstructure containing residual coarse grained regions co-existing with regions of heavily deformed material with a high dislocation density.

- At 300°C the AE was significantly reduced due to the occurrence of dynamic recrystallization.
- Four pass ECAP processed specimens, with their ECAP induced recrystallized structure with a grain size of 800 nm, show a reduced AE activity already at room temperature. As this material exhibited dynamic recrystallization during compression tests at 200°C and 300°C, AE signals under these conditions were very weak if any.
- The average size of dynamically recrystallized grains increases with increasing strain imposed by ECAP.
- Dynamic recrystallization occurs during the deformation of ECAPed specimens at high temperatures.

b) Microstructure and texture evolution with strain due to ECAP

- The first pass (1P) of ECAP results in the formation of a new texture component inclined by about 40° relatively to the initial texture.
- The bimodal character of the microstructure remains unchanged up to 4P of ECAP.
- Further ECAP pressing (8 and 12P) results in a completely refined microstructure.
- The refinement of large grains occurs gradually with increasing ECAP passes by dynamic rotation recrystallization mechanism.
- The grain size was reduced by a factor of about 100–200 through ECAP processing.

4.3 Mechanical and fatigue properties of cast and wrought AZ31

- Mechanical properties of cast material are inferior to those of wrought alloy.
- Hot rolled and ECAPed alloy exhibited substantially higher ultimate tensile strength, fatigue life and endurance limit than cast alloy.
- Subsequent ECAP processing does not result in further improvement of fatigue properties of hot rolled alloy despite the marked grain refinement it produces, most probably due to the texture effects and a change in the character of grain boundaries.
- Control of complex interplay of all these factors poses a challenge to ''grain boundary engineering'' aimed at optimization of the alloy properties.

5. Acknowledgement

This work was financially supported through the research program MSM 0021620834 of Ministry of Education of the Czech Republic.

6. References

Agnew, S.R., Lillo, T.M., Macheret, J., Stoica, G.M., Chen, L., Lu, Y., Fielden, D., Liaw, P.K. (2001). Assessment of equal channel angular extrusion processing of magnesium alloys, *Proceedings of the Magnesium Technology Symposium,* pp. 243–247, New Orleans, Louisiana, February 11–15.

Agnew, S.R., Mehrotra, P., Lillo, T.M., Stoica, G.M., Liaw, P.K. (2005). Crystalographic texture evolution of three wrought magnesium alloys during equal channel angular extrusion, *Mater Sci Eng.,* A408, 72-78.

ASTM (1994). *Test Methods of Tension Testing Wrought and Cast Aluminium-and Magnesium-Alloy Products. Annual Book of ASTM Standards.* ASTM B 557-94 (1994). West Conshohocken, PA, ASTM International, vol. 02.02.

Barnett, M.R. , Keshavarz, Z., Beer, A.G., Atwell, D. (2004). Influence of grain size on the compressive deformation of wrought Mg-3Al-1Zn, *Acta Mater.,* 52, 5093–5103.

Bohlen, J., Chmelík, F., Dobroň, P., Kaiser, F., Letzig, D., Lukáč, P., Kainer, K.U. (2004). Orientation effects on acoustic emission during tensile deformation of hot rolled magnesium alloy AZ31, *J. Alloys Compd.*, 378, 207–213.

Botten, R., Wu, X., Hu, D., Loretto, M.H. (2001). The significance of acoustic emission during stressing of TiAl-based alloys. Part I: Detection of cracking during loading up in tension, *Acta Mater.*,49, 1687-1691.

Cáceres, C.H., Griffiths, J.R., Davidson, C.J., Newton, C.L. (2002). Effects of solidification rate and ageing on the microstructure and mechanical properties of AZ91 alloy, *Mater. Sci. Eng.,A 325*, 344–355.

Chmelík, F., Ziegenbein, A., Neuhäuser, H., Lukáč, P. (2002). Investigating the Portevin–Le Châtelier effect by the acoustic emission and laser extensometry techniques, *Mater. Sci. Eng,.* A 324, 200–207.

Corby, C., Cáceres, C.H., Lukáč, P. (2004). Serrated flow in magnesium alloy AZ91*Mater. Sci. Eng.* A387-389, 22-24.

Emley, E.F. (1996). *Principles of Magnesium Technology*, Pergamon Press, 978-0849355547, London.

Estrin, Y., Yi, S., Brokmeier, H.G., Zúberová, Z., Yoon, S.C., Kim, H.S., Hellmig, R.J. (2008). Microstructure, texture and mechanical properties of the magnesium alloy AZ31, *Int. J. Mater. Res.*, 99, 50-55

Friesel, M., Carpenter, S.H. (1984). Acoustic emision investigation during the deformation of pure Mg and AZ31B alloy. *J. Acoustic Emission,* 3, 11-17.

Heiple, C.R., Carpenter, S.H. (1987). Acoustic emission produced by deformation of metals and alloys, *J. Acoustic Emission*, 6, 215-237.

Ion, S.E., Humphreys, F.J., White, S.H. (1982). Dynamic recrystallization and the development of microstructure during the high temperature deformation of magnesium, *Acta Mater.*, 30, 1909-1919.

Ishikawa, K., Watanabe, H., Mukai, T. (2005). High temperature compressive properties over a wide range of strain rates in an AZ31 magnesium alloy, *J. Mater. Sci.,* 40, 1577–1582.

Kaiser, F., Letzig, D., Bohlen, J., Styczynski, A., Hartig, Ch., Kainer, K.U. (2003). Anisotropic Properties of Magnesium Sheet AZ31, *Mater. Sci. Forum,* 419–422, 315-320.

Kaiser, J. (1953). Erkenntnisse und Folgerungen aus der Messung von Geräuschen bei Zugbeanspruchung von Metallischen Werkstoffen*, Arch. Eisenhüttenwes., 24, 43-45.*

Kamado, S., Ashie, T., Yamada, H., Sanbun, K., Kojima, Y. (2000). Improvement of tensile properties of wrought magnesium alloys by grain refining, *Mater. Sci. Forum,* 350–351, 65–72.

Kiesewetter, N., Schiller, P. (1976). The acoustic emission from moving dislocations in aluminium, *Phys. Status Solidi,* (a) 38, 569–576.

Kim, H.K., Lee, Y.I., Chung, C.S. (2005), Fatigue properties of a fine-grained magnesium alloy produced by equal channel angular pressing, *Scripta Mater.,* 52, 473-77.

Kim, W.J., Hong, S.I., Kim, Y.S., Min, S.H., Jeong, H.T., Lee, J.D. (2003). Texture development and its effect on mechanical properties of an AZ61 Mg alloy fabricated by equal channel angular pressing, *Acta Mater.*, 51, 3293-3307.

Král, R., Dobroň, P., Chmelík, F., Koula, V., Rydlo, M., Janeček, M. (2007). A qualitatively new approach to acoustic emission measurements and its application to pure aluminium and Mg-Al alloys, *Kovove Mater.,* 45, 159-163.

Lamark, T.T., Chmelík, F., Estrin, Y., Lukáč P. (2004). Cyclic deformation of a magnesium alloy investigated by acoustic emission, *J. Alloys & Comp.*, 378, 202-206.

Mabuchi, M., Iwasaki, H., Yanase, K., Higashi, K. (1997), Low temperature superplasticity in an AZ91 magnesium alloy processed by ECAE, *Scripta Mater.*, 36, 681-686.

Máthis, K., F. Chmelík, F., Trojanová, Z., Lukáč, P., Lendvai, J. (2004). Investigation of some magnesium alloys by use of acoustic emission technique, *Mater. Sci. Eng.,* A 387–389, 331–335.

Máthis, K., Chmelík, F., Janeček, M., Hadzima, B., Trojanová, Z., Lukáč, P. (2006). Investigating deformation processes in AM60 magnesium alloy using the acoustic emission technique, *Acta Mater.,* 54, 5361.

Matsubara, K., Miyahara, Y., Horita, Z., Langdon, T.G. (2003). Developing superplasticity in a magnesium alloy through a combination of extrusion and ECAP, *Acta Mater.*, 51, 3073-3084.

Mukai, T., Yamanoi, M., Watanabe, H., Higashi, K. (2001). Ductility enhancement in AZ31 magnesium alloy by controlling its grain structure, *Scripta Mater.,* 45, 89–94.

Polmear, I.J. (1992), *Magnesium Alloys and Their Applications*, Mordike, B.L. , F. Hehmann F. (Eds.), , DGM, Oberursel, pp. 201

Richeton, T., Dobroň, P., Chmelík, F., Weiss, J., Louchet, F. (2006). On the critical character of plasticity in metallic single crystals, *Mater. Sci. Eng.,* A424, 190-195.

Segal, V.M. (1995). Materials processing by simple shear, *Mater. Sci. Eng.,* A197, 157.

Tan, J.C, Tan, M.J. (2002). Superplasticity in a rolled Mg-3Al-Zn alloy by two-stage deformation method, *Scripta Mater.,* 47, 101–106.

Somekawa, H., Mukai, T. (2006). Fracture thoughness in Mg-Al-Zn alloy processed by equal channel angular extrusion, *Scripta Mater.*, 54, 633-638.

Trojanová, Z., Cáceres, C. (2007). On the strain to the onset of serrated flow in AZ91 alloy, *Scripta Mater.,* 56, 793-796.

Valiev, R.Z., Islamgaliev R.K., Alexandrov, I.V. (2000), Bulk Nanostructured Materials from Severe Plastic Deformation, *Prog. Mater. Sci.*, 45, 103-189.

Vinogradov, A., Merson, D.,L., Patlan, V., Hashimoto, S. (2003). On the mechanism of unstable plastic flow in an austenitic FeMnC TWIP steel, *Mater. Sci. Eng.,* A341, 57-73.

Watanabe, H., Mukai, T., Ishikawa, K., Higashi, K. (2003). Superplastic behaviour of an ECAE processed ZK60 magnesium alloy, *Mater. Sci. Forum*, 419-422, 557-562.

Yin, D.L., Zhang, K.F., Wang, G.F., Han, W.B. (2005). Warm deformation behaviour of hot-rolled AZ31 Mg alloy, *Mater. Sci. Eng.,* A392, 320-325.

Yoshida, Y. , Arai, K., Itoh, S., Kamado, S., Kojima, Y. (2004). Superplastic deformation of AZ61 magnesium alloy having fine grains, *Mater. Trans.*, 45, 2537-2541.

Zhang, P., Watzinger, B., Kong, P.Q., Blum, W. (2000). Microstructural evolution during creep of Mg-Al alloy AZ91hp, *Key Eng. Mater.* 171–174, 609–616.

Zúberová, Z., Estrin, Y., Lamark, T.T., Janeček, M., Hellmig, R.J., Krieger, M. (2007), Effect of equal channel angular pressing on the deformation behaviour of magnesium alloy AZ31 under uniaxial compression, *Jour. Mat. Proc. Technol.*, 184, 294-299.

4

Thermo - Physical Properties of Iron - Magnesium Alloys

Krisztina Kádas[1,2], Hualei Zhang[1], Börje Johansson[1,3], Levente Vitos[1,2,3] and Rajeev Ahuja[1,3]
[1]*KTH Royal Institute of Technology*
[2]*Research Institute for Solid State Physics and Optics*
[3]*Uppsala University*
[1,3]*Sweden*
[2]*Hungary*

1. Introduction

According to the common phase diagrams, iron and magnesium are almost immiscible at ambient pressure Massalski (1986). In the liquid phase, the solubility of Mg in Fe is of the order of 0.025 atomic percent (at.%). The maximum solid solubility of Fe in Mg is 0.00041 at.% and the Fe content in Mg at the eutectic point is less than 0.008 at.% (Haitani et al., 2003). Below 1273 K the solubility of Mg in α-Fe is below the detection limit and about 0.25 at.% Mg can be solved in $\delta-$Fe at the monotectic temperature. The immiscibility of Fe and Mg at ambient conditions is in line with the well-known Hume-Rothery rules, according to which more than 15% atomic size difference between alloy constituents hinders solid solution formation (Massalski, 1996). In spite of the negligible solubility of Mg in Fe, several Fe-rich metastable Fe-Mg solid solution have been synthesized.
According to the pioneering work by Hightower *et al.* (Hightower et al., 1997), mechanical alloying produced Fe-Mg substitutional solid solutions with up to 20 at.% Mg and having the body centered cubic (bcc) crystallographic phase of α-Fe. Later, using the similar alloying procedure, Dorofeev *et al.* (Dorofeev et al., 2004; Yelsukov et al., 2005) found that about $5-7$ at.% Mg in α-Fe forms supersaturated solid solution. These authors suggested that the driving force for the formation of Fe-Mg solid solutions is associated with the excess energy of coherent interfaces in the Fe-Mg nanocomposite, which facilitates incorporation of Mg into α-Fe. Indeed, based on semiempirical thermodynamic calculations, Yelsukov *et al.* (Yelsukov et al., 2005) obtained 6 kJ/mol for the enthalpy of formation for Fe-Mg solid solutions, compared to 20 kJ/mol calculated for the corresponding Fe-Mg nanocomposites. In addition to the mechanical alloying techniques, pressure was also found to facilitate the solid solution formation between Fe and Mg. Dubrovinskaia *et al.* (Dubrovinskaia et al., 2004) reported that at pressures around 20 GPa and temperatures up to 2273 K, the solubility of Mg in bcc Fe was increased to 4 at.%. They found that the lattice parameter of the bcc Fe-Mg alloy increased approximately by 0.6 % per at.% Mg. Furthermore, recent experimental measurements in combination with theoretical simulations demonstrated that at the megabar pressure range more than 10 at.% Mg could be dissolved in liquid Fe, which then could be quenched to ambient conditions (Dubrovinskaia et al., 2005). The mechanism behind the

high-pressure alloying is the much larger compressibility of Mg compared to that of Fe.
Most of the theoretical and experimental investigations of the Fe-Mg solid solutions so far focused on the phase diagram, crystallographic structure, nanostructure, grain boundaries and segregation. However, much less is known about the mechanical properties of Fe-rich Fe-Mg alloys. Here we present a systematic first-principles study of the effect of Mg on the elastic properties of ferromagnetic bcc Fe-Mg alloys. We calculate the single-crystal and polycrystalline elastic parameters by using the all-electron exact muffin-tin orbitals method (Andersen et al., 1994; Vitos et al., 2000; Vitos, 2001) in combination with the coherent-potential approximation (Soven, 1967; Gyorffy, 1972; Vitos et al., 2001; Vitos, 2007). Since at ambient conditions, the Fe-rich Fe-Mg alloys were found to adopt the ferromagnetic bcc structure (Hightower et al., 1997; Dorofeev et al., 2004; Dubrovinskaia et al., 2005), all calculations are performed for this magnetic and crystallographic phase. Using Mösbauer spectroscopy, Hightower *et al.* (Hightower et al., 1997) found that bcc Fe-Mg alloys encompassing ~ 18 at.% Mg possess large chemical heterogeneities. According to that study only few Fe atoms have Mg atoms as first-nearest neighbors and the Mg atoms cluster into Fe-depleted zones on the bcc lattice. On the other hand, Dorofeev *et al.* (Dorofeev et al., 2004; Yelsukov et al., 2005) determined the effect of nearest neighbor and next nearest neighbor Mg atom on the hyperfine magnetic field of Fe nuclei in Fe-Mg alloys containing $5-7$ at.% Mg. Moreover, the $Fe_{0.96}Mg_{0.04}$ synthesized by Dubrovinskaia *et al.* (Dubrovinskaia et al., 2004) at high temperature and moderate pressures was reported to be homogeneous. It is also noticeable the excellent agreement obtained between the experimental and theoretical equation of states for $Fe_{0.96}Mg_{0.04}$, the latter obtained for completely random alloy (Dubrovinskaia et al., 2005). These findings indicate that clustering of Mg atoms is less significant in Fe-rich alloys. Because of that, we limit the present study to $Fe_{1-x}Mg_x$ alloys with $0 \leq x \leq 0.1$ and assume random distributions of the Mg atoms on the parent lattice.
In order to be able to assess the results obtained for Fe-Mg alloys at ambient condition, here we also present some results obtained for random $Fe_{1-x}Cr_x$ alloys with $0 \leq x \leq 0.1$. It is well-known that Fe-Cr constitute the basis for stainless steels. The Fe-Cr alloys, except the high temperature Fe-rich γ-phase and the σ-phase observed around equimolar concentrations, adopt the bcc structure (Hultgren et al., 1973). At normal operating temperatures, these bcc alloys are ferromagnetic with Curie temperatures around $900-1050$ K (Hultgren et al., 1973). For $x \lesssim 0.1$ and $T \gtrsim 600$ K, the Fe-Cr system is fully miscible, whereas the nucleation or spinodal (α') decomposition driven clustering occurs at higher Cr concentrations (Tavaresa et al., 2001; Cieslak et al., 2000). Nevertheless, it has been shown (Olsson et al., 2003; 2006) that the energetics of Fe-Cr alloys with $\lesssim 20$ at.% Cr are well described using the substitutional disordered ferromagnetic bcc phase.
The composition and the structure of the Earth's solid inner core are still unknown. The core is considered to be made of iron-rich alloys containing 5-15% nickel (Anderson, 1989) and one or more light elements (McDonough, 2003). Based on seismic observations, different models have been constructed to describe the physical properties of the Earth's interior. The most widely accepted of these models is the "Preliminary Reference Earth Model" (PREM, (Dziewonski & Anderson, 1981)), which provides the radial distribution of elastic properties, seismic quality factors and densities. The physical properties of pure iron at core conditions have been extensively studied both experimentally (Singh et al., 1998; Mao et al., 1998; Dubrovinsky et al., 2000) and theoretically (Stixrude & Cohen, 1995; Söderlind et al., 1996; Steinle-Neumann et al., 1999; Laio et al., 2000; Vočadlo et al., 2000; Steinle-Neumann et al., 2001; Belonoshko et al., 2003; Qiu & Marcus, 2003; Belonoshko et al., 2007), and they have

been found to differ significantly from those of the PREM model. In 2001, Hemley and Mao proposed that pure iron has a nonmagnetic hexagonal closed-packed (hcp) structure (ϵ-Fe) at Earth's core pressures and temperatures (Hemley & Mao, 2001). Lately, the body-centered cubic (bcc) phase of iron was suggested to be present in the inner core, (Ross et al., 1990; Matsui & Anderson, 1997; Belonoshko et al., 2003; 2007; 2008), although its stability at core conditions is still in discussion (Vočadlo et al., 2003; Vočadlo, 2007). It has been shown recently (Mikhaylushkin et al., 2007) that because of the subtle energy difference between the different phases of Fe at core conditions, the presence of any of the hcp, face-centered cubic (fcc) or bcc phases can not be ruled out in the Earth's inner core.

The higher density of pure iron compared to that of the Earth's core indicates the presence of light element(s) in this region. In the past few years, notable effort has been made to study iron-rich alloys at core conditions, covering nickel (Vočadlo et al., 2006; Kantor et al., 2007; Dubrovinsky et al., 2007), silicon (Lin et al., 2002; Vočadlo et al., 2003; Chen et al., 2007) and sulphur (Vočadlo et al., 2003; Chen et al., 2007) as alloying elements. However, none of these proposed composition models were in full agreement with seismic observations.

Magnesium, one of the most abundant of Earth elements, which does not alloy with iron at ambient conditions, has just recently been proposed as a possible component of the Earth's core, when Dubrovinskaia et al. have shown that high pressure promotes the solubility of Mg in iron (Dubrovinskaia et al., 2004; 2005). On the other hand, today, magnesium is often classified as a litophile element (McDonough & Sun, 1995; Allegre et al., 1995), and therefore its presence in the core is precluded. This classification is based on two main arguments. First, it is believed that the consistency between the relative amount of Mg in the Earth's mantle and in the chondritic models, makes the occurrence of Mg in the core unlikely. Second, it is thought that metallic Mg in the core would require extremely reducing conditions. Indeed, based on oxygen fugacity, the occurrence of metallic Mg is rather improbable (Robie et al., 1978) at mantle conditions. However, the oxygen fugacity significantly increases with increasing temperature for Mg, indicating that at inner core conditions the presence of Mg should not be ruled out (Robie et al., 1978). Furthermore, the ionic character of metal oxides at the extreme conditions of the core, is not yet fully understood. In addition, Si, which also has lower oxygen fugacity, than the redox state of the Earth's mantle, is widely accepted as a possible component of the inner core.

Recently we showed that Mg is a strong candidate light element of the inner core (Kádas et al., 2008a; Kádas, Vitos, Johansson & Ahuja, 2009). Here, without examining the partition of Mg into the core, we describe the thermo-physical properties of hcp and bcc iron-magnesium alloys at the conditions of the Earth's inner core. We demonstrate the effect of Mg alloying on the hexagonal axial ratio, elastic constants, density and sound wave velocities, and show that the shear modulus and the transverse sound velocity of hcp Fe are notably reduced by Mg (Kádas et al., 2008a). Though the calculated shear moduli and sound velocities of hcp Fe-Mg alloys still differ significantly from those of the core as provided by seismic observations, even at 10 atomic % Mg content, Mg alloying changes the elastic properties of hcp iron in such a way that the differences to the seismic data decrease. At core conditions, we predict that 5-10% Mg stabilizes bcc Fe both dynamically and thermodynamically (Kádas, Vitos, Johansson & Ahuja, 2009), and we give an electronic structure explanation of this phenomenon. We demonstrate that the physical properties of bcc Fe-Mg alloys containing 5-10% Mg in fact reproduce those of the inner core: the calculated density, elastic moduli and sound velocities of bcc Fe-Mg alloys are consistent with seismic data. Therefore the bcc-structured Fe-Mg alloy seems to be amongst the strongest candidate models for the Earth's solid inner core.

2. Theory

2.1 Computational method

The present calculations are based on density functional theory (DFT) (Hohenberg & Kohn, 1964) formulated within the Perdew-Burke-Ernzerhof generalized gradient approximation for the exchange-correlation functional (Perdew et al., 1996). The Kohn-Sham equations (Kohn & Sham, 1965) were solved using the exact muffin-tin orbitals (EMTO) method (Andersen et al., 1994; Vitos et al., 2000; Vitos, 2001). The substitutional disorder was treated within the coherent-potential approximation (CPA) (Soven, 1967; Gyorffy, 1972; Vitos et al., 2001; Vitos, 2007). From the self-consistent charge density the total energy was calculated using the full-charge density technique (Kollár et al., 2000).

The EMTO method is an improved screened Korringa-Kohn-Rostoker method (Andersen et al., 1994), where the full potential is represented by overlapping muffin-tin potential spheres. By using overlapping spheres one describes more accurately the exact crystal potential, when compared to the conventional muffin-tin or non overlapping methods (Andersen et al., 1998; Vitos, 2001). Further details about the EMTO method and its self-consistent implementation can be found in Refs. (Vitos et al., 2000; Andersen et al., 1994; Vitos, 2001; Vitos et al., 2001; Vitos, 2007). The EMTO approach ensures the accuracy needed for the calculations of anisotropic lattice distortions in random alloys. It has been applied successfully in the *ab initio* study of the thermo-physical properties of random Fe-based alloys (Vitos et al., 2002; 2003; Olsson et al., 2003; Vitos et al., 2006; Dubrovinskaia et al., 2005; Kádas et al., 2008a; Kádas, Vitos, Johansson & Ahuja, 2009; Zhang et al., 2009; 2010), simple and transition metal alloys (Taga et al., 2005; Huang et al., 2006; Zander et al., 2007; Vitos, 2001; Magyari-Köpe, Grimvall & Vitos, 2002; Magyari-Köpe et al., 2004; Ahuja et al., 2009; Delczeg-Czirjak et al., 2009; Kádas, Lindquist, Erikssson, Johansson & Vitos, 2009; Sahlberg et al., 2009) and solid solutions (Magyari-Köpe et al., 2001; Magyari-Köpe, Vitos, Johansson & Kollár, 2002; Landa et al., 2002; Magyari-Köpe, Vitos, G. Grimvall & Kollár, 2002; Hu et al., 2007; Kádas et al., 2008b; Hu et al., 2008).

2.2 Calculation of elastic constants

2.2.1 Body-centered cubic elastic constants

There are three independent elastic constants in a body centered cubic system: C_{11}, C_{12} and C_{44}. They can be obtained by calculating the total energy as a function of small strains δ applied on the parent lattice. In the present application, the cubic shear constant, $C' = (C_{11} - C_{12})/2$ was obtained using volume-conserving orthorhombic deformation,

$$\begin{bmatrix} \delta_o & 0 & 0 \\ 0 & -\delta_o & 0 \\ 0 & 0 & \frac{\delta_o^2}{1-\delta_o^2} \end{bmatrix}. \tag{1}$$

and C' was determined from $\Delta E_o = 2VC'\delta_o^2 + O(\delta_o^4)$.

Applying the monoclinic strain

$$\begin{bmatrix} 0 & \delta_m & 0 \\ \delta_m & 0 & 0 \\ 0 & 0 & \frac{\delta_m^2}{1-\delta_m^2} \end{bmatrix}, \tag{2}$$

C_{44} was calculated from $\Delta E_m = 2VC_{44}\delta_m^2 + O(\delta_m^4)$.

C_{11} and C_{12} were separated by using C' and the cubic bulk modulus $B = (C_{11} + 2C_{12})/3$.

2.2.2 Hexagonal closed-packed elastic constants

In a hexagonal closed-packed system there are five independent elastic constants: $C_{11}, C_{12}, C_{13}, C_{33}$ and C_{44}. They were obtained from the bulk modulus,

$$B = \frac{C_{33}(C_{11} + C_{12}) - 2C_{13}^2}{C_S}, \tag{3}$$

where $C_S = C_{11} + C_{12} + 2C_{33} - 4C_{13}$, the logarithmic volume derivative of the hexagonal lattice parameter,

$$\frac{d\ln(c/a)_0}{d\ln V} = -\frac{C_{33} - C_{11} - C_{12} + C_{13}}{C_S}, \tag{4}$$

and three isochoric strains (Steinle-Neumann et al., 1999). By varying the c/a ratio at a given volume and applying the strain

$$\begin{bmatrix} \delta_h & 0 & 0 \\ 0 & \delta_h & 0 \\ 0 & 0 & \frac{1}{(1+\delta_h)^2} - 1 \end{bmatrix}, \tag{5}$$

C_S was calculated from $\Delta E_h = VC_S\delta^2 + O(\delta^3)$, where δ is the magnitude of the strain, and $\Delta E_h = E(\delta_h) - E(0)$ is the energy difference of the strained and unstrained systems. To determine $C_{66} = (C_{11} - C_{12})/2$, we applied an orthorhombic strain

$$\begin{bmatrix} \delta_o & 0 & 0 \\ 0 & -\delta_o & 0 \\ 0 & 0 & \frac{\delta_o^2}{1-\delta_o^2} \end{bmatrix}, \tag{6}$$

leading to the energy change $\Delta E_o = 2VC_{66}\delta_o^2 + O(\delta_o^4)$. Applying the monoclinic strain

$$\begin{bmatrix} 0 & 0 & \delta_m \\ 0 & \frac{\delta_m^2}{1-\delta_m^2} & 0 \\ \delta_m & 0 & 0 \end{bmatrix}, \tag{7}$$

C_{44} was determined from $\Delta E_m = 2VC_{44}\delta_m^2 + O(\delta_m^4)$.

2.2.3 Polycrystalline elastic constants

There are several different techniques for averaging the single-crystal data. We use Hill (Hill, 1952) averaging method to investigate the polycrystalline bulk (B) and shear moduli (G). According to the Hill averaging method, the polycrystalline B and G are given as the arithmetic average of the Voigt (Voigt, 1889) and Reuss (Reuss, 1929) limits. In the crystal aggregates, Voigt method assumed a uniform strain, while Reuss proposed a uniform stress. Accordingly, for a cubic crystal, the polycrystalline shear modulus is

$$\begin{aligned} G &= (G_V + G_R)/2, \\ G_R &= 5(C_{11} - C_{12})C_{44}(4C_{44} + 3C_{11} - 3C_{12})^{-1}, \\ G_V &= (C_{11} - C_{12} + 3C_{44})/5. \end{aligned} \tag{8}$$

where the G_R and G_V are the Reuss and Voigt bounds, respectively.

For cubic crystal, the Voigt and Reuss bounds are identical with the single-crystal bulk modulus, i.e.,

$$\begin{aligned} B &= (B_{\mathrm{V}} + B_{\mathrm{R}})/2, \\ B_{\mathrm{R}} &= B_{\mathrm{V}} = (C_{11} + 2C_{12})/3, \end{aligned} \tag{9}$$

Using a variational method, Hashin and Shtrikman (Hashin & Shtrikman, 1962) derived more rigorous upper and lower bounds for B and G. For cubic lattices with $C' < C_{44}$, these bounds are

$$\begin{aligned} B_{\mathrm{u}} &= B_{\mathrm{u}} = \frac{C_{11} + 2C_{12}}{3}, \\ G_{\mathrm{l}} &= C' + 3\left(\frac{5}{C_{44} - C'} + 4\beta_1\right)^{-1}, \\ G_{\mathrm{u}} &= C_{44} + 2\left(\frac{5}{C' - C_{44}} + 6\beta_2\right)^{-1}, \end{aligned} \tag{10}$$

where

$$\begin{aligned} \beta_1 &= \frac{3(B + 2C')}{5C'(3B + 4C')}, \\ \beta_2 &= \frac{3(B + 2C_{44})}{5C_{44}(3B + 4C_{44})}. \end{aligned} \tag{11}$$

For $C' > C_{44}$, the upper and lower bounds are reversed.

2.3 Application to iron-magnesium systems

The cubic elastic constants of the random ferromagnetic bcc $Fe_{1-x}Mg_x$ ($0 \leq x \leq 0.1$) alloys at ambient conditions were calculated as a function of the chemical composition. At each concentration the theoretical equilibrium volume and the bulk modulus were derived from an exponential Morse type function (Moruzzi et al., 1988) fitted to the *ab initio* total energies of bcc structures calculated for seven different atomic volumes. In order to obtain the two cubic shear moduli C' and C_{44}, we used volume-conserving orthorhombic and monoclinic deformations as described, e.g., in Ref. (Vitos, 2007).

The polycrystalline Young's modulus (E) and the Poisson ratio (ν) are connected to B and G by the relations

$$\begin{aligned} E &= 9BG/(3B + G), \\ \nu &= (3B - 2G)/(6B + 2G). \end{aligned} \tag{12}$$

Finally, the polycrystalline elastic Debye temperature (Θ) was calculated from the longitudinal and transversal sound velocities obtained from B, G, and the average alloy density (see, e.g., Ref.(Vitos, 2007)).

In the present electronic structure and total energy calculations, the one-electron equations were solved within the scalar-relativistic and soft-core approximations. The Green function was calculated for 16 complex energy points distributed exponentially on a semicircular contour. In the basis set we included s, p, d, and f orbitals ($l_{max} = 3$), and the one-center expansion of the full charge density was truncated at $l^h_{max} = 8$ (Vitos, 2007). The electrostatic correction to the single-site coherent potential approximation was described using the

screened impurity model (Korzhavyi et al., 1995) with screening parameter of 0.6. The radii of the overlapping muffin-tin spheres of Fe, Mg, and Cr were chosen to be equal to the average atomic sphere radius.
To calculate the two cubic shear constants, C' and C_{44}, for bcc iron-magnesium alloys at core conditions, the total energy was computed for six different orthorhombic and monoclinic distortions ($\delta_{o/m}$=0.00, 0.01, ..., 0.05). The bulk modulus was determined from an exponential Morse-type function (Moruzzi et al., 1988) fitted to the total energies of the non-distorted bcc structure (δ=0) calculated for 10 different volumes. Finally, C_{11} and C_{12} were separated by using C' and the cubic bulk modulus B.
To determine the elastic constants for hcp iron-magnesium alloys, the total energy was calculated for six different orthorhombic and monoclinic distortions ($\delta_{o/m}$=0.00, 0.01, ..., 0.05) to determine C_{66} and C_{44}, respectively, and for nine hexagonal distortions ($\delta_h = -0.04, -0.03, ..., 0.00, ..., 0.04$) to obtain C_S. The sound velocities were determined by solving the secular equation, as it is given by Grimvall (Grimvall, 1999).
The temperature effect in the elastic constants calculated at fixed volume was taken into account via the Fermi-Dirac distribution of the electrons and neglecting the phonon contributions. We used the Debye model to account for the lattice vibration effects in the Gibbs energy. In the self-consistent EMTO calculations, the one-electron equations were treated within the scalar relativistic and soft core approximations. The EMTO Green's function was calculated for 16 energy points. In the EMTO basis set s, p, d and f orbitals were included for both hcp and bcc Fe-Mg systems. In the case of the strained hcp structures 9744 $k-$points were used in the irreducible part of monoclinic Brillouin zones. For the strained bcc structures, 22000 k-points were used in the irreducible part of the monoclinic Brillouin zones. The Hashin-Shtrikman averages (Hashin & Shtrikman, 1962) were applied to calculate the shear and Young moduli, and the sound velocities of bcc Fe-Mg alloys at Earth's core conditions. The total charge density was expanded in spherical harmonics, including terms up to l_{max}=10.

3. Iron-magnesium alloys at ambient conditions

In this chapter we review the thermo-physical properties of ferromagnetic body-centered cubic iron-magnesium alloys at ambient conditions.

3.1 Equation of state and formation energy

In this section, we investigate the composition dependence of the equation of state and formation energy of ferromagnetic bcc $Fe_{1-x}Mg_x$ ($0 \leq x \leq 0.1$) random alloys. For comparison, we also show results obtained for Fe-Cr alloys. The composition dependence of $a(x)$ is shown in Fig. 1 (left panel) along with the experimental data for Fe-Mg (Hightower et al., 1997; Dorofeev et al., 2004) and Fe-Cr (Sutton & Hume-Rothery, 1955; Pearson, 1958). Compared to slight increase on bcc Fe by Cr, Mg strongly enlarge lattice parameter of bcc Fe as shown in Fig. 1 (left panel).
Since the lattice constant of bcc Fe is by ~ 0.019 Å smaller than that of B2 Cr, based on Vegard's rule we would predict a linear $a(x)$ with slope of $\Delta a(x)/\Delta x \sim 0.2 \times 10^{-3}$ Å per at.% Cr. However, both the experimental and the theoretical lattice parameters deviate from this simple linear trend as shown in Fig. 1 (left panel). The EMTO lattice parameter reaches a maximum value between 7.5 and 10 at.% Cr and remains above the lattice parameter of pure Fe for all concentrations considered here. Using the theoretical values below $c = 0.1$, the theoretical slope of $a(x) \sim 1.7 \times 10^{-3}$ Å is larger than the average experimental value of

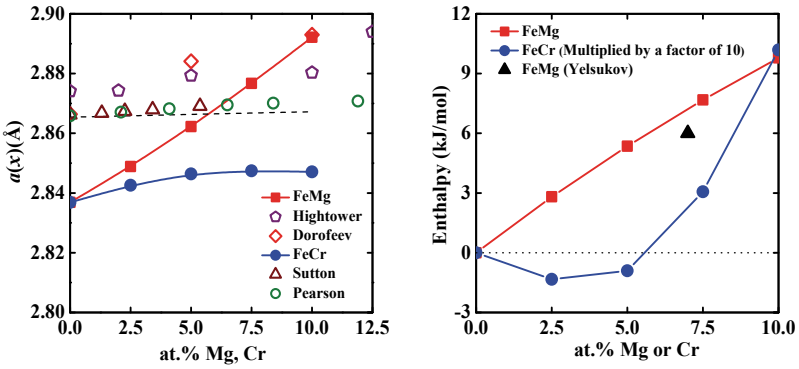

Fig. 1. Theoretical (EMTO, solid symbols connect with lines) lattice parameter (left panel) of ferromagnetic bcc Fe-Mg random alloys as a function of Mg concentration. The experimental data (open symbols) are from Ref. (Hightower et al., 1997) (Hightower) and Ref. (Dorofeev et al., 2004) (Dorofeev). For comparison, theoretical (EMTO) and available experimental Ref. (Sutton & Hume-Rothery, 1955)(Sutton) and Ref. (Pearson, 1958)(Pearson) lattice constant of ferromagnetic bcc Fe-Cr random alloys are also shown.The dashed line for Fe-Cr is obtained from Vegard's rule. Theoretical (EMTO) enthalpy of formation (right panel) for ferromagnetic bcc Fe-Mg random alloy. For comparison, the enthalpy of formation for Fe-Cr is also shown. The latter has been multiplied by 10 to match the scale. The predicted value by Yelsukov *et al.* (Yelsukov et al., 2005) for $Fe_{0.93}Mg_{0.07}$ is shown by triangle.

$\sim 0.5 \times 10^{-3}$ Å per at.% Cr (Pearson, 1958), but is in perfect agreement with the former *ab initio* calculation based on special quasi random structures (Olsson et al., 2006).

For the atomic radius of hcp Mg we obtained 1.764 Å, which agrees well with the experimental value of 1.77 Å (Young, 1991). Using this atomic radius and that of pure Fe (1.40 Å), for the bcc $Fe_{1-x}Mg_x$ alloys Vegard's rule predicts a lattice parameter with slope of $\Delta a(x)/\Delta x \sim 3.6 \times 10^{-3}$ Å per at.% Mg. The present EMTO results, shown in Fig. 1 (left panel), give 5.5×10^{-3} Å increase per at.% Mg. Moderate lattice expansion upon Mg addition to Fe was also reported by Hightower *et al.* (Hightower et al., 1997) and Dorofeev *et al.* (Dorofeev et al., 2004). In their measurements, the average lattice expansion below $x = 0.1$ was 0.6×10^{-3} and 2.7×10^{-3} Å per at.% Mg, respectively. Thus, similar to Fe-Cr, the present theoretical $\Delta a(x)/\Delta x$ seems to overestimate its experimental counterparts. On the other hand, the local experimental slope between 10 and 12.5 at.% Mg by Hightower *et al.* reaches 5.4×10^{-3} Å per at.% Mg, which is very close to the present value obtained for random solid solution. Surprisingly, our calculated density change of 11% obtained for $x = 0.1$ is in perfect agreement with the average experimental value measured below 10 at.% Mg (Fig. 1 in Ref.(Hightower et al., 1997)).

According to the experimental phase diagram, the solid solubility of Mg in Fe, and vice versa, is very small (Massalski, 1986), meaning that the formation energy of Fe-Mg alloy should be large and positive. In Fig. 1 (right panel) we compare the formation enthalpy of Fe-Mg with that of Fe-Cr. For the standard states, we use the ferromagnetic bcc Fe, the antiferromagnetic B2 Cr, and the experimental hexagonal closed packed (hcp) Mg with $c/a = 1.624$. The present enthalpy of formation for Fe-Cr shows a local negative minimum and becomes positive near 5.5% Cr, in good accordance with that reported in Refs. (Olsson et al., 2003; Korzhavyi et al., 2009).The enthalpy of formation for Fe-Mg, on the other hand, is found to increase monotonously up to 10 kJ/mol obtained for $Fe_{0.90}Mg_{0.10}$. This result is in line with the

predicted enthalpy of formation for Fe-Mg by de Boer *et al.* (de Boer et al., 1988) and also with that calculated by Yelsukov *et al.* (Yelsukov et al., 2005) for $Fe_{0.93}Mg_{0.07}$.

3.2 Single crystal elastic constants

For each Mg concentration x,the elastic constants were calculated at the corresponding theoretical equilibrium lattice parameter $a(x)$. The present theoretical single-crystal elastic constants $C_{ij}(x)$ of ferromagnetic bcc $Fe_{1-x}Mg_x$ ($0 \leq x \leq 0.1$) random alloys are plotted in Fig. 2 as a function of Mg content. We find that all elastic constants decrease nearly linearly with Mg addition. The theoretical $C_{11}(x), C_{12}(x), C'(x)$, and $C_{44}(x)$ for $x = 0.1$ change by about $-36.3\%, -34.2\%, -38.2\%$, and -8.2%, respectively, compared to the corresponding values for pure Fe. The monotonously decreasing trends of the $C_{ij}(x)$ of Fe-Mg (Fig. 2) indicating the absence of electronic topological transition in Fe-rich Fe-Mg random solid solutions.

Before turning to the polycrystalline elastic moduli, we discuss the effect of local lattice relaxation (LLR) around the impurity atoms on the single-crystal elastic constants. The LLR effect, neglected in the CPA calculations, is expected to become important in systems with large volume mismatch. Here we use a supercell technique to establish the order of magnitude of the effect of LLR on the C' elastic constant of Fe-Mg and Fe-Cr solid solutions. The 2x2x2 bcc supercell contained one Mg (or Cr) atom and 15 Fe atoms. First we calculated the tetragonal elastic constant of $Fe_{15}Mg_1$ ($Fe_{15}Cr_1$) using ideal bcc underlying lattice with lattice constant fixed to that obtained in a CPA calculation performed for the bcc $Fe_{0.9375}Mg_{0.0625}$ ($Fe_{0.9375}Cr_{0.0625}$) random alloy. Next we relaxed the first 8 nearest neighbor (NN) Fe atoms around the impurity atom and recalculated C' for the relaxed structure. In these calculations, we used ~ 2500 uniformly distributed k-points in the irreducible wedge of the Brillouin zone. Results from the supercell calculations are summarized in Table 1. We find that in $Fe_{15}Mg_1$ the equilibrium Fe-Mg distance is $\sim 0.8\%$ larger than the equilibrium Fe-Fe bond length in pure bcc Fe. This figure may be contrasted with $\sim 0.1\%$ contraction of the Fe-Cr distance in the Fe-Cr system relative to the Fe-Fe bond length. Comparing the tetragonal elastic constant calculated for the supercell having the ideal bcc structure (C'_u) to that calculated for the supercell with relaxed Fe-impurity distance (C'_r), we can estimate the LLR effect in C'. In $Fe_{15}Mg_1$ this effect is ~ 0.7 GPa and in $Fe_{15}Cr_1 \sim 0.2$ GPa. Since the alloying effects for both systems are significantly larger than the above LLR effects (Fig. 2), we conclude that the composition dependence of the elastic parameters of Fe-Mg and Fe-Cr systems is well captured by the present EMTO-CPA approach.

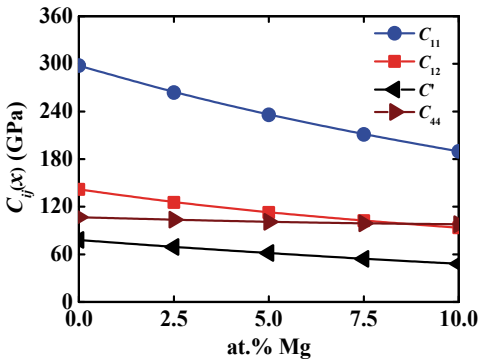

Fig. 2. Theoretical (EMTO) single-crystal elastic properties of ferromagnetic bcc Fe-Mg random alloys as a function of Mg concentration.

system	C'_u	δ_{NN}	C'_r
$Fe_{15}Mg_1$	56.61	0.8 %	57.33
$Fe_{15}Cr_1$	77.40	-0.1 %	77.57

Table 1. Results of the supercell calculations for $Fe_{15}Mg_1$ and $Fe_{15}Cr_1$ systems. δ_{NN} is the relaxation of the first nearest neighbor Fe atoms around the impurity atom. C'_u and C'_r (in GPa) are the tetragonal elastic constants obtained for the supercells without and with local lattice relaxation, respectively.

3.3 Polycrystalline elastic constants

The theoretical polycrystalline elastic moduli for ferromagnetic bcc $Fe_{1-x}Mg_x$ ($0 \leq x \leq 0.1$) random alloys are displayed as a function of Mg content in Fig. 3. Similar to the single-crystal elastic constants (Fig. 2), the polycrystalline elastic moduli also decrease with Mg content. These results could in fact be anticipated if, for instance, we take into account that the theoretical bulk modulus of hcp Mg is significantly smaller than that of bcc Fe. However, the actual slope of B in Fig. 3 is much larger than that predicted from the ~ 157 GPa difference between the theoretical bulk moduli of Fe and Mg by assuming a linear composition dependence for $B(x)$. We find that for $x = 0.1$, $B(x), G(x), E(x)$, and $B/G(x)$ decrease by about 35.2%, 21.7%, 23.9%, and 17.3%, respectively, relative to those of pure Fe. Above 7.5 at.% Mg, the calculated $B/G(x)$ ratio of Fe-Mg alloys drops below the brittle-ductile limit of 1.75 set by Pugh (Pugh, 1954), implying that Mg addition makes the ferromagnetic bcc Fe-Mg alloys brittle.

The theoretical Poisson's ratio ($\nu(x)$) and Debye temperature ($\Theta(x)$) of Fe-Mg are shown in Fig. 4, for comparison theoretical and experimental (Speich et al., 1972) Poisson's ratio and Debye temperature of Fe-Cr are also shown. For Fe-Cr, the Poisson's ratio slightly decreases with Cr concentration up to 10 at.% Cr, in line with the experimental data (Speich et al., 1972). The Debye temperature exhibits a monotonous enhancement with Cr content. In $Fe_{0.9}Cr_{0.1}$, the calculated Poisson's ratio decreases by 9.97% and the Debye temperature enhances by 4.45% with respect to that for pure Fe.

For Fe-Mg, both of them exhibit a nearly linear decreasing dependence on the chemical

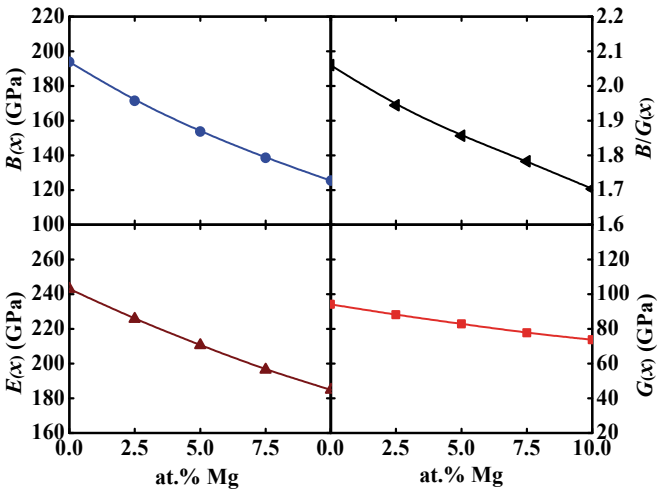

Fig. 3. Theoretical (EMTO) polycrystalline elastic properties of ferromagnetic bcc $Fe_{1-x}Mg_x$ ($0 \leq x \leq 0.1$) random alloys as a function of Mg concentration.

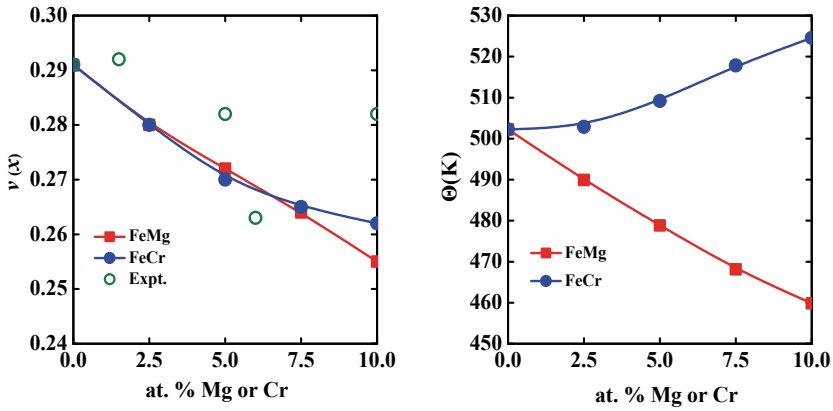

Fig. 4. Theoretical (EMTO) Poisson's ratio (left panel) and Debye temperature (right panel) of ferromagnetic bcc $Fe_{1-x}Mg_x$ ($0 \leq x \leq 0.1$) random alloys as a function of Mg concentration. For comparison, theoretical and experimental (Speich et al., 1972)Poison's ratio and Debye temperature for Fe-Cr are also shown.

composition. At 10 at.% Mg, the Poisson's ratio and Debye temperature are by 12.37% and 8.45%, respectively, smaller than those corresponding to pure Fe. This Debye temperature drop when going from Fe to $Fe_{0.90}Mg_{0.1}$ is expected to give a phonon vibration energy contribution which stabilizes the solid solution. To estimate this effect, we make use of the high-temperature expansion of the phonon energy (Grimvall, 1976). Namely, for two solids with similar Debye temperatures, the vibrational free energy difference is $\Delta F^{\rm vib} \approx 3k_{\rm B}T(\Delta\Theta/\Theta)$, where T is the temperature, $\Delta\Theta/\Theta$ is the relative Debye temperature and $k_{\rm B}$ the Boltzmann constant. We write the phonon free energy of formation for $Fe_{1-x}Mg_x$ as $\Delta F^{\rm vib}(x) = x\left[F^{\rm vib}(x) - F^{\rm vib}({\rm Mg})\right] + (1-x)\left[F^{\rm vib}(x) - F^{\rm vib}({\rm Fe})\right]$, where $F^{\rm vib}(x)$, $F^{\rm vib}({\rm Mg})$, and $F^{\rm vib}({\rm Fe})$ are the vibrational free energies for $Fe_{1-x}Mg_x$, Mg, and Fe, respectively. For $x = 0.1$ we have $\left[\Theta(0.1) - \Theta({\rm Fe})\right]/\Theta({\rm Fe}) \approx -0.0845$ and $\left[\Theta(0.1) - \Theta({\rm Mg})\right]/\Theta({\rm Mg}) \approx 0.406$, where for the Debye temperature of Mg we used 327 K (Grimvall, 1999). Using these relative Debye temperatures, we arrive at $\Delta F^{\rm vib}(0.1) \approx -0.884 \times 10^{-3} T$ kJ/mol/K (referring to mole of atoms). For comparison, the configuration entropy for $Fe_{0.90}Mg_{0.1}$, evaluated within the mean-field approximations, is $\Delta F^{\rm conf}(0.1) \approx -2.70 \times 10^{-3} T$ kJ/mol/K. It is worth noting that according to Fig. 1 (right panel), the total thermal free energy $\Delta\left[F^{\rm vib}(0.1) + F^{\rm conf}(0.1)\right] = -3.584 \times 10^{-3} T$ kJ/mol/K would stabilize the random $Fe_{0.90}Mg_{0.1}$ solid solution at ~ 2790 K, *i.e.* above the melting point of Fe.

4. Iron-magnesium alloys at Earth's core conditions

In this chapter we review the thermo-physical properties of hexagonal closed-packed and body-centered cubic iron-magnesium alloys at high pressure (and high temperature), up to the conditions of the Earth's solid inner core. We discuss the relevance of the theoretical results to the inner core.

4.1 Hexagonal closed-packed iron-magnesium alloys

In the following, we demonstrate the elastic properties of hexagonal closed-packed iron-magnesium alloys at high pressures and zero temperature (Kádas et al., 2008a).

Volume	C_{11}	C_{33}	C_{12}	C_{13}	C_{44}	
51.0	1545.5	1760.8	709.1	540.3	346.7	present work
49.6	1533.0	1544.0	846.0	835.0	583.0	Expt.[a]
50.0	1675	1835	735	645	415	LAPW[b]
49.9	1625.0	1867.6	809.3	639.2	356.5	APW+lo[c]
50.9	1510	1450	460	673	414	FP-LMTO[d]

[a] Ref. Mao et al. (1998)
[b] Ref. Steinle-Neumann et al. (1999)
[c] Ref. Qiu & Marcus (2003)
[d] Ref. Söderlind et al. (1996)

Table 2. Theoretical and experimental elastic constants (in GPa) of nonmagnetic hcp Fe at $\sim$50 Bohr^3/atom. All the theoretical results were obtained at zero temperature, while measurements were performed at room temperature.

In order to check the accuracy of our method, we compare the present results obtained for pure nonmagnetic hcp Fe to the available experimental and ab initio theoretical data at V=$\sim$50 Bohr^3/atom volume (Table 2).
We obtain a reasonable agreement both with theoretical and experimental results. The present theoretical values agree with the full-potential linearized-augmented plane-wave (LAPW, (Steinle-Neumann et al., 1999)), full-potential augmented plane-wave plus local orbital (APW+lo, (Qiu & Marcus, 2003)) and full-potential linear muffin-tin orbitals (FP-LMTO, (Söderlind et al., 1996)) results within $\sim$20%, except C_{12}, where the FP-LMTO method provides significantly smaller value than the other ab initio methods. We find larger deviations from the X-ray diffraction measurements (Mao et al., 1998) for C_{13} and C_{44}, where the experiment provides notably larger values than any theoretical methods, even if we take into account that the experimental volume is a little bit smaller than any of the theoretical ones.

4.1.1 Equation of state

Prior to the calculation of the equation of state, we need to optimize the hexagonal axial ratio, c/a, at each V volume for pure Fe and hcp Fe-Mg alloys. Panel (a) in Fig. 5 shows that c/a increases with increasing pressure for pure Fe and Fe-Mg alloys (Kádas et al., 2008a). However, the change in c/a is rather small, in the whole studied pressure range, it increases by 0.7%, 0.6% and 0.5% in pure Fe, $Fe_{0.95}Mg_{0.05}$ and $Fe_{0.9}Mg_{0.1}$, respectively. We obtain the lowest c/a values for pure Fe, and find that c/a increases with Mg content. Compared to pure Fe, the average change in c/a is 0.3% in $Fe_{0.95}Mg_{0.05}$, and 0.6% in $Fe_{0.9}Mg_{0.1}$. We note that the experimental c/a values for pure iron in the 34.8-300.6 GPa pressure range (Mao et al., 1990) are very scattered and they vary between 1.575 and 1.602.
The theoretical equation of state is shown in Fig. 5 (b). At any pressure, the volume increases with increasing Mg content compared to pure iron. This can be explained with the larger atomic size of Mg: its metallic atomic radius is 27% larger than that of Fe. As the pressure increases, the change in volume with increasing Mg concentration decreases, which can be understood by considering that Mg has a much higher compressibility, than Fe (Dubrovinskaia et al., 2005).

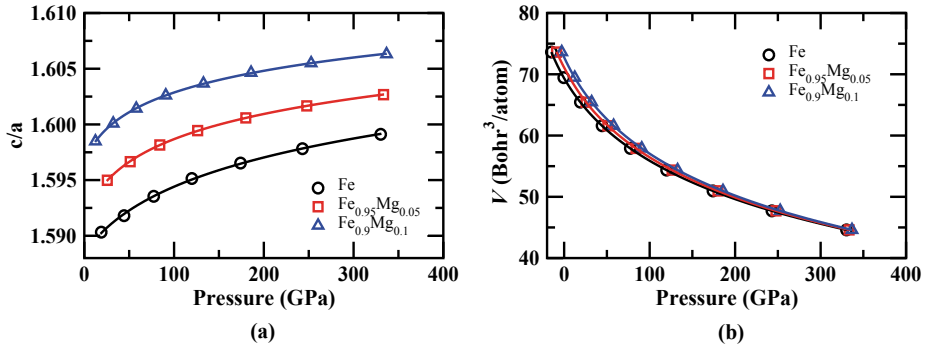

Fig. 5. Theoretical pressure dependency of the hexagonal axial ratios (c/a) and the volume of pure hcp Fe (circles), $Fe_{0.95}Mg_{0.05}$ (squares) and $Fe_{0.9}Mg_{0.1}$ (triangles).

4.1.2 Single crystal elastic constants

The theoretical elastic constants of Fe, $Fe_{0.95}Mg_{0.05}$ and $Fe_{0.9}Mg_{0.1}$ at different volumes are shown in Table 3.

All the elastic constants follow a normal decreasing behavior with increasing volume. Their average changes in this volume interval are ΔC_{11}=-70%, ΔC_{33}= -69%, ΔC_{12}=-77%, ΔC_{13}=-79% and ΔC_{44}=-62%. We observe monotonous change with the Mg concentration at each volume: C_{11}, C_{33} and C_{44} decrease with increasing Mg content, while C_{12} and C_{13} slightly increase. $C_{66} = (C_{11} - C_{12})/2$ decreases with increasing Mg concentration. We calculate the largest variations for C_{44}: compared to pure iron, it decreases by 14% in $Fe_{0.95}Mg_{0.05}$ and 27% in $Fe_{0.9}Mg_{0.1}$ at V=44.6 Bohr^3/atom. Both pure hcp Fe and Fe-Mg alloys are mechanically stable in the whole pressure range considering the following stability criteria (Grimvall, 1999), $C_{11} > |C_{12}|$, $C_{33}(C_{11} + C_{12}) > 2C_{13}^2$, $C_{11}C_{33} > C_{13}^2$ and $C_{44} > 0$, which are fulfilled at any volume and Mg content.

Volume	C_{11}	C_{33}	C_{12}	C_{13}	C_{44}
		Fe:			
44.602	2257.1	2597.4	1151.2	873.3	476.6
50.965	1545.5	1760.8	709.1	540.3	346.7
65.450	676.8	773.9	240.5	179.2	178.8
		$Fe_{0.95}Mg_{0.05}$:			
44.602	2159.2	2503.2	1169.1	869.6	411.6
50.965	1476.3	1707.6	739.3	544.6	303.9
65.450	653.4	767.9	264.3	187.6	157.4
		$Fe_{0.9}Mg_{0.1}$:			
44.602	2036.5	2398.7	1206.2	875.7	348.5
50.965	1399.3	1650.5	775.7	552.9	261.2
65.450	633.1	752.0	289.9	196.1	136.6

Table 3. Theoretical elastic constants (in GPa) of hcp Fe and hcp Fe-Mg alloys at different volumes (in Bohr^3/atom). These volumes correspond to pressures between approximately 18 and 340 GPa.

4.1.3 Polycrystalline elastic constants

In the following, we examine the effect of Mg alloying on the physical properties of iron, and compare our theoretical results to those of the PREM model. Panel (a) in Fig. 6 shows that Mg decreases the bulk modulus, B, at any pressure. We find that B of the $Fe_{0.9}Mg_{0.1}$ alloy is in an excellent agreement with PREM data of the inner core. We note, however, that our calculations were performed at zero temperature, and according to the theoretical results of Steinle-Neumann et al., B increases in Fe with increasing temperature (Steinle-Neumann et al., 2001).

Examining the effect of alloying on the density, we find that the increasing Mg concentration decreases it at any given pressure (Fig. 6 (b)). However, the densities of Fe-Mg alloys do not reach those of the inner core reported in the PREM model, not even at 10% Mg content. The shear modulus decreases with increasing Mg content (Fig. 6 (c)). Though at core pressures 10% Mg alloying reduces the shear modulus by 23%, compared to pure iron, it is still insufficient to reproduce shear moduli of the inner core. For the sound velocities, we find that the longitudinal (compressional) sound wave velocity, v_P, slightly decreases with increasing Mg alloying (Fig. 6 (d)), and even at 10% Mg concentration, we calculate about 20% larger values than those of the PREM values at the Earth's inner core. The transverse (shear) sound velocity, v_S, decreases to a larger extent with increasing Mg content than v_P. Although at core pressures 10% Mg alloying reduces v_S by 12%, compared to pure iron, we obtain here ∼45% larger values than those expected in the inner core. We note that both the

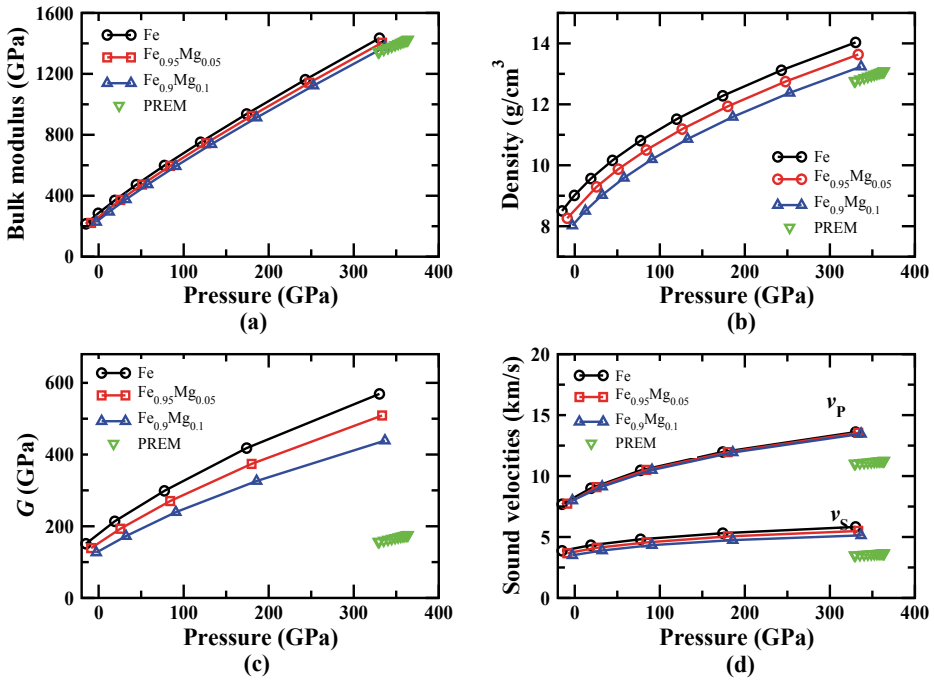

Fig. 6. Theoretical bulk modulus (a), density (b), shear modulus, G (c), and sound velocities (d) of pure hcp Fe (circles), $Fe_{0.95}Mg_{0.05}$ (squares) and $Fe_{0.9}Mg_{0.1}$ (triangles) as a function of pressure. v_P and v_S denote longitudinal and transverse sound velocities, respectively. Seismic data as given in the PREM model are shown for comparison (inverted triangles).

present calculated v_P and v_S values, being in linear relation with the density, fulfill Birch's law (Birch, 1961) at any Mg concentration.
In summary, investigating the elastic properties of iron-rich hcp Fe-Mg alloys, containing 5 and 10 atomic % Mg, up to pressures of the Earth's inner core, we found that in these systems the increasing Mg content decreases the bulk modulus, density and both the longitudinal and transverse sound velocities. Mg alloying changes the elastic properties of hcp iron in such a way that the differences to the PREM values decrease. Our results indicate that Mg should be considered as a possible component of the Earth's inner core. In addition, we note that agreement between the calculated value of the bulk modulus and that of PREM is not a sufficient test for a compositional model of the inner core, as has been noted in the literature before.

4.2 Body-centered cubic iron-magnesium alloys

I the following, we demonstrate the thermo-physical properties of body-centered cubic iron-magnesium alloys at high pressure and high temperature (Kádas, Vitos, Johansson & Ahuja, 2009).

4.2.1 Equation of state

We calculated the equation of state for pure bcc Fe, as well as for bcc $Fe_{1-x}Mg_x$ ($Fe_{0.95}Mg_{0.05}$ and $Fe_{0.9}Mg_{0.1}$) alloys at zero temperature (Fig. 7). For comparison, for pure Fe both the nonmagnetic (NM) and ferromagnetic (FM) states were considered. Figure 7 shows that the volumes of NM and FM bcc Fe are notably different at low pressure, but the volume difference gradually decreases with increasing pressure and disappears around ≈300 GPa. This is in line with the gradually vanishing calculated ferromagnetic moment on Fe. We also modelled the high temperature paramagnetic phase using the disordered local magnetic moment (DLM) approach. The DLM was proven to describe the effect of loss of the net magnetic moment accurately above the transition temperature (Oguchi et al., 1983). Our calculated DLM moments rapidly vanish with pressure and become zero already at ∼10 GPa. The effect of Mg-alloying can be observed in Fig. 7. At low pressures, the volume of Fe-Mg alloys increases with the Mg content, due to the larger atomic size of Mg. Since Mg has higher compressibility, than Fe, the change in volume with increasing Mg concentration decreases

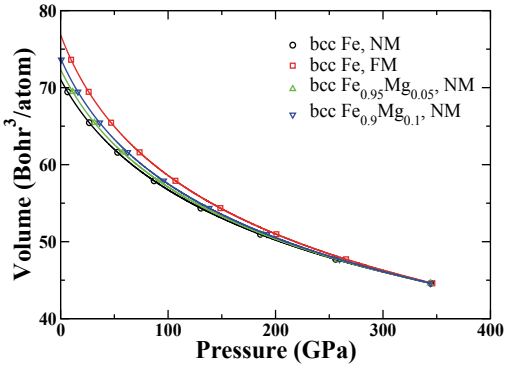

Fig. 7. Calculated equation of state for nonmagnetic (NM) and ferromagnetic (FM) pure bcc Fe (denoted by black circles and red squares, respectively), NM bcc $Fe_{0.95}Mg_{0.05}$ (red triangles), and bcc $Fe_{0.9}Mg_{0.1}$ alloys (blue inverted triangles).

with increasing pressure. The volume difference between pure Fe and Fe-Mg alloys practically vanishes at core pressures (329-364 GPa (Dziewonski & Anderson, 1981)).

4.2.2 Single crystal elastic constants

The zero temperature shear elastic constants, C', C_{44}, and the bulk modulus, B, calculated at different V volumes for for pure bcc Fe, $Fe_{0.95}Mg_{0.05}$ and $Fe_{0.9}Mg_{0.1}$ alloys are shown in Fig. 8 (solid lines). At T=0 K, pure bcc Fe is dynamically unstable, since one of its elastic constants, the tetragonal shear modulus (C') is negative at each volume. In addition, C' shows an anomalous behavior: it increases with increasing volume. However, C' remains negative at each volume, even in $Fe_{0.9}Mg_{0.1}$. We calculate $(\Delta C'/\Delta V)_{Fe}$=7.6 GPa/Bohr^3 for pure iron, and $(\Delta C'/\Delta V)_{Fe_{0.95}Mg_{0.05}}$=4.1 GPa/Bohr^3 and $(\Delta C'/\Delta V)_{Fe_{0.9}Mg_{0.1}}$=1.7 GPa/Bohr^3 for the alloys. C_{44} and B follow a normal decreasing behavior with increasing volume.

At T=7000 K, in our calculations, pure bcc Fe is still unstable at high pressures, i.e. at small volumes. Namely, at V=44.60 Bohr^3/atom, we calculate C'=-43.71 GPa for Fe at T=7000 K. We find that small amount of magnesium addition stabilizes dynamically the bcc phase of Fe-Mg alloys. At the lowest core temperature (∼5000 K), we obtain $C'(Fe_{0.91}Mg_{0.09})$=6.4 GPa at 355 GPa. However, at higher temperature, i.e. closer to the centre of the core, significantly less Mg is sufficient for dynamical stability. For instance, at 7000 K already 5 at.% Mg addition leads to positive C' for the bcc phase (Fig. 8). C_{44} and B decrease with increasing volume in both pure Fe and in Fe-Mg alloys at T=7000 K. The high temperature bulk moduli are slightly larger than those calculated at zero temperature (Fig. 8).

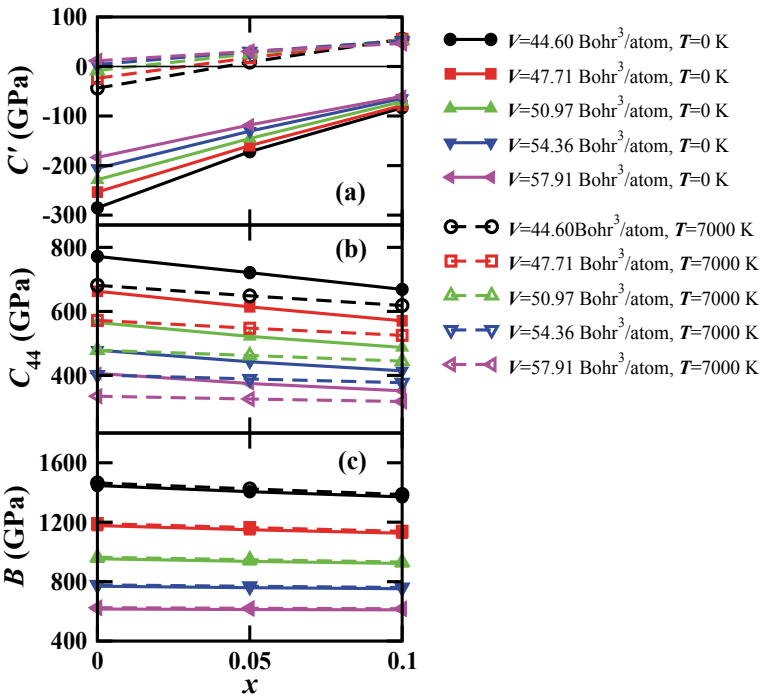

Fig. 8. Single crystal elastic constants, C', C_{44}, and the bulk modulus, B, as a function of Mg concentration, x, calculated at different V volumes at zero temperature (solid lines) and at T=7000 K (dashed lines). The horizontal black line in panel (a) corresponds to C'=0 GPa.

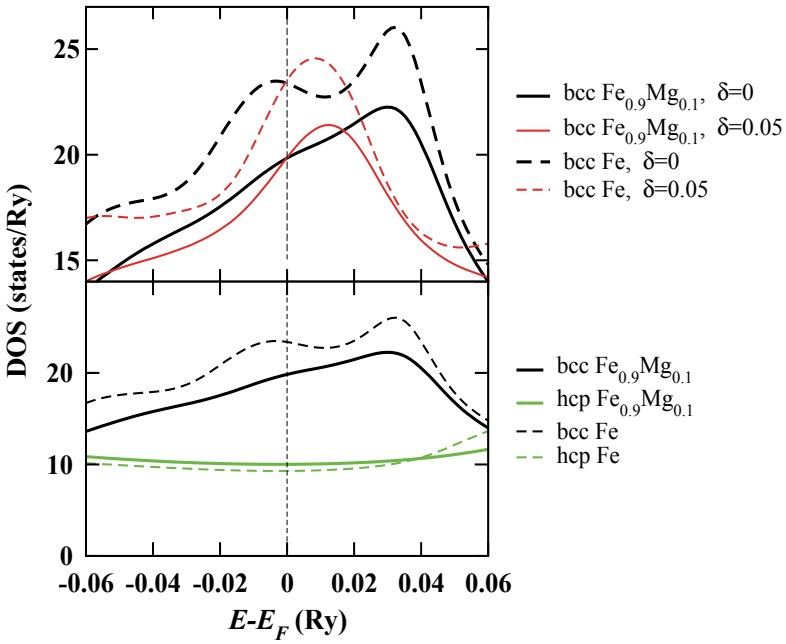

Fig. 9. Electronic density of states of Fe at T=0 K for an energy window corresponding to ∼5000-8000 K. Lower panel: density of states of Fe and $Fe_{0.9}Mg_{0.1}$ in the bcc and hcp phases, respectively. Upper panel: density of states for non-distorted bcc Fe and $Fe_{0.9}Mg_{0.1}$ (δ=0) and for distorted bcc Fe and $Fe_{0.9}Mg_{0.1}$ (δ=0.05). Similar orthorhombic distortions have been used to compute the tetragonal cubic shear modulus C'. Vertical dashed lines denote the Fermi level.

To understand the role of Mg on the dynamical stability of the bcc phase, we follow the effect of the orthorhombic distortion δ (used to compute C') on the bcc DOS (Fig. 9, upper panel). In bcc Fe, the orthorhombic distortion splits the degenerated d peak located around -7 mRy below E_F (corresponding mainly to the e_g states), pushing one d band towards negative energies and one d band above the Fermi level. Because of that, the DOS between -40 mRy and E_F decreases, which gives a substantial negative contribution to the electronic energy. Consequently, the total energy decreases upon lattice distortion yielding a large negative tetragonal shear constant for bcc Fe (C'_{Fe}=-285 GPa at 0 K and 44.6 $Bohr^3$/atom). This mechanism is responsible for the dynamical instability of bcc Fe at core pressures and low temperatures. In Fe-Mg alloys, the above effect is greatly diminished. Due to the chemical disorder, the DOS is much smoother near the Fermi level in $Fe_{0.9}Mg_{0.1}$ compared to that in pure Fe (Fig. 9, upper panel, black solid line). As a result, the energy decrease upon lattice distortion is less dominant for the alloy than for pure Fe. This leads to a significantly larger C' for Fe-Mg than for Fe already at low temperatures ($C'_{Fe_{0.9}Mg_{0.1}}$=-83 GPa at 0 K and 44.6 $Bohr^3$/atom).

The marked difference between the bcc and hcp DOS's near E_F (Fig. 9) is also reflected in the temperature effects. The electron excitations are more significant in the case of the bcc structure than for the hcp structure. This is because, first the DOS at E_F is notably larger in the bcc phase, and second the DOS at E_F is very irregular in the bcc phase in contrast to the almost

constant DOS in the hcp phase. The increasing temperature increases C' of bcc Fe, because of the strong increase in the electronic entropy with distortion. This gives positive contribution to the Gibbs free energy. In pure Fe at 6000 K, the electronic entropy term in the Gibbs free energy (-TS_e) is increased by 3.1 mRy with orthorhombic distortion, compared to that of the non-distorted system. In $Fe_{0.9}Mg_{0.1}$, -TS_e is increased by 1.7 mRy in the distorted structure, which indicates that the dynamical stabilization effect of temperature is larger in pure Fe than in Fe-Mg alloys. However, this can not compensate the large chemical stabilization effect of Mg present already at low temperatures. Accordingly, we calculate C'(Fe)=-77 GPa and $C'(Fe_{0.9}Mg_{0.1})$=37.0 GPa at 6000 K and 44.6 Bohr^3/atom (356 GPa).

4.2.3 Polycrystalline elastic constants

The polycrystalline shear modulus (G) can not be defined for dynamically unstable systems. Accordingly, in the following, we examine the polycrystalline elastic constants at T=7000 K temperature, for the dynamically stable bcc Fe-Mg alloys, and reveal the effect of Mg alloying on the elastic properties. The Hashin-Shtrikman averages (Hashin & Shtrikman, 1962) of the shear modulus (G), the Young modulus (E), the polycrystalline anisotropy (A), and the longitudinal (v_P) and transversal (v_S) sound velocities calculated for bcc $Fe_{0.95}Mg_{0.05}$ and $Fe_{0.9}Mg_{0.1}$ alloys at different volumes and at T=7000 K are shown in Fig. 10. The shear modulus follows a normal decreasing behavior with increasing volume in both alloys (Fig. 10, panel (a)). Between V=44.60 and V=57.91 Bohr^3/atom G decreases by 20% in $Fe_{0.95}Mg_{0.05}$, and 39% in $Fe_{0.9}Mg_{0.1}$. The shear modulus increases with Mg alloying at each volume considered here. The change in G, due to the increased Mg content, diminishes with increasing volume. This is because G decreases almost linearly with increasing volume in $Fe_{0.9}Mg_{0.1}$, while in $Fe_{0.95}Mg_{0.05}$ $|\Delta G/\Delta V|$ increases with increasing volume. G is 49% larger in $Fe_{0.9}Mg_{0.1}$ than in $Fe_{0.95}Mg_{0.05}$ at V=44.60 Bohr^3/atom, and the corresponding difference in G is only 15% at V=57.91 Bohr^3/atom.

Magnesium enhances the stiffness of bcc Fe at T=7000 K, as the Young moduli, $E = 9BG/(3B + G)$, are higher in $Fe_{0.9}Mg_{0.1}$ than in $Fe_{0.95}Mg_{0.05}$ at each volume (panel (b) in Fig. 10). In $Fe_{0.9}Mg_{0.1}$, E decreases approximately linearly with increasing volume (i.e. with decreasing pressure), while in $Fe_{0.95}Mg_{0.05}$ $|\Delta E/\Delta V|$ increases with increasing volume. Because of this, the change in E due to 5% Mg addition diminishes with increasing volume: E is 47% larger in $Fe_{0.9}Mg_{0.1}$ than in $Fe_{0.95}Mg_{0.05}$ at V=44.60 Bohr^3/atom, and this difference is reduced to 14% at V=57.91 Bohr^3/atom.

In polycrystalline materials,

$$A = \frac{G_V - G_R}{G_V + G_R} \tag{13}$$

can be used as a measure of elastic anisotropy, where G_V and G_R are the Voigt and Reuss shear moduli (Grimvall, 1999). In an isotropic material, the Voigt and Reuss averages of the shear moduli are equal, so that A=0. The more anisotropic a material is, the larger A value it has. The bcc Fe-Mg alloys considered here are highly anisotropic: A varies between 0.90 and 0.51 in $Fe_{0.95}Mg_{0.05}$, and it changes between 0.53 and 0.37 in $Fe_{0.9}Mg_{0.1}$. The anisotropy is larger in $Fe_{0.95}Mg_{0.05}$ than in $Fe_{0.9}Mg_{0.1}$ at each volume (Fig. 10, panel (c)), indicating that the increasing Mg content decreases the anisotropy of the alloys. For both alloys the anisotropy decreases with increasing volume. As a comparison, we note, that there is a significant difference in anisotropy between the two phases, namely the bcc and hcp phases of pure Fe. Hexagonal Fe is almost isotropic: A=0.02 at V=44.60 Bohr^3/atom (Kádas et al.,

2008a). In this phase, Mg alloying does not change anisotropy notably: at the same V=44.60 Bohr^3/atom volume, A=0.03 in hcp $Fe_{0.95}Mg_{0.05}$, and A=0.04 in hcp $Fe_{0.9}Mg_{0.1}$.

The longitudinal sound velocity can be calculated as $v_P = \sqrt{\frac{B+4G/3}{\varrho}}$, where ϱ is the density. The longitudinal sound velocity decreases linearly with increasing volume (panel (d) in Fig. 10) in both $Fe_{0.95}Mg_{0.05}$ and $Fe_{0.9}Mg_{0.1}$. Since $B \gg G$ in these alloys, we find that $v_P \sim \sqrt{B}$, which in turn follows a linear trend with volume. Increasing Mg content raises v_P at each V volume.

The transversal sound velocity, $v_S = \sqrt{G/\varrho}$, monotonically decreases with increasing volume in $Fe_{0.9}Mg_{0.1}$ (panel (e) in Fig. 10). In $Fe_{0.95}Mg_{0.05}$, v_S follows a different behavior: it increases with increasing volume up to V=50.97 Bohr^3/atom, and decreases above V=54.36 Bohr^3/atom. The trend in v_S vs. volume obtained for $Fe_{0.95}Mg_{0.05}$ and $Fe_{0.9}Mg_{0.1}$ can be explained by v_S being approximately proportional to $\sqrt{G}$ in bcc Fe-Mg alloys. The transversal sound velocity is raised by increasing Mg content at each volume.

4.3 Implications for the Earth's inner core

Iron-based alloys at high pressure and temperature are relevant to the Earth's solid inner core. There are extreme conditions in this part of our planet: the pressure varies between 329 and 364 GPa (Dziewonski & Anderson, 1981), and the temperature changes between 5000 and 8000 K (Hemley & Mao, 2001).

We showed in Section 4.1.3 that Mg alloying changes the elastic properties of hcp iron in such a way that the differences to the PREM values decrease. However, the shear modulus and both the longitudinal and transversal sound velocities significantly differ from those

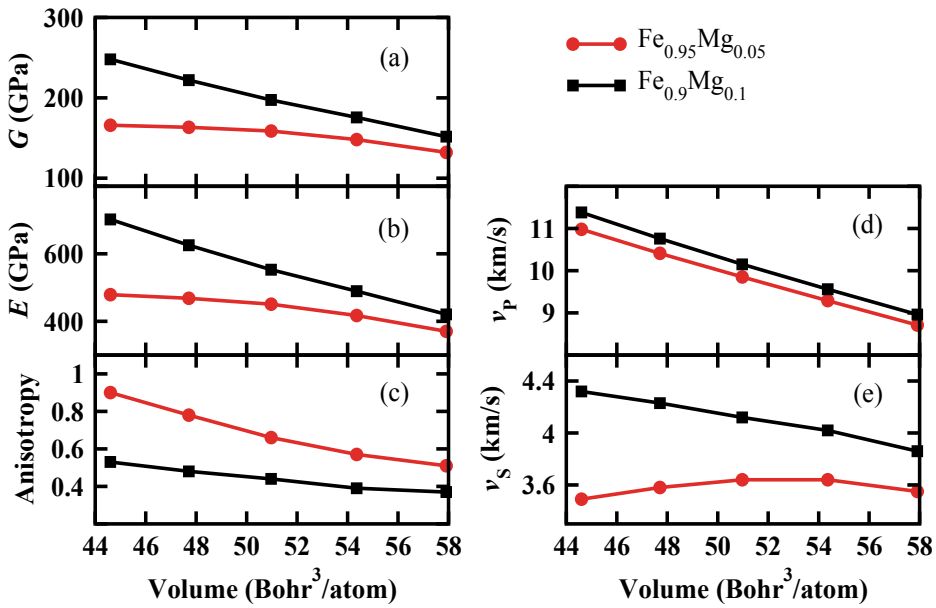

Fig. 10. Shear (G) and Young moduli (E), polycrystalline anisotropy, and longitudinal (v_P) and transversal (v_S) sound velocities of bcc $Fe_{0.95}Mg_{0.05}$ (red circles) and $Fe_{0.9}Mg_{0.1}$ alloys (black squares) at different V volumes, at T=7000 K temperature.

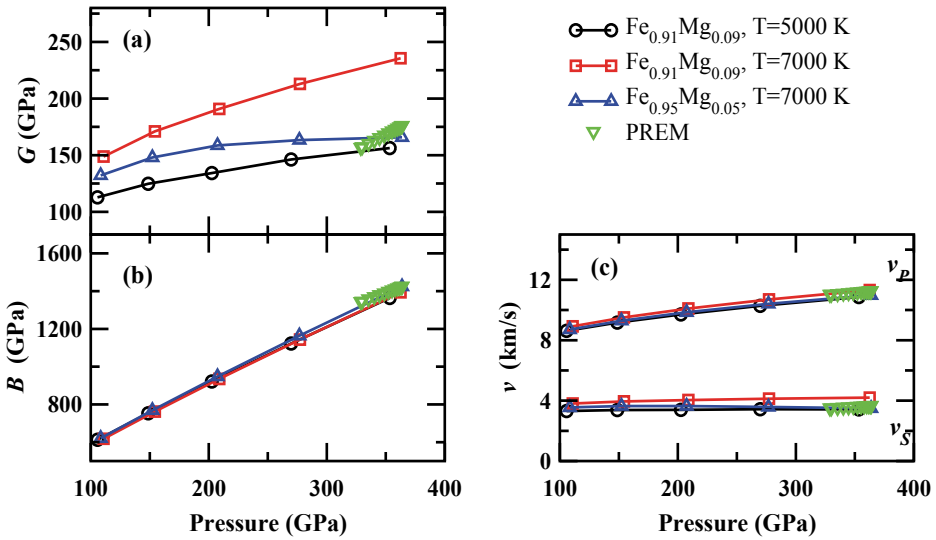

Fig. 11. Shear and bulk moduli, and sound velocities of bcc Fe-Mg alloys. Calculated shear moduli (a), bulk moduli (b) and sound velocities (v_S shear wave and v_P compressional wave velocities, panel (c)) are displayed for $Fe_{0.91}Mg_{0.09}$ at temperatures of T=5000 K (circles) and T=7000 K (squares), and for $Fe_{0.95}Mg_{0.05}$ at T=7000 K (triangles). Seismic data as given in the PREM model (Dziewonski & Anderson, 1981) are shown for comparison (inverted triangles).

of the PREM values at the Earth's inner core. The electronic DOS of hcp Fe (Fig. 9) indicates that the electronic excitations are not as significant in the hcp phase of Fe than in the bcc phase. Therefore we do not expect dramatic changes in the elastic constants at high temperature, compared to zero temperature. Accordingly, one may not expect significantly better agreement in the shear modulus and sound velocities of hcp Fe-Mg alloys with PREM data at high temperature than at T=0 K.

Therefore, in the following we focus on bcc-structured alloys, and we compare the theoretical high-temperature elastic properties of bcc Fe-Mg alloys with seismic data of the inner core, as given in the PREM model (Dziewonski & Anderson, 1981).

The calculated density of the bcc $Fe_{0.91}Mg_{0.09}$ alloy is 13.17 g/cm^3 at 5000 K and 350 GPa, which shows an excellent agreement with the corresponding core density (Dziewonski & Anderson, 1981), the deviation being 1.6%. The present density is smaller than 13.58 g/cm^3 obtained from ab initio molecular dynamics simulations (Belonoshko et al., 2007) for pure bcc iron at 356.7 GPa. In Fig. 11, we compare the shear (G) and bulk (B) moduli, as well as compressional (v_P) and shear (v_S) wave velocities of $Fe_{0.91}Mg_{0.09}$ at 5000 and 7000 K, and those of $Fe_{0.95}Mg_{0.05}$ at 7000 K with the PREM data. The shear modulus of $Fe_{0.91}Mg_{0.09}$ at 5000 K is in very good agreement with the seismic data, the deviation being -7.8% at 353 GPa (panel (a)). The figure also demonstrates that G increases with increasing temperature at constant Mg content. However, at higher temperatures smaller amount of Mg can stabilize bcc Fe, and G sensitively decreases with decreasing Mg concentration. Accordingly, $G(Fe_{0.95}Mg_{0.05})$ at 7000 K agrees excellently with those of the core: the present theoretical value at 363 GPa differs by -5.8% from the seismic data. The calculated bulk moduli (Fig. 11 (b)) are also very close to those of the inner core (Dziewonski & Anderson, 1981). $B(Fe_{0.91}Mg_{0.09})$ differs from the seismic data by -2.5% and -2.1% at 5000 and 7000 K, respectively, while the deviation

for $Fe_{0.95}Mg_{0.05}$ at 7000 K is only -0.1%. The compressional (P-wave) velocity also shows an excellent agreement with PREM (Fig. 11 (c)). At core pressures, the deviations between theoretical and PREM v_P values are -2.9% and 0.6% for $Fe_{0.91}Mg_{0.09}$ at 5000 K and 7000 K, respectively, and -2.5% for $Fe_{0.95}Mg_{0.05}$ at 7000 K. It has been shown (Vočadlo, 2007) that both bcc and hcp phases of pure Fe, as well as FeS and FeSi have significantly higher shear wave velocities than those deduced from seismology. At the same time, the present theoretical shear wave velocity (Fig. 11 (c)) agrees well with PREM for $Fe_{0.91}Mg_{0.09}$ at 5000 K: the difference being -5.4% at 353 GPa. At 7000 K and 362 GPa, the deviation between theoretical and PREM v_S values is somewhat larger (14.6%). However, v_S decreases with decreasing Mg content, and we obtain an excellent agreement (-4.8%) with seismic data for $Fe_{0.95}Mg_{0.05}$ at 7000 K and 363.8 GPa.
In summary, a bcc-structured Fe-Mg alloy containing 5-10% Mg in fact reproduces the physical properties of the Earth's inner core, as given in the PREM model, which makes it a very strong candidate structural model for the core.

5. Conclusions

Using the EMTO method in combination with the coherent-potential approximation, we have calculated the single-crystal and polycrystalline elastic properties of ferromagnetic bcc Fe-Mg random alloys encompassing up to 10 at.% Mg. At ambient conditions, all elastic parameters of ferromagnetic bcc Fe-Mg decrease in an almost linear manner with Mg addition. In general, Mg is found to have a more pronounced impact on the elastic properties of Fe-based alloys than that of Cr. In particular, the B/G ratio decreases by 17.3% when 10% Mg is added to bcc Fe, indicating that Mg reduces the ductility of Fe. According to the classical solid-solution strengthening models (Vitos & Johansson, 2007; Labusch, 1972), the large alloying effects obtained for the Fe-Mg alloys should result in an enhanced mechanical hardness. These predictions are subject for further theoretical investigations and call for well designed experimental studies on the mechanical properties of Fe-rich Fe-Mg solid solutions. We showed that at Earth's core pressures, Mg alloying changes the elastic properties of hcp iron in such a way that the differences to the seismic data decrease. The calculated shear moduli and sound velocities of hcp Fe-Mg alloys still differ significantly from those of the core as provided by seismic observations, even at 10% Mg content. We showed that at the conditions of the inner core 5-10% Mg stabilizes bcc Fe both dynamically and thermodynamically, and we gave an electronic structure explanation of this phenomenon. We demonstrated that the physical properties of bcc Fe-Mg alloys containing 5-10% Mg reproduce those of the inner core: the calculated density, elastic moduli and sound velocities of bcc Fe-Mg alloys are consistent with seismic data. Therefore the bcc-structured Fe-Mg alloy is amongst the strongest candidate models for the Earth's solid inner core.

6. Acknowledgments

The Kami Research Foundation, the Swedish Research Council, the Swedish Foundation for Strategic Research, the Swedish Energy Agency, the Swedish Foundation for International Cooperation in Research and Higher Education, and the China Scholarship Council are acknowledged for financial support. The calculations were performed on UPPMAX and HPC2N resources.

7. References

Ahuja, B. L., Arora, G., Ahmed, G., Rathor, A., Sharma, V., Kádas, K. & Ahuja, R. (2009). A study of electron momentum density and charge transfer in W-Cu system, *J. Alloys and Comp.* 467: 595–599.

Allegre, C. J., Poirier, J. P., Humler, E. & Hofmann, A. W. (1995). The chemical-composition of the Earth, *Earth Planet. Sci. Lett.* 134(3-4): 515–526.

Andersen, O. K., Arcangeli, C., Tank, R. W., Saha-Dasgupta, T., Krier, G., Jepsen, O. & Dasgupta, I. (1998). *in: Tight-Binding Approach to Computational Materials Science, edited by P. E. A. Turchi and A. Gonis and L. Colombo, MRS Symposia Proceedings No. 491*, Materials Research Society, Pittsburgh. pp. 3–34.

Andersen, O. K., Jepsen, O. & Krier, G. (1994). *in: Lectures on Methods of Electronic Structure Calculations, edited by O. K. Andersen and A. Mookerjee*, World Scientific, Singapore. pp. 63.

Anderson, D. (1989). *Theory of Earth*, Blackwell Scientific Publications, Oxford. pp. 366.

Belonoshko, A. B., Ahuja, R. & Johansson, B. (2003). Stability of the body-centered-cubic phase of iron in the Earth's inner core, *Nature* 424: 1032–1034.

Belonoshko, A. B., Skorodumova, N. V., Davis, S., Osiptsov, A. N., Rosengren, A. & Johansson, B. (2007). Origin of the low rigidity of the Earth's inner core, *Science* 316: 1603–1605.

Belonoshko, A. B., Skorodumova, N. V., Rosengren, A. & Johansson, B. (2008). Elastic anisotropy of Earths inner core, *Science* 319: 797–800.

Birch, F. (1961). Composition of the Earth's mantle, *Geophys. J. Royal Astronomical Soc.* 4: 295–311.

Chen, B., Gao, L., Funakoshi, K. I. & Li, J. (2007). Thermal expansion of iron-rich alloys and implications for the Earth's core, *Proc. Natl. Acad. Sci. USA* 104: 9162–9167.

Cieslak, J., Dubiel, S. M. & Sepiol, B. (2000). Mossbauer-effect study of the phase separation in the Fe-Cr system, *J. Phys.: Condens. Matter.* 12: 6709–6717.

de Boer, F. R., Boom, R., Mattens, W. C. M., Miedema, A. R. & Niessen, A. K. (1988). *Cohesion in Metals: Transition Metal Alloys, Vol. 1, edited by F. R. de Boer and D. G. Pettifor*, North-Holland, Amsterdam.

Delczeg-Czirjak, E. K., Delczeg, L., Ropo, M., Kokko, K., Punkkinen, M. P. J., Johansson, B. & Vitos, L. (2009). Ab initio study of the elastic anomalies in Pd-Ag alloys, *Phys. Rev. B* 79: 085107.

Dorofeev, G. A., Elsukov, E. P. & Ul'yanov, A. L. (2004). Mechanical alloying of immiscible elements in the Fe-Mg system, *Inorg. Mater.* 40: 690–699.

Dubrovinskaia, N., Dubrovinsky, L., Kantor, I., Crichton, W. A., Dmitriev, V., Prakapenka, V., Shen, G., Vitos, L., Ahuja, R., Johansson, B. & Abrikosov, I. A. (2005). Beating the miscibility barrier between iron group elements and magnesium by high-pressure alloying, *Phys. Rev. Lett.* 95: 245502.

Dubrovinskaia, N., Dubrovinsky, L. & McCammon, C. (2004). Iron-magnesium alloying at high pressures and temperatures, *J. Phys. Cond. Mat.* 16: S1143–S1150.

Dubrovinsky, L., Dubrovinskaia, N., Narygina, O., Kantor, I., Kuznetzov, A., Prakapenka, V. B., Vitos, L., Johansson, B., Mikhaylushkin, A. S., Simak, S. I. & Abrikosov, I. A. (2007). Body-centered cubic iron-nickel alloy in Earth's core, *Scince* 316: 1880–1883.

Dubrovinsky, L. S., Saxena, S. K., Tutti, F., Rekhi, S. & LeBehan, T. (2000). In-situ X-ray study of thermal expansion and phase transition of iron at multimegabar pressure, *Phys. Rev. Lett.* 84: 1720–1723.

Dziewonski, A. M. & Anderson, D. L. (1981). Preliminary reference Earth model, *Phys. Earth*

Planet. Inter. 25: 297–356.
Grimvall, G. (1976). Polymorphism of metals .3. theory of temperature-pressure phase-diagram of iron, *Phys. Scr.* 13: 59–64.
Grimvall, G. (1999). *Thermophysical Properties of Materials*, Elsevier, North-Holland, Amsterdam. pp. 70-78.
Gyorffy, B. L. (1972). Coherent-potential approximation for a nonoverlapping-muffin-tin-potential model of random substitutional alloys, *Phys. Rev. B* 5: 2382–2384.
Haitani, T., Tamura, Y., Motegi, T., Kono, N. & Tamehiro, H. (2003). Solubility of iron in pure magnesium and cast structure of Mg-Fe alloy, *Mater. Sci. Forum* 419-422: 697–702.
Hashin, Z. & Shtrikman, S. (1962). A variational approach to the theory of the elastic behaviour of polycrystals, *J. Mech. Phys. Solids* 10: 343–352.
Hemley, R. J. & Mao, H. K. (2001). In-situ studies of iron under pressure: new windows on the Earth's core, *Int. Geol. Rev.* 43: 1–30.
Hightower, A., Fultz, B. & R. C. Bowman, J. (1997). Mechanical alloying of fe and mg, *J. Alloys Compd.* 252: 238–244.
Hill, R. (1952). The elastic behaviour of a crystalline aggregate, *Proc. Phys. Soc. A* 65: 349–354.
Hohenberg, P. & Kohn, W. (1964). Inhomogeneous electron gas, *Phys. Rev.* 136: B864–B871.
Hu, Q., Kádas, K., Hogmark, S., Yang, R., Johansson, B. & Vitos, L. (2007). Predicting hardness of covalent/ionic solid solution from first principles theory, *Appl. Phys. Lett.* 91: 121918.
Hu, Q. M., Kádas, K., Hogmark, S., Yang, R., Johansson, B. & Vitos, L. (2008). Hardness and elastic properties of covalent/ionic solid solutions from first-principles theory, *J. Appl. Phys.* 103: 083505.
Huang, L., Vitos, L., Kwon, S. K., Johansson, B. & Ahuja, R. (2006). Thermoelastic properties of random alloys from first-principles theory, *Phys. Rev. B* 73: 104203.
Hultgren, R., Desai, P. D., Hawkins, D. T., Gleiser, M. & Kelley, K. K. (1973). *Selected Values of the Thermodynamic Properties of Binary Alloys*, American Society for Metals, Metals Park, Ohio. pp. 694-703.
Kádas, K., Lindquist, M., Erikssson, O., Johansson, B. & Vitos, L. (2009). Magnetism-driven anomalous surface alloying between Cu and Cr, *Appl. Phys. Lett.* 94: 172507.
Kádas, K., Vitos, L. & Ahuja, R. (2008a). Elastic properties of iron-rich hcp Fe-Mg alloys up to Earth's core pressures, *Earth Planet. Sci. Lett.* 271: 221–225.
Kádas, K., Vitos, L. & Ahuja, R. (2008b). Theoretical evidence of a superconducting transition in doped silicon and germanium driven by a variation of chemical composition, *Appl. Phys. Lett.* 92: 052505.
Kádas, K., Vitos, L., Johansson, B. & Ahuja, R. (2009). Stability of body-centered cubic iron-magnesium alloys in the Earth's inner core, *Proc. Natl. Acad. Sci. USA* 106: 15560–15562.
Kantor, A. P., Kantor, I. Y., Kurnusov, A. V., Kuznetsov, A. Y., Dubrovinskaia, N. A., Krisch, M., Bossak, A. A., Dmitriev, V. P., Urusov, V. S. & Dubrovinsky, L. S. (2007). Sound wave velocities of fcc Fe-Ni alloy at high pressure and temperature by mean of inelastic X-ray scattering, *Phys. Earth Planet. Inter.* 164: 83–89.
Kohn, W. & Sham, L. J. (1965). Self-consistent equations including exchange and correlation effects, *Phys. Rev.* 140: A1133–A1138.
Kollár, J., Vitos, L. & Skriver, H. L. (2000). *in: Electronic Structure and Physical Properties of Solids: the uses of the LMTO method, Editor H. Dreyssé, Lectures Notes in Physics*,

Springer-Verlag, Berlin. pp. 85.
Korzhavyi, P. A., Ruban, A. V., Abrikosov, I. A. & Skriver, H. L. (1995). Madelung energy for random metallic alloys in the coherent potential approximation, *Phys. Rev. B* 51: 5773–5780.
Korzhavyi, P. A., Ruban, A. V., Odqvist, J., Nilsson, J.-O. & Johansson, B. (2009). Electronic structure and effective chemical and magnetic exchange interactions in bcc Fe-Cr alloys, *Phys. Rev. B* 79: 054202.
Labusch, R. (1972). Statistical theories of solid solution hardening, *Acta Metall.* 20: 917–927.
Laio, A., Bernard, S., Chiarotti, G. L., Scandolo, S. & Tosatti, E. (2000). Physics of iron at Earth's core conditions, *Science* 287: 1027–1030.
Landa, A., Chang, C.-C., Kumta, P. N., Vitos, L. & Abrikosov, I. A. (2002). Phase stability of $Li(Mn_{100-x}Co_x)o_2$ oxides: an ab initio study, *Solid State Ionics* 149: 209–215.
Lin, J. F., Heinz, D. L., Campbell, A. J., Devine, J. M. & Shen, G. (2002). Iron-silicon alloy in Earth's core?, *Science* 295: 313–315.
Magyari-Köpe, B., Grimvall, G. & Vitos, L. (2002). Elastic anomalies in Ag-Zn alloys, *Phys. Rev. B* 66: 064210.
Magyari-Köpe, B., Vitos, L., G. Grimvall, B. J. & Kollár, J. (2002). Low-temperature crystal structure of CaSiO3 perovskite: An ab initio total energy study, *Phys. Rev. B* 65: 193107.
Magyari-Köpe, B., Vitos, L. & Grimvall, G. (2004). Anomalous behavior of lattice parameters and elastic constants in hcp Ag-Zn alloys, *Phys. Rev. B* 70: 052102.
Magyari-Köpe, B., Vitos, L., Johansson, B. & Kollár, J. (2001). Parametrization of perovskite structures: an ab initio study, *Acta Crystallogr., Sect. B: Struct. Sci* 57: 491–496.
Magyari-Köpe, B., Vitos, L., Johansson, B. & Kollár, J. (2002). High-pressure structure of ScAlO3 perovskite, *J. Geophys. Res.-Solid Earth* 107: 2136–2141.
Mao, H. K., Shu, J., Shen, G., Hemley, R. J., Li, B. & Singh, A. K. (1998). Elasticity and rheology of iron above 220 GPa and the nature of the Earth's inner core, *Nature* 396: 741–743.
Mao, H. K., Wu, Y., Chen, L. C. & Shu, J. F. (1990). Static compression of iron to 300 GPa and $Fe_{0.8}Ni_{0.2}$ alloy to 260 GPa: implications for composition of the core, *J. Geophys. Res.* 95: 21737–21742.
Massalski, T. B. (1986). *Binary Alloy Phase Diagrams, edited by T. B. Massalski*, American Society for Metals, Metals Park, Ohio. Vol.1.
Massalski, T. B. (1996). *in: Physical Metallurgy, Structure and Stability of Alloys, Vol.1, edited by R. W. Cahn and P. Haasen*, North-Holland, Amsterdam. pp. 134.
Matsui, M. & Anderson, O. L. (1997). The case for a body-centered cubic phase (α') for iron at inner core conditions, *Phys. Earth Planet. Inter.* 103: 55–62.
McDonough, W. F. (2003). *in: Treatise on geochemistry, Editor R. W. Carlson*, Elsevier, New York. pp. 547-568.
McDonough, W. F. & Sun, S. S. (1995). The composition of the Earth, *Chem. Geol.* 120: 223–253.
Mikhaylushkin, A. S., Simak, S. I., Dubrovinsky, L., Dubrovinskaia, N., Johansson, B. & Abrikosov, I. A. (2007). Pure iron compressed and heated to extreme conditions, *Phys. Rev. Lett.* 99: 165505.
Moruzzi, V. L., Janak, J. F. & Schwarz, K. (1988). Calculated thermal properties of metals, *Phys. Rev. B* 37: 790–799.
Oguchi, T., Terakura, K. & Hamada, N. (1983). Magnetism of iron above the Curie temperature, *J. Phys. F: Met. Phys.* 13: 145–160.
Olsson, P., Abrikosov, I. A., Vitos, L. & Wallenius, J. (2003). Ab initio formation energies of

Fe-Cr alloys, *J. Nucl. Mater.* 321: 84–90.
Olsson, P., Abrikosov, I. A. & Wallenius, J. (2006). Electronic origin of the anomalous stability of fe-rich bcc Fe-Cr alloys, *Phys. Rev. B* 73: 104416.
Pearson, W. B. (1958). *A handbook of lattice spacings and structures of metals and alloys*, Pergamon Press, Belfast. pp. 532.
Perdew, J. P., Burke, K. & Ernzerhof, M. (1996). Generalized gradient approximation made simple, *Phys. Rev. Lett.* 77: 3865–3868.
Pugh, S. F. (1954). XCII. relations between the elastic moduli and the plastic properties of polycrystalline pure metals, *Philos. Mag.* 45: 823–843.
Qiu, S. L. & Marcus, P. M. (2003). Elasticity of hcp nonmagnetic Fe under pressure, *Phys. Rev. B* 68: 054103.
Reuss, A. (1929). Calculating the limit of mishkristallen flowing due to the plastizitatsbeding for monocrystals, *Z. Angew. Math. Phys.* 9: 49.
Robie, R. A., Hemingway, B. S. & Fisher, J. R. (1978). *Thermodynamic properties of minerals and related substances at 298.15 K and 1 bar (105 pascals) pressure and at higher temperatures*, U.S. Geological Survey Bulletin 1452, Washington.
Ross, W., Young, D. A. & Grover, R. (1990). Theory of the iron phase diagram at Earth core conditions, *J. Geophys. Res.* 95: 21713–21716.
Sahlberg, M., Beran, P., Nielsen, T. K., Cerenius, Y., Kádas, K., Punkkinen, M. P. J., Vitos, L., Eriksson, O., Jensen, T. R. & Andersson, Y. (2009). A new material for hydrogen storage; $ScAl_{0.8}Mg_{0.2}$, *J. Solid State Chem.* 182: 3113–3117.
Singh, A. K., Mao, H. K., Shu, J. & Hemley, R. J. (1998). Estimation of single-crystal elastic moduli from polycrystalline X-ray diffraction at high pressure: application to FeO and iron, *Phys. Rev. Lett.* 80: 2157–2160.
Söderlind, P., Moriarty, J. A. & Wills, J. M. (1996). First-principles theory of iron up to earth-core pressures: Structural, vibrational, and elastic properties, *Phys. Rev. B* 53: 14063–14072.
Soven, P. (1967). Coherent-potential model of substitutional disordered alloys, *Phys. Rev.* 156: 809–813.
Speich, G. R., Schwoeble, A. J. & Leslie, W. C. (1972). Elastic constants of binary iron-base alloys, *Metall. Trans.* 3: 2031–2037.
Steinle-Neumann, G., Stixrude, L. & Cohen, R. E. (1999). First-principles elastic constants for the hcp transition metals Fe, Co, and Re at high pressure, *Phys. Rev. B* 60: 791–799.
Steinle-Neumann, G., Stixrude, L., Cohen, R. E. & Gülseren, O. (2001). Elasticity of iron at the temperature of the Earth's inner core, *Nature* 413: 57–60.
Stixrude, L. & Cohen, R. E. (1995). High-pressure elasticity of iron and anisotropy of Earth's inner core, *Science* 267: 1972–1975.
Sutton, A. L. & Hume-Rothery, W. (1955). *Philos. Mag.* 46: 1295–1309.
Taga, A., Vitos, L., Johansson, B. & Grimvall, G. (2005). Ab initio calculation of the elastic properties of $Al_{1-x}Li_x$ ($x \leq 0.2$) random alloys, *Phys. Rev. B* 71: 014201.
Tavaresa, S. S. M., de Noronha, R. F., da Silva, M. R., Neto, J. M. & Pairis, S. (2001). *Mater. Res.* 4: 237.
Vitos, L. (2001). Total-energy method based on the exact muffin-tin orbitals theory, *Phys. Rev. B* 64: 014107.
Vitos, L. (2007). *The EMTO Method and Applications, in: Computational Quantum Mechanics for Materials Engineers*, Springer-Verlag, London.
Vitos, L., Abrikosov, I. A. & Johansson, B. (2001). Anisotropic lattice distortions in random

alloys from first-principles theory, *Phys. Rev. Lett.* 87: 156401.
Vitos, L. & Johansson, B. (2007). Applied parallel computing. state of the art in scientific computing, lecture notes in computer science, springer-verlag berlin heidelberg, B. kagström et al. (eds.), 4699: 510–519.
Vitos, L., Korzhavyi, P. A. & Johansson, B. (2002). Elastic property maps of austenitic stainless steels, *Phys. Rev. Lett.* 88: 155501.
Vitos, L., Korzhavyi, P. A. & Johansson, B. (2003). Stainless steel optimization from quantum mechanical calculations, *Nat. Mater.* 2: 25–28.
Vitos, L., Korzhavyi, P. A. & Johansson, B. (2006). Evidence of large magnetostructural effects in austenitic stainless steels, *Phys. Rev. Lett.* 96: 117210.
Vitos, L., Skriver, H. L., Johansson, B. & Kollár, J. (2000). Application of the exact muffin-tin orbitals theory: the spherical cell approximation, *Comp. Mat. Sci.* 18: 24–38.
Voigt, W. (1889). The relation between the two elastic moduli of isotropic materials, *Ann. Phys. (Leipz.)* 38: 573.
Vočadlo, L. (2007). Ab initio calculations of the elasticity of iron and iron alloys at inner core conditions: Evidence for a partially molten inner core?, *Earth Planet. Sci. Lett.* 254: 227–232.
Vočadlo, L., Alfè, D., Gillan, M. J., Wood, I. G., Brodholt, J. P. & Price, G. D. (2003). Possible thermal and chemical stabilization of body-centered-cubic iron in the Earth's core, *Nature* 424: 536–539.
Vočadlo, L., Brodholt, J., Alfè, D., Gillan, M. J. & Price, G. D. (2000). Ab initio free energy calculations on the polymorphs of iron at core conditions, *Phys. Earth Planet. Inter.* 117: 123–137.
Vočadlo, L., Dobson, D. P. & Wood, I. G. (2006). An ab initio study of nickel substitution into iron, *Earth Planet. Sci. Lett.* 248: 147–152.
Yelsukov, E. P., Dorofeev, G. A. & Ul'yanov, A. L. (2005). Mechanism and kinetics of mechanical alloying in an immiscible Fe-Mg system, *Czech. J. Phys.* 55: 913–920.
Young, D. A. (1991). *Phase Diagrams of the Elements*, University of California Press, Berkeley.
Zander, J., Sandström, R. & Vitos, L. (2007). Modelling mechanical properties for non-hardenable aluminium alloys, *Comp. Mat. Sci.* 41: 86–95.
Zhang, H. L., Johansson, B. & Vitos, L. (2009). Ab initio calculations of elastic properties of bcc Fe-Mg and Fe-Cr random alloys, *Phys. Rev. B* 79: 224201.
Zhang, H. L., Punkkinen, M. P. J., Johansson, B., Hertzman, S. & Vitos, L. (2010). Single-crystal elastic constants of ferromagnetic bcc Fe-based random alloys from first-principles theory, *Phys. Rev. B* 81: 184105.

5

Precipitates of γ–$Mg_{17}Al_{12}$ Phase in AZ91 Alloy

Katarzyna N. Braszczyńska-Malik
Institute of Materials Engineering
Technical University of Częstochowa
Poland

1. Introduction

Magnesium alloys are light metallic structural materials with a unique combination of properties, which are very attractive in such applications as the automobile, aerospace and electronic industries (Mordike & Ebert, 2001). The use of magnesium alloys has become significant due to a one-third lower density of magnesium compared with aluminium, improved damping ability, a higher resistance to corrosion and better mechanical properties. In lightweight magnesium alloys, aluminium constitutes the main alloying element, chiefly because of its low price, availability, low density and the advantageous effects on corrosion and strength properties (Smola et al., 2002). The AZ91 alloy (contains about 9 wt.% Al and 1 wt.% Zn, with addition of about 0.4 wt.% Mn) is the most widely used magnesium alloy exhibiting a good combination of high strength at room temperature, good castability and excellent corrosion resistance. According to the phase diagram (Fig. 1) the microstructure of Mg–Al alloys is generally characterized by a solid solution of aluminium in magnesium (an α phase with a hexagonal closely-packed, hcp structure) and the γ-phase.

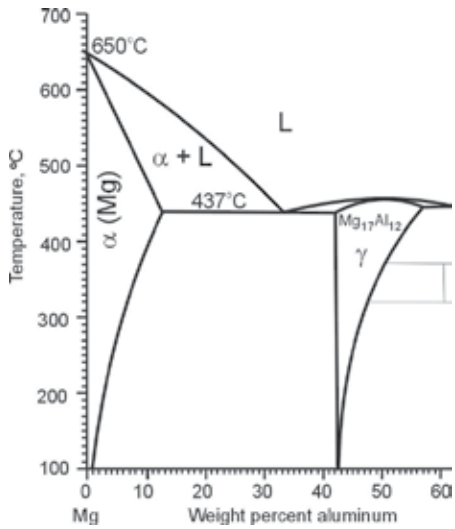

Fig. 1. Fragment of Mg–Al phase diagram (adopted from (ASM Handbook Committee, 1986))

The γ-phase (called also β-phase) is an intermetallic compound with a stoichiometric composition of $Mg_{17}Al_{12}$ (at 43.95 wt.% Al) and an α-Mn–type cubic unit cell. Young modulus of γ-phase is about 80 GPa whereas for magnesium only 45 GPa. In comparison with binary Mg–Al, new phases do not appear in commercial ternary alloys with zinc (like AZ91) when the Al to Zn ratio is larger then 3:1. In this case, the zinc substitutes aluminium in the γ-$Mg_{17}Al_{12}$ phase, creating a ternary intermetallic compound $Mg_{17}Al_{11.5}Zn_{0.5}$ or $Mg_{17}(Al,Zn)_{12}$ type (Braszczyńska-Malik K.N., 2005; Bursik & Svoboda, 2002 ; Celotto, 2000; Gonzalez-Martinez et al., 2007; Gharghouri et al., 1998; Celotto & Brastow, 2001).

2. The γ phase in as-cast AZ91 alloy

According to the equilibrium phase diagram, in Mg-Al alloys (Al concentration to 12.9 wt.%) after solidification process only one α-phase should occur. Non-equilibrium solidification condition cause the formation of large crystal of the primary γ-phase, depleted in alloying elements, and pushing the Al admixture away into interdendritical spaces. At the last stage of solidification the α + γ binary eutectic is formed at 473 K. In Mg-Al alloys eutectic can be fully or partially divorced dependent on aluminum content and solidification condition. Solidification conditions during gravity cast of magnesium alloys are effective in microstructure of casts. Differences in characteristic temperatures obtained during solidification of AZ91 alloy in cold steel and sand modulus (rod samples with a 200 mm diameter) are given in Fig. 2. Results were obtained from derivative thermal analysis (DTA) carried out by using a Cristaldigraph PC computer recorder. DTA curves were collected from thermocouple NiCr-NiAl with a 1.5 mm diameter, located directly into moulds. Measurements were archived with a sampling time of 0.2 s for steel mould and 1 s for sand mould. According to presented DTA results in a steel mould the AZ91 alloy solidified only 15 seconds whereas in sand mould (at the same size) about 680 seconds (Braszczyńska-Malik & Zyska, 2010).

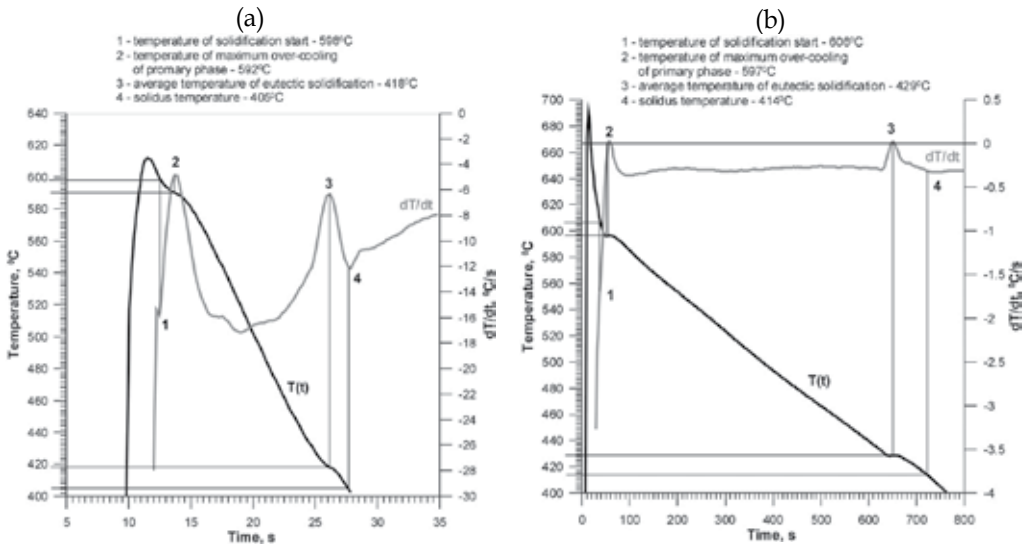

Fig. 2. DTA results: solidification curve T(t) and their first derivative dT/dt obtained for AZ91 alloy solidified in a steel (a) and sand mould (b)

Fig. 3 and 4 show microstructure of AZ91 magnesium alloy solidified in steel and sand moulds, respectively (rod samples with a 200 mm diameter). In both cases, the dendritical microstructure is characterised by the presence of α solid solution and the binary α + γ eutectic. Dendrite arms space (DAS) is visible high for alloy solidified in a sand mould. For samples cast into a steel mould, central areas of dendrites were strongly depleted in aluminium whereas near eutectic regions aluminium concentration was higher (Fig. 3b). Such aluminium distribution is very often observed in gravity cast AZ91 alloy. Differences in alloying elements distribution in microstructure were presented in Fig. 5 as the results of SEM+EDX analysis. Additionally, the presence of a small amount of manganese in commercial magnesium-aluminium alloys additionally causes the formation of aluminium-manganese intermetallic compounds Al_8Mn_5 or $Al_{11}Mn_4$ (Fig. 3b) (Braszczyńska-Malik K.N., 2005; Ohno et al., 2006).

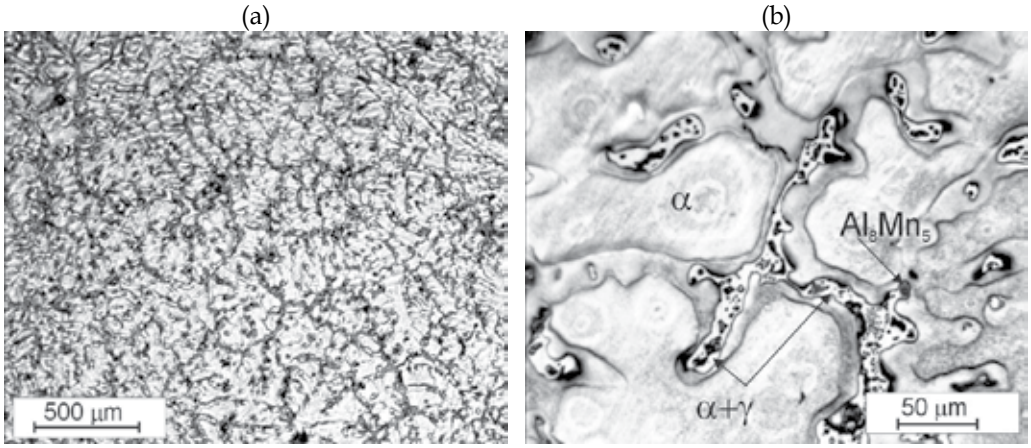

Fig. 3. Microstructure of AZ91 alloy; cast into a steel mould; light microscopy

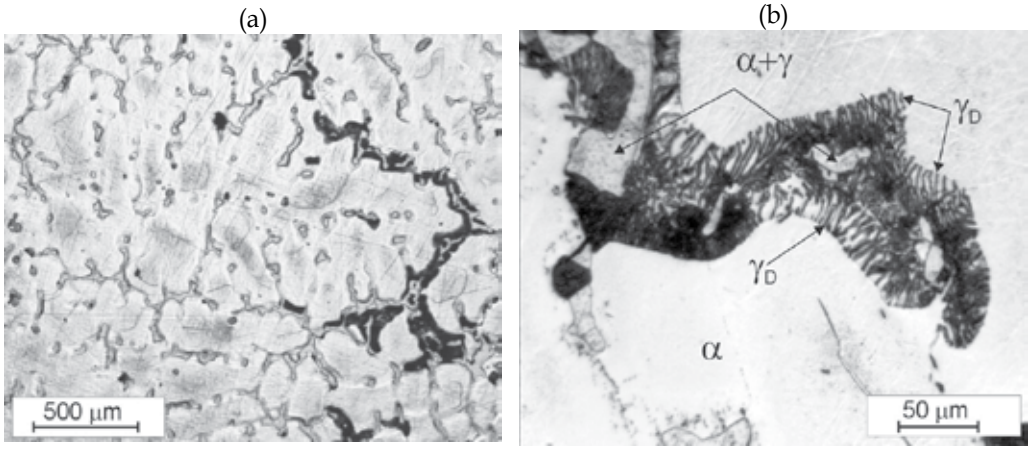

Fig. 4. Microstructure of AZ91 alloy; cast into a sand mould; light microscopy
(γ_D – discontinuous precipitates)

In the case of the alloy solidified in a sand mould, dark areas observed in Fig. 3a constitute regions of γ-phase discontinuous precipitates. Discontinuous precipitates (γ_D) formed from supersaturated solid solution (like areas marked as 2 in Fig. 5) due to slow cooling down of casts below the solvus temperature. Discontinuous precipitates are typical for AZ91 magnesium alloy gravity casts into sand moulds, where cooling of cast is slow. Characteristic lamellar structure of plate-like γ-phase is shown in Fig. 4b.

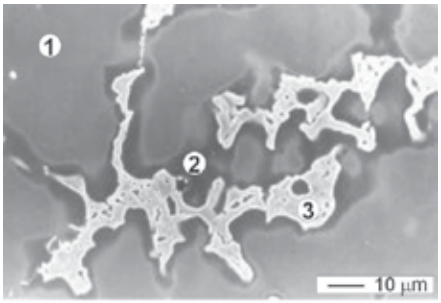

Point	Element	wt.%	at.%
1	Mg	95.03	95.50
	Al	4.97	4.50
2	Mg	90.10	91.27
	Al	9.33	8.52
	Zn	0.57	0.21
3	Mg	61.67	65.77
	Al	33.73	32.41
	Zn	4.60	1.82

Fig. 5. SEM image of AZ91 alloy; cast into a steel mould (a) and EDX analysis from points marked in the SEM image (b)

Analogical microstructure is observed in high-pressure die casts of Mg-Al alloys. Fig. 6 shows microstructure of AZ91 alloy from cast obtained using an Idra cold chamber machine (320 tone locking force). The microstructure consists of primary α phase and α + γ partially divorced eutectic (Braszczyńska-Malik et al., 2008).

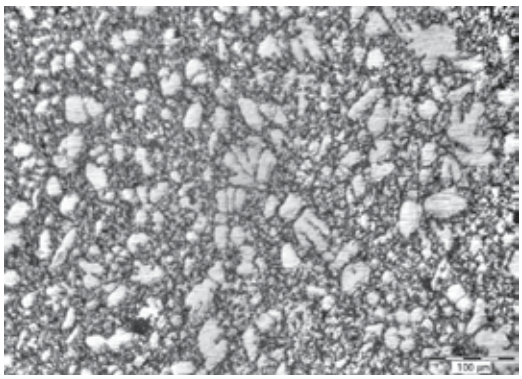

Fig. 6. Microstructure of AZ91 alloy; high-pressure die-casting; light microscopy

3. The γ phase in AZ91 alloy after heat treatment (discontinuous and continuous precipitation)

Magnesium-aluminium alloys are susceptible to heat treatment due to the variable solubility of their alloying elements in a solid state with temperature (Fig. 1). The maximum solid solubility of aluminium in magnesium is reasonably high at 12.9 wt.% Al at an eutectic temperature of 710 K whereas the equilibrium concentration at 473 K is about 2.9 wt.% Al. Solution annealing of the AZ91 alloy at 693 K caused a total dissolution of the α+γ eutectic and homogenised the aluminium throughout the matrix. The time necessary to obtain the homogeneous microstructure consisting of solid solution grains is very long (minimum 24 h) due to very slow diffusion of aluminium in a magnesium solid state. It should also be noted, that the Al_8Mn_5 intermetallic compound is not involved in heat treatment (Braszczyńska-Malik, 2009 a). The microstructure obtained after solution annealing is shown in Fig. 7.

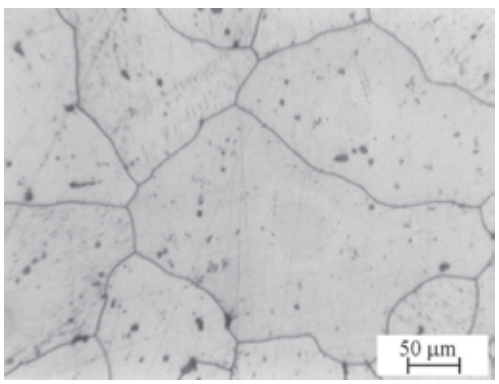

Fig. 7. Microstructure of AZ91 alloy after solution annealing at 693 K for 24 h; light microscopy

During conventional heat treatment, involving solution annealing at about 690 K for a minimum of 24 h, followed by ageing at about 430 K for 16 h (T6 conditions), the precipitation process appears and the formation of γ phase precipitates occurs. During γ phase precipitation, neither Gunier-Preston zones nor other metastable phases are formed (Dully et al. 1995). The microstructure of the AZ91 alloy after ageing of the supersaturated solid solution at 423 K for 16 h (T6 conditions) is characterized by the presence of fine, plate-like, discontinuous γ precipitates. Fig. 8 shows a typical microstructure of the AZ91 alloys after this heat treatment. The γ phase precipitates had a lamellar morphology with a marked anisotropy of growth.

However, precipitation occurring in supersaturated alloys can take place either continuously or discontinuously. During both discontinuous and continuous precipitation reactions, representing a solid-solid phase transformation, a supersaturated solid solution (α_0) decomposes into a new solute-rich precipitate (γ) and a less-saturated, near-equilibrium, initial phase (α) with the same crystal structure as the α_0. The differences between discontinuous and continuous precipitation consist in the nucleation places and growth. Discontinuous precipitation (DP) is the cellular growth of alternating plates of the secondary phase and near-equilibrium matrix phase at high angle boundaries. This heterogeneous reaction leads to the formation of a lamellar structure behind a moving grain boundary.

Continuous precipitation (CP) proceeds by a different mechanism, where precipitates of the γ phase nucleate and grow inside the α_0 grains. In most alloys, nevertheless, these two types of precipitates can also occur simultaneously (Braszczyńska, 2002; Cerri & Barbagallo, 2002; Bradai et al., 2001; Bettles, 2003; Nie et al., 2001).

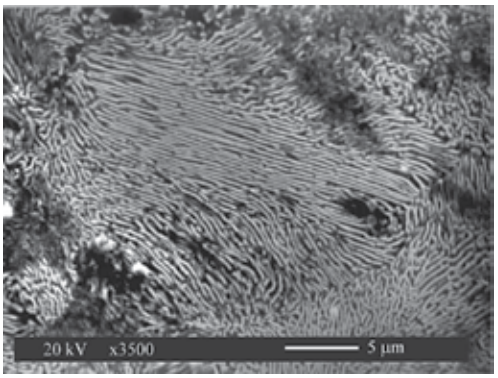

Fig. 8. Discontinuous precipitates in AZ91 alloy after ageing supersaturated solid solution at 423 K for 16 h; SEM

Figs. 9-10 show typical SEM images representing the variation in precipitation morphology with the temperature. At the temperature of 545 K both continuous and discontinuous precipitates were observed. The light areas in Fig. 9a represent typical colonies of discontinuous lamellar precipitates growing from the grain boundaries. Additionally, after ageing at this temperature, small continuous precipitates inside the grains were observed. Fig. 9b illustrates fine continuous precipitates observed after ageing for 2 h at 545 K. The same results were obtained after ageing at 473 K and 543 K for binary Mg-9 wt.% Al alloy (Braszczyńska-Malik, 2009 a).

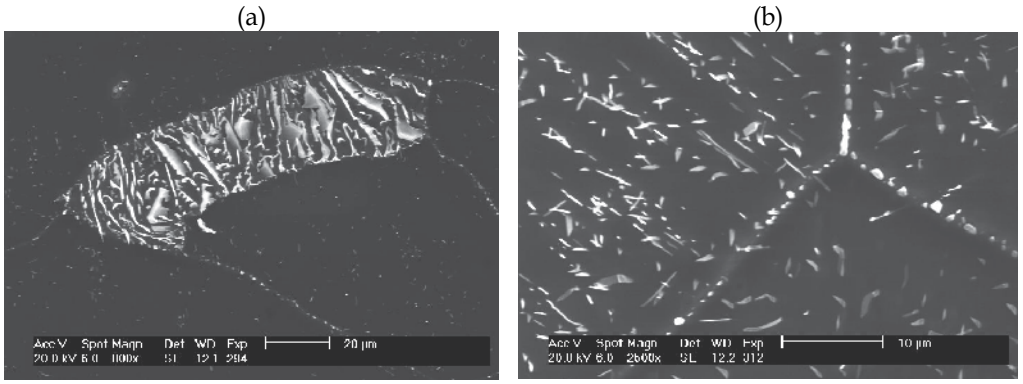

Fig. 9. Discontinuous (a) and continuous (b) precipitates of γ phase in AZ91 alloy after ageing at 545 K; SEM

A different situation was observed after ageing supersaturated alloys at 623 K. Although in the samples aged for 1 h the presence of γ precipitates at the grain boundaries was also revealed (Fig. 10a), the process of its growth was quickly stopped. Ageing of the AZ91 alloy at 623 K for 2 h caused the occurrence only of continuous precipitates also with a visible

orientation relationship with the matrix grains (Fig. 10b). It should be noted, that at this temperature (623 K) typical colonies of discontinuous precipitates did not occur. The same results were observed for the binary Mg-9 wt.% Al alloy (Braszczyńska-Malik, 2009 a).

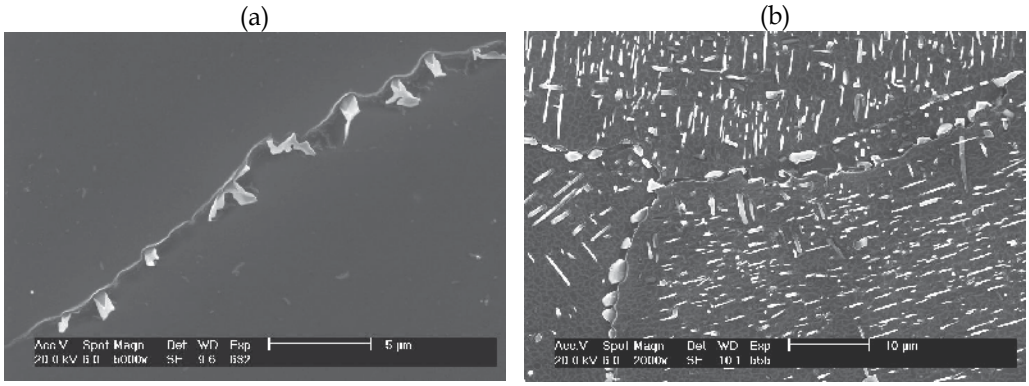

Fig. 10. Precipitates of γ phase at grain boundary (a) and continuous precipitates (b) in AZ91 alloy after ageing at 623 K; SEM

As was revealed, for the AZ91 alloy, discontinuous and continuous precipitates can occur simultaneously or competitively, dependently on the ageing temperature. After ageing at 423 K typical colonies of discontinuous precipitates were observed whereas at 623 K only continuous precipitates were formed inside grains. It proved that continuous precipitation tends to be favoured at high temperatures (i.e. close to the solvus curve) whereas at low temperatures of ageing, discontinuous precipitation invades all the samples. The presented observations also indicate that at an intermediate temperature range both discontinuous and continuous precipitates can be observed. The same results were obtained for the commercial AZ91 alloy and experimentally binary Mg-9 wt.% Al alloy (Braszczyńska-Malik, 2009a). It confirmed, that zinc present in the commercial alloy not does influence the precipitate type. It should also be noted, that the volume fraction of continuous precipitates increased with ageing temperature. Nevertheless, the mutual ratio of the discontinuous and continuous precipitates in each sample is practically not evident, because it depends on the local conditions for nucleation and growth in the grains and at grain boundaries. Additionally, as could be expected, the time necessary for nucleation and growth of precipitates decreases with ageing temperature. As well known, the volume fraction of regions transformed by discontinuous precipitation essentially depend on reaction front velocity, interlamellar spacing, average composition of the solute-depleted α lamellae, temperature, solute content and conditions of the grain boundaries (Bradai et al., 2001; Bradai et al. 1999; Braszczyńska 2002; Maitrejean et al., 1999; Zięba, 2000). The phase transformation during continuous precipitation is mainly described as the sequential or simultaneous processes of nucleation, growth and impingement (Celotto, 2000; Celotto & Bastow 2001; Duly et al. 1995). In both cases, reduction of the driving force for propagation and impediment of nucleation may be the limiting factors. However, a simple dependence describing the dominant type of precipitation did not seem to exist. It should also be noted, that at all temperatures, grain boundaries tend to be rapidly decorated by arrays of heterogeneous γ precipitates testifying that the grain boundaries are the first and privileged places of nucleation for precipitates.

Additionally, the amount of continuous precipitates very strongly depends on the number of crystal defects within the matrix which may act as heterogeneous nucleation sides. It well known, that besides the grain boundaries, the various nucleation sizes are: vacancies, dislocations, stacking faults and solid free surfaces. One possibility is the heterogeneous nucleation of continuous precipitates on vacancies. On the other hand, vacancies also determine the volume diffusion mechanism. Due to comparable Al and Mg atom diameters, vacancy diffusion can be dominant in the investigated alloys. Solution annealing and quenching result in a higher (non-equilibrium) vacancy concentration. If a concentration of vacancy is lower (i.e. near-equilibrium) continuous precipitates of the γ phase cannot occur.
As expected for a higher temperature the diffusion became faster, resulting in an increase of volume precipitates. Moreou et al. (1971) have found that the volume diffusion coefficient (D_V) for aluminium in magnesium can be determined using:

$$D_V = 12x10^{-4} \exp\left(\frac{-144x10^3}{RT}\right) \quad \mathrm{m}^2/\mathrm{s} \tag{1}$$

Discontinuous precipitation is described by Sundquist, Cahn, Hillert, Turnbull or Petermann-Hornbogen models (Bradai et al., 1999; Maitrejean et al., 1999) whereas continuous precipitation by the Austin and Ricket (A–R) equation or the well-known Avrami equation, which is also known as the Johnson–Mehl–Avrami–Kolmogorov (JMAK) equation (Celotto, 2000). For consistency, the grain boundary diffusivities for discontinuous precipitation can be evaluated using the Petermann-Hornbogen equation (Bradai et al., 1999; Zieba, 2000):

$$s\delta D_{gb} = \frac{RT}{-8\Delta G}\lambda^2 \nu \tag{2}$$

where D_{gb} is the grain boundary diffusion coefficient, δ - the grain boundary width, s - the segregation factor, ν - the velocity for the process, ΔG - the total driving force, R - the gas constant, T - the absolute temperature of the process and λ is the interlamellar spacing.
Bradai et al. (1999) has determined the Arrhenius parameters as the pre-exponential factor $(s\delta D_{gb})_0 = 1.15x10^{-6}$ m^3/s and the activation energy for grain boundary diffusion: Q_{gb} = 105.3 kJ/mol. A different value of Q_{gb} = 128 kJ/mol was reported by Amir & Gupta (1995). On the other hand, the grain boundary diffusion coefficient, D_{gb}, can be calculated from equation (2) assuming s = 1 and δ = 0.5 nm, according to (Bradai et al., 1999). In Fig. 11 the diffusion coefficients, D_v (from equation (1)) and D_{gb} (from equation (2) where the pre-exponential factor ($s\delta D_{gb}$) was evaluated from the Arrhenius plot) were presented. The obtained values show that the volume diffusion coefficient is approximately 6-7 orders of magnitude less than the diffusion coefficient for the grain boundary. At lower temperatures the process of secondary precipitation is controlled by grain boundary diffusion. It causes discontinuous precipitates to form earlier at the grain boundaries in characteristically shaped colonies of lamellae. As the temperature increases, bulk diffusion becomes faster, which tends to favour continuous precipitation. Continuous precipitation reduces the amount of chemical driving energy available for both the initiation and propagation of discontinuous precipitates. So if the continuous precipitation process started inside the grains then discontinuous precipitates are stopped.

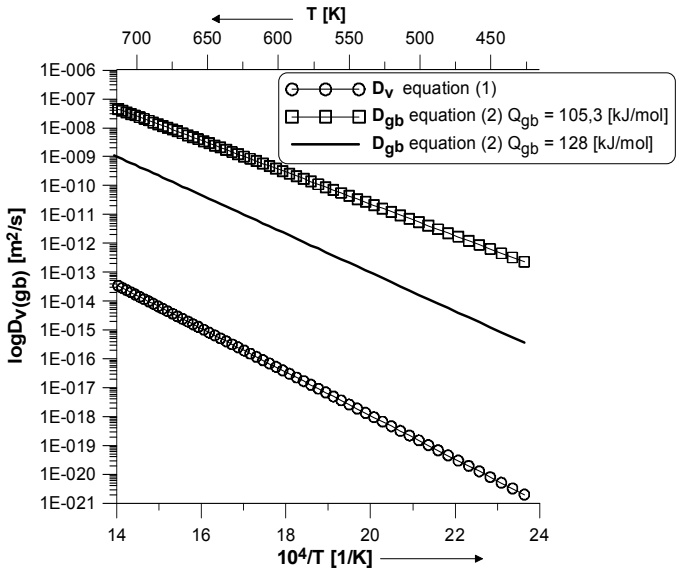

Fig. 11. Volume (D_V) and grain boundary (D_{gb}) diffusion coefficient for aluminium in magnesium based on [19, 25, 27] data

For both precipitates, the predominant orientation relationship (OR) is the Burgers OR, namely: $(0001)_\alpha \parallel (0\,\bar{1}\,0)_\gamma$ and $[2\,\bar{1}\,\bar{1}\,0]_\alpha \parallel [111]_\gamma$ (Braszczyńska-Malik, 2005; Celotto & Bastow, 2001; Zhang et al., 2003). Additionally, other ORs were also reported in Mg-Al based alloys, i.e. the Crawley OR (Celotto, 2000; Gharghouri et at., 1998), the Porter OR (Celotto, 2000), the Gjömmes-Östrmoe OR (Zhang et al., 2003; Nie et al., 2001) or the Potter OR (Nie et al., 2001; Bradai et al. 1999).

Precipitates with the Burgers OR are parallel to the basal plane of the matrix, i.e. $(0001)_\alpha$ whereas precipitates with optional ORs lie on the prism plane of the magnesium i.e. $(1\,\bar{1}\,00)_\alpha$ and they are perpendicular to the basal plane of the matrix. The strain caused by the γ phase precipitate may be seen clearly from its eigenstrain matrix. In this case, the hcp α phase must be transformed to a regular cubic γ phase. During transformation, the coordinates system of matrix $x_1^\alpha - x_2^\alpha - x_3^\alpha$ must be changed to the coordinates of precipitate $\xi_1^\gamma - \xi_2^\gamma - \xi_3^\gamma$. Fig. 12 shows a scheme of the transformation α phase to the γ precipitate according to the Burgers OR and the Crawley OR. Transformations for the Porter OR and the Gjömmes-Östrmoe OR are analogical to those presented for the Crawley OR.

The lattice deformation matrix A to change the α lattice into the γ lattice can be written as:

a. for the Burgers OR:

$$A^{\rightarrow B} = \begin{pmatrix} \frac{a_\gamma\sqrt{3}}{\kappa a_\alpha} & 0 & 0 \\ 0 & \frac{\sqrt{11}a_\gamma}{3\kappa a_\alpha\sqrt{3}} & 0 \\ 0 & 0 & \frac{a_\gamma\sqrt{2}}{\kappa c_\alpha} \end{pmatrix} - \delta_{ij} \tag{3}$$

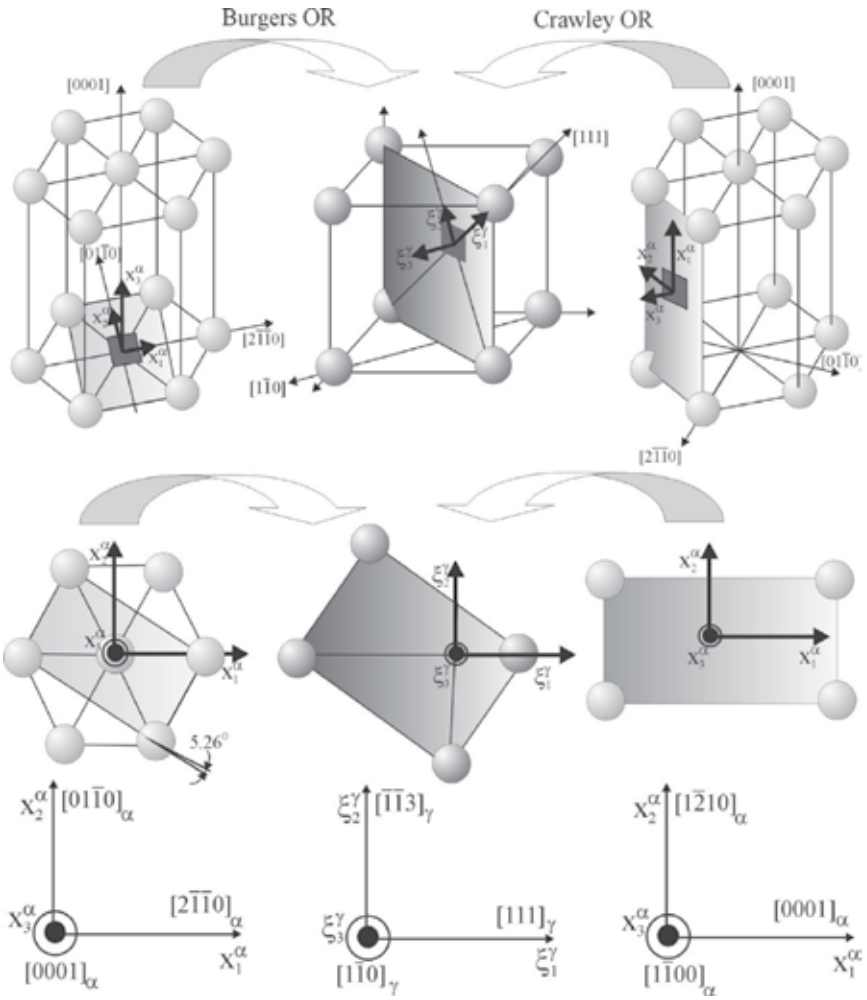

Fig. 12. Scheme of hcp α-phase matrix lattice transformation to γ precipitate lattice

b. for the Crawley OR:

$$A^{\rightarrow C} = \begin{pmatrix} \frac{a_\gamma\sqrt{3}}{\kappa c_\alpha} & 0 & 0 \\ 0 & \frac{a_\gamma\sqrt{3}}{\kappa a_\alpha\sqrt{2}} & 0 \\ 0 & 0 & \frac{a_\gamma\sqrt{2}}{\kappa a_\alpha\sqrt{3}} \end{pmatrix} - \delta_{ij} \tag{4}$$

where δ_{ij} is the Kronecker delta, a_α, c_α are the lattice parameters of the α phase, a_γ is the lattice parameter of the γ phase, and κ is a multiplication factor introduced due to the large difference in lattice parameters between the α and γ phase (Braszczyńska-Malik, 2005). Additionally, rigid-body rotation, δ_{ij}, by $\varpi = 5.26°$ is necessary to realize the Burgers OR:

$$\lambda_{ij} = \begin{pmatrix} \cos\varpi & -\sin\varpi & 0 \\ \sin\varpi & \cos\varpi & 0 \\ 0 & 0 & 1 \end{pmatrix} \tag{5}$$

Therefore, the total transformation matrix to include the change in the crystal structure becomes:

a. for the Burgers OR

$$\varepsilon_{ij}^{\xi\to B} = \begin{pmatrix} -0.0512 & -0.009 & 0 \\ -0.009 & 0.0472 & 0 \\ 0 & 0 & -0.046 \end{pmatrix} \tag{6}$$

b. for the Crawley OR

$$\varepsilon_{ij}^{\xi\to C} = \begin{pmatrix} -0.12 & 0 & 0 \\ 0 & 0.0053 & -0.0012 \\ 0 & -0.0012 & 0.0714 \end{pmatrix} \tag{7}$$

The obtained results suggest the presence of coherent boundaries with slight lattice deformation between the magnesium matrix and γ precipitates. It is known that the interphase boundary may be coherent if the lattice incoherence is less than 0.1. Low values obtained from transformation matrices (equation (6) and (7)) explain both plate-like morphology of precipitates and its visible anisotropy of growth.

4. The γ phase in AZ91 alloy after equal-channel angular pressing

The grain refinement is very important in magnesium alloys because they have poor formability and limited ductility at room temperature rooted in their hexagonal close-packed (hcp) crystal structure. In the past decade, efforts have been concentrated on thermomechanical processing for grain size refinement using methods of severe plastic deformation (SPD) (Valiev et al., 2000). SPD techniques, such as equal channel angular pressing (ECAP) (Valiev et al., 2000; Valiev & Langdon, 2006; Chen et al., 2008; Ravi Kumar et al., 2003; Wang et al., 2008), accumulative roll bonding (ARB) (Jiang et al., 2008; Saito et al., 1999) or high-pressure torsion (HCP) (Zhilyaev & Longdon, 2008; Zhiyaev et al., 2003), have been applied to the grain refinement of magnesium alloys on bulk materials. The influence of ECAP process on precipitation in AZ91 magnesium alloy was also investigated (Braszczyńska-Malik, 2009 b). The ECAP die used in the presented investigation was designed to obtain a maximum shear strain of about 1.15 during each pass. It contained an inner contact angle Φ equal to 90° and corner angle Ψ of 0°. The billets (with 11.8 mm of diameter and 50 mm of length) were processed at a pressing rate of 5 mm/min. using a plunger attached to a hydraulic press on an Instron machine. All the pressings were conducted using route B_C where the billet is rotated 90° (clockwise) around the lengthwise axis between each pass. For each separate pressing, the samples were coated with molybdenum disulphide (MoS_2) as a lubricant. AZ91 alloy was heat treatment before ECAP (solution annealing – 698 K, 24 h – Fig. 7)

Figs. 13 and 14 show microstructure of AZ91 alloy after 4 ECAP passes at 553 and 623 K. The presented results indicated that the microstructure of the AZ91 alloy processed by ECAP at 553 and 623 K via the B_C pressing route at a rate of 0.16 mm/s consisted of α matrix phase equiaxal grains of about 10 μm in size (Fig. 13) and spherical precipitates located particularly inside the grains (Figs. 13 and 14). The observed precipitates were unequivocally identified as the γ phase (Fig. 14). The microstructure observations carried out on both the transverse and the longitudinal sections of the pressed samples provides direct evidence of the spherical shape of precipitates with a maximum size of about 1 μm. It is well known that equilibrium morphology is a shape that minimizes the total energy which is composed of two parts: elastic strain energy and interfacial energy.

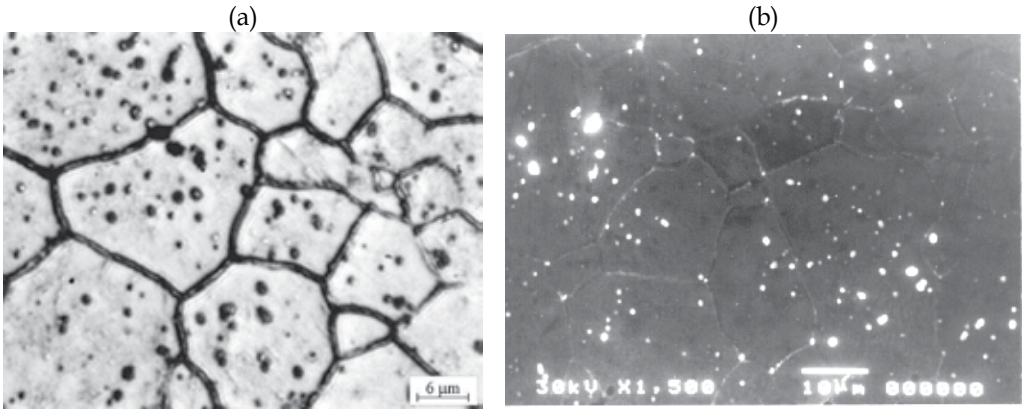

Fig. 13. Spherical precipitates of γ phase in AZ91 alloy after ECAP at 553 K; light microscopy (a), SEM (b)

On the other hand, the analysed planes (basal and prism planes) in hcp magnesium are simultaneously the main slip planes. For magnesium with a c/a ratio equal to 1.624 the main slip system is {0001}<11 $\bar{2}$ 0>. It is well known that the three main dislocations determined as (i) **a** type with Burgers vector 1/3[11 $\bar{2}$ 0], (ii) **c** type with Burgers vector 1/2[0001] and (iii) **c+a** type with Burgers vector 1/3[11 $\bar{2}$ $\bar{3}$] can operate in magnesium (Woo, 2000; Mathis et al., 2004). In case of unfavourable orientation of the main slip system to external stress or in higher temperatures, different slip systems e.g. {1 $\bar{1}$ 00}<11 $\bar{2}$ 0> and {1 $\bar{1}$ 01}<11 $\bar{2}$ 0> can also operate. In works concerning hot working of magnesium alloys (Koike et al. 2003; Yoo et al. 2001) however, an <a> cross slip and energetically favorable junction between glissile <a> and sensile **c** dislocations on a {1 $\bar{1}$ 00} prism plane seem to be predominant. The dissolution of an **a** dislocation on the basal plane to Shockley partial dislocations connected with a single stacking fault is also possible. However, plastic deformation during SPD processes especially of magnesium alloys at high temperatures appears to be more composite and complicated. For example, in the present case, the supersaturated solid solution exhibited higher than equilibrium solute atoms concentration, which could form atmospheres generating dislocation locking. It should also be noted that the deformation of hcp magnesium alloys caused the formation of twins, especially the $\{1\bar{1}02\}_{matrix}$ || $\{0\bar{1}12\}_{twin}$ type (Christian & Mahajan, 1995; Braszczyńska- Malik et al., 2006).

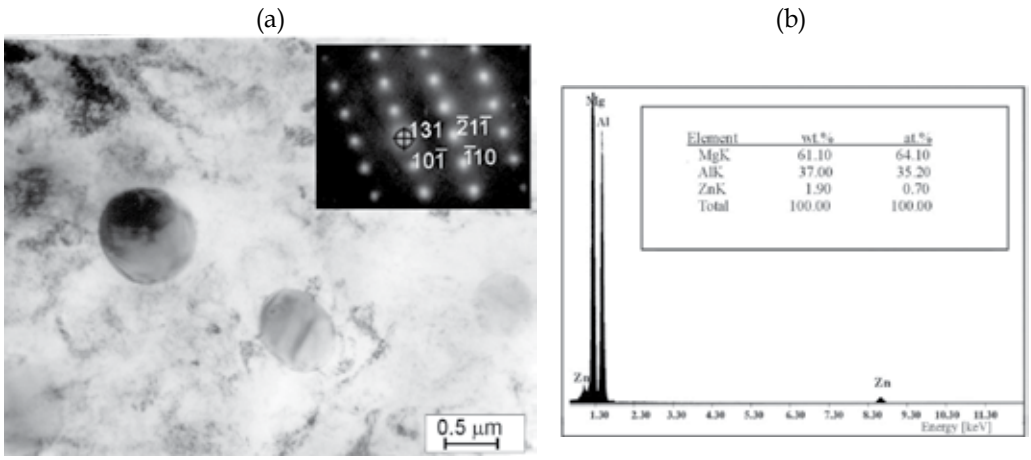

Fig. 14. TEM image of spherical precipitates of γ phase in AZ91 alloy after ECAP at 623 K (a), and result of EDX analysis obtained from one of precipitate (b)

In most published works (Janecek et al., 2007; Su et al., 2006; Kulyasova et al., 2009; Braszczyńska-Malik & Froyen, 2005; Braszczyńska- Malik et al., 2006) the microstructure of magnesium alloys processed by the ECAP technique was characterized by strong deformation and high density of dislocations and twins. Introducing a high dislocation density and strong disordering of the matrix lattice during severe plastic deformation can preclude formation of a coherent boundary between the matrix and growing γ precipitates. If precipitate growth proceeds during continuous plastic deformation, then the plate-like shape of precipitates is unfavourable. In this case the spherical shape of precipitates can be the most energetically favorable. On the other hand, the high density of crystal defects introduced inside α−phase grains during plastic deformation act as privileged sites for the heterogeneous nucleation of precipitates. Additionally, high dislocation density (and other defects like vacancies) caused faster diffusion of solute atoms in the magnesium matrix which were effective in reducing the time necessary for the nucleation and growth of precipitates (in comparison to precipitation during heat treatment). For this reason also, spherical precipitates were observed especially inside matrix grains which is clearly seen in Fig. 13.

In the present case, a new spherical shape of γ precipitates was obtained in the AZ91 alloy processed by ECAP at a maximum shear strain of about 1.15 during each pass and at a pressing rate of 0.16 mm/s. The applied ECAP parameters allowed the attainment of severe plastic deformation introducing strong disordering of the magnesium lattice. On the other hand, the temperature and time were suitable for the growth of precipitates during deformation. Thus, the selected process parameters allowed the attainment of new spherical precipitates of the γ phase.

7. Conclusion

1. In as-cast microstructure of AZ91 magnesium alloy the γ phase is mainly constituent of more or less divorced eutectic (but it should also be noted that in slow cooling down casts it my also creates discontinuous precipitates).

2. After ageing of supersaturated solid solution at 423 K only discontinuous precipitates are observed whereas at 623 K only continuous once are revealed in the microstructure of AZ91 alloy. At intermediate ageing temperatures both discontinuous and continuous precipitates of the γ phase occur.
3. The spherical shape of γ precipitates can be obtained due to correlate precipitation and magnesium matrix deformation processes (Fig. 15).

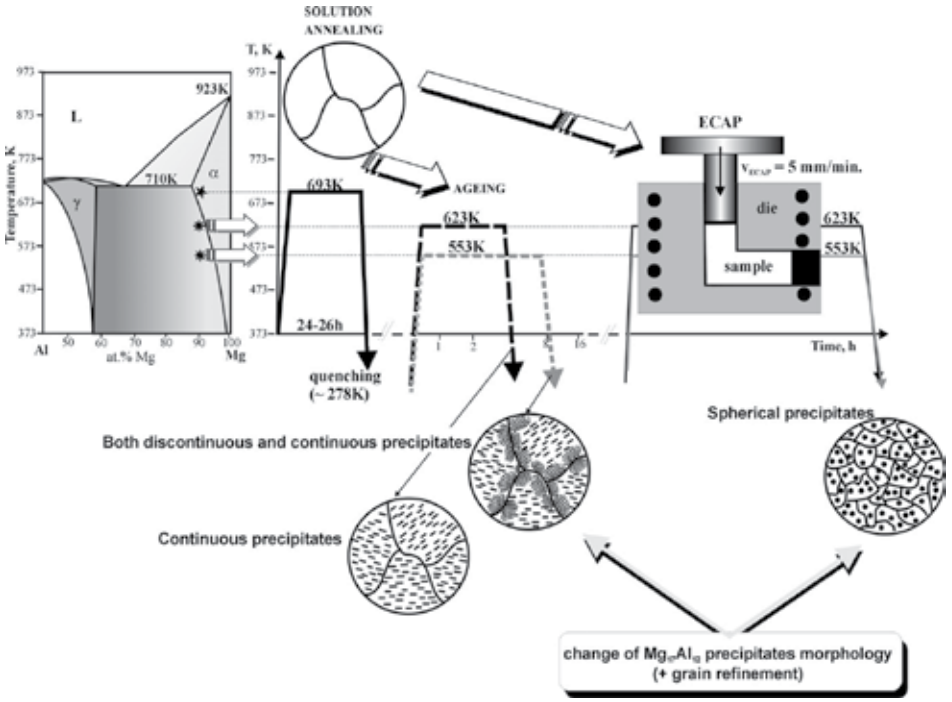

Fig. 15. Scheme of obtained results

8. References

Amir, Q.M. & Gupta, S.P. (1995). Cellular precipitation and precipitate coarsening in a Mg-Al alloy, Canadian Metallurgical Quarterly, Vol. 34, Issue 1, (January 1995) pp. 43-50, ISSN: 00084433

ASM Handbook Committee (1986). Binary alloys phase diagrams, Metals Park, ISBN: 0-87170-261-4, Ohio

Bettles C.J. (2003). The effect of gold additions on the ageing behavior and creep properties of the magnesium alloy AZ91E, Materials Science and Engineering A, Vol. 348, Issue 1-2, (May 2003) pp. 280-288, ISSN 09215093

Bradai D., Kadi-Hanifi M., Zięb, P.. Kuschke W. M. & Gust W. (1999) The kinetics of the discontinuous precipitation and dissolution in Mg-rich Al alloys, Journal of Materials Science, Vol: 34, Issue 21, (November 1999) pp. 5331 – 5336, ISSN 0022-2461

Bradai D., Zieba P., Bischoff E. & Gust W. (2001). A new mode of the discontinuous dissolution reaction in Mg-10 wt.% Al alloy, Materials Chemistry and Physics, Vol. 72, Issue 3, (December 2001) pp. 401-404, ISSN: 02540584

Braszczyńska K.N. (2002). The microstructure of a Mg-10 wt.% Al alloy, Zeitschrift fuer Metallkunde, Vol. 93, Issue 8,(August 2002) pp. 845-850, ISSN: 00443093

Braszczyńska-Malik K.N. (2005). The study on the shaping of the microstructure of magnesium-aluminium alloys, Publisher: WIPMiFS PCz., ISBN 83-87745-72-3, Częstochowa *(in Polish)*

Braszczyńska-Malik K.N. (2009 a). Discontinuous and continuous precipitation in magnesium-aluminium type alloys, Journal of Alloys and Compounds, Vol. 477, Issue 1-2, (May 2009) pp. 870-876, ISSN 0925-8388

Braszczyńska-Malik K.N. (2009 b). Spherical shape of γ-$Mg_{17}Al_{12}$ precipitates in AZ91 magnesium alloy processed by equal-channel angular pressing, Journal of Alloys and Compounds, Vol. 487, Issues 1-2, (November 2009) pp. 263-268, ISSN 0925-8388

Braszczyńska-Malik K.N. & Froyen L. (2005). Microstructure of AZ91 alloy deformed by equal channel angular pressing, Zeitschrift fuer Metallkunde, Vol. 96, Issue 8, (August 2005) pp. 913-917, ISSN: 00443093

Braszczyńska-Malik K.N., Lityńska L. & Baliga W. (2006) Transmission electron microscopy investigations of AZ91 alloy deformed by equal-channel angular pressing, Journal of microscopy, Vol. 224, (October 2006) pp. 15-17, ISSN 0022-2720

Braszczyńska-Malik. K.N., Zawadzki I., Walczak W. & Braszczyński J. (2008). Mechanical properties of high-pressure sie casting AZ91 magnesium alloy, Archives of Foundry Engineering, Vol. 8, Issue 4, (October-December 2008) pp. 15-18, ISSN 1897-3310

Braszczyńska-Malik K.N. & Zyska A. (2010). Influence of solidification rate on microstructure of gravity cast AZ91 magnesium alloy, Archives of Foundry Engineering, Vol. 10, Issue 1, (January-March 2010) pp. 23-26, ISSN 1897-3310

Bursik J. & Svoboda M. (2002). A HREM and Analytical STEM Study of Precipitates in an AZ91 Magnesium Alloy, Microchimica Acta, Vol. 139, Issue 1-4, 39-42, ISSN 0026-3672

Celotto S. (2000). TEM study of continuous precipitation in Mg–9 wt%Al–1 wt%Zn alloy , Acta Matrialia, Vol. 48, Issue 8, (May, 2000) pp. 1775-1787, ISSN 1359-6454

Celotto S. & Bastow T.J. (2001). Study of precipitation in aged binary Mg–Al and ternary Mg–Al–Zn alloys using ^{27}Al NMR spectroscopy, Acta Materialia, Vol. 78, Issue 5, (November 1998), 1137-1149, ISSN1359-6454

Cerri E. & Barbagallo S. (2002). The influence of high temperature exposure on aging kinetics of a die cast magnesium alloys, Mater Letters, Vol. 56, No. 5, (November 2002) pp. 716-720, ISSN 0167577X

Chen B., Lin D-L., Jina L., Zeng X-Q. & Chen L. (2008). Equal-channel angular pressing of magnesium alloy AZ91 and its effects on microstructure and mechanical properties, Materials Science and Engineering A, Vol. 483-484, Issue 1-2 C, (June 2008) pp. 113-116, ISSN: 09215093

Christian J.W. & Mahajan S. (1995). Deformation twinning, Progress in Materials Science, Vol. 39, Issue 1-2, (1995) pp. 1-157, ISSN: 00796425

Duly D, Cheynet MC, & Brechet Y. (1995) On the competition between continuous and discontinuous precipitations in binary Mg-Al alloys, Acta Metallurgica et Materialia, Vol. 43, Issue 1, (January 1995) pp. 101-106, ISSN: 1359-6454

Figueiredo R.B. & Langdon T.G. (2009). Principles of grain refinement and superplastic flow in magnesium alloys processed by ECAP, Materials Science and Engineering A, Vol. 501, Issue 1-2, (February 2009) pp. 105-114, ISSN: 09215093

Gharghouri M.A., Weatherly G.C. & Embury D.J. (1998). The interaction of twins and precipitates in a Mg-7.7at.% Al alloy, Philosophical Magazine A; Vol. 78, Issue 5, (November 1998) pp. 1137-1149, ISSN 01418610

González-Martínez R., Göken J., Letzig D., Steinhoff K., Kainer K.U. (2007). Influence of aging on damping of the magnesium–aluminium–zinc series, Journal of Alloys and Compounds, Vol. 437, Issue 1-2, (June, 2007) pp.127-132, ISSN 0925-8388

Janecek M. & Popov M., Krieger M.G., Hellmig R.J. & Estrin Y. (2007). Mechanical properties and microstructure of a Mg alloy AZ31 prepared by equal-channel angular pressing, Materials Science and Engineering A, Vol. 462, Issue 1-2, (July 2007) pp. 116-120, ISSN: 09215093

Jiang L., Perez-Prado M.T., Gruber P.A., Arzt E., Ruano O.A. & Kassner M.E. (2008). Texture, microstructure and mechanical properties of equiaxed ultrafine-grained Zr fabricated by accumulative roll bonding, Acta Materialia, Vol. 56, Issue 6, (April 2008) pp. 1228-1242, ISSN: 13596454

Koike J., Kobayashi T., Mukai T., Wanatabe H., Suzuki M., Maruyama K. & Higashi K. (2003) The activity of non-basal slip systems and dynamic recovery at room temperature in fine-grained AZ31B magnesium alloys, Acta Materialia, Vol. 51, Issue 7, (April 2003) pp. 2055-2065, ISSN: 13596454

Kulyasova O., Islamgaliev R., Mingler B. & Zehetbauer M. (2009). Microstructure and fatigue properties of the ultrafine-grained AM60 magnesium alloy processed by equal-channel angular pressing, Materials Science and Engineering A, Vol. 503, Issue 1-2, (March 2009) pp. 176-180, ISSN: 09215093

Maîtrejean S., Verona M., Bréchet Y. & Prudy G.R. (1999). Morphological instabilities in Mg-7.7 at % Al, Scripta Materialia, Vol. 41, Issue 11 (November 1999) pp. 1235-1240, ISSN: 13596462

Máthis K., Gubicza J. & Nam N.H. (2005). Microstructure and mechanical behavior of AZ91 Mg alloy processed by equal channel angular pressing, Journal of Alloys and Compounds, Vol. 394, Issue 1-2, (May 2005) pp. 194-199, ISSN: 09258388

Máthis K., Nyilas K. & Axt A. (2004). The evolution of non-basal dislocations as a function of deformation temperature in pure magnesium determined by X-ray diffraction, Acta Materialia, Vol. 52, Issue 10, (June 2004) pp. 2889-2894, ISSN: 13596454

Mordike B. & Ebert T. (2001). Magnesium properties-applications-potential, Materials Science and Engineering A; Vol. 302, Issue 1, (April 15, 2001) pp. 37-45, ISSN 0921-5093

Moreau G., Cornet J. & Calais D. (1971). Acceleration de la diffusion chimique sous irradiation dans le systeme aluminium-magnesium, Journal of Nuclear Materials, Vol. 38, Issue 2, (February 1971) pp.197-202, ISSN: 00223115

Nie J. (2003). Effects of precipitate shape and orientation on dispersion strengthening in magnesium alloys, Scripta Materialia, Vol, 48, Issue 8, (14 April 2003) pp. 1009-1015, ISSN 13596462

Nie J.F., Xiao X.L., Luo C.P. & Muddle B.C. (2001). Characterization of precipitate phases in magnesium alloys using electron microdiffraction, Micron, Vol. 32, Issue 8, (2001) pp. 857-863, ISSN: 09684328

Ohno M., Mirkovic D. & Schmid-Fetze R. (2006), Liquidus and solidus temperatures of Mg-rich Mg–Al–Mn–Zn alloys, Acta Materialia, Vol. 54, Issue 15, (September 2006) pp. 3883-3891, ISSN: 13596454

Ravi Kumar N.V., Blandin J.J., Desrayaund C., Montheillet F. & Surey M. (2003) Grain refinement in AZ91 magnesium alloy during thermomechanical processing, Materials Science and Engineering A, Vol. 359, Issue 1-2, (October 2003) pp. 150-157, ISSN: 09215093

Saito Y., Utsonomiya H., Tsuji N. & Sakai T. (1999). Novel ultra-high straining process for bulk materials development of the accumulative roll-bonding (ARB) process, Acta Materialia, Vol. 47, Issue 2, (January, 1999) pp. 579-583, ISSN: 13596454

Smola B., Stulikova I., von Buch F. & Mordike B.L. (2002). Structural aspects of high performance Mg alloys design. Materials Science and Engineering A; Vol. 324, Issue 1-2, (February, 2002) pp. 113-117, ISSN 0921-5093

Su C.W., Lu L. & Lai M.O. (2006). A model for the grain refinement mechanism in equal channel angular pressing of Mg alloy from microstructural studies, Materials Science and Engineering A, Vol. 434, Issue 1-2, (October 2006) pp. 227-236, ISSN: 09215093

Valiev R.Z., Islamgaliev R.K., & Alexandrov I.V. (2000) Bulk nanostructured materials from severe plastic deformation, Progress in Materials Science, Vol. 45, Issue 2, (March 2000), pp. 103-189, ISSN: 00796425

Valiev R.Z. & Langdon T.G. (2006). Principles of equal-channel angular pressing as a processing tool for grain refinement, Progress in Materials Science, Volume 51, Issue 7, (September 2006) pp. 881-981, ISSN: 00796425

Wang X-S., Jin L., Li Y. & Guo X-W. (2008). Effect of equal channel angular extrusion process on deformation behaviors of Mg-3Al-Zn alloy, Mater Letters, Vol. 62, Issue 12-13, (April 2008) pp. 1856-1858, ISSN: 0167577X

Woo C.H. (2000). Defect accumulation behaviour in hcp metals and alloys, Journal of Nuclear Materials, Vol. 276, Issue 1, (January 2000) pp. 90-103 , ISSN: 00223115

Yoo M.H., Agnew S.R., Morris J.R. & Ho K.M. (2001). Non-basal slip systems in HCP metals and alloys: Source mechanisms, Materials Science and Engineering A, Vol. 319-321, (December 2001) pp. 87-92, ISSN: 09215093

Zhang M.X. & Kelly P.M. (2003). Crystallography of $Mg_{17}Al_{12}$ precipitates in AZ91D alloy, Scripta Materialia, Vol. 48, Issue 5, (March 2003) pp. 647-652, ISSN 13596462

Zhilyaev A.P. & Langdon T.G. (2008). Using high-pressure torsion for metal processing: Fundamentals and applications, Progress in Materials Science, Vol. 53, Issue 6, (August 2008) pp. 893-979, ISSN: 00796425

Zhilyaev A.P., Nurislamova G.V., Kim B.K., Baro M.D. , Szpunar J.A. & Langdon T.G. (2003). Experimental parameters influencing grain refinement and microstructural

evolution during high-pressure torsion, Acta Materialia, Vol. 51, Issue 3, (February 2003) pp. 753-765, ISSN: 13596454

Zięba P. (2000). Recent progress in the energy-dispersive X-ray spectroscopy microanalysis of the discontinuous precipitation and discontinuous dissolution reactions, Materials Chemistry and Physics, Vol. 62, Issue: 3, (February 2000) pp. 183-213, ISSN: 0254-0584

6

Evaluation Method for Mean Stress Effect on Fatigue Limit of Non-Combustible Mg Alloy

Kazunori MORISHIGE, Yuna MAEDA,
Shigeru HAMADA and Hiroshi NOGUCHI
Department of Mechanical Engineering, Faculty of Engineering, Kyushu University
JAPAN

1. Introduction

Structures are commonly loaded with a mean stress. Therefore, it is necessary to investigate the influence of the mean stress on the fatigue strength of the structural materials. Fatigue strength of a material, whose fatigue crack is initiated from an inclusion, strongly depends on the size of the inclusion. The fatigue strength of the material is quite variable. Therefore, if we test the effect of the mean stress on the fatigue strength of this material, the effect would be hidden in the scatter and the effect becomes uncertain. In this study, we propose an evaluation method for the mean stress effect of the inclusion-induced scattered fatigue strength using the non-combustible Mg alloy AMX602B (X=Ca) (Sakamoto et al., 1997; Chang et al., 1998; Akiyama et al., 2000). We discuss the equivalence of an artificial defect and an actual defect (inclusion).

Figure 1 shows the *S-N* diagram for the smooth specimens of the non-combustible Mg alloy AMX602B (X=Ca) by the authors (Kitahara et al., 2005; Kitahara et al., 2006; Fujii et al., 2008; Masaki et al., 2008). The relationship between the load stress and the fatigue life of the smooth specimens significantly varies. Moreover, no non-propagating crack was observed in the unbroken specimens. The condition of the surface of the fatigue fracture origin is shown in Fig. 2. The fracture originated at a non-metallic inclusion.

There have been several studies that investigated the effect of the mean stress on the fatigue strength of the conventional Mg alloy (Forrest, 1962; Heywood, 1962; Osgood, 1970; Ogarevic & Stephens, 1990; Akiyama et al., 2000). Forrest (Forrest, 1962) reported that the effect of the mean stress on the fatigue strength of a Mg alloy can be evaluated using the modified Goodman diagram. In contrast, Heywood (Heywood, 1962) and Osgood (Osgood, 1970) reported that the fatigue strength of a Mg alloy under a high mean stress became low and that the fatigue life evaluation using the modified Goodman diagram may not be conservative prediction. However, the reason why the fatigue strength under a high mean stress decreases has not been clarified.

In this study, rotating-bending fatigue tests and tension-compression fatigue tests were carried out on specimens with an artificial defect (a small hole or a small crack). Especially, we examined why the fatigue strength under a high mean stress decreases and whether the fatigue strength at $N = 10^7$ under a mean stress can be applied to an estimation using the modified Goodman diagram. The fatigue testing of the small holed specimens and the small

cracked specimens was first performed, and the characteristics of the fatigue strength at $N = 10^7$ under a high tensile mean stress were investigated. Moreover, the size dependence of the fatigue strength with a small crack was investigated. Based on the results of the fatigue testing of smooth, small hole and the small crack specimens, the influence of the mean stress on the fatigue strength at $N = 10^7$ of the smooth specimens was considered, and the validity of the application of the modified Goodman diagram was investigated.

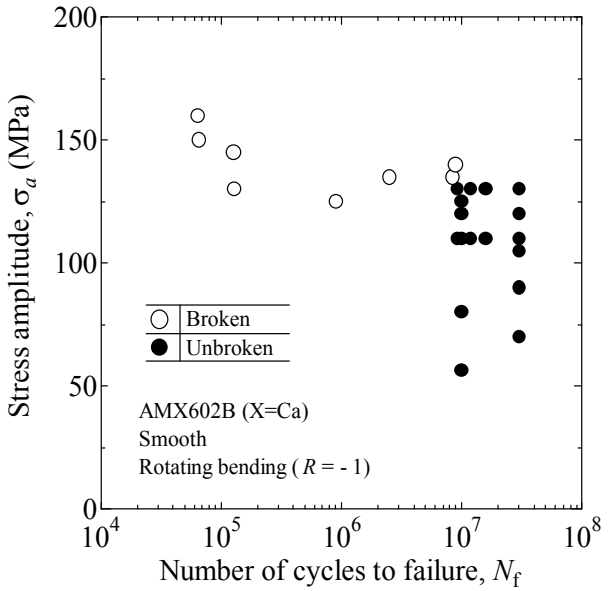

Fig. 1. *S-N* diagram for the smooth specimens (Kitahara et al., 2005; Kitahara et al., 2006; Masaki et al., 2008)

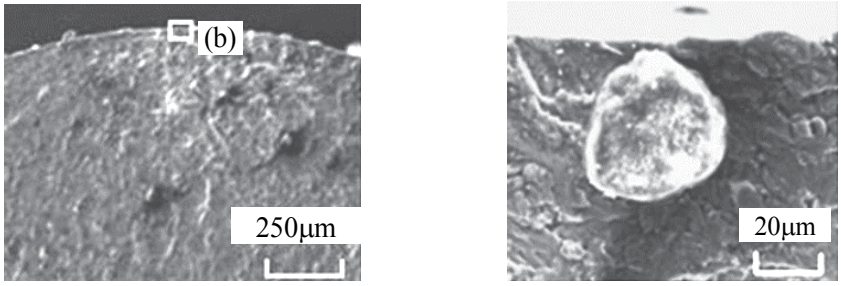

(a) Fracture surface around the fracture origin (b) Magnification of fracture origin

Fig. 2. Non-metallic inclusion observed at fatigue fracture origin of the non-combustible Mg alloy (AMX602B (X=Ca)) smooth specimens (rotating-bending) (Kitahara et al., 2005; Kitahara et al., 2006)

2. Characteristics of non-combustible Mg alloy

In order to stop global warming and solve the energy problem, improvement in the fuel consumption by the weight saving of vehicles is now being advanced. In this case, the use of

a magnesium (Mg) alloy is attracting attention because the Clarke number of Mg is high, and Mg has the lowest density of commercial metals.

The non-combustible Mg alloy used in this study is a material which has an improved resistance of being easy to burn by the addition of about 2% calcium (Ca) to the conventional Mg alloy (Sakamoto et al., 1997; Chang et al., 1998; Akiyama et al., 2000; Masaki et al., 2008). Figure 3 shows the relationship between the ignition point and the Ca content of the Mg alloys (Sakamoto et al., 1997). The ignition point of the non-combustible Mg alloy is about 300K higher than that of the conventional Mg alloy. Therefore, the non-combustible Mg alloy can be safely used in casting and metal cutting compared to the conventional Mg alloy. The non-combustible Mg alloy does not need special protection from atmospheric gases or a special flux in the case of casting. Therefore, working in air can be done similar to that for an aluminum alloy. Consequently, an improvement in the problem of high cost, which is one of the concerns of the conventional Mg alloy, is expected.

In order to utilize the non-combustible Mg alloy in practical use as a structural material, it is necessary to determine the fatigue strength characteristics. The fatigue strength characteristics have been investigated for the Mg alloy until now (Forrest, 1962; Heywood, 1962; Osgood, 1970; Ogarevic & Stephens, 1990). The *S-N* diagram characteristics of the Mg alloy are reported as follows: though a clear fatigue limit is not shown, the strength gradually decreases with an increase in the cycles to failure up to a high cycle region (Forrest, 1962; Heywood, 1962; Osgood, 1970; Ogarevic & Stephens, 1990).

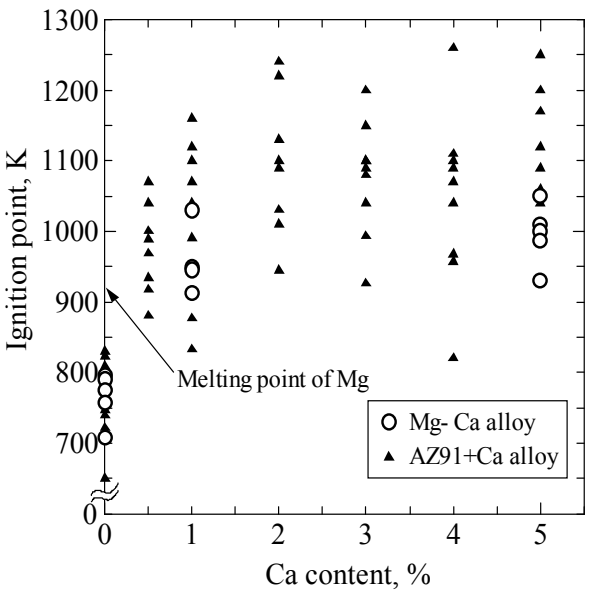

Fig. 3. Relationship between ignition point and Ca content for Mg alloys (Sakamoto et al., 1997)

With the addition of Ca, inclusions increase in the non-combustible Mg alloy (Akiyama et al., 2000). Therefore, it is necessary to consider the influence of inclusions in the case of the fatigue strength characteristics evaluation. The fatigue strength at $N = 10^7$ for the smooth specimens of the three types of the non-combustible Mg alloys (AMX602B (X=Ca), AZX312D (X=Ca), AZX912D (X=Ca)) using a rotating-bending fatigue testing machine was investigated by the authors (Kitahara et al., 2005; Kitahara et al., 2006; Fujii et al., 2008;

Masaki et al., 2008). As a result, it was clarified that the fatigue fracture origin in the non-combustible Mg alloy was due to a non-metallic inclusion as shown in Fig. 2. The non-metallic inclusion is shown in Fig. 2(b). No non-propagating crack at $N = 10^7$ was observed. The fatigue strength at $N = 10^7$ could be estimated using the size of the non-metallic inclusion at the fracture origin (Kitahara et al., 2005; Kitahara et al., 2006). The fatigue strength of the non-combustible Mg alloy was almost the same as that of the conventional Mg alloy.

Figure 4 shows the results of having compared the relationship of the tensile strength and the fatigue strength at $N = 10^7$ in the non-combustible Mg alloy with the relationship of the tensile strength and the fatigue strength at $N = 2\times10^7$ for the conventional Mg alloy (Heywood, 1962). Although the fatigue strength at $N = 10^7$ of the non-combustible Mg alloy has some scatter due to the size of the inclusions, it turns out to be comparable to the conventional Mg alloy in tensile strength.

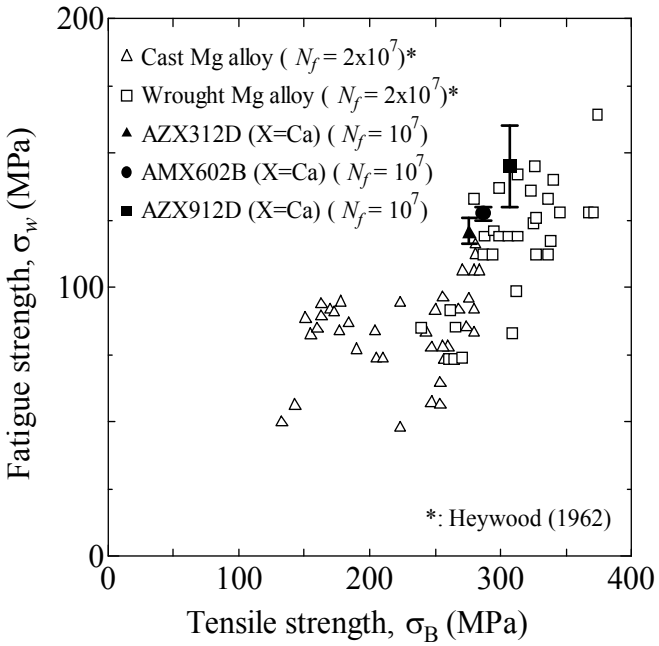

Fig. 4. Relationship between rotating-bending fatigue strength and tensile strength for Mg alloys

3. Experimental procedure

The material used in this study is an extruded non-combustible Mg alloy AMX602B (X=Ca) (extrusion ratio: 3). Its mean grain size is 5 μm. Table 1 shows the chemical composition. Table 2 shows the mechanical properties. Young's modulus, tensile strength and elongation of AMX602B (X=Ca) are the same as those of a conventional Mg alloy. Figure 5 shows the specimen configurations for the rotating-bending fatigue test and tension-compression fatigue test. Three types (smooth, with a small hole and with a small crack) of specimens were prepared. For the non-combustible Mg alloy, if a smooth specimen is used for the

fatigue test, the inclusion of various sizes serves to initiate a fatigue crack, the fatigue strength at $N = 10^7$ varies (Kitahara et al., 2005; Kitahara et al., 2006; Fujii et al., 2008; Masaki et al., 2008), and the influence of the mean stress on the fatigue strength at $N = 10^7$ cannot be studied in detail. In order to correctly determine the fatigue strength at $N = 10^7$, a small hole or a small crack is then introduced in the test specimen. The size of the hole and the crack are slightly larger than the inclusion. This specimen then enabled us to study the influence of the mean stress in detail. Moreover, the reason for having introduced two kinds of artificial defects (a small hole or a small crack) is for the inclusion to clearly show, which is equivalent to a actual defect, a small hole or a small crack.

The surfaces of the specimens are buff-polished using alumina (particle size: 0.05μm). For the small hole specimens, as shown in Fig. 5 (c), a small hole ($d_1 = h_1 = 100$μm) is introduced in the specimen surface after surface polishing. For the small crack specimens, as shown in Fig. 5 (d), a small hole ($d_2 = h_2 = 50$μm) is introduced in the specimen surface after surface polishing, and a small crack ($2a \approx 160$μm) is introduced in the specimen surface by fatigue loading. After that, in order to relieve residual stress caused by introducing the small crack, the specimens are annealed in vacuum for 1 hour at 200°C. The size of the small hole and the small crack are arranged to be the same value: 100μm when the $\sqrt{area}$ parameter model (Murakami, 2002a) is applied. The $\sqrt{area}$ is the square root of the projected "*area*" of an inclusion onto a plane perpendicular to the maximum principal stress. Figure 6 shows the definition of the $\sqrt{area}$. Though we are concerned about the influence on the fatigue strength by the difference in a processing method between each test specimen, it is shown clearly that the influence of vacuum annealing on the fatigue strength at $N = 10^7$ is small (to be described).

Moreover, in order to investigate the size dependence of the fatigue strength of the small crack specimens at $N = 10^7$, the test specimens which have 349μm, 650μm or 918μm length crack were prepared. Rotating-bending fatigue tests were also used for the small crack specimens.

The test machines used for this study are the Ono-type rotating-bending fatigue test machine and the hydro-servo tension-compression fatigue testing machine. Fatigue tests were performed in air at room temperature. The frequency for the rotating-bending fatigue tests is 50Hz, for tension-compression fatigue tests of smooth and the small hole specimens is 20Hz and those for tension-compression fatigue tests of small crack specimens are 30Hz and 35Hz. The replica method was used to observe the specimen surface successively.

Al	Ca	Mn	Zn	Si	Fe	Cu	Ni	Be	Mg
5.98	1.89	0.34	0.002	0.029	<0.001	0.001	<0.001	0.001	Bal.

Table 1. Chemical composition (non-combustible Mg alloy AMX602B (X=Ca))

Young's modulus	Tensile strength	0.2% proof stress	Elongation	Vickers hardness
E (GPa)	σ_B (MPa)	$\sigma_{0.2}$ (MPa)	ε_B (%)	HV (kgf/mm^2)
46	287	210	14	69

Table 2. Mechanical properties (non-combustible Mg alloy AMX602B (X=Ca))

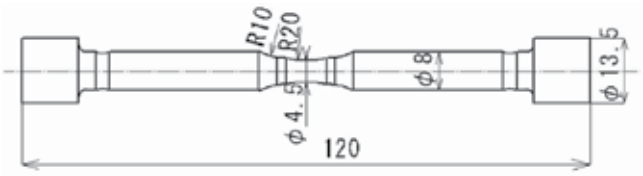

(a) For tension-compression fatigue test (T-C)

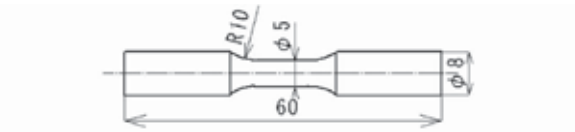

(b) For rotating-bending fatigue test (R-B)

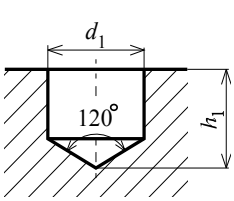

(c) Small hole (d_1 = h_1 = 0.1)

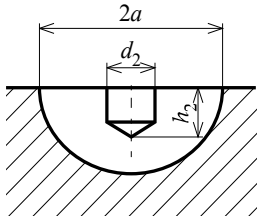

(d) Small crack (2a = 0.16, 0.35, 0.65, 0.92)

Fig. 5. Shapes and dimensions of the specimens (dimensions in mm)

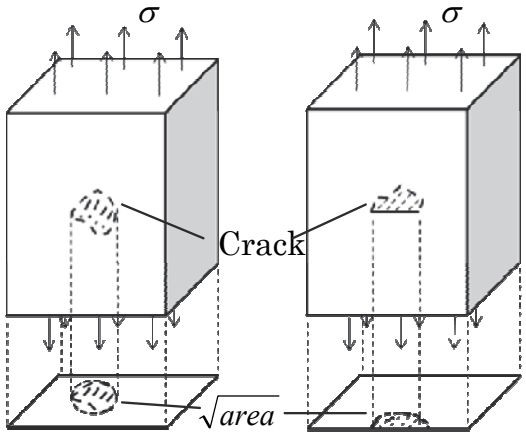

(a) Interior crack (b) Surface crack

Fig. 6. Definition of $\sqrt{area}$

4. Results and discussion

4.1 Fatigue strength at $N = 10^7$ characteristic of the small hole and the small crack specimens by rotating-bending fatigue test

Figure 7 shows the *S-N* diagram for the specimens with the small hole and the small crack under the rotating-bending fatigue test. In Fig. 7, the results for the vacuum-annealed small

hole specimens are also shown. When vacuum annealing was carried out, we were concerned about the fatigue strength at $N = 10^7$ changing, but in this study, the fatigue strength at $N = 10^7$ after vacuum annealing has not changed. Therefore, the influence on the fatigue strength at $N = 10^7$ by the difference in residual stress of the processing method is small, and we can compare the fatigue strength of the small hole specimens, the small crack specimens and the smooth specimens.

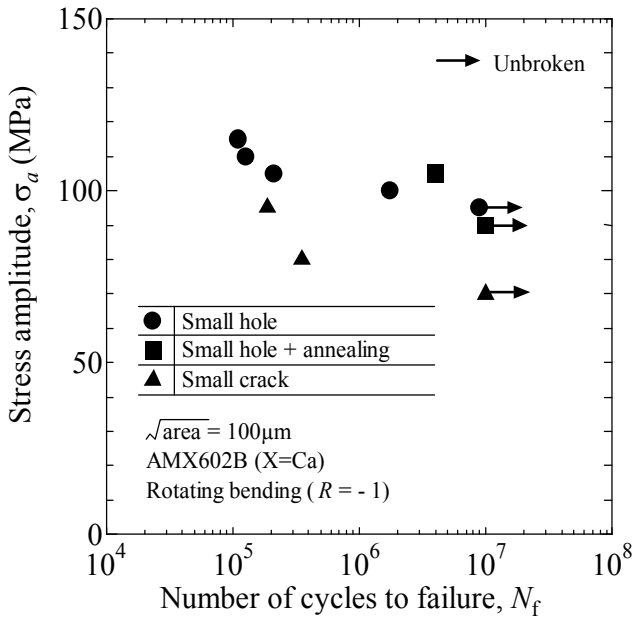

Fig. 7. *S-N* data for the small hole and the small crack specimens

The fatigue strength at $N = 10^7$ of the specimens with the small hole and the small crack was 95MPa and 70MPa, respectively. The fatigue strength at $N = 10^7$ of the specimens with the small hole is about 30% higher than that of the small crack, and effects of defect shape exist (effect of stress concentration level).

Figure 8 shows micrographs around the small hole and the small crack. No crack was observed under the fatigue strength at $N = 10^7$ in the small hole specimen. Otherwise, a nonpropagating crack was observed under the fatigue strength at $N = 10^7$ in the small crack specimen.

Because the small hole specimen and the small crack specimen have a comparable defect size $\sqrt{area}$, when a crack is initiated from the small hole, the stress intensity factor which acts on the crack in the small hole specimen becomes almost equal to the stress intensity factor which acts on the small crack specimen. If one assumes that the crack has been initiated from the small hole, the fatigue strength at $N = 10^7$ of the small hole specimens and the small crack specimen should become comparable. However, in this study, there is about a 30% difference between the fatigue strength at $N = 10^7$ of the small hole specimens and that of the small crack specimens. Therefore, the fatigue strength at $N = 10^7$ of the small hole specimens is determined by the crack-initiating critical stress, and the fatigue strength at $N = 10^7$ of the small crack specimens is determined by the crack-propagating critical stress.

That is, the reason why the fatigue strength at $N = 10^7$ of the small hole specimens is higher than that of the small crack specimens is that the stress amplitude required in order for a crack to be initiated from a small hole is higher than the stress amplitude required for a crack to propagate.
Therefore, effects of the defect shape (effect of stress concentration level) on the fatigue strength at $N = 10^7$ do exist.

4.2 Effect of the mean stress on the fatigue strength at $N = 10^7$ characteristics of the small hole and the small crack specimens

Figure 9 shows endurance data for specimens with a small hole or a small crack. The fatigue strength at $N = 10^7$ of the specimens with a small hole was 30 ~ 150% higher than that of the specimens with a small crack under tensile mean stress. The effects of defect shape (effect of stress concentration level) on the fatigue strength at $N = 10^7$ exist.
On the other hand, when the mean stress is as high as 100MPa or more (σ_m > 100MPa), the small hole specimens show a different fatigue behavior from that of the small crack specimens. As in the report by Heywood (Heywood, 1962) or Osgood (Osgood, 1970), the fatigue strength at $N = 10^7$ suddenly decreased as the mean stress became high. In order to clarify the reason why only the small hole specimens suddenly decreases in fatigue strength at $N = 10^7$ under a high tensile mean stress, the endurance diagram was considered by dividing it into two domains (Domain I and Domain II).
Domain I is defined as the mean stress σ_m = 0 to 100MPa domain. This is the domain in which the fatigue strength of the small hole specimens falls gradually and the fatigue strength at $N = 10^7$ of the small crack specimens suddenly decreases compared with the small hole specimens as the mean stress becomes high.
Nisitani & Okasaka (Nisitani & Okasaka, 1973) has reported as follows on the influence of the mean stress affecting the crack initiation and crack propagation. Because the magnitude of stress amplitude is the main factor in crack initiation, the influence of the mean stress is small, and because stress amplitude and the magnitude of the maximum stress are the main factors in crack propagation, the influence of the mean stress is large.
Therefore, because the fatigue strength at $N = 10^7$ of the small hole specimens is the crack-initiation critical stress, the magnitude of stress amplitude becomes important and it is thought that the influence of the mean stress affecting the fatigue strength at $N = 10^7$ of the small hole specimens is small. Moreover, the fatigue strength at $N = 10^7$ of the small crack specimens is the crack-propagation limit; therefore, the stress amplitude and the magnitude of the maximum stress become important, and it is thought that the influence of the mean stress on the fatigue strength at $N = 10^7$ of the small crack specimens is larger than that on the small hole specimens.
Domain II is defined as the mean stress σ_m = 100 to 190MPa domain. This is the domain in which the fatigue strength of the small hole specimens suddenly decreases and the fatigue strength at $N = 10^7$ of the small crack specimens falls gradually as the mean stress becomes high.
In order to clarify the cause of the fatigue strength at $N = 10^7$ of the small hole specimens suddenly decreasing under a high tensile mean stress, the condition near the small hole in the test was observed in detail. As a result, static cracks from a small hole under a high tensile stress had occurred during the time of the first loading in the fatigue testing. A photograph of the static cracks observed around the small hole is shown in Fig. 10.

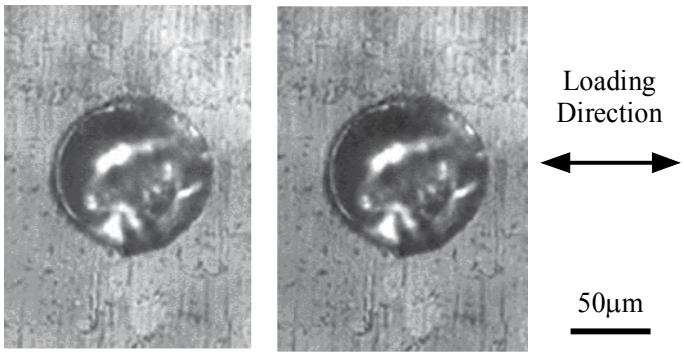

(1) $N = 0$ (2) $N = 10^7$

(a) Small hole specimen under σ_a = 95MPa (no crack)

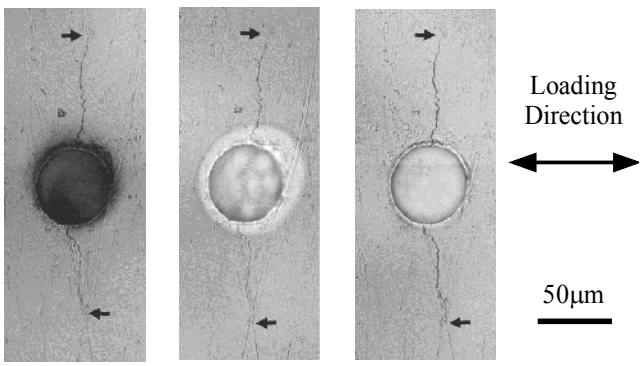

(1) $N = 0$ (2) $N = 1.15 \times 10^6$ (3) $N = 10^7$

(b) Small crack specimen under σ_a = 70MPa

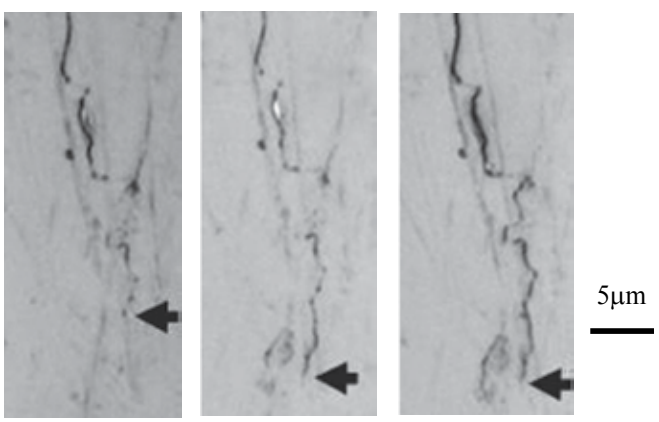

(1) $N = 0$ (2) $N = 1.15 \times 10^6$ (3) $N = 10^7$

(c) Crack tip of the small crack specimen under σ_a = 70MPa (Magnification of (b)) (nonpropagating crack)

Fig. 8. Micrographs around small hole and small crack (non-combustible Mg alloy AMX602B (X=Ca))

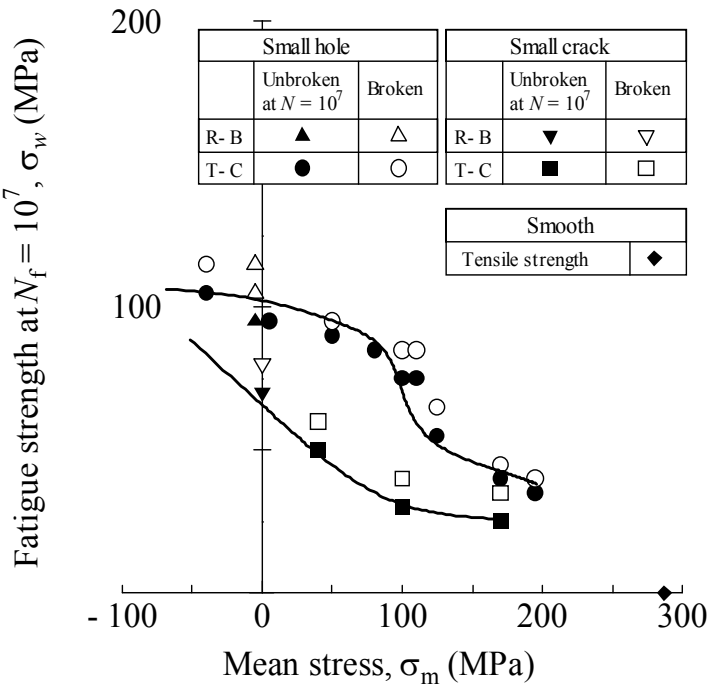

Fig. 9. Endurance data for the small hole and the small crack specimens (non-combustible Mg alloy AMX602B (X=Ca))

As shown in Fig. 9, the fatigue strength at $N = 10^7$ of the small hole specimens is higher than the fatigue strength at $N = 10^7$ of the small crack specimens by about 30 ~ 150%, and it shows the influence of defect shape (effect of stress concentration level). Therefore, the reason that the fatigue strength at $N = 10^7$ suddenly decreases under a high tensile mean stress in the small hole specimens is as follows: it falls when the shape of the defect changes from a small hole to a small crack and the fatigue strength at $N = 10^7$ of the small hole specimens approaches the fatigue strength at $N = 10^7$ of the small crack specimens, because static cracks were initiated from a small hole during the time of the first loading. That is, in the small hole specimens, unless it comes under a high tensile mean stress during which static cracks are initiated from the small hole, the fatigue strength at $N = 10^7$ does not fall. Kang et al. (Kang et al., 2007) has also reported that the fatigue limit fell due to a static crack in research on high strength prestrained steel.

In addition, the reason why the fatigue strength at $N = 10^7$ of the small hole specimens is slightly higher under a high tensile mean stress than the fatigue strength at $N = 10^7$ of the small crack specimens is considered to be as follows. The crack initiated in the small hole specimens at the time of the first loading is not a fatigue crack but a static crack, and the static crack has been strongly influenced by crack closure due to plastic deformation near the small hole, so that the crack opening stress is then higher than that of the small crack specimens.

Kondo et al. (Kondo et al., 2003) has reported the small crack opening stress of steel as follows regarding the fatigue strength characteristics of the small crack specimens under a high tensile mean stress ($R = 0.5$): under a high mean stress, the crack closure is not

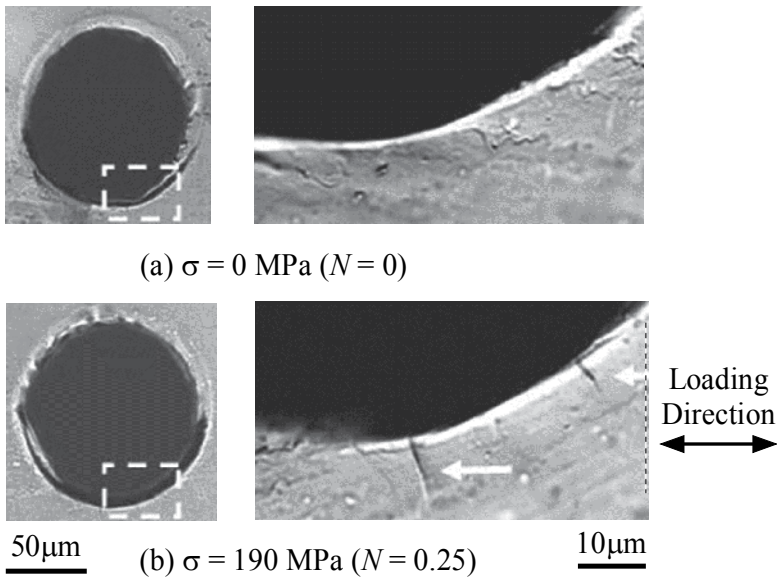

Fig. 10. Micrographs of static cracks observed during the first loading (arrow indicates static crack)

observed, so that the threshold stress intensity factor range, ΔK_{th} is the same value as the effective threshold stress intensity factor range, $\Delta K_{eff,\,th}$.

Therefore, the reason why the fatigue strength at $N = 10^7$ of the small crack specimens falls gradually in this research is considered to be because the fatigue strength at $N = 10^7$ of the small crack specimens becomes close to the effective threshold stress intensity factor range, $\Delta K_{eff,\,th}$, for a high tensile mean stress.

Figure 11 shows the relationship between the defect size $\sqrt{area}$ of the smooth specimens, the small hole specimens and the small crack specimens and their fatigue strength. In order to compare the fatigue strength of the smooth specimens with the results for the small crack specimens, the results of extrapolating the relation between the defect size $\sqrt{area}$ and the fatigue strength at $N = 10^7$ using the experimental results for a crack length of about 50μm ($\sqrt{area}$ = 30μm) in which crack length is sufficiently larger than the size of a few grain are shown. The slope of extrapolation was set to 1/6 (Murakami, 2002b) which reported to be good agreement with many materials.

The relationship for the smooth specimens between the defect size $\sqrt{area}$ and the fatigue strength is closer to the relationship for the small hole specimens than the relationship for the small crack specimens. Moreover, the fatigue strength at $N = 10^7$ of the smooth specimens is high compared with that of the small crack specimens. Therefore, it is thought that in the fatigue strength at $N = 10^7$, the fatigue behavior of the smooth specimens shows the near fatigue behavior of the small hole specimens. That is, the fatigue strength at $N = 10^7$ of the smooth specimens is thought to be the crack initiation limit. The effect of the mean stress on the fatigue strength at $N = 10^7$ is considered as follows. Under the high mean stress in which a static crack is initiated, the fatigue strength at $N = 10^7$ falls; however, the fall in fatigue strength at $N = 10^7$ is smooth under the mean stress in which a static crack is not

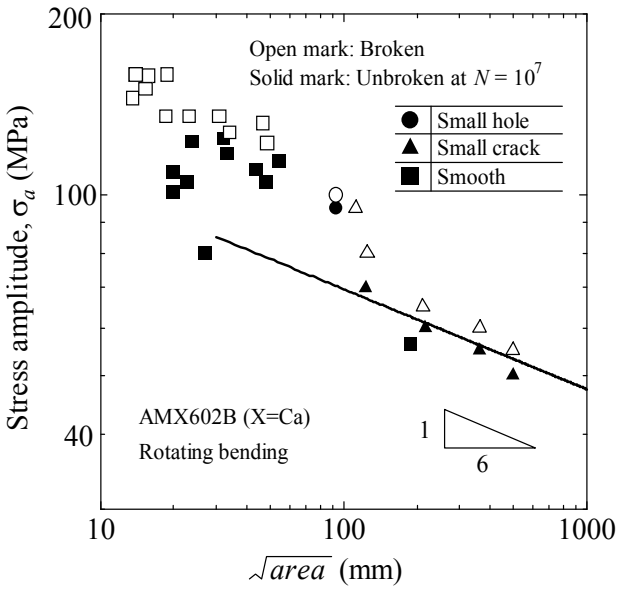

Fig. 11. Relationship between stress amplitude and defect size

initiated. Like the fatigue behavior of the small hole specimens, unless it is examined on the smooth specimens, a nonpropagating crack is indeed not observed. As shown in Fig. 12, when the loading of the high tensile stress was carried out, the static crack was initiated from the inclusion.

4.3 Application validity of the modified Goodman diagram

Figure 13 shows the endurance data for the smooth specimens. In the fatigue test results for the smooth specimens, the highest fatigue strength at $N = 10^7$ was applied, because the application of the highest fatigue strength created a severe modified Goodman diagram. The fatigue strength at $N = 10^7$ of the small hole specimens (Fig. 5) is also shown in the figure by a dashed line. The fatigue strength at $N = 10^7$ of the smooth specimens is higher than that of the small hole specimens in the range of $\sigma_{max} < \sigma_{0.2}$. From these results, the mean stress influence on the fatigue strength at $N = 10^7$ can be evaluated on the safety side using the modified Goodman diagram in the practical stress range ($\sigma_{max} < \sigma_{0.2}$).

Meanwhile, a static crack is initiated also in the smooth specimens, and there is a possibility that the fatigue strength at $N = 10^7$ may suddenly decrease under a high tensile mean stress. However, the tensile stress at which a static crack is initiated in a smooth specimens exceeds 0.2% proof stress, and the range under the mean stress which is considered to cause the fall fatigue strength at $N = 10^7$ in the smooth specimens is not a practical stress range ($\sigma_{max} < \sigma_{0.2}$).

4.4 Discussion of the effect of the mean stress on the fatigue strength of other Mg alloys

The possibility that the fatigue strength falls due to a static crack initiated under a high tensile mean stress in other Mg alloys is considered. In order for the fatigue strength to fall due to a static crack, the following two points are required. (i) The static crack is initiated by

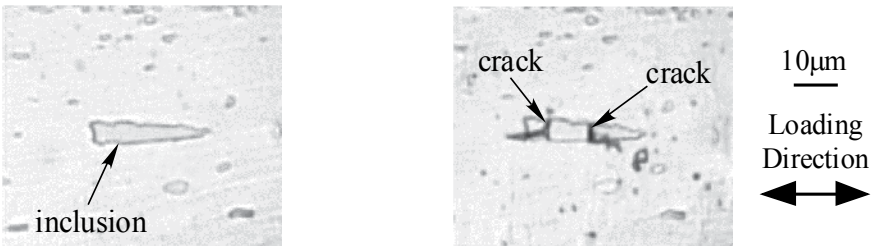

(a) σ = 0MPa, N = 0 (b) σ = 235MPa, N = 0.25

Fig. 12. Small static cracks initiated from inclusion at the first loading (non-combustible Mg alloy AMX602B (X=Ca))

the loading of a high tensile stress. (ii) The crack-initiation critical stress is higher than the fatigue crack-propagation critical stress, and once a crack is initiated, the fatigue strength will fall.

Elongation of many Mg alloys is about 10% (The Japan Magnesium Association, 2000). Because the elongation is small, it is thought that a static crack is initiated by a high tensile stress load. Moreover, because a clear fatigue limit is not defined for smooth specimens of many Mg alloys, the crack-initiation critical stress of the smooth specimens is higher than the fatigue crack-propagation critical stress, and once a crack is initiated, the fatigue strength is thought to fall.

Therefore, also in other Mg alloys, it is thought that the fatigue strength falls due to static crack initiation like that in the small hole specimens in this research. One can say that, also in other Mg alloys, unless the alloy is under a high tensile mean stress during which a static crack is initiated, it is thought that the influence of the mean stress on the fatigue strength can be evaluated using the modified Goodman diagram.

Furthermore, the difference in the opinions of Forrest (Forrest, 1962), Heywood (Heywood, 1962) and Osgood (Osgood, 1970) can also be explained based on the considerations described above. The report of Forrest (Forrest, 1962) summarized the influence of the mean stress on the fatigue strength of the Mg alloy which does not have much of a difference in the fatigue crack-propagation critical stress and the crack-initiation critical stress, and it is thought that the fatigue strength did not suddenly decrease under the high tensile mean stress. The reports of Heywood (Heywood, 1962) and Osgood (Osgood, 1970) summarized the influence of the mean stress affecting the fatigue strength of the Mg alloy which shows a difference in the fatigue crack-propagation critical stress and the crack-initiation critical stress, and the fatigue strength suddenly decrease under the high tensile mean stress; if the modified Goodman diagram is used for evaluation of fatigue strength, it is thought that it may not be conservative prediction.

5. Conclusions

Using the smooth specimens, the small hole specimens and the small crack specimens of the non-combustible Mg alloy AMX602B (X=Ca), the influence of the mean stress on the fatigue strength at $N = 10^7$ was investigated. We especially investigated the validity of applying the modified Goodman diagram to determine why the fatigue strength suddenly decreases

under a high tensile mean stress and why the mean stress affected the fatigue strength at $N = 10^7$. The conclusions are as follows.

1. We proposed an evaluation method for the mean stress effect of the inclusion-induced scattered fatigue strength. The proposed method involves fatigue testing using specimens with an artificial defect.
2. Using the non-combustible Mg alloy, whose fatigue strength shows an inclusion-induced scattering, the mean stress effect of the fatigue strength was evaluated.
3. In the range of σ_m = 0 to 100MPa, the fatigue strength at $N = 10^7$ of the small hole specimens was higher than that of the small crack specimens by 30 to 150%.
4. In the range of σ_m > 100MPa, the fatigue strength at $N = 10^7$ of the small hole specimens suddenly decreased due to static cracks initiating around the small hole during the first loading.
5. In the practical stress range ($\sigma_{max} < \sigma_{0.2}$), the fatigue strength at $N = 10^7$ of the smooth specimens was estimated using the modified Goodman diagram.

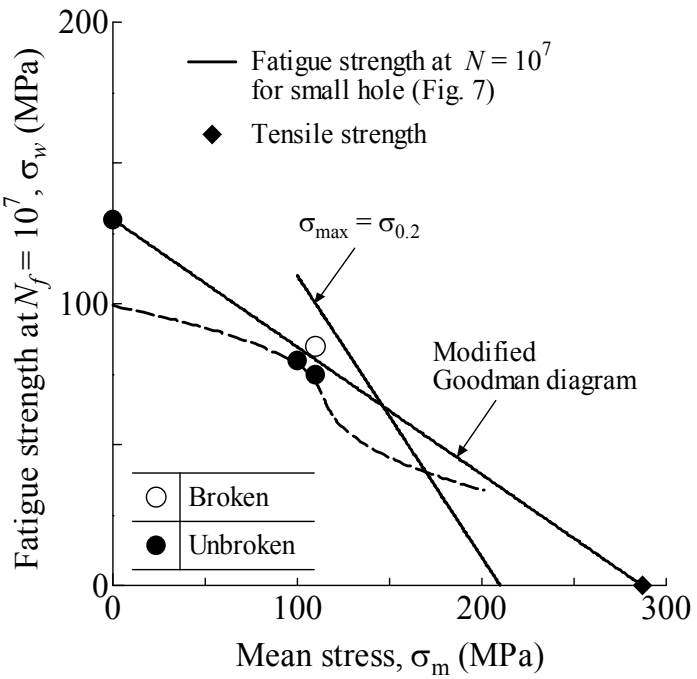

Fig. 13. Endurance data for the smooth specimens (non-combustible Mg alloy AMX602B (X=Ca))

6. References

Akiyama, S., Ueno, H. & Sakamoto, M. (2000). Purification of Molten Non-combustible Magnesium Alloy (in Japanesea). *Journal of Japan Foundry Engineering Society*, Vol. 72, No. 8 (521-524), ISSN: 13420429

Chang, S-Y., Matsushita, M., Tezuka, H. & Kamio, A. (1998). Ignition prevention of magnesium by simultaneous adding of calcium and zirconium. *International Journal of Cast Metals Research*, Vol. 10, No. 6 (345-351), ISSN: 13640461

Forrest, P. G. (1962). *Fatigue of Metals*, Pergamon Press, ISBN: 0080097294, Oxford, (75, 95-103)

Fujii, T., Morishige, K., Hamada, S., Noguchi, H., Sakamoto, M. and Ueno, H. (2008). Fatigue Strength Characteristics of Non-Combustible Mg Alloy. *Journal of Solid Mechanics and Materials Engineering*, Vol. 2, No. 6 (763-770) ISSN: 18809871

Heywood, R. B. (1962). Designing Against Fatigue, Chapman and Hall Ltd., ISBN: 0412068206, London, (69-70)

Kang, M., Aono, Y. & Noguchi, H. (2007). Effect of prestrain on and prediction of fatigue limit in carbon steel. *International Journal of Fatigue*, Vol. 29, No. 9-11 (1855-1862) ISSN: 01421123

Kitahara, Y., Shimazaki, H., Yabu, T., Noguchi, H., Sakamoto, M. &Ueno H. (2005). Influence of inclusions on fatigue characteristics of non-combutible Mg alloy. *Materials Science Forum*, Vol. 482 (359-362) ISSN: 02555476

Kitahara, Y., Ikeda, K., Shimazaki, H., Noguchi, H., Sakamoto, M. & Ueno H. (2006). Fatigue strength characteristics of non-combustible Mg alloy: 1st report, quantitative comparison among fatigue strengths of three non-combustible Mg alloys (in Japanese). *Transactions of the Japan Society of Mechanical Engineers A*, Vol. 72, No. 717 (661-668) ISSN: 03875008

Kondo, Y., Sakae, C., Kubota, M. & Kudou T. (2003). The effect of material hardness and mean stress on the fatigue limit of steels containing small defects. *Fatigue and Fracture of Engineering Materials and Structures*, Vol. 26, No. 8 (675-682) ISSN: 8756758X

Masaki, K., Ochi, Y., Kakiuchi, T., Kurata K., Hirasawa, T., Matsumura, T., Takigawa, Y. & Higashi, K. (2008). High Cycle Fatigue Property of Extruded Non-Combustible Mg Alloy AMCa602. *Materials Transactions*, Vol. 49, No. 5 (1148-1156) ISSN: 13459678

Murakami, Y. (2002a). *Metal Fatigue: Effects of Small Defects and Nonmetallic inclusions*, Elsevier, ISBN: 0080440649, Amsterdam, (16-19)

Murakami, Y. (2002b). *Metal Fatigue: Effects of Small Defects and Nonmetallic inclusions*, Elsevier, ISBN: 0080440649, Amsterdam, (60-62)

Nisitani, H. & Okasaka, K. (1973). Effect of mean stress on fatigue strength crack strength and notch radius at branch point, under repeated axial stresses. *Transactions of the Japan Society of Mechanical Engineers*, Vol. 39, No. 317 (49-59) ISSN: 00290270

Ogarevic, V. V. & Stephens, R. I. (1990). Fatigue of magnesium alloys. *Annual Review of Materials Science*, Vol. 20, No. 1 (141-177), ISSN: 00846600

Osgood C. C. (1970). Fatigue Design, Wiley-Interscience, ISBN: 0471657115, New York, (433-439)

Sakamoto, M., Akiyama, S., Hagio, T. & Ogi, K. (1997). Control of oxidation surface film and suppression of ignition of molten Mg-Ca alloy by Ca addition (in Japanesea). *Journal of Japan Foundry Engineering Society*, Vol. 69, No. 3 (227-233) ISSN: 13420429

The Japan Magnesium Association (2000). *Handbook of advanced magnesium technology (in Japanese)*, Kallos Publishing, ISBN: 4874320147, Tokyo, (447-460)

7

Fatigue Endurance of Magnesium Alloys

Mariana Kuffová
Armed Forces Academy of General Milan Rastislav Stefanik
The Slovak Republic

1. Introduction

Magnesium alloys belong to the important light alloys. For wide utilization of Mg-alloys it is significant to know their properties, including the fatigue properties.
The fatigue of construction materials is a degradation process of irreversible changes in material properties caused by cyclic loading. Gradual accumulation of damage under repeated mechanical stress of the specimen, part of fabrication, known as the fatigue process, is conditioned by a great number of factors. Investigation of characteristics of the fatigue process depends on the kind of mechanical stress, the characteristic of testing machines and equipments. The criterion of material resistance to repeated stress is still the fatigue limit, expressed by the stress amplitude σ_a or the plastic deformation amplitude ε_{ap} under whose action material will endure an infinite number o cycles (fatigue limit σ_c), or at least a number of loading cycles determined in advance. The Wöhler curve in coordinates σ_a – log N, or ε_a – log N, is constructed on the basic of long-term tests of a great number of specimens. According to the respect of the fracture mechanics regularities, there is the dependence of fatigue crack growth on stress intensity factor ($da/dN = f(K_a)$) and threshold value of stress intensity factor K_{ath}. The importance of fatigue is tied foremost to safety of persons, which life is dependent on the reliability of given device operation (Nečas & Kelemen, 2010).
Cracks initiate and propagate from pre-existing flaws, material defects, or design features (fatter holes or sharp corners). In the fact, most fatigue is widespread, as hundreds, or even thousands of cracks are manifested in cyclic loading. The net effect of numerous fatigue cracks located in the same general area is that they synergistically interact reducing the structure's residual strength. However, the single-crack concept is still important, because ultimately, catastrophic failure can occur when a single crack goes critical and in the process envelops other adjacent cracks in zippering effect.

2. Available information about fatigue properties of magnesium alloys

Two basic methods are employed to predict and determine potential fatigue locations. The first is full-scale fatigue testing, which is performed during the development process. These tests are employed to ascertain the expected durability. Experimental fatigue tests can be performed under the low frequency cyclic loading, at frequencies to 2000 Hz (usually at $f \leq 200$ Hz) or under the high frequency cyclic loading ($f \approx 20$ kHz). In particular, fatigue tests are very expensive, since they require a lot of human and machine time. Using of high frequency cyclic loading allow us to obtain relevant information about fatigue endurance

and fatigue properties in areas of high and very high number of cycles ($N = 1.10^9 – 1.10^{12}$) . Decreasing of expenses as well as increasing of efficiency of whole process of mechanical design and providing of operability during the overall lifetime of parts and machineries allow us to make progress in the field of the utilization of the computational technologies and the application of numerical methods for the solution of huge amount of mechanical engineering praxes' problems. Nowadays we have several commercial programs at our disposal which allow us to solve the crack propagation. Many authors have dealt with influence of the crack growth on the functionality of the particular parts from global point of view. Available simulation programs for the simulation of fatigue crack growth can be generally divided into numerical and analytical ones. The numerical programs (FRANC/FAM, FRANC3D, ADAPCRACK3D, CRACK-TRACER, ZENCRACK) are able to predict the crack path in arbitrary 2-D or 3-D structures by using the finite element or boundary element method, meshless method, the material point method. The lifetime is mostly calculated using linear damage accumulation. However, they are often very time consuming. On the other hand, analytical programs (NASGRO, ESACRACK, AFGROW) are very fast because no model has to be built, no meshing has to be done and the analysis is very rapid. But in many cases the analytical solutions for a number of selected problems do not match the real geometry and boundary conditions very well (Sander & Richard, 2006).

2.1 Fatigue endurance of magnesium alloys under low frequency cyclic loading

Fatigue tests for particular magnesium alloys were carried out by authors ((Bursk, 1997), (Cllaper & Watz, 1956), (Goodenberger, 1990)) to obtain relevant information about their fatigue endurance under low frequency cyclic loading. Their chemical composition and mechanical properties are shown in Tab. 1.

Alloy	**Al**	**Zn**	**Mn**	**Cu**	**Si**	**Fe**	**Ni**	**Zr**	**Rm**	**Re**	**A**
Wrought	**[wt %]**								**[MPa]**		**[%]**
AZ31B	3.0	1.0	0.2	-	-	-	-	-	260	200	15
AZ61A	6.5	1.0	0.15	-	-	-	-	-	310	230	16
ZK60A	-	5.5	-	-	-	-	-	0.4	305	205	16
AM503	0.01	0.01	1.62	0.02	0.006	0.007	0.003	-	200	107	6
Cast											
AZ63A	6.8	3.1	0.33	0.009	0.04	0.009	0.001	-	260	168	6,9
AZ91B	9.0	0.68	0.13	-	-	-	-	-	230	160	3
AZ91E	8.97	0.54	0.12	0.01	0.01	0.003	0.001	-	318	142	12

Table 1. Chemical composition and mechanical properties of particular magnesium alloys

Experimental fatigue tests were realised under different frequencies (3.5 ÷ 50 Hz), in air, at the temperature of surroundings and the criterion of failure was the final fracture. From the measured results, dependences applied stress – number of cycles, $\sigma_a = f(N)$, were plotted. The results for wrought and cast magnesium alloys are depicted in Fig. 1.

Fatigue limit σ_c of magnesium alloys has been determined in the range 70 ÷ 150 MPa at the terminal number of cycles $N = 1.10^7$ cycles, Table 2 and Fig. 1.

During the experimental fatigue tests, the influence of particular factors on the fatigue lifetime was observed. The authors have noted that the fatigue endurance of magnesium alloys is influenced by surface conditions. Sharp notches, small radii, fretting and corrosion

are more likely to reduce fatigue life than variations in chemical compositions or heat treatment. Removing the relatively rough as-cast surfaces of castings by machining improves fatigue properties of the castings, what is depicted in Fig. 2 (Avedesian & Baker, 2000). The influence of the microstructure on fatigue lifetime is conditioned by homogeneity

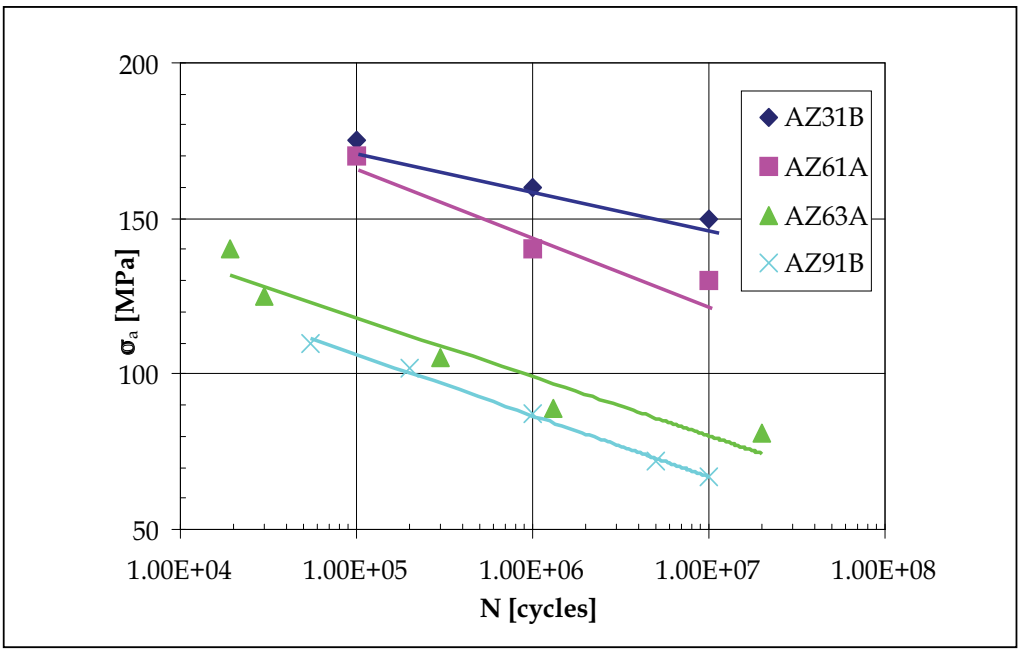

Fig. 1. Dependence $\sigma_a = f(N)$ of particular magnesium alloys

Mg - alloys	AZ 31B	AZ 61A	AZ 63A	AZ 91B
R	0.25	0.25	-1	-1
σ_c [MPa]	150	130	85	70

Table 2. Fatigue limit σ_c of particular magnesium alloys

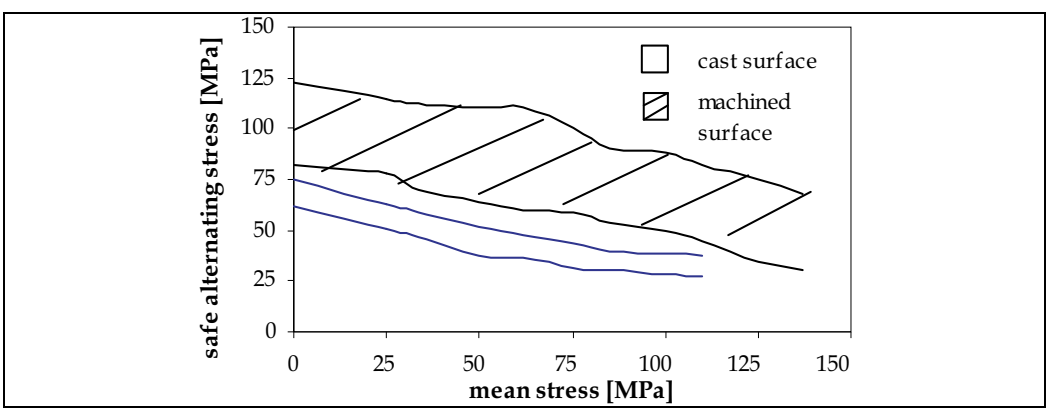

Fig. 2. Influence of the surface quality on the fatigue properties of magnesium alloys

of the microstructure. During the ageing, the homogeneous and inhomogeneous cell structure is created and has influence on the dependence $\sigma_a = f(N)$ (Ishikawa et al., 1997).
When fatigue is the controlling factor in design, every effort should be made to decrease the severity of stress raisers. Use of generous fillets in re-entrant corners and gradual changes of section greatly increase fatigue life. Conditions in which the effects of one stress raiser overlap those of another should be eliminated. Cold working the surfaces of critical regions by rolling or peening to achieve appreciable plastic deformation produces residual compressive surface stress and increases fatigue life. Surface rolling of radii is especially beneficial to fatigue resistance because radii generally are the locations of higher-than-normal stresses.
The initiation of fatigue cracks in magnesium alloys is related to slip in preferable oriented grains and is often related to the existence of micropores. The initial stage of fatigue crack growth usually occurs from quasicleavage, which is common in hexagonal close-packed structures. Further crack growth micromechanisms can be brittle or ductile and trans- or intergranular, depending on metallurgical structure and environmental influence.
On the basis of experimental tests, the authors came to the conclusion that: The dependence fatigue crack growth rate da/dN on the stress intensity factor amplitude ΔK increases with the increasing value of asymmetry coefficient R. The fatigue properties of magnesium alloys decrease with the increasing content of aluminium. Authors (Zheng et al., 2000) observed the influence of loading frequency and heat treatment on the fatigue crack growth rate in magnesium alloy AZ 91HP. The results show that the fatigue crack growth rate in the die-cast magnesium alloy has increased with the frequency decrease. Crack growth can be reduced as a consequence of dissolving annealing or can be increased after ageing. Casting magnesium alloys contain pores filled with air which reduce mechanical properties of the products. Pores have caused the blowholes and deformation during the heat treatment. The studies of fatigue crack growth in magnesium alloy AZ 91D which did not contain pores, have shown two facts. For the low values of ΔK the crack growth is discontinuous and for higher values of ΔK it is continuous. These facts confirm that fatigue crack growth is influenced by heat treatment and environment. It is relationship between growth rate and free surface oxidation. The fatigue crack growth is higher in the air than in argon. The brittle oxidizing film on the free fatigue surface is the cause of it. The ageing increases fatigue crack growth and decreases K_{fc}. However, it shows that ageing does not influence ΔK_{th} ((Ishikawa et al., 1995), (Shibusawa et al., 1997)).
A fundamental study of the corrosion fatigue of magnesium alloys found that both stress-corrosion and corrosion-fatigue cracks propagated in a mixed transgranular - intergranular mode. Corrosion fatigue crack growth is accelerated by the same environments as those that accelerate stress corrosion crack growth. The boundary between regions II and III in sodium bromide solutions of the da/dN versus ΔK curve is higher than the stress corrosion threshold, which occurs at much lower stress intensity.

2.2 Fatigue endurance of magnesium alloys under high frequency cyclic loading

Information about fatigue endurance of magnesium alloys under high frequency cyclic loading is rare. Authors in papers ((Mayer et al., 1997), (Stanzl et al., 1984), (Laird & Charsley, 1982), (Papakyriacou et al., 2001), (Mayer, 1998)) determined fatigue endurance of high pressure die cast magnesium alloys AZ 91HP, AM 60 Hp and AS 21HP under high frequency loading. Fatigue tests of magnesium alloys with chemical composition, shown in tab. 3 were carried out in the air, with temperature 20 ÷ 22 °C and warm air with temperature 125°C and final number of cycles was $N = 1.10^9$ cycles.

Mg - alloys	Al	Zn	Mn	Si	Fe	Cu	Ni	Ce
	[wt %]							
AZ 91 HP	8.9	0.79	0.21	0.01	0.003	0.001	0.001	-
AM 60 HP	6.1	0.01	0.29	0.01	0.003	0.002	0.001	-
AS 21 HP	2.2	< 0.01	0.16	0.98	< 0.01	< 0.002	< 0.001	0.073

Table 3. Chemical composition of particular magnesium alloys

Experimental results which were obtained are depicted in Fig. 3 and measured value of fatigue limit σ_c (N = 1.10^9 cycles) including fatigue limit σ_c (N = 1.10^7 cycles) for particular magnesium alloys are shown in Table. 4. Results of fatigue experiments with AZ 91HP are shown in Fig. 3. Specimens which did not fail are marked with an arrow. Data points for load amplitudes equal or higher than 52 MPa (ambient air, T = 20 ÷ 22 °C) and 42 MPa (warm air, T = 125 °C) are approximated using an exponential function, and the lines indicate a probability for fracture of 50 %. In both environments numbers of cycles to failure greater than about 1.10^7 cycles are rare, and a well defined fatigue limit exists. No specimen failed within 1.10^9 cycles at load levels of 38 MPa (ambient air, T = 20 ÷ 22 °C) and 33.5 MPa (warm air, T = 125 °C), respectively.

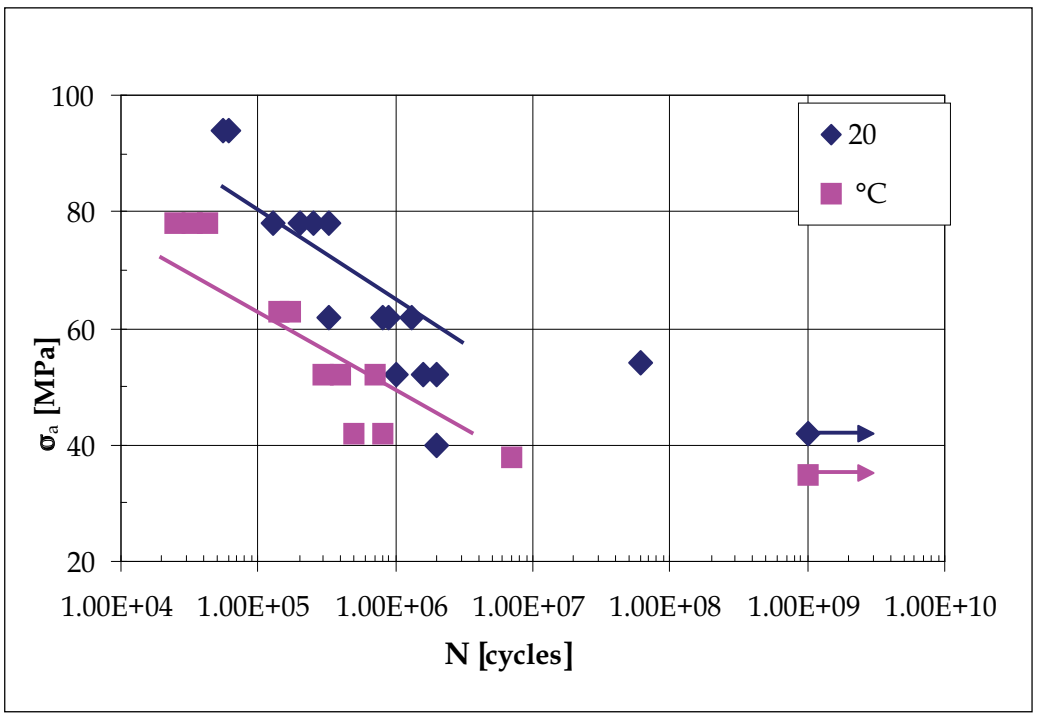

Fig. 3. Dependence $\sigma_a = f(N)$ of magnesium alloy AZ 91HP

A comparison between the S – N curves of AZ 91HP, AM 60HP and AS 21HP is depicted in Fig. 4. In ambient air environment AM 60HP shows longer fatigue life and a higher fatigue limit than AZ 91HP. Fatigue limit in magnesium alloys AZ 91D and AS 21HP is decreasing in approximately 20 % if the temperature increases from 20 ÷ 22 °C to 125°C. Fatigue properties of AS 21HP are worse than those of AZ 91HP and of AM 60HP.

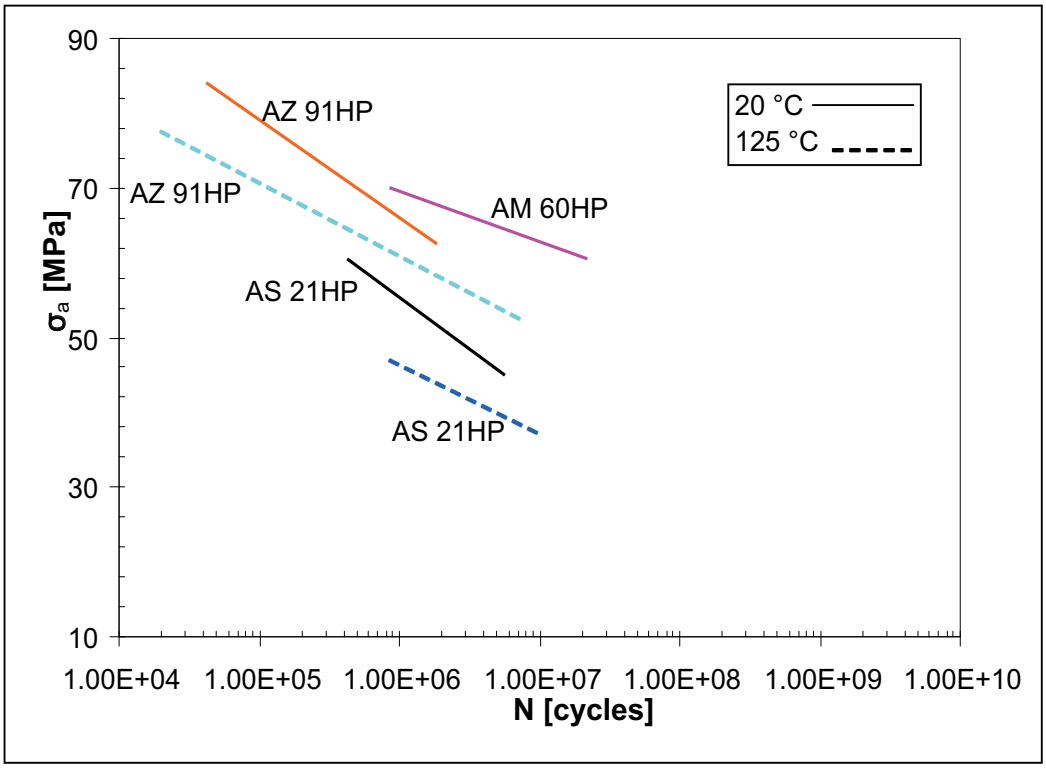

Fig. 4. The comparison of dependence $\sigma_a = f(N)$ of particular magnesium alloys

Fatigue limit		σ_c [MPa]			
Mg - alloy	**Number of cycles**	**N = 1.10⁹**		**N = 1.10⁷**	
	Temperature	**20 °C**	**125 °C**	**20 °C**	**125 °C**
AZ 91HP		38	33.5	52	42
AM 60HP		43	-	52	-
AS 21HP		28	21	40	25

Table 4. Fatigue limit σ_c at number of cycles N = 1.10⁷ and 1.10⁹ cycles for particular magnesium alloys

Experimental bars after fatigue tests were undergone a fractographic analysis. Voids were observed on the surfaces of all broken AZ 91HP and AM 60HP specimens, and in crack initiation area on 37 of 40 broken AS 21HP specimens. Fig. 5 shows such a void as an example for that kind of casting defect on the fracture surface of an AZ 91HP specimen which was cycled with load amplitude of 52 MPa and broken after 1.92x10⁶ cycles. Some places on the surface of the void show dendrite arms, which indicates that voids are shrinkage, formed during cooling of the melt. Voids serve as starting points for the formation of fatigue cracks. Further crack growth then is transcrystalline in all three investigated materials irrespective of load level and temperature.

Voids generally had a very irregular shape and it was sometimes difficult to clearly find the border of that casting defect. In the crack initiation area of some specimens not one but several voids of different size were concentrated.

Subdividing the fatigue process into fatigue crack initiation and crack growth until final failure, voids shorten both fatigue periods. Voids cause stress concentration in nearby material and facilitate crack initiation. Stress amplitude, size, shape and site of a void as well as possibilities for slip in adjacent grains influence the number of cycles to form an initial crack. With increasing size of the casting defects the probability for early crack initiation is increasing (Mayer at al., 1997).

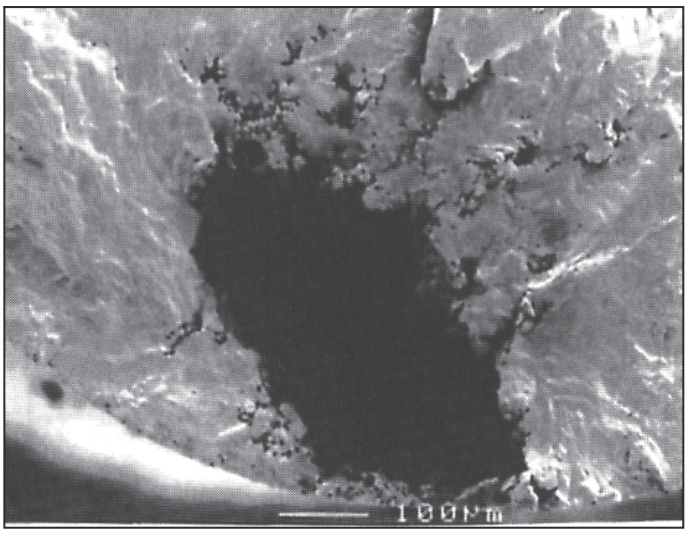

Fig. 5. Void in the fatigue crack initiation area of AZ 91HP under high frequency cyclic loading

An influence of the heat treatment (T6a – dissolving annealing and artificial ageing, T4 – dissolving annealing) on fatigue endurance (dependence $\sigma_{max} = f(N)$) for magnesium alloy AZ 91D is presented by authors (Ishikawa et al., 2001), and shown in Fig. 6. For both heat treatment the specimens did not fail in the area of number of cycles $N = 1.10^6 \div 1.10^7$ cycles. For that area, magnesium alloy AZ 91D with heat treatment T6a showed better fatigue properties. Authors supposed with respect to the dependence $\sigma_{max} = f(N)$ that the mechanism of failure was different in dependence on the stress level.

An influence of environment and porosity on fatigue endurance of magnesium alloys was observed in author's work (Mayer et al., 1999). Fatigue experiments were performed in ambient air (temperature 20 ÷ 22 °C) and in a saltwater spray (5wt% iodized sodium chloride dissolved in water). Specimens were excited to longitudinal resonance vibrations at ultrasonic frequencies (≈ 20 kHz). The results of fatigue experiments are depicted in Fig. 7. Lines indicated a fracture probability of 50%. In ambient air, failures beyond 1.10^7 cycles were rare and the *S-N* curve became parallel to the abscissa in the high-cycle regime. Because no specimen failed within 1.10^9 cycles at a stress level of 38 MPa that stress amplitude was defined as the fatigue limit of that material.

In saltwater spray, no significant reduction of fatigue lifetimes, in comparison to ambient air, was found for cycles-to failure below 1.10^7 cycles, and the fatigue date coincided within the range of scatter. For higher numbers of cycles, however, an influence of the corrosive fluid on fatigue properties was observed. The *S-N* curve decreased in the regime above 1.10^7 cycles, an in contrast to the ambient air environment, no fatigue limit was found.

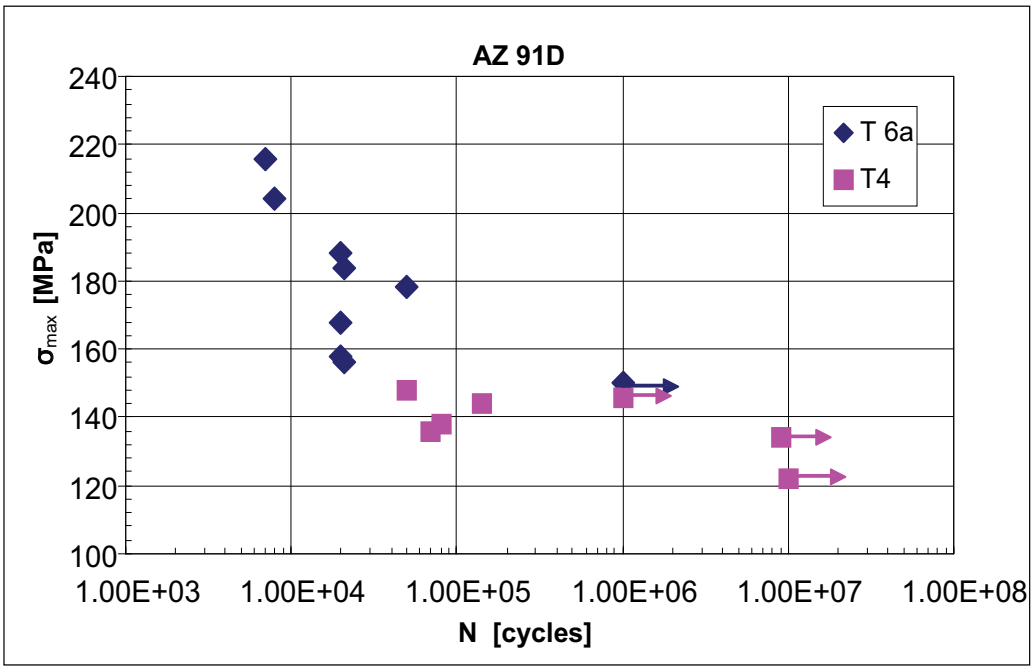

Fig. 6. Dependence $\sigma_{max} = f(N)$ for magnesium alloy AZ 91D after heat treatment

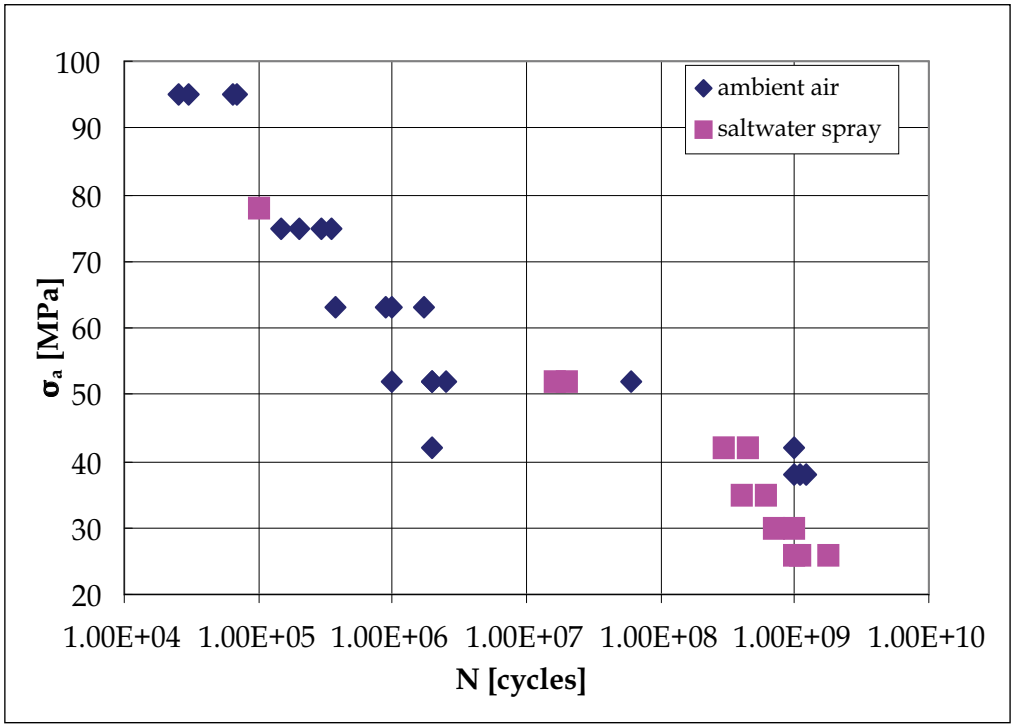

Fig. 7. Results of endurance fatigue tests on AZ 91HP in ambient air at 20 °C and in saltwater spray

If the number of cycles-to-failure was below 1.10^7, the fracture surfaces of AZ 91HP specimens fatigued in ambient air and saltwater spray were similar. Fatigue cracks emanated from voids in both cases, and the fracture surfaces showed transgranular crack propagation with no significant influence of the corrosive fluid. At very high numbers of cycles-to-failure (1.10^8 and above), cyclic loading in corrosive fluid led to the formation of corrosion pits on the surface of the material. The depth of pits increased approximately linearly with exposure time of the specimen. The lifetime in saltwater spray was not only shorted due to accelerated crack growth, but additionally by the notch effect of those pits which caused local stress concentrations and enabled crack initiation at low applied stress amplitudes. However, AZ 91HP did not show nearly as deep corrosion pits after 42 h corrosion attack if no cyclic loading had been applied. The testing times at ultrasonic frequencies below 1.10^7 (f = 20 kHz, t = 8 min.) cycles-to-failure probably were too short to lead to a strong corrosive effect in that material. Magnesium alloy AZ 91HP did not show fatigue limit in saltwater spray (Mayer et al., 1999). Ambient air had significant influence on the fatigue crack growth in the threshold regime. Threshold value of stress intensity factor K_{ath} measured in vacuum was 30 ÷ 85 % higher than in ambient air. The influence of air humidity decreased at higher fatigue crack growth rates at ultrasonic frequencies. Accelerated fatigue crack growth in magnesium alloys at high growth rates was caused by absorbed hydrogen which had weakened bond between atoms (Lynch, 1988) or hydrogen diffusion which caused embrittlement of material (Makar et al., 1993). A significant reduction in lifetimes was found for sand-cast AZ 91E-T6 when specimens were cycled at conventional frequencies (25 Hz) in saltwater.

The influence of porosity was observed on the fracture surfaces of all AZ 91HP specimens which showed in ambient air that voids were crack initiation points. Most fatigue cracks started at voids on the surface or close to the surface of the specimens, which meant that such flaws were more detrimental than defects in the inner sections of the material. Fatigue crack growth was transcrystalline, irrespective of the load level. Stress concentrations near voids were the source of crack initiation. The increase of the nominal stress in the remaining cross-section was limited. Because a larger initially broken area caused higher cyclic stress intensity amplitude, the crack growth period at a certain cyclic load was shorter for larger flaws. Most fractured specimens failed below $1 \div 2.10^7$ cycles, and the *S-N* curve at higher number of cycles was approximately parallel to the abscissa. The rather low fatigue limit of AZ 91HP was attributed to the manufacturing process leading to relatively large casting voids and it was not an inherent property of that magnesium cast alloy. Fatigue tests of magnesium alloy AZ 91HP produces with different casting techniques showed that the *S-N* curve determined permanent mould-casted AZ 91HP material without voids lain above the *S-N* of die-cast AZ 91HP, however, it decreased in the entire investigated regime between $1.10^5 \div 1.10^9$ cycles and did not show a fatigue limit. In cases where specimens failed after more than 1.10^7 cycles, cracks emanated from voids in the inner section of the material. It meant that fatigue cracks grew mainly under vacuum conditions.

3. Fatigue endurance of magnesium alloys AZ 91D and AZ 63HP

3.1 Experimental materials

Fatigue experiments were performed with the sand-cast magnesium alloys AZ 91D and AZ 63 HP after heat treatment T4 – dissolving annealing according to Fig. 8. AZ 91D is the most frequently using alloy, mostly in automobile industry. AZ 63 HP is alloy with high purity and reduced content of copper, ferrum and silicon.

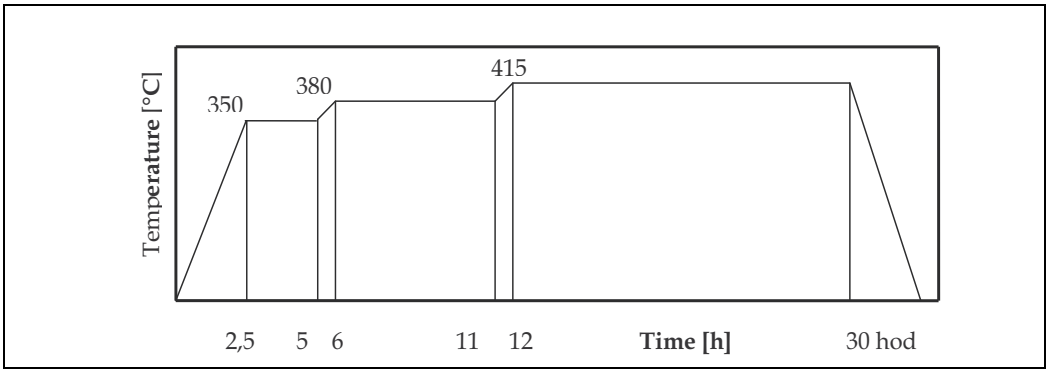

Fig. 8. Heat treatment regime of magnesium alloys AZ 91 and AZ 63HP

Magnesium alloys were delivered after being cast into sand moulds in the form of half-finished products, i.e. plates with dimensions 21 x 100 x 200 mm (Fig. 9a) and blocks with dimensions 70 x 160 x 160 mm (Fig. 9b). Due to non-uniform hardening in the course of experimental material cooling, specimens were taken from the block and the plate edge as well as the plate middle (Fig. 9).

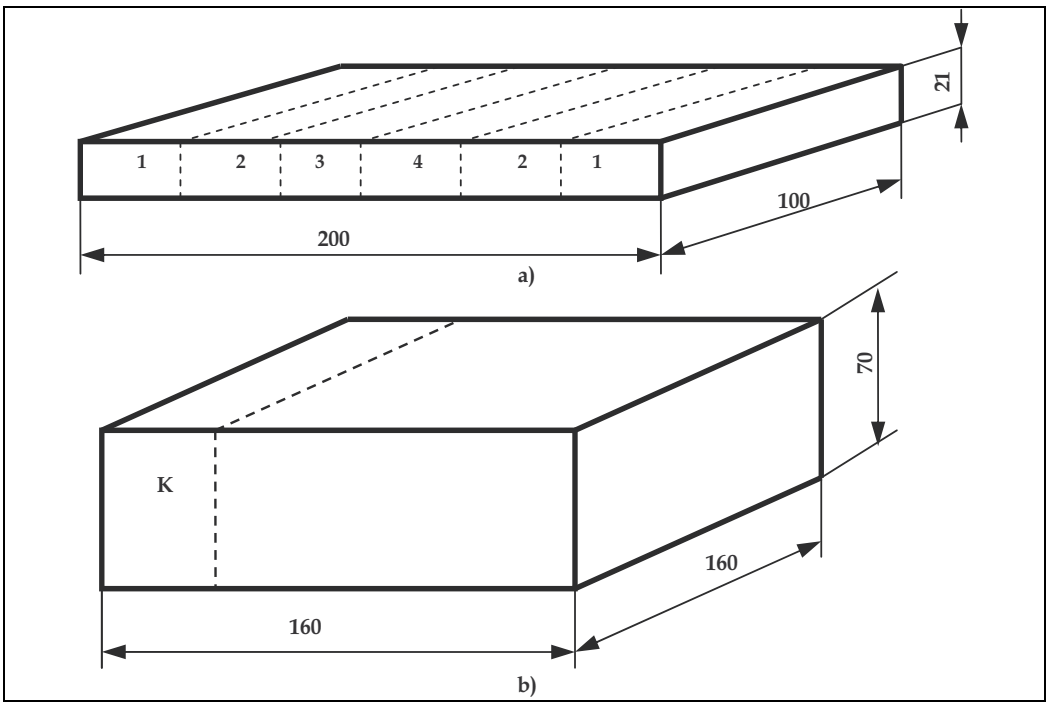

Fig. 9. Taking, marking and using of specimens, a – plate, b – block
1, 2 – fatigue test, metallographic analysis, Brinell hardness test, tensile test
– marked **plate edge**
3, 4 – fatigue test, metallographic analysis, Brinell hardness test
– marked **plate middle**
K – fatigue test, metallographic analysis, Brinell hardness test, falling-weight test
– marked **block**

Chemical composition and mechanical properties of magnesium alloys AZ 91D and AZ 63HP are shown in Tab. 5, Tab. 6 and Tab. 7.

Mg-alloy	Al	Zn	Mn	Si	Cu	Fe	Be	Pb
AZ 91D	7.98	0.63	0.22	0.045	0.007	0.013	0.0003	0.057
AZ 63HP	5.28	2.65	0.21	0.028	0.002	0.003	0.0003	0.037

Tab. 5. Chemical composition (wt %) of magnesium alloys AZ 91D and AZ 63HP

Mg- alloy	Rm [MPa]	Re [MPa]	A_5 [%]	Z [%]	KCU 2 [J.cm^{-2}]
AZ 91D	223	76	8	0.5	4.4
AZ 63HP	121	59	6.2	0.3	6.6

Tab. 6. Mechanical properties of magnesium alloys AZ 91D and AZ 63HP

Mg - alloy	Plate edge	Plate middle	Block
AZ 91D	64.2	65.5	67.5
AZ 63HP	63.6	63.0	60.6

Tab. 7. Value of Brinell hardness test, $HB_{2.5/62.5/30}$ for magnesium alloys AZ 91D and AZ 63HP

Microstructure of magnesium alloy AZ 91D specimens after heat treatment (Fig. 8) is presented in Fig. 10. Specimens for metallographic analysis were taken from block, plate edge as well as plate middle. Microstructure of the specimens taken from the block (Fig. 10a) was the complicated heterogeneous structure which was extremely influenced by the cooling rate and therefore the microstructure after heat treatment was considerably influenced by microstructure of half-finished product. The structure was created by non-uniform large dendritic grains of phase δ (grain size 2) and discontinuous eutectic (γ + δ) precipitated on the grain boundaries. The eutectic was created by fine lamellas of phase γ (electron compound $Al_{12}Mg_{17}$) with huge number of voids (black points). Phase γ was in attendance in the form of primary precipitated massive phase (precipitated on the dendrite boundaries) which was surrounded by the eutectic. Presence of the voids was characteristic for the whole structure. Microstructure of the specimens taken from the plate with the thickness 21 mm (Fig. 10b, c) was created by polyedric grains of phase δ. The grain size was not the same in the whole cast body. Bigger grain was observed in specimens taken from the plate middle (grain size 4) (Fig. 10b) when compared to the specimens taken from the plate edge (grain size 5) (Fig. 10c). At some places, within the grain boundaries there was found the presence of small amount of discontinuous precipitate consisting of fine lamellas of phase γ (electron compound $Al_{12}Mg_{17}$) in matrix of δ phase. In that case, there were observed the characteristic meandering grain boundaries with the rest of lamellar precipitate (Fig. 12a).

Character of the microstructure of magnesium alloy AZ 63HP was mainly given by different chemical composition (lower content of Al, higher content of Zn). As a consequence, the microstructure was mostly characterized by phase δ and small amount of the precipitate. Microstructure of the specimens taken from the block (Fig. 11a) was created by non-uniform polyedric phase δ (grain size 1 - 2) with the areas of lamellar precipitate on the grain boundaries. Black places presented the presence of voids. Microstructure of the specimens

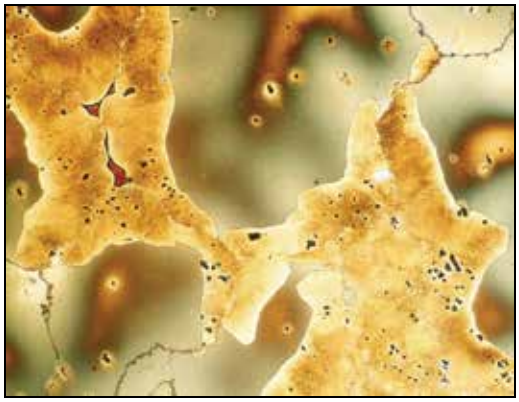

(a) the block 70 x 160 x 160 mm x 100

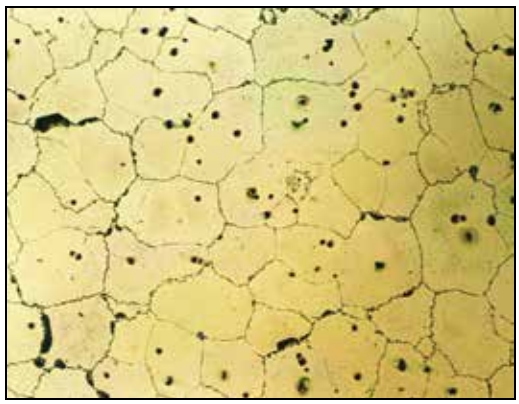

(b) the plate 21 x 100 x 200 mm the middle, x 100

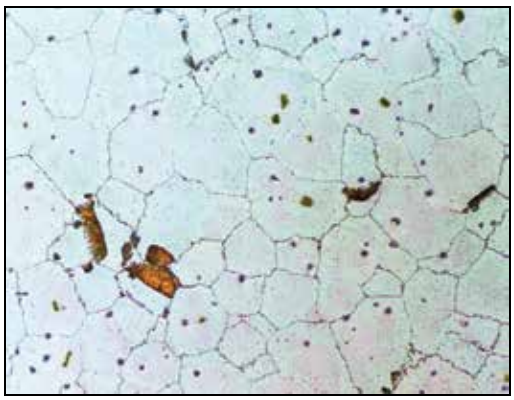

(c) the plate 21 x 100 x 200 mm the edge, polarized light x 100

Fig. 10. Microstructure of magnesium alloy AZ 91D after heat treatment T 4, etch. 5 % molybdenum acid

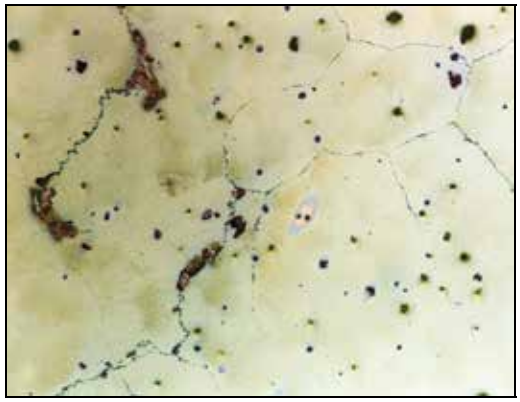

(a) the block 70 x 160 x 160 mm x 100

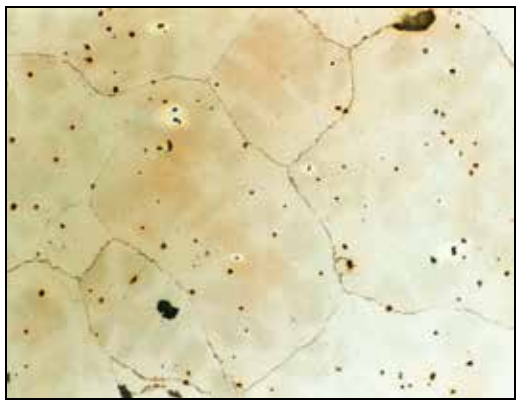

(b) the plate 21 x 100 x 200 mm the middle x 100

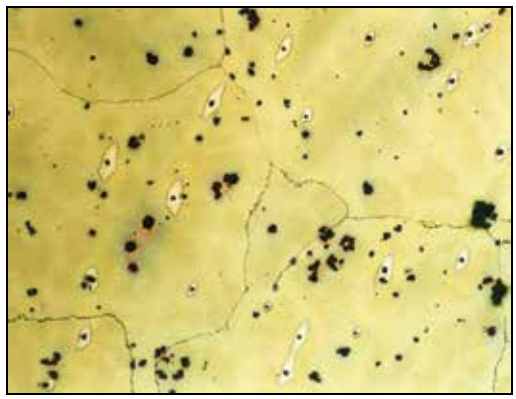

(c) the plate 21 x 100 x 200 mm the edge x 100

Fig. 11. Microstructure of magnesium alloy AZ 63HP after heat treatment T 4, etch. 5 % molybdenum acid

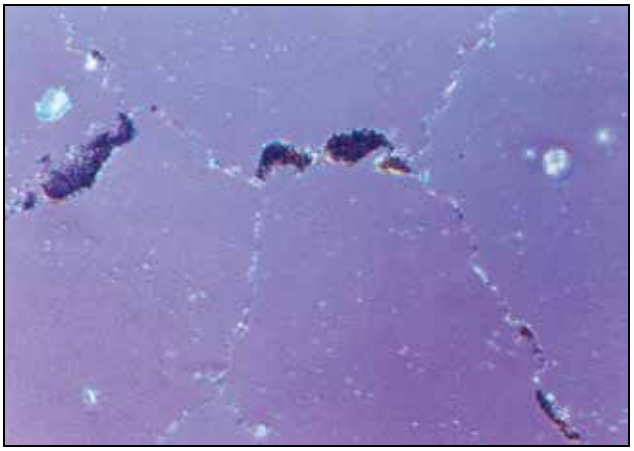

(a) Mg – alloy AZ 91D, the plate middle x 500

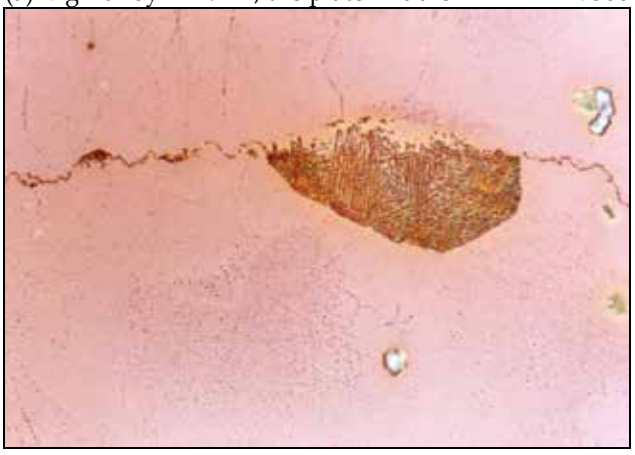

(b) Mg – alloy AZ 63HP, the plate edge, the lamellar precipitate x 500

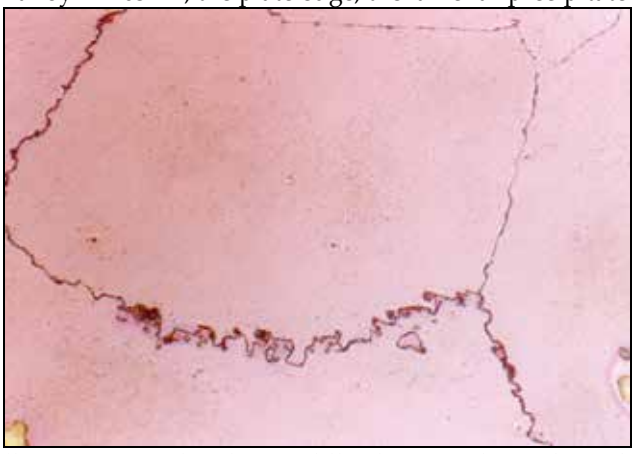

(c) Mg – alloy AZ 63HP, the plate middle, the meandering boundaries x 500

Fig. 12. Details of microstructure of Mg – alloys AZ 91D and AZ 63HP after heat treatment T4, etch. 5 % molybdenum acid, polarized light

taken from the plate was analogical (Fig. 11b, c). The presence of lamellar precipitate was sporadically observed in the specimens taken from the plate middle (Fig. 11b). Detail of the lamellar precipitate is shown in Fig. 12b. There were observed the characteristic meandering grain boundaries of phase δ (grain size 1) with the rest of the precipitate. The presence of lamellar precipitate (Fig. 11c) was not identified in the structure of the specimens taken from the plate edge (grain size 2 - 3). The grain boundaries were markedly meandering and the rest of the lamellar precipitate (Fig. 12c) was observed on the grain boundaries.
Assessment of the individual effects of particular types of precipitate morphologies on the properties of the material is difficult as all of them exist in the same material. Generally these kind of cellular microstructures are considered as detrimental to the toughness of the material. When evaluating the effect of discontinuous precipitation on mechanical properties the nodule size should also be considered. Elimination of this type of precipitation reaction in Mg based alloys would be desirable as it is also claimed to accelerate creep at high temperatures. Furthermore, this would allow for more extensive continuous precipitation leading to better strengthening effect. Coarse γ particles at the grain boundaries are the product of a divorced eutectic reaction from the Al enrich part of the liquid metal that solidifies the last in a casting. The continuous precipitation products in AZ 91 are known to nucleate on dislocations, twin boundaries and interiors. Slower cooling rates increase the amount of discontinuous precipitation (Kaya et al., 2000).

3.2 Experimental fatigue tests of magnesium alloys AZ 91D and AZ 63HP

The testing bars using in experimental works were designed to be in accord with recommendations ((Salama & Lamerand, 1982), (Puškár et al., 1987)) to follow the resonance conditions. Testing bars for the observation of the dependence $\sigma_a = f(N)$ which shape and dimensions are depicted in Fig. 13, were in the middle, the working area softly ground and polished in order to eliminate the surface influence on the fatigue properties. They were made from the specimens taken from the plate edge and plate middle (Fig. 9a) as well as from the block (Fig. 9b). Testing bars for fatigue crack growth observation, Fig. 14, had a flat shape with the ground and polished surface in the working area and in the middle of it was made artificial notch with the diameter 1 mm as a stress concentrator for fatigue crack growth. They were made from specimens taken from the plate middle.

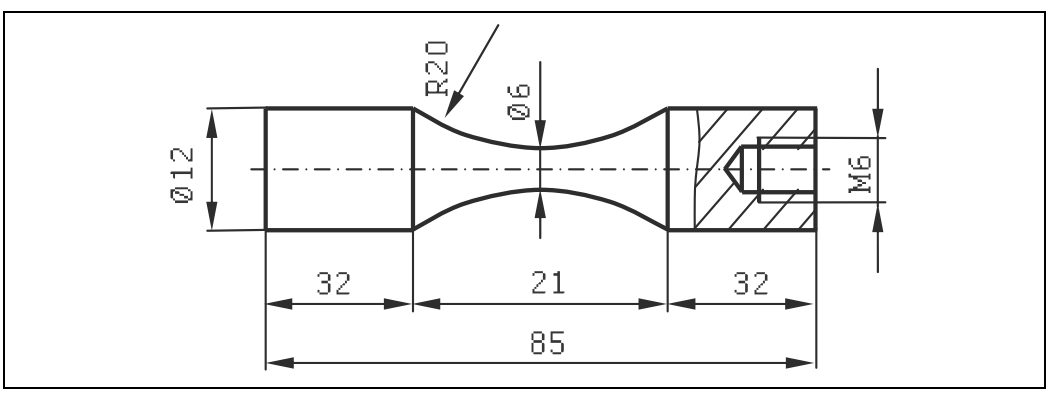

Fig. 13. Shape and dimension of bars using to determination of dependence $\sigma_a = f(N)$, HFCL

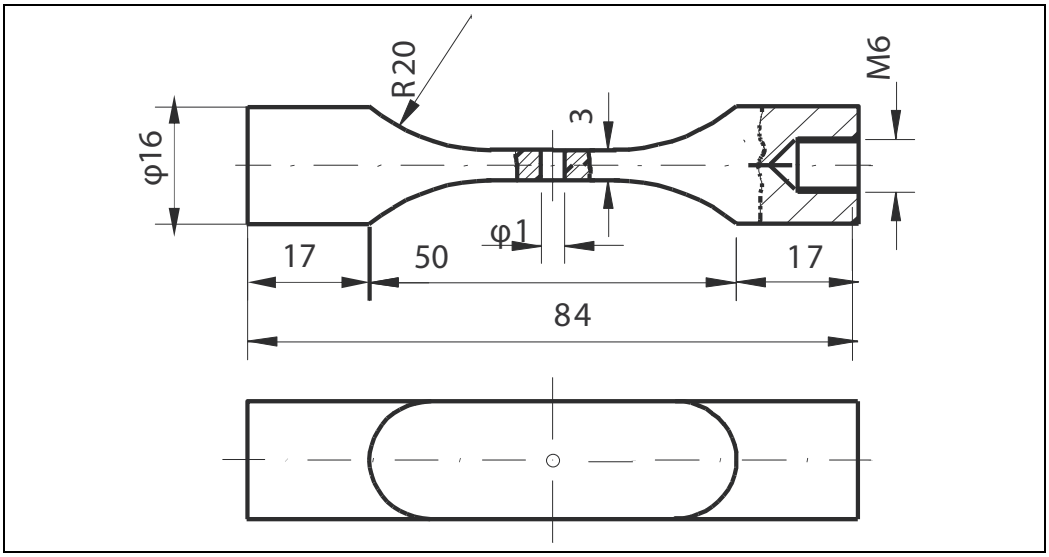

Fig. 14. Shape and dimension of bars using to determination of the dependence $da/dN = f(K_a)$, HFCL

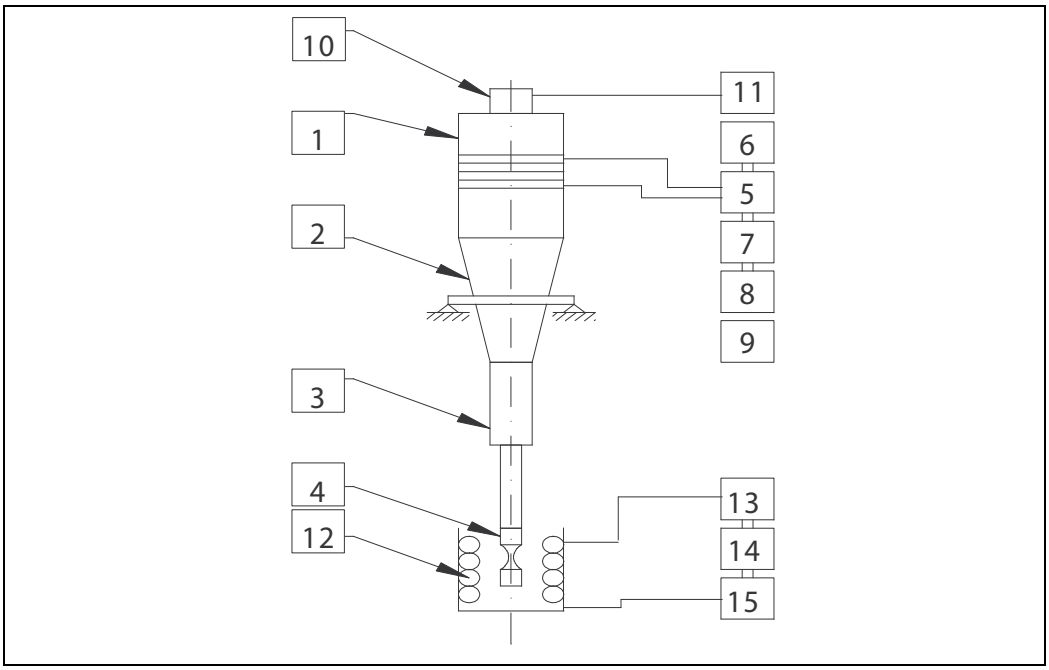

Fig. 15. Schematic device CAFS, HFCL (Puškár, 1997),
(1)- piezoelectric transducer, (2) – conical concentrator, (3) – stepped concentrator, (4) – testing bar, (5) – ultrasonic generator, (6) – automatic frequency balancer, (7) – frequency meter, (8) – printer, (9) – stop watch, (10) – sensor of amplitude displacement, (11) – milivoltmeter, (12) – cooling solution, (13) – thermostat, (14) – water pump, (15) – header.

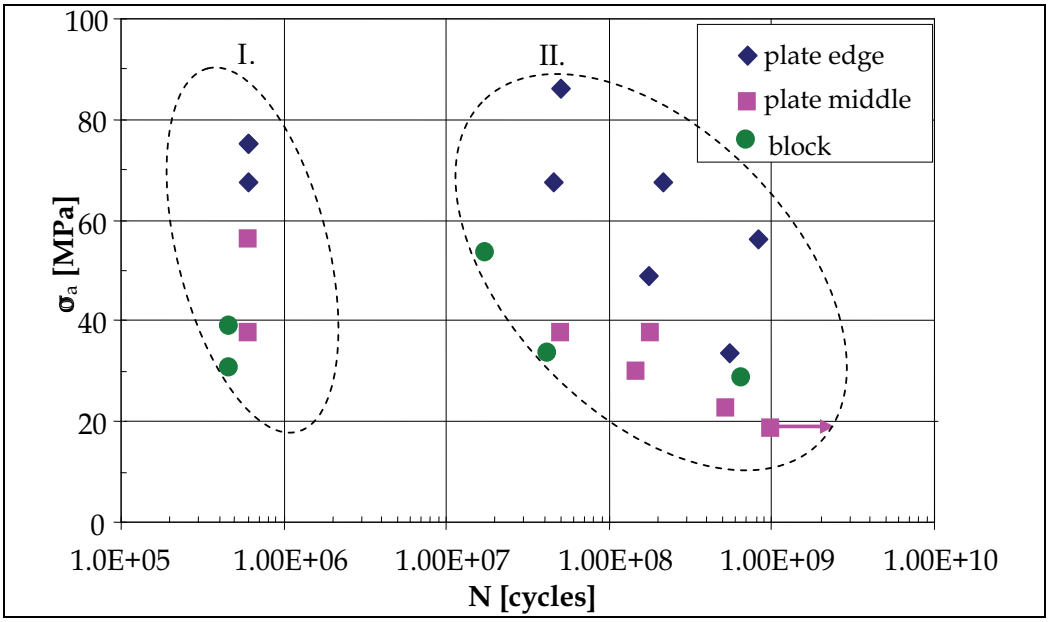

Fig. 16. Experimentally obtained dependences $\sigma_a = f(N)$ for magnesium alloy AZ 91D, HFCL

Fatigue tests were carried out on the experimental device CAFS (Complex Acoustic Fatigue Strength) (Fig. 15) under the high frequency cyclic loading in the very high- cycle regime (N = 1.10^9 cycles) using the high frequency resonance method. Using that method, bars were excited to longitudinal resonance vibrations at ultrasonic frequencies (≈ 20 kHz). That led to sinusoidal cyclic loading with maximum load amplitude in the centre of the bar. The fatigue experiments were performed with constant cyclic loads and no static preload was superimposed, load ratio R = -1. An amplitude control unit guaranteed that the prestated and the actual displacement amplitudes agreed within 99 % during experiments. Because crack growth increased the compliance of the bars and reduced the resonance frequency, control of the loading frequency was necessary. The bars were cycled until they failed or up to N = 1.10^9 cycles if they did not fail (marked by arrow).

Fatigue experiments were performed in ambient air, temperature 20 ± 10°C. During the test the bar was cooling in solution of NaOH.

The obtained results of experimental measurements are depicted in Fig. 16 for magnesium alloy AZ 91D and in Fig. 17 for magnesium alloy AZ 63HP.

Shape of the dependence $\sigma_a = f(N)$ for the testing bars made from the specimens taken from the plate edge was observed in the range N = $6.10^5 \div 1.10^9$ cycles. Bars which did not fail are marked with an arrow. From the Fig. 16, it is obvious that the stress amplitude σ_a decreases with the increasing number of loading cycles within the range. The stress amplitude σ_a is 75 MPa for N = 6.10^5 cycles and σ_a = 56 MPa for N = 8.10^8 cycles. A difference of the stress amplitudes is conceived $\Delta\sigma_a$ = 19 MPa. Similar shape of the dependence is observed for testing bars taken from the plate middle. The decrease of stress amplitude σ_a with the increasing number of cycles-to-failure is evident from the Fig. 16 (σ_a = 56 MPa for N = 6.10^5 cycles, σ_a = 18 MPa for N = 1.10^9 cycles, the difference of the stress amplitudes is $\Delta\sigma_a$ = 38 MPa). Because no bars failed within 1.10^9 cycles at a stress level of 18 MPa, this stress amplitude is defined as a fatigue limit of this material. For this experimental material, Mg –

alloy AZ 91D the considerable scatter of results of number of cycles N at the particular stress levels σ_a is characteristic. The dependence $\sigma_a = f(N)$ for testing bars taken from the block has slightly declining character (nearly parallel to the coordinates of number of cycles). The stress amplitude σ_a is 38 MPa for N = 5.10^5 cycles and σ_a is 30 MPa for N = 7.10^8 cycles. The difference of the stress amplitudes is $\Delta\sigma_a$ = 8 MPa. The results are considerably influenced by the place of bars taking.

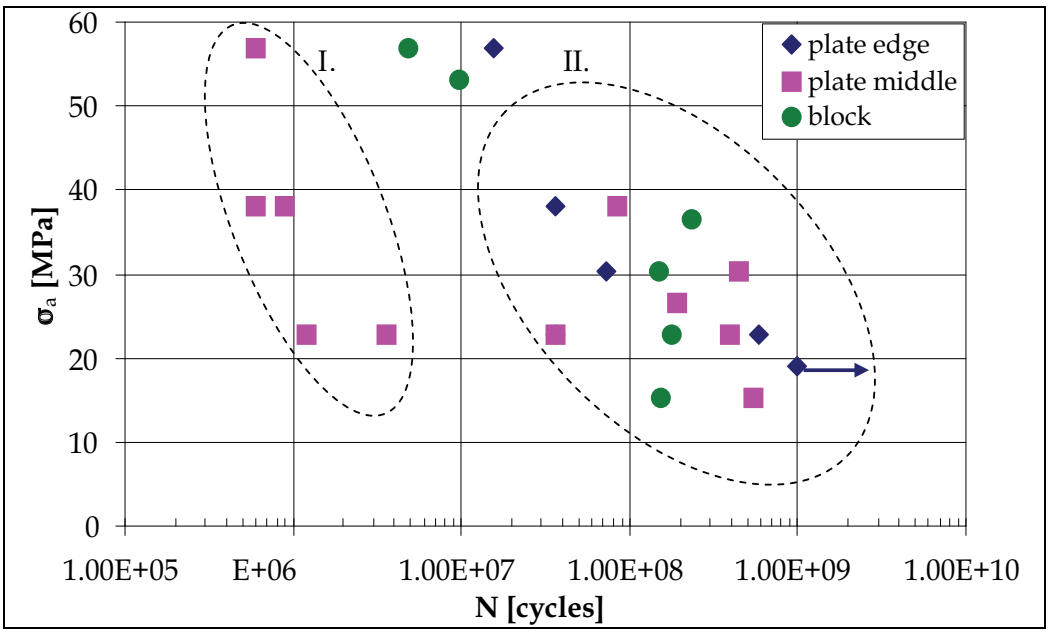

Fig. 17. Experimentally obtained dependences $\sigma_a = f(N)$ for magnesium alloy AZ 63HP, HFCL

The scatter of results of magnesium alloy AZ 63HP (Fig. 17) depended on the place of the bars taking is not as substantial as for the alloy AZ 91D. The shape of the dependence $\sigma_a = f(N)$ for testing bars made from the specimens taken from the plate edge has a decreasing character within the range N = $1.8x10^7$ cycles to N = 1.10^9 cycles. The difference of amplitude $\Delta\sigma_a$ = 39 MPa (σ_a = 57 MPa for N = $1.56x10^7$ cycles and σ_a = 18 MPa for N = $1.\ 10^9$ cycles). The scatter on one stress level is small – one order. After N = 1.10^9 cycles testing bar at the stress level σ_a = 18 MPa did not fail and it is considered as the fatigue limit. Decreasing shape of dependence $\sigma_a = f(N)$ was observed for testing bars made from the specimens taken from the plate middle as well. Decrease of the stress amplitude has slight character (σ_a = 57 MPa for N = 6.10^5 cycles and σ_a = 15 MPa for N = 5.10^8 cycles). The difference of amplitude $\Delta\sigma_a$ = 42 MPa . For the testing bars made from the specimens taken from the block was observed the most considerable decrease within the range N = 4.10^6 to N = 2.10^8 cycles. The difference of amplitude $\Delta\sigma_a$ = 42 MPa (σ_a = 57 MPa for N = 4.10^6 cycles and σ_a = 15 MPa for N = 1.10^8 cycles)

For the magnesium alloys AZ 91D and AZ 63HP, the fatigue crack growth was observed on the testing bars (Fig. 14). The testing bar was initially excited by stress amplitude σ_a, in which the crack started growing. The stress amplitude was decreased gradually unless the crack stopped without failure. Those cycled bars were observed by a light microscope (Fig. 18, 19) and an electron microscope (Fig. 20, 21).

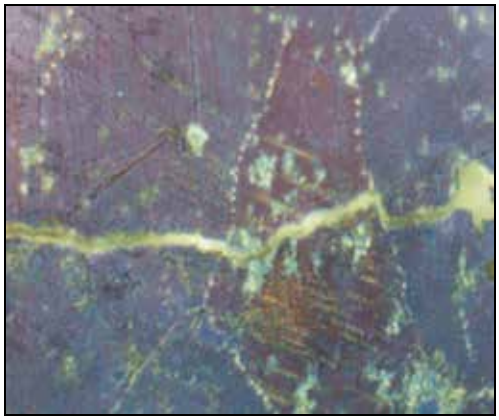

(a) transcrystalline fatigue crack growth x 400

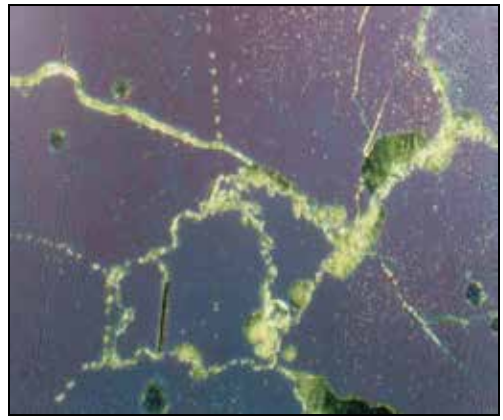

(d) transcrystalline fatigue crack growth through the intermetallic particle x 400

(b) transcrystalline fatigue crack growth along the grain boundaries x 400

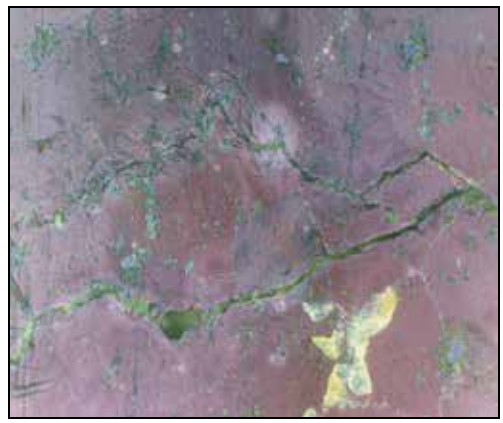

(e) fatigue crack branching x 200

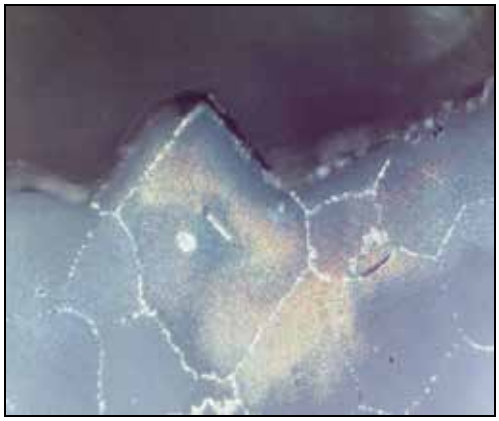

(c) fatigue fracture contour x 200

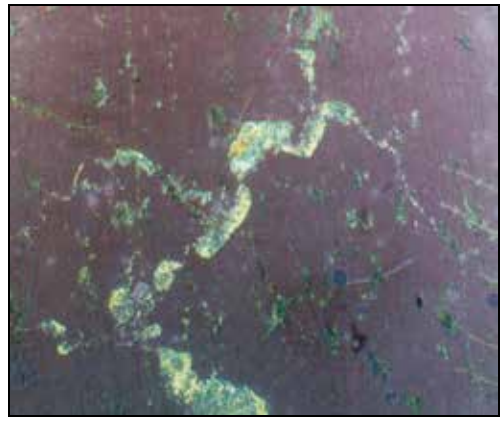

(f) fatigue crack end x 400

Fig. 18. Fatigue crack growth in magnesium alloy AZ 91D, light microscopy

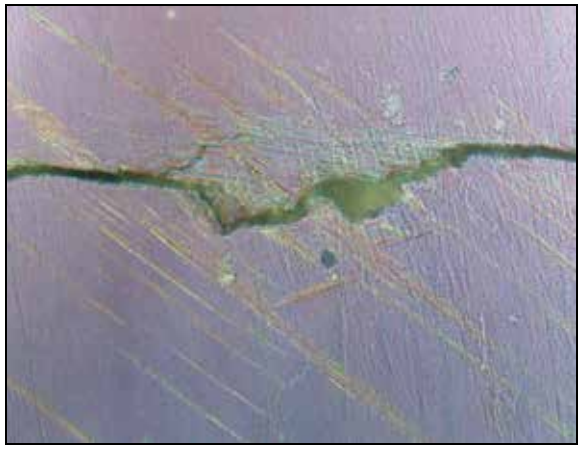

a) transcrystalline fatigue crack growth with the slip bands x 400

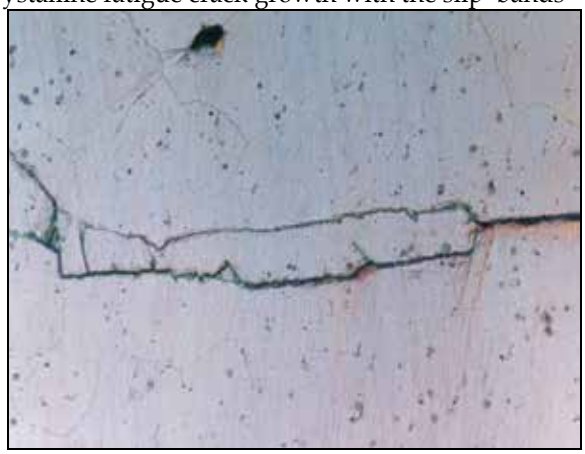

b) fatigue crack branching x 100

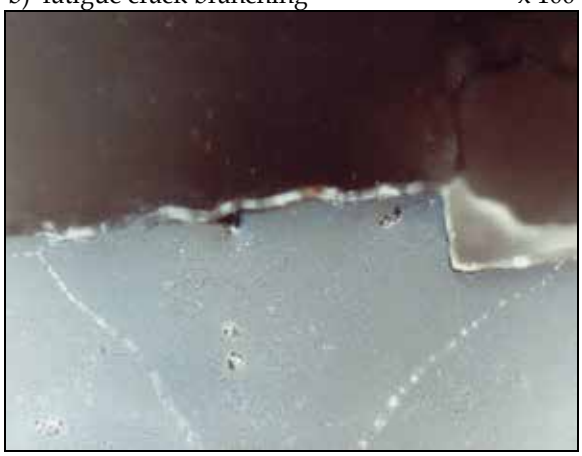

c) fatigue fracture contour x 200

Fig. 19. Fatigue crack growth in magnesium alloy AZ 63HP, light microscopy

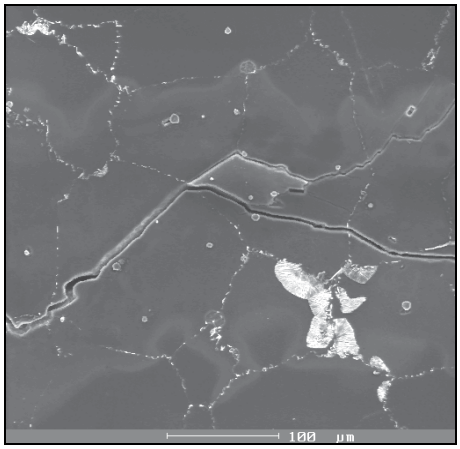

Fig. 20. Fatigue crack growth trajectory in Mg – alloy AZ 91D, S.E.M.

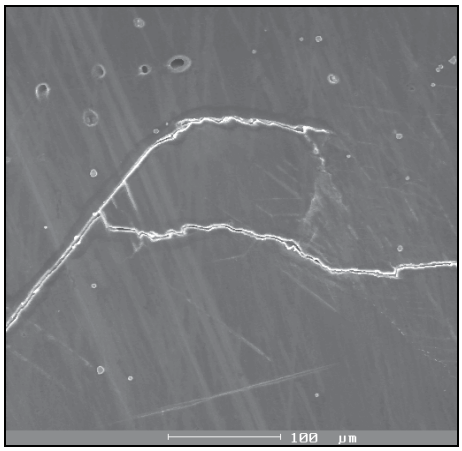

a) fatigue crack branching

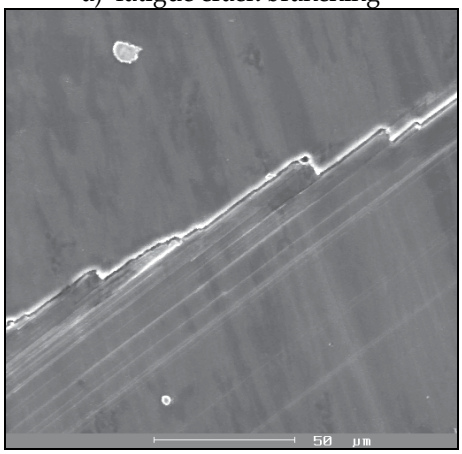

b) steps with slip bands

Fig. 21. Fatigue crack growth trajectory in Mg-alloy AZ 63HP, S.E.M.

The main fatigue crack grew in magnesium alloy AZ 91D transcrystallicaly (Fig. 18a, 19a) despite the lamellar precipitate and rest of lamellar eutectic precipitated on the grain boundaries. At higher value of stress intensity factor K_a the fatigue crack trajectory was less dissected and propagation of fatigue cracks was accompanied by intensive slip what was proved by slip bands in the vicinity of the fatigue crack (Fig. 18a). With gradually decreasing value of stress intensity factor K_a the trajectory of fatigue cracks became more dissected and the propagating crack started to copy their boundaries in their vicinity in some of the grains (Fig. 18b). Sporadically there was observed also intercrystalline crack growth (Fig. 18c, 20) as a consequence of weakening of grain boundaries by precipitate or eutectic. When the fatigue crack grew through the intermetallic particles those particles were damaged by brittle failure and the fatigue crack did not change its direction (Fig. 18d). At near-threshold values of stress intensity factor, there occurred branching of cracks as well as an extensive network of secondary cracks (Fig. 18e). When the fatigue crack reached the threshold value of stress intensity factor K_{ath} the fatigue crack growth was stopped (Fig. 18f). The main fatigue crack in the magnesium alloy AZ 63HP propagated transcrystallicaly and its growth was accompanied by slip with the intensive slip bands in its vicinity (Fig. 19a). At lower value of stress intensity factor K_a, there occurred crack branching (Fig. 19b) and formation of secondary ineffective cracks (Fig. 21a). There were observed the steps (Fig. 19c), during the fatigue crack growth, which presence was accompanied by characteristic slip bands orientated perpendicularly to fatigue crack growth direction (Fig. 21b). The main crack stopped as soon as reached threshold value of stress intensity factor K_{ath}.

The fractographic analysis was performed on the testing bars after fatigue tests. There were observed the fracture surfaces of particular testing bars at low stress levels σ_a in the area of number of cycles $N = 3.6 \times 10^7$ to $N = 6.61 \times 10^8$ cycles. As it was proved by metalographic analysis, final structure was considerably influenced by place of specimen's taking. Variety of structure as well as scatter of results at the same stress levels σ_a was showed during fatigue tests as well as by fractographic analysis.

In magnesium alloy AZ 91D, there were observed testing bars broken at stress level $\sigma_a = 30$ MPa. Number of cycles-to-failure at that stress level was $N = 5.57 \times 10^8$ cycles (testing bar made from specimen taken from the plate edge), $N = 1.8 \times 10^8$ cycles (testing bar made from specimen taken from the plate testing bar made from specimen taken from the plate middle) and $N = 6.61 \times 10^8$ cycles (testing bar made from specimen taken from the block).

Observed testing bars of magnesium alloy AZ 63HP were broken at the stress level $\sigma_a = 22.8$ MPa. Number of cycles-to-failure was for particular bars followed: $N = 3.6 \times 10^7$ cycles (testing bar made from specimen taken from the plate edge), $N = 3.65 \times 10^7$ cycles (testing bar made from specimen taken from the plate middle) and $N = 1.78 \times 10^8$ cycles (testing bar made from specimen taken from the block).

Magnesium alloy AZ 91D was delivered as casting with characteristic casting defects which influenced the fatigue crack initiation, their growth, possibly stop. Amount of casting defects depended on the place of specimen's taking (Fig. 22, 23, 24). The highest amount of casting defects was observed on the specimens taken from the plate middle (Fig. 23), which occurred not only on the surface (Fig. 23a) but also within whole section (Fig. 23b). The casting defects extended to surface of testing bars (Fig. 22a, 23a, 24a) were place of fatigue crack initiation, rarely there were undersurface defects. There were observed not only fatigue failure but also fissile and ductile failure (Fig. 23b) as a consequence of local overload in the proximity of defects. Casting defects occurred very often and sometimes formed large

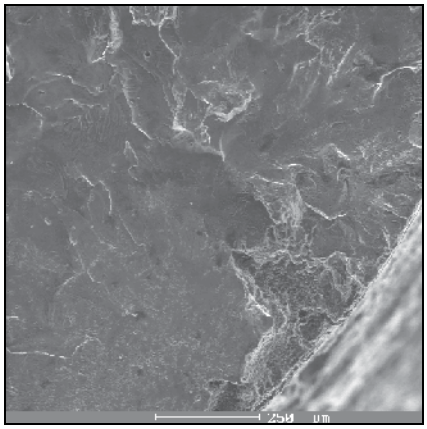

(a) fatigue crack initiation

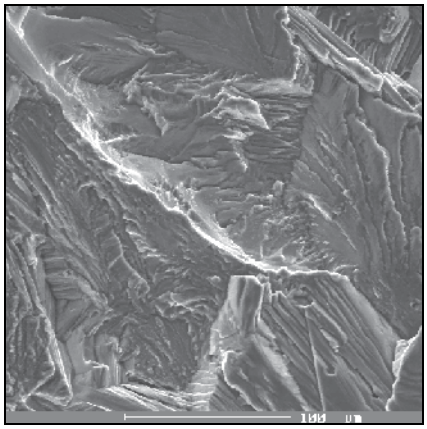

(b) fatigue failure

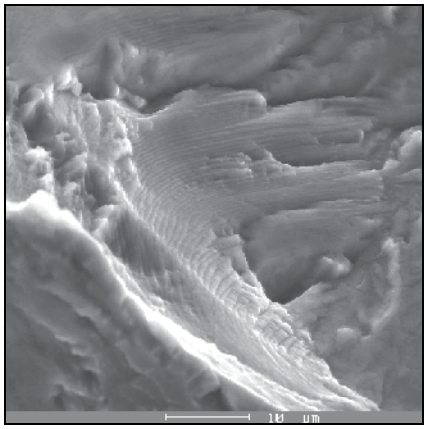

(c) ripples

Fig. 22. Magnesium alloy AZ 91D, the plate edge, S.E.M.

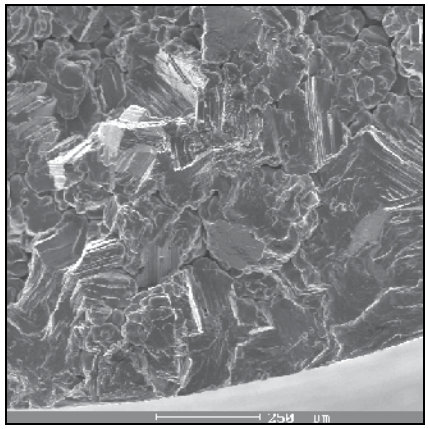

(a) fatigue crack initiation

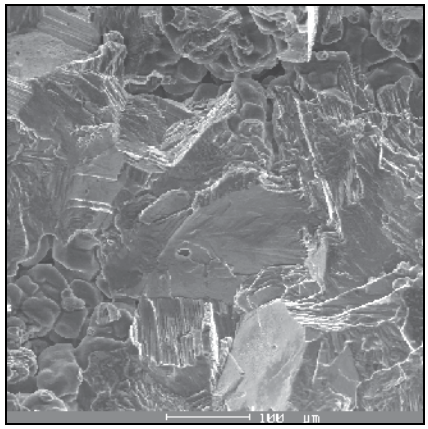

(b) casting defects, mixed mode of failure

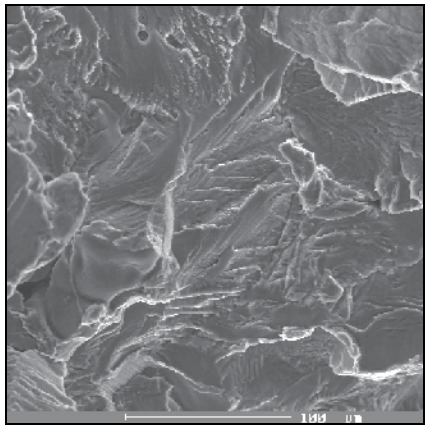

(c) fatigue failure

Fig. 23. Magnesium alloy AZ 91D, the plate middle, S.E.M.

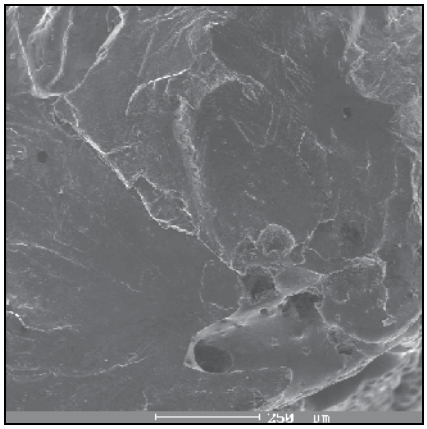

(a) fatigue crack initiation

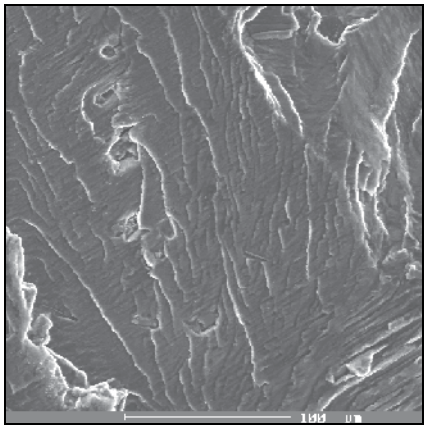

(b) fatigue failure

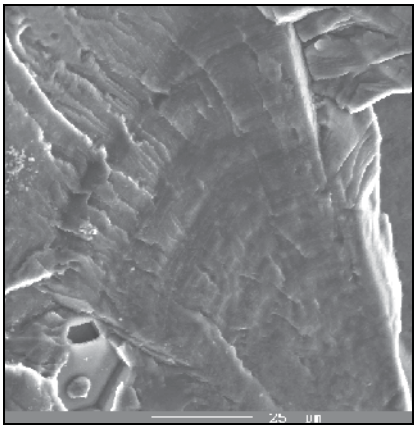

(c) ripples

Fig. 24. Magnesium alloy AZ 91D, block, S.E.M.

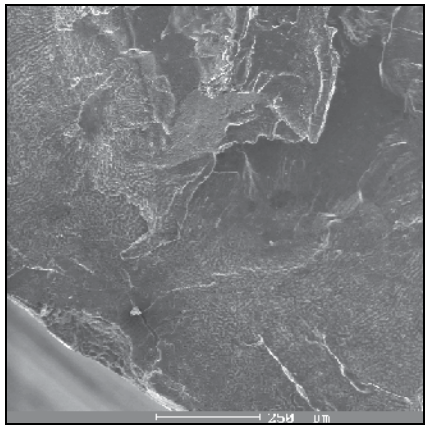

(a) fatigue crack initiation

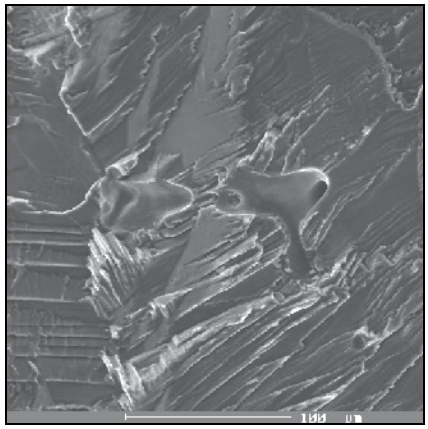

(b) ripples

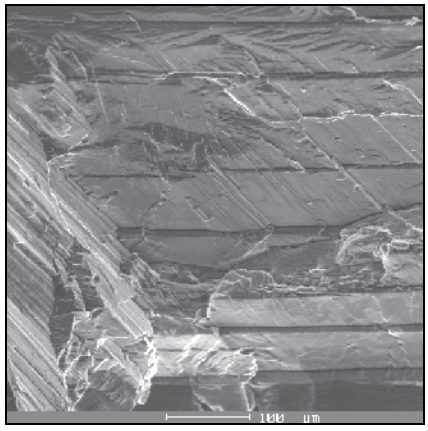

(c) twins

Fig. 25. Magnesium alloy AZ 63HP, the plate edge, S.E.M.

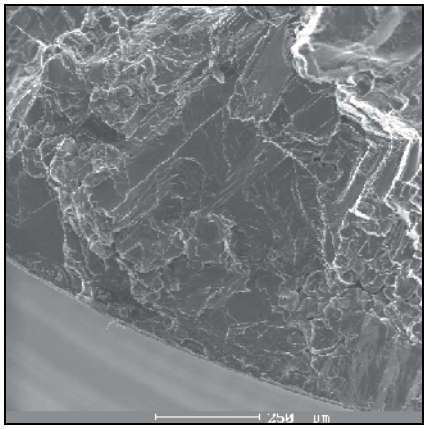

(a) fatigue crack initiation

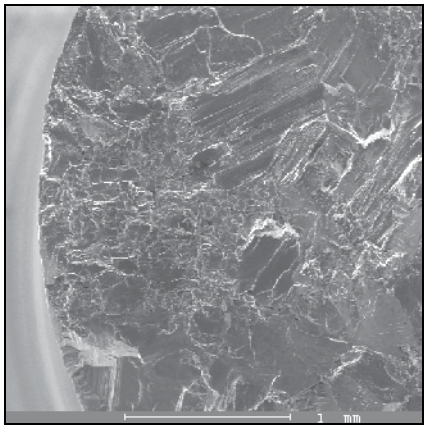

(b) fatigue crack initiation from two places

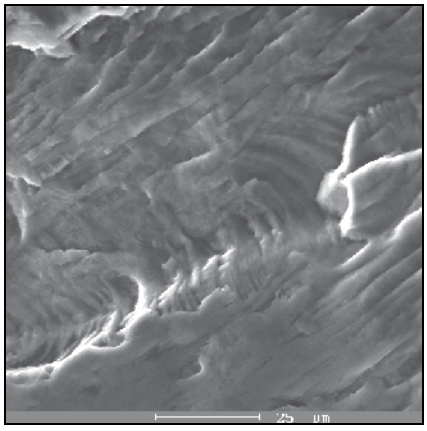

(c) ripples

Fig. 26. Magnesium alloy AZ 63HP, the plate middle, S.E.M.

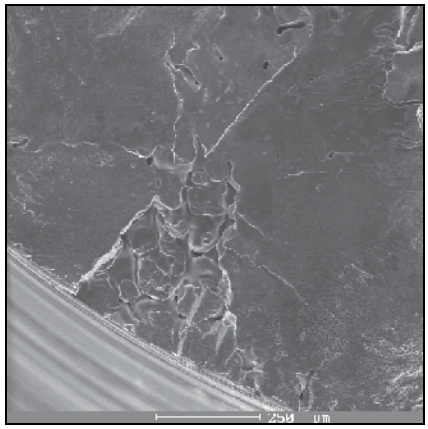

(a) fatigue crack initiation

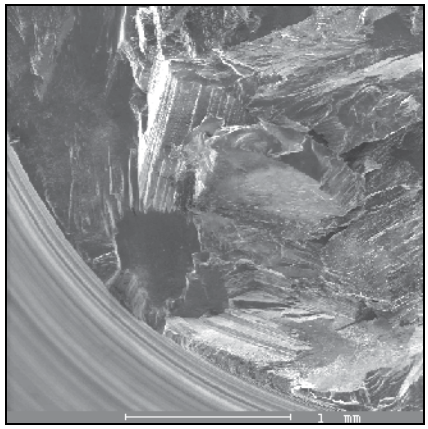

(b) intercrystalline fissile failure

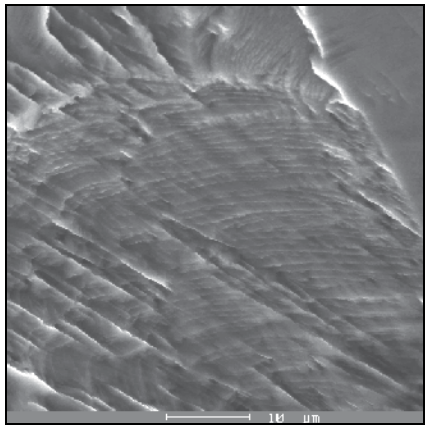

(c) ripples

Fig. 27. Magnesium alloy AZ 63HP, the block, S.E.M.

network. Parts of fracture surfaces which showed fatigue failure (Fig. 22b, 23c, 24b) had mostly transcrystalline character and intercrystalline failure made only negligible part. Despite relief's fracture there were possible to observe the fine ripples (Fig. 22c, 24c). Scatter of results at the same stress level was influenced by character of the structure and presence of casting defects.

Fractographic analysis of fracture surfaces carried out on the testing bars taken from the magnesium alloy AZ 63HP showed that fatigue cracks were initiated from the surface of all testing bars. Amount of voids situated on the surface depended on the place of specimen's taking. Presence of the voids on the specimens taken from the plate edge and the block was rare but on the specimens taken from the plate middle they were observed within whole fracture surface. Casting defects were mostly microscopically small but they served as an initiation place of fatigue cracks (Fig. 25a, 26a, 27a). On the fracture surfaces there were possible to observe fatigue crack initiation from two (Fig. 26b) or more places. Fatigue crack growth had mainly transcrystalline mode and there were visible the fine ripples on the investigated surface (Fig. 25b, 26 c, 27c). Fracture surfaces had generally mixed mode with not only the transcrystalline fatigue failure but also intercrystalline fissile failure (Fig. 25b, 27b). In some cases, fatigue crack stopped in the places of casting defects. On the testing bars taken from the plate edge, there were observed the twins (Fig. 25c) which pointed up during the fatigue crack growth as a consequence of either hexagonal lattice deformation or influence of local weakening of material by network of casting defects.

3.3 Simulation of fatigue crack growth in magnesium alloy AZ 91D

Fatigue crack growth in magnesium alloy AZ 91D was simulated using finite-element software ADINA (Automatic Dynamic Nonlinear Analysis) which is suitable for solving large variety of problems. Reliability of modeling is in greater rate supplied by the accuracy in material properties, boundary conditions and last but not least in modeling of proper material behavior at crack tip including singularity if zero radius is presented. Linear and nonlinear fracture mechanics analysis can be performed with ADINA system including computation of conservation criteria (J-integral, energy release rate) in 2D and 3D finite element models. Two different numerical methods are available for the computation of the conservation criteria – the line contour method and the virtual crack extension method. The fracture mechanics allows performing an analysis with only one crack however. The crack line or surface can be located on the boundary or inside of the finite element model.

ADINA is thus fully capable of solving fracture mechanics problems in general with large amount of options in stack under various loading conditions or thermal conditions utilizing wide variety of material models. Also there is the ability to model rupture criteria and thus it is possible to model material damage caused by cavities or impurities and its progression under cyclic load.

The microstructure of the material represented by tightly packed grains was modeled by using the finite-element software ADINA. The geometry of each grain was modeled by Pro/Engineer software and was exported as a plain surface in IGES file to ADINA, where a 2D dynamic analysis was performed. For the analysis each surface representing individual grain of the microstructure was discretized using finite element mesh. In this case quadratic elements were used, which means that unknown quantities were approximated by a polynomial of second order inside of each element. Due to large gradients in secondary fields, it is necessary to use very fine discretisation in the vicinity of the crack to achieve reasonable accuracy. The only factor limiting the fineness of the mesh is of course available

hardware, but for extremely fine mesh a lower numerical stability can be expected. Multi-linear plastic material model was used in the simulation. The properties of the alloy were obtained experimentally as a dependence of displacement of the specimen on the applied force. Afterward the stress-strain curve was imported into ADINA and allocates each element. The analysis was performed by using large deformations and large displacements incorporated into the mathematical model.

Each grain was considered as a standalone body and contact conditions between each pair of grains were implemented. In the microstructure model a stress concentrator was made (Fig. 28). Issue of damage propagation of materials in the microstructure is considerable demanding for the exact model. It is because of some effects are manifested in the atomic structure and they can be described by the continuum mechanics only by certain optimal conditions or on the base of experimental measures, eventually by other specific numerical methods. Because of this, the mesh in the vicinity of the stress concentrator has to be very fine (Fig. 29). On the boundaries was applied a cyclic load with amplitude 30 MPa and with frequency 25 Hz in a pull-push fashion.

The load amplitude by which the propagation of micro-failure occurs is fully dependent on non-homogeneity of the material. A redistribution of stress was influenced by the cyclic nature of the applied load. Even though the stress is applied in uniform manner on the structure, it does not act in the same way on each grain in the structure. Most of the stresses are cumulated in the region with certain non-homogeneity in the microstructure. In this case an artificially created cavity acts as a concentrator. The propagation of material damage was governed similarly to crack propagation, where a plastic zone (Fig. 30) is created in the vicinity of the crack tip in which a plastic strain is accumulated due to cyclic loading.

The deformation process at the crack tip depends significantly on the mechanical properties of the material and on the environment in which the loading occurs. All, limited plastic deformation, equal values of intensity factor and equal coefficients of asymmetry of the

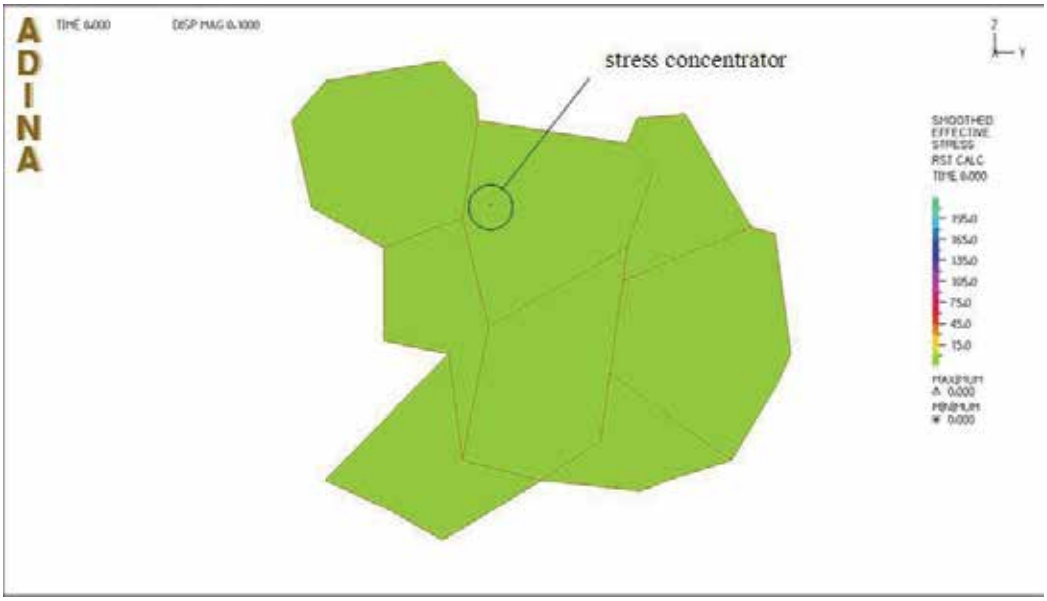

Fig. 28. Model of the microstructure with artificial notch before load

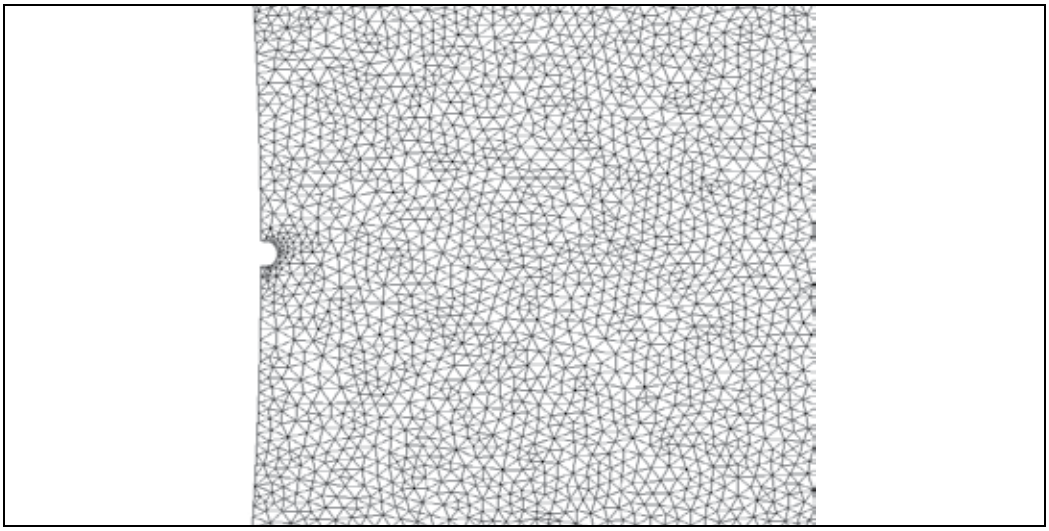

Fig. 29. Mesh in the surrounding of the stress concentrator

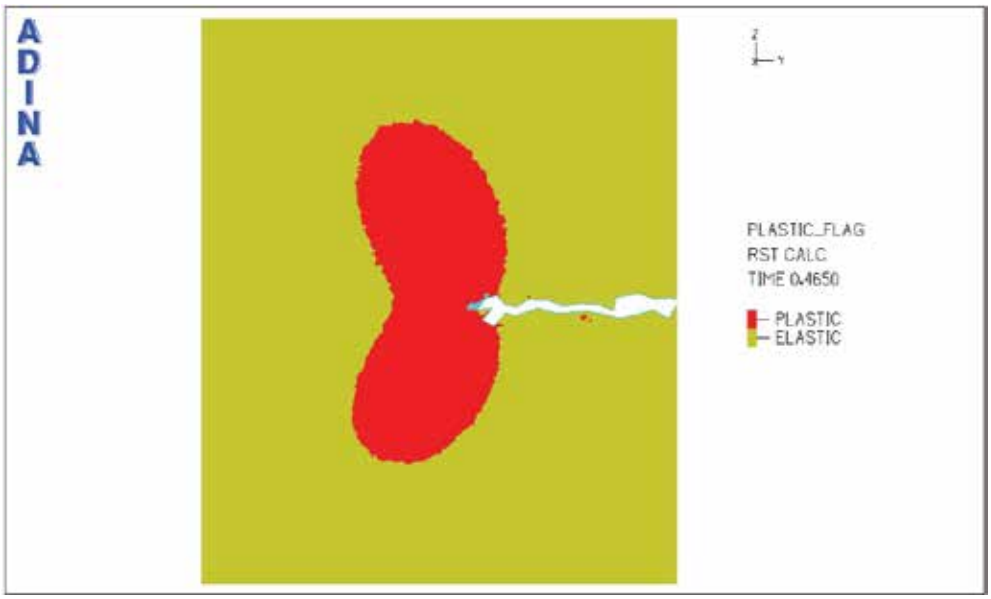

Fig. 30. Plastic zone at the crack tip

cycle do not guarantee the same magnitude and form of plastic zone ahead of the crack tip. Once the critical value of the plastic strain is reached in the vicinity of the crack tip, a material damage occurs and the crack propagates (Fig. 31). The crack propagation occurs in the direction of maximal shear stress and its direction gradually changes into direction perpendicular to the direction of applied load. The orientation of main stresses inside of each grain is changing depending on the orientation of the grains, on their shape and on the spread of the damage. The crack acts upon this by changing the direction on the grain boundaries, but due to the damage in the grain can do so even inside of the grain.

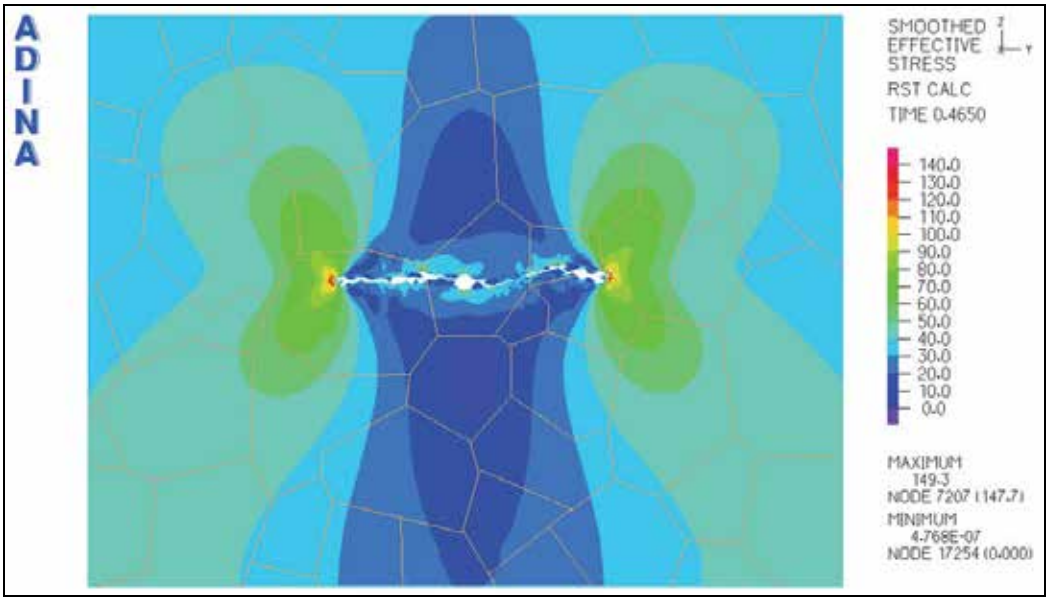

Fig. 31. Fatigue crack growth in magnesium alloy AZ 91D by ADINA

4. Discussion

The results of fatigue test carried out in magnesium alloys AZ 91D and AZ 63HP under high frequency cyclic loading as well as simulation of fatigue crack growth in Mg – alloy AZ 91D are comparable to results of authors mentioned in this chapter.

The initial stage of fatigue is so-called crack-free stage, where the dislocation density increases and different dislocation structures may be generated by micro-plastic deformation. Interactions between dislocations and other structural constituents influence the macroscopic properties (e.g. hardening, softening). This cyclic behaviour during the crack-free stage strongly depends on the initial microstructure and therefore the different magnesium alloy systems and their heat treatments have to be considered to evaluate the cyclic behaviour during fatigue. At first, cyclic hardening was observed in pure magnesium. This effect was also found in some magnesium alloys, which are mainly based on the Mg-Al or Mg-Li systems. The attention is drawn to different heat treatment and their microstructures. In the as-cast (F) and dissolving annealing (T4) usually cyclic hardening occurs, which can be generally attributed to the increase of dislocation density during microplastic deformation. On the contrary, age-hardened alloys show a non-uniform behaviour: the cyclic loading can either lead to hardening or softening, depending on the type of the precipitates. Age-hardened magnesium alloys based on the Mg-RE or Mg-Zn system tend to show cyclic softening due to the presence of coherent precipitates. These precipitates can easily been cut by dislocations, therefore reducing the size of the precipitates, leading to cyclic softening. In contrary, age-hardened magnesium alloys based on the Mg-Al system form incoherent precipitates, which are difficult to cut by dislocations and therefore stable during cyclic loading. Owing to the fact that these precipitates are not efficient to pin dislocations, the cyclic hardening effect of the Mg-Al based alloys seems to be mainly based on the increment of dislocation density. This cyclic hardening effect happens

within approximately the first 10 000 cycles. A generalization of the cyclic behaviour of magnesium alloys is not possible due to the differences in microstructure of the alloy systems and their heat treatment (Potzies & Kainer, 2004).

Like in the other metals, fatigue cracks in magnesium alloys also initiate at slip bands developed by cyclic micro-plastic deformation. The deformation modes of hexagonal structures are rather complex compared to the cubic system. Due to the hexagonal structure of magnesium, dislocation movement at room temperature predominantly occurs in basal slip (0001) planes in the <1120> directions, while pyramidal slip in {1011} <1120> and prismatic slip in {1010} <1120> is more favourable at higher temperatures. An alternative non-basal deformation mode in hcp structures is the twinning in {1012}, {1011}, {1122} and {1121} – planes, where {1012}-twinning is the most common in magnesium. Twinning is an important deformation mechanism in (uniaxial) monotonic deformation but also concerning cyclic micro-plastic deformation during fatigue.

The appearance of fatigue slip bands is only noticed in defect-free material, and despite their good castability, magnesium alloys tend to contain casting defects. The formation of casting defects often depends on the solidification morphology, which in the case of magnesium alloys is mainly endogenously, due to the large solidification range. The large solidification range of most magnesium alloys leads to a formation of microshrinkage, which is additionally favoured by the dendritic grain structure. Another reason for the formation of casting defects may lie in the processing route of the high pressure die casting, which is primarily used for many magnesium alloys. Due to the high casting speeds, the melt flow as non-lamilar and air can be entrapped causing porosity when the melt solidifies. As a consequence, high stress concentrations at casting defects initiate fatigue cracks instead of the afore-mentioned fatigue slip bands. In the presence of casting defects like pores or microshrinkage the crack initiation stage can be reduced to a negligible extent, reducing the lifetime of the component altogether. On the other hand, in defect free material the crack initiation stage - especially at lower stresses - is significantly greater than the crack propagation stage and can be up to 90 % of the total fatigue life. An additional important factor which has to be considered for crack initiation is the condition of the surface and edge layer of the specimens. As already well known, as-cast material usually tends to show higher fatigue lives than machined specimens due to the fine grain edge layer which is removed during the machining.

As it is depicted in Fig. 15 and 16, there are observed two areas of investigated results (area I and II) dependent on number of cycles. There are considered different micromechanisms of failure, surface fatigue crack initiation and undersurface fatigue crack initiation (Mayer, 1998). Fatigue crack initiation in the gigacycle regime seems to occur essentially inside the bars and not at the surface as is observed for shorter lives. So we can model three types of crack initiation in a cylindrical bar with a polished surface depending on whether it is low-cycle (1.10^4 cycles), megacycle (1.10^6 cycles) or gigacycle (1.10^9 cycles) fatigue. For the smallest number of cycles to rupture, the crack initiation sites are multiple and on the surface, while at 1.10^6 cycles, there is only one initiation site, but, for the higher numbers of cycles-to-failure, the initiation is located at an internal zone. An explanation of this phenomenon is that cyclic plastic deformation in the plane stress condition becomes very small in the gigacycle regime. In this case, internal defects or large grain size play a role, in competition with surface damage. The effect of environment is quite small in the gigacycle regime as the initiation of short cracks is inside the bars. The surface plays a minor role

especially if it is smooth. Inclusion can be active crack initiation sites, especially if the load ratio is high. The porosities can initiate a crack in competition with inclusions, especially when the load ratio is low, particularly in pull-push (Bathias, 1999). Another explanation of fatigue crack initiation in gigacycle regime is by stress concentration between two or more grains where a long grain boundary is located perpendicular to the pull stress and therefore it works as an internal notch.

After the crack initiation, the short crack usually advance in an angle of 45°to the load and are strongly influenced by the microstructure, e.g. grain boundaries, and the orientation of the basal (0001) slip bands. During propagation the cracks grow and change their orientation, being perpendicular to the load. The fatigue crack propagation can be either trans- or intercrystalline. In the as-cast (F) of AZ 91, for example, the brittle intermetallic $Al_{12}Mg_{17}$ at the grain boundaries favours interdendritic cracking. Additionally, high crack tip driving forces tend to promote crack propagation through the $Al_{12}Mg_{17}$ phase, while lower loads assist crack propagation through the primary alpha-Mg grains. The crack growth is additionally assisted by the connection of different microcracks or – especially in material with casting defects – cracks, which developed between pores or microshinkage (Potzies & Kainer, 2004).

Concerning the crack propagation rate, magnesium and its alloys in general, show a very low fracture toughness, which therefore promotes a higher crack propagation rate than in other light metal. Furthermore, the crack propagation rate strongly depends on the individual microstructure (type of alloy, heat treatment) and the micro structural constituents, e.g. precipitates. In age-hardened (T6) ternary Mg-Li based alloy and Mg-Nd and Mg-Zn based alloys the precipitates formed can cause a decelerating effect on the crack propagation, while in the age-hardened (T6) and as-cast (F) magnesium alloy AZ 91 the $Al_{12}Mg_{17}$ intermetallic, rather increases the crack propagation rate. To improve the fatigue crack propagation resistance of the Mg-Al based alloys, additional elements can be used to form intermetallics with higher fracture toughness. Yttrium and neodymium added to AZ 91 are found to show a beneficial effect on the fracture toughness, leading to the reduction in the fatigue crack propagation rate. Beside, different mechanical surface treatments (e.g. shot-peening, deep-rolling) can be used to modify the edge layer. The increased near-surface dislocation density and the implemented compressive residual stresses significantly reduce the crack propagation rate, increasing the fatigue lives although the crack initiation is accelerated due to the increased surface roughness (Potzies & Kainer, 2004).

Fatigue crack propagation of long cracks is customarily divided in three regimes. Regime A or near-threshold is of great practical importance and it is characterized by complex testing procedures and by the influence of many experimental and material factors. Regime B or Paris's regime has been extensively studied becauasae of its usefulness for the damage tolerant approach to the fatigue design of aerospace structure (Kelemen, 2004). Regime C characterizes the rapid crack extension to final fracture. The main characteristics that differentiate Regime A and B are extension to final fracture. The near-tip plasticity and its relationship with a typical material microstructural feature, such aas the average grain size, can be used to discriminate between regimes A and B. The near-threshold regime in metals is generally associated with a crack tip plasticity largely confined to select crystallographic planes with a reversed-shear mode of growth. Crack deflections due to mmicrostructural heterogeneity can lead to mixed-mode displacements on the microscopic level and a faced fracture surface. These displacements cause mismatch between upper and lower crack faces

which in turn results in a positive closure load. Here attention is devoted to the roughness-induced crack closure (RICC) because it is strongly influenced by the material microstructure and it is associated to a zigzag crack pattern. RICC is promoted by: a) low stress intensity factor levels where the plastic zone is smaller than the average grain diameter, b) small crack opening displacements (e.g. low ΔK and low R-ratios) of a size comparable to surface asperities, c) coarse grained microstructures, d) periodic deflections of the crack due to grain boundaries, second-phase particles and composite reinforcement, e) enhanced slip irreversibility. Fatigue crack paths in a coarse-grained material become complicated even at relatively high stress intensities. The resulting crack tortuosity involves several mechanisms and tends to reduce the effective stress intensity range, ΔK_{eff}, below the nominal applied range, ΔK.

RICC limits the minimum stress intensity, hook or ´lock-up´ mechanisms limit the maximum stress intensity and branching produces true elastic shielding. Tortuosity also increases the ratio of the true length to that projected on the plane of the stress axis reducing the energy release rate. The crack path is a result of a series of mechanisms associated with different stages of fatigue crack growth. When the plastic zone extends over a number of grains due to a high ΔK or to a fine-grained material, quasi continuum mechanisms are operative. A rectilinear Mode I crack path, also termed a Stage II fatigue crack, occurs during fatigue crack propagation of long cracks. A dual- slip system is active at the crack tip, and the crack growth process involves simultaneous or alternating flow along this slip system.

When crack growth rates are reduced toward threshold conditions specific features can be observed. A stage I crack growth, occurring predominantly by single shear in the direction of the primary slip system, can develop because the plastic zone becomes smaller of the average grain size. Crack propagation is characterized by crack deflection from grain to grain (Nicoletto et al., 2003).

The corrosion fatigue has been tested in different aqueous solutions, but most investigations have been performed with sodium chloride solutions. Generally, the influence of corrosion fatigue shows a significant reduction in fatigue life of magnesium components with different impacts depending on the selected solutions. In the presence of aqueous solutions the fatigue crack initiation, which is more influenced by the corrosive environment than the crack propagation, often starts at cracked regions in the corrosion layer, which mainly consists of magnesium hydroxide. Due to the lower specific volume of magnesium hydroxide compared to the magnesium substrate, the layer fractures easily and corrosion can continue within the voids. These voids can act as additional initiation sites for fatigue failure. To avoid degradation of the surface, special surface treatments or coatings are therefore advisable. Anodizing, chromating or sealing with epoxy resins are possible surface treatments to form protective layers. Additionally, fatigue cracks can also initiate at corrosion pits developed by local galvanic corrosion at precipitates or impurities. These corrosion pits become more effective in high cycle fatigue regimes with low load amplitudes. To avoid local galvanic corrosion, usually high purity alloys (HP) are used. Besides corrosion induced damage of the surface, casting defects, like ores or microshrinkage are very effective origins for fatigue cracks. Despite the additional corrosive attack at these casting defects, the fatigue life is not further reduced compared to the fatigue life in air.

Besides corrosion, elevated temperatures are another critical environment for magnesium alloys and lead to lower mechanical properties already of 120°C and above. The results show a significantly decreasing fatigue life with increasing temperature, due to greater plastic strain amplitudes, which promotes the initiation of fatigue cracks (Potzies & Kainer, 2004).

5. Conclusion

Magnesium alloys show a high specific strength and are therefore increasingly used for light-weight constructions in automobile industry. Any moving causes vibrations leading to cyclic loading in the components. To predict the behaviour of the material under the influence of cyclic loading it is vital to understand the fatigue behaviour of magnesium alloys.
The technique of ultrasonic fatigue is especially appropriate to perform fatigue experiments in very high-cycle regime of 1.10^9 and more within reasonable testing times, whereas extremely long testing times (months or years) would be needed with all other conventional testing equipment.
To improve the fatigue behaviour of magnesium alloys, two different main approaches are possible: surface modification to improve the fatigue resistance (mechanical surface treatment) and /or corrosion resistance (coating), improvement of the bulk material to decelerate crack initiation (avoid casting defects) or to reduce the crack propagation rate (increase fracture toughness).
The first approach can be realized by techniques of mechanical surface hardening treatments, which improve the fatigue resistance by introducing compressive residual stresses into the surface layer. The compressive residual stress and the increment of surface hardness decelerate the process of fatigue crack initiation by reducing the dislocation movement. By using roller burnishing even the corrosion fatigue resistance can be improved.
Another possibility to decelerate the fatigue crack initiation, especially when the magnesium components are exposed to a corrosive media, is the use of surface coatings. These coatings reduce the corrosive attack and therefore the formation of corrosive induced cracks and corrosion pits, which often act as fatigue crack initiation sites.
Considering the second approach by improving the bulk material, the focus should be set on reducing the casting defects by using new or optimized casting techniques. Advanced or new processes, like vacuum pressure die casting or semi-solid processing respectively, enable a reduction of porosity in cast components, increasing the fatigue life. Reducing the porosity, additionally decreases the scatter and therefore improving the reliability.
Besides reducing casting defects, adding certain alloying elements to increase the fracture toughness is a further option to improve the fatigue behaviour of magnesium alloys. Yttrium and neodymium have been found to increase the fracture toughness of AZ 91 and reduce the crack propagation rate. Though a possible option, this effect is less pronounced, compared to minimizing the porosity.
Depending on the demand of certain mechanical properties and the exposure to detrimental environments, several opportunities are available to improve the fatigue behaviour and increase the fatigue life of magnesium alloys (Potzies & Kainer, 2004).
To apply the full potential of weight reduction by using magnesium alloys, especially in transportation applications, further investigations are still necessary to fully understand the fatigue behaviour of magnesium alloys and to transfer the knowledge for further alloy development and component design.

6. References

Avedesian, M. M. (1999). *ASM Specialty Handbook, Magnesium and Magnesium Alloys*, Michael Avedesian and Hugh Baker, ISBN 0871706571

Bathias, C. (1999) There is no infinite fatigue life in metallic materials, *Fatigue Fract Engng Mater Struct,* Vol. 22, No. 7, (July 1999), pp. 559-565, ISSN 8756-758X

Bursk, R.S.(1987). *Magnesium Products Design*, Marcel Dekker, New York.

Cllaper, R. B. & Watz, J. A. (1956). Determination of Fatigue Crack Initiation and Propagation in a Magnesium Alloys, In: *ASTM STP 196*, 1956, p. 111

Goodenberger, D. (1990). *Fatigue and Fracture Behavior of AZ91E – T6 Sand Cast Alloy*. Masters's thesis, The University of Iowa

Ishikawa K.; Kobayashi, Y. & Ito, T. (1995). Characteristics of Fatigue Crack Propagation in Heat Treatable Die Cast Magnesium Alloy. *Proccedingsof 124th TMS Annual Meeting*, pp. 449-460, Las Vegas, 1995,USA

Ishikawa, K.; Kobayashi, Z.; Kaneko, T. & Shibusawa, T. (1997). Precipitated Structures and Mechanical Properties of AZ 91D Magnesium Alloy. *Nippon Kinzoku Gakaishi - Journal of the Japan Institute of Metals*, Vol. 61, No. 10, (June, 1997) 1031-1036, ISSN 0021-4876

Ishikawa, K.; Kobayashi, Y. & Kentarou, K. (2001) Abstract Endurance Limit and Fatigue Crack Propagation of Magnesium Alloys, *Proceedings of Fatigue in the Very High Cycle Regime*. pp. 199-205, Wiena, June 2001, Austria

Kaya, A.A. ; Uzan, P. ; Eliezer, D. & Aghion, E. (2000). Electron microscopical investigation of as cast AZ 91D alloy. *Materials Science and Technology*, Vol. 16, No. 9 (September 2000) 1001-1006, ISSN 0267-0836

Kelemen, M. (2004) Ground Search and Rescue Service, *Proceedings of Aerospace medicine and 1st Annual Intern. Forum on Disaster Medicine,* pp. 38, Košice, June 2004, Košice

Laird, C. & Charsley, P. (1982) Strain Rate Sensitivity Effects in Cyclic Deformation and Fatigue Fracture. *Proceedings of Ultrasonic Fatigue*, Champion; Pa ; October 1981. pp. 187-205

Lynch, S. P. (1998) Environmentally Asisted Cracking: Overwiev of Evidence for an Adsorption – Induced Localised – Slip Process. *Acta Met.*, Vol. 36, No. 10, (October 1988) 2639 –2661, ISSN 1359-6454

Makar, G. L.; Kruger, J. & Sieradzki, K. (1993) Stress Corrosion Cracking of Rapidly Solidified Magnesium – Aluminium Alloys. *Corrosion Sci.*, Vol. 34, No. 8 (August 1993), 1311-1323, ISSN 0010-938X

Mayer H.; Rösch, R.; Lipowsky, H.; Zettl, B.; Papakyriacou, M. & Stanzl-Tschegg, S.E. (1997). Fatigue Properties of High Pressure die Cast Magnesium Alloys, *Proceedings of Magnesium 97*, pp. 145 – 150, Dead Sea, June 1997, Israel

Mayer, H. (1998) Application of Ultrasonic Frequencies in Fatigue. *Kovové materially-Metallic Materials*, Vol. 36, No. 3, (1998), 213-219 , ISSN 0023-432X

Mayer, H. ; Lipowsky, H. ; Papakyriacou, M.; Rosch, R.; Stich, A. & Stanzl–Tschegg, S. (1999) Applications of Ultrasound for Fatigue Testing of Lightweight Alloys, *Fatigue Fract.Engng. Mater.Struct.*, Vol. 22, No. 7, (July 1999) 591-599, ISSN 8756-758X

Nečas, P. & Kelemen, M. (2010). *War on insecurity: calling for effective strategy!,* The centre of educational literature, ISBN 978-611-01-0023-6, Kiev

Nicoletto, G.; Konečná, R. & Pirondi, A. (2003) Fatigue Crack Paths in Coarse – grained Magnesium. *Proceedings of Fatigue Crack Paths*. Pp. 1-8, Parma, September 2003, Italy

Papakyriacou, M. ; Mayer, H. ; Pypen, C. ; Jr H.P. & Stanzl-Tschegg, S.E.(2001) Influence of Loading Frequency on High – Cycle Fatigue Properties of b.c.c. and h.c.p. Metals, *Material Sci. Eng*. A,Vol. 308, No. 1-2, (June 2001) 143-152, ISSN 0921-5093

Potzies, C. & Kainer, K.U. (2004) Fatigue of Magnesium Alloys. *Advanced Engineering Materials*, Vol. 6, No. 5, (May 2004) 281-289, ISSN 1438-1656

Puškár, A.; Bokůvka, O.; Palček, P. & Meško J. (1987) Inštrumentalizácia a metodiky únavových skúšok pri ultrazvukovej frekvencii zaťažovania, *Strojírenství*, Vol. 37, No. 9, 1987, 507-513

Salama, K. & Lamerand, R.K. (1982) Ultrasonic Fatigue, *Met. Society*, AIME, New York,

Sander, M. & Richard, H.A. (2006). Fatigue crack growth under variable amplitude loading Part II : analytical and numerical investigations. *Fatigue Fract. Engng. Mater. Struct.*, Vol. 29, No. 4, (april 2006) 303-319I, SSN 8756-758X

Shibusawa, T ; Kobayashi, Y. & Ishikawa, K. (1997). Fatigue Crack Propagation in Die – cast AZ 91D Magnesium Alloy. *Nippon Kinzoku Gakaishi - Journal of the Japan Institute of Metals*, Vol. 61, No. 4, (September, 1997) 298-302, ISSN 0021-4876

Stanzl, S.E.; Hollanek, W. & Tschegg, E.K. (1984) Fatigue and Fracture Under Variable – Amplitude Loading at Ultrasonic Frequency, *Advances in Fracture Research*, Ed. S. R. Valuri et al., 3645-3651, Pergamon Press

Zheng, L.; Yan – Chun, L.; Zhong – Guang, W.; Yue, W. & Zhong – Yang, L. (2000). Influence of Load Frequency and Heat Treatment on Fatigue Crack Propagation Rate of Die – casting Alloy AZ 91HP. *Hangkong Cailia Xuebao – Journal of Aeronautical Materials*, Vol. 20, No. 1, (January, 2000) , 7-20, ISSN 1005-5053

8

Ultrasonic Grain Refinement of Magnesium and Its Alloys

M. Qian[1] and A. Ramirez[2]
[1]*The University of Queensland, School of Mechanical and Mining Engineering*
Australian Research Council (ARC) Centre of Excellence for Design in Light Metals
Brisbane QLD 4072
[2]*Aix-Marseille Université and CNRS, UMR 6242, IM2NP*
Campus de Saint Jérôme, Case 142, 13397 Marseille Cedex 20,
[1]*Australia*
[2]*France*

1. Introduction

Achievement of a uniform fine grain structure in cast magnesium (Mg) alloys is desired as it improves structural uniformity, reduces segregation and associated casting defects, enhances consistency in performance, and facilitates the solid-state forming of various wrought Mg products. Inoculation is a standard grain-refining practice for commercial cast alloys. However, many commercial alloy systems do not have an established inoculating agent or chemical grain refiner. In the context of Mg alloys, although aluminium-free Mg alloys can be readily grain-refined with zirconium (Emley, 1966; Qian & Das, 2006; Qian, 2006), it has proved difficult to grain-refine the more common Mg-Al based alloys by inoculation (StJohn et al., 2005; Qian & Cao, 2005). Alternative approaches to grain-refining these alloys are desirable.

Ultrasonic irradiation during solidification is one such alternative that has proved to be effective for Mg-Al based alloys, first demonstrated in the former USSR countries (Abramov, 1994; Eskin, 1998). It is also effective in grain-refining other metallic materials (Eskin, 1998; Jian et al., 2005; Jian et al., 2006a; Liu et al., 2007; Xu et al., 2008) and ice (Zhang et al., 2001). The recent renewed interest in the process for Mg alloys (Jian et al., 2006b; Ramirez & Qian, 2007; Zhang et al., 2007; Liu et al., 2008; Ramirez et al., 2008; Ramirez et al., 2009; Qian & Ramirez, 2009; Qian et al., 2009; Qian et al., 2010a) is driven by its potent grain-refining capability, ease of operation, and requirement for inexpensive equipment. In addition, the melt surface is left almost undisturbed during irradiation. As a result, there is little concern over contamination by oxidation. In fact, molten Mg and its alloys are particularly suited to ultrasonication for structural refinement, partially because of their low viscosity (η), where $\eta_{Mg} = 1.25 \times 10^{-3}$ N s m^{-2} at 651 °C (Brandes & Brook, 1992), being almost the same as that of water, where $\eta_{Water} = 1.002 \times 10^{-3}$ N s m^{-2} at 20°C (Lide, 2001). Low viscosity implies low attenuation (see Eq.(2)), which is important for the structural refinement of a large volume of melt. However, the lack of fundamental understanding of the ultrasonic refining process has largely restricted its development and application.

This chapter reviews the current understanding of ultrasonic grain refinement (UGR) of Mg and its alloys and discusses issues that are central to UGR, including the characteristics of UGR of Mg alloys, the dependence of UGR on solute or alloy chemistry, the attenuation in liquid Mg alloys, and the mechanisms of UGR.

2. Ultrasonic irradiation

Ultrasonic irradiation, in general, can be divided into direct and indirect ultrasonication depending on the melting point of the liquid and its chemical reactivity with the sonotrode, also referred to as ultrasonic horn or radiator. Fig. 1 illustrates the two approaches (Qian et al., 2009). The sonotrode is often made of titanium (Ti-6Al-4V) or stainless steel or niobium because of their high efficiency in transmitting ultrasound, chemical inertness to many liquids, dimensional stability, and mechanical performance at elevated temperatures. Dimensional instability can distort both the frequency and amplitude leading to undesirable performance while low chemical inertness under high-intensity ultrasonication will reduce the lifespan of the sonotrode apart from contaminating the liquid. The direct approach is preferred for ultrasonication of low melting point metals such as Mg and Al. The indirect approach is useful for ultrasonicating high melting point or reactive liquids. In the chemical processing industry, indirect ultrasonication has long been used to accelerate chemical reactions, where hundreds of ultrasonic transducers are often mounted onto the outside walls of a vessel to promote intense irradiation or vibration.

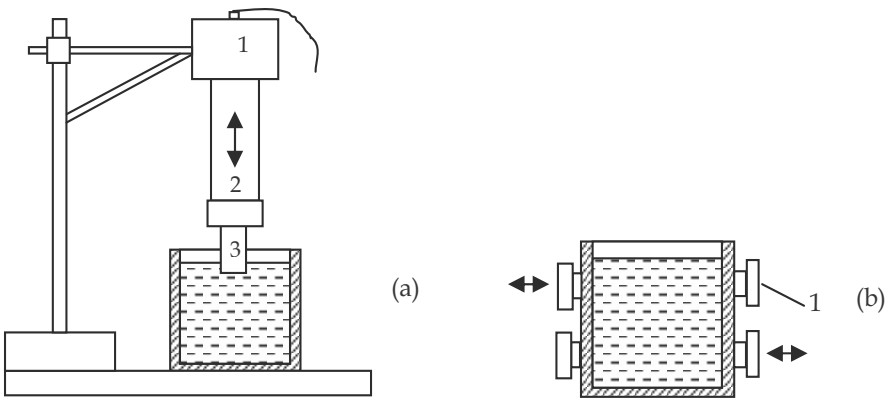

Fig. 1. (a) Direct ultrasonication: 1. ultrasonic transducer; 2. waveguide which amplifies the signal; 3. sonotrode or radiator. (b) Indirect ultrasonication: 1. transducer. Arrows denote the vibration directions, typically at a frequency of 20 kHz (Qian et al., 2009).

A commercial ultrasonic system (Fig. 1a) typically consists of a 20 kHz ultrasonic generator, a waveguide, and a sonotrode through which ultrasonic energy is transmitted to molten Mg. The intensity of ultrasonic irradiation (I) is defined by (Eskin, 1998)

$$I = \frac{1}{2}\rho c(2\pi fA)^2 \tag{1}$$

where ρ is the liquid density (ρ = 1.59 g cm^{-3} for molten Mg), c is the speed of sound, where c = 1500 m s^{-1} in molten Mg (Ramirez et al., 2008), f is the frequency, typically 20 kHz, and A is the amplitude of ultrasound. It has been established that cavitation is essential for

effective UGR and for fully developed cavitation to occur in molten light metals, the ultrasound intensity needs to be ≥ 80-100 W cm^{-2} (Eskin, 1998). The intensity can be controlled through the amplitude. For instance, I = 105, 425, 950 and 1700 W cm^{-2} corresponding to A = 7.5, 15, 22.5, and 30 μm, respectively, by Eq. (1). The amplitude of 7.5 μm is thus almost the minimum amplitude necessary for effective UGR of molten Mg. The maximum amplitude is normally < 50 μm as the resultant intensity is already significant. For instance, I = 1700 W cm^{-2} at A = 30 μm, which is ~ 20 times the threshold required for the development of full cavitation. The amplitude can be increased to 72 μm by reducing the diameter of the sonotrode to ~ 12 mm and changing the waveguide length. However, that will greatly reduce the sonotrode-melt contact interface and confine the irradiation to the vicinity of the sonotrode. In practice, it is important to ensure a maximum sonotrode-melt interface for volumetric irradiation with a well-performing amplitude (≤ 30 μm).

3. Materials and ultrasonic irradiation process

The results presented in Sections 4-8 are based on the experiments described below. Pure Mg (99.98%), binary Mg-Al and Mg-Zn alloys containing 1%, 3%, 6% and 9% of solute (all in wt.%), and three benchmark commercial Mg alloys, AZ31 (Mg-3%Al-1%Zn), AJ62 (Mg-6%Al-2%Sr), and AZ91 (Mg-9%Al-1%Zn), were irradiated during solidification. Pure Mg and binary alloys were irradiated at the maximum amplitude 30 μm while each commercial alloy was irradiated at four amplitudes, 7.5, 15, 22.5, and 30 μm.

Ingot samples of 70 mm diameter were prepared. In each experiment, 350 g of charge was melted in a clay-graphite crucible (inner diameter: 70 mm) at 730°C. After melting and alloying (for binary alloys), the crucible was withdrawn from the furnace and cooled in air. The cooling rates prior to nucleation varied between 0.76 K s^{-1} and 0.99 K s^{-1} according to the cooling curves recorded. The cooling conditions were consistent as the melt solidified in hot crucibles. This ensures that the difference in the grain size observed results mainly from the ultrasonication process and solute content.

Ultrasonic irradiation was applied through a 20 kHz commercial system (Sonic Systems Ltd, UK). Both the waveguide and sonotrode are made of Ti-6Al-4V. The sonotrode is a 25mm diameter rod with a flat radiating surface. Titanium has a negligible solubility in molten Mg (< 200 ppm at 650°C), favouring a long lifespan and minimum contamination. The melt was irradiated at 680°C by dipping the sonotrode into the crucible for 180 s. Two irradiation experiments were carried out for each condition to ensure reproducibility of results. Each irradiated ingot was sectioned longitudinally. An entire section was polished, etched, and examined. The average grain size (d) and standard deviation (σ) for each set of data reported were determined from measurements in six fields of view at 100 times. On average, about 73% of the measurements fall between $d \pm \sigma$ and 94% of the data fall between $d \pm 1.5\sigma$. The grain density, G_ρ, grains/mm^3, is calculated from the grain size assuming spherical grains.

4. Ultrasonic grain refinement of pure magnesium

The presence of an alloying element in molten Mg may alter the liquid property, for instance, its surface tension or viscosity. Accordingly, this may affect its response to ultrasonic irradiation. It is thus necessary to establish the effectiveness of ultrasonic irradiation for the grain refinement of pure Mg.

Fig. 2a shows the macro-structure of a pure Mg ingot sample solidified without ultrasonic irradiation (Ramirez & Qian, 2007). The ingot exhibited fully developed columnar grains extending to the centre, indicative of adequate purity (99.98%) of the melt. It has been shown that reducing the purity of Al from 99.99% to 99.8% will promote a columnar-to-equiaxed grain transition under conditions of forced air cooling of the melt surface in a graphite crucible (Ohno, 1987).

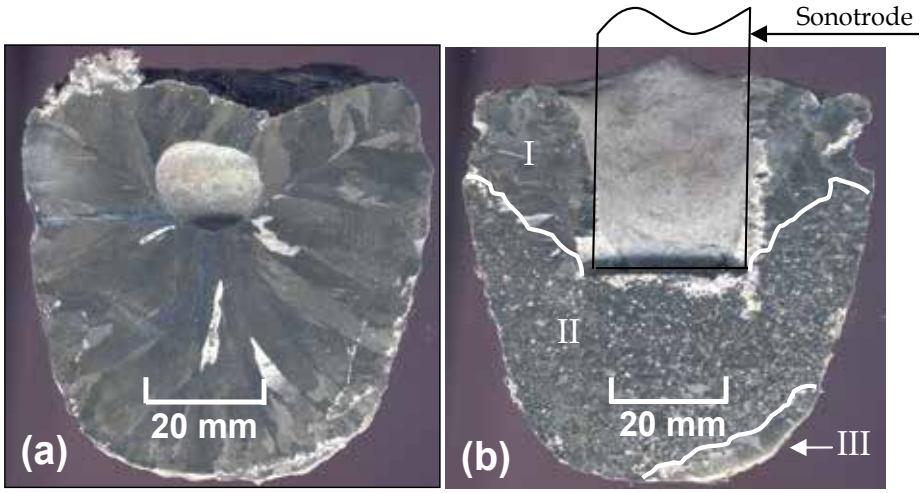

Fig. 2. Grain structures of pure magnesium: (a) without ultrasonication and (b) with ultrasonication at a nominal intensity level of 1700 W cm^{-2} (Ramirez & Qian, 2007).

Fig. 2b shows an irradiated sample, where the Ti sonotrode was dipped 35 mm into the melt. Three distinct zones are observed: a top columnar zone surrounding the sonotrode (Zone I); a nearly equiaxed zone beneath the sonotrode (Zone II); and a narrow columnar zone at the bottom (Zone III). It is interesting to note that despite the large cooling cylindrical surface of the sonotrode and the vibrations applied perpendicularly to the melt surface (Fig. 1a), UGR occurred almost exclusively below the submerged radiating face while columnar growth prevailed adjacent to the cylindrical face. The grain size is minimum (260 μm) below the radiating face and increases with ultrasound propagation distance.

Titanium has a strong growth restriction factor for Mg by the Mg-Ti phase diagram. To clarify the influence of the likely dissolution of the Ti sonotrode in the melt on the UGR, the Ti content in twelve pure Mg and AZ31 ingot samples solidified with and without ultrasonication was analysed with Inductively Coupled Plasma - Atomic Emission Spectroscopy (ICP-AES). The Fe content was also analysed as Ti is a potent iron remover. The ICP-AES analyses Ti and Fe contents down to 10 ppm each.

Table 1 lists the Ti and Fe contents obtained. There is no detectable change in the Ti content in pure Mg ingot samples after ultrasonication at 680 °C for 180 s. This is logical considering the high melting point of Ti, short ultrasonication time, and low solubility of Ti in molten Mg (~ 200 ppm at 680 °C). These results confirmed that Ti does not have any appreciable influence on the significant grain refinement observed.

The observations shown in Fig. 2b thus reflects the grain-refining capability of high-intensity ultrasonication for pure Mg, in the absence of solute, under slow cooling conditions.

Ingot sample	Before ultrasonication		After ultrasonication	
	Ti (ppm)	Fe (ppm)	Ti (ppm)	Fe (ppm)
Pure Mg	<10	51	13	35
Pure Mg	<10	30	<10	23
Pure Mg	<10	37	<10	37
AZ31	<10	31	<10	25
AZ31	<10	41	<10	11
AZ31	<10	13	<10	17

Table 1. Ti and Fe contents in pure Mg and AZ31 ingot samples ultrasonicated with an immersed 25mm diameter titanium sonotrode for 180 seconds at 680 °C (Qian et al., 2009)

5. Ultrasonic grain refinement of magnesium alloys – General observations

Ultrasonic irradiation of, either binary or multi-component commercial Mg alloys, resulted in much more potent structural refinement than that of pure Mg. Fig. 3 shows the grain structure of an ingot sample of AZ31 solidified without ultrasonication, and Figs. 4 and 5 show the refined structures of AZ31 and AZ91, respectively (Ramirez & Qian, 2007).

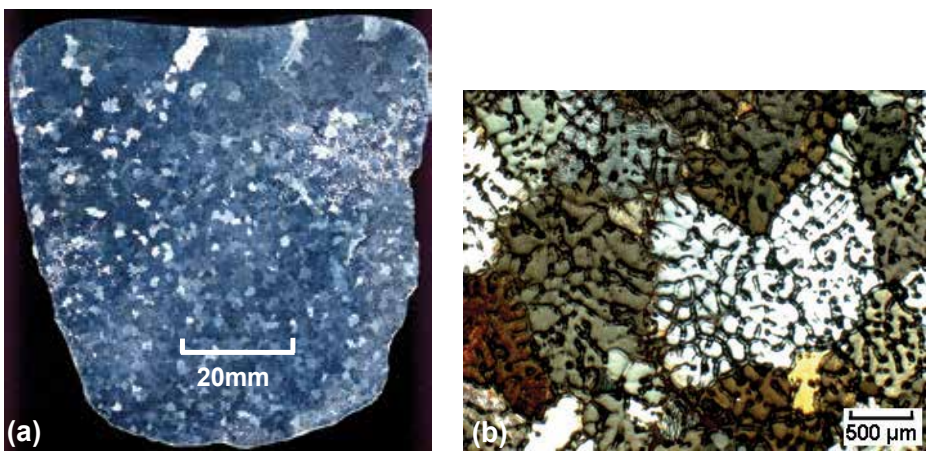

Fig. 3. Grain structures of AZ31 without ultrasonic exposure (Ramirez & Qian, 2007).

Ingot samples of AZ31 solidified without ultrasonic exposure showed coarse dendritic structure throughout the ingot, Fig. 3. The average grain size is about 2,000 μm although some dendrites have grown to ~ 4,000 μm. The macro-structure of an ingot solidified under ultrasonic irradiation and identical cooling conditions is shown in Fig. 4a. Fig. 4 b-c displays the refined equiaxed grain structures at different depths below the radiating face. The average grain size at 5 mm below the radiating face is 107 μm, demonstrating substantial UGR compared with the dendritic grains shown in Fig. 3b. The refinement decays with increasing distance from the radiating face. Far from the radiator (see Fig. 4 d, 65 mm away) rosette-like or dendritic grains are noticeable, suggesting that the local ultrasonication intensity is critical to the grain-refining process.

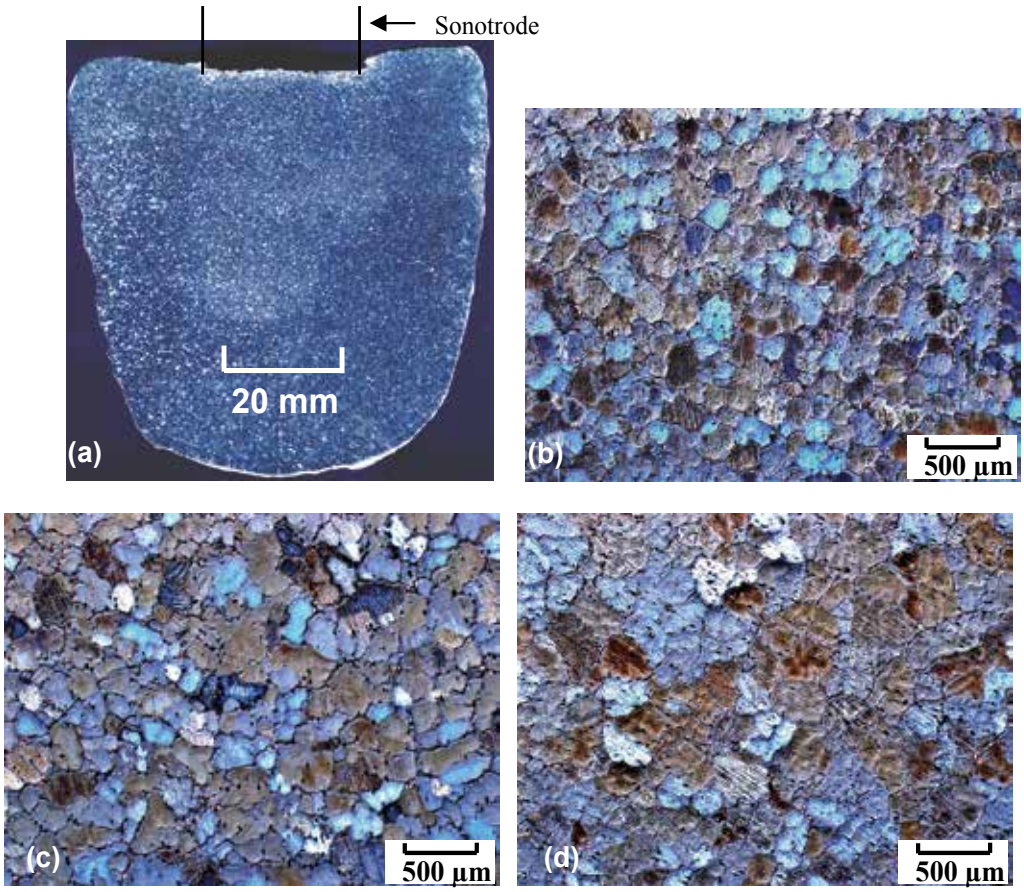

Fig. 4. Grain structures observed in an ingot sample of AZ31 solidified under ultrasonic irradiation at a nominal intensity level of 1700 W cm^{-2}. The insertion depth of the sonotrode was 1 mm. Micrographs (b), (c) and (d) were taken from 5 mm, 15 mm and 65 mm below the sonotrode radiating face, respectively (Ramirez & Qian, 2007).

Similar experiments were conducted on AZ91 in order to further assess the grain-refining potential of ultrasonic irradiation for Mg-Al based alloys. The grain structures of AZ91 ingot samples cast without ultrasonic irradiation (not shown here) are similar to those of AZ31 (Fig. 3). The average grain size is also about 2,000 µm under the slow cooling conditions used, although AZ91 was expected to have a finer grain size than AZ31 due to its high Al content.

However, ultrasonic irradiation made a substantial difference. AZ91 was found to be much more responsive to ultrasonic irradiation than both AZ31 and pure Mg. The attendant grain size is much finer and the overall grain structure is more uniform and equiaxed (Fig. 5) than the grain structures shown in Fig. 4 for AZ31. Ultrasonic irradiation of AJ62 resulted in grain refinement between AZ31 and AZ91. High-intensity ultrasonic irradiation is clearly more effective than carbon inoculation for Mg-Al based alloys; its grain-refining potency is close to that of Zr for Al-free magnesium alloys in terms of the attendant grain sizes (Ramirez et al., 2008).

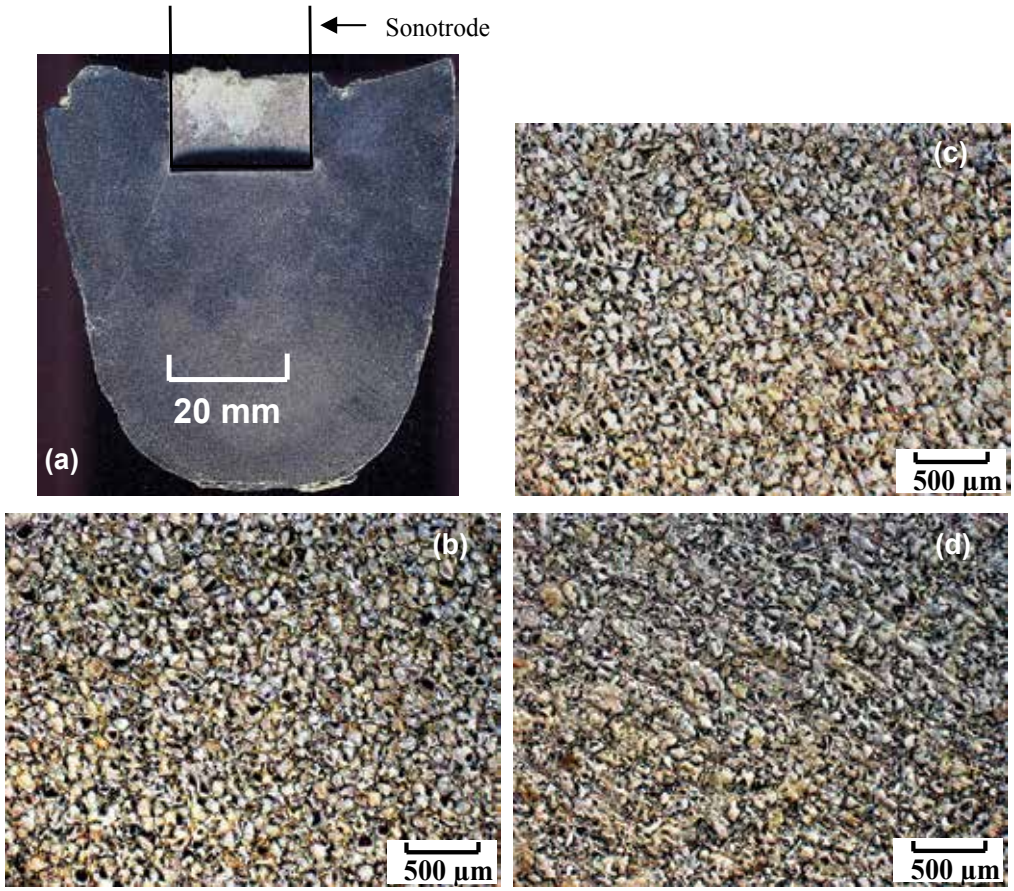

Fig. 5. Grain structures of an AZ91 ingot sample solidified under ultrasonic irradiation at a nominal intensity level of 1700 W cm^{-2}. The insertion depth of the sonotrode was ~ 20 mm. Micrographs (b), (c) and (d) were taken from 5 mm, 15 mm and 45 mm below the sonotrode radiating face, respectively (Ramirez & Qian, 2007).

From pure Mg to AZ31, AJ62 and AZ91, there is a consistent indication that alloy chemistry affects the UGR of Mg alloys. A detailed assessment of the effect of solute on the UGR of Mg alloys will be presented in Section 6.2, which shows that the presence of adequate solute is crucial to attaining excellent UGR of Mg alloys.

6. Ultrasonic grain refinement of magnesium alloys – Detailed analyses

6.1 Grain size distribution

A detailed analysis of the grain size distribution along five different directions of grain-refined ingot samples of AZ31, shown schematically in Fig. 6a, was carried out. The results are summarised in Fig. 6b (1 mm insertion depth of the sonotrode) and Fig. 6c (20-25 mm insertion depth). Very similar grain size distribution patterns were observed.

A number of features can be seen from the grain size distribution shown in Fig. 6.

i. The grain size is the finest immediately below the ultrasonic radiator and increases with increasing distance from the radiating face in all directions.

ii. The grain size along the direction perpendicular to the ultrasonic radiator, i.e. the principal propagation direction or Direction 1 in Fig. 6a, is finer than the grain sizes observed along other directions at the same distance from the radiator.
iii. The grain size distribution is symmetrical to the principal direction, Direction 1. As can be seen, Directions 2 and 3, and Directions 4 and 5, are symmetrical. The grain size distributions overlap along these symmetrical directions.
iv. Similar grain sizes are obtained, irrespective of the immersion depth of the sonotrode, at a given distance below the radiator.
v. Although the grain size increases with increasing distance from the radiator, the ultrasonic treatment is effective throughout the volume of the melt (some rosette-like grains are observed at ~ 65 mm away from the sonotrode).

These characteristics are typical of the UGR of Mg alloys.

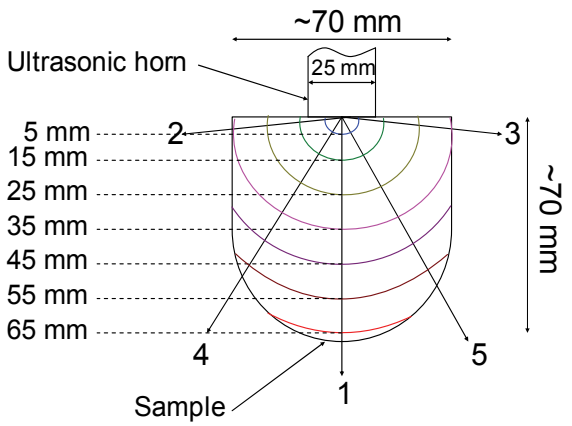

(a)

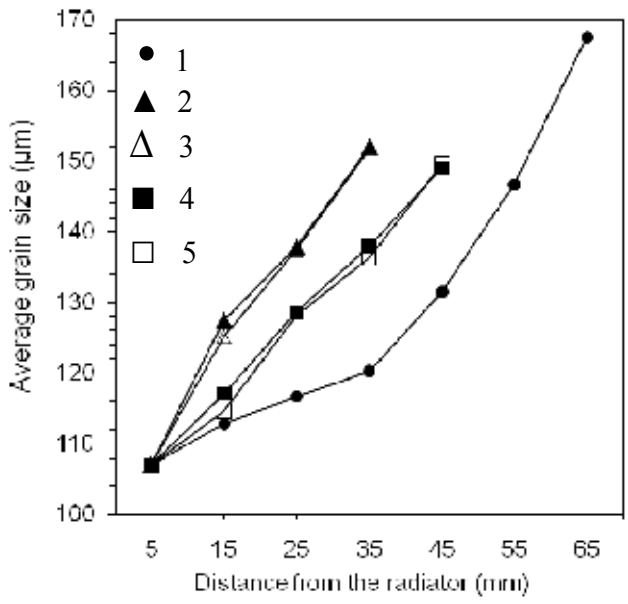

(b)

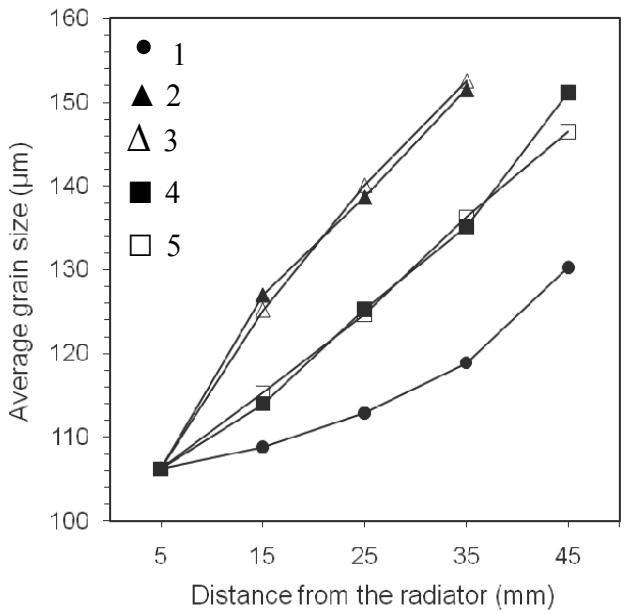

(c)

Fig. 6. Grain size distributions along five selected directions on polished ingot samples of AZ31 solidified under ultrasonic irradiation at a nominal intensity level of 1700 W cm^{-2}. Fig. 6a illustrates the five selected directions. The immersion depth of the sonotrode in the ingot sample for Fig. 6b is 1 mm and 20-25 mm in the ingot sample for Fig. 6c (Qian et al., 2009).

6.2 The role of solute atoms

From a solute re-distribution standpoint, liquid alloys that solidify in a high-intensity ultrasound field are subjected to high-frequency (at 20,000 Hz), small amplitude (10-50 μm) vibrations. Additionally, the collapse of bubbles (cavitation) produces violent local mixing and acoustic streaming. These dynamic conditions are expected to result in a relatively uniform distribution of solute ahead of the advancing solid-liquid interfaces and thereby diminish the growth-restriction role of solute in grain nucleation and growth.

Fig. 7 shows the average grain size versus solute content for binary Mg-Al and Mg-Zn alloys solidified without and with ultrasonic irradiation (Qian et al., 2010). Despite the substantial refinement from coarse dendritic grains to fully equiaxed fine grains, it is intriguing to note that the dependence of grain size on solute content is similar with and without ultrasonic exposure for both groups of alloys. A more detailed analysis of the role of solute will be shown in Fig. 9 and Fig. 12.

Fig. 8 a-d shows the average grain size as a function of ultrasound power represented by the square of amplitude, A^2, according to Eq. (1), and solute content for commercial magnesium alloys, AZ31, AJ62 and AZ91 (Qian et al., 2010). Without ultrasonic irradiation, all three commercial alloys solidified to dendritic grains with an average grain size of ~ 2,000 μm (see Fig. 3) under slow cooling conditions (Ramirez et al., 2008). Substantial grain refinement was obtained of each alloy even at the minimum irradiation intensity 105 W cm^{-2} ($A^2 = 7.5^2$ μm^2). These observations support Eskin's finding that an irradiation intensity level of 80-100

W cm^{-2} is required for fully developed cavitation to occur in light alloys (Eskin, 1998). They also indicate that the ultrasonic power was transmitted effectively through the titanium sonotrode, where molten magnesium wets solid titanium well (Kondoh et al., 2010).
The following observations can be made from Fig. 8 a-d.

- The average grain size decreases with increasing ultrasonic irradiation intensity but the reduction mainly occurs from 7.5^2 μm^2 to 22.5^2 μm^2; the benefits of further increasing the irradiation intensity from 22.5^2 μm^2 to 30^2 μm^2 are small.
- Increasing solute content from AZ31 to AJ62 or AZ91 consistently outweighed increasing irradiation intensity from 7.5^2 μm^2 (I_{min}) to 30^2 μm^2 (I_{max}), which represents an increase by *15 times*, i.e., (30/7.5)^2-1, at all depths. An example is illustrated in Fig. 8a, where the shorter arrowed dashed line depicts the effectiveness of increasing irradiation intensity from I_{min} to I_{max} while the longer arrowed dashed line depicts that of increasing solute content from AZ31 to AJ62 at the minimum irradiation intensity I_{min} (7.5^2 μm^2).

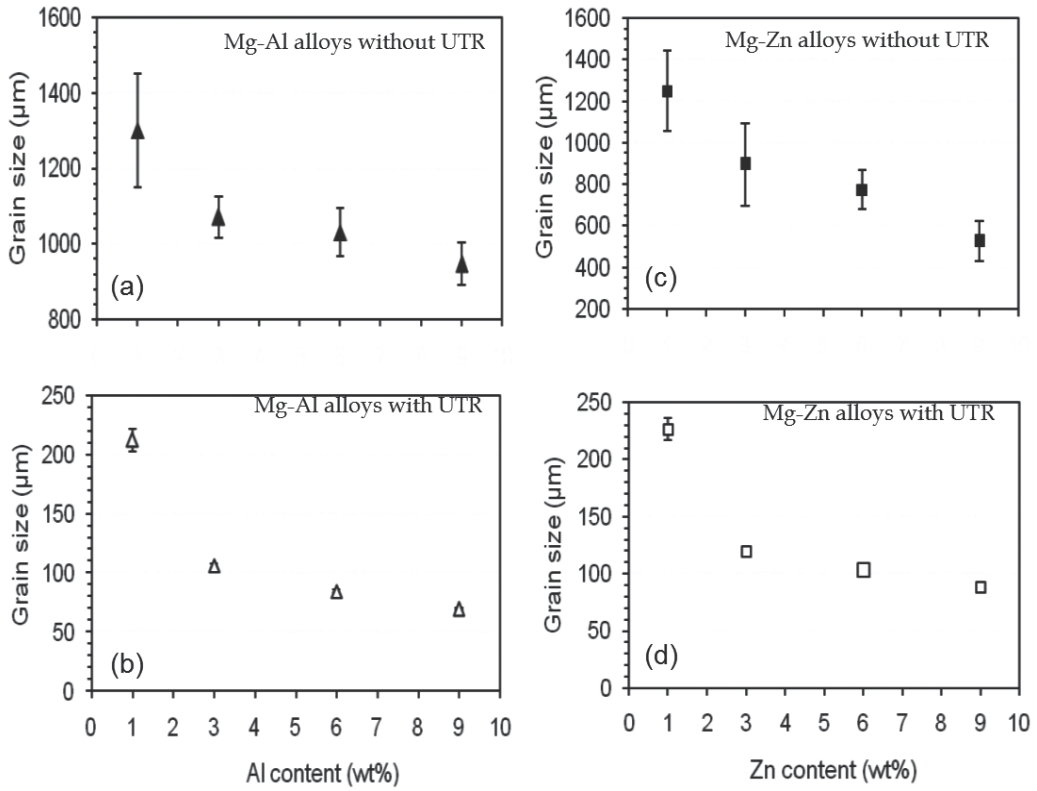

Fig. 7. Average grain size versus solute content for binary alloys without and with ultrasonication at I = 1700 W cm^{-2}. The grain size was measured at 15 mm below the radiating face. UTR: ultrasonic irradiation (Qian et al., 2010)

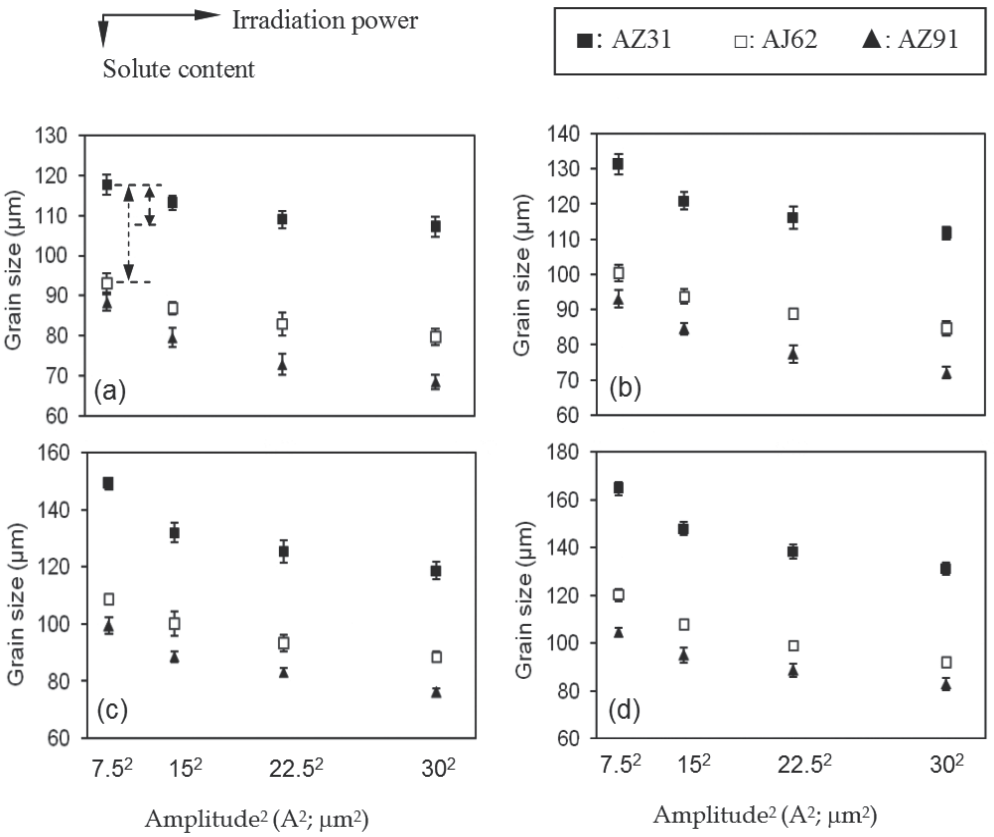

Fig. 8. Average grain size at different depths below the radiating face versus ultrasonication intensity ($I \propto A^2$) for AZ31, AJ62 and AZ91: (a) 5 mm; (b) 15 mm; (c) 30 mm; and (d) 45 mm (Qian et al., 2010)

- The *proportional* difference in the grain size between each of the alloys, for example, AZ31 and AZ91 where $d_{AZ91} \approx 0.64 d_{AZ31}$, remains approximately constant at all depths, irrespective of irradiation intensity in the range from 7.5^2 μm² to 30^2 μm². This suggests that there is little interaction between the solute content and ultrasonic irradiation intensity beyond the threshold level (7.5^2 μm²) for cavitation.
- The minimum grain size of AZ31 attained at I_{max} = 1700 W cm^{-2} (30^2 μm²) is still much greater than the grain size of AJ62 attained at I_{min} = 105 W cm^{-2} (7.5^2 μm²), although the difference in the irradiation intensity is $I_{max}/I_{min} \approx 16$ times. In contrast, the difference in the solute (Al) content between AZ31 and AJ62 is only from 3% to 6%. This further indicates that solute plays a far more important role in determining the achievable minimum grain size than the irradiation intensity.

An alternative way of evaluating the effect of solute on UGR is by examining the grain density, G_ρ, which is more closely linked to the nucleation rate. Table 2 lists the grain density calculated from the average grain size by assuming spherical grains. The grain density in each alloy that solidified in the hot crucible without ultrasonic irradiation is negligible (< 5 grains/mm³) and therefore not listed in Table 2.

Solute content (wt.%)	Mg-Zn alloys Grain density (grains mm^{-3})	Mg-Al alloys Grain density (grains mm^{-3})	Commercial alloys Grain density (grains mm^{-3})
0	64	64	64
1	165	205	
3	1116	1599	1559 (AZ31: 3%Al)
6	1722	3245	3744 (AJ62: 6%Al)
9	2793	5640	5788 (AZ91: 9%Al)

Table 2. Grain densities of binary Mg-Zn and Mg-Al and commercial AZ31, AJ62 and AZ91 alloys calculated from the grain size at 15 mm below the sonotrode-melt interface, irradiated at $A^2 = 30^2$ μm^2 (Qian et al., 2010)

The grain density increases enormously with increasing solute content under the same irradiation conditions. For instance, it increased from 205 to 5640 grains/mm^3 with increasing Al content from 1% to 9%. In fact, the grain density and solute content exhibit an unexpected linear relationship for each alloy system. Fig. 9 shows the results (Qian et al., 2010). Also indicated is the grain density of pure Mg irradiated under similar conditions.
Fig. 9 reveals that there must be adequate solute present in each alloy for significant grain refinement ($G_\rho \geq 2000$ grains/mm^3 or $d \leq 100$ μm) to occur by ultrasonic irradiation. Under the slow cooling conditions used, it requires a minimum of ~ 6.5% Zn for binary Mg-Zn alloys and a minimum of ~ 3.5% Al for binary Mg-Al alloys. Commercial grade AZ31 is just about all right as it contains 3%Al and 1%Zn. This benchmark wrought Mg alloy can thus be effectively refined by ultrasonic irradiation, although having a higher solute content will further enhance the refinement as shown by AJ62 and AZ91 in the same plot.

6.3 The role of wall crystals

Wall crystals can play an important role in metal solidification as demonstrated by Ohno (Ohno, 1987). The melt surface vibration experiments performed by Ohno (Ohno, 1987; Qian et al., 2009) are essentially similar to the application of ultrasonic vibration to the melt surface through a bar-type titanium sonotrode, which traverses perpendicularly to the melt surface as illustrated in Fig. 1a. Apart from transmitting ultrasonic energy, the titanium sonotrode, whose diameter varies from a few millimeters to over 100 mm depending on the volume of the liquid, also acts as a big chill to absorb and conduct heat away from the melt due to the substantial difference in the melting point of Ti (1660°C) and the melt temperature (≤ 800°C for light metals). Accordingly, it is anticipated that the immersed surface of the Ti sonotrode will provide a primary cold surface for the formation of wall crystals. Also, it would seem reasonable to further assume that many such wall crystals will separate from the surface of the Ti sonotrode due to the high frequency (20 kHz) transverse movements of the rod and consequently play an important role in the UGR of light metals. Hence understanding the role of wall crystals in ultrasonic refinement will help understand the mechanism by which ultrasonication refines the microstructure and facilitate designing a more efficient ultrasonic refining system.

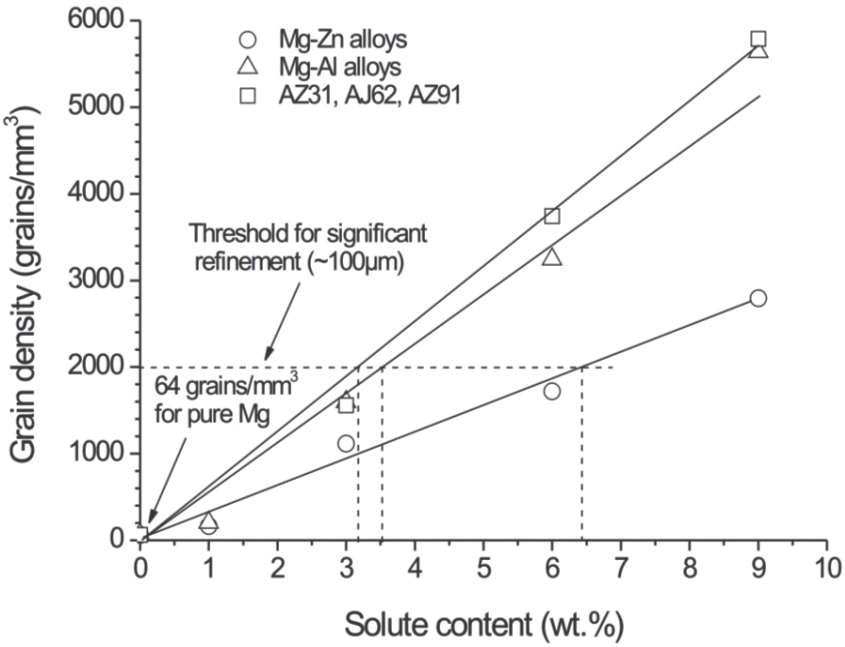

Fig. 9. Grain density versus solute content for magnesium alloys irradiated at 1700 W cm^{-2} or $A^2 = 30^2$ μm^2 (Qian et al., 2010)

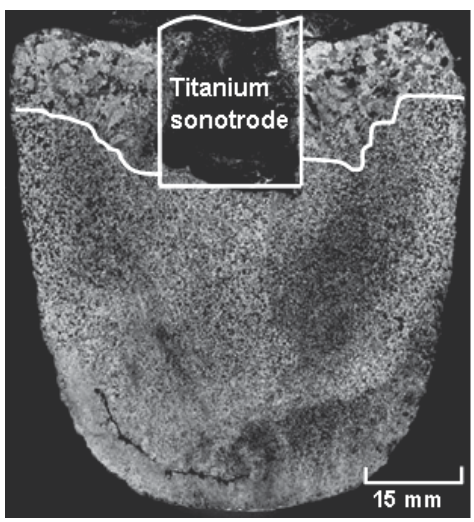

Fig. 10. Ultrasonic refinement of AZ31 at a nominal intensity level of 1700 W cm^{-2}.

Fig. 2b shows that ultrasonic grain refinement of pure Mg occurs only below the radiating face; little refinement was observed adjacent to the cylindrical face of the sonotrode immersed in the melt. To clarify if the observation occurs only to pure Mg, similar immersion experiments were conducted on AZ31. Fig. 10 shows the macro-structure of an AZ31 ingot sample solidified under ultrasonic irradiation (Qian et al., 2009), where the titanium sonotrode was submerged about 25 mm into the melt. Similarly, ultrasonic grain

refinement was observed almost exclusively below the radiating face. The borderlines that distinguish the refined and unrefined regions are indicated in Fig. 10.

Considering that the colder sonotrode surface provides an effective surface for nucleation due to its chill effect and transverse motion, the occurrence of columnar growth around the cylindrical sonotrode face for both pure Mg (Fig. 2b) and AZ31 (Fig. 10) indicates that the anticipated formation and detachment mechanism was ineffective. More interestingly, as shown by Fig. 6b and c, the actual grain sizes and grain size distribution patterns are almost independent of the insertion depth of the ultrasonic radiator. This demonstrates negligible influence of the chill surface (source of wall crystals) on the observed refinement.

The formation of columnar zones around the cylindrical face of the immersed sonotrode can be explained as follows. The efficient chill effect of the sonotrode produces a large thermal gradient around the cylindrical face and promotes directional growth of nucleated crystals perpendicular to the sonotrode. However, the lack of convection in this region will deter the detachment and melting of the crystals at their base thereby favouring coarse columnar growth. In addition, the small amplitude of vibration (30 μm) of the sonotrode is probably inadequate to mechanically shear off the wall crystals from the sonotrode surface before columnar growth occurs. According to Ohno (Ohno, 1987), once a solid shell of columnar grains forms on a cold contact with high cooling capacity, it will be difficult for the columnar crystals to separate even though movement of molten metal still exists. On the other hand, it is plausible that some wall crystals have formed and separated from both the surfaces of the sonotrode and the crucible walls, but the total population is negligible compared to the number of the crystal nuclei created by cavitation-enhanced nucleation. Under the experimental conditions, the minimum grain size of a pure Mg ingot sample is about 2,000 μm (see Fig. 2a, edge of the ingot at the bottom). This roughly corresponds to a grain density of ~ 0.24 mm^{-3}. In contrast, the grain density attained in pure Mg immediately below the radiating face is ~ 100 mm^{-3} (average grain size: 260 μm), which is about 400 times the grain density originating from the wall crystals. The wall crystal effect is thus fairly negligible under the experimental conditions even if the mechanism has been operative during ultrasonication.

7. Ultrasonic attenuation in molten magnesium alloys

Similar to propagation in water, when an ultrasonic wave travels through a liquid metal, its amplitude (A) and intensity (I) attenuate with distance. Consequently, ultrasonication will be confined to a limited volume of the liquid beyond which the intensity is insufficient to induce desired structural refinement. It is thus necessary to understand the process both for effective UGR and the design of a performing ultrasonic system.

The Stokes-Kirchhoff relation allows prediction of the attenuation coefficient α of an ultrasonic wave in a liquid by the addition of a viscous component α_v and a thermal component α_T in the form (Sahu, 1984; Awasthi & Murthy, 1985; Kuttruff, 1991)

$$\alpha = \alpha_v + \alpha_T = \frac{2\pi^2}{\rho c^3}\left[\frac{4}{3}\eta + \lambda_T\left(\frac{1}{c_v} - \frac{1}{c_p}\right)\right] f^2 \tag{2}$$

In Eq. (2), ρ is the density (kg m^{-3}), c is the velocity of ultrasound (m s^{-1}) in the liquid, η is the viscosity (N s m^{-2}), λ_T is the thermal conductivity (W m^{-1} K^{-1}), f is the ultrasonic frequency (Hz), and c_v and c_p are specific heats at constant volume and pressure, respectively (J kg^{-1} K^{-1}). However, it has been found that the predictions given by Eq. (2) for low melting point metals (< 350°C) are much smaller than the experimental measurements (Sahu, 1984; Awasthi & Murthy, 1985). For molten Mg (T_m = 650°C), ρ = 1590 kg m^{-3}, c =1500 m s^{-1} (Ramirez et al., 2008), η = 1.25 mN s m^{-2}, λ_T = 78 W m^{-1} K^{-1}, and c_p = 1.36 J g^{-1} K^{-1} (Brandes, and Brook, 1992), where for most liquids, c_p/c_v = 1.0-1.1. Eq. (2) gives α = (2.45-10.89)×10^{-6} m^{-1} for molten Mg with respect to f = 20 kHz. The predicted value of α is too small and contradicts experimental observations.

A practical approach has recently been proposed to assess the ultrasonic attenuation in light metals and alloys (Qian & Ramirez, 2009). For Mg alloys, the attenuation can be assessed by the variations of the grain density with propagation distance in relation to the ultrasonication intensity applied (Qian & Ramirez, 2009). Fig. 11 (a) to (c) depicts the variations of the grain density (G_ρ) for AZ31, AJ62 and AZ91 along the principal propagation direction (Direction 1 in Fig. 6) with respect to different ultrasonic amplitudes. A detailed analysis revealed that the reduction in G_ρ with propagation distance is best described, in an exponential form of $G_\rho = G_\rho(0)e^{-\alpha x}$, where $G_\rho(0)$ is the grain density at the radiating face in the solidified sample and α is attenuation coefficient. The exponential curves of best fit are shown in Fig. 11 for each condition.

Table 3 summarizes the characteristic attenuation coefficients (α) for each alloy determined from Fig. 11. As expected, α exhibited dependence on alloy composition, where a significant decrease in the value of α was observed with increasing solute content from 3%Al to 6%Al but a further increase of the solute content to 9%Al resulted in only a marginal decline. A low attenuation coefficient implies that the molten alloy can be readily ultrasonicated. So, both AJ62 and AZ91 are more ultrasonicatable than AZ31. Consequently,

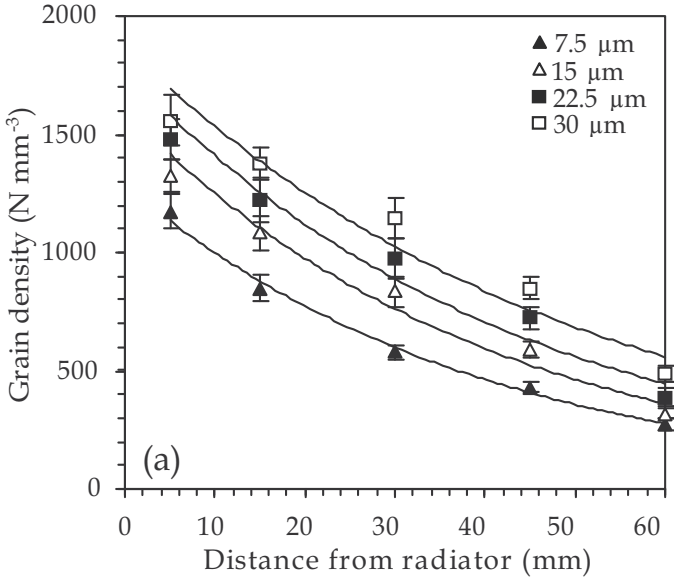

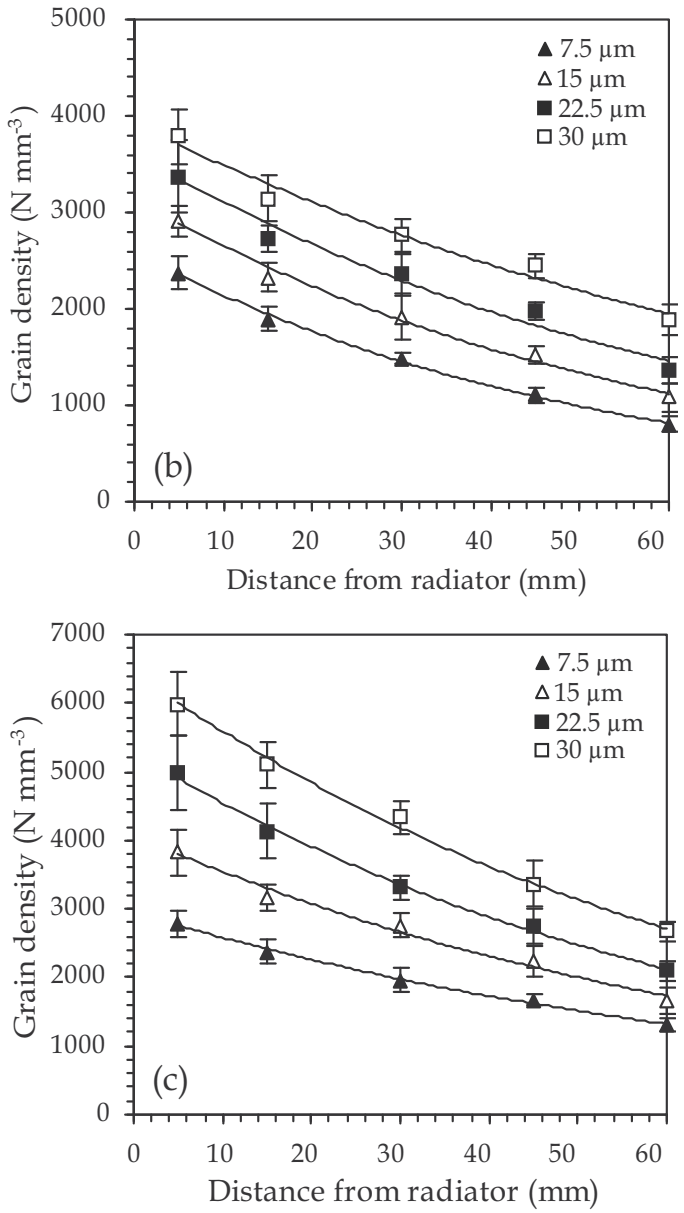

Fig. 11. Grain density versus propagation distance along the principal propagation direction with respect to different amplitudes for (a) AZ31, (b) AJ62 and (c) AZ91.

to exploit the structural refining potential of ultrasonic irradiation, it is important to develop low attenuation coefficient alloys. Alloy chemistry plays a critical part in this regard. This also provides a means of controlling the attenuation behaviour in molten Mg alloys. The characteristic attenuation coefficient determined for AZ31 was validated by comparing predictions with experimental observations from ultrasonicating 140 mm diameter ingot samples, and also with Eskin's work (Qian & Ramirez, 2009).

Liquid alloy (wt.%)	Attenuation coefficient α (mm^{-1})	Standard deviation (mm^{-1})
Mg-3Al-1Zn (AZ31)	0.0234	0.002394
Mg-6Al-2Sr (AJ62)	0.015825	0.003241
Mg-9Al-1Zn (AZ91)	0.01435	0.000742

Table 3. Characteristic ultrasonic attenuation coefficients in liquid Mg alloys (Qian & Ramirez, 2009).

Attenuation is a concern for the structural refinement on a large scale. Alloy design can effectively mitigate the problem according to the attenuation coefficient results listed in Table 3.

8. Mechanism of ultrasonic grain refinement

The influence of ultrasonic irradiation on structural refinement is based on the physical phenomena arising out of high-intensity ultrasound propagation through liquid. Several mechanisms have been proposed and the major ones may be summarised as cavitation-induced dendrite fragmentation, cavitation-enhanced heterogeneous nucleation, and vibration-stimulated separation of wall crystals.

The cavitation-induced dendrite fragmentation hypothesis assumes that the shock waves generated from the collapse of bubbles lead to fragmentation of dendrites, which are redistributed through acoustic streaming, thereby increasing the number of crystals (Flemings, 1974). The cavitation-enhanced heterogeneous nucleation theory is further explained by three different mechanisms. The first is based on the pressure pulse–melting point (T_m) mechanism (Hunt & Jackson, 1966), where the pressure pulse arising from the collapse of bubbles alters T_m according to the Clapeyron equation. An increase in T_m is equivalent to increasing the undercooling so that an enhanced nucleation event is expected. It has been estimated that at the collapse point of a gas-filled bubble in water the pressure produced is of the order of between 1000 and 4000 atm (Knapp et al., 1970). The attenuation of the maximum-pressure intensity is proportional to $1/r$, where r is the distance from the collapse centre. At a distance of $r/R = 2$, where R is the bubble radius, the pressure is estimated to be of the order of 200 to 1000 atm (Knapp et al., 1970). Using the Clapeyron equation and the typical parameters for magnesium summarised in (Qian, 2006), we found that the increase in the melting point of magnesium or undercooling by a pressure pulse of one atmosphere is about 0.00647 K. For nickel it is about 0.0027 K (Chalmers, 1964). For a given pressure pulse of 1000 atmospheres, that is equivalent to introducing an "additional undercooled zone" with $\Delta T = 6.47$ K. This will suffice to trigger nucleation on most substrates present in the undercooled zone. The second is based on cavitation-enhanced wetting (Eskin, 1998), which assumes that cavities and cracks on the substrate surfaces and insoluble non-metallic inclusions that either pre-exist in the melt or form on cooling during solidification, can be wetted by the melt under the pressure pulse from the collapse of the bubbles. Consequently, this enables these substrates to act as effective nucleation sites (Eskin, 1998). The third mechanism assumes that rapid adiabatic expansion of gas inside the bubbles created during cavitation undercools the liquid at the bubble-liquid interfaces

resulting in nucleation on the bubble surfaces (Hunt J. D. & Jackson, 1966; Jian et al., 2005). Collapsing of these bubbles will distribute the nuclei into the surrounding liquid producing a significant number of nuclei in the liquid.

The wall crystal hypothesis was proposed by Ohno (Ohno, 1987). It was suggested that vibration refines the microstructure by two means. First, since a molten metal is constantly covered with oxide films, the contact of the molten metal with the mould walls or a cold contact surface can hardly be uniform under usual conditions. Vibration could disrupt the covering oxide films promoting wetting of the mould walls by the molten metal. This enhances the nucleation of the wall crystals on the mould or cold contact surfaces. The second aspect is that vibration promotes the separation of the crystals of a thin necked shape from the mould walls due to the local shaking and/or shearing effects caused by vibration. These two effects combine together to produce a substantial number of crystal nuclei responsible for the refinement. Recent work has clarified that the wall crystal mechanism does not play any appreciable role in the UGR of Mg alloys (Qian et al., 2009).

The role of solute was not considered in the mechanisms proposed previously. It is clear from Figs. 8 and 9 that solute plays a decisive role in the UGR of Mg alloys. This generally goes against the perception that solute homogenisation could be enhanced under ultrasonic induced fluid flow reducing the growth restriction effect. Solidification under ultrasonic irradiation is known to be more dynamic compared with solidification under quiescent conditions (Chalmers, 1964). An immediate question that follows is: what are the roles that ultrasonic irradiation and solute each play in the structural refinement? A new mechanism is proposed below for ultrasonic grain refinement of Mg alloys.

First, high-intensity ultrasonic irradiation plays a key role in producing the first batch of nuclei or crystallites in the effectively irradiated volume near the sonotrode by enhanced nucleation, due to enhanced wetting of the insoluble nucleating particles and/or the pressure effect on melting point. These crystals are then continuously dispersed into other parts of the melt as nuclei or crystallites by the dynamic effects generated by ultrasonic irradiation. In a direct ultrasonication process, the sonotrode was immersed below the melt surface in the middle of the melt. Crystals are thus dispersed from the middle of the melt towards the crucible walls. Without ultrasonic irradiation the chance of creating a large number of initial nuclei and having them dispersed in the bulk melt at the same time are generally very limited. This is because nuclei originating from either the mould wall reaching and then surviving in the bulk superheated melt would have been very small in number. In contrast, high-intensity ultrasonication directly creates nuclei in the irradiated bulk melt. Therefore it fundamentally changes the sequence of solidification compared to conventional ingot solidification. Second, the high-frequency (20,000 Hz) and small amplitude (7.5-30 μm) vibrations in conjunction with the strong cavitation effects help dissipate heat from the effectively irradiated volume so that many of the crystals formed in the melt have a better chance to survive. This differs from the low survival rate of wall crystals in conventional ingot solidification. On the other hand, new crystals are being continuously generated by ultrasonic irradiation to serve as fresh nuclei or growing fronts. Ultrasonic irradiation thus acts as a continuous crystal generator to inoculate the solidifying melt with a large number of *initial crystallites*. For instance, in the case of AZ91, the number of grains formed under ultrasonic irradiation is in the order of 5788/mm^3 (Table 2) compared to a negligible grain density of 0.24 (~ 2,000 μm grain size) under the same slow cooling conditions.

Once the initial crystallites are generated in an alloy melt by ultrasonic irradiation, growth of each crystal will lead to solute enrichment ahead of each growing front. The attendant constitutional supercooling (ΔT_{cs}) will further induce nucleation on nearby most potent available nucleants when ΔT_{cs} is greater than the undercooling required for nucleation (ΔT_n) (Qian et al., 2010b). The concept has been formulated on a rigorous basis to predict grain formation in Al, Mg and Ti alloys solidified under various conditions (Qian et al., 2010b). It confirms the existence of a fundamental linear relationship between the average grain size d and the growth restriction factor $Q = m_l \cdot c_0 \cdot (k-1)$, where c_0 is the solute concentration, m_l the slope of the liquidus, and k the solute partition coefficient. The linear relationship assumes

$$d = a + D \cdot \Delta T_n / (v \cdot Q) \tag{3}$$

where a is a constant, D is diffusion coefficient and v is growth velocity. A detailed account has been given of the historical evolution of this linear relationship in the work referenced (Qian et al., 2010b).

Fig. 12 plots the average grain size obtained at 15 mm (Fig. 12a) and 30 mm (Fig. 12b) below the radiating face for AZ31, AJ62 and AZ91 versus $1/Q$ with respect to each intensity level applied. An excellent linear relationship was observed. The average grain size versus $1/Q$ at other depths below the radiating face showed similar linear relationships.

It is clear from Fig. 9 that the presence of solute considerably enhances grain density. In fact, only a very low number of crystals in the order of 64/mm^3 (Table 2) would survive to produce the final grain structure if no solute were present. This suggests that the development of a constitutionally undercooled region around each initial crystallite may be critical in ensuring the survival of the ultrasonically produced crystallites. This explains the strong dependence of grain size on solute composition shown in Fig. 12.

It should be noted that the formation of a sufficient number of initial crystallites or presence of numerous nucleating particles is essential to the ultrasonic grain-refining process, particularly for commercial alloys in which native nucleants are often poisoned by impurities (Cao et al., 2005). For example, without ultrasonication, little effect of solute was observed in the three commercial alloys when solidified under the same slow cooling conditions (Ramirez et al., 2008), where they all showed a similar coarse grain structure of d ≈ 2,000 μm. This is because there were few active nucleants operating in these alloys to initiate the growth-restriction effect of solute. This was confirmed by the negligible grain density of 0.24 grains/mm^3 (d ≈ 2,000 μm) observed in each solidified alloy ingot (Ramirez et al., 2008). Accordingly, it supports the idea that ultrasonic irradiation is a nucleation facilitator or crystallite generator. However, the degree of survival of these crystallites is determined by the solute content of the alloy.

In a continuous ultrasonic irradiation process, as the effect of solute develops ahead of the growing crystals, new crystallites will be continuously generated and dispersed into other parts of the melt. This development will gradually extend into the entire melt where the growth restriction effect of solute similarly applies. So, once the irradiation intensity is above the cavitation threshold, which means that the irradiation applied is able to generate a sufficient number of initial crystals, the subsequent development of the solidification process will be mainly determined by the growth restriction role of solute. Ultrasonic grain

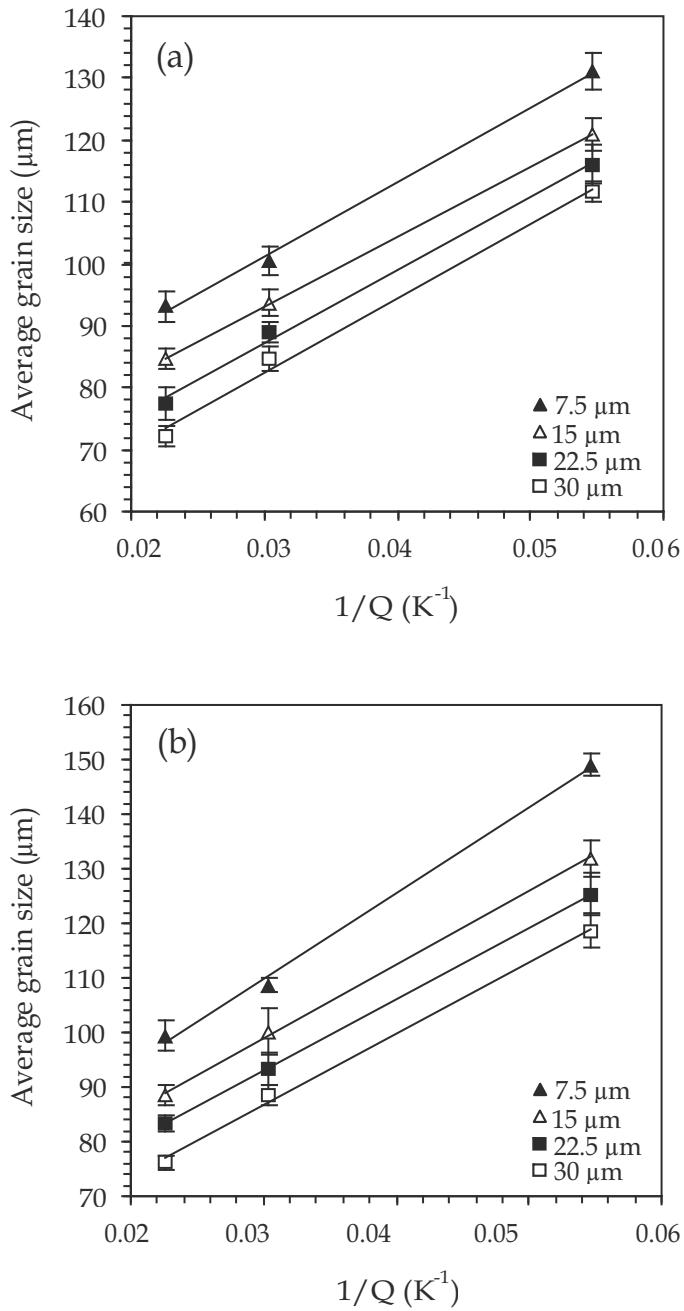

Fig. 12. Average grain size measured at 15 mm (a) and 30 mm (b) below the radiating face versus 1/*Q* for AZ31, AJ62 and AZ91 (Qian & Ramirez, 2009).

refinement of Mg alloys thus arises from the combined effects of ultrasonic irradiation and solute. Both effects are important to ensure significant refinement. There is little need to pursue extremely high irradiation intensity levels. Instead, it appears to be more important to exploit the effect of solute through alloy design by using an appropriate level of irradiation intensity such as $A^2 = 15^2$ μm^2 or 22.5^2 μm^2. Finally, it should be noted that solute affects the physical properties of a liquid alloy including the surface tension and viscosity, which may affect cavitation. Any detailed assessment of such influences will facilitate the selection of solutes for ultrasonic grain refinement.

The proposed mechanism explains most observations made from this study. Given the importance of solute under ultrasonic irradiation in ensuring a fine grain structure, the proposed mechanism is expected to apply to ultrasonic irradiation of all alloy systems that are made up of growth restricting elements. Regarding the inference that ultrasonic irradiation showed little influence on solute redistribution even at the irradiation intensity level of 1700 W cm^{-2}, our proposal is that the dynamic effects from ultrasonic irradiation may only affect the solute boundary layer by a limited amount over a short timescale; they do not largely interfere with the evolution of an appreciable constitutional undercooling zone. This needs to be examined in greater detail in the future.

9. Summary and conclusions

- Ultrasonic irradiation of magnesium alloys at intensity levels above the melt cavitation threshold leads to significant structural refinement (≥ 2,000 grains/mm^3 or ≤ 100 μm grain size) *only in the presence of adequate solute*. Without solute, high-intensity (1700 W cm^{-2}) ultrasonic irradiation of pure magnesium results in grain densities only in the order of 64 grains/mm^3 while in the presence of 9%Al the grain density increases to 5640 grains/ mm^3 under the same irradiation conditions. Grain refinement of magnesium alloys by ultrasonic irradiation shows strong dependence on solute content.
- For significant grain refinement to occur by ultrasonic irradiation, the minimum solute required is ~ 6.5%Zn for binary Mg-Zn alloys and ~ 3.5%Al for binary Mg-Al alloys under cooling conditions of 0.76 - 0.99 K s^{-1}. Commercial grade AZ31 is just about all right as it contains 3%Al and 1%Zn.
- Increasing solute content at an appropriate irradiation intensity level (i.e. above the cavitation threshold) is more effective for grain refinement than substantially increasing irradiation intensity. The difference in the grain size between two magnesium alloys solidified under ultrasonic irradiation is mainly determined by the solute content rather than the irradiation intensity. In view of these, there is little need to pursue excessive irradiation.
- The primary role of ultrasonic irradiation is to produce the initial crystallites by enhanced nucleation in the effectively irradiated melt volume. The role of solute with a high growth-restriction factor is twofold. Firstly, the constitutionally undercooled region developed around each growing initial crystallite protects them from remelting. Growth of these crystals then generates constitutional undercooling sufficient to cause further grain nucleation in regions away from the sonotrode. Ultrasonic grain refinement of Mg alloys arises from the combined effects of solute and irradiation and both effects are important.

- The effect of ultrasonic irradiation on solute redistribution in a solidifying magnesium alloy seems rather limited even at a substantial intensity level such as 1700 W cm^{-2}. Solute plays a similar role with and without high-intensity ultrasonic irradiation.
- Ultrasonic grain refinement occurs almost exclusively below the radiating face of the sonotrode; little refinement is observed in the solidified ingot adjacent to the immersed cylindrical face of the cold titanium sonotrode, which oscillates perpendicularly to the melt surface at an amplitude of 30 μm and a frequency of 20 kHz. The insertion depth of the sonotrode in the melt has no impact on the resulting ultrasonic refinement. The formation and separation of wall crystals from the titanium sonotrode has negligible influence on the observed refinement.
- Ultrasonic grain refinement is symmetrical to the principal ultrasound propagation direction; the grain size along the principal propagation direction is the smallest at the same distance from the radiating face. The grain size increases with increasing distance from the radiating face in all directions.
- Attenuation of ultrasound intensity in molten Mg alloys can be effectively assessed according to the variations of the grain density with propagation distance. Metallographic analyses reveal that the dependence of grain density on ultrasound propagation distance obeys an exponential law with respect to different amplitudes. The attenuation of ultrasound amplitude with propagation distance can be described by the same exponential law. The characteristic attenuation coefficients in three benchmark molten magnesium alloys, AZ31 (Mg-3Al-1Zn), AJ62 (Mg-6Al-2Sr) and AZ91 (Mg-9Al-1Zn), have been determined. The coefficient is alloy dependent.
- High-intensity ultrasonic irradiation is more potent than carbon inoculation for Mg-Al based alloys; its grain-refining potency is close to that of Zr for Al-free magnesium alloys (Ramirez et al., 2008).

10. Acknowledgements

Financial support from the UK government's Engineering and Physical Sciences Research Council (EPSRC) is acknowledged. Magnesium Elektron Ltd., UK is acknowledged for both financial support and provision of experimental materials. Useful discussions with Dr A. Das of the School of Engineering, Swansea University, Singleton Park, Swansea, SA2 8PP, UK are acknowledged.

11. References

Abramov O. V. (1994). *Ultrasound in Liquid and Solid Metals*, CRC Press, ISBN 0801649307, Boca Raton, FL.

Awasthi O. N. & Murthy B. V. S. (1985). *Phys. Lett*. A, Vol. 108, 119-122, ISSN 0375-9601.

Brandes E. A. & Brook G. B. (1992). *Smithells Metals Reference Book* (7th ed.), Butterworth-Heinemann, ISBN 0408046228, Oxford.

Cao P., Qian M. & D.H. StJohn (2005). *Scripta Mater.,* Vol. 53, 841-844, ISSN 1359-6462.

Chalmers B. (1964). *Principles of Solidification*, 86-89, John Wiley, ISBN 0471143251, NY.

Emley E. F. (1966). *Principles of Magnesium Technology*, Pergamon, ISBN 0080106730, Oxford.

Eskin G. I. (1998). *Ultrasonic Treatment of Light Alloy Melts*, Gordon & Breach, ISBN 905699042X, Amsterdam.

Flemings M. C. (1974). *Solidification Processing*, 300, McGraw-Hill, ISBN 007021283X, NY.

Hunt J. D. & Jackson K. A. (1966). *J. Appl. Phys.,* Vol. 37, 254-257, ISSN 0021-8979.

Jian X., Xu H., Meek T. T. & Han Q. (2005). *Mater. Lett.*, Vol. 59, 190-193, ISSN 0167-577X.

Jian X., Meek T. T. & Han Q. (2006a). *Scripta Mater.*, Vol. 54, 893-896, ISSN 1359-6462.

Jian X., Meek T., Geer T. & Han Q. (2006b). *Magnesium Technology 2006*, pp. 103-107, ISBN 978-0-87339-620-2, San Antonio, TX, March 2006, TMS, Warrendale, PA.

Knapp R. T., Daily J. W. & Hammitt F. G. (1970). *Cavitation*, 143-145, McGraw-Hill, NY.

Kondoh K., Kawakami M., Imai H., Umeda J. & Fujii H. (2010). *Acta Mater.*, Vol. 58, 606-614, ISSN 1359-6454.

Kuttruff H. (1991). *Ultrasonics: Fundamentals and Applications*, 209, Elsevier, ISBN 1851665536, London.

Lide D. R. (2001). *CRC Handbook of Chemistry and Physics* (82nd ed.), 6-3, CRC Press, ISBN 0849304822, Boca Raton.

Liu X., Osawa Y., Takamori S. & Mukai T. (2008). *Mater. Sci. Eng. A*, Vol. 487, 120-123, ISSN 0921-5093.

Liu Q., Zhai Q., Qi F. & Zhang Y. (2007). *Mater. Lett.*, Vol. 61, 2422-2425, ISSN 0167-577X.

Ohno A. (1987). *Solidification: The Separation Theory and Its Practical Applications*, Springer, ISBN 3540182330, Berlin.

Qian M. & Cao P. (2005). *Scripta Mater.,* Vol. 52, 415-419, ISSN 1359-6462.

Qian M. & Das A. (2006). *Scripta Mater.,* Vol. 54, 881-886, ISSN 1359-6462.

Qian M. (2006). *Acta Mater.,* Vol. 54, 2241-2252, ISSN 1359-6454.

Qian M. & Ramirez A. (2009). *J. Appl. Phys.*, Vol. 105, 013538, ISSN 0021-8979.

Qian M., Ramirez A. & Das A. (2009). *J. Crystal Growth*, Vol. 311, 3708-3715, ISSN 0022-0248.

Qian M., Ramirez A., Das A. & StJohn D. H. (2010a). *J. Crystal Growth*, Vol. 312, 2267–2272, ISSN 0022-0248.

Qian M., Cao P., Easton M. A., McDonald S. D. & StJohn D. H. (2010b). *Acta Mater.*, Vol. 58, 3262–3270, ISSN 1359-6454.

Ramirez A. & Qian M. (2007). *Magnesium Technology 2007*, pp. 127-132, ISBN 978-0-87339-663-9, Orlando, FL, February, 2007, TMS, Warrendale, PA.

Ramirez A., Qian M., Davis B. & Wilks T. (2009). *Inter. J. Cast Metal. Res.*, Vol. 22, 260-263, ISSN 1364-0461.

Ramirez A., Qian M., Davis B., Wilks T. & StJohn D. H. (2008). *Scripta Mater.*, Vol. 59, 19-22, ISSN 1359-6462.

Sahu K. C. (1984). *Phys. Lett. A*, Vol. 102, 370-372, ISSN 0375-9601.

StJohn D. H., Qian M., Easton M. A., Cao P. & Hildebrand Z. (2005). *Metall. Mater. Trans. A*, Vol. 36, No. 7, 1669-1679, ISSN 1073-5623.

Xu Z., Yan J., Chen W. & Yang S. (2008). *Mater. Lett.*, Vol. 62, 2615-2618, ISSN 0167-577X.

Zhang X., Inada T., Yabe A., Lu S. & Kozawa Y. (2001). *Inter. J. Heat Mass Transfer*, Vol. 44, 4533-4539, ISSN 0017-9310.

Zhang Z. Q., Le Q. C. & Cui J. Z. (2007). *Mater. Sci. Forum*, Vols. 546-549, 129-132, ISSN 0255-5476.

9

Bulk Ultrafine-Grained Magnesium Alloys by SPD Processing: Technique, Microstructures and Properties

Jinghua JIANG and Aibin MA
Hohai University
P.R.China

1. Introduction

Mg alloys are very attractive as the lightest metallic structural materials and have great potential for applications in automotive, aerospace and electronic industries. However, their usages are still limited due to some undesirable properties of castings (such as strength, ductility, creep and corrosion resistance) and few fabricating methods besides conventional ingot metallurgy processing. Since grain refinement is generally believed to have beneficial effect on properties of Mg alloys, fabrication of bulk ultrafine-grained (UFG, grain size less than 1μm) alloys using the new conceptual metal forming process - severe-plastic-deformation (SPD) should attract considerable attention (Azushima et al., 2008).

During the last decade, SPD processing has been evolving as a rapidly progressing direction of modern materials science that is aimed at developing materials with new mechanical and functional properties for advanced applications. As well known, all Mg alloys (except for some special Li-containing alloys) exhibit a hexagonal crystal structure, leading to severe limitations in their ductility, strength and creep resistance. This inherent difficulty maybe be reasonably overcame by some special processing of SPD, such as equal-channel angular pressing (ECAP), accumulative rolling bonding (ARB), high pressure torsion (HPT), etc. Enhanced properties have been obtained after these SPD processes in various Mg alloys. For example, ZK60 Mg alloy processed by ECAP (with the grain size to ~0.8μm) is superplastic at a testing temperature of 473K with an optimum ductility of ~1310% when using an initial strain rate of $2.0\times10^{-4}s^{-1}$ (Figueiredo et al., 2006). Mg-9Li-1Zn alloy had the greater increase in tensile strength of about 41.8MPa and the least decrease in elongation of about 25% at room temperature (Chang et al., 2006). UFG ZE41A alloy after enough ECAP passes obtains higher corrosion resistance besides superior mechanical properties (about 120% higher in yield strength and 75% larger in elongation at room temperature after 32 passes) (Ma et al., 2009).

SPD fabrication of bulk UFG Mg alloys is becoming one of the most actively developing areas in the field of advanced structural and functional Mg alloys. SPD-produced UFG materials are fully dense and their large geometric dimensions make them attractive for efficient practical applications. Today, SPD techniques are emerging from their domain of laboratory-scale research into commercial production of various UFG materials (Valiev et al., 2009). In this chapter, we will consider these new trends in SPD processing used to produce bulk UFG Mg alloys and highlight some key results on the development of the

UFG alloys science and applications. The aim is to better understand the relationships between microstructure and properties of SPD materials, and exploit novel SPD processing routes for fabricating UFG Mg alloy with enhanced properties.

2. Developing SPD techniques for grain refinement

SPD processes may be defined as metal forming processes to fabricate UFG materials, via introducing an ultra-large plastic strain into a bulk metal without any significant change in the overall dimensions. The main objective is to produce lightweight parts with high mechanical behaviours and environmental harmony, since the well accepted notion of the Hall-Petch equation suggests that a decrease in grain size leads to an increase in yield strength. Due to an ever-increasing interest in fabricating materials with extremely small grain sizes, various SPD techniques are now available, including ECAP, ARB, HPT, cyclic extrusion compression (CEC), repetitive corrugation and straightening (RCS), torsion extrusion, severe torsion straining (STS), cyclic closed-die forging (CCDF), super short multi-pass rolling (SSMR), etc. We report here the principles and new trends of those major SPD processes, and discuss its application in fabricating UFG magnesium alloys.

2.1 The principles of SPD techniques

Equal channel angular pressing, known also as equal-channel angular extrusion (ECAE), was first introduced by Segal et al. (1981) at an institute in Minsk in the former Soviet Union. It is at present the most developed SPD processing technique, which may be used for grain refinement of solid metals billet and consolidation of metallic powder to obtain new and unique properties. Fig.1 shows the schematic representation of ECAP process and a typical facility (Berbon et al., 1999). During ECAP a rod-shaped billet is side extruded through a die constrained within a channel that is bent at an abrupt angle. Since the cross-sectional dimensions of the billet remain unchanged, the pressings may be repeated to attain exceptionally high strains. The equivalent strains, ε introduced in ECAP is determined by a relationship as follows (Iwahashi et al., 1996):

$$\varepsilon = \frac{N}{\sqrt{3}}\{2\cot(\frac{\phi}{2}+\frac{\psi}{2}) + \psi \cos ec(\frac{\phi}{2}+\frac{\psi}{2})\ \} \tag{1}$$

where N is the pass number through the die, ϕ is the angle of intersection of two channels and ψ is the angle subtended by the arc of curvature at the point of intersection. When ϕ = 90˚and ψ = 0°, the total strain from the above equation is ε = 1.15 N. During repetitive pressing, the shear strain is accumulated in the billet, leading ultimately to a UFG structure.
For these billets inserted within the channel, it is convenient to develop processing routes in which the billets are rotated by increments of 90˚ between each separate pass. This leads four fundamental process of metal flow during ECAP, as shown in Fig.2. In route A, the billet is pressed without rotation. In route B_A and B_C, the billet is rotated by 90˚ in an alternate direction or the same direction between consecutive passes, respectively. In route C, the sample is rotated by 180˚ between consecutive passes. From these macroscopic distortions shown in Fig.2, the influence of the processing route on the development of an UFG microstructure can be considered. When using a die with ϕ = 90˚, route B_C is generally the most expeditious way to develop a UFG structure consisting of homogeneous and equiaxed grains with high angle grain boundaries. Matsubara et al. (2003) and Lin et al.

(2005) fabricate the UFG Mg alloys via a two-stage extrusion plus ECAP. The original coarse grain size can be reduced to around 0.7 μm after extrusion at 300˚C and subsequent 8-pass ECAP at 200˚C. There has been numerous recent modification of conventional ECAP that are designed to yield more efficient grain refinement (Valiev & Langdon, 2006), including the incorporation of a backpressure and the development of continuous ECAP processing.

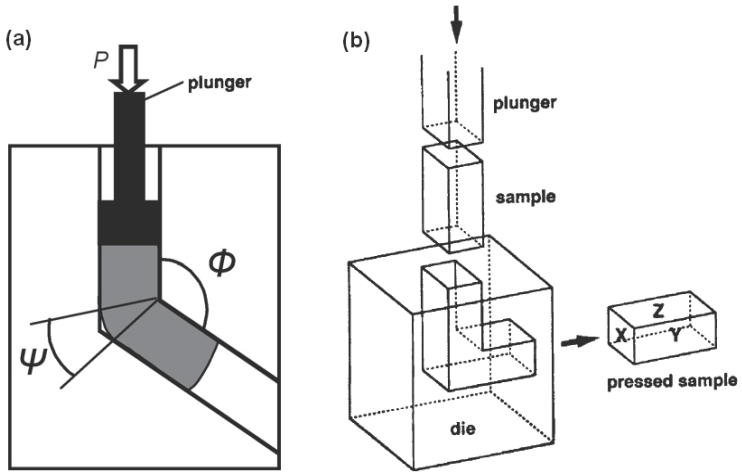

Fig. 1. Schematic illustration of ECAP process (a) and a typical facility (b): the X, Y and Z planes denote the transverse plane, the flow plane and the longitudinal plane, respectively.

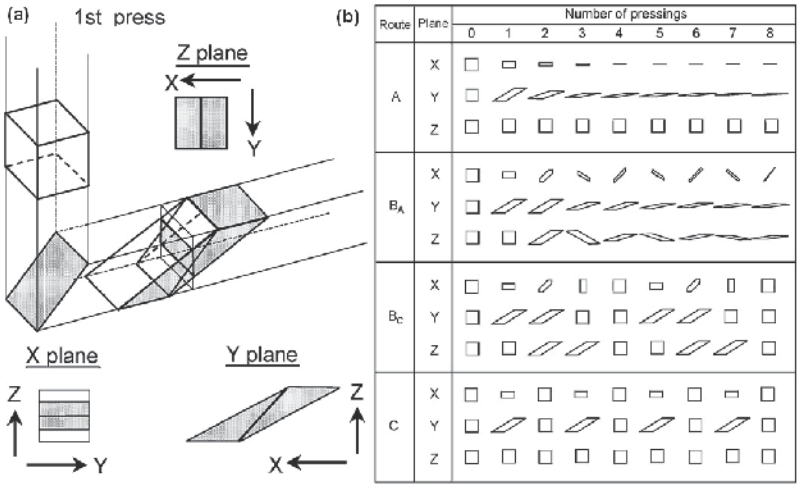

Fig. 2. Fundamental process of metal flow during ECAP. (a) The deformation of a cubic element on a single pass ([a] Furukawa et al, 2001) . (b) Shearing characteristics for four different processing routes (Furukawa et al, 1998) .

Accumulative roll-bonding process was first developed by Saito et al. (1998), which principle is represented systematically in Fig.3. First, a sheet is rolled to reduce one-half of the thickness in a prerolled condition, and then cut into two halves that are stacked together. Their

interfaces are surface-treated in advance to enhance the bonding strength. The stacking sheets are then rolled again to one-half thickness and sectioned into two halves again. Conventional roll-bonding, cutting, pre-treating and stacking of sheets are repeated in the process, so that very large plastic strain can be accumulated in the sheet. The strain after n cycles of the ARB process can be expressed as ε_N=0.80N (Saito et al. ,1999). This process has recently been applied successfully for dramatic grain refinement of AZ61 Mg alloy (Del Valle et al., 2005). ARB process is applicable to produce large sheet of bulk UFG Mg alloys. However, the UFG structure produced by ARB is not three-dimensionally equiaxed but rather there is a pancake-like structure elongated in the lateral direction.

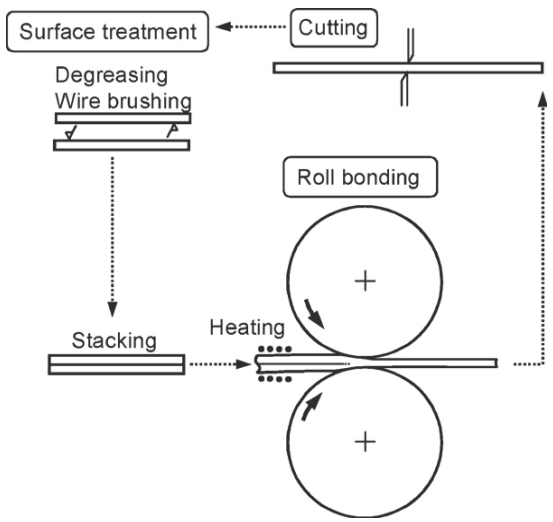

Fig. 3. Diagrammatic representation of the accumulative roll-bonding (Saito et al. ,1999)

High-pressure torsion (HPT) process refers to the processing of metals whereby samples, generally in the form of a thin disk, are subjected to a compressive force and concurrent torsional straining (Bridgman et al., 1935).The principle of HPT is illustrated schematically in Fig.4. The disk located in a closed die is compressed by a very high pressure, and plastic torsional straining is achieved by rotation of one of the anvil. The equivalent strain according to the von Mises yield criterion is given by

$$\varepsilon = \frac{2\pi nr}{\sqrt{3}l} \tag{2}$$

where r is the distance from the axis of the disk sample, n is the number of rotation and l is the thickness of the sample. For Mg alloys which are not processed easily by ECAP, HPT is more effective in producing exceptionally small grain sizes (Zhilyaev & Langdon., 2008). This process provides an opportunity for achieving significant grain refinement, often to the nm level, and exceptionally high strength. The disadvantages of the conventional HPT are that the relatively small disk is not available for the production of large bulk materials, and the microstructures created are dependent on the applied pressure and the location within the disc. It is reasonable to anticipate that HPT processing may be an effective tool for producing small parts used in a range of industrial and medical applications.

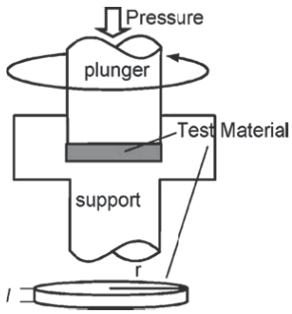

Fig. 4. Diagrammatic representation of the thin disc-HPT process (Valiev et al. ,1991)

Cyclic extrusion compression process is performed by pushing a billet from one cylindrical chamber of diameter D to another with equal dimensions through a die with diameter d (markedly smaller than D), which principle is represented schematically in Fig. 5. The billet is extruded repeatedly backwards and forwards within the chamber, and preserves the original shape with large strain deformation after N passes. The accumulated equivalent strain is approximately given by

$$\varepsilon = 4N \ln(D / d) \tag{3}$$

where N is the number of deformation cycles, D is the chamber diameter and d is the channel diameter . This process is better suited for processing soft material such as Mg alloys. However, the strain introduced in the forward extrusion may be cancelled by the strain introduced on the backward extrusion. The strains reached with this process are much high than those with any unidirectional SPD technique, but the microstructure are similar for extra dislocation annihilation due to cyclic straining character (Richert et al., 2003).

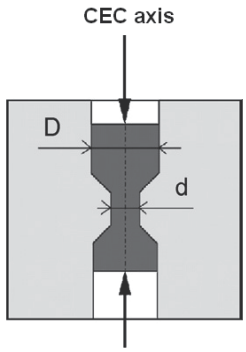

Fig. 5. Schematic illustration of cyclic extrusion compression process

SPD processing has been developed extensively over the last decade and the polycrystalline Mg alloys produced by various SPD techniques exhibit unique and attractive characteristics including excellent strength at ambient temperature. Although those techniques have been typically used for laboratory-scale research, materials processed by SPD are now receiving serious consideration for potential use in a wide range of products. For successful commercialization of UFG materials, the requirement of economically feasible production is necessary and raises several new problems in the development of SPD techniques.

2.2 Continuous SPD pressing

It is known that UFG materials with unique mechanical and physical properties can be produced by SPD, and the key to the wide commercialization is to lower their processing cost and waste through continuous processing. Although ECAP is an effective route to UFG billets by imposing large shear strains, the conventional process has some limitations for commercialization. In particular, the limited length of the billets makes ECAP a discontinuous process with low production efficiency and high cost. Several attempts have been made to develop continuous SPD processes, such as rotary-die ECAP (Nishida et al., 2001), equal channel angular drawing (ECAD) (Alkorta et al., 2002), continuous cyclic bending (CCB) (Takayama et al., 2002), repetitive corrugation and straightening (RCS) (Huang et al., 2001), continuous shear deformation process (conshearing) (Saito et al., 2000), continuous confined strip shearing (C2S2) (Lee et al., 2002) , continuous frictional angular extrusion (CFAE) (Huang et al., 2007), ECAP-Conform(Raab et al., 2004) . The ARB and RCS process using a rolling mill are effective to continuously manufacture UFG sheets or plates; however, the bad quality of interface bonding, poor ductility or edge-cracks need be eliminated for industrial application. Although the total strain can be largely accumulated in CCB, UFG microstructures have not been developed (Tsuji et al., 2003) .

Fig.6 presents the schematic illustration of a rotary-die (RD) ECAP process. The die contains two channels with the same cross-sections intersecting at the center to remove the limitation in the conventional ECAP, i.e. the sample must be removed from the die and reinserted again in each step. By the RD-ECAP apparatus, a billet can be repetitive pressed with a back pressure. Ma et al. (2009) reported that the UFG ZE41A Mg alloy after 16 passes of RD-ECAP is more uniform with average grain size of about 1.5μm. In the similar way, Rosochowski et al. (2002) developed a method to reduce the repetitive number by increasing the number of channel turns in the die. These ECAP processes have been used only in the laboratory for low productivity, and continuous ECAP processing techniques (e.g. ECAD, conshearing and C2S2) are developed for mass production of long metal bars and strips. However, ECAD cannot be use effectively for multi-pass processing due to cross-sectional reduction higher than 15% (Alkorta et al., 2002). A schematic illustration of the C2S2 machine used for continuous confined strip shearing is presented in Fig.7. This newly developed technique was termed dissimilar channel angular pressing (DCAP) to distinguish this technique with the conventional ECAP. The DCAP process can impart the shear deformation to long and thin metallic sheets without significant changes in their cross-sectional area (Lee et al., 2001; Lee et al. , 2002). However, these techniques should be developed for further improvement of microstructure uniformity and properties.

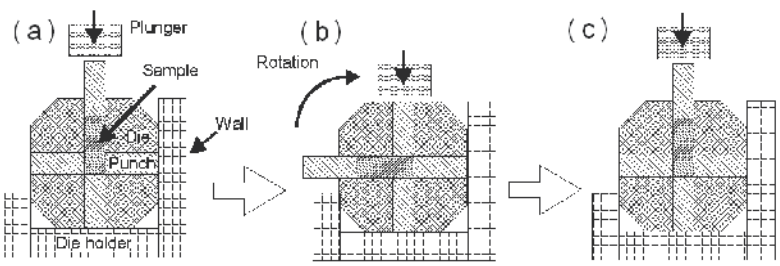

Fig. 6. The RD-ECAP process via pressing route A: (a) initial state, (b)after one pass and (c) after 90˚die rotation

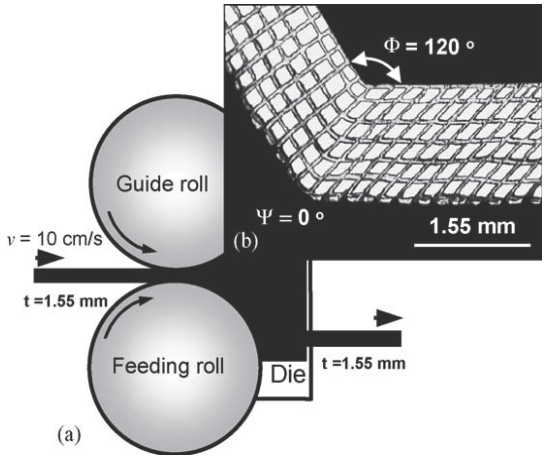

Fig. 7. (a) A schematic illustration of the C2S2 machine used for continuous confined strip shearing based on DCAP; (b) optical micrograph showing the shear deformation pattern recorded from the side surface of the specimen processed by DCAP (Han et al,2004).

Recently, the combining ECAP with the Conform process (Raab et al, 2004) is developed to continuously process UFG materials for large-scale commercial production. The principle of the ECAP-conform process is represented schematically in Fig.8. The workpiece is driven forward by frictional forces on the three contact interfaces with the groove. The workpiece is constrained to the groove by the stationary constraint die, which forces the workpiece turn by shear deformation as in a regular ECAP process. The continuous nature of the process makes it promising for successfully producing UFG materials on a large scale, in an efficient and coat-effective manner. However, further study is necessary to investigate its ability with respect to grain refinement and properties improvement of various UFG materials.

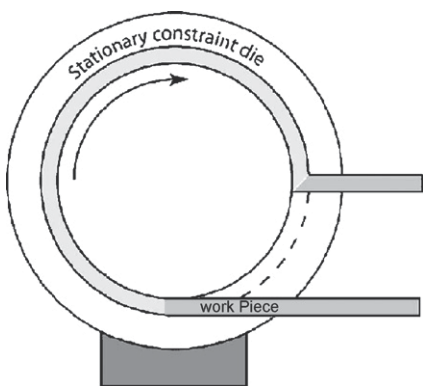

Fig. 8. Schematic illustration of the ECAP-Conform process.

2.3 Combined SPD processing

Recently, the combined processes of ECAP and conventional metal forming (such as cold rolling, forging or extrusion) were developed to improve properties of UFG materials with effective shaping of long-sized semi-products (sheets, rods). The principle of the combined process of ECAP and cold rolling is represented schematically in Fig. 9 (Azushima et al.,

2002). Cheng et al. (2007) used the process of equal-channel angular rolling (ECAR) to produce AZ31 Mg alloy sheets with improved ductility. The high-speed-ratio differential speed rolling (HRDSR) technique was developed to induce a large shear deformation in an Mg sheet during rolling. By this technique, UFG Mg alloy sheets with a low intensity of basal fiber texture could be produced and obtained with high strength and high ductility (Kim et al., 2007). By applying ECAR and HRDSR in sequence, one can effectively control the grain size and texture of AZ31 sheets, resulting in the increase of its strength and ductility (Kim et al., 2009). This shows great prospects for applying SPD processing to commercial production of UFG Mg alloys.

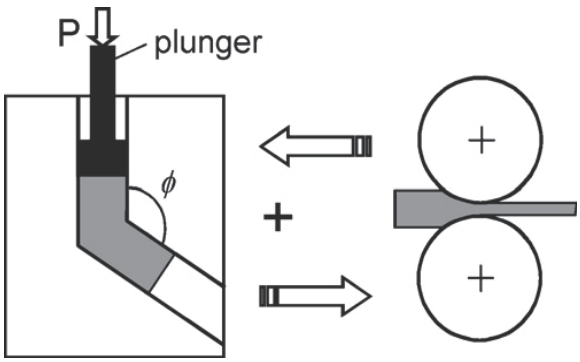

Fig. 9. Principle of the combined process of ECAP process and cold rolling.

3. Structural features and deformation behaviors in SPD-produced bulk UFG Mg alloys

Bulk UFG Mg alloys produced by SPD techniques have been arguably the hottest research area in the recent years (Máthis et al., 2005), because UFG materilas have sufficient room temperature ductility and superplasticity at high strain rates (Weertman et al., 1999). Although the successful attainment of UFG pure Mg by SPD is very difficult due to a limit of slip systems in hexagonal close-packed (hcp) systems, it is possible to obtain remarkable grain refinement in Mg-based alloys. An early attempt to achieve significant grain refinement in AZ91 alloy by ECAP was successful , which obtained a grain size of 1 μm with an elongation of 660% at 6×10^{-5} s^{-1} and 200 ˚C(Mabuchi et al., 1997). Ma et al. (2009) found that the tensile yield strength, ultimate strength, elongation to failure of UFG ZE41A Mg alloy are all remarkably increased after a large number of ECAP passes. However, the combination of high strength and good ductility is rare in their coarse-grained counterparts. It is well known that the mechanical behaviors of materials are determined by their deformation mechanisms, while the deformation mechanisims are controlled by the structures of the materials. The unique mechanical behaviors of UFG Mg alloys are believed to be caused by the unique deformation mechanisims operating in the UFG materials.

3.1 Structural evolution during SPD processes

Jin et al (2006) investigated the microstructure evolution of AZ31 Mg alloy ECAP-processed at 498K to clarify the process of grain refinement. SEM examinations showed that the grains of AZ31 Mg alloy were refined significantly with the mean grain size of 1.91μm after

extruded eight passes (in Fig.10). TEM examination revealed that after the first pass, the structure comprises a mixture of sub-boundaries, low angle grain boundaries (LAGBs) and high angle grain boundaries (HAGBs, misorientation angle >15˚). Dislocations were induced at the initial stage of extrusion and rearranged to form dislocation boundaries and sub-grain

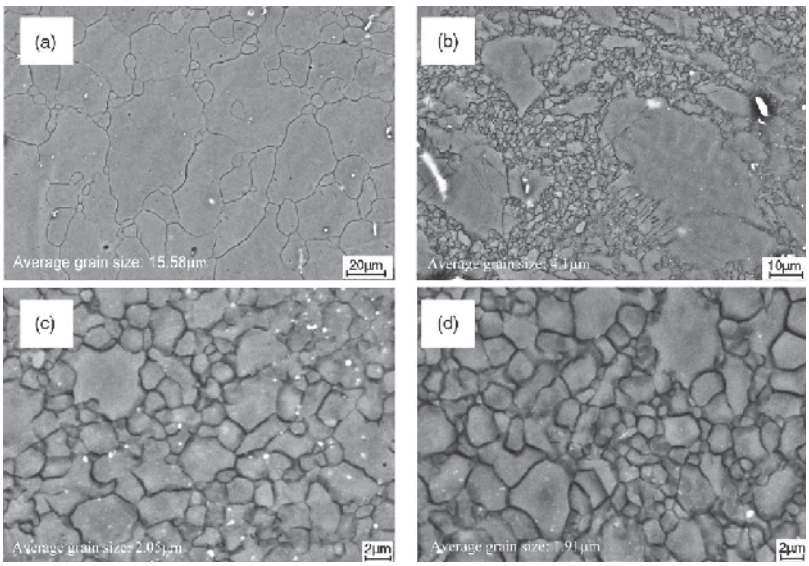

Fig. 10. SEM photographs of AZ31 alloy: (a) original condition, (b) after one pass, (c) after four passes and (d) after eight passes of ECAE at temperature 498 K.(Jin et al , 2006)

boundaries during deformation (see Fig.11). As strain increased, the newly created dislocations in subgrains were absorbed by the subboundaries and the misorientation between subboundaries increased and evolved to LAGBs and HAGBs. The frequency of LAGBs decreased and the frequency of HAGBs increased from four passes to eight passes, however the grain sizes have not been changed (see Fig.10 c and d). It means that grain refinement of ECAPed AZ31 alloy is pronounced at the initial stage of ECAP and further deformation forms more HAGBs but does not provide further refinement.

Precipitate-hardened Mg alloys or Mg-based composites can easily achieve a UFG structure due to the effective pining effect from the precipitates or added ceramic particles on the grain boundaries (Morisada et al, 2006; Lee et al., 2006; Chang et al., 2006). For pure Mg or solute solution hardened Mg alloys (such as AZ31) with a low content of alloying elements, it is difficult to achieve a UFG microstructure due to the rapid growth kinetics of the single-phase grains. Li et al. (2004) reported that dynamic recrystallization (DRX) caused the grain refinement of ECAPed AZ31 Mg alloy due to the effect of the deformation temperature and the total strain or the strain rate occurred in the SPDed material. The SPD process led to homogeneous equiaxed grains and many small subgrains, so that the microstructure became finer and more homogeneous with increasing ECAP passes up to a critical value. The effect of deformation temperature is significant as high temperature is favorable for grain growth. The DRX grain size is finer corresponding to the lower ECAP temperature. Ma et al.(2009)observes microstructure characterization of the ZE41 alloy after various ECAP passes at 603K. As shown in Fig. 12, primary as-cast ZE41 alloy has equiaxed grains with the size of around 80μm. The alloyed elements of Zn and RE exist as $Mg_{12}Zn_{13}$ and $REMg_{12}$

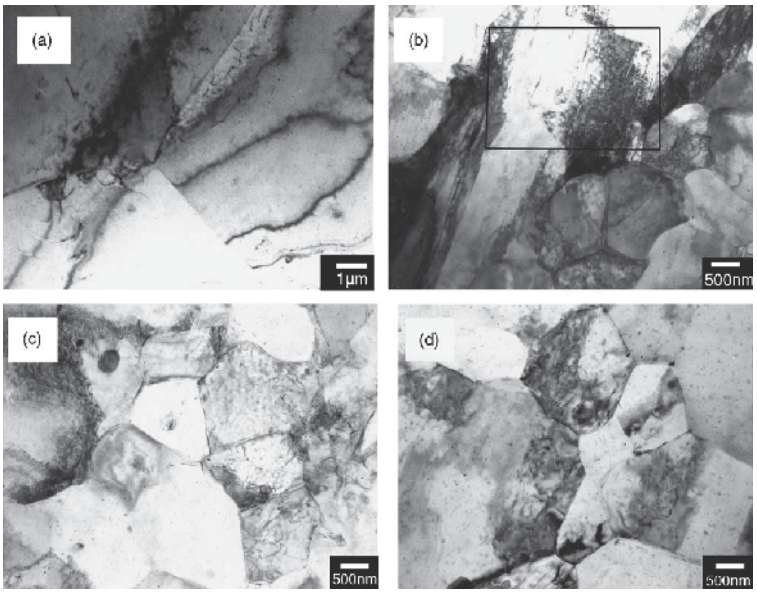

Fig. 11. TEM photographs of as-extrusion and ECAP AZ31 alloy, (a) as-extrusion, (b) ECAP one pass at 498 K, (c) ECAP four passes at 498K and (d) ECAP eight passes at 498 K.

compounds at Mg grain boundaries at room temperature, while zirconium crystals are also concentrated at the grain boundaries (Avedesian et al., 1999). After 8 passes of ECAP, the structure is formed by large particles or large long grains with 70μm in length, and ultrafine grains or particles (about 1μm in diameter). The large long grains take more percentage compared with ultra-fine grains in the 8-passes sample. Obviously, DRX of Mg alloys plays a key role in refining grains into sub-micrometer range. The more the pressing pass, the higher the degree of deformation and the greater the amount of recrystallization finished. After 16 passes of pressing, the microstructure of this alloy shows ultrafine Mg grains but includes a few large particles with 5-8μm in size. As increasing the ECAP passes to 32, this alloy possess a complete recrystallization microstructure, which is more uniform with average grain size of about 1.5μm and no large particle or large grain is found. With further ECAP processing at the same temperature, grain size remains stable.

Accumulative roll bonding is also proved to be an efficient and inexpensive grain refinement method for Mg-Al-Zn alloys (Perez-Prado et al., 2004) . The final grain size obtained is similar to that achieved by other SPD techniques such as ECAP (Mabuchi et al., 1999). Increasing the Al content results in finer microstructures, albeit more heterogeneous. Several examples of the beneficial effects of precipitation in the stabilization of ultrafine grains via SPD are given in the literature ([b] Furukawa et al., 2001). Second, a larger Al content in solution retards the movement of dislocations, hindering recovery, and this may also result in finer grains. Thus, the homogeneity of the microstructure can be improved by increasing the number of rolling passes.

Grain orientation distribution (texture) plays an important role in improving mechanical properties of the hexagonal metals and alloys (Mukai et al., 2001; Agnew et al., 2004),because these materials usually have quite high plastic anisotropy in their single crystals. Thus the textures in the hexagonal alloys after the ECAP processing were investigated carefully. It is known that moderate to strong level of complex textures can be

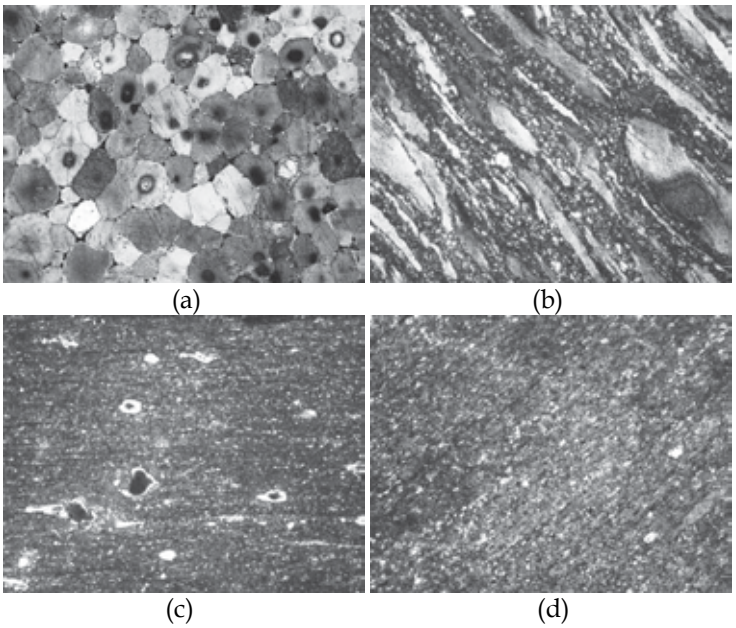

Fig. 12. Optical microstructures of the ZE41 alloy before and after ECAP: (a) as-cast alloy; (b) 8 passes; (c) 16 passes; (d) 32 passes of pressing.

induced during various deformation routes available in ECAP (Ferrase et al., 2004) . Liu et al. (2004) reported that ECAP can not only refine the grain size, but also modify the texture type of the Mg–3.3%Li alloy. Two quite different and strong textures are formed in the Mg–3.3%Li alloy after the two ECAP processes with the routes A and Bc (see in Fig.13). Recrystallization occurs during both the ECAP processes, but the extents of recrystallization are different for route A and Bc. The combined effect of grain refinement and texture modification caused by ECAP can improve the strength and ductility of the alloy simultaneously.

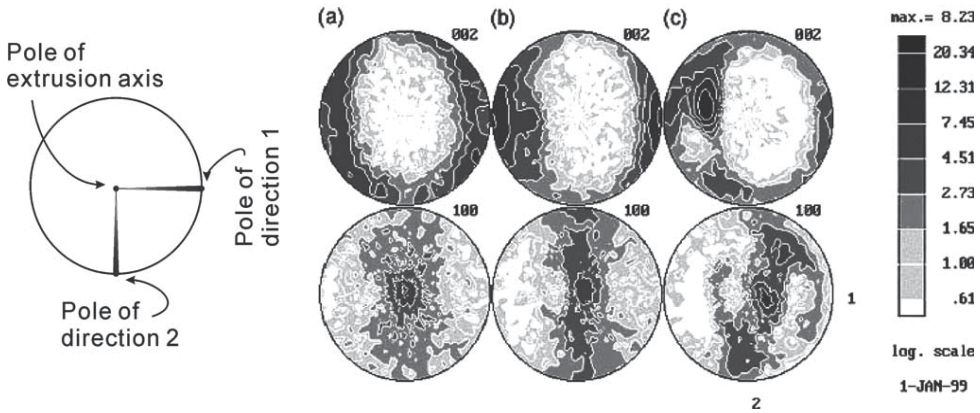

Fig. 13. (002) and (100) pole figures of Mg-3.3%Li alloy for (a) conventionally extruded samples, (b) 4-passes ECAP by A routes and (c) 4-passes ECAP by Bc routes (Liu et al.,2004).

Del Valle et al.(2006) reported that the texture and grain size has a great influence on work hardening and ductility of polycrystalline Mg alloy after SPD process. In addition to the direct effect of texture through the change in the orientation factor for basal and prismatic slip, effects were found on dynamic recovery and the appearance of stage II of work hardening. Dynamic recovery is enhanced with increasing deviation of the basal planes from the ideal orientation. The grain size refinement causes a strong decrease in the hardening rate due to a contribution of grain boundary sliding to deformation.
Recently, Gan et al.(2009) presented the texture evolution in pure Mg for ECAP processing between one and four passes, along with the associated pole figures. Yapici et al. (2009) investigated the texture evolution of four different hexagonal close packed materials (pure Zr, pure Be, AZ31 Mg alloy and Ti-6Al-4V) after varies passes of ECAP. The resulting textures demonstrated a common feature where the basal poles were aligned along the most highly elongated direction of the sheared grains. Their texture evolutions is striking similar, irrespective of the initial material properties (c/a ratio, impurity content, grain size, texture) and processing conditions. It is suggested that basal slip acts as the common plasticity mechanism leading to the similar texture evolutions. Therefore, UFG Mg alloys with optimum mechanical properties can be realized faster by reducing-cost processing experiments and texture measurements.

3.2 Enhanced mechanical properties by SPD processing

Grain refinement is an effective method to improve mechanical behaviours of Mg alloys at room temperature (Valiev et al., 2000; Zheng et al., 2008), because Hall–Petch slope in Mg alloys is very pronounced (210±60 MPa $\mu m^{1/2}$ vs. 115 MPa $\mu m^{1/2}$ in Al alloys) (Jones et al., 1998). However, the studies on the effect of grain size on the properties of ECAPed Mg-Li alloys indicate that the UFG alloys exhibit the inverse Hall–Petch relation (Kim et al., 2009), due to a transition from power-law breakdown (grain boundary diffusion-controlled GBS) to a grain-size-independent mechanism (pipe diffusion-controlled slip creep). An interesting ductility enhancement at room temperature in UFG Mg alloys has been attributed to the texture changes produced by SPD (Mukai et al., 2001). Obviously, both grain refinement and texture modification have great influence on mechanical properties in Mg alloys (Agnew et al., 2004) .
Tong et al. (2009) investigated mechanical properties of UFG Mg–5.12 wt.% Zn–0.32 wt.% Ca alloy produced by 4-passes ECAP at 250°C (average grain size : 0.7μm) . The ECAPed alloy exhibited lower yield stress and ultimate tensile strength at room temperature, indicating that the texture softening effect was dominant over the strengthening from grain refinement. The ductility of the ECAPed alloy was increased to 18.2%, and the grain refinement caused an obvious decrease in work hardening rate. The elongation was improved in the ECAPed Mg–Zn–Ca alloy with lower work hardening, which was different from some ECAPed Mg alloys with grain size larger than 2μm. These alloys showed high elongation with high work hardening rate (Agnew et al., 2004; Ko et al., 2006). This suggested that grain size plays a major role in the strain hardening behavior of ECAPed Mg alloys compared with the texture effect. The improved tensile elongation in the ECAPed alloy may be attributed to non-basal slip and grain boundary sliding (GBS), in addition to basal slip. [a] Koike et al.(2003) reported that non-basal slip was induced in fine grained Mg alloys by compatibility stress that operated to maintain continuity at grain boundaries. Thus, the activity of non-basal slip near grain boundaries would be helpful for the

improvement of ductility in the ECAPed Mg alloy. GBS was observed to occur at room temperature in AZ31 alloy with average grain size of 8μm, and the ratio of the strain by GBS to total strain is about 8% ([b] Koike et al.,2003). Therefore, the GBS might be also responsible for deformation of the ECAPed alloy at room temperature.

Ma et al. (2009) found that ECAPed ZE41A aeronautic Mg alloy for 8 passes at 603K has higher tensile strength but relatively lower ductility than the unpressed sample from room temperature to 423K (see in Fig.14), whereas the tensile yield strength, ultimate strength, elongation to failure of UFG alloy after enough passes are all remarkably increased (about 120% higher in yield strength and 75% larger in elongation at RT after 32 passes). The UFG Mg alloy pressed at elevated temperature underwent DRX, resulting in more uniform

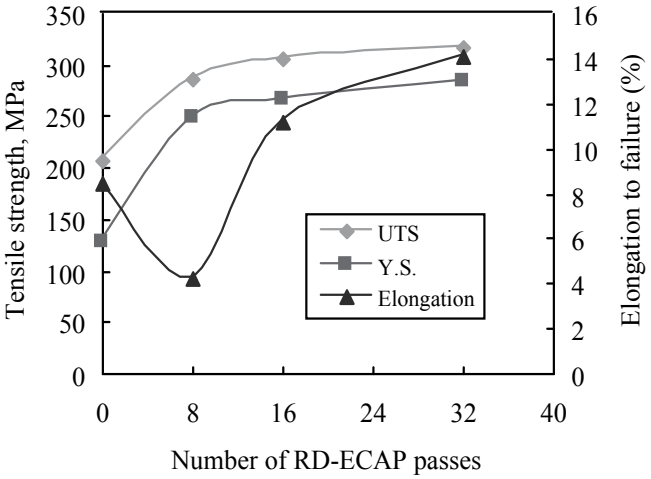

Fig. 14. Tensile strength and plasticity of ZE41A Mg alloy at room temperature as a function of the number of ECAP passes:

α phase with average grain size of about 1.5μm. The simultaneous improvement of its strength and ductility at service temperature was due to higher fraction of high-angle grains boundaries combined with a low dislocation density.

The high fraction of HAGB introduced by SPD make microstructure of UFG Mg alloy conducive to the occurrence of GBS and thus to the advent of superplastic flow. It was shown in Fig.15 that the 1%Ca-AZ80 Mg alloy produced by HRDSR (average grain size: 0.8μm) exhibits a maximum elongation of ~ 700% at $0.3\times10^{-3}s^{-1}$ at 523K(Kim et al., 2010). Excellent low-temperature superplasticity (<573K) was also observed in the ECAPed Mg alloys: elongations to failure are 810% and 570% at a strain rate of $3\times10^{-3}s^{-1}$ for ZK60 and AZ91 alloys, respectively (Chuvil'deev et al., 2004). These results confirm the potential for utilizing SPD processing in achieving exceptional superplastic ductilities with the SPD-processed ultrafine microstructure. Currently, superplastic metals are formed industrially within the strain-rate range of $\sim10^{-3}$ s^{-1} to $10^{-2}s^{-1}$. Since the strain rate is proportional to $(1/d)^2$, it is apparent that SPD processing and production of bulk UFG Mg alloy has the potential of achieving very rapid superplastic flow and thereby substantially reducing the forming times in industrial operations.

The fatigue properties are key features for a successful use of UFG Mg alloys. Fine-grained materials are known to exhibit a lower resistance of fatigue crack growth. Because the

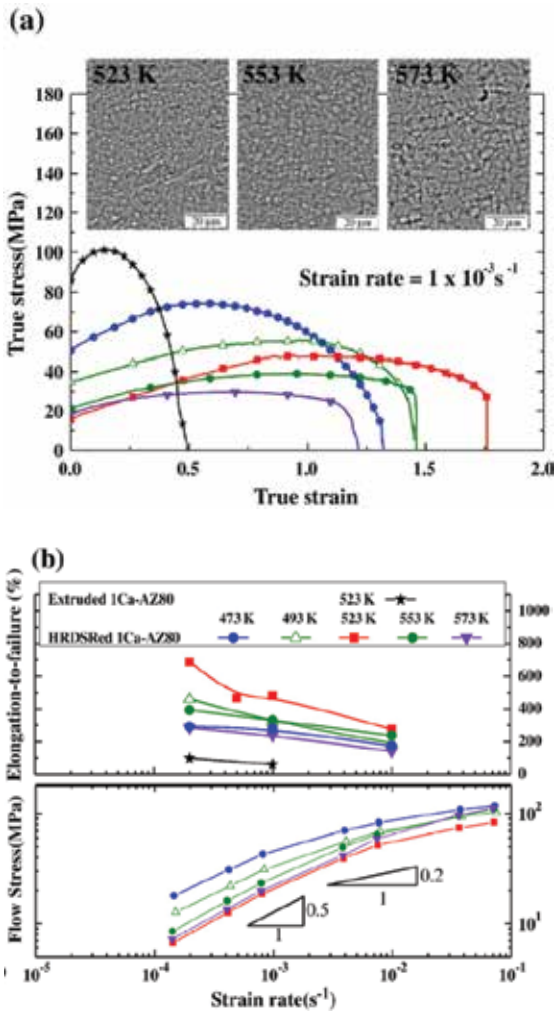

Fig. 15. (a) True stress—true strain curves for the extruded and HRDSRed 1Ca-AZ80 Mg alloy at $1\times10^{-3}s^{-1}$ at various temperatures. The insert presents the HRDSRed microstructures taken before the tensile loading at the three temperatures. (b) [Top] Tensile elongation of the extruded and HRDSRed alloys as a function of the strain rate at various temperatures [Bottom] The SRC results for the HRDSRed alloy at temperature ranges of 473K-573K.

plastic deformation zone in the fine-grained materials is normally larger than the grain size, a reverse slip of the dislocations during unloading is often impossible so that the accumulation of damage is large during cycling (Suresh et al., 1998) . However, Kim et al. (2005) found that ECAPed AZ31 Mg alloy exhibited a lower crack growth rate and lower fatigue limit than the coarse grained counterpart (see in Fig.16) unlike other UFG materials which have a lower threshold and higher fatigue crack growth rates (Vinogradov et al., 1999; Kim and Choi et al., 2003). It seems that enhanced ductility due to grain refinement in the ECAPed AZ31 alloy resulted in increasing crack growth resistance because of its better ability to accommodate plastic strains during cycling. Higo et al. (1981) observed a $d^{-1/2}$ dependence of crack propagation threshold (ΔK_{th}) for copper alloys. Therefore, the

influence of grain size on the fatigue properties of UFG materials seems to be very complex due to the interaction between several intrinsic and extrinsic factors. Zúberová et al. (2007) also reported that the fatigue lifes of ECAPed AZ31 alloy (average grain size of about 1 to 2μm) are superior to that of the squeeze-cast alloy in the low-cycle and high-cycle regions.

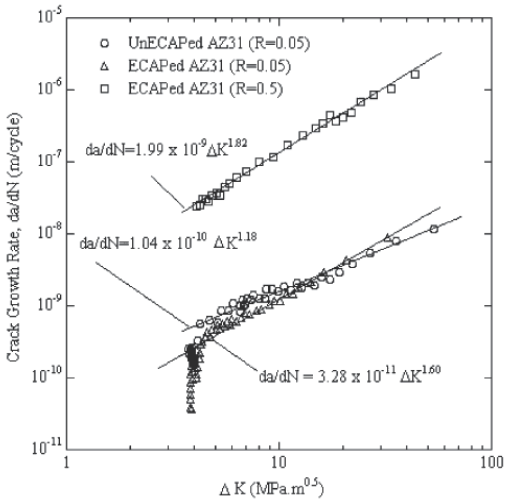

Fig. 16. A comparison of fatigue crack growth behavior of the unECAPed and ECAPed AZ31 alloys.

3.3 Deformation mechanism of SPD-produced UFG Mg alloys

The unique mechanical properties of SPD-produced UFG Mg alloys are attributed to their unique deformation mechanisms different from their coarse-grained counterparts. The deformation mechanisms include full dislocation and partial dislocations slip, deformation twinning, wide stacking faults, grain-boundary sliding and grain rotations. The activation and signification of each mechanism depend on intrinsic material properties (such as stacking-fault energy and shear modulus), structural features (such as grain size) and external factors (such as SPD temperature and applied stress). With decreasing grain size, full dislocation slip decreases but partial dislocation emits from grain boundaries become significant (Zhu et al., 2003; Yamakov et al., 2004). A transition from twinning to slip dominated flow is found for grains sizes less than a few micrometers (Zheng et al., 2008). Moreover, GBS and grain rotation may become significant deformation mechanism, leading to abnormal Hall–Petch relationship.

Table 1 summarizes the microscale deformation mechanism that have been inferred or identified in ECAPed Mg alloys. The initial texture had the effect of increasing the non-basal activity. Kim et al (2003) noted a decrease from an initial axisymmetric texture of 7.0mr (multiply random) in AZ61 Mg alloy to 5.6mr after first pass and then to 2.8mr after second pass. Agnew et al.(2005) showed that texture development in ECAPed AZ31 evolved differently depending on their initial extruded texture. Basal, prismatic or some combination of the two are most dominant in the first pass, and pyramidal <c+a> and twinning are less so. One plausible reason for the common features in the one-pass hcp textures is the predominance of <a>-slip.

Materals	ECAP processing				Deformation mechanism	Reference
	T/°C	Φ/ψ	Passes	routes		
AZ31	200,300	90°	1-4	A	basal,prismatic, pyramidal<c+a>	Agnew et al., 2005
ZK60	260-325	90°	1-4	A	basal,prismatic, pyramidal<c+a>	Agnew et al., 2005
WE43	260-325	90°	1-4	A	basal,prismatic, pyramidal<c+a>	Agnew et al., 2005
Mg-4Li	260	90°	1-4	A	basal,prismatic	Agnew et al., 2005
AZ31	200	90°/37°	1st		basal,prismatic, tensiling twinning	Yoshida et al., 2003
AZ31	250	90°/37°	1st		basal,pyramidal<c+a>	Yoshida et al., 2003
AZ61	275	90°/30°	8	Bc	basal,prismatic	Kim et al., 2003
Mg-3.3%Li	250	90°	4	Bc	basal,prismatic, pyramidal<c+a>	Liu et al.,2004

Table 1. Recent studies on microscale deformation mechanism in ECAPed Mg alloys .

The deformation modes are high dependent on the temperature and alloys. Increasing the temperature can alter the type of deformation mechanism (such as from twinning to slip), the relative activity of these mechanism and the fraction of recrystallized grains. During high-temperature ECAP processing, the differences between the critical resolved shear stresses (CRSS) of the basal slip and those of the nonbasal slip modes are lower. Therefore, it is possible that prismatic and <c+a> pyramidal modes are activated, in combination with basal slip, producing observable changes in texture evolution after the first pass. [a] Agnew et al.(2005) found that both initial texture effects and alloying had large effects on texture evolution of various Mg alloys. Two alloys (AZ80 and AZ31) with similar solid-solution Al content but different initial textures had the same texture evolution dominated by basal slip, while Mg-4Li alloy had a different one-pass texture due to the non-basal activity promoted by Li. As shown in Table 1, deformation mechanisms of ECAPed Mg alloys will also be highly dependent on processing routes and passes. Each route has a different "entry" texture that may invoke different deformation modes. With increasing the ECAP pass, twinning will not be favoured over slip due to the combination of grain refinement and high processing temperature. A dislocation process with possibly some fine-scale twinning at grain boundaries must be the primary deformation mechanism at room temperature for UFG Mg alloys.

Due to the low-symmetry crystal structure, a grain in Mg alloys needs to call up a combination of several possible slip or twinning modes to accommodate deformation. The choice depends heavily on their crystallographic orientation. Unlike cublic materials (fcc and bcc), not every hcp material uses the same set of slip and twinning modes. For the same orientation, one type of hcp crystal would use one or two slip modes, while another type would use a combination of twinning and slip (Beyerlein & Tóth, 2009). Zheng et al.(2008) found that the compressive stress–strain curve of an ECAPed Mg–Zn–Y–Zr alloy includes a short region with high strain hardening rate, followed by a long steady state region with

very low strain hardening rate (see Fig.17a) . The grain size is significantly refined and the basal planes are inclined about 45° to the extrusion direction. These effects may impede the activation of $\{10\bar{1}2\}$ twinning in compression. The reduced grain size may be the most important cause for the suppression of twinning, because the twinning stress increases with decreasing grain size. Fig. 17(b) shows a typical microstructure of the ECAPed Mg alloys after a compressive true strain of 0.6 at a strain rate of 1.67×10^{-3} s^{-1} at 423 K. No visible twins indicated that at lower strains, plastic flow is dominated by dislocation motion. The suppression of twinning may also result in low strain hardening. In addition, the UFG structure of the ECAPed alloy is scarcely modified after compression to higher strains. This may be due to the restriction of grain growth by the dispersion of fine I-phase (quasi-crystalline icosahedral phase) and precipitates in the alloy. The enhanced strain rate sensitivity, low strain hardening rate of the ECAPed alloy together with the microstructures after compression indicate that different deformation mechanisms are active in the UFG ECAP-processed and as-extruded alloy. They may include thermally activated climb-controlled annihilation of lattice dislocations in or near grain boundaries (May et al., 2005) as well as GBS and Coble creep.

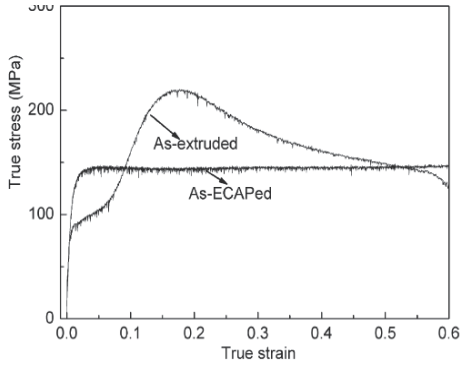

(a)

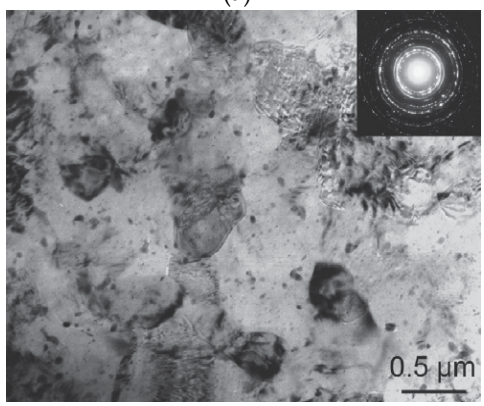

(b)

Fig. 17. (a) Compressive true stress–true strain curves at a strain rate of 1.67×10^{-3} s^{-1} at 423K for the ECAPed and extruded Mg-Zn-Y-Zr alloys. (b) Microstructure of the ECAPed alloy after compression (The insert presents the diffraction pattern taken with a 9μm aperture).

Special mention should be made of GBS as another possible deformation mechanism in UFG Mg alloys. When the grain size is very small, GBS has been predicted to be a deformation mechanism by MD simulations (Meyers et al.,2006). This mechanism was reported in pure Mg with a fairly large grain size of about 1 mm at room temperature by Hauser et al. in 1956. Later, Gifkins and Langdon (1964) analyzed the possibility of GBS at room temperature in Mg and Mg alloys with grain sizes of 100-300μm. They claimed that GBS does not occur at room temperature and that the step formation was due to different amounts of shear localized in neighboring grains. In contrast, Koike et al.(2003) have recently reported the occurrence of GBS at room temperature in d = 8 μm AZ31 alloy, and determined the strain contribution by measuring the displacements of marked lines at the surface. The ratio of GBS strain to total strain was estimated to be near to 8%. Kim et al. (2009) also observed deviations from the Hall–Petch relationship in Mg-Li alloy with a grain size of 1 μm and proposed the negative slope observed in the Hall–Petch plot is related to transition from pipe diffusion -controlled slip creep to grain boundary diffusion-controlled GBS. The critical grain size associated with abnormal Hall–Petch behavior is predicted to vary depending on the strain rate and diffusivity.

4. Corrosion resistance of SPD-processed Mg and Mg alloys

Grain refinement is proved to be favorable to improving mechanical properties of pure Mg and its alloys, but the precise effect of grain size on corrosion at a fundamental level is not widely understood. There is only limited attention that is focused on electrochemical properties of SPDed Mg and its alloys. As well known, the standard electrode potential of Mg (-2.37 V_{NHE}) is the lowest among metallic elements, and thus Mg and its alloys have poor corrosion resistance in comparison with other conventional metallic structural materials. This shortcoming limited their industrial applications (Jönsson et al.,2007; Ambat et al., 2000), therefore particular attention should be paid to corrosion resistance improvement of Mg and its alloys in aggressive environments (e.g. Cl^--containing aqueous media). Their low corrosion resistance in aqueous media are mainly related to high permeability and low stability of Mg hydroxide film (Nordlien et al., 1997), and high sensitivity of Mg to impurities and alloying elements that promote internal galvanic attacks (Volovitch et al., 2009) . Recent related work in the authors' group has shown that the corrosion rate of ECAPed pure Mg was increased in NaCl aqueous solution but UFG ZE41A alloy by ECAP had slower corrosion rates compared to coarse grained one (Song et al., 2010; Jiang et al., 2009). The outcomes of such work indicated that grain refinement by SPD, in some cases, was beneficial to reduced corrosion resistance. The provenience of a particular grain structure is of crucial importance and that there are factors other than the grain size that control corrosion response. Herein, the corrosion of SPDed Mg and its alloys are focused in order to address a critical fundamental knowledge gap in the assessment of Mg corrosion as a function of grain size and grain character.

4.1 Corrosion characteristics of UFG pure Mg

Recently, the potential effect of grain size on corrosion of pure Mg was investigated by processing the UFG specimens using ECAP and surface mechanical attrition treatment (Birbilis et al., 2010; Song et al., 2010). Some relevant prior works indicated that significant variation in corrosion rate depend on decreasing grain size when used individual mechanical processing techniques, while no clear trend in the dependence of corrosion properties on the grain size when examined independently of mechanical processing.

Song et al.(2010) found that the ECAPed pure Mg after 6 passes at 573K, compared with as-cast one (800~1500 μm), obtained finer grains (50~100 μm) but was fined slightly with further pressing. The strain-induced grain refinement with more crystalline defects weakened corrosion resistance of pure Mg, resulting in more and deeper pits after in-situ corrosion, higher mass-loss rate immersed in NaCl solution, larger *I*corr values in polarization curves and lower fitted *R*t values in EIS plots. However, the enhanced initial open-circuit-potential (OCP) values indicate better weather resistance. Furthermore, corrosion improvement can be expected by reducing defects via subsequent annealing.
Op'tHoog et al.(2008) investigated corrosion behaviors of pure Mg produced by a variety of mechanical or thermo-mechanical processes and annealed at 250 °C. Fig. 18 presents the average grain sizes as a function of annealing time and corrosion current versus grain size for pure Mg. For the cast specimens, a weak linear decrease in corrosion current with decreasing grain size was found. SMAT process is believed to induce an extremely high free energy state in the near-surface region , resulting in an increased corrosion current response despite decreasing grain size. Overall, the ECAPed specimens exhibit better corrosion

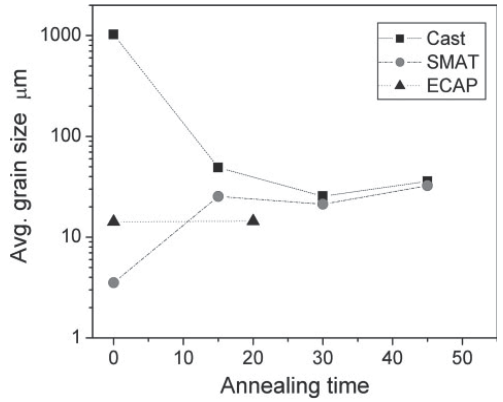

(a)

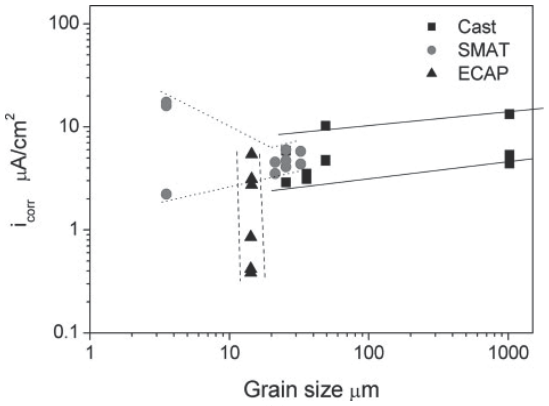

(b)

Fig. 18. (a) Average grain sizes as a function of annealing time for pure Mg (in minutues). (b) Corrosion current versus grain size for pure Mg (Data sets have been grouped according to processing method). (Op'tHoog et al. 2008)

resistance with notably lower values of *i*corr, compared with that of the SMATed and as-cast specimens. The distinct difference in corrosion behavior strongly indicated that grain size may not be the only factor in tailoring corrosion properties through thermo-mechanical processing. Recently, A hypothesis was given that the increased density of grain boundaries with high misorientation, formed during continued ECAP processing, can promote a more coherent oxide (Birbilis et al.,2010).

The natural oxide layer of Mg is not stable in aqueous solutions (below about pH 11) and easily crack owing to high compression stresses within the oxide layer (geometrical mismatch with respect to the hexagonal Mg lattice) (Kainer et al, 2003). By deliberately introducing a large volume fraction of grain boundaries in the bulk material, the mismatch may be diminished with the development of a more coherent, uniform and protective file on Mg surface. Potentiodynamic polarisation data (Op'tHoog et al., 2008), collected upon Mg specimens in various conditions, suggested that ECAP treatment simultaneously lower the anodic and cathodic kinetics, thus improving the surface oxide quality by modifying the substrate structure of Mg. For SMATed specimens, the surface film quality is not improved due to increased LAGB density via a peening mechanism and massive residual stresses. Recent studies suggest that major residual stresses are detrimental to electrochemical behavior (Uhlenhaut et al., 2009).

We would like to emphasise that there is a lack of literature on purely microstructural effects on corrosion of SPDed Mg, particularly in the absence of alloying elements. If the grain structure is varied with isolated effects of chemistry, the potential effect of grain size on corrosion could be determined. General speaking, electrochemical response of Mg can be controlled through microstructural variations via SPD procedures. For improving corrosion resistance of pure Mg, the provenience of a particular UFG structure is of crucial importance. And the high fraction of HAGB and the low residual stress (surface free energy) in UFG Mg can also be expected, which depends sensitively on the SPD processing.

4.2 Corrosion behaviors of UFG Mg alloys

UFG Mg alloys processed by SPD method are potentially attractive since they exhibit higher strength and better ductility in comparison with their coarse-grained counterparts. However, electrochemical properties of SPDed materials have received only limited attention and the effect of grain size on corrosion behavior of UFG Mg alloys is not widely understood. Alloying elements and its distribution have also great effect on electrochemical responses of UFG Mg alloys . Therefore, particular attention should be paid to the relationship between corrosion behavior and microstructure changes of UFG SPDed Mg alloys with various alloying elements to meet the needs of structural applications.

Hamu et al. (2009) investiged the relation between microstructure and corrosion behavior of ECAPed AZ31 Mg alloy for 4 passes at 350˚C. All the electrochemical measurements were performed in 3.5% NaCl saturated with $Mg(OH)_2$ with a pH 10.5 , at which Mg can cover itself with more or less protective oxide or hydroxide which inhibits the dissolution reaction. After initial ECAP passes, the "bimodal" microstructure with coarse grains surrounded by fine ones was observed. The grain structure, however, became visibly uniform with further ECAP deformation. The average grain size was considerably reduced from over 30 μm (as-received) to below 10μm. Clearly, processing at a temperature well above 0.5 *T*m was more effective and this might be attributed to the suppression of DRX and grain growth. TEM observation showed that the density of the dislocations in the ECAPed alloys (extrusion

ratio 98.99%) increases significantly around small second phases (average size of 150 nm) and grain boundaries, and there apparently existed lots of twins (see Fig.19). Although the grain size after ECAP process was similar to the grain size after conventional extrusion (extrusion ratio 91.34%), a sharp increase in the corrosion rate and relatively less noble behavior for the ECAPed AZ31 are caused due to a higher density of dislocation and twins, i.e relatively higher deformation energy. The corrosion resistance of AZ31 Mg alloys following conventional extrusion was increased due to smaller grain size in comparison to that as received one (see Fig.20). Therefore, once fully recrystallized structured are formed with increasing the pass number of ECAP, the electrochemical potential of the Mg matrix may be nobler with decreasing the anodic dissolution due to the lower dislocation density.

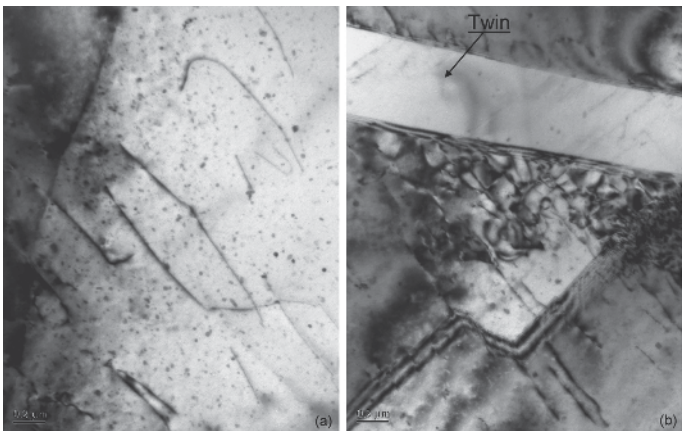

Fig. 19. Typical microstructures of the ECAPed AZ31 alloy for 4 passes at 350˚C (extrusion ratio 98.99%). (a) dislocation arrangements; (b) structure of the twins. (Hamu et al., 2009)

Our recent studies proved that significant grain refinement has beneficial effect on corrosion resistance of ZE41A Mg alloy through a large number of ECAP passes (Jiang et al., 2009). After ECAP over 16 passes at 603K, ultrafine equiaxial grains (about 2.5μm) were obtained with homogeneously dispersed fine secondary particles (about 5-8μm) due to plastic-induced grain refinement accommodated by DRX. The ECAPed sample had lower corrosion susceptibility with increasing ECAP passes (see Fig.21).The lower corrosion current density and nobler corrosion potential correlated with large number of pressing passes were attributed to the low tendency toward localized corrosion after homogenization of broken secondary phase on ultra-fine grained Mg matrix. Fig.22 exhibits SEM micrographs of the corroded surface of ECAPed ZE41A alloy immersed in 35g/L NaCl for 30min. Obviously, there are micro-crackings on the corroded surface of the 8-, 16-, and 32-pass samples, probably due to the presence of residual internal stress. The 60P-passes sample appears to be more resistant to corrosive attack, because the complete DRX of the deformed microstructure reduces the tendency toward stress corrosion cracking and pitting. It is well known that DRX decreases the residual internal stress and intragranular dislocation density of the deformed microstructure and leads to the presence of higher fraction of HAGB. The residual internal stress in ECAPed sample is adverse to partial protective layer adhered on Mg matrix, therefore it should be eliminated as complete as possible. It means that the percentage of DRX has great effect on corrosion resistance of UFG ZE41A alloy with fine and homogeneous secondary particles.

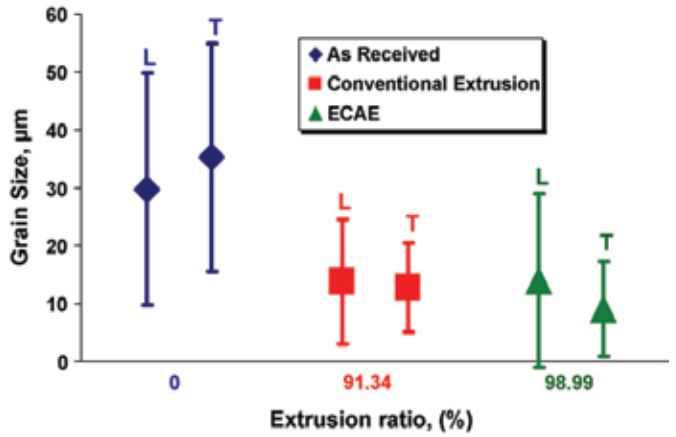

(a)

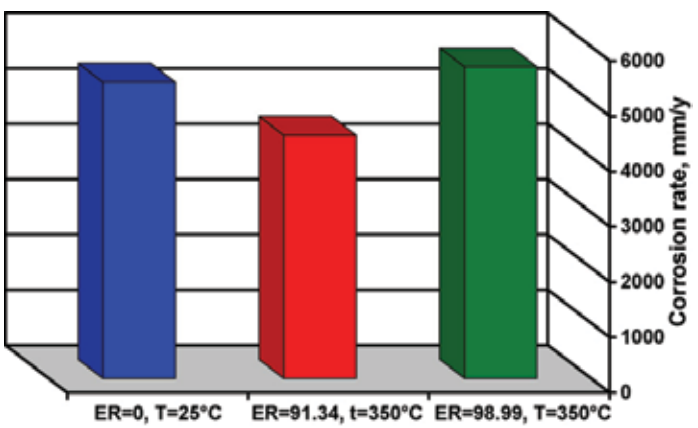

(b)

Fig. 20. Variation in grain size (a) and corrosion rate (b) of AZ31 Mg alloy in different extrusion ratios(ER). (Hamu et al. , 2009)

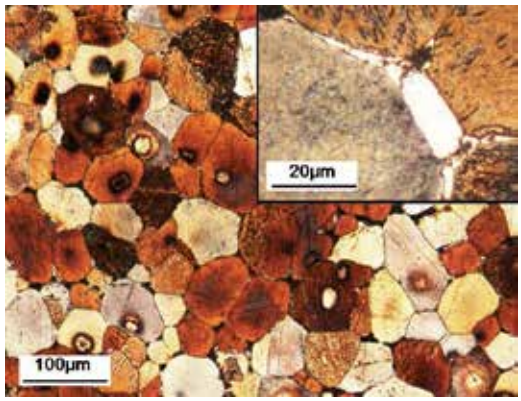

(a)

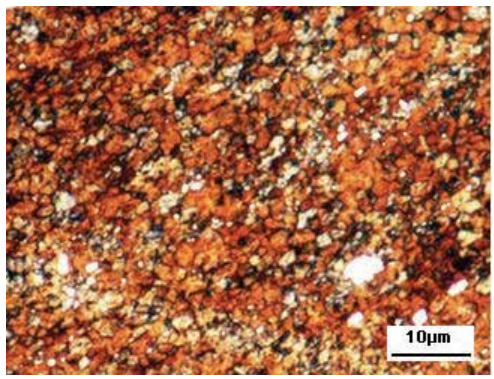

(b)

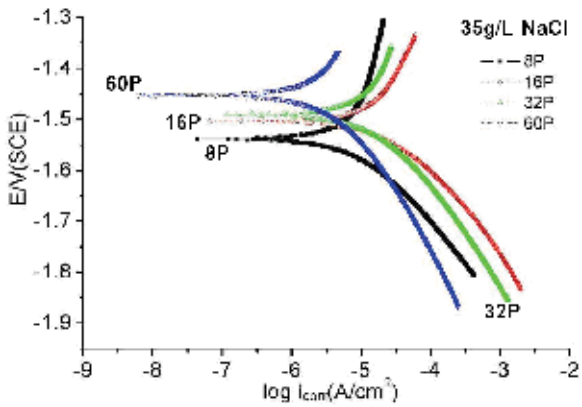

(c)

Fig. 21. Micrographs and potentiostatic polarization curve of ZE41A Mg alloy. Optical microstructure for (a) as-received one and (b) after 32 passes ECAP; (c) polarization curve of ECAPed alloy in 35g/L NaCl aqueous solution.

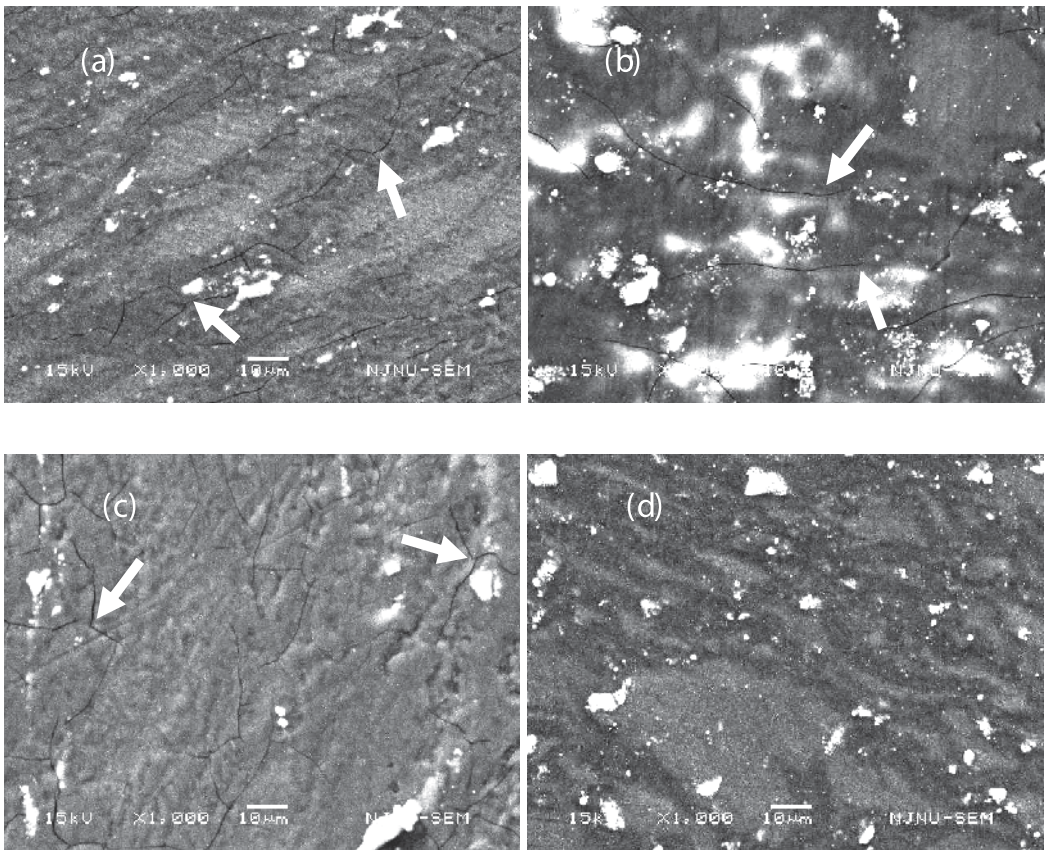

Fig. 22. SEM surface morphologies of the ECAPed ZE41A with various passes after 30 min immersion in 35g/L NaCl solution: (a) 8passes, (b)16passes,(c)32passes, and (d) 60passes.

In general, ECAP is effective in improving the corrosion resistance of Mg-based alloy. Large number of ECAP pass within the temperature range of DRX is necessary to obtain UFG structure with low dislocation density and residual internal stress, thus leading to low anodic dissolution. Otherwise, internal galvanic corrosion attack on Mg alloy is strongly influenced by the distribution and morphology of secondary phases.The enhanced corrosion resistance of UFG ZE41A Mg alloy proves that enough passes of ECAP within the temperature range of DRX can endow UFG bulk alloy with higher resistance to electrochemical attack besides exceptional mechanical advantages. It means that fabricating UFG materials by SPD method can be developed a new strategy for improving the comprehensive properties of structural materials. The UFG Mg alloy processed by ECAP method is attractive for some potential applications.

4.3 Criteria for optimizing the corrosion resistance

Based on the fundamental aspects of the corrosion behaviours of SPDed Mg alloys, attempts to enhance the corrosion resistance of UFG Mg-based materials must therefore aim at enhancing the homogenization and stability of UFG microstructures, reducing residual stress and dislocation density, and at the same time, improving the corrosion prevention of

the natural passivated layer on Mg substrate. In detail, the following points are considered to play an important role:

a. Stability and homogenization of UFG microstructure.

Although a fundamental knowledge of corrosion behaviour varied with the individual microstructures of Mg alloy is still lacking, recent studies present that UFG microstructure with high fraction of HAGB, low residual stress and intragranular dislocation density is advantageous to the electrochemical behaviour. In order to achieve the optimum corrosion resistance, the fully recrystallized structure without grain growth is expected during SPD. The microstructure stability is strongly affected by SPD process parameters, in particular by the route and pass number of ECAP and the amount and the kind of impurities of the Mg alloys used. Uniform distribution of fine secondary particles may inhibit significant grain growth of the matrix phases of Mg alloys SPD-processed at the temperature range of DRX and reduce the tendency toward localized corrosion, thus resulting in relatively high corrosion resistance. It means that suitable annealing treatments have a positive effect on the corrosion behaviour of UFG Mg alloy after initial passes ECAP, while a large number of ECAP can enhance the corrosion resistance due to a complete recrystallization of the UFG microstructure. Introducing fine and homogeneous secondary particles is crucially important to inhibit the grain growth during SPD, resulting in the formation of UFG microstructure with low residual stress and high fraction of HAGB.

b. Production of stable protective layer

In moist air, Mg-based materials naturally tend to form a thin passivated layer, which consists mainly of $Mg(OH)_2$ and hydrated oxide components of alloying elements. Judged by the Pilling-Bedworth ratio, the natural passivated layer on Mg alloy is no dense and cannot protect the metal in the long term due to geometric mismatching. However, satisfactory surface protective layer is capable to be formed on the UFG Mg containing alloying elements such as Al, Zn and rare earth. These elements exercise a positive influence on the corrosion stability of the surface of Mg, which effect on corrosion response of SPDed Mg should be throughly investigated. Recent studies present that the improved corrosion resistance seems to arise from rapid formation of passive films due to an increase in grain boundaries and dislocations in the UFG materials, but no impurities segregated to grain boundaries.

5. Summary and outlook

Several new trends in SPD processing for fabrication of bulk ultrafine-grained Mg alloys have been presented in this chapter, based on recent results in a global world. Presently new tasks, connected with economically feasible production of UFG Mg alloys, started to be solved through decreasing the material waste, obtaining homogeneous structure and advanced properties in bulk billets and products. Although ECAP is an effective route to UFG billets by imparting large shear strains, the conventional process has some limitations for commercialization. Studies focused on continued ECAP technique of bulk UFG Mg alloys, as well as their structural features and potential for obtaining extraordinary properties, are of special interest.

Because of their small grain sizes, UFG Mg alloys after SPD processing exhibit high strength and ductility, superplasticity, enhanced corrosion resistance, and other attractive properties. Microstructure characteristic and principal properties of bulk UFG Mg alloys processed by

various SPD procedures are briefly surveyed, with emphasis on their mechanical properties and corrosion behaviour after ECAP procedure. Our focus is on the effect of the grain size on intrinsic mechanical and corrosion response of UFG Mg alloys, without paying detailed attention to subtle microstructural differences in these materials. It appears that more systemic studies are needed to tailor the ECAP-processing conditions for obtaining microstructures favourably affecting mechanical properties and corrosion resistance. To obtain the benefit of the high strength and good ductility of UFG Mg alloy, a through understanding of their deformation models is imperative but also challenging. Despite years of research, a consensus on the deformation mechanism of UFG Mg alloy processed by SPD has not yet been reached. Partial dislocation emission from grain boundaries and grain-boundary sliding may become significant deformation mechanism with decreasing grain size, resulting in significantly increasing ductility and strength. As concerns the corrosion resistance of UFG Mg, these seem to be also enhanced in comparison to their coarse-grained counterparts, although the extent of the improvement clearly depends on the processing methods. The interior dislocation and HAGB densities in UFG Mg alloy play an important role in oxide formation and corrosion susceptibility, which potential effect on corrosion should be determined. Anyway, fabricating UFG materials by SPD method can be developed a new strategy for improving the comprehensive properties of structural Mg-based materials, which are attractive for some potential, marketable applications.

6. References

Agnew, S.; Horton, J.; Lillo, T. & Brown. D. (2004) Enhanced ductility in strongly textured Mg produced by equal channel angular processing. *Scripta Mater.,* Vol. 50, (Febr. 2004) Pages 377-381, ISSN: 1359-6462.

[a] Agnew, S.; Mehrotra, P.; Lillo, T.; Stoica, G. & Liaw, P. (2005). Texture evolution of five wrought Mg alloys during route A equal channel angular extrusion: Experiments and simulations. *Acta Mater.*, Vol. 53, (June 2005) Pages 3135-3146, ISSN: 1359-6454.

[b] Agnew, S.; Mehrotra, P.; Lillo, T.; Stoica, G. & Liaw, P. (2005) Crystallographic texture evolution of three wrought Mg alloys during equal channel angular extrusion. *Mater. Sci. Eng. A*, Vol. 408, (Nov. 2005) pages 72–78, ISSN: 0921-5093.

Alkorta, J.; Rombouts, M.; Messemaeker, J. ; Froyen, L. & Sevillano J. (2002). On the impossibility of multi-pass equal-channel angular drawing. *Scripta Mater.,* Vol. 47, (July 2002) Pages 13-18, ISSN:1359-6462.

Ambat, R.; Aung, N. & Zhou, W. (2000). Evaluation of microstructural effects on corrosion behaviour of AZ91D Mg alloy. *Corros. Sci.*, Vol.42 , (August 2000) Pages 1433-1455, ISSN:0010-938X.

Avedesian, M. & Baker, H. (1999). *Mg and Mg Alloys*, ASM International, ISBN: 0-87170-657-1,USA.

Azushima, A.; Aoki, K.; Asada, Y. & Kimura, Y. (2002). High strengthening by combination process of shear deformation and rolling. *Proceedings of 2002 Japanese Spring Conference on Technology of Plasticity*, pp.309-310, ISBN:0919-1925, Chiba, May 2002, JSTP, Tokyo (in Japanese).

Azushima, A.; Kopp, R.; Korhonen, A.; Yang, D.; Micari, F.; Lahoti, G.; Groche, P.; Yanagimoto, J. ; Tsuji, N.; Rosochowski, A. & Yanagida, A. (2008). Severe plastic

deformation (SPD) processes for metals. *CIRP Annals - Manufacturing Technology*, Vol.57, (Oct. 2008) Pages 716-735, ISSN: 0007-8506.

Berbon, B.; Furukawa, M.; Horita, Z.; Nemoto, M. & Langdon, T. (1999). Influence of pressing speed on microstructural development in equal-channel angular pressing. *Metall. Mater. Trans.*, Vol.30, No.8, (Aug. 1999) Pages 1989-1997, ISSN: 1073-5623.

Beyerlein, I. & Tóth, L. (2009) Texture evolution in equal-channel angular extrusion. *Prog. Mater .Sci.*, Vol.54, (June. 2009) Pages 427-510, ISSN: 0079-6425.

Birbilis, N.; Ralston, K.; Virtanen, S.; Fraser, H. & Davies, C. (2010) Grain character influences on corrosion of ECAPed pure magnesium. *Corros. Eng. Sci. Techn.*,Vol.45, (June 2010) Pages 224-230, ISSN:1478-422X

Bridgman, P. (1935) Effects of High Shearing Stress Combined with High Hydrostatic Pressure. *Physical Review*, Vol.48, (Nov. 1935) Pages 825-847.

Chang, C.; Wang, Y.; Pei, H.; Lee, C. & Huang, J. (2006) On the Hardening of Friction Stir Processed Mg-AZ31 Based Composites with 5-20% Nano-ZrO2 and Nano-SiO2 Particles. *Mater. Trans.* , Vol.47, (Dec. 2006) Pages 2942-2949,. ISSN: 1345-9678.

Chang, T. ; Wang, J. ; Chu, C. & Lee, S. (2006). Mechanical properties and microstructures of various Mg–Li alloys. *Mater. Letters*. Vol.60, (Nov. 2006) Pages 3272-32763. ISSN: 0167-577X

Cheng, Y.; Chen, Z. & Xia, W. (2007). Effect of crystal orientation on the ductility in AZ31 Mg alloy sheets produced by equal channel angular rolling. *J. Mater. Sci.* , Vol.42, (May 2007) Pages 3552-3556, ISSN: 0022-2461.

Chuvil'deev, V.; Nieh, T.; Gryaznov, M.; Sysoev, A. & Kopylov, V. (2004) Low-temperature superplasticity and internal friction in microcrystalline Mg alloy processed by ECAP. *Scripta Mater.*, Vol.50, (March 2004) Pages 861-865, ISSN:1359-6462.

Del Valle, J.; Pérez-Prado M. & Ruano, O. (2005). Accumulative roll bonding of a Mg-based AZ61 alloy. *Mater. Sci. Eng. A* , Vol. 410-411, (Nov. 2005) Pages 353-357, ISSN: 0921-5093

Del Valle, J.; Carreno, F. & Ruano, O. (2006). Influence of texture and grain size on work hardening and ductility in Mg-based alloys processed by ECAP and rolling. *Acta Mater.*, Vol.54 , (Sept. 2006) Pages 4247-4259, ISSN:1359-6454.

Ferrase, S.; Segal, V.; Kalidindi, S. & Alford, F. (2004). Texture evolution during equal channel angular extrusion: Part I. Effect of route, number of passes and initial texture. *Mater. Sci. Eng. A* , Vol. 368 (March 2004) Pages 28-40, ISSN: 0921-5093.

Figueiredo, R. & Langdon, T. (2006) . The development of superplastic ductilities and microstructural homogeneity in a Mg ZK60 alloy processed by ECAP. *Mater. Sci. Eng. A*. Vol.430, (Aug. 2006) Pages 151-156, ISSN: 0921-5093.

Furukawa, M.; Iwahashi, Y.; Horita, Z.; Nemoto, M. & Langdon, T. (1998) The shearing characteristics associated with equal-channel angular pressing. *Mater. Sci. Eng. A*, Vol. 257, (Dec. 1998) Pages 328-332, ISSN: 0921-5093.

[a] Furukawa, M.; Horita, Z.; Nemoto, M. & Langdon, T. (2001) Review: Processing of Metals by Equal-channel Angular Pressing. *Journal of Material Science*, Vol.36, No.12, (June 2001) Pages 2835-2843, ISSN: 0022-2461.

[b] Furukawa, M.; Utsonomiya, A.; Matsubara, K.; Horita, Z. & Langdon, T. (2001) Influence of Mg on grain refinement and ductility in a dilute Al–Sc alloy. *Acta Mater.*, Vol.49, (Oct. 2001) Pages 3829-3838, ISSN: 1359-6454.

Gan, W. ; Zheng, M. ; Chang, H.; Wang, X.; Qiao, X.; Wu, K.; Schwebke, B. & Brokmeier H. (2009). Microstructure and tensile property of the ECAPed pure Mg. *J. Alloys Compd*, Vol.470, (Feb. 2009) Pages 256-262, ISSN: 0925-8388.

Gifkins, R. & Langdon, T. (1964). On the question of low temperature sliding at grain boundaries. *J. Inst. Metals* , Vol .93 , Pages 347-352

Raab, G.; Valiev, R.; Lowe, T. & Zhu, Y. (2004). Continuous Processing of Ultrafine Grained Al by ECAP-Conform. *Mater. Sci. Eng. A* , Vol.382, (Sept. 2004) Pages 30-34, ISSN: 0921-5093.

Hamu, G.; Eliezer, D. & Wagner, L. (2009) The relation between severe plastic deformation microstructure and corrosion behavior of AZ31 Mg alloy. *J. Alloys Compd*, Vol.468, (Jan. 2009) Pages 222–229, ISSN: 0925-8388.

Han, J.; Oh, K. & Lee J. (2004) Effect of accumulative strain on texture evolution in 1050 Al alloys processed by continuous confined strip shearing. *Mater. Sci. Eng. A* , Vol.387–389, (Dec. 2004) Pages 240-243, ISSN: 0921-5093.

Hauser, F. , Landon, P. & Dorn, J. (1956). Deformation and fracture mechanisms of polycrystalline Mg at low temperatures. *Trans. Am. Soc. Metals*, Vol.48, (Oct. 1956) Pages 986-1002.

Higo, Y.; Pikard, A. & Knott, J. (1981). Effects of grain size and stacking fault energy on fatigue-crack-propagation thresholds in Cu-Al aluminium alloys. *Met. Sci* ., Vol.15, (June 1981) Pages 233-240, ISSN: 0306-3453.

Huang, J.; Zhu, Y.; Jiang, H. & Lowe, T. (2001) Microstructures and dislocation configurations in nanostructured Cu processed by repetitive corrugation and straightening. *Acta Mater.,* Vol.49, (May 2001) Pages1497-1505. ISSN: 1359-6454.

Huang, Y. & Prangnell, P. (2007) Continuous frictional angular extrusion and its application in the production of ultrafine-grained sheet metals. *Scripta Mater.* , Vol.56, (March 2007) Pages 333-336, ISSN:1359-6462

Iwahashi, Y.; Wang, J.; Horita, Z.; Nemoto, M. & Langdon, T. (1996) Principle of equal-channel angular pressing for the processing of ultra-fine grained materials. *Scripta Mater.* , Vol.35 , (July 1996) Pages 143-146, ISSN: 1359-6462.

Jiang,J.; Ma, A.; Saito, N.; Shen, Z.; Song, D.; Lu, F.; Nishida, Y.; Yang, D. & Lin, P. (2009) Improving corrosion resistance of RE-containing magnesium alloy ZE41A through ECAP. *Journal of Rare Earths*, Vol.27, (Oct. 2009) Pages 848-852, ISSN: 1002-0721.

Jin, L.; Lin, D.; Mao, D. ; Zeng, X.; Chen, B. & Ding, W. (2006). Microstructure evolution of AZ31 Mg alloy during equal channel angular extrusion. *Mater. Sci. Eng. A* , Vol.423, (May 2006) Pages 247 – 252 , ISSN: 0921-5093.

Jones, H. & Lavernia, E. (1998) in: *Elements of Rapid Solidification: Fundamentals and Applications*.. Otooni, M. A. (Ed.), Page 135, Springer, ISBN: 3540617914, Berlin

Jönsson, M.; Persson & D.; Thierry, D.(2007) Corrosion product formation during NaCl induced atmospheric corrosion of Mg alloy AZ91D. *Corros. Sci*., Vol. 49 (March 2007) Pages 1540-1558, ISSN: 0010-938X.

Kainer, K. (2003) *Mg Alloys and Technol.* Wiley-VCH, ISBN: 9783527602049, Germany

Kim, W.; Hong, S.; Kim, Y.; Min, S. ; Jeong, H. & Lee, J.(2003) Texture development and its effect on mechanical properties of an AZ61 Mg alloy fabricated by equal channel angular pressing. *Acta Mater.,* Vol.51 ,(June 2003) Pages 3293-3307, ISSN: 1359-6454.

Kim, H.; Choi, M. ; Chung, C. & Shin, D. (2003) Fatigue properties of ultrafine grained low carbon steel produced by equal channel angular pressing. *Mater Sci Eng A* , Vol.340, (Jan. 2003) Pages 243-250 , ISSN: 0921-5093.

Kim, H.; Lee, Y. & Chung, C. (2005) Fatigue properties of a fine-grained magnesium alloy produced by equal channel angular pressing. *Scripta Mater.*, Vol.52, (June 2005) Pages 473-477, ISSN: 1359-6462.

Kim, W.; Lee, J.; Kim, W. , Jeong, H. & Jeong, H. (2007) Microstructure and mechanical properties of Mg–Al–Zn alloy sheets severely deformed by asymmetrical rolling. *Scripta Mater.*, Vol.56, (Febr. 2007) Pages 309-312, ISSN: 1359-6462.

Kim, W.; Yoo, S.; Chen, Z. & Jeong, H. (2009) Grain size and texture control of Mg–3Al–1Zn alloy sheet using a combination of equal-channel angular rolling and high-speed-ratio differential speed-rolling processes. *Scripta Mater* , Vol.60, (May 2009) Pages 897-900, ISSN: 1359-6462.

Kim, W. (2009) Explanation for deviations from the Hall – Petch Relation based on the creep behavior of an ultrafine-grained Mg – Li alloy with low diffusivity. *Scripta Mater*, Vol.61, (Sept. 2009) 652-655, ISSN: 1359-6462.

Kim, W. & Lee, Y. (2010) Enhanced superplasticity of 1 wt.%Ca-AZ80 Mg alloy with ultrafine grains. *Materials letters*, Vol. 64, (Aug. 2010) Pages 1759-1762, ISSN: 0167-577X.

Ko, Y.; Shin, D. ; Park, K. & Lee, C. (2006) An analysis of the strain hardening behavior of ultra-fine grain pure titanium. *Scripta Mater.* Vol.54, (May 2006) Pages 1785-1789, ISSN: ISSN: 1359-6462.

[a] Koike, J.; Ohyama, R.; Kobayashi, T.; Suzuki, M.& Maruyama, K. (2003)Grain-boundary sliding in AZ31 Mg alloys at room temperature to 523 K. *Mater Trans*, Vol.44, (Apr. 2003) Pages 445-451, ISSN: 1345-9678.

[b] Koike, J.; Kobayashi, T.; Mukai, T. ; Watanabe, H.; Suzuki, M.; Maruyama, K. & Higashi, K. (2003) The activity of non-basal slip systems and dynamic recovery at room temperature in fine-grained AZ31B Mg alloys. *Acta Mater.*, Vol. 51, (Apr. 2003) Pages 2055-2065, ISSN: 1359-6454.

Lee, C. ; Huang, J. & Hsieh, P. (2006) Mg based nano-composites fabricated by friction stir processing. *Scripta Mater.*, Vol. 54 ,(April 2006) Pages1415-1420, ISSN: 1359-6462.

Lee, J.; Seok, H.; Han, J. & Chung, Y. (2001) Controlling the textures of the metal strips via the continuous confined strip shearing (C2S2) process. *Mater. Res. Bull.*, Vol.36, (March 2001) Pages 997-1004., ISSN: 0025-5408.

Lee, J. ; Seok, H. & Suh, J. (2002) Microstructural evolutions of the Al strip prepared by cold rolling and continuous equal channel angular pressing. *Acta Mater.*, Vol.50, (Sept. 2002) Pages 4005-4019, ISSN: 1359-6454.

Li, Y.; Liu, Y.; Ngai , T.; Zhang, D.; Guo, G. & Chen, W. (2004) Effects of die angle on microstructures and mechanical properties of AZ31 Mg alloy processed by equal channel angular pressing . *Trans Nonferrous Met Soc China*, Vol.14, (Feb. 2004) Pages 53-57, ISSN:1003-6326.

Lin, H.; Huang, J. & Langdon, T. (2005) Relationship between texture and low temperature superplasticity in an extruded AZ31 Mg alloy processed by ECAP. *Mater. Sci. Eng. A*, Vol.402, (Aug. 2005) Pages 250-257, ISSN: 0921-5093.

Liu, T.; Wang, Y. ; Wu, S.; Peng, R. ; Huang, C.; Jiang, C. & Li, S. (2004) Textures and mechanical behavior of Mg – 3.3%Li alloy after ECAP. *Scripta Mater.*, Vol.51, (Nov. 2004) Pages 1057-1061 , ISSN: 1359-6462.

Ma, A. ; Jiang, J. ;Saito, N.; Ichinori, S.; Yuan, Y. ; Yang, D. & Nishida Y. (2009). Improving both strength and ductility of a Mg alloy through a large number of ECAP passes. *Mater. Sci. Eng. A* , Vol. 513-514 , (July 2009) Pages 122-127, ISSN: 0921-5093.

Mabuchi, M.; Iwsaki, H. ;Yanase, K.& Higashi, K. (1997) Low temperature superplasticity in an AZ91 Mg alloy processed by ECAE. *Scripta Mater.*, Vol.36, (March 1997) Pages 681-686, ISSN: 1359-6462.

Mabuchi, M.; Ameyama, K.; Iwasaki, H. & Higashi, K. (1999) Low temperature superplasticity of AZ91 Mg alloy with non-equilibrium grain boundaries. *Acta Mater.*, Vol.47,(May 1999) Pages 2047-2057, ISSN: 1359-6454.

Máthis, K.; Gubicza, J. & Nam, N. H. (2005) Microstructure and mechanical behavior of AZ91 Mg alloy processed by equal channel angular pressing . *J. Alloys Compd*, Vol.394, (May 2005), Pages 194-199, ISSN: 0925-8388.

Matsubara, K.; Miyahara, Y. ; Horita, Z. & Langon, T.G. (2003). Developing superplasticity in a Mg alloy through a combination of extrusion and ECAP. *Acta Mater.*, Vol.51, (June 2003) Pages 3073-3084, , ISSN: 1359-6454.

May, J.; Höppel, H. W. & Göken, M. (2005). Strain rate sensitivity of ultrafine-grained aluminium processed by severe plastic deformation. *Scripta Mater.*,Vol.53 (July 2005) Pages 189-194, ISSN: 1359-6462.

Meyers, M.; Mishra, A. & Benson, D. (2006) The deformation physics of nanocrystalline metals: experiments, analysis, and computations. *JOM*, Vol.58, (April 2006) Pages 41-48, ISSN:1047-4838

Morisada, Y.; Fujii, H.; Nagaoka, T. & Fukusumi, M. (2006) Nanocrystallized Mg alloy – uniform dispersion of C_{60} molecules. *Scripta Mater.* , Vol.55, (Dec. 2006) Pages1067-1070, ISSN: 1359-6462.

Mukai, T.; Yamanoi, M.; Watanabe, H. & Higashi, K. (2001) Ductility enhancement in AZ31 Mg alloy by controlling its grain structure. *Scripta Mater.*, Vol.45, (July 2001) Pages 89-94, ISSN: 1359-6462.

Nishida, Y.; Arima, H.; Kim, J. & Ando, T. (2001) Rotary-die equal-channel angular pressing of an Al – 7 mass% Si – 0.35 mass% Mg alloy. *Scripta Mater.*, Vol. 45, (Aug. 2001) Pages 261-266, ISSN: 1359-6462.

Nordlien, J. H.; Ono, S. ; Masuko, N. & Nisancioglu, K. (1997) A TEM investigation of naturally formed oxide films on pure Mg. *Corros. Sci.*, Vol.39, (Aug. 1997) Pages 1397-1414, ISSN: 0010-938X.

Op'tHoog, C.; Birbilis, N. & Estrin Y. (2008) Corrosion of pure mg as a function of grain size and processing route. *Adv. Eng. Mater.*, Vol.10,(May 2008) Pages 579-582, ISSN:1438-1656.

Perez-Prado, M. ; Valle, D. & Ruano, O. (2004) Grain refinement of Mg-Al-Zn alloys via accumulative roll bonding. *Scripta Mater.*, Vol.51, (Nov. 2004) Pages 1093-1097, ISSN: 1359-6462.

Raab, G. ; Valiev, R. ; Lowe, T. & Zhu, Y. (2004) Continuous Processing of Ultrafine Grained Al by ECAP Conform. *Mater. Sci. Eng. A*, Vol. 382 (Sept. 2004) Pages 30-34, ISSN: 0921-5093.

Richert, M.; Stüwe, H. ; Zehetbauer, M. ; Richert, J.; Pippan, R., Motz, C. & Schafler, E. (2003). Work hardening and microstructure of AlMg5 after severe plastic deformation by cyclic extrusion and compression. *Mater. Sci. Eng. A*, Vol.355, (Aug. 2003) Pages 180-185, ISSN: 0921-5093.

Rosochowski, A. & Olejnik, L. (2002) Numerical and Physical Modeling of Plastic Deformation in 2-turn Equal Channel Angular Extrusion. *Journal of Materials Processing Technology*,Vol.125-126, (Sept. 2002) Pages 309-316, ISSN: 0924-0136.

Saito, Y.; Tsuji, N.; Utsunomiya, H.; Sakai, T.& Hong, R.(1998) Ultra-fine grained bulk aluminum produced by accumulative roll-bonding (ARB) process. *Scripta Mater.*, Vol.39, (Oct. 1998) Pages 1221-1227, ISSN: 1359-6462.

Saito, Y.; Utsunomiya,H., Tsuji, N. & Sakai, T. (1999) Novel ultra-high straining process for bulk materials—development of the accumulative roll-bonding (ARB) process. *Acta mater.*, Vol.47, (Jan. 1999) Pages 579-583, ISSN:1359-6454.

Saito, Y.; Utsunomiya, H.; Suzuki, H. & Sakai, T. (2000) Improvement in the r-value of aluminum strip by a continuous shear deformation process. *Scripta Mater.*, Vol.42, (June 2000) Pages 1139-1144, ISSN: 1359-6462.

Segal, V. ; Reznikov, V. ; Drobyshevskiy, A. & Kopylov, V. (1981) Plastic working of metals by simple shear. *Russian Metall*, No.1, Pages 99-105, ISSN: 0036-0295.

Song,D.; Ma, A.; Jiang, J.; Lin, P.; Yang, D. & Fan, J. (2010) Corrosion behavior of equal-channel-angular-pressed pure magnesium in NaCl aqueous solution. *Cor. Sci.*, Vol. 52, (Febr.) Pages 481-490, ISSN: 0010-938X

Suresh, S. (1998). *Fatigue of materials*. Cambridge University Press, ISBN: 0521570468, Cambridge.

Takayama, Y.; Saigo, Y.; Takahashi, R. & Kato, H. (2002) . Changes in microstructure and crystallite orientation distribution by continuous cyclic bending and annealing in a commercial purity titanium. *J. Jpn. Inst. Light Met.*, Vol. 52 , Pages 566-571, ISSN: 0451-5994.

Tong, L.; Zheng, M.; Chang, H.; Hu, X. & Wu, K. (2009) Microstructure and mechanical properties of Mg-Zn-Ca alloy processed by equal channel angular pressing. *Mater. Sci. Eng. A*, Vol.523, (Oct. 2009) Pages 289-294, ISSN: 0921-5093.

Tsuji , N.; Saito, Y.; Lee, S. & Minamino, Y. (2003) ARB (Accumulative Roll-Bonding) and other new techniques to produce bulk ultrafine grained materials. *Adv. Eng. Mater.* Vol.5, (Jun. 2003) Pages 338-344, ISSN: 1438-1656.

Uhlenhaut, D. I.; Furrer, A.; Uggowitzer P. J. & Löffler, J. F. (2009) Corrosion properties of glassy Mg70Al15Ga15 in 0.1 M NaCl solution . *Intermetallics*, Vol.17, (Oct.2009)Pages 811-817, ISSN:0966-9795.

Valiev, R. ; Krasilnikov, N. & Tsenev, N. (1991) Plastic Deformation of Alloys with Submicron-grained Structure. *Mater. Sci. Eng. A*, Vol.197, (May 1991) Pages 35-40, ISSN: 0921-5093.

Valiev, R.; Islamgaliev, R. & Alexandrov, I. (2000) Bulk nanostructured materials from severe plastic deformation. *Prog. Mater. Sci.* Vol. 45, Pages 103-189, ISSN: 0079-6425.

Valiev, R. & Langdon, T. (2006) Principles of equal-channel angular pressing as a processing tool for grain refinement. *Prog. Mater .Sci.*, Vol.51, (Sep. 2006) Pages 881-981, ISSN: 0079-6425.

Valiev, R. & Nazarov, A. (2009). Bulk nanostructured materials by SPD processing, In: *Bulk nanostructured materials*, Zehetbauer, M.J. & Zhu, Y.T.(ed.), 21-48,Willey-VCH, ISBN:978-527-315246, Weinheim.

Vinogradov, A.; Nagasaki, S.; Patlan, V. ; Kitagawa, K. & Kawazoe, M. (1999). Fatigue properties of 5056 Al-Mg alloy produced by equal-channel angular pressing. *Nanostruct Mater*, Vol.11, (Oct. 1999) Pages 925-934, ISSN: 0965-9773.

Volovitch, P.; Allely, C. & Ogle, K. (2009) Understanding corrosion via corrosion product characterization: I. Case study of the role of Mg alloying in Zn–Mg coating on steel . *Corros. Sci.*, Vol. 51, (June 2009) Pages 1251-1262, ISSN: 0010-938X.

Weertman, J. ; Farkas, D.; Hemker, K; Kung, H.; Mayo, M. & Mitra, R. (1999). Structure and mechanical behavior of bulk nanocrystalline materials . *Mater Res Soc Bull*, Vol.24, Pages 44-50, ISSN: 0883-7694.

Yamakov, V.; Wolf, D.; Phillpot, S., Mukherjee, A. & Gleiter, H. (2004). Deformation-mechanism map for nanocrystalline metals by molecular-dynamics simulation. *Nature Mater.*, Vol.3, (Dec. 2003) Pages 43-47, ISSN: 1476-1122.

Yapici, G. &Karaman, I. (2009) Common trends in texture evolution of ultra-fine-grained hcp materials during equal channel angular extrusion. *Mater. Sci. Eng. A*, Vol. 503, (Mar. 2009) Pages 78-81, ISSN: 0921-5093.

Yoshida, Y.; Cisar, L.; Kamado, S.; Koike, J. & Kojima, Y. (2003) Texture Development of AZ31 Mg Alloy during ECAE Processing. *Mater Sci Forum*, Vol. 419-422, (Jan. 2003) Pages 533-538, ISSN: 0255-5476.

Zheng, M.; Xu, S.; Qiao, X.; Wu, K.; Kamado, S. & Kojima, Y.(2008) Compressive deformation of Mg–Zn–Y–Zr alloy processed by equal channel angular pressing . *Mater. Sci. Eng. A*, Vol. 483-484, (June 2008) Pages 564-567, ISSN: 0921-5093.

Zhilyaev, A. & Langdon T. (2008) Using high-pressure torsion for metal processing: Fundamentals and applications. *Prog. Mater .Sci.*, Vol. 53, (Aug. 2008) Pages 893-979, ISSN: 0079-6425.

Zhu, Y.; Huang, J.; Gubicza, J.; Ungár, T.; Wang, Y.; Ma,. E. & Valiev, R. (2003) Nanostructures in Ti processed by severe plastic deformation. *J. Mater Res.*,Vol.18, (Aug. 2003) Pages 1908-1917, ISSN: 1862-5282.

Zúberová, Z.; Kunz, L.; Lamark, T.; Estrin, Y. & Janeček, M. (2007) Fatigue and tensile behavior of cast, hot-rolled, and severely plastically deformed AZ31 Mg alloy. *Metall Mater Trans*, Vol. 38, (Sept. 2007) Pages 1934-1940, ISSN: 1073-5623.

10

Mechanical Properties of Fine-Grained Magnesium Alloys Processed by Severe Plastic Forging

Taku Sakai and Hiromi Miura
UEC Tokyo (The University of Electro-Communications)
Japan

1. Introduction

Magnesium (Mg) and its alloys have recently attracted growing interest especially in the automobile industries due to their excellent specific properties, as one of the lightest structural materials (Mordike & Ebert, 2001). To date, most of Mg products have been fabricated by casting, in particular, by die-casting because of its high productivity, suitable strength, acceptable quality and dimensional accuracy. The intrinsic poor formability and limited ductility at ambient temperature due to the hexagonal close-packed (hcp) crystal structure and the associated insufficient independent slip systems, however, greatly restricts their practical usage. Then Mg and its alloys are categorized in hard plastic materials and its products of structural light materials are not a lot fabricated by plastic working such as rolling, forging and other forming processes. During warm and hot working, on the other hand, there are several non-basal slip systems operated in addition to the basal slip plane leading to increase of the plastic workability. It is also known that fine-grained structures are frequently developed in Mg alloys after warm and hot working to relatively low strains. The plastic workability of such fine-grained alloys can be much improved accompanied by superplasticity. It has been studied recently (Humphrey & Hatherly, 2004, Valiev & Langdon, 2006) that severe plastic deformation (SPD), such as equal channel angular pressing (ECAP), high pressure torsion (HPT), accumulative roll-bonding, multi-directional forging (MDF), etc., is carried out on many metallic materials, leading to the development of ultrafine-grained (UFGed) structures in a whole volume of the products. The present authors have studied thermomechanical processing for development of UFGed Mg alloys by using MDF under decreasing temperature conditions, and succeeded much in improvement of the plastic workability as well as the mechanical properties at ambient temperature, as described in the following sections.

The aim of the present chapter is to review our current studies on (1) the mechanical and microstructural behaviors as well as the grain refinement mechanism operating in Mg alloys during a single-pass compression, (2) outstanding effect of MDF on acceleration of rapid grain refinement under decreasing temperature conditions, and (3) improvement of the mechanical properties of fine-grained Mg alloys processed by MDF. The mechanical properties and characteristics of superplasticity are investigated in tension at various temperatures and strain rates, and the microstructural and textural changes taking place

during tensile deformation are examined. The mechanisms of new grain development taking place during plastic working and the deformation mechanisms operating in fine-grained Mg alloys are discussed in details.

2. Experimental procedure

2.1 Materials and thermomechanical procedure

Commercial Mg alloys, such as AZ31, AZ61, etc., were provided as hot-extruded rods. Cylindrical samples of 8 mm in diameter and 12 mm in height were prepared from the rod with the axis aligned along the extrusion (longitudinal) direction and mainly used for studying the deformation behaviors during a single-pass compression. Another type of samples was a rectangular shape with the dimensions of the axis ratio of 2.22: 1.49: 1 and used for studying the deformation behaviors and the processes of grain refinement taking place during MDF. The MDF employed is carried out with changing the loading axis at an angle of 90° through three mutually perpendicular axes (i.e. x to y to z to x to …..) from pass to pass (Fig. 1). When a pass strain is kept as $\Delta\varepsilon = 0.8$, the dimension ratio above mentioned does not change in each compression and so MDF can be carried out repeatedly to severe large accumulated strains. Then these samples machined were annealed at 733 K for 7.2 ks and furnace cooled, leading to the evolution of almost equiaxed grains with a diameter of about 22.3 μm (see Fig. 4(a)).

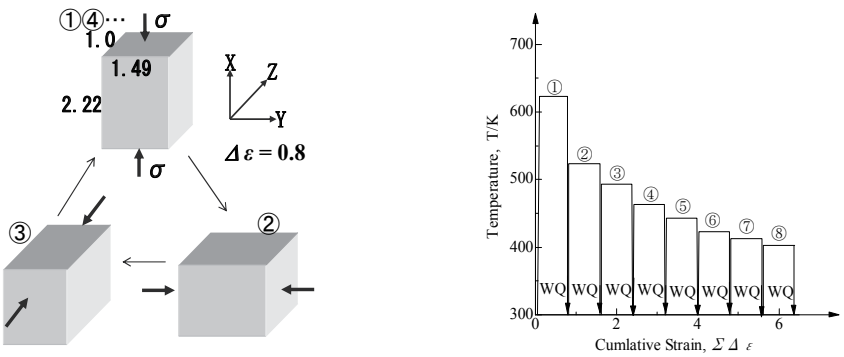

Fig. 1. Schematic illustration of the thermo-mechanical processing used in MDF with continuous decreasing temperature in each pass. (a) The loading direction is changed in 90° with pass to pass (x→y→z→x⋯). A pass strain $\Delta\varepsilon$ is 0.8. (b) Deformation temperature is decreased from 623K to 423K in each MDF. WQ indicates water quenching.

Multiple forgings were carried out in compression by using the rectangular samples with a dimension of 31 mm in length, 21 mm in width and 14 mm in thickness or with the other dimension of around 60 x 40 x 27 mm^3, which were machined from the as-extruded rod parallel to the extrusion direction. Compression were carried out at constant true strain rates in a modified Instron-type testing machine which was equipped both a vacuum vessel and a quenching apparatus (Sakai & Takahashi, 1991). The later made a sample possible to quench in water within 1 s after hot deformation was ceased for freezing the as-deformed microstructures. The samples were deformed either isothermally in single-pass compression or in repeated MDF at various temperatures between 473 K and 673 K. MDF was also

performed under decreasing temperature conditions pass by pass from 623 K to 403 K because of promotion of rapid grain refinement (Fig. 1). The samples MDFed were cut along a plane parallel to the last compression axis for microstructural observation, which was carried out by using optical microscopy (OM), transmission electron microscopy (TEM) under an accelerating voltage of 200 kV and scanning electron microscopy (SEM) in corporating an orientation imaging microscopy (OIM) system

2.2 Tensile test

A strong texture was developed with the basal plane, i.e. {0001}, roughly perpendicular to final forging direction in the fine-grained Mg alloy, which is typical for compressed hcp-metals (see Fig. 7) (Rollet & Wright, 1998). Three perpendicular directions of the Mg samples MDFed were defined as L (=X), LT (=Y) and ST (=Z), respectively, as shown in Figs. 1 and 2. Two types of tensile specimens were machined from the Mg plate MDFed for studying mainly (1) the mechanical properties at room and elevated temperatures, and partly (2) influence of the texture anisotropy on the properties. For tensile tests of the formers (1), the specimens with the gauge dimension of 6 mm in length, 3 mm in width, and 0.7 mm in thickness were machined from the Mg plate parallel to the L-ST plane. These correspond to the 0° specimen in Fig. 2(b). For tensile tests of the latters (2), three kinds of tensile specimens with a gauge dimension of 10 × 4 × 1 mm^3 were machined from the Mg products MDFed, as shown schematically in Fig. 2(b). The tensile axes for each specimen were inclined at 0°, 45° and 90° to the basal plane, respectively. Hereafter these specimens are denoted as the 0°, 45° and 90° ones.

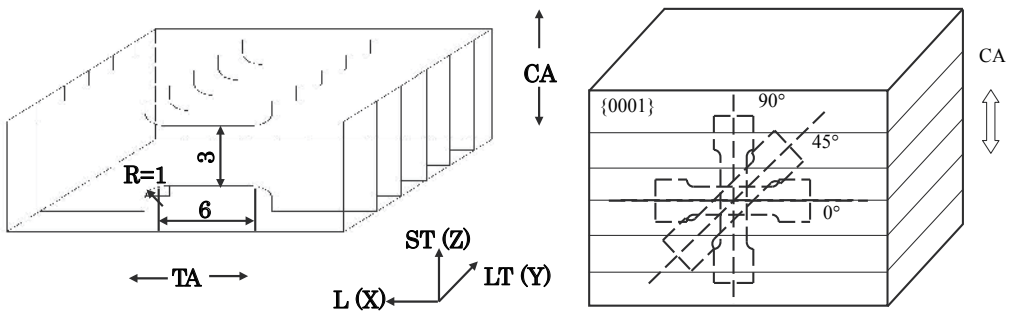

Fig. 2. (a) Tensile specimens, machined parallel to L-ST plane of MDFed Mg alloy, for studying mechanical properties and superplasticity of fine-grained Mg alloy. These correspond to the 0° ones in (b). (b) Tensile specimens for studying effect of the texture anisotropy of MDFed Mg alloy on mechanical behaviors. Tensile axes are inclined at 0°, 45° and 90° to the basal plane, which is roughly perpendicular to final compression axis (CA).

Tensile tests were conducted in vacuum by using an Instron-type testing machine, which was equipped with a hydrogen gas quenching apparatus (Xing et al., 2007). Tensile tests were carried out at temperatures from 298 K to 473 K and at initial strain rates from around 10^{-6} s^{-1} to 10^{-2} s^{-1}. The specimens were heated and kept for 0.6 ks at each test temperature, and then tensile tested, followed by rapid cooling at a rate of around 0.5 Ks^{-1} for freezing as-deformed microstructures. The microstructures were examined by using OM and OIM. The texture changes were also examined.

3. Mechanical and microstructural behaviors during hot compression

A series of the true stress-true strain (σ–ε) curves in compression at a true strain rate of 3×10^{-3} s^{-1} for an annealed Mg alloy AZ31 is represented in Fig. 3 (Yang et al., 2003). At high temperatures above 573 K, the σ–ε curves show work softening following a smooth stress peak at low strain, followed by steady-state like flow at high strains. Such flow behaviors are generally similar to those of conventional discontinuous dynamic recrystallization (dDRX) behavior appearing in cubic metals, where new grains with high angle boundaries (HABs) are dynamically nucleated and then followed by their growth in large distance, that is two-step reactions (Sakai & Jonas, 1984, 2001). At low temperatures below 523 K, in contrast, the σ–ε curve shows rapid work hardening in low strain and a sharp stress peak at around ε = 0.2, and then work softening followed by steady state flow at high strains. The σ–ε curve at 473 K exhibits a sharp and higher stress peak of above 300 MPa at around ε = 0.2, immediately followed by brittle fracture.

Typical microstructural changes and the corresponding σ - ε curve for the Mg alloy deformed at 673 K and at 3 x 10 $^{-3}$ s^{-1} are shown in Fig. 4 (Yang et al., 2003). The relatively smooth grain boundaries of the initial structure (Fig. 4(a)) are frequently corrugated and fine grains are partly evolved near the boundaries at around the peak strain ε_p = 0.12 where the stress peak appears (Fig. 4(b)). It was observed from the surface morphology that several deformation bands based on **kink bands** (Higashida et al., 1986) are frequently evolved and traversed or intersected in some grain interiors. The boundaries of these bands can be seen in the OIM map in Fig. 5(a). At a strain of 0.3, where strain softening clearly takes place, new fine grains are developed in colony along most the grain boundaries accompanied with grain boundary sliding and grain rotation (Fig. 4(c)). Further straining to around 0.5, where a steady state flow starts to take place, there are equiaxed new grains developed homogeneously and almost fully in the whole area (Fig. 4(d)). The results in Fig. 4 are almost similar to the previous ones reported by Ion et al., 1982 and Sitdikov & Kaibyshev, 2001. The close relationship between the flow softening behavior and the development of a new grain structure looks like the same as that of conventional dDRX in cubic metals (Sakai & Jonas, 1984, 2001).

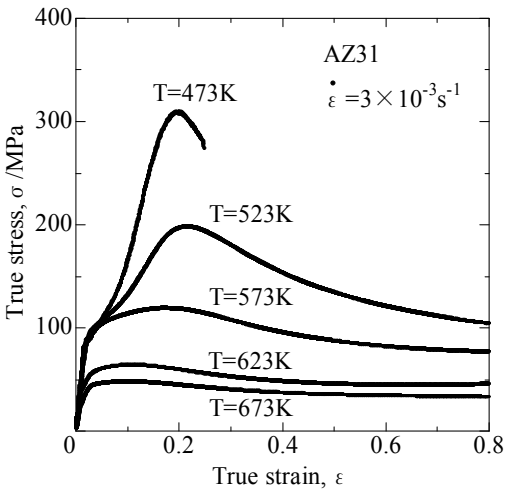

Fig. 3. Temperature effect on true stress-true strain curves of as-annealed AZ31 alloy with a grain size of 22.3 μm during single pass compression at a true strain rate of 3×10^{-3} s^{-1}.

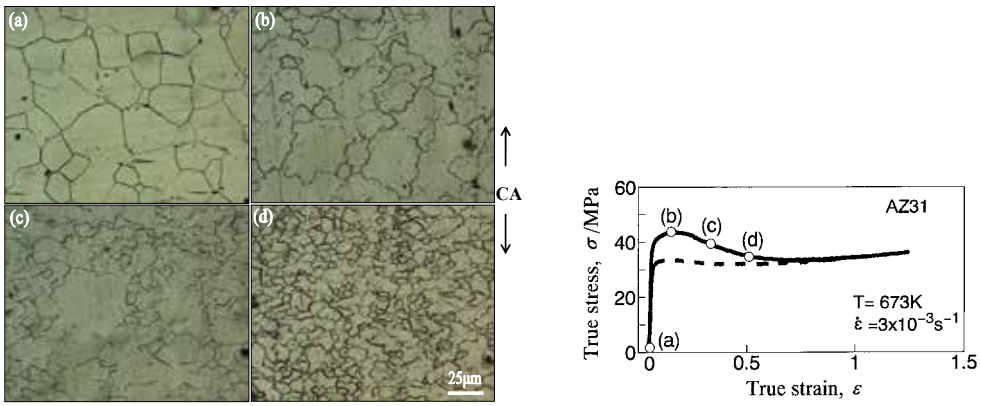

Fig. 4. Typical optical microstructures and the corresponding true stress-true strain curve of AZ31 alloy deformed to various strains at 673 K and at 3 x 10 $^{-3}$s^{-1}, followed by water quenching. The compression axis (CA) was parallel to the extrusion direction of the alloy. (a) $\varepsilon = 0$, (b) $\varepsilon = 0.1$, (c) $\varepsilon = 0.3$ and (d) $\varepsilon = 0.5$.

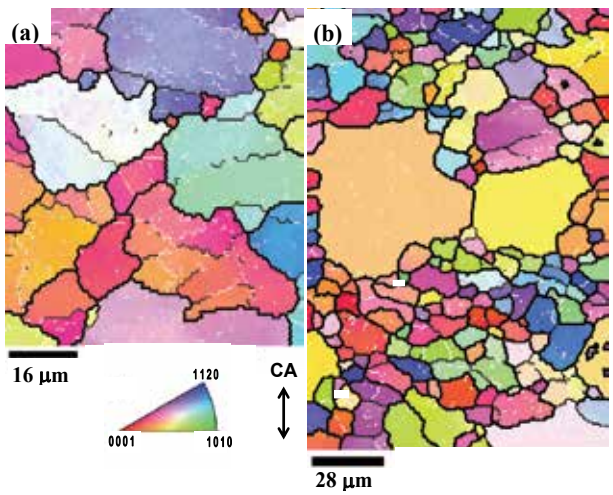

Fig. 5. Typical OIM maps of AZ31 alloy deformed to strains of (a) 0.10 and (b) 0.30 at 673 K and at 3 x 10 $^{-3}$ s $^{-1}$.

Typical OIM micrographs for the sample deformed to strains of 0.1 and 0.3 at 673 K are shown in Fig. 5 (Yang et al., 2003). Different colors for each grain and even in grain interiors indicate different crystallographic orientations defined in the inverse pole figure. HABs with misorientations more than 15° are delineated by thick-black lines, while low-angle boundaries in the range of 4° and 15° by thin-black lines and those in the range 2°- 4° by white lines. It is seen in Fig. 5(a) that fine grains are partly evolved along grain boundaries corrugated, and new boundaries with medium angle misorientations are developed in some regions of corrugated boundaries. Such a process of new grain formation may be similar to that appearing in conventional dDRX in cubic metals, i.e. the bulging of part of serrated grain boundaries (Sakai & Jonas, 1984, 2001). New boundaries with low to medium angle misorientations are also evolved in some grain interiors and some of them intersect with

each other. These new boundaries with low misorientation angles correspond to those of kink bands and so similar to transition bands or microbands (Humphreys & Hatherly, 2004). It is interesting to note in Fig. 5(a) that several initial grains are fragmented by the formation of such kink bands and the crystal orientation of each region fragmented is slightly changed in a grain interior even at $\varepsilon = 0.1$.

A typical OIM micrograph for a strain of 0.3 is depicted in Fig. 5(b). In the strain range over around ε_p, where a work softening takes place, the fraction of new grains rapidly increases and finally an equiaxed new grain structure is homogeneously developed in $\varepsilon > 0.5$ throughout the material. It is seen in Fig. 5 (b) that crystal orientation of each new grain evolved are almost randomly distributed and some rather coarser grains are retained in the fine grained regions. It is noted here that small angle subboundaries related to kink bands are not developed in these retained grain interiors. It was remarkable to note that the average size of new grains evolved is roughly similar to that of the regions fragmented by kink band and also does not change during further deformation to high strains. This suggests that each fragmented region surrounded by low to medium angle boundaries may transform in-situ to a grain with HABs and also scarcely grow during further deformation.

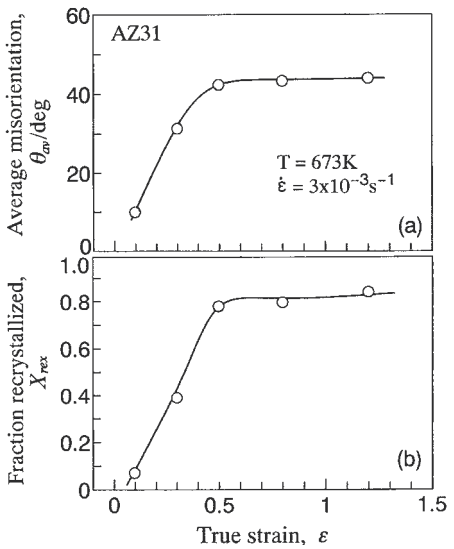

Fig. 6. Strain dependence of (a) average misorientation of (sub)grain boundaries, θ_{av}, and (b) fraction dynamically recrystallized, X_{rex}, of AZ31 alloy deformed at 673 K and at 3 x $10^{-3}s^{-1}$.

Changes, with increasing deformation, of the average misorientation (θ_{av}) and of the volume fraction of a new grain structure (X_{rex}) measured in OIM maps are depicted in Fig. 6 (Yang et al., 2003). Both the θ_{av} and X_{rex} start to increase at around the peak strain and rapidly rise during work softening, finally approaching saturation values at high strains, i.e. about 43°and 0.85, respectively. It is interesting to note in Fig. 6(b) that new grains are not fully developed even under a steady state flow in high strain. Such a result has not been reported in conventional dDRX of cubic metals. All of the results mentioned above suggest that new grain evolution in the Mg alloy may be not resulted from conventional dDRX, but a series of strain-induced reactions, that is essentially similar to **continuous DRX (cDRX)**. This will be discussed in section 4 in detail.

Finally, let us discuss a possible relationship between work softening after the peak stress and texture change occurring during compression. The extruded Mg rod with a strong texture, as mentioned above, is confirmed by the results of Fig**. 7** (Yang et al., 2002, 2003). Here the L-direction sample at $\varepsilon = 0$ has the basal plane of hcp lattice lying parallel to the extrusion direction and so the compression direction. According to the method employed by Ion et al. (1982), relative intensity of the texture orientations measured in the OIM data is plotted against φ, the angle between the compression axis and the {0001} texture. It is seen in Fig. 7 that the initial texture of the L-direction sample is reoriented gradually by compression. Namely, the alignment of the basal planes initially parallel to the compression axis is gradually rotated by compression and approaches perpendicular to the compression axis in high strain. The initial texture of the T-direction sample, prepared from the extruded rod aligned along the transverse direction, in contrast, was scarcely changed by compression and the relative intensity increased with increasing strain. It is quite possible to note, therefore, that work softening taking peace only in the L-direction sample can not result from new grain development due to DRX, but also the initial texture in which slip hardly takes place changing to the softer or stable one, that is the **geometrical softening**. It is also well understood why an appreciable work softening does not take place in the T-direction sample because of no clear change in the texture.

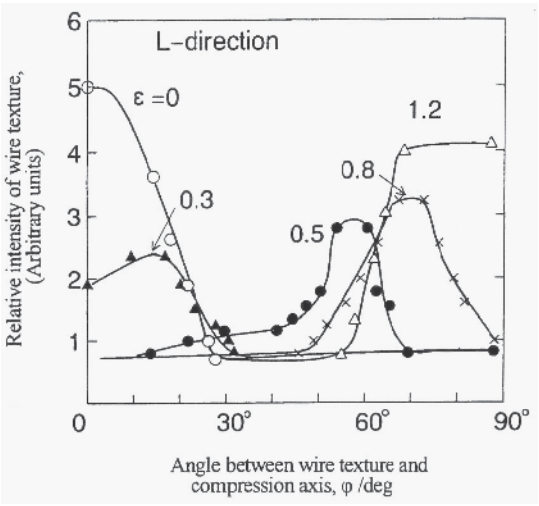

Fig. 7. Changes in the distribution of wire texture, with the basal planes lying parallel to the extruded direction, with compression at 673K. The axes of the L- direction samples is parallel to the extrusion direction.

4. Mechanisms of grain refinement in Mg alloy

It is seen from the experimental results and discussion in section 3 that hot deformation behavior of the Mg alloy AZ31 is closely related to the new grain formation due to the operation of DRX. Some results are, however, not similar to those of conventional dDRX taking place in cubic metals, although some previous studies on Mg alloys discuss that dDRX takes place during hot deformation (Ion et al., 1982, Sitdikov & Kaibyshev., 2001, Miura et al., 2005). So let us summarize briefly new grain formation due to dDRX taking

place in cubic metals during hot deformation. It is well known (Sakai & Jonas, 1984, 2001) that new grains are mostly evolved along the initial grain boundaries which are serrated by preceding hot deformation, and DRX nucleation occurs by operation of the bulge mechanism of the following process. Grain boundary sliding and/or grain boundary zone shearing first operates at appropriate serrated boundaries, leading to development of inhomogeneous local strains as well as strain or orientation gradients developed from grain boundaries towards grain interiors (Miura et al., 1994, 2007, Belyakov et al., 1998, Wusatowska-Sarnek et al., 2002). With further deformation, dislocation boundary and/or twin boundary is easily evolved in near the extrapolated places of the prior grain boundaries, resulting in acceleration of the separation of the bulged region from the parent grains and then dynamic formation of new grains. Finally these new grains can grow towards grain interiors because of large gradients of strain energy developed, finally leading to a full development of new grains in a whole volume.

The mechanisms of DRX nucleation taking place in Mg alloy will be discussed now. During early hot deformation of Mg alloy, kink bands are frequently formed in the regions of corrugated grain boundaries and also crossed in grain interiors. Then the misorientation and the number of the boundaries of kink band rapidly rise with further deformation (Fig.6). Then the regions fragmented by kink bands are bounded by HABs, but do not grow with further deformation. These regions finally result in evolution in-situ of new grains assisted by dynamic recovery. It is concluded, therefore, that the dynamic formation of new grains discussed above can result from a series of strain-induced continuous reactions, that is essentially similar to cDRX and actually a one-step phenomenon, i.e. new grains are nucleated homogeneously throughout the material and can scarcely grow (Sakai & Jonas, 2001). In contrast, conventional dDRX involves a two-step process, i.e. the nucleation of new grain surrounded by HABs followed by their long distance migration. It should be noted in cDRX of Mg alloy that a new grain structure can not be fully developed throughout the material even in high strain (Fig. 6). In retained original grains surrounded by new fine grains, kink bands may be hardly developed, because constrained deformation by surrounding grains can be relaxed by grain boundary sliding and dynamic recovery, etc., which take frequently place in the fine grained regions during deformation.

It has been recently reported, by the way, that UFGs are developed in many cubic metallic materials by **severe plastic deformation (SPD)**, such as ECAP, HPT, MDF, etc., and considered to be resulted from strain-induced continuous reactions, i.e. cDRX (Belyakov et al., 2001, Humphreys & Hatherly, 2004, Sakai et al., 2008). So let us discuss the process of strain-induced grain formation in Mg alloy as well as in cubic metals during SPD. The continuous increase in misorientations between (sub)grain boundaries evolved during deformation is an essential feature of cDRX, and the kinetics can be discussed by using the relationship between the average (sub)grain boundary misorientation (θ_{AV}) and total accumulated strain (Sakai et al., 2008). The θ_{AV} – ε relationships for Al alloy 2219 ECAPed at 523 K (Mazurina et al., 2008), a pure Cu MDFed at 195 K to 473 K (Gao et al., 1999, Belyakov et al., 2001, Kobayashi et al., 2007) and Mg alloy AZ31 compressed at 673 K are represented in Fig. 8. The data of AZ31 is the same as those in Fig. 6. It is remarkable to note in Fig. 8 that the kinetics of grain formation clearly depends on materials and is highest in the Mg alloy AZ31. The process of misorientation increase can be virtually subdivided into three stages in Fig. 8. The first stage is characterized by a rapid rise in θ_{AV} followed by a small plateau at a level of about 5°. Then the misorientation starts to increase again rapidly after some critical strain ε_c, i.e. this is in the second stage. The third stage corresponding to large strains, the

θ_{AV} approaches its saturation level. The fraction of HABs vs. strain (F_{HAB} – ε) curves are also similar to those in the θ_{AV} – ε curves in Fig. 8 (Sakai et al., 2008). The F_{HAB} is scarcely developed at below ε_c (the first stage) and then the F_{HAB} starts to increase in the second stage and approaches a saturation value in high strain (the third stage). It is also clearly seen in Fig. 8 that temperature effect on the kinetics of grain refinement in Cu is negligible small in the first and second stages of the evolutional process. However, the kinetics of new grain formation in the third stage slows down with decrease of deformation temperature. As a result, the saturation level of θ_{AV} at large strains is remarkably lower for deformation at lower temperature.

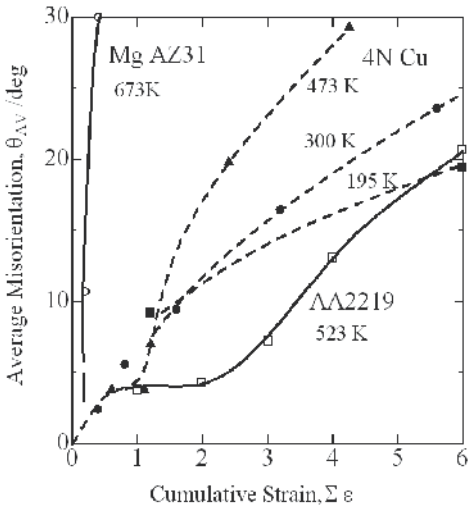

Fig. 8. Relationships between average misorientation angle of strain-induced (sub)grain boundaries and cumulative strain of Al alloy 2219 ECAPed at 523 K, pure Cu MDFed at 195 K, 300 K and 473 K, and Mg alloy AZ31 compressed at 673 K.

Now let us discuss the mechanisms for strain-induced grain formation operating in cubic metals during SPD and also in Mg alloy during light deformation, respectively. The structural changes leading to the submicrocrystalline structure after large strains by SPD of cubic metals can be illustrated by a schematic drawing in Fig. 9 (Sakai et al., 2008). In the first stage of the process, i.e. $0 < \varepsilon < \varepsilon_c$, early deformation brings about high density dislocations that are homogeneously arranged in cellular substructure. The initiation of rapid increase in θ_{AV} over ε_c can be resulted from the introduction of deformation bands such as **microshear bands** (**MSBs**) in cubic metals, followed by the fragmentation of original grains in the second stage of the process. The crystal orientation of small adjacent domains separated by a sharp MSB, *e.g.* the domains labeled with A and B in Fig. 9(a), seems to be the same at around ε_c. The new fine grains are preferably evolved inside the MSBs and, especially, at their intersections (Fig. 9(b)). The fraction of the UFGed structure gradually increases with increasing the number of MSB. It can be concluded, therefore, that a full evolution of new fine grains in cubic metals must need a full development of MSB in a whole volume that is promoted by further SPD. In Mg alloys, on the other hand, kink bands in replacement of MSB are frequently developed in grain interiors after hot deformation to much low strains and these fragmented regions can become in-situ new grains with HABs

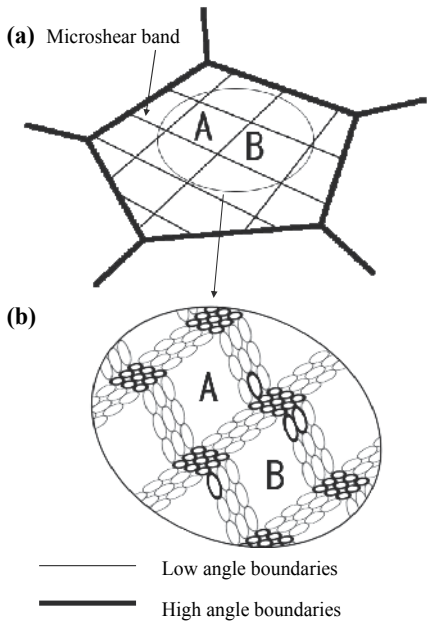

Fig. 9. Schematic drawing of the development of (a) microsher bands at low strains and (b) subsequent formation of new grains at the intersections and along the microshear bands at large strains in cubic metals.

in low strain (Fig. 8). This means that kink bands do not need to be fully evolved in high density in a whole volume of Mg alloys. If MSBs are changed to kink bands in the model of Fig. 9(a), new grains can be fully developed in a whole volume even after light deformation, because grain formation can result from grain fragmentation due to introduction of kink bands in the case of Mg alloy.

5. Effect of MDF on grain refinement

It is discussed in section 4 that dynamic grain refinement taking place in Mg alloy during hot deformation can be based on grain fragmentation due to kink band evolving in original grain interiors and so controlled by strain-induced continuous reactions assisted by dynamic recovery, i.e. cDRX. The new grain development starts to take place at low strains and rapidly approach a saturation state at strains over $\varepsilon > 0.5 - 0.6$ (Figs. 4 and 6). At the same time, the basal plane roughly parallel to the compression axis in extruded Mg rod gradually rotates and approaches perpendicular to the compression axis at around $\varepsilon > 1$ (Fig. 7). On the other hand, kink bands are concurrently formed roughly perpendicular to the basal plane in low strain (Yang et al, 2006) and so new fine grains may not be fully generated throughout the material during a single-pass compression (Fig. 6). Aiming to break this difficulty, any effect of the change of the loading direction on further grain refinement has been studied systematically by using the same Mg alloy AZ31. It has been also known in Mg alloys that dynamic grain sizes evolved in high strain decrease with decreasing deformation temperature (Galiyev et al. 2001, Sitdikov & Kaibyshev 2001). Then if Mg alloy is repeatedly MDFed with decreasing temperature, grain refinement is expected to take place more rapidly and effectively.

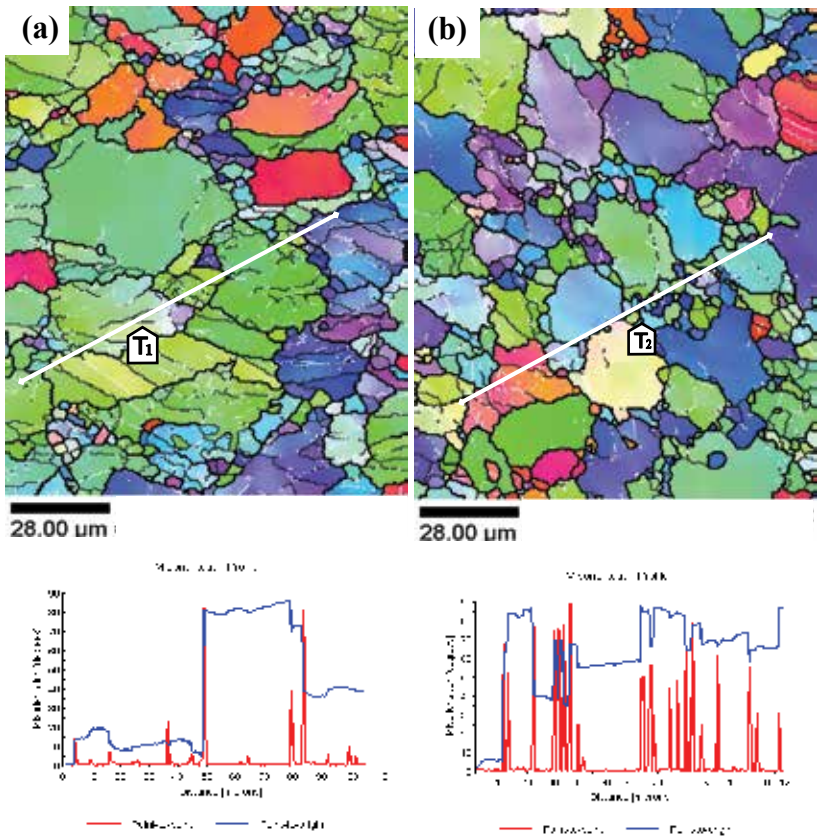

Fig. 10. OIM maps of Mg alloy AZ31 deformed to ε= 0.3 at 573 K by (a) a single- and (b) two-directional compression with changing the loading direction. Point-to-point misorientations and lattice rotation measured along the lines T_1 and T_2.

A typical effect of MDF on grain evolution can be seen in Fig. 10 (Yang et al., 2007), where two typical OIM micrographs show the microstructures developed during single- and two-directional compression at a lower temperature of 573 K. The former sample was compressed once to $\varepsilon = 0.3$ and the latter one deformed twice to $\Delta\varepsilon = 0.15$ in each direction, resulting in a same total strain, i.e. $\Sigma\ \Delta\varepsilon = 0.3$. The distribution of point-to-point misorientation (θ) and cumulative disorientation ($\Sigma\theta$) developed along the lines T_1 and T_2 are also represented in Fig. 10. Under a single-directional compression, kink bands developed mainly in one direction, which are roughly perpendicular to the compression axis (Fig. 10 (a)). Misorientation angle of deformation-induced boundaries does not exceed 20° in original grain interiors after a single-directional compression. Under two-directional compression with changing the loading direction, in contrast, the development of kink bands and their intersection as well as new grains takes place more frequently at a same total strain (Fig. 10 (b)). It is remarkable to note that kink bands are developed in various directions accompanied by changing the loading direction, leading to rapid formation of new grain boundaries with misorientations of over 20°. Such results in Fig. 10 strongly suggest that MDF may be a more effective method on strain-induced grain refinement taking place in Mg alloys. It can be seen in Fig. 10 that, in addition to the above mechanisms,

mechanical twinning may effectively contribute to the grain fragmentation in coarse grains, in particular, under decreasing temperature conditions (Sitdikov et al., 2003, Miura et al., 2007, Yang et al., 2007).

Let us discuss the process of grain refinement taking place in the Mg alloy during MDF under dropping temperature condition. MDF with a pass strain of 0.8 was carried out on the same Mg alloy AZ31 with decreasing temperature from 623 K to 403 K from pass to pass. Fig. 11 shows typical true stress-cumulative strain ($\sigma - \Sigma\Delta\varepsilon$) curves during repeated MDF under decreasing temperature condition and also during isothermal MDF at 623 K (Xing et al., 2008). The first flow curve at 623 K shows a sharp stress peak followed by work softening and subsequently steady-state like flow at high strains. The amounts of the peak stress and work softening after the peak decrease with repeated isothermal MDF at 623 K (broken line), while the flow stresses of around 40 MPa appearing in high cumulative strain do not change during MDF. On the other hand, the σ–$\Sigma\Delta\varepsilon$ curves during MDF with decreasing temperature condition are depicted by solid line in Fig. 11. During early MDF at higher temperatures, they show work softening following a peak stress and then followed by steady-state flow. With dropping the processing temperature, the values of flow stress increase accompanying with decrease in the amount of work softening after the stress peak.

At temperatures below 493 K, steady-state flow appears without a peak stress as well as flow softening. It is interesting to note that the $\sigma - \varepsilon$ curve for the as-annealed sample at 473 K (see Fig. 3) and that appearing at around $\Sigma\Delta\varepsilon$ =3 during MDF at 473 K in Fig. 11 is clearly different from each other. Namely, the flow stress peak for the annealed sample is 310 MPa a ε =0.2 and then brittle fracture occures (Fig. 3) and, in contrast, that appearing during MDF at 473 K is about 128 MPa which is about one-third of the former. Furthermore, the MDF processing is successful to deform the Mg alloy to cumulative large strains up to $\Sigma\Delta\varepsilon$ =5.6 at 403 K which is below than 0.5T_m (T_m is the melting point).

Typical grain structural changes taking place during MDF under decreasing temperature condition is represented in Fig. 12 (Xing et al., 2008). It is seen in Fig. 12 that strain-induced grain sizes developed decrease sensitively with decreasing temperature from 623 K to 403 K

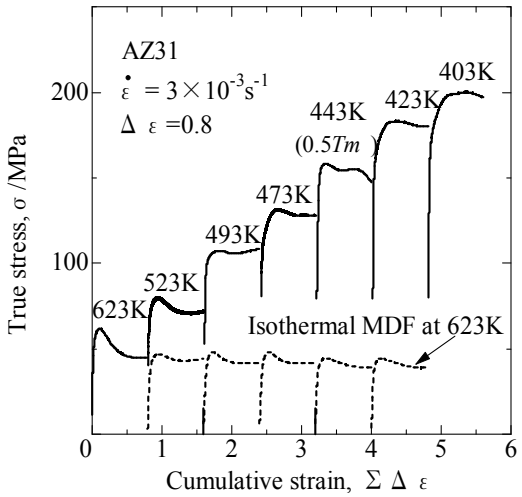

Fig. 11. True stress-true strain curves of AZ31 alloy during isothermal MDF at 623K (broken line) and MDF under decreasing temperature condition from 623K to 403K (solid line).

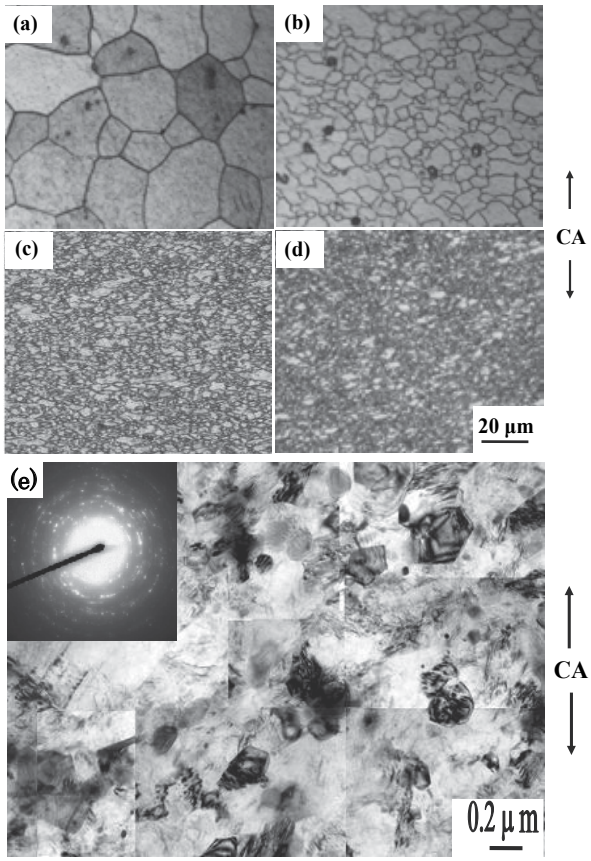

Fig. 12. Optical ((a) to (d)) and TEM (e) microstructures with the diffraction pattern evolved in Mg alloy AZ31 during MDF with continuous decreasing temperature in each pass. (a) As annealed, (b) T = 623 K, $\Sigma\Delta\varepsilon$ = 0.8, (c) T = 523 K, $\Sigma\Delta\varepsilon$ =1.6, (d) T = 473K, $\Sigma\Delta\varepsilon$ =3.2, and (e) T = 403K, $\Sigma\Delta\varepsilon$ =5.6.

during MDF. Fig. 12 (e) shows a typical TEM microstructure and the selected area diffraction (SAD) pattern developed in the sample deformed to $\Sigma\Delta\varepsilon$ = 5.6 at 403 K. Many diffraction points with a streak in the SAD pattern suggest that rather large internal stresses can be evolved in this strain-induced grain structure (Belyakov et al., 2000). The SAD pattern in Fig. 12 (e), showing almost uniform and fully continuous rings, suggests that this microstructure is composed of polycrystalline UFGs surrounded by HABs. The average grain size of 0.23 μm is almost fully developed after 7th-pass compression to $\Sigma\Delta\varepsilon$ = 5.6 at 403 K. Changes in the average grain size evolved in the Mg alloy AZ31 during isothermal MDF at 623 K and during MDF under decreasing temperature condition are represented by a broken line and a solid line in Fig. 13, respectively (Xing et al., 2008). The average grain size developed during isothermal MDF is almost constant within the experimental scatters and about 6.7 μm at strains up to $\Sigma\Delta\varepsilon$ =4.8. On the other hand, the dynamic grain size evolved during MDF with dropping temperature condition decreases drastically with repeated MDF. Such an excellent grain refinement taking place during MDF is also observed in another Mg alloy AZ61 (Miura et al., 2008, 2010). It is concluded, therefore, that the MDF

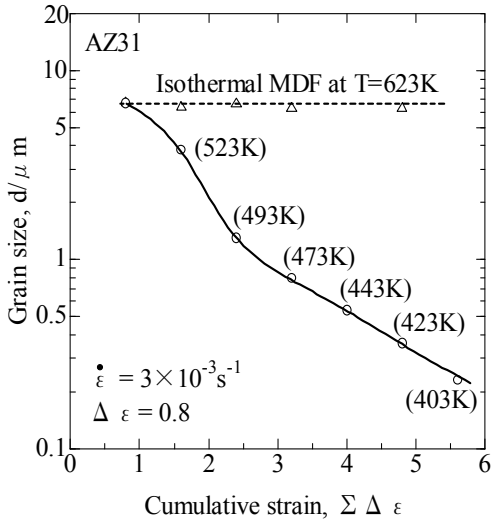

Fig. 13. Grain size changes in Mg alloy AZ31 during MDF with $\Delta\varepsilon$ = 0.8 at a temperature of 623K (broken line) or with decreasing temperature from 623K to 403K (solid line).

processing under dropping temperature conditions may be a most effective method for promotion of grain refinement in Mg alloys.

The relationship between the average grain size and the flow stress developed during MDF with dropping temperature as well as that for single-pass compression at high temperature is depicted in Fig. 14 (Xing et al., 2005, 2008). The symbols of triangle and circle indicate the data obtained by MDF and a single-pass compression at high temperature, and open and solid marks indicate the results obtained by using OM and TEM, respectively. Fig. 14 suggests that grain size may approach to 0.1 μm or less than it with further MDF at lower temperature. Such strain-induced grain sizes can be expressed by two power law functions of flow stress, i.e. $\sigma = k\, d^{-N}$, where k and N are constants, in the region of flow stress above

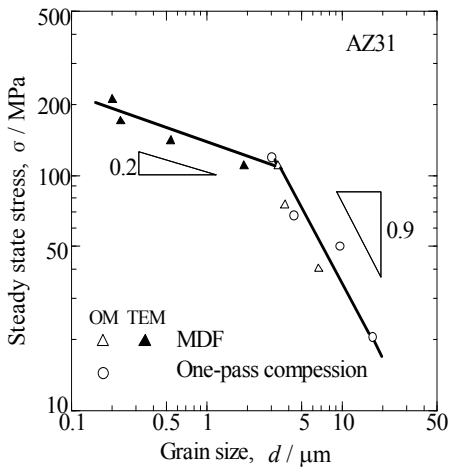

Fig. 14. Relationship between flow stress and strain-induced grain size developed during MDF and one-pass compression for Mg alloy AZ31.

or below around 100 MPa. The grain size exponent is N = 0.9 in the region of σ < 100 MPa, where deformation is carried out at higher temperatures above 0.5 T_m. In contrast, N is about 0.2 in the region of σ > 100 MPa, where MDF is performed below around 0.5 T_m. The relationship between flow stress and dynamic grain size developed in Cu and Ni-20%Cr is also roughly similar to the results in Fig. 14; namely, N is 0.75 in the region of lower stresses below 200 MPa and N = 0.3 in that of higher stresses (Belyakov et al., 2001, Dudova et al., 2010). It is interesting to note that a similar type of the relationship is held between σ and d irrespective of different recrystallization mechanisms operating in different materials, i.e. dDRX and cDRX. In pure Cu and Ni-20%Cr, dDRX and cDRX can operate in the regions of lower flow stresses and higher ones, respectively. On the other hand, only cDRX can take place in hcp Mg alloy irrespective of the flow stress regions, as discussed above.

6. Mechanical properties of fine-grained Mg alloy

Tensile specimens were machined from the Mg plate MDFed parallel to the L-ST plane, as shown in Fig. 2 (a). An UFGed structure with d = 0.36 μm was developed in this plate MDFed to $\Sigma\Delta\varepsilon$ =4.8 with decreasing temperature from 623 K to 423 K. The tensile axis is perpendicular to the final compression axis, CA (see Fig. 2(a)). Tensile tests were carried out at 298 K and at 8.3×10^{-3} s^{-1}. Fig.15 shows changes in the true stress-nominal strain (σ - ε_n) curves with strain-induced grain size at 293 K (Xing et al., 2008). The σ - ε_n curve of the 22.3 μm sample shows a monotonous work hardening following yielding and then a stress peak just before fracture at a total elongation of about 35%. It is remarkable to note in Fig. 15 that the yield and peak stresses just before fracture increase remarkably accompanying with rather large magnitude of work hardening and moderate total elongation with decreasing grain size. The σ - ε_n curve of the 0.36 μm sample shows the highest yield stress over 400 MPa and the peak stress of 526 MPa at a total elongation of 13%. This yield stress is almost 5.3 times larger than that for the as-annealed sample. Fig. 16 shows the relationships between yield flow stress at a strain of 0.2% (σ_y) or room-temperature hardness (H_v) and the average grain size (d) developed during MDF (Xing et al., 2005, 2008). The results of H_v and σ_y are represented by open and solid circles, respectively. It is noted in Fig.16 that the relationship between H_v or σ_y and d can be approximated by the following Hall-Petch equations (1) and (2) with almost similar slopes of 0.23 and 0.21.

$$H_v = 500 + 0.23\, d^{-1/2} \quad (1)$$

$$\sigma_y = 80 + 0.21\, d^{-1/2} \quad (2)$$

Here the data for the as-annealed samples are not taken into account because they do not contain deformation- induced high-density dislocations. The highest values of H_v and σ_y for the UFGed sample are over about 2 and 4 times larger than those for the annealed one, respectively. It is concluded that excellent improvement of the mechanical properties of Mg alloy can be attained by MDF processing under decreasing temperature conditions.

It is remarkable to note in Fig. 15, on the other hand, that mechanical properties of the UFGed Mg alloy are excellent for not only strength, but also ductility at ambient temperature. It has been reported in (Humphrey & Hathery, 2004, Valiev & Langdon, 2006) that such excellent mechanical properties can be attained in various UFGed materials processed by SPD. Recently, Tsuji et al. (2002) investigated the grain size dependence of room temperature strength as well as ductility of an UFGed Al alloy and an interstitial free

(IF) steel processed by the accumulative roll-bonding (ARB) method. Fig.17 shows the relationships between uniform elongation (ε_u) and strain-induced grain size (ε_u - d) for Al alloy and IF steel processed by ARB and also of the present Mg alloy processed by MDF. It can be seen in Fig.17 that grain size dependence of ε_u is almost the same in the Al and IF steel irrespective of the different crystal lattice. It is remarkable to note that the

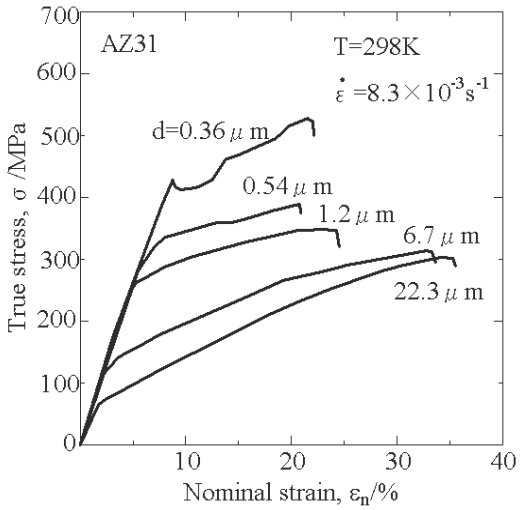

Fig. 15. Effect of strain-induced grain size on true stress-nominal strain (σ - ε_n) curves at 298K for Mg alloy AZ31 processed by MDF under dropping temperature condition.

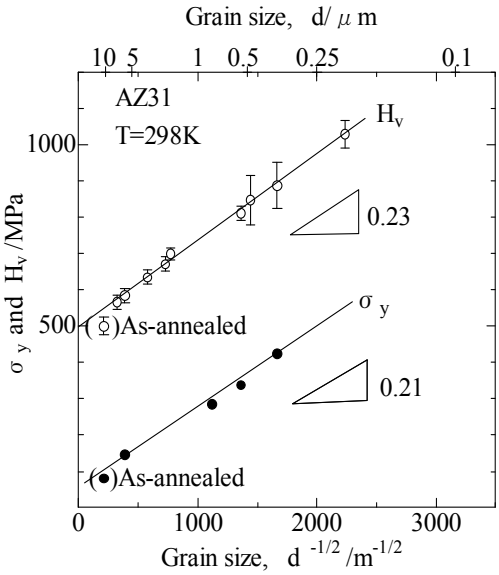

Fig. 16. Relationships between yield stress or hardness measured at 298K and strain-induced grain size developed by MDF of Mg alloy AZ31.

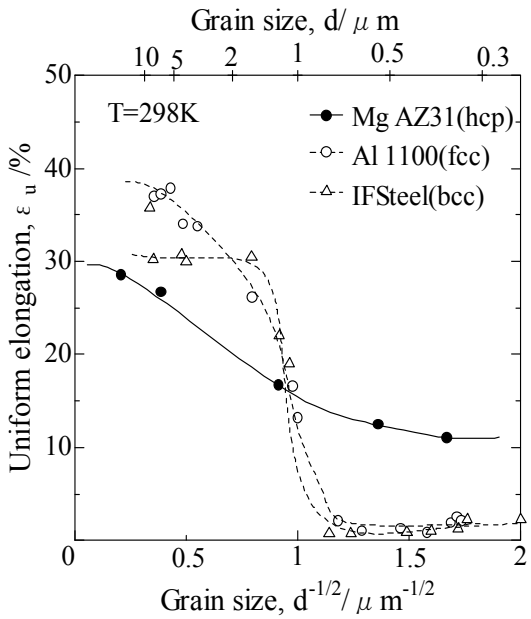

Fig. 17. Grain size dependence of uniform elongation measured in tensile tests at 298 K for Mg alloy AZ31, Al alloy 1100 and IF steel processed by severe plastic deformation. The data for Al 1100 and IF steel are reported by Tsuji et al., 2002.

uniform elongation of these metals suddenly drops to a few per cent at the grain sizes below around 1μm. In contrast, the uniform elongation of the Mg alloy does not show any drastic dropping at any grain sizes investigated and decreases gradually with decreasing grain size, and is always more than 13% even in the UFGed region. Tsuji et al. discuss that the dropping of uniform elongation taking place at grain sizes below 1 μm may be resulted from small or even negative work-hardening rate after yielding appearing in these UFGed materials, that is plastic instability.

By the way, Koike et al. (2003) studied dislocation microstructures developed by tensile deformation at room temperature for a polycrystalline Mg alloy AZ31. They observed in a 50 μm coarse-grained sample that non-basal **a** + **b** dislocations active only near grain boundaries, while basal **a** dislocations are dominant in grain interiors. In a 7 μm fine grained Mg alloy, in contrast, non-basal **a** + **b** dislocation segments are around 40% of the total dislocation density even in the grain interiors. If the data obtained by Koike et al. can be extrapolated to a range of submicron grain size, non-basal **a**+ **b** dislocations may be more activated to develop in grain interiors by compatibility stress concentration. This may activate various kinds of slip systems operating in non-basal and basal planes, and then result in relatively large work-hardening as well as moderate uniform elongation appearing in the UFGed Mg alloy, as can be seen in Fig. 17.

7. Superplasticity of fine-grained Mg alloys

Typical true stress-nominal strain (σ - ε_n) curves at various strain rates and elevated temperatures from 393K to 473K are shown in Fig. 18 (Xing et al., 2007, 2008). Strain rate

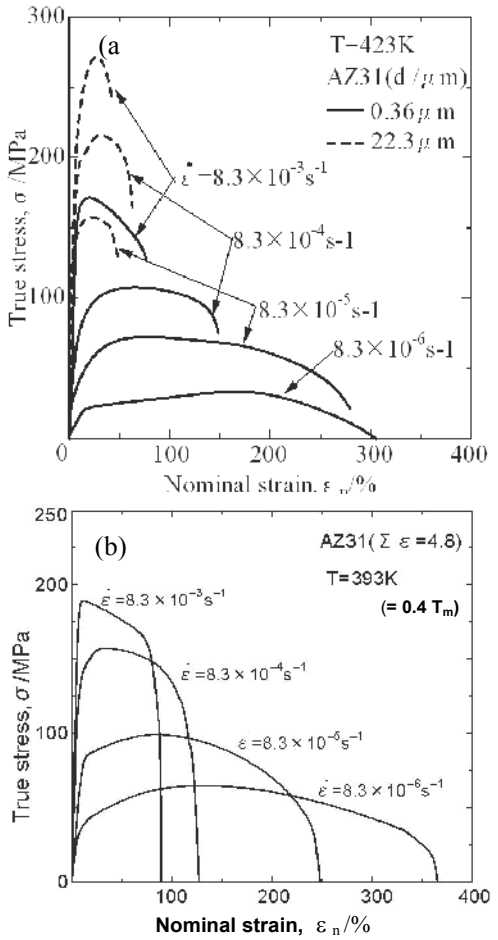

Fig. 18. (a) Effect of grain size on the strain rate dependence of true stress-nominal strain (σ - ε_n) curves at 423K and (b) strain rate dependence of σ - ε_n curves at 393 K (= 0.4 T_m) for Mg alloy AZ31 processed by MDF under dropping temperature conditions.

dependence of the flow stress peak (σ_p) and the total elongation to fracture (ε_T) are represented in Fig. 19. At the highest strain rate of around 10 $^{-2}$ s^{-1}, the σ - ε_n curves show a sharp stress peak in low strain, followed by work softening and then fracture at strains of about 100%. With decreasing strain rate, σ_p rapidly decreases and conversely ε_T increases from 100% to above 300%. At 393K and at 8.3×10 $^{-6}$s^{-1}, ε_T attains to the maximum of around 370%. A similar superplasticity was observed also in MDFed Mg alloy AZ61 (Miura et al., 2008). The superplasticity occurs at relatively low temperature (around 0.4 T_m), and so this may be defined as low temperature superplasticity. It is well known (Edington et al., 1976, Higashi et al., 1996, Nieh et al., 1997) that superplasticity can appear accompanying with a typical stress exponent ($n = \partial \ln \dot{\varepsilon} / \partial \ln \sigma$) of less than 3 and with an ε_T of above 200%. In the present experiments, however, n is always larger than 5 at strain rates investigated, while ε_T is always over 200% in strain rate below 10 $^{-3}$ s^{-1}. This result is contrast with those of general superplastic materials. This will be discussed later in detail.

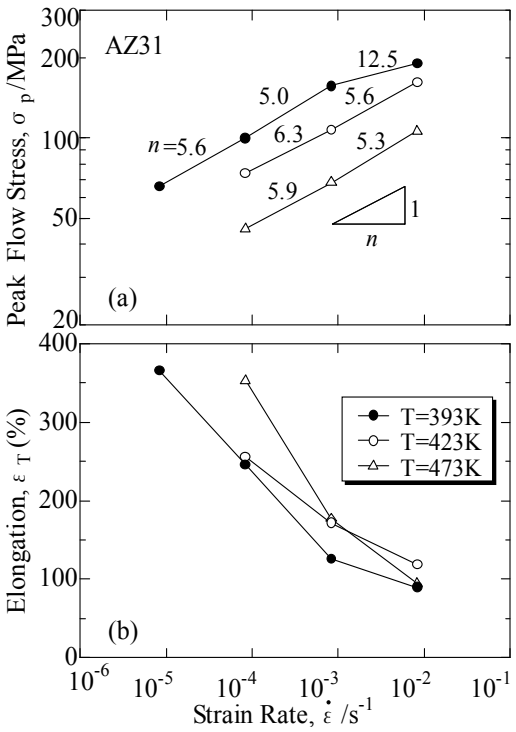

Fig. 19. Strain rate dependence of (a) peak flow stress σ_p and (b) total elongation to fracture ε_T of MDFed Mg alloy tested at 393K, 423K and 473K.

Fig. 20 shows changes in the strain-induced grain size with strain and strain rate at 473 K (Xing et al., 2007). The intial grain size of 0.36 μm in the as-MDFed samples increased to 2.2 μm during heating and keeping at 473 K before tension. It is seen in Fig. 20 that a grain structure developed by MDF is sensitively changed not only by strain rate, but also straining itself during tensile deformation. At $8.3\times10^{-5}s^{-1}$, grain size rapidly increases and attains to a peak value of 4.6 μm at $\varepsilon \cong 100\%$ and then gradually decreases to 4.1 μm at $\varepsilon \cong 350\%$. At $8.3\times10^{-4}s^{-1}$, grain size slightly increases to 2.5 μm at $\varepsilon \cong 100\%$ and then does not change in high strain. At the highest strain rate of 8.3×10^{-3} s^{-1}, in contrast, grain size decreases to 1.97 μm in early deformation and then gradually decreases with straining. At the same time, the strong texture of near {0001}; i.e. the basal plane of hcp lattice roughly parallel to the tensile axis, did not change during tensile deformation up to strain of 350% (Xing et al., 2007) (see also Fig.21). It is concluded, therefore, that the grain size of the fine-grained Mg alloy remarkably changes during superplastic deformation and, in contrast, the deformation texture is hardly changed.

Let us discuss such a characteristic superplasticity appearing in the MDFed fine-grained Mg alloy and the reason why the stress exponents are always over 3. It is generally accepted that superplasticity of fine grained materials can be controlled mainly by grain boundary sliding and so expressed by the following equation (Edington et al., 1976, Higashi et al., 1996, Nieh et al., 1997),

$$\dot{\varepsilon} = k \cdot d^{-p} \cdot \sigma^{n} \cdot \exp(-Q / RT) \tag{3}$$

where k is a constant, p is the grain size exponent, n is the stress exponent, Q is the apparent activation energy for deformation, and R is the gas constant. The n in equation (3) is obtained in the case that an initial grain size does not change during deformation. It is noted in Fig. 20 that the grain size changes depend sensitively on strain and strain rate in Mg alloy, while the changes of grain size with deformation are relatively small at high strains. The grain size developed in low strain is assumed here to be roughly constant at high strains and to depend mainly on strain rate. The relationship between the peak flow stress (σ_p) and the grain size (d) developed at around a strain associated with σ_p can be approximated by a power law function expressed by the following equation.

$$\sigma_P = k_1 \cdot d^{-N} \tag{4}$$

here k_1 and N are constants. N = 0.9 was obtained from the experimental data of Figs. 18 and 20. On the other hand, if the stress exponent is designated by n' in the present case, where d changes with deformation according to equation (4), the relationship between $\dot{\varepsilon}$ and σ_p can be approximated by equation (5).

$$\dot{\varepsilon} = k_2 \cdot {\sigma_P}^{n'} \tag{5}$$

It is seen in Fig. 19 that n' ranges from 5 to 6.3. Then the following relationship is derived from equations (3), (4) and (5).

$$n' = n + \frac{p}{N} \tag{6}$$

It has been reported in many superplastic metals and alloys (Edington et al., 1976, Higashi et al., 1996, Nieh et al., 1997) that p ranges from 2 to 3. If n' = 5 - 6.3 in Fig. 19, N = 0.9 and p = 2 - 3 are given in equation (6), the n takes a value of 2.8 - 3.0. This is almost similar to the

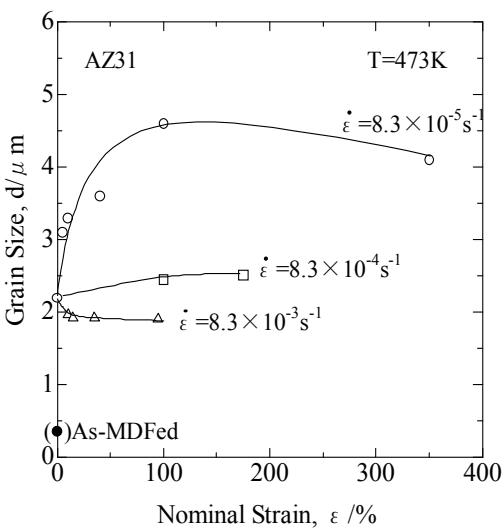

Fig. 20. Effect of strain rate on changes in average grain size with tensile deformation of MDFed Mg alloy at 473K.

typical values reported in general superplastic materials. It is concluded, therefore, that the true stress exponent of around 3 apparently increases to the experimental one of $n' = 5$ - 6.3 because the initial grain size changes sensitively with deformation.

Next let us discuss the texture change in the fine-grained Mg plate taking place during superplasticity. Fig. 21 shows OIM micrographs for a same position in the L-ST surface deformed at 473K and at 8.3×10^{-5} s^{-1} (Xing et al., 2007). It is seen in Fig. 21 that the crystal orientations of the grains marked by a, b, c and d hardly change within experimental scatters during tensile straining from $\varepsilon = 5\%$ to $\varepsilon = 40\%$. It is interesting to note that the new grains indicated by arrows in Fig.21 (b) appear in the adjoining area of the grains c and d for a strain interval between 5% and 40%. This suggests that some grains in a lower grain layer of L-ST plane may be moved to an upper layer accompanied by grain boundary sliding during deformation, that is, Fig. 21 may be an evidence for operation of the grain-switching mechanism in Mg alloy (Ashby & Verrall, 1997). It is concluded from the present study that superplasticity of fine-grained Mg alloy processed by MDF can be controlled mainly by grain boundary sliding, and at the same time grain coarsening and refinement takes place during deformation, while grain rotation hardly takes place. It is interesting to note that grain rotation hardly takes place irrespective of the operation of grain boundary sliding, and grain refinement takes place during early deformation at higher strain rate or later one at low strain rate (Fig. 20). These unusual results in Mg alloy should be investigated in more detail in the near future.

Finally let us examine the influence of the texture anisotropy of the MDFed Mg alloy on tensile deformation. Three kinds of tensile specimens, i.e. the 0°, 45° and 90°ones in Fig. 2 (b), were used for the tests. Tensile tests were performed at initial strain rates ranging from 5×10^{-5} s^{-1} to 5×10^{-3} s^{-1} and at 423 K. Typical true stress - nominal strain (σ - ε_n) curves are

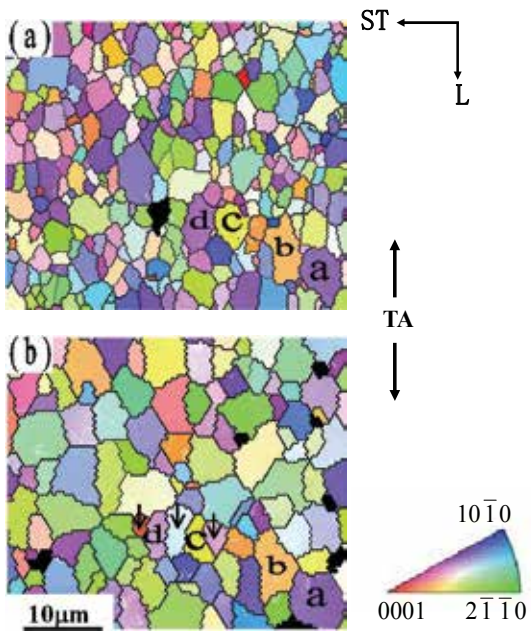

Fig. 21. OIM micrographs in L-ST surface at a same position during tensile deformation at 473 K and at 8.3×10^{-5} s^{-1}. (a) $\varepsilon = 5\%$ and (b) $\varepsilon = 40\%$

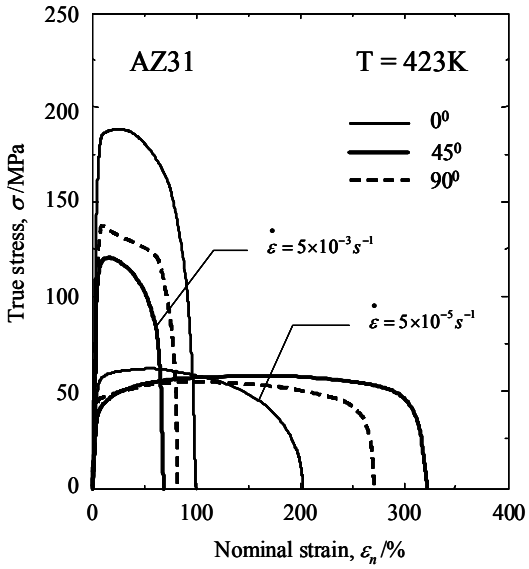

Fig. 22. True stress-nominal strain curves of MDFed Mg alloy AZ31 with different starting textures at strain rates of 5 x 10^{-5} s^{-1} and 5 x 10^{-3} s^{-1}.

represented in Fig. 22 (Zhang et al., 2009). At a higher strain rate of 5 × 10^{-3} s^{-1}, the curves show a stress peak just after yielding followed by strain softening and fracture at relatively low strain. Flow stresses decrease clearly in the order of the 0°, 90° and 45°specimen, and total elongations to failure (ε_f) of below 100% also decrease in the same order. At a lower strain rate of 5 × 10^{-5} s^{-1}, in contrast, flow curves show lower flow stresses of one-second to one-forth of those at 5 × 10^{-3} s^{-1} and large elongations to failure of over 200%. It is interesting to note that total elongations to failure increase from about 200% to 320% in the order of the 0°, 90° and 45° specimen. It is found in Fig. 22 that the mechanical properties of the present AZ31 alloy processed by MDF are sensitively affected by not only strain rate, but also the texture.

The initial texture dependence of σ_p and ε_f is depicted in Fig. 23 (Zhang et al., 2009). Anisotropy of peak flow stress resulting from the initial texture appears significantly at a higher strain rate of 5 × 10^{-3} s^{-1}. The anisotropy of σ_p decreases with decrease in strain rate and is difficult to be detected at a lower strain rate of 5 × 10^{-5} s^{-1}. However, yield stress (σ_y) at 5 × 10^{-5} s^{-1} decreases in the order of the 0°, 90° and 45° specimen, which is a similar dependence of σ_p at higher strain rates. On the other hand, texture anisotropy of ε_f also appears clearly at a strain rate of 5 × 10^{-5} s^{-1}, where all the values of ε_f are over 200%, i.e. about 320% for the 45° specimen, 280% for 90° specimen and the smallest one of 200% for 0° specimen. ε_f decreases rapidly with increase in strain rate and the anisotropy of ε_f becomes small at 5 × 10^{-3} s^{-1}.

Let us discuss such different tensile behavior appearing in the 45° or 90° specimens and in the 0° one. In the 0° specimen, slipping on basal plane and grain rotation accompanied by grain boundary sliding hardly take place during superplastic deformation, as discussed in Fig. 21. In the 45° specimen, in contrast, slip by dislocation motion additionally and easily takes place on the basal plane inclined 45° to the tensile axis and grain refinement due to cDRX may also take place in high strain during tensile deformation (see Fig. 20). This is why

larger total elongation to failure appears at 5×10^{-5} s^{-1} in the 45° or 90° specimen rather than in the 0°specimen. The various initial textures of the present alloy change with straining and approach the same stable texture in large tensile strain, i.e. the basal plane parallel to tensile axis (Zhang et al., 2009). It is concluded that superplastic deformation of the present fine-grained Mg alloy processed by MDF can be controlled mainly by not only grain boundary sliding, but also dislocation motion and grain refinement or coarsening taking place due to the operation of cDRX. The 0° specimen, in contrast, show a minimum elongation to fracture because of no texture change during tensile deformation. As a result, total elongation to failure can be affected sensitively by the initial texture of Mg specimens. However, these results should be also systematically investigated in more detail in the near future.

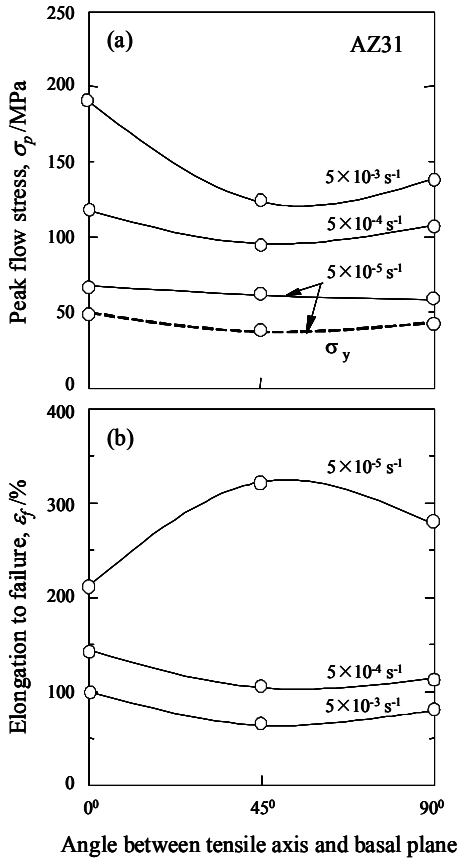

Fig. 23. Changes in (a) peak flow stress σ_p (and σ_y) and (b) elongation to failure ε_f with initial textures of MDFed AZ31 alloy tested at 423K and at various strain rates.

8. Conclusions

In magnesium (Mg) alloys categorized as hard plastic materials, fine grains are developed at relatively low strains during warm and hot working. In this chapter, optimum dynamic processes for fine grain development are studied in multi-directional forging (MDF) under decreasing temperature conditions by using commercial Mg alloys, such as AZ31, AZ61, etc.

The fine-grained Mg products processed by MDF can result in much improvement of the mechanical properties at ambient temperature and low temperature superplasticity. The main results are summarized as follows.

1. Dynamic grain evolution in Mg alloy can be resulted from grain fragmentation by kink band taking place in original grain interiors, and so controlled by deformation-induced continuous reactions assisted by dynamic recovery, i.e. continuous DRX. The grain refinement process taking place during deformation is accelerated by multi-directional forging (MDF), which is carried out with changing the loading direction from pass to pass accompanying with decrease in temperature.
2. The average grain size developed during MDF is almost constant during isothermal forging, while the one evolved under dropping temperature condition from 623 K to 403 K (< 0.5 Tm) decreases drastically with repeated MDF and approaches 0.23 μm at $\sum\Delta\varepsilon = 5.6$.
3. From the results of room temperature tensile tests for MDFed Mg alloys with a grain size of 0.36 μm, the sample shows the highest yield stress over 400 MPa and the peak flow stress of 526 MPa at a total elongation of 13%. The mechanical properties of the ultrafine grained Mg alloy are excellent for not only strength, but also ductility at ambient temperature, because various types of dislocations can be activated to operate in finer grain interiors.
4. From the results of tensile tests carrying out at temperatures from 393 K to 473 K and at various strain rates, the total elongation to fracture increases from 100 % to above 300 % and attains to the maximum of around 370 % at 393 K and at 8.3×10^{-6} s^{-1}. It is concluded that low temperature superplasticity can take place in the fine-grained Mg alloys processed by MDF. The mechanisms operated are analyzed and discussed in detail.

9. Acknowledgements

The authors are intended to Drs. Belyakov, Jonas, Kaibyshev, Sitdikov, Xing & Yang for stimulating discussions. They also acknowledge with gratitude the financial support received the following sources: the Ministry of Education, Science and Culture for some Grants-in-Aid for Scientific Research, the Japan Research Institute Advanced Copper-Base Materials and Technologies, and the Light Metals Educational Foundation, Japan, under several grants of scientific research.

10. References

Ashby, M.F. & Verrall, R.A. (1973). Diffusion-accommodated flow and superplasticity. *Acta Met.*, 21, 149-163.

Belyakov, A., Miura, H. & Sakai, T. (1998). Dynamic recrystallization under warm deformation of a 304 type stainless steel. *Mater. Sci. and Eng. A*, 255, 139 -147.

Belyakov, A., Sakai, T., Miura, H. & Kaibyshev, R. (2000). Strain-induced submicro-crystalline grains developed in austenitic stainless steel under severe warm deformation, *Philos. Mag. Letters*, 80, 711-718.

Belyakov, A., Sakai, T., Miura, H. & Tsuzaki, K. (2001). Grain refinement in copper under large strain deformation, *Philosophical Magazine A*, 81, 2629-2643.

Dudova, N., Belyakov, A., Sakai, T. & Kaibyshev, R. (2010). Dynamic recrystallization mechanisms operating in a Ni-20%Cr alloy under hot-to-warm working. *Acta Materialia*, 58, 3624-3632.

Edington, J., Melton, K.N. & Cutler, C. P. (1976). Superplasticity. *Progress in Materials Science*. 21, 61-170.

Galiyev, A., Kaibyshev, R. & Gottstein, G. (2001). Dynamic recrystallization in pure magnesium. *Acta Mater.* 49, 1199-1207.

Gao, W., Belyakov, A., Miura, H. & Sakai, T. (1999). Dynamic recrystallization of copper polycrystals with different purities, *Mater. Sci. and Eng. A,* 265, 233 - 239.

Higashi, K., Mabuchi, M. & Langdon, T.G. (1996). High-strain-rate superplasticity in metallic materials and the potential for ceramic materials. *ISIJ Intl*., 36, 1423-1438

Higashida, K., Takamura, J. & Narita, N. (1986). The formation of deformation bands in f.c.c. crystals. *Mater. Sci. Eng.*, 81, 239-258.

Humphreys, F.J. & Hatherly, M. (2004). *Recrystallization and related annealing phenomena* (Second edition), (Elsevier, UK).

Ion, S.E., Humphreys, F.J. & White, S.H. (1982). Dynamic recrystallization and the development of microstructure during the high temperature deformation of magnesium. *Acta Metall.* 30, 1909- 1919.

Kobayashi, C., Sakai, T., Belykov, A., & Miura, H. (2007). Ultrafine grain development in copper during multidirectional forging at 195 K. *Phil. Mag. Letters,* 87, 751-766.

Koike, J., Kobayashi, T., Mukai, T., Watanabe, H., Suzuki, M., Maruyama, K. & Higashi, K., (2003). The activity of non-basal slip systems and dynamic recovery at room temperature in fine-grained AZ31B magnesium alloys. *Acta Mater.* 51 (2003), 2055-2065.

Mazurina, I., Sakai, T., Miura, H., Sitdikov, O. & Kaibyshev, R. (2008). Grain refinement in aluminum alloy 2219 during ECAP at 250 ^{o}C. *Mater. Sci. Eng. A*, 473, 297-305.

Miura, H., Aoyama, H. & Sakai, T. (1994). Grain boundary misorientation effect on dynamic recrystallization of Cu-Si bicrystals. *J. Jpn Inst. Metals*, 58, 267-275.

Miura, H., Yang, X., Sakai, T., Mogawa, R., Watanabe, T., Miura, S., & Jonas, J.J. (2005). High temperature deformation and extended elongation of Mg single crystals, *Phil. Mag.*, 85, 3553-3565.

Miura, H., Sakai, T., Mogawa, R., & Jonas, J.J. (2007). Nucleation of dynamic recrystallization and valiant selection in copper bicrystals, *Phil. Mag.,* 87, 4197-4209.

Miura, H., Yang, X. & Sakai, T. (2008). Evolution of ultra-fine grains in AZ31 and AZ61 Mg alloys during multi-directional forging and their properties, *Mater. Trans.,* 49, 1015-1020.

Miura, H, Yu, G., Yang, X. & Sakai, T. (2010). Microstructure and mechanical properties of AZ61 Mg alloy prepared by multi directional forging, *Trans. Nonferrous Metals Society of China*, 20 (in press).

Mordike, B.L. & Ebert, T. (2001). Magnesium properties - applications - potential. *Mater. Sci. Eng*. A. 302, 37-45.

Nieh, T.G., Wadsworth, J. & Sherby, O.D. (1997). *Superplasticity in metals and ceramics*, (Cambridge University Press).

Rollet, A.D. & Wright S.I. (1998). Typical textures in metals. In: *Texture and anisotropy,* Kocks, U.F., et al., (Ed.), 178-238, Cambridge University Press.

Sakai, T. & Jonas, J.J. (1984). Dynamic recrystallization: mechanical and microstructural consideration, *Acta Metalrgica.* 32, 189-209

Sakai, T. & Takahasi, C. (1991). Flow softening of 7075 aluminum alloy under hot compression, *Mater. Trans., JIM.* 32, 375-382.

Sakai, T. & Jonas, J.J. (2001). Plastic deformation: role of recovery and recrystallization, In: *Encyclopedia of Materials Science and Technology*, Buschow, K.H., et al., (Ed.), 7079-7084, (Elsevier, Oxford).

Sakai, T., Belyakov, A. & Miura, H. (2008). Ultrafine grain formation in ferritic stainless steel during severe plastic deformation, *Metall. Maters. Tra*ns. *A*, 39, 2206-2214.

Sitdikov, O. & Kaibyshev, R. (2001). Dynamic recrystallization in pure magnesium. *Mater. Trans.*, 42, 1928- 1937.

Sitdikov, O., Kaibyshev, R. & Sakai, T. (2003). Dynamic recrystallization based on twinning in coarse-grained magnesium. *Mater. Sci. Forum,* 419-422, 521- 526.

Tsuji, N., Ito, Y., Saito,Y. & Minamino, Y. (2002). Strength and ductility of ultrafine grained aluminum and iron produced by ARB and annealing. *Scripta Materialia*, 47, 893-899.

Valiev, R.Z. & Langdon, T.G. (2006). Principles of equal-channel angular pressing as a processing tool for grain refinement, *Prog. Mater. Sci.* 51, 881-981.

Wusatowska-Sarnek, A.M., Miura, H. & Sakai, T. (2002). Nucleation and microtexture development under dynamic recrystallization of copper, *Mater. Sci. and Eng. A,* 323, 177-186.

Xing, J., Soda, Y., Yang, X., Miura, H., & Sakai, T. (2005). Ultra-fine grain development in magnesium alloy AZ31 during severe large forging under decreasing temperature conditions, *Mater. Trans.,* 46, 1646-1650.

Xing, J., Yang, X., Miura, H., & Sakai, T. (2007). Superplasticity of magnesium alloy AZ31 processed by multi-directional forging, *Mater. Trans.*, 48, 1406-1411.

Xing, J., Yang, X., Miura, H. & Sakai, T. (2008). Mechanical properties of magnesium alloy AZ31 after sever plastic deformation, *Mater. Trans.,* 49, 69-75.

Yang, X., Ji, Z., Miura, H. & Sakai, T. (2009). Dynamic recrystallization and texture development during hot deformation of magnesium alloy AZ31, Trans. Nonferrous Metals Society of China, 19, 55-60.

Yang, X., Miura, H. & Sakai, T. (2003). Dynamic evolution of new grains in magnesium alloy AZ31 during hot deformation, *Mater. Trans.*, 44, 197 - 203.

Yang, X., Xing, J., Miura, H. & Sakai, T. (2006). Strain-induced grain refinement of magnesium alloy AZ31 during hot forging, *Materials Science Forum,* 503-504, 521-526.

Yang, X., Miura, H. & Sakai, T. (2007). Effect of initial grain size and strain path on grain refinement in magnesium alloy AZ31, *Materials Science Forum*, 539-543, 1632-1637.

Zhang, Z.-R., Xing, J., Yang, X., Miura, H. & Sakai, T. (2009). Anisotropy of low temperature superplasticity of ultrafine grained magnesium alloy AZ31 processed by multi-directional forging, *Mater. Sci. Tech.,* 25, 1442-1447.

11

Grain Refinement of Magnesium Alloy by Multiaxial Alternative Forging and Hydrogenation Treatment

Kunio Funami and Masafumi Noda
Department of Mechanical Science and Engineering, Chiba Institute of Technology
Japan

1. Introduction

Owing to their high specific strength, magnesium alloys are promising materials for use in various structural products whose weight is to be minimized. These alloys are drawing attention as materials with reduced environmental load since they save both resources and energy. However, these alloys have low strength and a small number of slip systems and are more difficult to work forming. Therefore, it is necessary to modify them, e.g., improve the mechanical properties and fatigue strength of the alloys, and reduce processing costs, which would help increase their industrial applications. To overcome the above-mentioned drawbacks, the formation of a fine-grained structure would be useful. For magnesium materials, the effect of fine-grained structure on the static mechanical properties, fatigue, and fracture toughness has been investigated to study their practical applicability(Nagata et al,2007). Such investigations are very important for increasing the use of magnesium alloys as industrial materials (Noda et al, 2009).

Microstructure control has been achieved through grain refinement by employing several strain work processes such as MA (Mechanical Alloying:Ameyama et al.,1998), ECAP (Equal Channel Angular Pressing:Berbon et al.,1999), ARB (Accumulative Roll-Bonding:Tsuji et al.,1999), and MAF (Multiaxial Alternative Forging:Noda et al.,2005 and Xing et al,2005). These methods were found to enhance strain energy in materials without changing their geometrical shapes. This means that under external deformation, it is necessary to produce in materials, as much as possible, a nonhomogeneous microstructure containing such as micro bands, shear bands, and lamellar boundaries. In the early stages of deformation, even a small increase in the number of dislocation pile-up sources influences the formation of dense dislocation walls and cells. Examples of such sources are static and dynamic recrystallization sources.

Magnesium alloys have high hydrogen absorbing capacity, similar titanium alloys, and readily form hydrides under suitable temperature and pressure (Yoshimura et al, 1994). Hydride precipitates of MgH_2 obtained in this treatment were useful for developing high-density dislocation pile-up sources. This refinement treatment, which involves the use of hydrogen, titanium alloy, and titanium composite alloy with dispersed TiC particles, resulted in a homogeneous, fine, and equi-axial structure(Machida et al,2004). It appears that the combination of a plastic deformation process and hydrogenation treatment has considerable potential to induce a fine-grained structure in a magnesium alloy (Ishida et al, 2007).

In this study, we combined the hydrogen absorption method and the MAF process for grain refinement of a material surface. Hydrogenation treatment involves producing the hydride compound MgH_2 in the magnesium alloy through hydrogen absorption, making use of magnesium's ability to absorb hydrogen, and using the resultant hydrogen compounds to trap defects; these defects are induced by severe strain working such as shot peening on a material surface subjected to recrystallization and heat treatment for grain refinement. We study the effectiveness of hydrogenation treatment and the MAF process for grain refinement; we attempt to improve the strength of magnesium alloys by carrying out grain refining by the MAF process, investigate the mechanical properties of the grains, and improve the workability of these fine-grained materials. When hydrogenation-dehydrogenation and shot peening techniques are used, the surface structure of fine-grained magnesium materials obtained by MAF becomes finer.
This study investigates the following:

1. effect of MAF on grain refinement in a magnesium alloy together with the microstructure formation process of MAFed magnesium alloy and its mechanism
2. effect of hydrogenation treatment using rolling working and shot peening working for plastic formation on the surface microstructure of the MAFed magnesium alloy
3. mechanical properties of a fine-grained magnesium alloy, that is, fatigue strength, fracture toughness, and crack propagation behavior, and the influence of grain size on the properties.

2. Effect of grain refinement by multiaxial forging

2.1 Specimen and processing method

The specimens we used were a commercially available magnesium AZ31 extruded material. The chemical composition of each material was Al (3.13 mass%), Zn (0.90 mass%), Mn (0.55 mass%), and Fe (0.003 mass%). Each had a cubic shape with an edge of 30 mm. Figure 1-1 shows the initial structure of the AZ31 material. The initial crystal structure of the extruded material is finer than that of the cast material, with the initial crystal grain diameter being 20 μm. However, the mechanical properties vary greatly in the direction of extrusion and in the direction perpendicular to it due to the effect of the processing strain. We subjected this material to multiaxial forging, as shown in Fig.1-2.
The processing temperature, speed, and draft rate were varied and the recrystallization temperature was considered as the reference. As shown in the figure, the processing

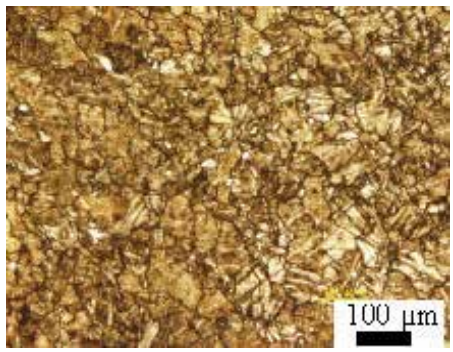

Fig. 1-1. Optical microstructure of as-received extrusion AZ31 magnesium alloys used.

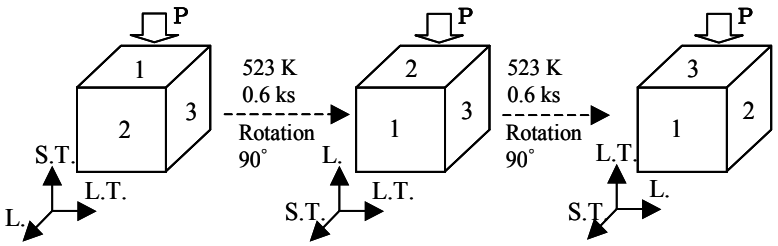

Fig. 1-2. Schematic illustration of the working process of the multi-axial alternative forging.

procedures comprised forging by alternately turning faces 1–3 by 90°. The execution of the forging process once for each of the faces was defined as one cycle. In any given cycle, forging was performed at a constant processing temperature, and the temperature was partially varied between cycles.

For forging codition as shown in Fig.1-2, forging of the specimens was started after maintaining the specimens at 523 K for 3.6 ks. They were again maintained at the same temperature for 0.6 ks again before proceeding to process the next face. The temperature at which the specimens were maintained was 523 K for cycles 1 and 2, 473 K for cycles 3–5, and 443 K for cycles 6–8. The specimens were cooled in water after processing. The draft rate for each face was controlled at 20% and the displacement rate at 1 mm/min. The specimens were processed for eight cycles, which corresponded to an equivalent strain of 4.8. Direction S.T. was the direction of extrusion for the extruded material.

The structures observation was made of the cast and extruded materials were observed after MAF processing, and the specimens were then subjected to the hardness test and tensile test. The dimensions of a specimen used for the tensile test were 1 mm (thickness), 3 mm (width), and 5 mm (length). The tensile test was conducted at room temperature and the initial strain rate was 8.3×10^{-3} s^{-1}. The hardness test was conducted using the micro-Vickers method, with an indentation load of 2.94 N and a period of 30 s. The crystal grain diameter was observed using optical microscopy and SEM and calculated by the section method. The internal structure of the specimens was observed using TEM.

2.2 Structural changes and grain refinement by multiaxial forging

2.2.1 Multicycle forging of magnesium alloy

The structure of a specimen forged for 6 cycles for the processing conditions shown in Fig.1-2 is shown in Fig.1-3; the structure was observed using optical microscopy. Although some coarse grains remain for both processing conditions, fine grains are found to be dominant overall. While the average grain diameter for processing condition was about 1 μm.

Large plastic strain is accumulated internally in the specimen due to free forging. However, strain distribution and accumulation in the material sides and section in contact with the compression plate, as well as the internal strain distribution and accumulation were not uniform.

Thus, the temperature of the material was not uniform when at which recrystallization began was not uniform, leading to difference in the formation of fine crystal grains with different sizes which are generated by dynamic recrystallization depending on the location and the formation of different substructures resulting in different substructures at different locations. However, uniform refinement became possible when the number of MAF processing cycles was increased.

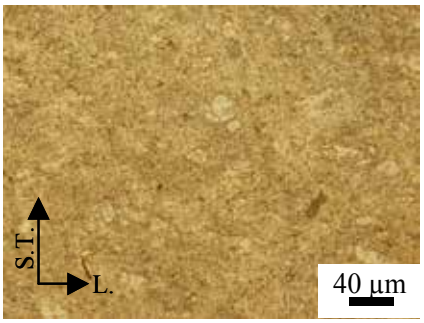

Fig. 1-3. Optical microstructure of 6 cycles MAFed AZ31 magunesium alloys by working condition as shown in Fig.1-2.

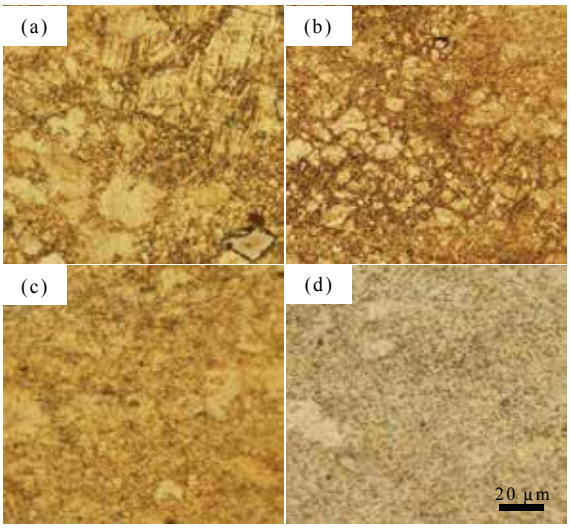

Fig. 1-4. Optical microstructure of MAFed AZ31Mg alloys under various forging process, (a) : 1cycle,(b) : 2cycle,(c) :5cycle and (d) : 8cycle.

The number of cycles in forging processing condition and the changes in the specimen structure are shown in Fig.1-4. The initial grain diameter at the beginning of the processing cycle was 20 μm; the grain diameters at the end of the first, second, fifth, and eighth MAF processing cycles were 15, 9, 4, and 1 μm. Deformation bands and twin crystals were formed by one-pass processing, in which forging was conducted in the extruding direction and fine grains were formed by dynamic recrystallization, and the crystal grains that were elongated in the extruding direction were deformed in a perpendicular direction, which makes the crystal grains larger in the extrusion plane and smaller in the perpendicular plane. At the same time, a kink band is formed within the crystal grain in the perpendicular plane, which refines the grains even further. Similarly, in two-pass processing, twin crystals, deformation bands, and kink bands were formed on the three planes of extrusion planes and perpendicular plane, and they tended to be the cores that triggered dynamic recrystallization. That is, the effects of refinement by segmentation of crystal grains were small in both the extrusion plane and perpendicular plane for one-pass processing, highlighting the formation of fine grains around the ground boundary.

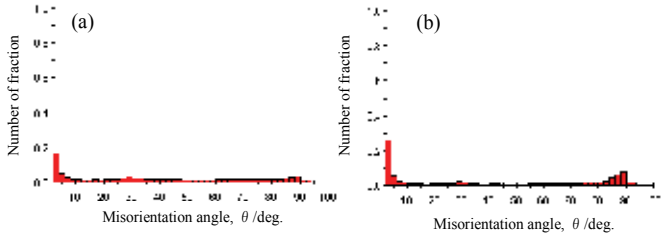

Fig. 1-5. Misorientation angle distribution of MAFed AZ31Mg alloys by working condition as shown in Fig.1-2, (a):1cycle and (b):5cycle.

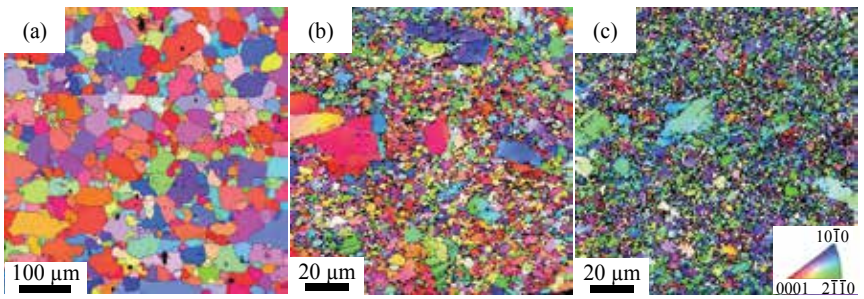

Fig. 1-6. IPF map of MAFed AZ31Mg alloys, (a):as-received extrusion material, (b): 1 cycle MAFed material, (c): 5 cycle MAFed material by forging working.

Further, crystal grains formed by refinement by segmentation were larger than fine grains formed around the grain boundary both in the extrusion plane and perpendicular plane in two-pass processing. Therefore, repeating this process in different directions, along the three axes, accelerates crystal grain refinement.

The misorientation angle distribution diagram, and IPF map (Figs.1-5 and Fig.1-6) obtained from EBSP analysis support the above-mentioned facts. Figure 1-5 shows the frequency of orientation difference of the adjacent crystal.

It is evident that the crystal grains become more uniform and refined as the number of MAF processing cycles is increased. Since the low-angle grain boundary with an orientation difference of 5° or less is formed by almost segmenting the coarse grains, it is assumed that it increases the grain boundary orientation difference after dynamic recrystallization and advances the refinement with an increase in the number of processing cycles.

2.2.2 Single-cycle forging of magnesium alloy

While the structure is increasingly refined as the number of MAF process cycles increases, it is desirable for the structural refinement to be conducted efficiently in a short period at the processing site. Therefore, we examined by to what extent refinement accelerated in one cycle by controlling the process temperature, speed, and process rate. The process conditions we used are provided in Table 1-1.

To minimize the forging count and obtain material with a refined structure, we processed the material only for one cycle and varied the temperature for each pass. The material we used had a larger size (dimension of one side: 100 mm).

Figure 1-7 shows an IPF map of the AZ31Mg alloy processed for one cycle under the forging conditions E. While the average grain diameter is 5 μm, there are island-like large crystal

Forging temperature : (Working temperature changes on each pass stage in cycles)				
Press ratio		1pass	2 pass	3 pass
E	20%	543 K	493 K	453 K
		Working speed (mm/min)		
		2		
F	30%	543 K	513 K	433 K
		Working speed (mm/min)		
		3	2	2

Table 1-1. MFA working condition in 1 cycle.

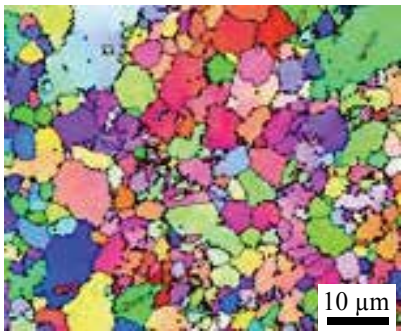

Fig. 1-7. Optical microstructure and IPF map by EBSP analysis of MAFed AZ31 Mg alloys by working condition E.

grains among fine crystal grains, showing a typical duplex grain size structure. EBSP analysis shows that these island-like large grains had many twin crystal/deformation bands. Figure 1-8 shows the IPF map and texture of the material forged for one cycle, which was further 50% hot-rolled under process conditions F. The axial direction of the bottom part of the rolled material is inclined in the plate thickness direction, which may imply large ductility.

The initial structures of the cast material and extruded material differ greatly, and the average crystal grain diameter for the materials after three cycles is 10 μm and less than or equal to 2 μm, respectively. The crystal grain diameter for both materials becomes equal

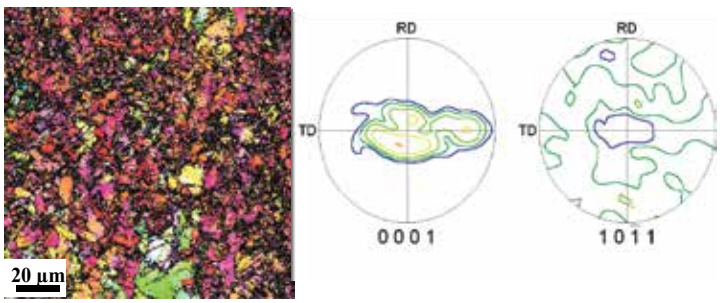

Fig. 1-8. IPF map and texture of MAFed AZ31 which carried out rolling processing 50% after forging process by working condition F.

after five cycles. However, the extruded material has a uniform, fine structure while the cast material has a duplex grain size structure that includes large crystals. Since refinement is accelerated quickly as a result of the MAF process facilitating the segmentation of the cell structure, forging of material with a unidirectional elongated structure by an extruding process occurs effectively.

2.3 Mechanical properties

To study the effects of an increase in the process count on the difference in the degree of work hardening acceleration, we checked the hardness of the cast material and extruded material processed under forging conditions as shown in Fig.1-2.

Although the process temperature is decreased in every few cycles, both materials hardened as the number of forging cycles increased, and the internal strain increased and saturated; these observations indicateding that any further increase in the number of process cycles would generate cracks. To form a fine structure by recrystallization thermal treatment, it is necessary that the increase in internal strain and uniformity of the strain distribution be controlled.

While both the cast material and extruded material increase in strength and elongation as the number of forging count increases, the deformation behavior varies depending on the degree of change in the internal structure due with increasing in cycle count; this variation is because their initial material conditions are different for the two materials. However, this increase reaches saturation after about five cycles for both materials.

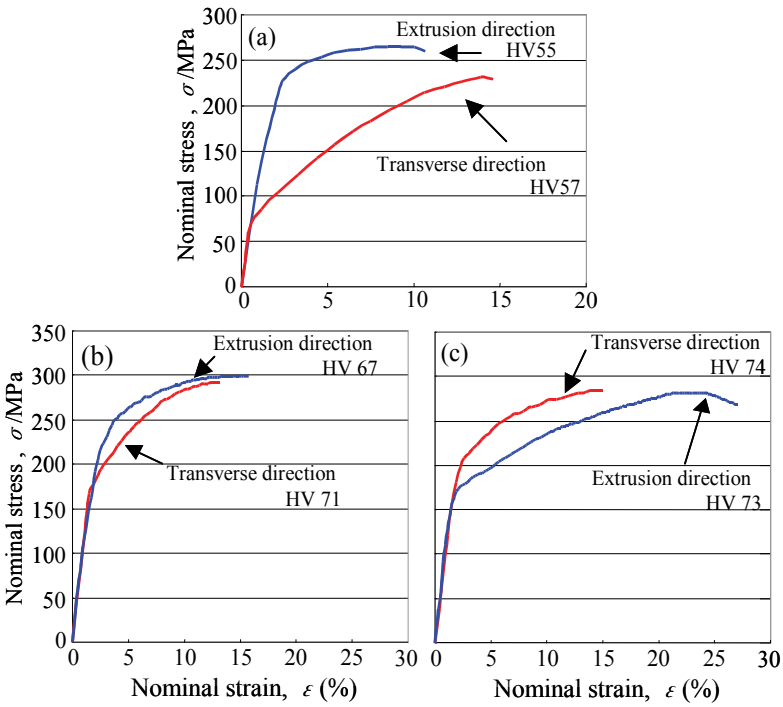

Fig. 1-9. Effect of MAF working process on nominal stress-strain curves of extrusion AZ31 Mg alloys, (a) : as-received extrusion material , (b) : 1cycle MAF working and (c) : 4cycle MAF working.

Figure 1-9 shows the change in the deformation behavior of the extruded material in the tensile direction when the number of forging cycles is increased. As shown in Fig.1-9(a), the received material had a proof stress that was three times greater and a tensile strength about 20% higher, while the total extension in the longitudinal direction was lesser than that in the vertical direction; the material properties in the longitudinal direction were improved by the extrusion process.
Upon forging these materials repeatedly, improvements in the tensile strength and proof stress reach saturation after several cycles, as shown in Subfigures (b) and (c). Although changes are not observed in the growth in the vertical direction compared to the initial material, anisotropy of the deformation strength decreases while the growth in the extruding direction increases by a factor of more than 2. This observation indicates the significant effect of forging. The growth in the vertical direction remains small because the distribution of fine structure is not uniform. That is, selection of the process load path and the process conditions is important for advancing refinement.

3. Surface structure refinement by hydrogenation treatment and its effects

From studies on hydrogenated materials, it has been confirmed that hydrogenation of magnesium materials yields magnesium hydride. The possibility of structural refinement has previously been shown for Ti materials by combining hydride formation and a strengthening process, and the hydride formation process in Mg alloys is similar to that in Ti materials. This section reports the results of using the recrystallization process for the structural refinement of Mg alloys; the variation of the dislocation density of the hydride relative to that of the subgrain is examined.

3.1 Materials and methods

We used a commercially available Mg alloy (AZ31B) extruded material as the specimens, similar to the investigation discussed in the previous section. We performed MAF processing on a cube with an edge of 90 mm under condition as shown in Fig.1-2. This pre-MAF processing increases the grain boundary area through crystal refinement and causes structural refinement of the entire base material.

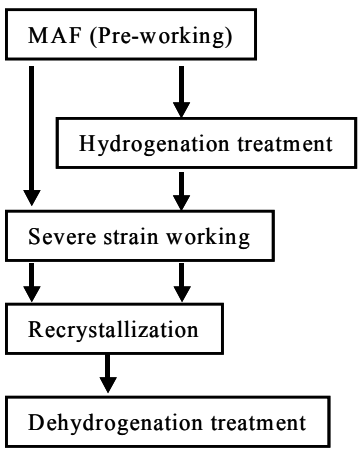

Fig. 2-1. Grain refinement working process by Hydrogenation process.

The processing also facilitates the entry and diffusion of hydrogen in the material at a low pressure during hydrogenation. The average crystal grain diameter is 6 μm after one cycle of MAF processing and about 2.5 μm after two cycles (forging temperature: 473 K), and the material continues to show a duplex grain size structure.
Figure 2-1 shows the structural refinement process that occurs during hydrogenation treatment. To introduce large surface strain, we performed shot peening, recrystallization thermal treatment, and dehydrogenation after the hydrogenation treatment.
During the hydrogenation treatment, the temperature and pressure were maintained at 593 K and 0.4 MPa under a hydrogen gas atmosphere for 6 h; subsequently, the hydrogen atmosphere was replaced with an Ar gas atmosphere, and the specimen was cool ding in water.

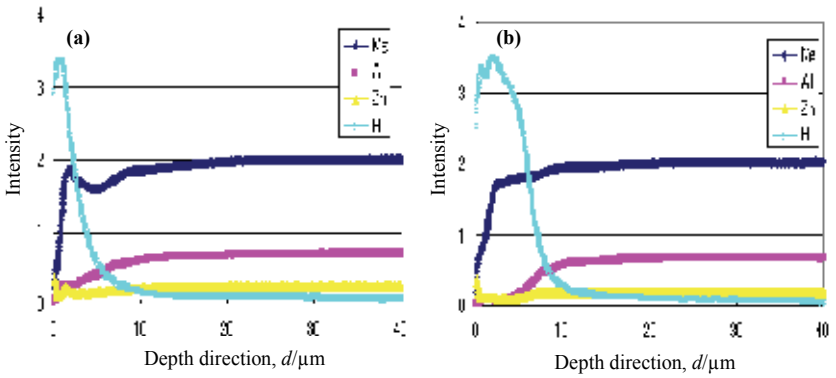

Fig. 2-2. Hydrogen content versus distance from surface of hydrogenated (a) :as-received sample and (b) :MAF worked sample by GDS measurement.

We used a dehumidified compressed air shooting system on a test piece that had been diffusion hydrogenated on the surface to shoot φ=0.5 mm in diameter steel balls from a height of 100 mm under 0.6 MPa compression. The shooting period was 120 s, and the average coarseness of the material surface at this point was Rc ≤ 60 μm. After shooting, recrystallization thermal treatment was performed at a recrystallization temperature of 433 K, which was calculated on the basis of the hardness measurement, and the maintenance period was 10 min; this was followed by dehydrogenation at a temperature of 453 K and a pressure of 0.8 Pa for 6 h.

3.2 Depth of hydride formation

Figure 2-2 shows the GDS analysis results, which indicate the residual hydrogen concentration in the depth direction after the hydrogenation of the specimen and the MAF test piece. Evidently, the material processed by MAF has hydrogen permeating deeper into it and has a larger total residual hydrogen than the specimen has. We measured the hydrogen storage amount using the inert gas fusion-thermal conductivity method and found that the value for the MAF-processed material reached 0.22 x 10^{-2} mass%. When compared to the value for the specimen 0.16 x 10^{-2} mass%, the value indicates that the hydrogen storage amount increases upon refining the structure. To study the relationship between the amount of hydrogen after hydrogenation following MAF processing and the crystal grain diameter for an Al-Mg alloy, we examined the results of a published study,

which involved tritium, on the separation rate and the relationship between the residual hydrogen amount and the grain diameter for certain rates of temperature increase.
According to the results, a primary peak of free diffusion dehydrogenation is observed at 353–373 K, and the separation largely depended on the grain diameter. A secondary separation peak for the separation of hydrogen trapped in dislocations or precipitation near the recrystallization temperature, and the amount of hydrogen separation in this secondary separation process also increase, as the processing strain in the material is high. Mg and hydrogen react and form MgH_2, a stable hydride with strong ion-binding property, during the hydrogenation treatment process of Al-Mg alloys. To identify where the hydride is located, we used a method to convert MgH_2 to AgH_2. The results show that MgH_2 was amply present near the grain boundary, especially at the triple point, but its distribution was not uniform.
The hydrogen separation tendency and conditions of hydride formation are expected to be similar for Mg alloys. Therefore, the depth and amount of hydrogen entering the specimen and MAF material differ depending on the extent of the difference between their structures. Furthermore, the presence of hydride in the depth direction was examined using X-ray analysis. Hydride was not observed in sections deeper than 0.5 mm from the surface of the MAF-processed material. Compared to this, the penetration was only up to a depth of 0.3 mm from the surface in the case of the specimen.

3.3 Relationship between shot-peening process and structural refinement

The changes in the hardness in the depth direction in the test piece of the MAF material processed by shot peening were examined. The hardness decreased rapidly for the section from the surface to 0.3-mm depth, indicating the effect of the shot-peening process.

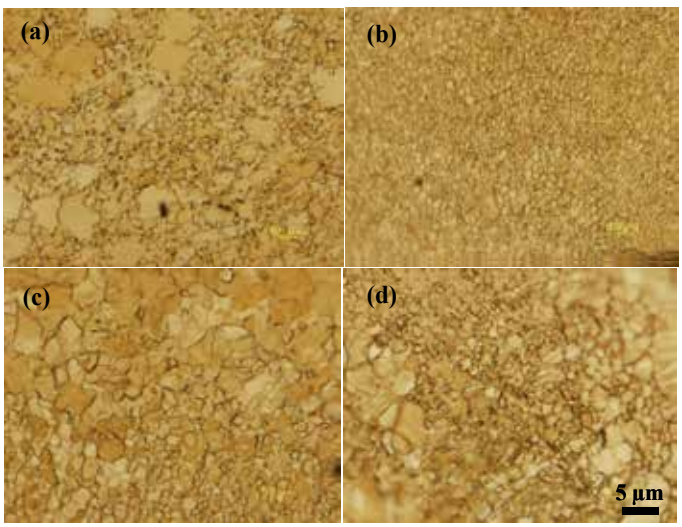

Fig. 2-3. Optical micrographs of MAF worked sample with various working treatment.
(a) : Initial structure of MAF worked sample, (b) :Sample subjected to hydrogenation treatment, shot peening work and recrystallization heat treatment,(c) :Dehydrogenated sample and (d) : Sample subjected to nonhydrogenation treatment, shot peening work and recrystallization heat treatment.

The changes in the structure of the MAF material after the shot peening process and the recrystallization thermal process with or without hydrogenation treatment are shown in Figure 2-3.
Subfigure (a) shows the initial structure of the MAF material. Subfigure (b) shows the structure after hydrogenation treatment, which was followed by the shot-peening process and recrystallization thermal process, and the lower photograph shows the surface of the sample for all subfigures.
Subfigure (d) shows the structure after the same treatment as that in the case of Subfigure (b) without hydrogenation. While changes in the crystal grain diameter due to the shot peeing, in the direction inward from the surface of the sample are significant regardless of hydrogenation treatment, the changes are greater in Subfigure (b) with hydrogenation, indicating that hydrogenation treatment is effective for structural refinement.
The effects of shot-peening process are also clearly observed. In addition, structural refinement is further accelerated near the surface of the hydrogenated material, and the recrystallized structure of the MAF material after hydrogen treatment shows gradient changes from the surface to a depth of about 0.2 mm. Subfigure (c) shows the structure of the recrystallized sample of Subfigure (b) after dehydrogenation.

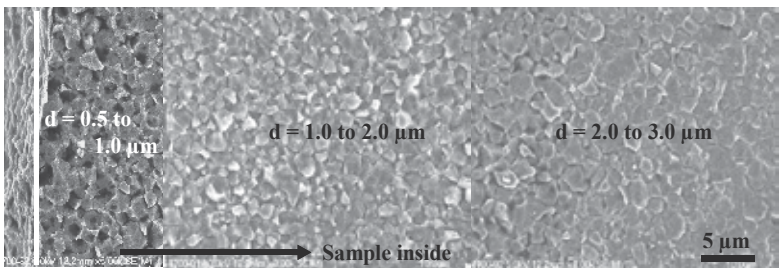

Fig. 2-4. Microstructure of MAFed sample surface beneath with hydrogenation,shot peening working, recrystallized heat treatment and dehydrogenation.

While ductility increased after dehydrogenation treatment, the structure showed grain growth since a temperature higher than the recrystallization temperature was used in the treatment to reduce the treatment period.However, grain growth was smaller than that observed in the specimen. The dehydrogenation conditions can be improved by adjusting the temperature and time. The grain diameter distribution in the gradient structure area after dehydrogenation treatment is shown in Fig.2-4.
Although we can observe grain growth caused by dehydrogenation, which is the final process, the process does not induce significant changes in the hydrogenated material.
Figure 2-5 shows the TEM structure near the surface of the specimen subjected to hydrogenation treatment and shot peening; an MAF material subjected to similar treatments is also shown. Figure 2-6 shows the inverse figure map of before and after hydrogenated treatment of MAF worked sample. Comparison of the structures evidently shows that the dislocation density for the MAF material after hydrogenation and shot peening (panel b) is higher, and it is also clear from the analysis pattern that the strain is higher for this material.
It also shows that there are many small-gradient grain boundaries with orientation differences of 5° or lesser. This fact indicates that there are many subgrains with a high dislocation density that are formed in the shot-peening process. Furthermore, the peak on the large-gradient side is caused by the generation of twin crystals, and it was confirmed by

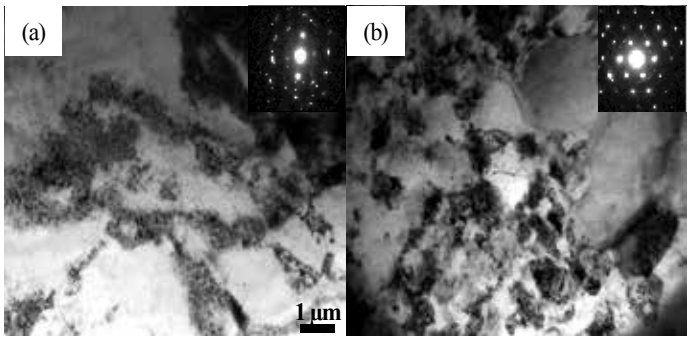

Fig. 2-5. TEM micrographs of as-received sample:(a) and MAF worked sample :(b)subjected to shot peening working following hydrogenation treatment.

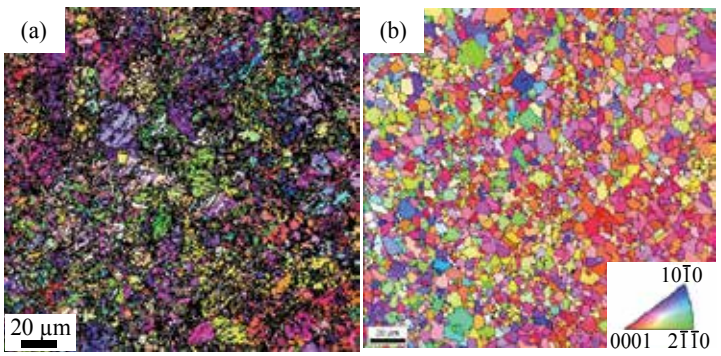

Fig. 2-6. Inverse pole figure maps of (a) : MAF worked sample and (b) : sample with hydrogenated treatment, shot peening working ,and before and after recrystallization heat treatment, respectively.

grain boundary orientation analysis (Fig.2-6(a)). This indicates that there is a high tendency for recrystallization cores to appear, and a finer structure is obtained after the subsequent recrystallization thermal process, as shown in Subfigure (b).

3.5 Mechanical properties of refined structure

The changes in Vickers hardness on the surface of the test pieces of the specimen and MAF-processed material after each treatment up to the dehydrogenation treatment were examined. Although the hardness increases dramatically after the shot-peening process, it decreases after the subsequent recrystallization and dehydrogenation.

Since the recrystallization temperature for the material is determined uniquely by considering the material processing history up to the point, it is impossible to change the recrystallization temperature conditions. However, the decrease in the hardness after dehydrogenation treatment can be controlled by improving the process conditions. The hardness of the MAF-processed material was greater than that of the specimen in all processes after hydrogenation treatment. Changes in the hardness are not caused by a change in the state of crystal orientation, but by a change in the internal strain; this fact was inferred from the TEM structure observations made after the shot-peening process (Fig.2-5 (b)).

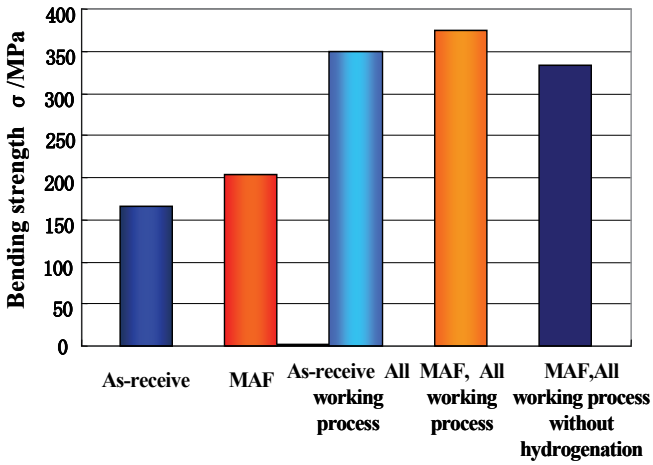

Fig. 2-7. Relationship of Bending strength and working process.

As described in the section on forging, the MAF process conditions we used may degrade the mechanical properties in the extrusion direction and the direction orthogonal to it, as well as the degree of anisotropy in the structure after MAF processing; however, the conditions do not increase the strength.

In comparison, the tensile test results obtained after dehydrogenation of the specimen and MAF-processed material show a significant change in strength after hydrogenation treatment. However, the strength of the MAF-processed material is only slightly larger than that of the specimen. This is because the thickness of the surface layer affected by hydrogenation treatment and the shot-peening process is about 10% of the sample thickness, and changes in the crystal grain diameter are not uniform.

We therefore conducted a transverse bending test after each surface treatment to observe the improvement in the mechanical properties of the surface layer more clearly. The results are presented in Fig.2-7.

A comparison between the combination of the shot-peening process and recrystallization process and the combination of the shot-peening process, hydrogenation treatment, and recrystallization thermal processing shows that the bending strength of the test piece subjected to the processes in the latter combination is higher by about 50 MPa. In addition, the bending strength doubles after the shot-peening process. These results indicate that the combination of MAF processing and the shot-peening process can endow a material with a large bending strength by changing the degree of structural refinement in the region from the surface to a finite depth and enhancing the fine structure on the surface. Improvement in fatigue strength may be expected in addition to heterogeneity of surface by utilizing these properties.

4. Effects of refined structure on toughness and fatigue strength

In this section, we study the crack growth behavior in fatigue characteristics from measurements of the fracture toughness of the AZ31Mg alloy material, which has a duplex grain size and refined structure, and examine the effects of surface treatment on fatigue limit improvement in order to study the dynamic mechanical properties of the materials considered in the previous two sections.

4.1 Fracture toughness

The materials we used were cast AZ31Mg alloy materials (average crystal grain diameter: 120 μm) and their forged versions with refined structures. The forged materials were made by subjecting them to one cycle of forging under forging conditions as shown in Fig.1-2 (average crystal grain diameter: 12 μm) and three cycles of forging under the same conditions (average crystal grain diameter: 10 μm). The bending test pieces prepared for toughness measurement had dimensions of 32 mm (length), 4 mm (width) and 8 mm (height), and they were prepared from a material that was 50%hot-rolled at the same temperature as the final forging temperature. Since the initial structure of cast materials is coarse, large crystal grains remain even after three cycles of forging, unlike extruded materials. We also used a material with a gradient structure that was obtained by large strain processing by shot peening and conducted a fracture toughness test, the 3-point bending test, to calculate the toughness value J_{IC}. The specimen shape is notched specimens with a length of 4 mm and a width of 1 mm at the center of the test piece by electric spark machining and introduced a fatigue precrack with a length of 1.25 mm at the tip.

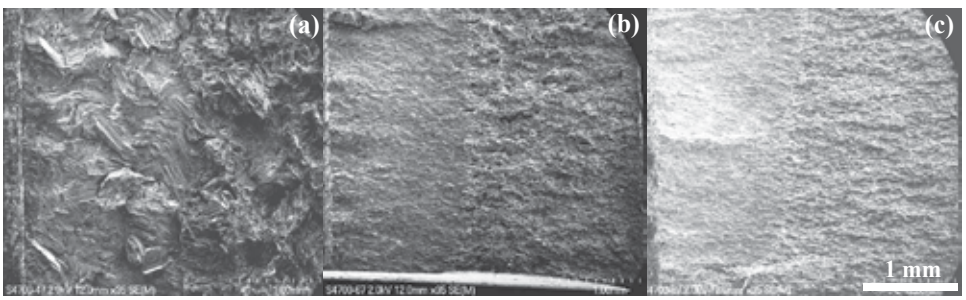

Fig. 3-1. Fracture surface by crack propagation with 3 point bending test (a) : cast material, (b) : MAFed material of 1cycle with 50% roll working,(c) : MAFed material of 3cycle with 50% roll working

The repeat load used for crack introduction conformed to the ASTM standard, and the frequency was 10 H_Z. We conducted a crack advance test using the 3-point bending test for a load rate of 0.1 mm/min and calculated the J integral on the basis of the load-load point displacement. The test pieces with accelerated cracks were cooled by liquid nitrogen and fractured by a Charpy impact machine to observe the fracture surface and measure the crack advance Δa. J_{IC} was calculated on the basis of the J—Δa relationship.

Figure 3-1 shows the fracture surface structure of the sample subjected to low-temperature fracture after the crack advance test. The fracture surface depends on the orientation of the crystal grain due to the effect of coarse grains, and a transgranular fracture surface with a fast advance rate is seen even on the fatigue precrack surface for the cast material (subfigure (a)).

Materials	K_{IC} [MPa $m^{1/2}$]
as cast	24
1cycle forging + 50% rolling	30
3cycle forging + 50% rolling	30

Table 3-1. Fracture toughness of cast and forged AZ31 Mg alloys.

Compared to this, subfigures (b) and (c) show similar crack advances with a relatively smooth fracture surface, and the differences in the fatigue precrack fracture surface and static crack advance range is evident. K_{IC} values calculated from K_{IC} are shown in Table 3-1. Forged materials show higher toughness values than cast materials. The K_{IC} values were identical for the one-cycle and 3-cycle materials.
The toughness values obtained by us were similar to the fracture toughness of commercial materials that is given in a published report (28 MPa $m^{1/2}$). Therefore, the structural refinement to crystal grains with a diameter of about 10 μm has little effect on the toughness value for the AZ31 in the cast material.

4.2 Refined structure and fatigue characteristics

The materials we used in the fatigue test were the AZ31 extruded material and the same material that was forged for one cycle under forging conditions B. The fatigue test was conducted using a tensile-compression round bar test piece with a diameter of 6 mm and a gage length of 15 mm along with a controlled load and 10 Hz frequency. We also used a 50 x 50 mm CT test piece with a plate thickness of 5 mm to observe the crack generation process.
The fatigue test results for the refined duplex grain size structures of the MAF-processed material are shown in Fig.3-2. While the durability limit for the extruded material varied dramatically depending on the direction of the test piece collection, such difference was not seen for the MAF-processed material, shown in figure. This tendency is identical to that in the case of tensile characteristics. Furthermore, the MAF material shows more drastic changes in the strength with time and with an increase in the repeated count for repeat count $N \leqq 4 \times 10^4$. This indicates that the crack advance rate was faster than changes in the stress amplitude.

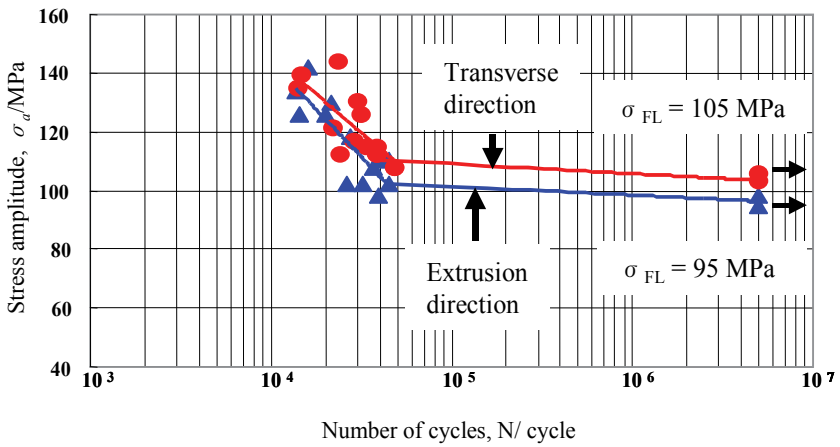

Fig. 3-2. S-N curves of MAFed AZ31Mg alloys.

The residual strain and residual stress have significant effects on the generation of fatigue cracks, and the residual stress in the extrusion direction of the extruded material was -135 MPa; and the value for the MAF-processed material was -4 MPa. In addition, the value for compression against tensile proof stress was approximately in the range 0.7 to 0.8. Compared to this, the value for the forged material was nearly 1.0.

When we studied the state of the fracture surface in the fatigue test, the state of fracture varied between the material loaded with stress amplitude near the durability limit under which fracture occurs for a repeat count of $N \geqq 10^5$ and the material fractured under large stress amplitude under which fracture occurs for a repeat count of $N \leqq 10^4$, The fracture surface was coarse in both materials when the load stress amplitude was large, and the crack accelerated vertically in the direction of the load, regardless of the uniformity/nonuniformity of the grain diameter. Compared to this, the results varied between the extruded material and the MAF-processed material when the stress amplitude was near the durability limit. The fracture mainly occurred as a transgranular fracture in the extruded material and the fracture surface was smooth due to the effect of the grain diameter.

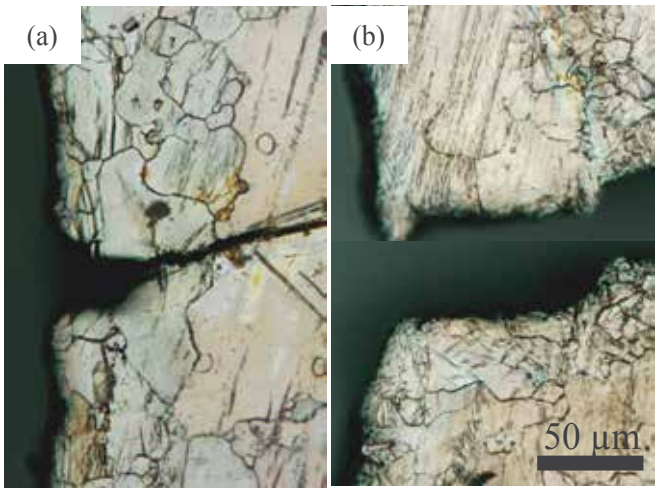

Fig. 3-3. Fatigue crack initiation behavior (a) : as-received ,(b) :MAF worked material .

However, fracture occurred with branching of cracks in concurrence with boundary fracture in the initial stages of fracture in the MAF-processed material. The effects of fine grains and coarse grains were clearly observed, and a twin crystal fracture was also seen in the case of coarse grains. Although it is expected that these effects would manifest in fatigue life as well, both the tensile strength and the ratio of fatigue strength did not show large changes in our experiment results, showing no significant difference in the crack advance rate between the materials. This coincides with the test results for the rolled material.

It is surmised that the durability limit is different for the two materials due to the timing of crack generation. Figure 3-3 shows the status near the crack generation in the specimen and the MAF material.

As shown in the figure, the crack propagates through the coarse crystal grain in the specimen. On the other hand, the crack propagates on the fine crystal boundaries in the MAF material. These cracks continue to advance for more than 90% of their total lifetime, and it is surmised that the initial crack generation and propagation timing greatly affect the total lifetime. However, this point needs to be examined in detail through further study.

Although the fatigue durability limit for the extruded material shows large differences between the extrusion direction and the direction perpendicular to it, this difference almost completely disappears in the MAF-processed material, showing a tendency similar to that for tensile proof stress. Furthermore, there is little difference in the state of fatigue crack propagation between the extruded material and MAF-processed material under high-amplitude loads, and the fracture surface conditions mainly give rise to transgranular fractures. However, the effect of crystal orientation appears locally in the low-amplitude range and grain boundary fracture is significant in the MAF-processed material. There was no significant difference between the materials with regard to the rate of the macroscopic crack propagation process during the total lifetime, and a large difference was observed until rapid crack advance. It is this crack generation and propagation process that the no uniform structure affects during the fatigue lifetime.

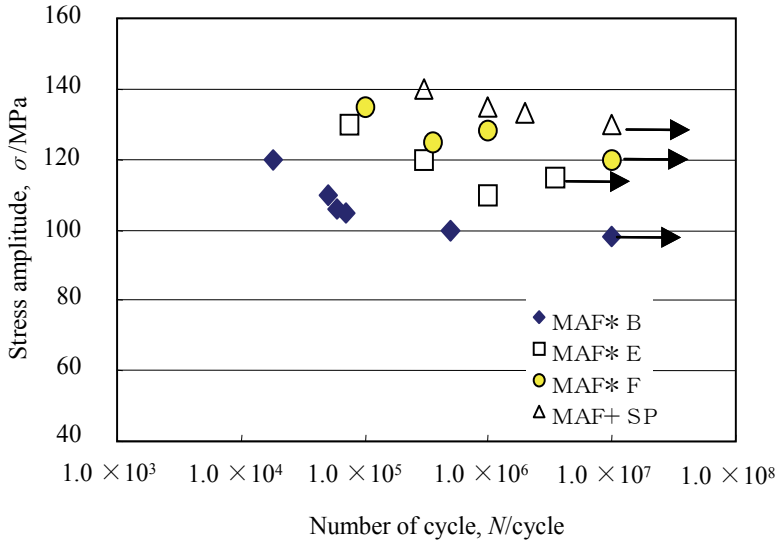

Fig. 3-4. S-N curves of MAFed AZ31 alloy by various forging condition working and fracture surfaces.

On the basis of these results, we conducted a fatigue test using a cube with an edge of 100 mm prepared from forged material processed by performing shot peening under forging conditions F. The test conditions were identical to those previously described. The fatigue test results are shown in Fig.3-4. The sample under forging conditions F was not processed thermally after forging. The crystal structure comprised mainly structural changes resulting from dynamic recrystallization, as described in Section 2, and it had a duplex grain size structure because it was processed only for one cycle.

However, traces of large deformation, such as twin crystals and sliding, remained in the coarse grains with diameters of 10–20 μm that remained as islands, indicating that the accumulation of strain. Fine crystals with diameters of several micrometers or smaller exist among the coarse grains, but the durability limit is improved to 120 MPa or greater.

Furthermore, the gradient structure shown in Fig.3-5 is formed when the surface treatment attempted in the previous section is carried out under forging conditions F. It is surmised that proof stress improvement and the generation of twin crystals were somewhat

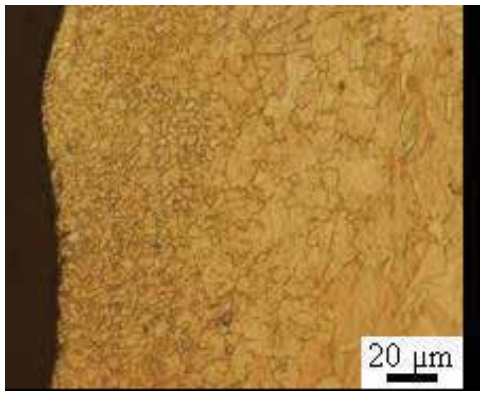

Fig. 3-5. Sub micron size microstructure at surface of AZ31 Mg alloy by MAF work, hydrogen treatment and shot penning with recrystallization treatment.

suppressed on the compressed side. It is possible to extend the lifetime by controlling the delay in crack generation timing by structural refinement and by controlling the delay in the crack advance rate by randomization of structural orientation based on our observation of crack generation behavior

5. Summary

We used commercially available materials, AZ31 and AZ61 magnesium alloys, and tried to refine their structure and improve their mechanical properties. Our findings are outlined below:

1. It was possible to obtain a fine structure with a crystal grain diameter of about 2–3 μm by properly selecting the process temperature for MAF processing, which is a type of large strain process. Although the degree of structural fineness and refinement advances with the number of repeated forging processes, they reach saturation in 4–5 cycles due to the limit in the tolerable work strain that can be introduced.
2. A structure with an average grain diameter of 5–6 μm can be obtained in one cycle of forging; however, such a structure is a duplex grain size structure. The degree of duplex grain size can be reduced by performing a recrystallization thermal process.
3. The method involving the use of hydrogenation requires a high-pressure hydrogen environment and it is of limited use. However, it is possible to refine the surface structure to the submicron level by using only shot peening for surface reinforcement and by performing a thermal process. Although the tensile strength improvement at room temperature resulting from structural refinement remained around 25%, the extension was improved by 30%.
4. Although the fracture toughness of a material with a crystal grain diameter of 10 μm improved only slightly relative to that of a commercially available material, it is still a dramatic improvement relative to the cast material. The durability limit in the fatigue test improved by 30% compared to the commercially available material when fine grain material was subjected to crystal refinement, and the anisotropy of strength in the material direction decreased upon forging. Its main effect is the increase in time until initial crack generation.

6. Future reserch

In this present study, it was clear that improvement mechanical properties and formability of magnesium alloys by Multi-axial alternative forging was effective thermo-mechanical and microstructure-controlled process. To make the surface layer with the more fine structure, the sever strain forming was combined with hydrogen adsorption processing and the way to make the structure of the material surface with the inclination organization has been developed. Our research topic in the future for practical applications is as follows.

1. To improve duplex microstructures formed by sever plastic deformation, optimized of heat treatment, plastic deformation process and microstructure controlled.
2. Evaluation of mechanical properties and formability of functional materials under several conditions.
3. Fabrication of bulk materials that has uniform microstructure and mechanical properties.

Mechanical properties of the multi-scale under various stress condition for design of practical goods application are investigated to reach the objective, and it aims at the optimization of microstructure, worked process, forming process and mechanical properties.

7. References

Ameyama,K.(1998). Low Temperature Recrystallization and Formation of an Ultra Fine (γ +σ) Micro- duplex Structure in a SUS316 Stainless Steel, *Scripta Mater*Vol.38:517-522

Berbon,P.,Komura,S.,Utsunomiya,A.,Z.horita,Z.,Furukawa,M.,N.Nemoto,N.&Langdon,T.(1999).An Evaluation of Superplasticity in Aluminum-Scandium Alloys Processed by Equal-Channel Angular Pressing, *Mater.Trans*Vol.40:772-778

Ishida,S.,Noda,M.,Funami,K.&Mori.H(2007).Grain Refinement and Mechanical Properties of Magune- sium Alloy by Hydrogenation Treatment, *Materials Science Forum* Vol.558-559:757-762

Machida,N.,Noda,M.,Funami,K.&Kobayashi,M.(2004).Effect of Hydrogenation Treatment on Grain Refinement of Reaction Sintered Ti-6Al-4V Alloy Composites,*Mater.Trans*Vol.45:2288-2294

Nagata,Y.,Noda,M.,Shimizu,H.,Funami,K.&Mori,H.(2007)Improvement of the Fatigue Characteristic of AZ31 Magunesium Alloy by Microstructure Control,*Materials Science Forum*Vol.558-559 :781 -786

Noda,M.,Funami,K.& Suwahara,Y.(2005).Effect of Constraint and Strain Path on Evolution of Ultra fine Grained Microstructure by Multi-axial Alternative Forging Materials, *Materials Science Forum* Vol.475 -479:3471-3474

Noda,M.&Funami,K.(2006).Deformation Behavior of Fine Grained Al-Mg Alloy under Biaxial Stress, *Materials Science Forum* Vol.503- 504:475-480

Tsuji,N.,Shiotsuki,K.&Saito,Y.(1999). Superplasticity of Ultra-Fine Grained Al-Mg Alloy Produced by Accumulative Roll-Bonding, *Mater.Trans*Vol.40:765-771

Yoshimura,H.,Kimura,K.,Hayashi,M.,Ishii,M.,Hanamura,T.&Takamura,J.(1994). Ultra-fine Equiaxed Grain Refinement and Improvement of Mechanical Properties of α+β

Type Titanium Alloys by Hydrogenation, Hot Working, Heat Treatment and Dehydrogenation, *Mater.Trans.JIM* Vol.35: 266-272

Xing,J.,Soda,H.,Yang,X.,Miura,H.&Sakai,T.(2005).Ultra-Fine Grain Development in an AZ31 Magnesium Alloy during Multi-Directional Forging under Decreasing Temperature Conditions, *Mater.Trans.* Vol.46: 1646-1650

12

Improving the Properties of Magnesium Alloys for High Temperature Applications

Kaveh Meshinchi Asl
School of Materials Science and Engineering,
Clemson University, Clemson
USA

1. Introduction

The demand to reduce the weight of components especially in automotive and aerospace industries has triggered renewed interest in magnesium alloys as a lightweight structural material. Magnesium which is a third lighter than aluminium is the lightest of the structural metals and is used in a diverse range of applications. This is because of their low density, high specific strength and stiffness, superior damping capacity, good electromagnetic shielding characteristics and good machinability [Khomamizadeh et al., 2005; Meshinchi Asl et al., 2009 (a); Mordike & Ebert 2001; Meshinchi Asl et al., 2009 (b)]. However, the number of commercially available magnesium alloys is still limited especially for applications at elevated temperatures. Increased applications of magnesium alloys for elevated temperature service require the development of low-cost alloys with good creep resistance and sufficiently high strength. The magnesium alloy that has received most attention is AZ91 (Mg-9Al-1Zn, wt.%) which is being used in approximately 90% of all magnesium cast products. While this alloy exhibits adequate tensile yield strengths at ambient temperature, it faces strong challenges such as fatigue and creep resistance and also strength at elevated temperatures [Gao et al., 2005; Wang et al., 2003; Meshinchi Asl et al., 2010; Kang et al., 2005].

Studies to understand the reasons for the poor mechanical behaviour of die cast Mg-Al alloys at elevated temperatures have focused on the near grain boundary regions where non-equilibrium interdendritic solidification produces a divorced eutectic microstructure of $Mg_{17}Al_{12}$ and magnesium. Recent studies have shown that discontinuous precipitation of the $Mg_{17}Al_{12}$ (β) intermetallic at elevated temperatures is more likely responsible for poor creep properties of these alloys [Moreno et al., 2003].

Considerable efforts have been made in recent years to improve the creep resistance of the Mg-Al based alloys via further alloying additions and the formation of thermally stable precipitates along grain boundaries to resist the deformation by grain boundary sliding. This limitation is attributed to the intermetallic phase $Mg_{17}Al_{12}$ under high temperatures. The alloys of Mg-Al-RE (Rare Earth) have been developed recently. Some studies were based on single RE elements but in this research Rare Earths were added as misch metal (MM). This is because Rare Earth elements have the similar behaviour and it is very economical to use misch metals instead of pure rare earths. In the present work the effects of

Rare Earth addition and aging heat treatment on the microstructure, mechanical properties and creep resistance of AZ91-RE magnesium alloys will be investigated. The effects of Si additions and Al content on the microstructure, some mechanical properties and creep resistance on magnesium alloys will also be discussed as another solution to produce high temperature resistance magnesium alloys.

As discussed before, magnesium alloys offer lightweight alternatives to conventional metallic alloys because of their low density. However in certain applications, lightweight alloys are subjected to sliding motion, thus wear resistance is becoming a key factor in these alloys. For critical automobile applications, wear properties of magnesium alloys are important. Despite the attractive range of bulk mechanical properties, a relatively poor resistance to fracture and wear is a serious hindrance against wider application of Mg alloys [Mehta et al., 2004]. Wear resistance can generally be enhanced by introducing a secondary phase(s) to the matrix material. In this fashion, the wear properties can be varied substantially through changes in the microstructure, the morphology, volume fraction and mechanical properties of the reinforcing phase, and the nature of the interface between matrix and reinforcement [Sharma et al., 2000; Lim et al., 2003; Oakley et al., 1995; Alahelistan & Bergamon, 1993; Lim et al., 2005]. Chen and Alpas (2000) performed testes on AZ91 magnesium alloy, reported a transition from mild to severe wear controlled by a critical surface temperature 347K above which severe wear occurred. They observed oxidation and delamination wear mechanisms in the mild wear regime..Lim et al. (2005) investigated the wear behaviour of Mg-Al alloy based composite reinforced with SiC particulates at various loads and speeds. They identified five different wear mechanisms operating singly or with others: abrasion, oxidation, delamination, adhesion, thermal softening and melting. More recently, Lim et al. (2005) experimented the nano-sizaed alumina reinforced magnesium-based composites. In these composites, increasing the reinforcing material up to 1.11 vol.% improved the wear resistance to 1.8 times relative to pure magnesium. Since the Rare Earths are added to the Mg alloys to improve the high temperature properties, it is essential to investigate the effect of Rare Earth content on the wear behaviour of AZ91 magnesium alloy.

2. Experimental details

Commercial pure magnesium, Aluminum and zinc (>99.9%) were used to prepare AZ91 alloy. Manganese was added as Al-25%Mn master alloy. Alloy was melted in a mild steel crucible and during the melting process, surface of the charge and the melt were protected by Magrex 36 flux. The RE was added to the melt at 750˚C. The melt was held at 750˚C for 30 min to make sure that the RE could be completely dissolved.

Rare earth elements (REs) were added by means of misch metal (MM) with nominal composition of 50% Cerium, 25% Lanthanum, 18% Neodymium and 7% Praseodymium. The reason of using misch metal instead of pure elements is the similar behavior of RE elements while it is very economical to use misch metals instead of pure rare earths. The melt was then held at 750˚C for 30 min to dissolve RE completely.

Finally the melt was stirred for 3 minutes (for oxide reduction) and after complete defluxing, it was poured at the pouring temperature of 750˚C into a permanent mold from mild steel which was preheated up to 300˚C. The chemical composition of the samples was determined by wet chemical analysis as shown in Table 1.

Metallographic samples were prepared by mounting them in cold setting resin. They were etched in 2% Nital aqueous solutions for 20 seconds. The microstructure and phase distribution was characterized by Olympus PME3 optical microscopy and Philips XL 40 scanning electron microscope (SEM). The elemental contents of various phases in the polished samples were determined by the energy dispersive X-ray spectroscopy (EDS) system of SEM. Tensile properties of samples were measured (ASTM-B557M standard) using an Instron 4400 at room and 140 ^{o}C temperatures (1 mm/min strain rate). The hardness was measured using Instron Brinell hardness tester. The averages of three measurements were reported for each experiment. For all the samples tested in this investigation, the samples were cut from the same place of the cast ingot and had the same microstructure in terms of grain size and precipitate distribution. Creep tests were performed in air using a creep test machine (ASTM-E139 standard). By plotting the displacement at various times which was measured using a strain gauge, the strain curves were obtained and the steady state strain rate was calculated.

Alloy code	Al	Zn	Mn	RE	Si	Mg
1	9.20	0.90	0.25	-	-	Rem.
2	8.90	0.85	0.30	1	-	Rem.
3	9.10	0.90	0.25	2	-	Rem.
4	4.10	0.90	0.25	2	-	Rem.
5	9.00	0.80	0.3	3	-	Rem.
6	8.95	0.85	0.30	-	0.25	Rem.
7	9.00	0.91	0.25	-	0.5	Rem.
8	9.10	0.90	0.30	-	1	Rem.
9	8.90	0.85	0.25	-	2	Rem.

Table 1. Chemical compositions of the samples investigated in wt. %.

Dry sliding wear test without lubricant according to ASTM G99 was conducted using a pin-on-disk apparatus. Pin specimens of diameter 5 mm and length 15 mm were prepared by machining of rods that followed out grinding up to 1200-grit silicon carbide, polishing with 0.05 μm diamond paste and alcohol and then cleaning with ultrasonic equipment in pure acetone. M35 hardened tool steel of 160 mm diameter and 65 HRc hardness was used as a counterface. After each test the disc surface was ground against 1200-grit SiC paper and cleaned with acetone. The experiments were performed under various stationary normal loads, sliding speeds and sliding distances. Weight loss values were determined from weight differences before and after the tests using a precise electronic balance with an accuracy of ±0.1 mg. Weight loss versus sliding distance curves were plotted and the wear rates were calculated. Frictional force was recorded for each test. In addition, contact surface temperature was detected with a sensitive thermocouple probe that placed in a narrow scratch in side with the axes of the pin. Throughout the tests, thermocouple connection with contact surface was controlled. Temperature against sliding distance curves also plotted.
The worn pins surfaces and wear debris accumulated during the tests were examined using a scanning electron microscopy and energy dispersive X-Ray spectroscopy to verify dominant wear mechanisms.

3. Result and discussion

3.1. Introducing the Mg-Al-RE alloys for high temperature applications and investigating the reasons of poor mechanical properties of Mg-Al based magnesium alloys at high temperatures

The microstructure of as-cast alloy 1 (AZ91) consists of two phases, α-Mg matrix and β ($Mg_{17}Al_{12}$) intermetallic compound in two kind of morphologies, eutectic β and precipitate of β due to decreasing of solubility of aluminum with decreasing temperature. According to the binary Mg-Al phase diagram, the composition of AZ91 alloy is close to the hypoeutectic Mg-Al alloys and the reason for formation of eutectic phases in a hypoeutectic alloy is the non-equilibrium solidification. By addition of REs as the form of cerium rich misch metal to AZ91 (alloy 1), a rod like $Al_{11}RE_3$ or Al_4RE intermetallic phase (the EDS pick of Al_4RE is like the $Al_{11}RE_3$) [Wang et al., 2003], was observed in the microstructure. More RE addition causes further decrease of β phase and coarsening of $Al_{11}RE_3$ phase in the microstructure. The EDX analysis of $Al_{11}RE_3$ phases is shown in Fig. 1.

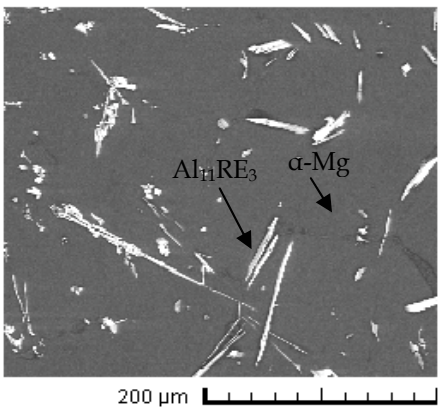

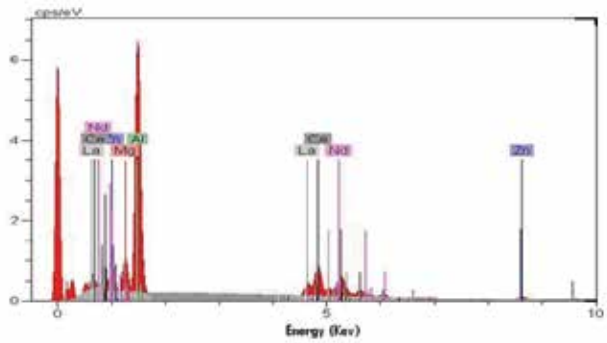

Element	At. %
Magnesium K	3.8
Aluminum K	71.4
Zinc K	1.7
Lanthanum L	6.4
Cerium L	10.8
Neodymium L	5.9

Fig. 1. $Al_{11}RE_3$ phase in the microstructure and energy dispersive X-ray analysis of the corresponding particle.

In the previous works it was observed that AZ91 alloy had poor mechanical properties at elevated temperatures. This was due to the low melting point of the β phase which can readily coarsen and soften at elevated temperatures [Moreno et al., 2001; Meshinchi Asl et al., 2010], thus REs were added to AZ91 alloy which result in the formation of $Al_{11}RE_3$ phase in the microstructure and has a high thermal stability [Khomamizadeh et al., 2005]. The microstructure of alloy 3 (AZ91 +2% RE) after solution treatment at 420°C for 24 h is shown in Fig. 1. After solution treatment all the β particles are dissolved in the matrix due to their low thermal properties but $Al_{11}RE_3$ needle shape particles remain unchanged due to relatively high melting point of needle shape $Al_{11}RE_3$ particles.

Fig. 2 shows the tensile properties of specimens tested at ambient and elevated temperatures. The results show that RE addition had little effect on ultimate tensile strength of the alloy at ambient temperature. However the RE addition greatly improved the high temperature tensile strength. This was due to the formation of $Al_{11}RE_3$ particles which reduced the amount of β particles in the matrix and had a relatively high thermal stability.

The most important result caused by RE addition was in creep resistance. Creep tests were performed on specimens over the temperature range of 135°C to 200°C and at an applied stress of 48-96 MPa. By measuring the slope of the curves, the steady state creep rate of the alloys can be calculated and it is shown in Table 2 for 200°C. The creep resistance of AZ91 alloy was poor but it can be seen that RE addition resulted in remarkable improvement of creep resistance and the lowest creep rate was obtained for 3% of RE.

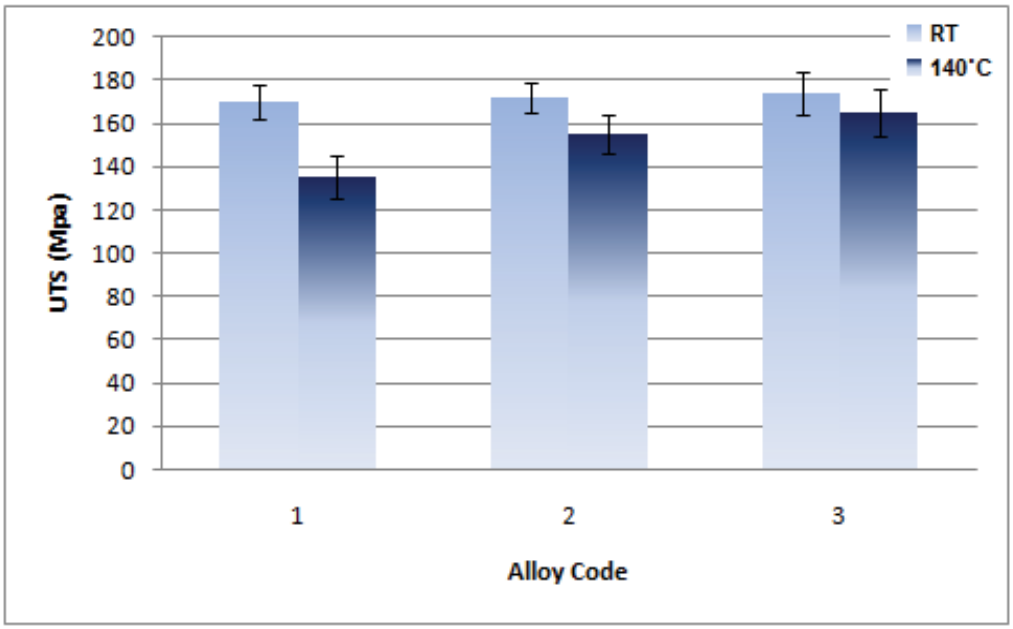

Fig. 2. Mechanical properties of the alloys investigated.

Alloy Code	$\dot{\varepsilon}$ (1/sec)				
	48 (Mpa)	58 (Mpa)	72 (Mpa)	82 (Mpa)	96 (Mpa)
1	$4.2x10^{-7}$	$8.1x10^{-7}$	$3.4x10^{-6}$	$2.1x10^{-5}$	$6.2x10^{-5}$
3	$5.1x10^{-8}$	$6.8x10^{-8}$	$1.4x10^{-7}$	$5.6x10^{-7}$	$8.2x10^{-7}$
4	$3.8x10^{-8}$	$5.2x10^{-8}$	$8.7x10^{-8}$	$3.5x10^{-7}$	$5.5x10^{-7}$

Table 2. Steady state creep rates of the alloys for different stresses in 200°C.

The conventional power law equation relating the minimum creep rate, $\dot{\varepsilon}$ min to the applied stress is:

$$\dot{\varepsilon} \text{ min} = A (\sigma/G)^n \exp(-Q/RT) \quad (1)$$

Both n and Q are parameters of the material and together may be used to identify the dominant creep mechanism for the material. By plotting logarithmically the minimum creep strain rate versus the applied stress σ, we can calculate the stress exponent, n. Plot of log ε. versus 1/T will yield the apparent activation energy, Q [Bettles, 2003; Meshinchi Asl et al., 2009 (b); Somekawa et al., 2005].

The stress exponent n~2 is generally reported for grain boundary sliding, while n=3~7 is for dislocation climb controlled creep, however, high n values for high stresses often indicate of power law breakdown [Bettles, 2003; Meshinchi Asl et al., 2009 (b)]. The activation energy for self diffusion in magnesium can be taken as 138 kJ mol^{-1}. The value of activation energy for boundary diffusion is estimated to be in the range 70-100 kJ mol^{-1} [Oakley et al., 1995. Meshinchi Asl et al., 2009 (b)]. At low stresses, the stress exponent for as cast AZ91 without REs was found to be 5.7 which is in the range of dislocation climb mechanism. However the activation energy lies between that for self diffusion and grain boundary diffusion, which was measured to be 119 kJ mol^{-1} for the AZ91. Together these two factors may indicate a mixed mode of creep behavior, with some grain boundary effects contributing to the overall behavior. SEM observations performed on specimens also showed a ductile dimple fracture mode of creep rupture for AZ91 alloy in 200°C as shown in Fig. 3.

For the AZ91-RE alloy the values of both parameters fit the values for dislocation climb controlled creep. The stress exponent was measured 3.2 and the activation energy was 143

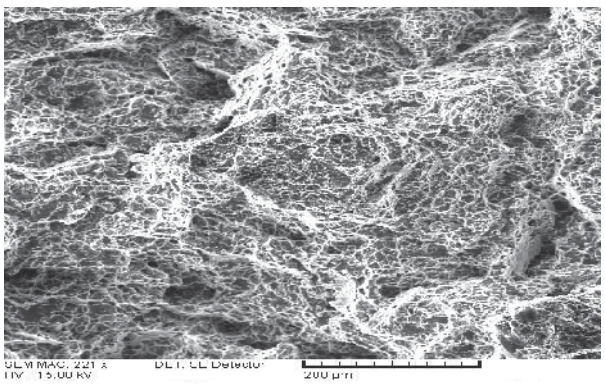

Fig. 3. Fractogragh of alloy 1 at 200°C after creep rupture.

kJ mol^{-1}. The activation energy is slightly higher that AZ91 alloys without REs which is due to its better creep resistance. The presence of thermally stable $Al_{11}RE_3$ needle shape particles along grain boundaries pin grain boundaries and hinder both grain boundary migration and sliding during high temperature exposure.
In Mg-Al based alloys, the β phase has the most strengthening effect on the alloys at room temperature however it has a low melting point and can readily soften and coarsen with increase of temperature. This is the main factor for poor creep resistance of these alloys and the grain boundaries are weakened because of softening and coarsening of the β phase and therefore sliding of grain boundaries has an important part in deformation mechanism at elevated temperatures. By adding REs the $Al_{11}RE_3$ needle shape phases along grain boundaries pin grain boundaries and contribute to improvement of creep resistance of the alloys.

3.2 Effects of aging heat treatment on ambient and high temperature properties of AZ91-RE magnesium alloy

The AZ91 alloy was heated at 400ºC for 24 h followed by water quenching (T4 heat treatment) and then aged at 180ºC for 20 h (T6 heat treatment). Fig. 4 shows the microstructure of the

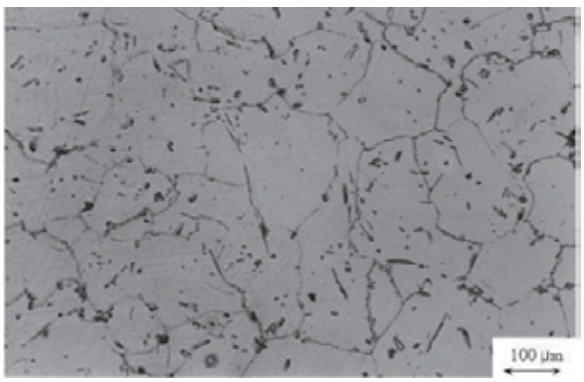

(a)

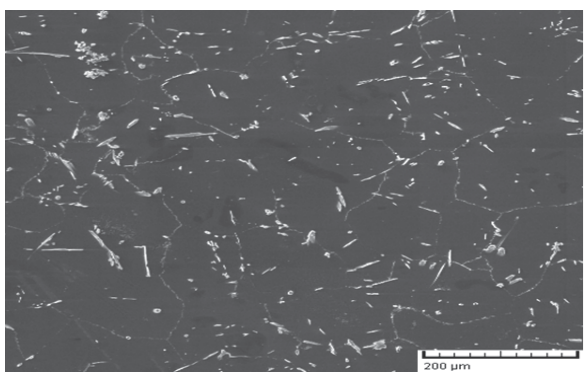

(b)

Fig. 4. Optical (a) and scanning electron microscope (b) image of microstructure of AZ91+2%RE (alloy 3) after T4 heat treatment where all the β particles are dissolved in the matrix but $Al_{11}RE_3$ particles remain unchanged after T4 heat treatment.

AZ91+2%RE alloy after T4 heat treatment. All the β particles are dissolved in the matrix due to their low thermal properties but $Al_{11}RE_3$ particles remain unchanged. This is because of relatively high melting point of needle shape $Al_{11}RE_3$ particles.
X-ray diffraction pattern of AZ91-2%RE alloy in the form of as-cast and also after T4 solution treatment are presented in Fig. 5. The pattern also indicates that other that α (Mg) and β ($Mg_{17}Al_{12}$) phases which are present in the AZ91 alloy, the $Al_{11}RE_3$ intermetallic phase is present in the microstructure of the alloy after RE addition. After the solution treatment, the related peaks of β phase disappear but the RE containing phase ($Al_{11}RE_3$) still remains in the pattern due to its high thermal stability.

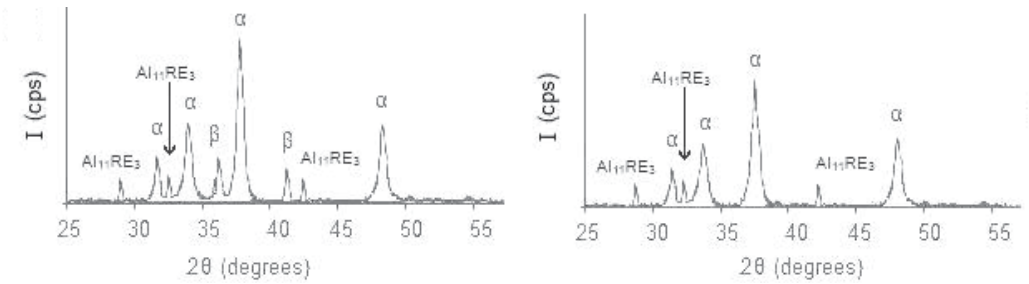

Fig. 5. X-ray Diffraction pattern of AZ91-2%RE alloy before solution treatment (left) and after solution treatment (right).

For the AZ91 alloy aged at 180ºC the formation of β precipitates occurred in two forms, discontinuous precipitation at the vicinity of grain boundaries (lamellar precipitation) which is dominant and continuous precipitation (fine plate shape precipitates) within grains. Discontinuous precipitation is the cellular growth of alternating layers of β-phase and near-equilibrium magnesium matrix at high-angle grain boundaries and is the main reason for poor mechanical properties of the alloy at elevated temperatures [Celotto, 2000; Wenwen et al., 2003].
In pure AZ91 alloy, the discontinuous β precipitates at grain boundaries are the main reason for poor mechanical properties of the alloy. Fig. 6 shows the fracture surface of AZ91 alloy

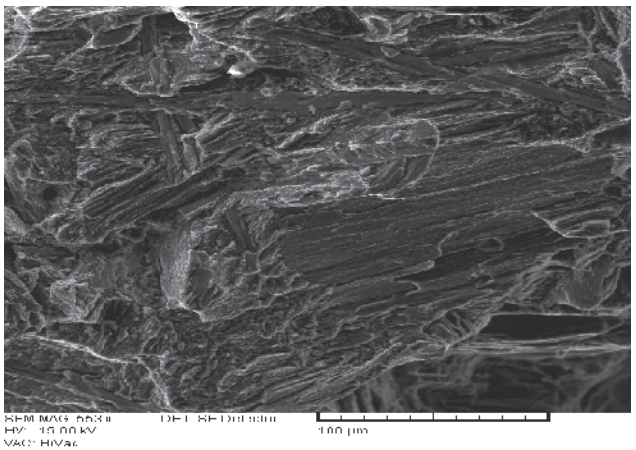

Fig. 6. Fracture surface of AZ91 alloy after the tensile test.

after the tensile test which is a cleavage kind of fracture. The cleavage facets could be easily seen on the fracture surface.
After the solution treated alloy is aged, the discontinuous precipitations which are dominant at the vicinity of grain boundaries form at early times of aging. Continuous precipitations form at longer times. Fig. 7 and Fig. 8 show the dissolution of β particles as the result of solution treatment and then formation of the discontinuous precipitation at grain boundaries after 5 hours of aging. The discontinuous precipitations in Mg-Al alloys exhibit different habit planes and morphologies. The most common morphologies of precipitates are long parallel precipitates and bush like precipitates [Dully et al., 1994].

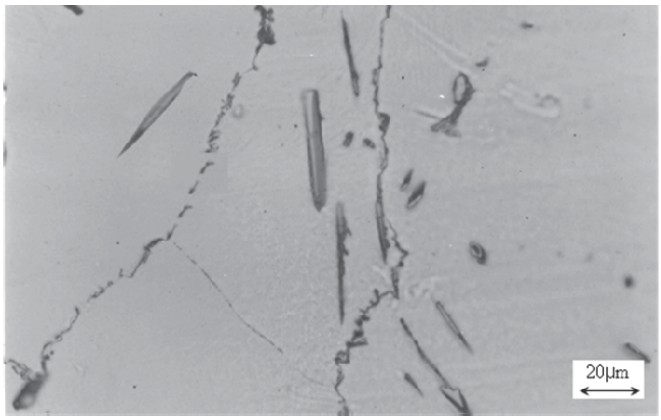

(a)

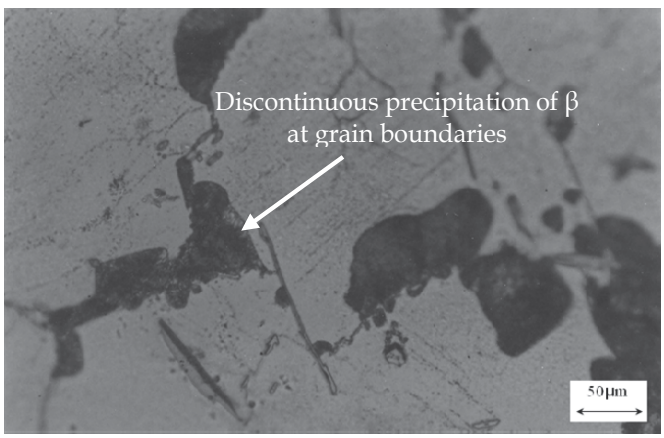

(b)

Fig. 7. Optical microscope image of AZ91+2%RE (alloy 3) after all the β particles are dissolved due to solution treatment (a) and after 5h of aging showing discontinuous precipitation at the vicinity of grain boundaries (b).

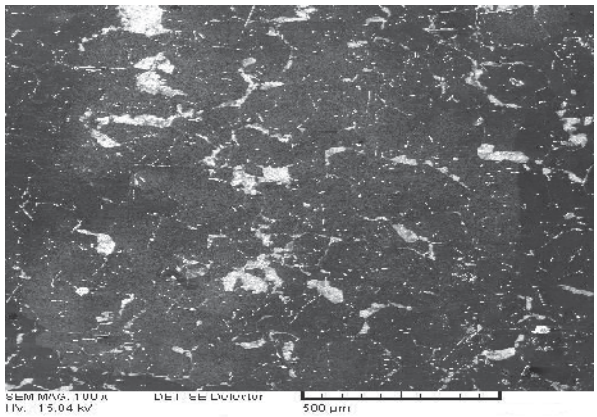

Fig. 8. Scanning electron microscope image of AZ91+2%RE (alloy 3) after 5 h of aging.

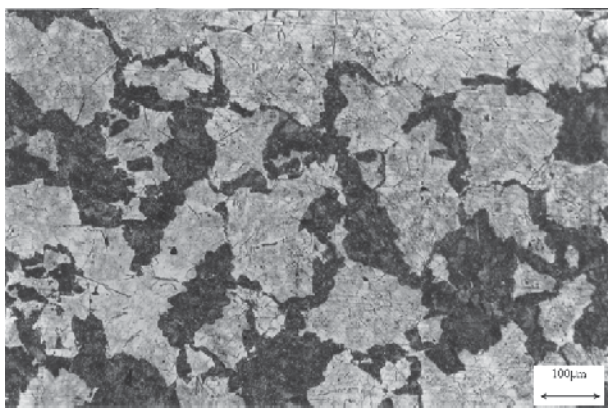

(a)

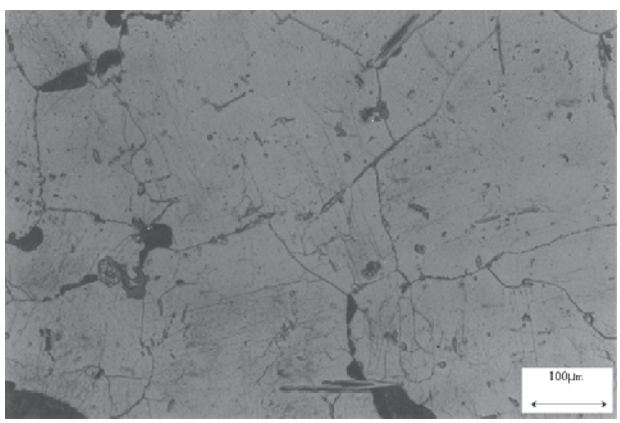

(b)

Fig. 9. Optical microscope image of alloy 2 after all the T6 aging treatment, showing β precipitates dominant (a) and alloy 5 after T6 heat treatment (b).

The discontinuous precipitation of β at grain boundaries readily coarsens and softens at elevated temperatures and thus weakens the grain boundaries at elevated temperatures. Therefore sliding of grain boundaries is an important factor in deformation of Mg-Al alloys at elevated temperatures.

It could be concluded that RE addition to AZ91 alloy decreases the amount of β particles in the microstructure (Fig. 9). After aging the rare earth inclusive alloys, the overall amount of β precipitates was greatly reduced and also the discontinuous precipitates were decreased in the microstructure.

Some of the mechanical properties of the alloys tested in this investigation are presented in Table 3. The creep resistance of the pure AZ91 alloy after aging heat treatment was decreased slightly compared to as cast specimens. This is due to the important role of β precipitates in the microstructure. While they are the main strengthening effect at room temperatures, the discontinuous precipitates of β are mainly distributed at grain boundaries. Their softening and coarsening weakens the grain boundaries at elevated temperatures (Table 4 and Fig. 10).

Alloy	Hardness (BHN)	Yield strength (Mpa)	UTS (Mpa)	UTS (Mpa)
			Room Temp.	140˚C
AZ91-2%RE	63	95	174	165
AZ91-2%RE followed by T4 and T6 treatment	65	97	179	168

Table 3. Mechanical properties of the alloys investigated.

After aging heat treatment of the AZ91 alloy, the discontinuous precipitates of β are dominant at grain boundaries and therefore weaken the grain boundaries at elevated temperatures and decrease the creep resistance of the alloy. Thus, despite good mechanical properties of aging heat treatment samples compared to as cast AZ91 alloy for applications at room temperature, these alloys should not be used at application conditions which involve elevated temperatures. By adding REs the metastable $Al_{11}RE_3$ needle shape phases along grain boundaries pin grain boundaries and contribute to improvement of creep resistance of the alloys.

Alloy Code	$\dot{\varepsilon}$ (1/sec)				
	48 (Mpa)	58 (Mpa)	72 (Mpa)	82 (Mpa)	96 (Mpa)
1	$4.2x10^{-7}$	$8.1x10^{-7}$	$3.4x10^{-6}$	$2.1x10^{-5}$	$6.2x10^{-5}$
1 (T4)	$3.5x10^{-7}$	$6.3x10^{-7}$	$8.1x10^{-7}$	$2.9x10^{-6}$	$5.4x10^{-6}$
1 (T6)	$7.8x10^{-7}$	$2.3x10^{-6}$	$6.5x10^{-6}$	$5.2x10^{-5}$	$1.8x10^{-4}$
3	$5.1x10^{-8}$	$6.8x10^{-8}$	$1.4x10^{-7}$	$5.6x10^{-7}$	$8.2x10^{-7}$
3 (T6)	$3.7x10^{-8}$	$5.1x10^{-8}$	$8.7x10^{-8}$	$1.2x10^{-7}$	$5.8x10^{-7}$

Table. 4. Steady state creep rates of the alloys for different stresses in 200^{o}C.

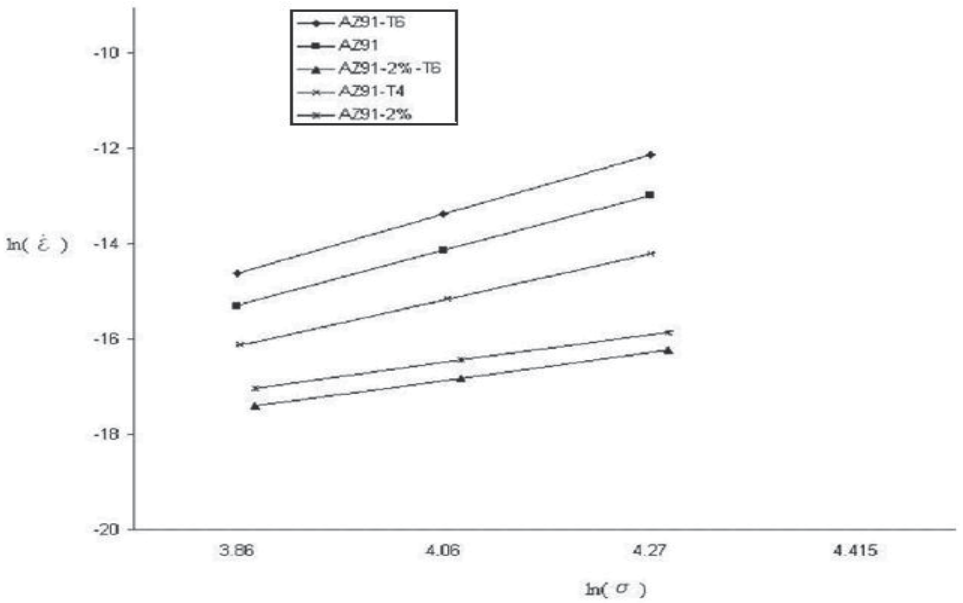

Fig. 10. Variation of creep rate with stress for alloys tested at 200°C.

3.3 Wear properties and its influence by Rare Earths addition

Wear rate under different normal loads for various sliding speeds were measured. The experiments were performed under 10, 20, 30, 50 and 100N stationary normal loads and sliding speeds of 0.25, 0.5 and 1.0 m/s at various sliding distances from 250 to 2000m. At constant sliding speed, applying higher normal load increases the wear rate generally. The wear rates increase abruptly at higher loads. The studies indicate that Rare Earth addition to AZ91 had no significant effect at lower sliding speeds. However it influences the wear rate at higher loads and speeds and show superior wear resistance compared with pure AZ91 alloy.

Studies suggest that there are five different operating wear mechanisms: abrasion, dalamination and gross plastic deformation more abundant and oxidation and adhesion less dominant. Abrasion is the prevailing wear mechanism at lower loads. Traces of parallel grooves can be distinguished on surfaces of most samples. These scratches may be attributed to hard asperities of counterface or detached particles that removed from disk or pin and placed in surface contact [Lim et al., 2003; Kumar & Kumar 2001; Cao et al., 1990].

With the wear process advancement, grooves become wider and deeper. Delamination mode of wear occurred when tests are conducted at sufficient high loads. Higher loads and longer sliding distances play an important role in increasing the probability of crack formation and growth.

High loads at long sliding distances result in severe plastic deformation on materials. As a result, edge cracks are fabricated. Due to intensive frictional heat of wear, AZ91 alloy locally melts and flows in the sliding direction [Chen & Alpas, 2000; Lim et al., 2003; Lim et al., 2005]. For more information on effect of Rare Earth addition on wear properties of AZ91 alloy, the readers can refer to Meshinchi Asl et al., 2010.

3.4 The effect of Al content and Si addition on the high temperature properties of Mg-Al alloys

Aluminum is an alloying addition often utilized to improve room temperature tensile properties by solid solution strengthening and precipitation of β intermetallic phase. At recent studies it is observed that the beneficial effects of Al appear to diminish because of microstructural instabilities at elevated temperatures [Moreno et al., 2003], thus alloy 4 was also investigated to compare the effect of reduction of Al in Mg-Al-RE alloys on microstructural and mechanical properties and creep behavior of these alloys, especially at elevated temperatures.

The RE elements don't have any reaction with magnesium as long as aluminum is in the melt [Khomamizadeh et al., 2005; Meshinchi Asl et al., 2009 (b)]. Thus, Al is consumed in $Al_{11}RE_3$ particles and the rest of Al interacts with Mg and forms the β phase. The reduction of Al in alloy 4 leads to decrease of β phase in the microstructure compared with alloy 3.

The addition of Si to AZ91 alloy results in the formation of Mg_2Si phase (Chinese Script) in the microstructure in addition to the $Mg_{17}Al_{12}$ particles. The only microstructural change between alloys with Si addition is the increase in the amount and size of Mg_2Si particles. On the other hand because the solid solubility of Si in Mg is negligible and Al and Si don't form any compound, the amount of β particles in the microstructure after the addition of Si to AZ91 alloy is constant. Thus, because the microstructre of the alloy after Si addition had no differences in the amount and distribution of β particles, the Si does not act as a refiner or modifier for the β phase. This behavior is unlike the effect of other alloying elements of AZ91 alloy such as REs which also modify the microstructure and decrease the β phase in the microstructure [Lu et al., 200]. This is due to the very little solubility between Al and Si which results in no changes in quantity of β phase after Si addition

Tensile properties show that alloy 3 with 2% RE and 9% Al had the best tensile properties at room temperature however at 140°C the tensile properties of alloy 4 is better. This is due to the decrease in β phases which are the main reason for poor mechanical properties of the AZ91 alloy at high temperatures.

The tensile strength of AZ91 alloy decreases with Si addition at room temperature. This reduction is due to the formation of brittle Mg_2Si Chinese Script particles. The amount of β phase in alloys with different Si addition is constant. However, with Si addition the amount of Mg_2Si Chinese Script phase increases which leads to a brittle microstructure. Although β phase is the most strengthening phase at room temperature in AZ91 alloy, the coarse brittle Chinese Script particles in the microstructure reduce the tensile properties at room temperature.

Creep tests indicate that alloy 4 with 2 weight percent of RE and lower Al content compared to alloy 3, had a slightly better creep resistance however alloy 3 has a better castability which is also important for industrial applications.

The most important result of Si addition was the improvement of the creep resistance of AZ91 alloy. Si addition resultes in remarkable improvement of creep resistance and alloy 7 with 1% of Si had a very lower creep rate compared to alloy 1. Thus Si addition results in significant increase in creep resistance of Mg-Al alloys.

For the alloy with 1 wt% Si addition, the stress exponent was 3.8 and the activation energy was measured 128 kJ mol^{-1}. Thus the values of both parameters fit the values for dislocation climb controlled creep.

The activation energy for alloy 4 is slightly higher than other alloys which is due to its better creep resistance. The presence of thermally stable Mg_2Si particles along grain boundaries which pin grain boundaries and hinder both grain boundary migration and sliding during high temperature exposure. This will yield to better creep properties in alloys with Si addition. The discontinuous precipitation of β are dominant at grain boundaries and weaken the grain boundaries at elevated temperatures. Therefore sliding of grain boundaries is an important factor in deformation of Mg-Al alloys at elevated temperatures. For more information the readers can refer to Meshinchi Asl et al., 2009 (a).

4. Conclusion remarks

- In AZ91 alloy the creep curves indicate a mixed mode of creep behavior, with some grain boundary effects contributing to the overall behavior. β ($Mg_{17}Al_{12}$) particles usually distributed at grain boundaries, have a low melting point and easily soften at high temperature, resulting in the previously mentioned behaviors.
- Addition of REs to Mg-Al alloys yields to the formation of thermally stable $Al_{11}RE_3$ needle shape particles which significantly improve creep properties of these alloys.
- The presence of thermally stable $Al_{11}RE_3$ needle shape particles along grain boundaries pin grain boundaries and hinder both grain boundary migration and sliding during high temperature exposure and therefore increase the creep resistance of the AZ91 alloy. For the AZ91alloy at low stresses, deformation is controlled by a mixed mode of dislocation climb mechanism with some grain boundary effects contributing to the overall behavior. Dislocation climb controlled creep is the dominant creep mechanism for the AZ91-RE alloys.
- Silicon addition to AZ91 alloy forms coarse Chinese Script Mg_2Si precipitates at the grain boundaries along with β ($Mg_{17}Al_{12}$). The addition of Si to AZ91 alloy doesn't modify the β phase morphology and also doesn't change the amount of β particles in the microstructure.
- Addition of Si to AZ91 alloy reduces the room tensile properties but improves the creep and elevated temperature tensile properties. After the Si addition, the sliding of grain boundaries is greatly suppressed due to morphological changes.
- The Mg-Al alloy with same RE addition and less Al content had better creep resistance. Thus despite good mechanical properties due to Al addition at room temperature, the Al content should be decreased for high temperature applications.
- In the AZ91 alloy, the formation of β precipitates occurred in two forms, discontinuous precipitation at the vicinity of grain boundaries (lamellar precipitation) and continuous precipitation (fine plate shape precipitates) within grains. The addition of REs in the form of misch metal (MM) to AZ91 alloy led to formation of needle shape $Al_{11}RE_3$ particles on the microstructure which have a high thermal stability and improve creep resistance of AZ91 alloy. It also decreases the amount of β particles in the microstructure and also decreases the discontinuous formation of precipitates at grain boundaries which have deleterious effect on mechanical properties of Mg-Al alloys at elevated temperatures.
- Abrasion, delamination and gross plastic deformation were identified as prevailing wear mechanisms. Abrasive wear activated at lower loads and sliding speeds. It

increased more wear rates for less ductile specimens of Rare Earth enriched. AZ91 alloy containing Rare Earth content show superior resistance to gross plastic deformation which operated at more severe wear conditions due to existence of $Al_{11}RE_3$ intermetallic phase which has attractive mechanical properties at elevated temperatures.

5. Acknowledgments

The author acknowledges Gary Kaufmann at the School of Materials Science and Engineering of Clemson University for his discussions which were thought provoking and inspiring.

6. References

Alahelistan, A. & Bergamon, F. (1993). Wear 165 (2) 221-226.
Alpas, A.T. & Zhang, J. (1992). Wear 155 83-104.
Archard, J.F.; (1953). J. of Applied Physics 24 981-988.
Bettles, C.J.; (2003). Materials Science and Engineering A 348 280-288.
Cao, L.; Wang, Y. & Yao, C.K. (1990). Wear 140 273-277.
Celotto, S.; (2000). Acta Mater. 48 1775-1787.
Chen, H. & Alpas, A.T. (2000). Wear 246 106-116.
Dully, D.; Cheynet, N.C. & Bercht, Y. (1994). Acta Metallurgica and Materialia 42 3843-3854.
Gao. X. et al., (2005). Scripta Materialia 53 1321-1326.
Jayamathy, M. et al., (2005). Mater. and Manu. Processes 20(2) 255-271.
Kang, D. H.; Park, S. & Kim, N. (2005). Materials Science and Engineering A 413-414 555-560.
Khomamizadeh, F.; Nami, B. & Khoshkhooei, S. (2005). Metallurgical and Materials Transactions A 3489-3494.
Kumar, S. & Kumar, B. (2001). Wear 247 191-201.
Lim, C.Y.; Lim, S.C. & Gupta, M. (2003). Wear 255 629-637.
Lim, C.Y.H.; Leo, D.K. & Ang, J.J.S. (2005).M. Gupta, Wear 259 620-625.
Lu, Y.; (2000). Materials Science and Engineering A 278 66-76.
Mehta, D.S.; Masood, S.H. & Song, W.Q. (2004). Journal of Materials Processing Technology 155-156 1526-1531.
Meshinchi Asl, K.; Tari, A. & Khomamizadeh, F. (2009). Materials Science and Engineering A 523 1–6 (a).
Meshinchi Asl, K.; Tari, A. & Khomamizadeh, F. (2009). Materials Science and Engineering A 523 27–31 (b).
Meshinchi Asl, K.; Masoudi, A. & Khomamizadeh, F. (2010). Materials Science and Engineering A 527 2027–2035.
Mordike, B.L. & Ebert, T. (2001). Materials Science and Engineering A 302 37-45.
Moreno, I.P. et al., (2001). Scripta Materialia 45 1423-1429.
Moreno, I.P. et al., (2003). Scripta Materialia 48 1029-1034.
Oakley, R.; Cochrane, R.F. & Stevens, R. (1995). Key Eng. Mat. 104-107 387-416.
Sharma, S.C.; Anand, B. & Krishma, M. (2000).Wear 241 33-40.
Sinha, S.K.; Reddy, S.Y. & Gupta, M. (2006). Tribology Int. 39 184-189.

Somekawa, H. et al., (2005). Materials Science and Engineering A 407 53-61.
Spigarelli, S.; (2000). Scripta mater. 42 397-402.
Wang, Y.; Wang, Q. & Ma, C. (2003). Materials Science and Engineering, A 342 178-182.
Wenwen, D. et al., (2003). Materials Science and Engineering A 356 1-7.

13

Microstructure and Properties of Elektron 21 Magnesium Alloy

Andrzej Kiełbus
Silesian University of Technology
Poland

1. Introduction

Magnesium is the lightest of metals used for constructional alloys. These alloys are characterised by low density and good mechanical properties (Mordike et al., 2001), however they are showed poor properties in elevated temperature (Mordike, 2002). Among various magnesium alloys, rare earth containing alloys are known to show good mechanical properties and excellent creep resistance (Avedesian et al., 1994). Mainly for these reasons, magnesium alloys have a widespread application in the motor vehicle and aircraft industries. The disadvantages are poor properties in elevated temperatures and high reactivity (Mordike, 2001). A range of alloys are commercially available from Mg-Al alloys to highest strength, high temperature Mg-Zr alloys with addition of yttrium. However alloys that contain yttrium have high associated cost due the difficulties in casting. Therefore there is a need for an alternative alloy which has similar properties to Mg-Y alloys, but with foundry handling and associated costs like non-yttrium containing alloys (Lorimer et al., 2003).

Magnesium alloys containing neodymium and gadolinium are interesting as light structural materials with high mechanical properties at room and elevated temperatures (Smola et al., 2002). Mg-Nd-Gd-Zr magnesium alloys are characterised by high-strength and good creep resistance to automotive and aerospace applications (Rokhlin et al., 1996). The rare earth elements have beneficial effect of on the creep properties, thermal stability of structure and mechanical properties of magnesium alloys (He et al., 2006).

Elektron 21 is new magnesium based casting alloy containing neodymium, gadolinium and zinc for used to approximately 200°C. This alloy has high strength, good corrosion resistance and excellent castability. Neodymium has a positive effect on tensile strength at elevated temperature, reduces porosity of casts and susceptibility to cracking during welding. Gadolinium, like neodymium shows a decreasing solid solubility as temperature falls, indicating potential for precipitation strengthening. Addition neodymium to Mg-Gd alloys reduces the solid solubility of gadolinium. It improves precipitation hardening response, at lower levels of gadolinium than the binary system offers. Zinc is added to magnesium alloys in sufficient quantities to achieve precipitation strengthening. It improves strength without reducing ductility. Zirconium, which does not form any phases with magnesium or alloying elements, contributes to the obtaining of a fine grain structure and improves the mechanical properties at an ambient temperature, castability and corrosion performance. Elektron 21 is being used in both civil and military aircraft and also in automobile (motorsport) industry (Lyon et al., 2005).

The scope of this book chapter is to provide the results of microstructure, mechanical properties, creep and corrosion investigations of Elektron 21 magnesium alloy in as-cast condition and after heat treatment.

2. Material and methodology

The material for the research was a sand casting Elektron 21 magnesium alloy. The chemical composition of this alloy is provided in Table 1.

Gd	Nd	Zr	Zn	Mn	Fe	Ag	TRE	Mg
1,2	2,7	0,49	0,4	0,001	0,003	0,01	4,2	balance

Table 1. Chemical composition of the Elektron 21 alloy (wt.%).

Sand casting was performed at 730, 780 and 830°C temperature. Castability has been investigated by determining the flow length with a mould featuring a spiral shaped cavity. The as-cast specimens were solution treated at 520 °C for 2÷48 h and quenched into water. Ageing treatments were performed at 200°C, 250°C and 300°C/4÷5000h with cooling in air. Thermal diffusivity was measured on LFA 427 Netzsch apparatus. The measurement was performed in the temperature range from 25 to 300 °C. The temperature was increased from ambient temperature to each test temperature (step 25°C). Thereafter, the thermal diffusivity measurement was carried out under isothermal conditions. The temperature of the rear surface of the specimen was measured with an InSb IR detector. Thermal diffusivity was calculated using the relation:

$$\alpha = 0{,}1388\frac{g^2}{t_{0,5}} \tag{1}$$

where:
g- is the thickness of the specimen, $t_{0,5}$- half- rise time, defined as the interval required for the rear surface temperature to reach one- half of the maximum temperature increase.
For the microstructure observation, an OLYMPUS GX71 metallographic microscope and a HITACHI S-3400N scanning electron microscope were used. TEM examination was carried out on a a Tecnai G² transmission electron microscope equipped with a high-angle annular dark-field detector and energy dispersive X-ray spectrometer.
For a quantitative description of the structure, stereological parameters describing the size and shape of the solid solution grains and phase precipitates were selected. To measure the stereological parameters, a program for image analysis "MET-ILO" was used. The procedure of converting the input image into a binary image to be used for grain size measurement is presented in Fig.1 and for intermetallic phase precipitates in Fig.2.
The examination of the mechanical properties was conducted on an MTS-810 machine at ambient (ca. 20°C) and 200°C temperature. Hardness tests have been performed with a Vickers indenter. Constant-load tensile creep tests were performed at 200°C and 250°C in the stress range 90÷150 MPa. Creep strain was measured by extensometers which were attached directly to the gauge section of specimens.
For corrosion test the specimens were exposed for 7 days to 3.5% NaCl saturated with $Mg(OH)_2$ solution maintained at ambient temperature, without stirring. Before the tests, the specimens were polished with SiC papers up to 1200 grit. After cleaning with acetone and

Picture A
gray image

Picture B
normalization, shadow correction, detection

Picture C
negative, edge removal

Picture D
manual correction, image for measurement

Fig. 1. The procedure of a quantitative evaluation of solid solution α-Mg grains in Elektron 21 alloy, LM.

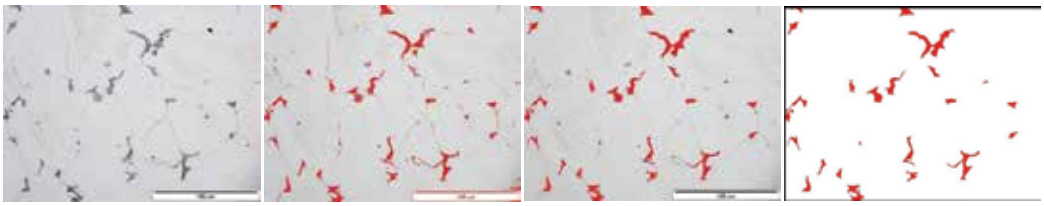

Picture A
gray image

Picture B
normalization, shadow correction, binarisation

Picture C
manual correction

Picture D
image for measurement

Fig. 2. The procedure of a quantitative evaluation of intermetallic phases precipitates in Elektron 21 alloy, LM.

drying, they were weighed to obtain their original weight (m_o) before corrosion. After immersion test, the corroded specimens were taken out of the solution, cleaned with distilled water and dried. They were then immersed in chromate acid (200g/dm^3 CrO_3 + 10g/dm^3 $AgNO_3$) to remove corrosion products. After that, the specimens were cleaned again with distilled water, rinsed with acetone and dried. The specimens were weighed on an analytical balance to an accuracy of ± 0.1 mg. The dried specimens were weighed (m_1) after immersion. The difference between m_o and m_1 is the corrosion weight loss (Δm). According the test results, the corrosion rate was calculated.

3. Results

3.1 As-cast state

The Elektron 21 alloy composed mainly of a solid solution structure α-Mg with eutectic α-Mg + Mg_3(Nd,Gd) on the grain boundaries. The Mg_3(Nd,Gd) phase (Fig. 3a) is a modification of Mg_3Nd phase with neodymium substituted by gadolinium without destroying the crystal structure, due to reasonably small difference in the atomic radii between gadolinium r_{Gd}=0,1802 nm and neodymium r_{Nd}=0,1821 nm. The regular precipitates of $MgGd_3$ phase have been also observed (Fig. 3b).

A quantitative evaluation of the Elektron 21 alloy microstructure has shown that the mean area of the solid solution α-Mg grain equals $\bar{A}$=649 μm^2, and the mean shape coefficient

value equals $\xi = 4\pi A/P^2 = 0.64$. The mean surface fraction of intermetallic phase, is V_V=6.55%, whereas the mean shape coefficient value is $\xi = 0.53$.

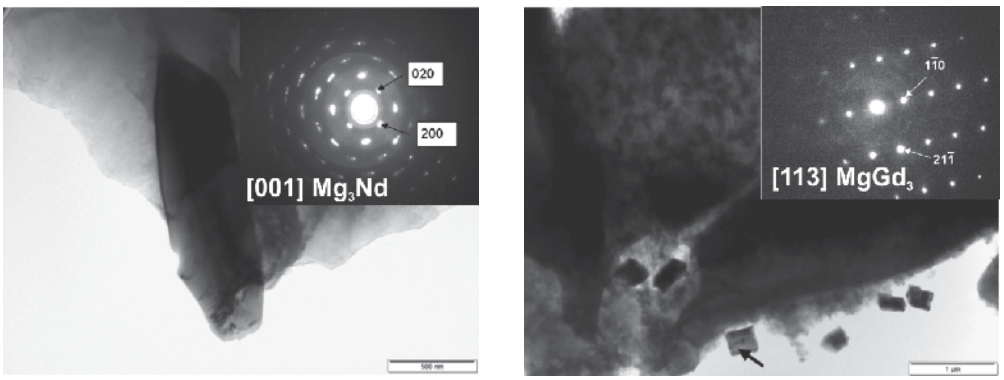

(a) (b)

Fig. 3. Microstructure of the Elektron 21 alloy in as-cast condition:
a) TEM image and corresponding diffraction pattern of Mg_3Nd phase
b) TEM image and corresponding diffraction pattern of $MgGd_3$ phase.

3.2 Castability

The castability of Elektron 21 alloy increase with the increase of casting temperature over the whole temperature range. Spiral casts of Elektron 21 alloy after casting from temperature 730, 780 and 830°C were showed in Fig. 4.

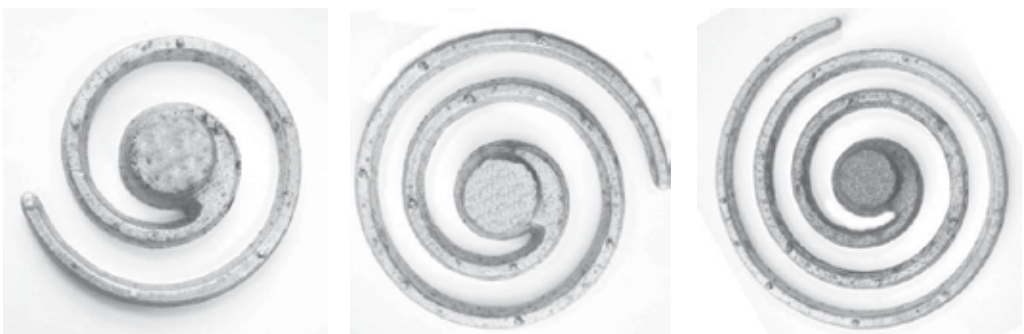

730°C Spiral length – 0,47 m | 780°C Spiral length – 0,57 m | 830°C Spiral length – 0,73 m

Fig. 4. Spiral casts of Elektron 21 alloy after fluidity test.

In Elektron 21 alloy after casting from 730°C the mean plane section area of α-Mg solid solution grains equals $\bar{A}$ = 384 μm² and the mean area fraction of intermetallic phase is A_A = 3,2%. Extension of the casting temperature to 780°C and 830°C brings slightly decrease of the mean plane section area of α-Mg grains respectively to $\bar{A}$ = 375μm² and $\bar{A}$ = 362μm², whereas the intermetallic phase quantity didn't change and equals A_A=~3,1%, irrespective of casting temperature (Fig.5).

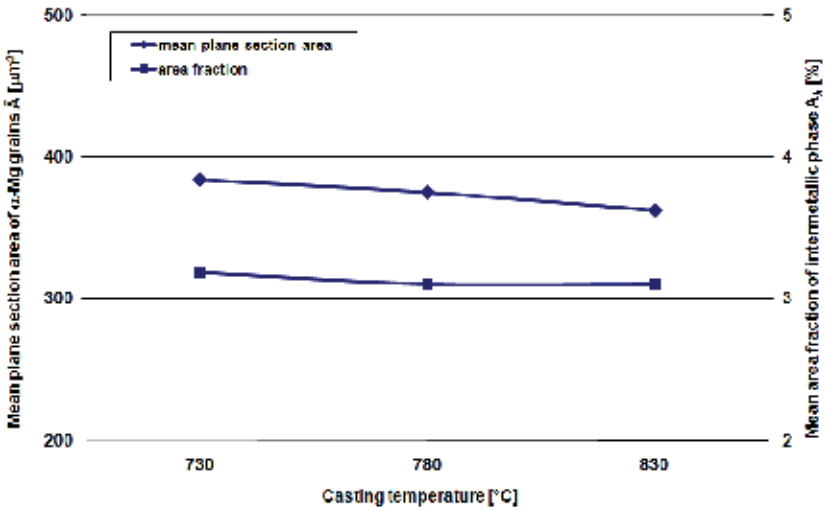

Fig. 5. The influence of casting temperature of Elektron 21 alloy on area fraction of the intermetallic phases and mean plane section area of α-Mg solid solution grains.

3.3 Heat treatment

Solution treatment

After solution treatment 520°C/water the $Mg_3(Nd,Gd)$ intermetallic phase dissolves in the matrix. 2-hours solution treatment causes a considerable (~3-times) decrease of the $Mg_3(Nd,Gd)$ phase area fraction to A_A=1.93%. The mean plane section area of α-Mg grains equals Ā=2186 μm² and is higher (also ~3-times) compared to the as-cast state (Fig. 6a). Extension of the solution treatment time to 8h brings about an even more considerable decrease of the phase area fraction to A_A=0.66%, whereas the mean plane section area of α-Mg grains grows to Ā =3091 μm² (Fig.6b).

Extension of the solution treatment time to 24 hours brings about an even more considerable decrease of the $Mg_3(Nd,Gd)$ phase quantity to A_A=0.5%, whereas the grain size grows to Ā =3200 μm² (Fig.7a). Even longer solution treatment time (48h) caused precipitation of a Nd-Gd intermetallic phase (probably $Nd_{0.5}Gd_{0.5}$ phase), however, it does not influence the solid solution grain mean area Ā = 3220 μm² (Fig.7b).

The influence of solution treatment time on the $Mg_3(Nd,Gd)$ phase quantity, the solid solution α-Mg grain size and hardness of Elektron 21 was presented on figures 8 and 9. After short time of solutioning (2h) the hardness of Elektron 21 alloy increase to 67 HV due to solution of neodymium and gadolinium in α-Mg matrix. Extension of the solution treatment time caused decreasing of hardness to 59 HV due to grain size grows. After 48h of solutioning, precipitation of a Nd-Gd intermetallic phase was observed which caused further decreasing of hardness to 47 HV.

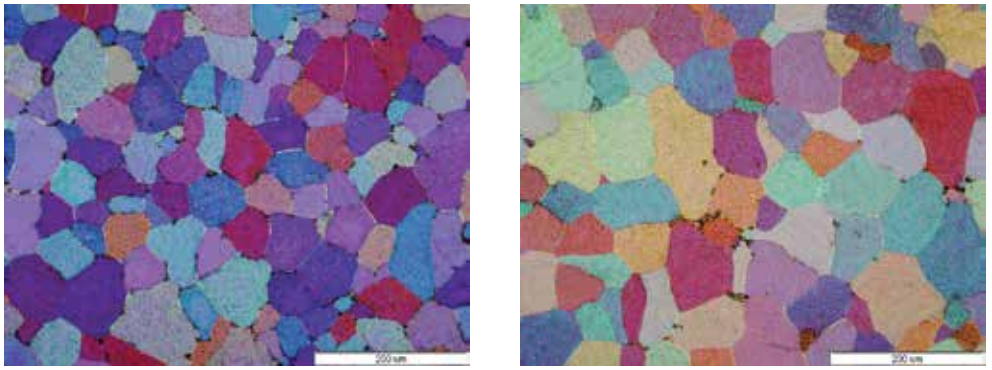

(a) (b)

Fig. 6. Microstructure of Elektron 21 alloy after solution treatment a) 520°C/2h/water, b) 520°C/8h/water, LM.

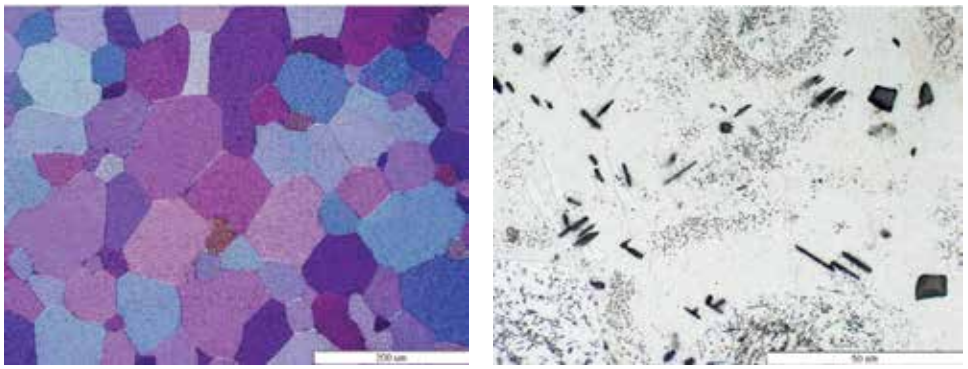

(a) (b)

Fig. 7. Microstructure of Elektron 21 alloy after solution treatment a) 520°C/24h/water, b) 520°C/48h/water, LM.

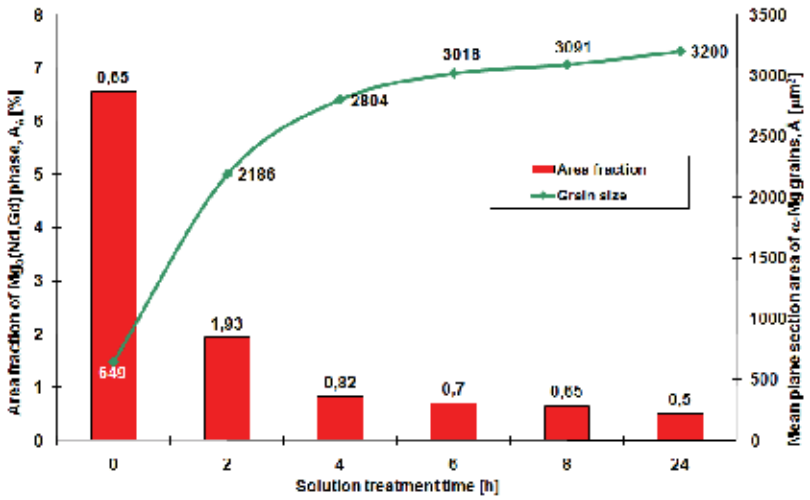

Fig. 8. Influence of the solution treatment time on the $Mg_3(Nd,Gd)$ phase quantity and the solid solution α-Mg grain size.

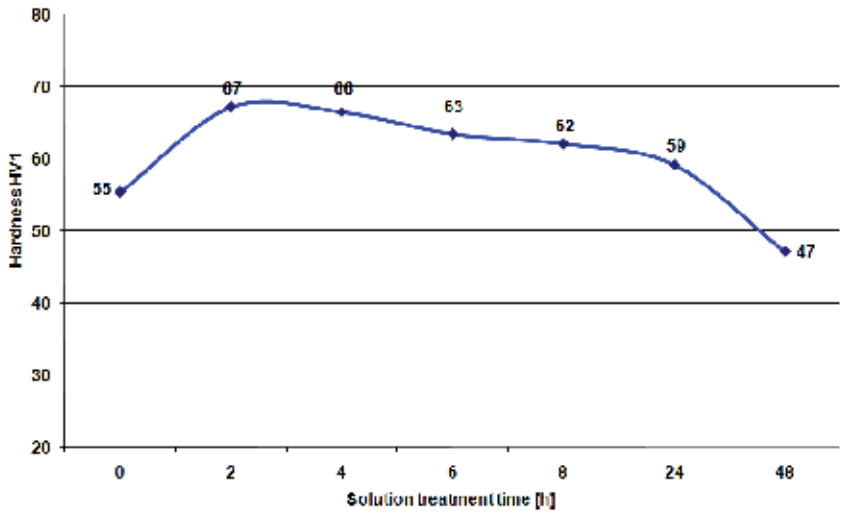

Fig. 9. Influence of the solution treatment time on the Elektron 21 hardness.

Ageing treatment

The microstructure of Elektron 21 alloy aged at 200 °C for 4 h contained thin precipitate platelets of β″ (Fig.10). The β″ platelets were approximately 8 nm in length and 2 nm thick. The β″ phase is fully coherent with the matrix. It has a $D0_{19}$ crystal structure (a=0,64 nm and c=0,52 nm) and is isomorphous with the $Mg_3X(RE)$ phase.

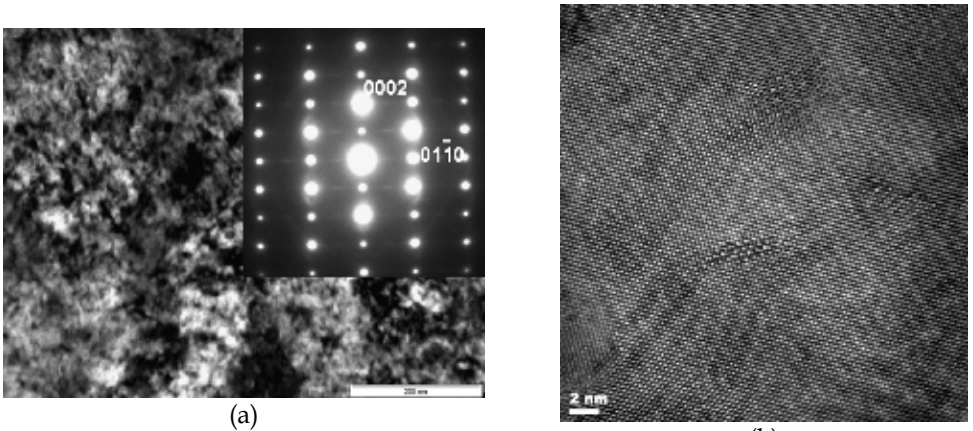

(a) (b)

Fig. 10. Microstructure of the Elektron 21 alloy aged at 200°C for 4h:
a) TEM image with corresponding (SAED) pattern, b) HRTEM image.

With continuous ageing for 16 h at 200 °C the microstructure contains except precipitates of β″, spherical particles of β′ (Fig.11). The β′ platelets were approximately 10÷15 nm in diameter and <10 nm thick. The intermediate β′ phase is metastable and semi coherent with the matrix. It has an orthorhombic crystal structure (a=0,64 nm, b=2,22 nm and c=0,52 nm).

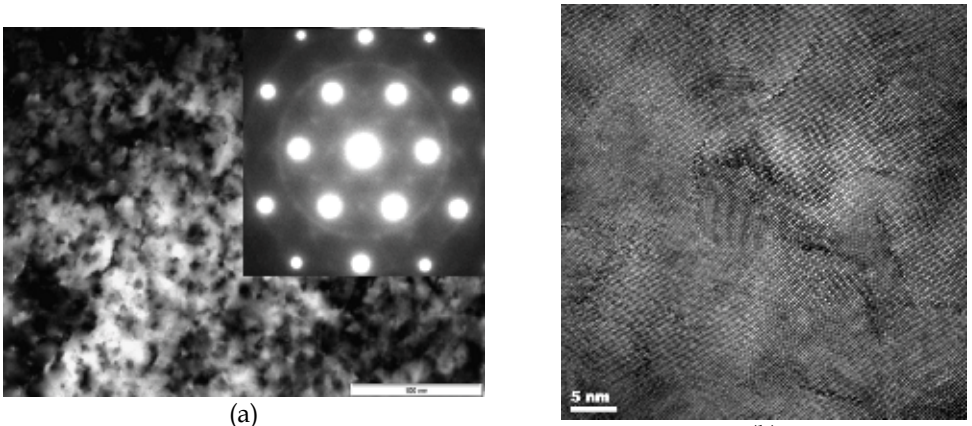

(a) (b)

Fig. 11. Microstructure of the Elektron 21 alloy aged at 200°C for 16h:
a) TEM image with corresponding (SAED) pattern, b) HRTEM image.

The microstructure of Elektron 21 alloy aged at 200 °C for 48h or aged at 250°C for 4 h consisted of enlarged β′ phase precipitates and the elongated, needle-shaped precipitates of equilibrium β phase (Fig.12). The precipitates of equilibrium β phase were formed between the β′ particles and nucleated preferentially in the strain field of the β′ phase. This phase formed heterogeneously on β′ particles. The β phase is non-coherent with the α-Mg matrix and is identified as Mg_3Nd phase. It has a face-centered cubic crystal structure (a=0.74 nm). Similarly in as-cast condition Mg_3Nd phase has the form of $(Mg)_3(Nd,Gd)$.

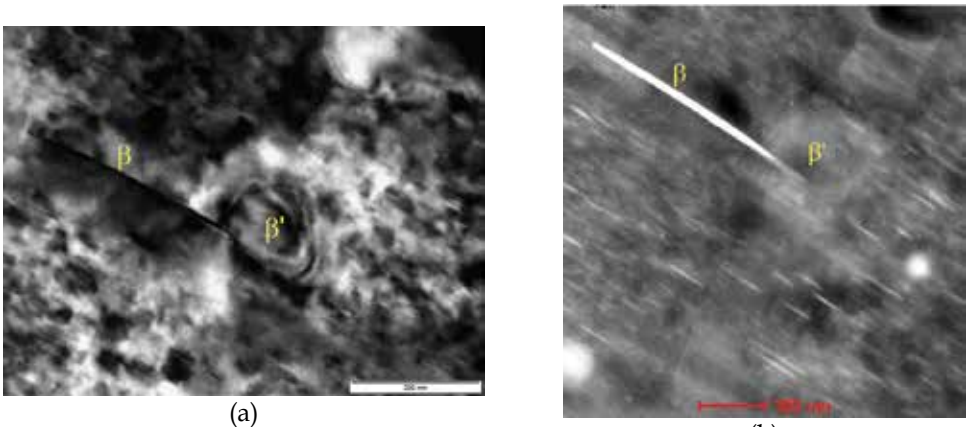

(a) (b)

Fig. 12. Microstructure of the Elektron 21 alloy aged at 250°C for 4h:
a) TEM image, b) STEM-HAADF image.

Ageing (300°C/500h) caused the precipitation of the globular particles of $Mg_{41}Nd_5$ phase (Fig.13a,b). Precipitates of Mg $(Nd,Gd)_3$ phase have been also observed (Fig.13c). Longer annealing caused the formation of the network consisted of $Mg_{41}Nd_5$ precipitates on α-Mg solid solution grain boundaries. The hardness evolution, as a function of ageing time for isothermal ageing at 200, 250 and 300 °C is shown in Fig. 14.

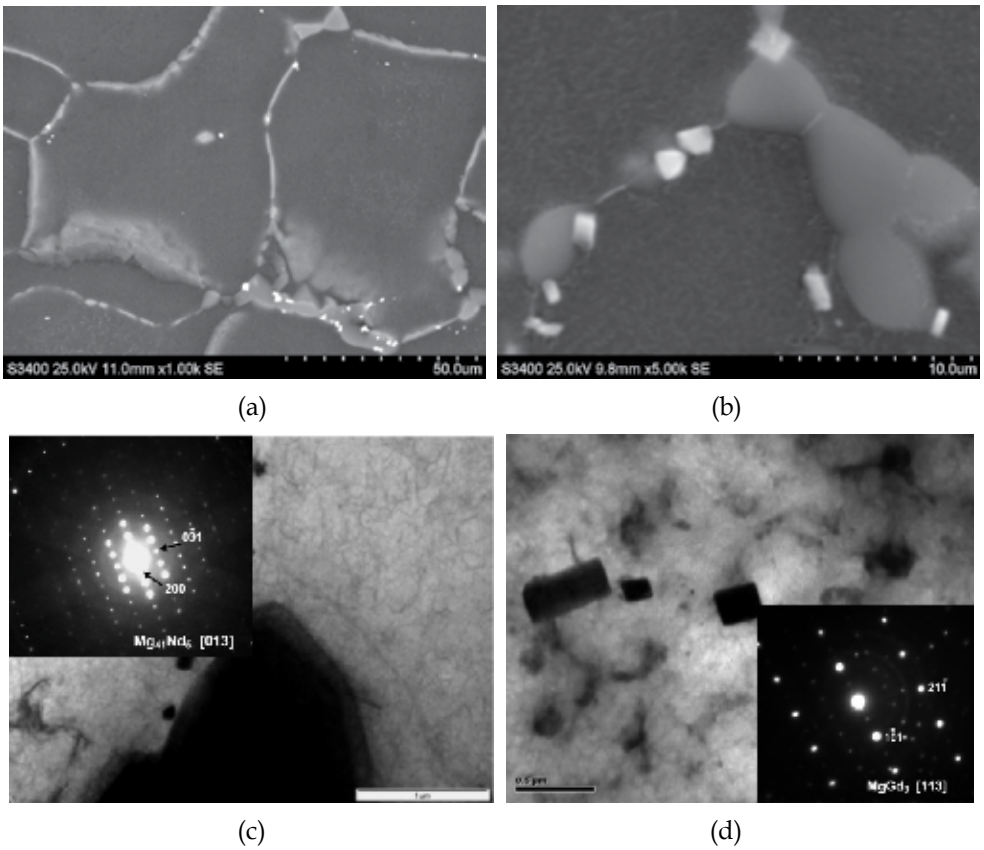

Fig. 13. Microstructure of the Elektron 21 alloy aged at 300°C for 500h:
a,b) SEM image ,d) TEM images

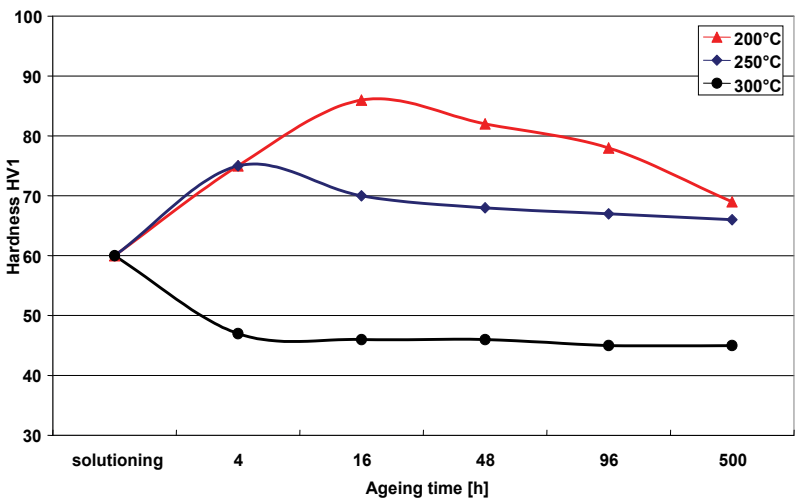

Fig. 14. Hardness evolution of the Elektron 21 alloy as a function of ageing time.

Elektron 21 alloy showed a remarkable hardening at 200°C temperature, and the peak hardness value can reach 87HV after ageing for 16 h at 200 °C due to the precipitation of β″ and β′ phases. The peak hardness was shortened with an increase of the ageing temperature. There wasn't any peak hardness in case of an alloy aged at 300°C.

3.4 Thermal diffusivity

The temperature dependences of the thermal diffusivity for the Elektron 21 alloy in as-cast state and after heat treatment is shown in figure 15. The thermal diffusivity of solution treated Elektron 21 alloy was determinate only in the temperature range from room temperature to 200°C. Above this temperature the influence of the phase transition on the thermal diffusivity is significant.

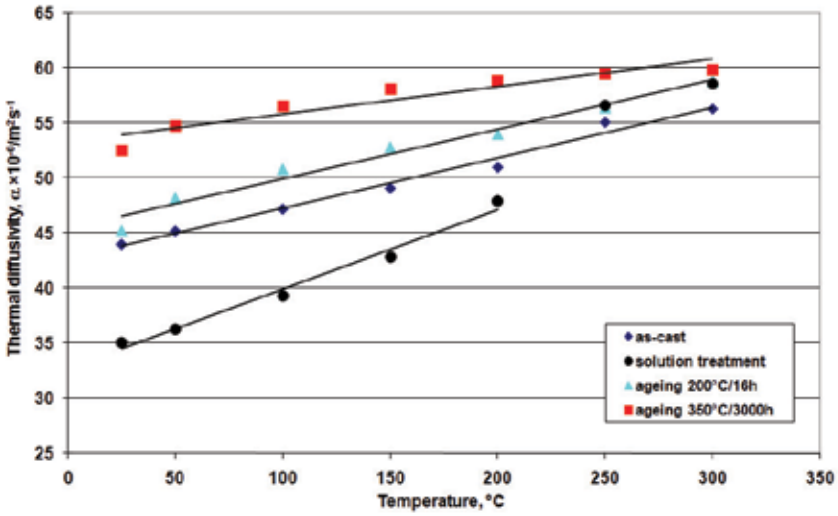

Fig. 15. Temperature dependence of the thermal diffusivity of Elektron 21 alloy, in as-cast condition and after heat treatment.

The thermal diffusivity of Elektron 21 alloy increase with the increase of temperature. The thermal diffusivity values (m^2s^{-1}) of this alloy are summarized in the following equations as a function of temperature.

Elektron 21 cast alloy

$$\alpha = 4{,}57\times10^{-2}T + 42{,}68$$

Elektron 21 solution-treated alloy

$$\alpha = 7{,}24\times10^{-2}T + 32{,}66$$

Elektron 21 aged at 200°C/16h

$$\alpha = 4{,}51\times10^{-2}T + 45{,}39$$

Elektron 21 aged at 350°C/3000h

$$\alpha = 2{,}5\times10^{-2}T + 53{,}29$$

Now we can discuss the influence of the content of the solute element in the α-Mg matrix on the thermal diffusivity of Elektron 21 alloy. This alloy after solution treatment showed low thermal diffusivity in this study because of its higher content of a solute element in the α-Mg

matrix. The high-temperature-aged Elektron 21 alloy in which the strengthening phases precipitated exhibited higher thermal diffusivity than its solution-treated state. The secondary phase precipitation consumed solute elements in the α-Mg matrix, leading to increase the thermal diffusivity of this alloy.

3.5 Creep properties

Curves of creep tests at 200°C are presented in Fig. 16 and at 250°C are shown in Fig. 17. The creep curves at 200 °C exhibit a well-defined primary and secondary stages.

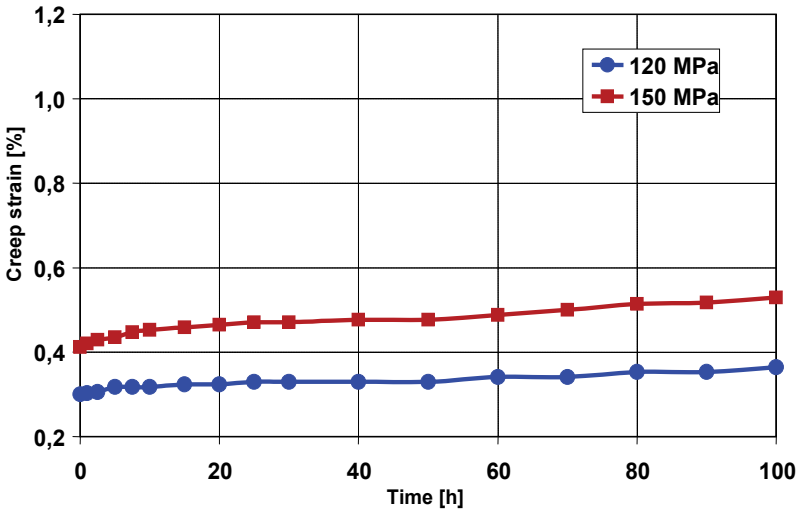

Fig. 16. Creep curves of Elektron 21 alloy (after T6 treatment) at 200°C under stresses of 120 and 150 MPa.

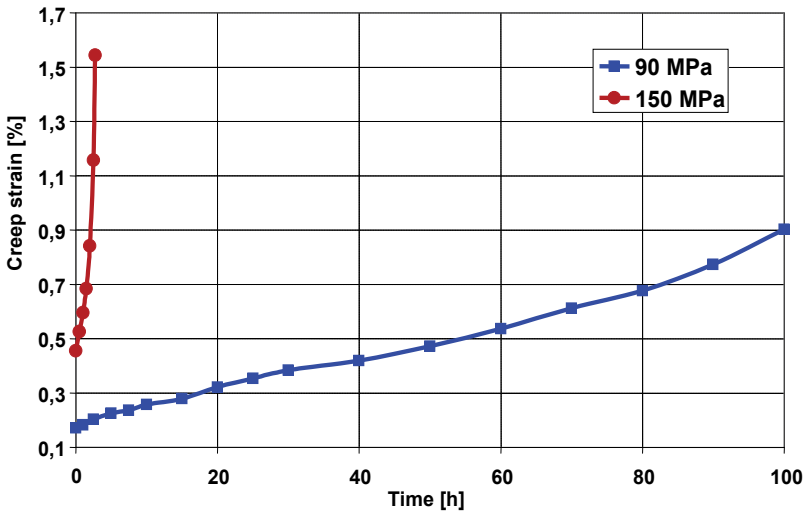

Fig. 17. Creep curves of Elektron 21 alloy (after T6 treatment) at 250°C under stresses of 120 and 150 MPa.

The creep strain at 200°C/100h varies from 0.36% (120 MPa) to 0.53% (150 MPa). The strain of the samples, which were crept at 250°C and at 90 MPa is equal 0.9%, whereas the specimen crept at 250°C and at 150 MPa has already ruptured after 2.7 h. For this sample, only tertiary stage was observed (Fig. 17). From the gradient of the secondary stage in the creep curves, the steady-state creep rate can be calculated and the results are shown in Table 2. Obviously, the steady-state creep rate and creep strain increased with the increase of in the test temperature and applied stress. This fact suggests that a high dislocation generation rate surpasses the annihilation rate.

		90 MPa	120 MPa	150 MPa
200°C	ε [%]	-	0.36	0.53
	$\dot{\varepsilon}$ [1/s]	-	$9.2 \cdot 10^{-10}$	$2.3 \cdot 10^{-9}$
250°C	ε [%]	0.9	-	1.54 (2,7h)
	$\dot{\varepsilon}$ [1/s]	$1.7 \cdot 10^{-8}$	-	-

Table 2. Creep elongation ε and creep rate in the secondary stage $\dot{\varepsilon}$ of Elektron 21 alloy after 100h of the test at different temperatures and stresses..

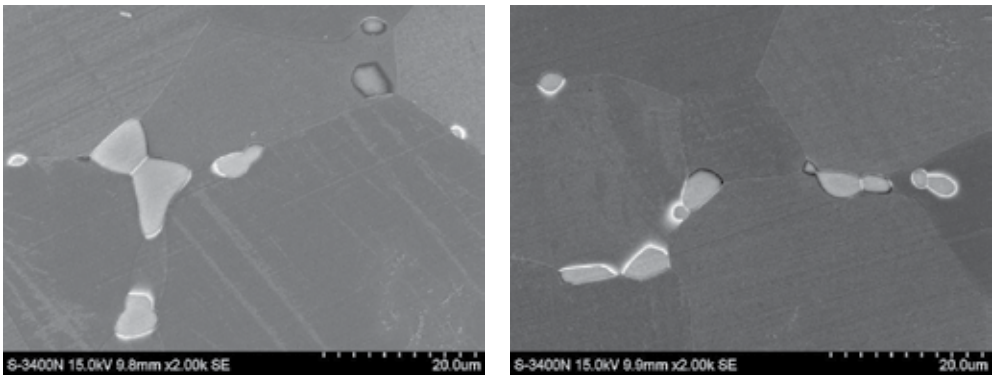

(a) (b)

Fig. 18. The microstructure of the Elektron 21 alloy after creep test at 150MPa/200°C.

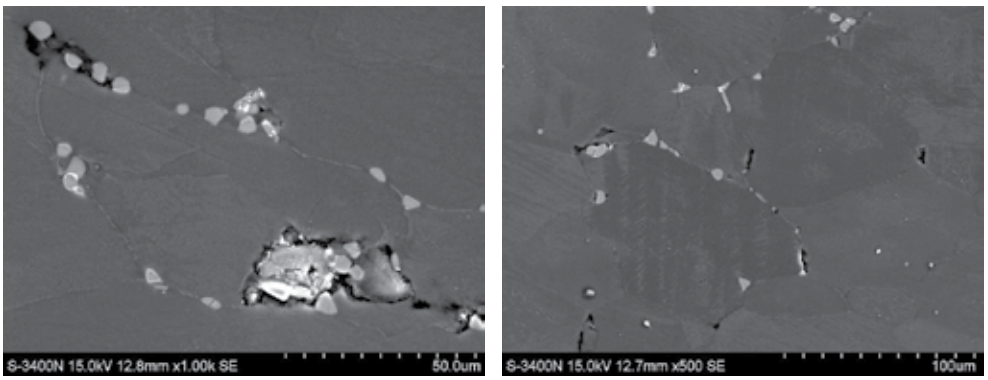

(a) (b)

Fig. 19. The microstructure of the Elektron 21 alloy after creep test at 90 MPa/250°C.

The microstructure of Elektron 21 alloy after creep test at 200°C/150 MPa (the secondary stage) is presented in Fig. 18. It can be seen that undissolved particles of the $Mg_3(Nd,Gd)$ phase are present in the microstructure of this alloy after T6 treatment. The cracks in these particles and voids accumulated at the interfacial boundary between α-Mg and $Mg_3(Nd,Gd)$ are visible after creep at 200°C/150 MPa. After creep test at 250°C/90 MPa (Fig. 19) numerous creep voids at the triple points are observed. Moreover, the large cracks, which were initiated under the stresses at the interfacial boundary are present in the microstructure of alloy investigated.

3.6 Corrosion resistance

Fig. 20 shows the typical surface features of the corroded specimens after 5 days of immersion test in 3.5% NaCl saturated with $Mg(OH)_2$ solution.

as cast | solutioning 520°C/8h | ageing 200°C/4h

ageing 200°C/16h | ageing 200°C/48h

Fig. 20. Corrosion morphologies of Elektron 21 alloys before and after heat treatment after 5 days of immersion test in 3.5% NaCl + $Mg(OH)_2$.

From the appearance of the specimen surface Elektron 21 in as-cast condition was more severely corroded than specimens after heat treatment. Only specimen after ageing 200°C/48 has similar morphology. The difference in macro-morphology of corroded specimens indicates different corrosion rates in dependence from heat treatment parameters. After five days, serious corrosion damage occurred on as cast state and aged 48h alloy over its entire surface, whereas the corrosion of remaining specimens was only appeared on part of the specimen surface. The comparison of the corrosion rates results obtained from immersion test in 3.5% NaCl are given in Fig. 21.

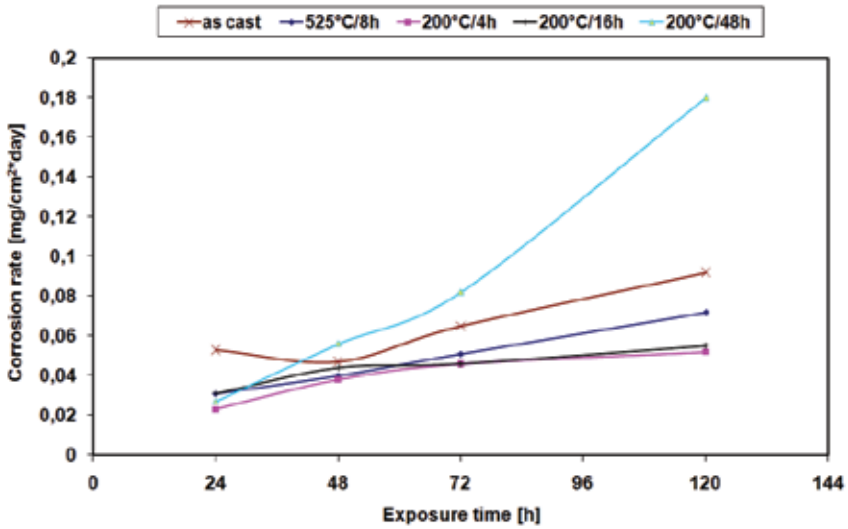

Fig. 21. Corrosion rates of Elektron 21 alloy before and after heat treatment during immersion test in 3.5% NaCl + $Mg(OH)_2$.

Fig. 22 shows the effect of heat treatment on the corrosion resistance of Electron 21 alloy after exposure in 3.5% NaCl + $Mg(OH)_2$ for 5 days.

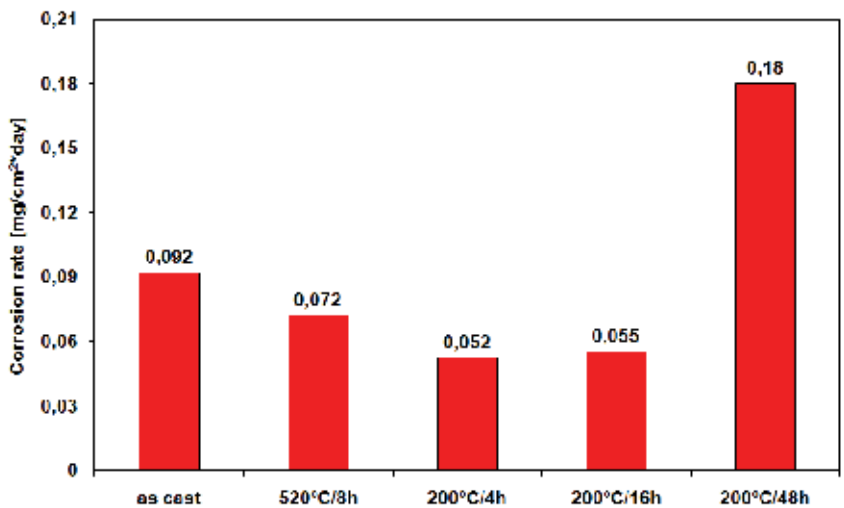

Fig. 22. Corrosion rates of Elektron 21 alloy after immersion test in 3.5% NaCl+$Mg(OH)_2$ for 5 days.

The corrosion rates of Elektron 21 alloy incresed with the increase of the exposure time and finally (after 5 days) reached maximum value 0.092 mg/cm^{-2}day^{-1}. After solution treatment (520°C/8h), the corrosion rate decrease due to dissolved of intermetallic phase precipitates and reached maximum value 0.072 mg cm^{-2} day^{-1}. Ageing at 200°C for 4h and 16h caused only slightly decrease of corrosion rate to value 0.052 and 0.055 mg cm^{-2} day^{-1}, respectively, due to precipitations of β' phase. While after ageing for 48 h the corrosion rate considerably

increase to value 0.188 mg cm^{-2} day^{-1} due to increase of the volume fraction and size of β′ phase and precipitations of equilibrium β phase.
The corrosion propagation was most uniform for the solution treatment condition. Corrosion rate decreases due to dissolution of intermetallic phase. Aged specimens (4h and 16h) were less corroded than as-cast alloy, and the difference in corrosion damage depends on ageing time. With increased ageing time, the volume fraction of precipitates increased gradually and these particles behaved as the cathodic sites and thus matrix attack is favored by micro galvanic cell formation.

4. Summary

The Elektron 21 alloy in as-cast condition is characterized by a solid solution structure α–Mg with eutectic α–Mg + Mg_3(Nd,Gd) intermetallic phase on grain boundaries and precipitates of $Mg(Nd,Gd)_3$. The castability of this alloy increase linearly with the increase of casting temperature over the whole temperature range. The increasing of the casting temperature causes slightly decrease of the mean plane section area of α-Mg solid solution grains whereas the volume fraction of the intermetallic phases didn't change.
The hardness of Elektron 21 alloy increase to 67HV after 2h of solutioning in 520°C due to solution of neodymium and gadolinium in α-Mg matrix. Extension of the solution treatment time caused decreasing of hardness to 59HV due to the mean plane section area of α-Mg solid solution grains grows and decrease of the area fraction of Mg_3(Nd,Gd) phase. After 48h of solutioning precipitation of a Nd-Gd intermetallic phase was observed which caused further decreasing of harness to 47HV.
In first stage of ageing process the product of the α–Mg decomposition are fully coherent and semi-coherent with the matrix precipitates of β″ and β′ phases, respectively. It causes an increase of hardness and the peak hardness (87 HV) was observed after 16 h of ageing at 200°C. Second stage is the formation of a stable equilibrium β (Mg_3Nd) phase. The β phase is non-coherent with the α–Mg matrix. Further ageing led to decrease of the hardness. The last stage of ageing assigned to formation of $Mg_{41}Nd_5$ phase. Long term annealing at 300°C/500÷5000h/air caused precipitation of globular $Mg_{41}Nd_5$ phases on solid solution grain boundaries. Also precipitates of $Mg(Nd,Gd)_3$ phase have been observed. The hardness of Elektron 21 alloy decrease to 45HV after 500h of annealing due to precipitation of these phases. Even longer annealing time (2000÷5000h) caused formation the network of $Mg_{41}Nd_5$ precipitatates on solid solution grain boundaries. However, it hasn't significant influence on the mean plane section area of α–Mg grains ($\bar{A}$ = ~3200 μm^2), the area fraction of $Mg_{41}Nd_5$ phase A_A=~5,5% and hardness 44HV
Generally, the investigated alloy showed that the decomposition of α–Mg supersaturated solid solution with increasing ageing time is as follows:

$$\alpha\text{–Mg} \rightarrow \beta'' \rightarrow \beta' \rightarrow \beta(Mg_3RE) \rightarrow Mg_{41}Nd_5.$$

The thermal diffusivity of Elektron 21 alloys was temperature and microstructure dependent. It was dependent on the content of the solute element in the α-Mg matrix. The solid solution of Nd and Gd in Mg has lower thermal diffusivity than alloy where the intermetallic Mg_3(Nd,Gd) phase is present. The formation of strengthening phases during ageing caused the consumption of the solute element in the α -Mg matrix, and improved the thermal conductivity of the alloy. The results confirm that the thermal diffusivity of Elektron 21 alloy depend on its thermal history.

Also corrosion behaviour of Elektron 21 alloy strongly depends on heat treatment condition. Corrosion rate of solutioned specimen is lower than those for as-cast due to dissolution of intermetallic phase precipitates and solution hardening. Lower corrosion rate of Elektron 21 alloy after short period of ageing (4h,16h) is caused by precipitation of metastable β′ phase. Higher corrosion rate of Elektron 21 alloy after ageing treatment at 200°C for 48h is caused by increase of β′ size and its volume fraction and also due precipitation of equilibrium β phases in microstructure.

5. Acknowledgement

The present work was supported by the Polish Ministry of Science and Higher Education under the research projects No N N507 451334 and PBR N R15-0015-04/2008.

6. References

He S.M., Zeng X.O., Peng L.M., Gao X., Nie J.F., Ding W.J., (2006). Precipitation in a Mg–10Gd–3Y–0.4Zr (wt.%) alloy during isothermal ageing at 250°C, *Journal of Alloys and Compounds,* Vol. 421 (2006), pp. 309–313.

Lyon P., Syed I., Wilks T., (2005). The influence of alloying elements and heat treatment upon properties of Elektron 21 (EV31A) alloy, *Magnesium Technology 2005,* pp. 303-308.

Rokhlin L., Nikitina N., Dobatkina T., (1996). Solid-state phase equilibria in the Mg corner of the Mg-Gd-Sm phase diagram, *Journal of Alloys and Compounds,* Vol. 239, (1996) pp. 209-213.

Smola B., Stulikova I., von Buch F., Mordike B., (2002),.Structural aspects of high performance Mg alloy design, *Materials Science and Engineering A* Vol. 324, (2002), pp. 113-117.

Mordike B., Eberr T., (2001). Magnesium: Properties-applications-potentials, *Materials Science and Engineering* A, Vol. 302, Issue 1 (2001) pp.37-45.

Mordike B., (2002). Creep-resistant magnesium alloys, *Materials Science and Engineering A*, Vol. 324 (2002), pp.103-112

Avedesian M., Baker H., (1994). Magnesium and Magnesium Alloys, *ASM Speciality Handbook*, ASM International, The Materials Information Society (1994).

Mordike B., (2001). Development of highly creep resistant magnesium alloys, *Journal of Material Processing Technology* Vol. 117 (2001), pp.391-394.

Lorimer G., Apps P., Karimzadech H., King J., (2003). Improving the performance of Mg-Rare Earth alloys by the use of Gd or Dy additions. *Materials Science Forum* Vols. 419-422 (2003), pp.279-284.

14

Magnesium Sheet; Challenges and Opportunities

Faramarz Zarandi and Stephen Yue
McGill University
Canada

1. Introduction

Where light-weight components are desired, e.g. in automotive and aerospace applications, magnesium can provide an important advantage over other structural materials such as aluminum and steel. The density of magnesium is two thirds that of aluminum and a quarter that of galvanized steel. The combination of low density and reasonable strength of magnesium leads to a specific strength, which is much higher than that of steel or aluminum. Stiffness is often as important as strength and, with respect to bending stiffness, magnesium offers major advantages over both steel and aluminum. Using more magnesium would significantly decrease the weight of automobiles, which is one of the important goals in automobile design. However, usage of magnesium lags far behind that of aluminum. To date, most magnesium applications in the automobile industry are in the form of die cast parts. Wrought magnesium, particularly in the form of sheet, represents a tremendous growth opportunity in the application of magnesium, e.g. inner door panel, engine bonnet, seat components, roof, and fenders. The use of magnesium sheet is, however, severely limited because of: (a) the high cost of magnesium sheet, (b) the poor room temperature ductility of magnesium, and (c) the relatively high propensity to corrosion.

Sheet materials are required to display sufficient formability when subjected to bending stresses during fabrication into parts. The poor plastic flow characteristics of magnesium at room temperature have considerably hampered its sheet applications. Essentially, because magnesium has a hexagonal close packed (*hcp*) structure, active slip systems at low temperatures are mainly limited to those involving basal planes. This is because the critical resolved shear stress (CRSS) for basal plane slip in magnesium single crystal is 100 times lower than that for non-basal plane slip (prismatic or pyramidal planes) near room temperature. Thus, the distribution of basal planes (0001) in magnesium plays an important role in determining formability at low temperatures. As the temperature increases, the CRSS of the non-basal slip systems decreases and, therefore, there is a significant increase in formability. Consequently, sheet forming at elevated temperatures is one possibility that is being contemplated, and there is considerable ongoing research in this general area, including those concerned with the viability of superplastic forming. In this chapter, the challenges to the production of magnesium sheet and the route toward overcoming them are explained. Then, deformation characteristics of magnesium and associated mechanisms are discussed.

2. Magnesium sheet production

Rolling is the usual process for sheet production. In early magnesium rolling practice, only extruded slabs were rolled. It was believed that an extruded slab had a more uniform microstructure and, hence, better rolling properties. The method of eliminating as-cast structure by press forging before rolling has also been extended to the production of sheet. This method offers no advantages over extrusion but is a useful alternative. Magnesium sheet can be also produced directly from cast slabs depending on the alloy, the degree of reduction, and final application of the sheet (Alico, 1945).

Magnesium sheets are conventionally made from magnesium shapes that are pre-conditioned cast slabs. In order to eliminate the as-cast structure, pre-conditioning is usually performed by heat treatment and hot deformation such as hot rolling. In laboratories, the as-cast ingot is usually pre-conditioned by hot extrusion, where large amounts of compressive deformation can be applied. AZ31, which has a nominal chemistry of Mg-3wt%Al-1wt%Zn, is the magnesium alloy currently favored for sheet production. Normally, the alloy is cast into a slab form and pre-conditioned in a block slab cogging mill. One drawback is that the slab surface is oxidized at high temperature. During rolling, the oxide film can be rolled into the sheet metal and deteriorate the sheet quality. Even though the oxide layer can be removed by chemical or mechanical demolition, these processes cause recesses, i.e. rough uneven and contaminated surfaces through a thickness of 10 to 15 mm that must be eliminated. On the surface, enriched contamination, compact oxide and inclusions, particles of second phases as well as microscopic and macroscopic defects, e.g. pores, increase the sheet susceptibility to cracking upon further deformation (Poss, 2003).

In order to prevent macrosegregation of the alloying elements, wrought magnesium alloys are preferably cast by Direct Chill (DC) machines. Despite rapid solidification of the narrow melt bath, the average grain size of the cast billet is large, depending on the billet diameter and casting parameters. In some cases, the cast billet has to be initially hot worked in order to avoid the brittleness effect of large grains and improve hot workability. The DC magnesium slab is often 300 mm by 1 m in cross section and 2 m long. The slab is normally first homogenized, for AZ31 typically at 480^{o}C, for several hours and hot rolled on a reversing hot mill to 5-6 mm thick. The hot rolling is normally performed at about 60 mpm. In the first rolling passes, the allowable reduction per pass is limited to 5-10% by the coarse grain structure of the cast feedstock which causes cracking. It is only after recrystallization and grain refinement that the strain per pass can be increased to 30-60%. The contact time between the slab and the rolls of the breakdown mill is quite short, and these rolls are seldom preheated. The rolls are often lubricated in the final passes. However, the best lubricant used today does not entirely solve one of the problems of magnesium hot rolling, namely, roll pickup in which magnesium oxide and metal cling to the rolls. As the rolling continues, this so-called roll pickup may be re-deposited upon the sheet, calling for careful cleaning at later stages. After breakdown, the slab is reheated to 315-370^{o}C and rolled in a flat or a coil finishing mill to final thickness. Prior to cold rolling, the hot rolled sheet is generally annealed at around 370^{o}C to ensure complete softening. Cold rolling is then carried out at speeds of 30 to 120 mpm. For rolling from 2 mm or thereabouts to thinner gauges, the process consists of a series of cold rolling operations with intermediate annealing treatments. The amount of reduction per pass varies from 1 to 5% and is sometimes as high as 10% in thin gauges. This latter part of the rolling process is time consuming with high operating costs and progressively tends towards lower metal yields.

Such a technology also requires expensive quality control procedures and substantial investment in equipment (Dow Chemical Company, 1943; Allen et al., 2001; Bach et al., 2006). This means that a standard magnesium sheet production consists of a complex DC casting, a homogenization treatment, and approximately 12-18 hot rolling passes in 2-3 heats. This is why magnesium sheet is expensive, even though the raw material costs can easily compete with aluminum.

Strip casting technology has been successfully used to produce aluminum sheet directly from the melt. This is also a potential process for production of magnesium sheet with considerably lower number of rolling passes. Therefore, the produced sheet would be much less expensive than the conventionally produced sheet. Single-belt and twin-belt strip casting technologies have been also studied. The principal advantages of these processes are that alloys with large solidification ranges can be produced easily and a high surface quality can be achieved owing to the 'moving die' principle. The twin-belt caster is more favored as less protective gases are required to protect the melt and the symmetrical cooling condition results in a homogeneous fine-grained microstructure. Nevertheless, the capability of twin-roll casting process, among other strip casting processes, has been more eagerly examined for magnesium sheet. Magnesium alloy strip with thicknesses less than 5-6 mm can be produced directly from the melt by twin-roll casting, reducing capital investment and operational costs (CSIRO, 2003). Commercial quality sheet samples from 2.3 to 5 mm thick have been successfully cast in standard alloys (AZ31, AZ61, AM60 and AZ91), along with a number of new magnesium wrought alloys. These samples have been rolled down to 0.5-0.6 mm gauges, using a novel finish-rolling schedule developed specifically for cast magnesium alloy sheet (Liang & Cowley, 2004). Near-rapid solidification achieved in twin-roll casting, through cooling rates ranging from 300 to several thousands of degrees per second, can potentially improve alloy properties by improving the homogeneity of microstructures (especially minimizing the size of manganese-rich particles), refining grain size, reducing segregation, increasing solid solubility, enhancing precipitate nucleation within the matrix, and generating a distribution of fine precipitates (CSIRO, 2003 & Masoumi et al., 2010a). The microstructure of a twin-roll cast AZ31 alloy, with about 5 mm thickness, consists of a columnar-grain zone from the surface to the mid-thickness region and an equiaxed-grain zone in the mid-thickness region. The secondary-dendrite arm spacing is within 5-6.5 μm range through the thickness and the width of the strip, which is much smaller than ~34 μm of a DC ingot AZ31 alloy (Nakaura & Ohori, 2005). The small dendrite arm spacing in a twin-roll cast AZ91 alloy improved the workability at elevated temperatures. The secondary-dendrite arm spacings can be transformed into recrystallized grains of 9-10 μm in diameter by hot rolling (Allen et al., 2001). Such a small grain size is expected to benefit superplasticity at elevated temperatures.

Hot-rolled twin-roll cast AZ91 sheet has exhibited an improvement of 60% in yield stress and 17-40% in UTS (Ultimate Tensile Strength) as compared to the sheets produced from the sand-cast (T6 temper) and die-cast (F temper) slabs (Allen et al., 2001). The fine precipitation within grains has definitely contributed to this improvement in mechanical properties. Moreover, it has been noted that casting AZ31 alloy close to the liquidus temperature promotes formation of spherical or nodular primary α-Mg, which is favorable for improved workability of AZ31 alloy (Yang et al., 2005). On the other hand, x-ray diffraction has shown that twin-roll casting results in a single α-Mg phase structure in AZ31B with aluminum as solute in α-Mg phase (Di et al., 2005). Hence, the single α-Mg phase, together with the small grain size and the absence of the $Mg_{17}Al_{12}$ phase in the microstructure, could lead to better formability in the twin-roll cast AZ series alloys.

Notwithstanding the fact that the sheet has better mechanical properties and the process is more economical, only alloys with small solidification ranges can be safely twin-roll cast. Otherwise, failures in the microstructure, e.g. hot cracking and centerline segregation, may occur due to the solidification conditions under rolling pressure. This could be the main drawback of twin-roll casting process that may limit the range of candidate compositions for magnesium sheet. Apart from this, twin-roll casting to produce AZ31 sheet has already experienced significant advances over the past decade. Recently, POSCO and RIST reported the production of AZ31 alloy strips through integration of twin-roll casting and multi-pass coil rolling processes (Jung et al., 2007). The coiled strips were 600 mm in width with thicknesses of 3–7 mm. However, much wider sheet is required for fabrication of automobile body panels, e.g. engine hood. Thus, one area of focus should be on producing larger sheets by improving twin-roll casting and coiling technologies. Additionally, the capability of twin-roll casting to produce fine dispersed particles should be utilized to develop novel magnesium alloys for sheet. Alloys in which poor formability is attributed to coarse particles, e.g. alloys with high aluminum content, could be potential candidates in this respect.

3. Thermomechanical processing

Magnesium sheet is required to undergo various thermomechanical treatments in order to produce various thicknesses and also develop desired mechanical properties for sheet fabrication, especially adequate formability to produce complex profiles. This would also contribute to the properties of the fabricated components, e.g. crashworthiness in automobile body panels. Therefore, it is important to have a thorough knowledge about the evolution of microstructure and viable deformation mechanisms in magnesium. This section will try to highlight the important topics in this area.

3.1 Recrystallization

Magnesium does not undergo any solid phase transformation. Consequently, recrystallization is essentially the sole effective mechanism to change the grain morphology in magnesium. Although both dynamic recrystallization (DRX) and static recrystallization (SRX), which occur during and after deformation, respectively, have been studied extensively in cubic metals with low to medium stacking fault energy (e.g. Sakai & Jonas, 1984; Sakai, 2000), there have been only a limited number of studies on DRX in *hcp* metals (Ion et al., 1982; Galiyev et al., 2001). Discontinuous recrystallization, characterized by nucleation of bulged or serrated grain boundaries, is known to be a preferred softening mechanism during hot deformation in materials with low to medium stacking fault energy where dynamic recovery is difficult. Although both high and low stacking fault energies have been reported in the literature, magnesium is usually considered to have low stacking fault energy. Therefore, the fact that the discontinuous recrystallization is rarely observed in deformed magnesium, except under high temperature and large straining conditions, has been a puzzle for sometime. Galiyev et al. have proposed a solution to this problem (Galiyev et al., 2003). They noticed that recrystallization always takes place in the area adjacent to the grain boundaries where basal dislocations cross-slip into non-basal planes. As a result, they assumed that splitting width of basal dislocations decreases and non-basal dislocations are formed leading to increased stacking fault energy that will enhance the dislocation rearrangement into cell structures. This assumption is also supported by the calculated values of stacking fault energy for basal and prismatic planes in magnesium, i.e. 78 and 255

mJm^{-2}, respectively (Galiyev et al., 2003; Sastry et al., 1969; Uesugi et al., 2003 & Watanabe et al., 2001). Thus, it appears that, although magnesium is generally considered as a low stacking fault energy metal, stacking faults near grain boundaries are mainly associated with non-basal dislocations and, hence, their energy is significantly high. In addition to the stacking fault energy, it has been also indicated that the constraints imposed by the lack of easily activated slip systems have an important effect on the DRX phenomenon in magnesium (Ion et al., 1982).

The kinetics of recrystallization in magnesium alloys is likely a complicated function of deformation temperature, strain, strain rate, deformation mode, grain size, and grain orientation. Therefore, it cannot be described by the usual Avrami equation. Dynamic evolution of new grains in magnesium alloys can be a result of continuous DRX, including twinning DRX and rotation DRX, under cold and warm deformation (Ion et al., 1982 & Galiyev et al., 2001). In contrast, discontinuous DRX, including the nucleation of new grains and their growth, takes place during deformation at high temperatures. It is well known that the dynamically recrystallized grain size in cubic metals is controlled by deformation condition, i.e. temperature and strain rate, irrespective of the initial grain size (Sakai & Jonas, 1984; Sakai, 2000). It is found, however, that the dynamically recrystallized grain size in magnesium alloys is clearly dependent not only on deformation conditions, but also on the initial grain size (Kaibyshev et al., 1994; Watanabe et al., 2001).

3.2 Microstructural evolution

The as-cast magnesium microstructure can consist of twins parallel to each other within one grain. Such twins can occupy about 12% of the entire material volume (Kaibyshev & Sitdikov, 1994). Plastic deformation yields two different structural components, the characteristics and volume fractions depending on strain. At temperatures up to 200°C, plastic deformation of magnesium produces extensive twinning on multiple systems and formation of dense dislocation pile-ups within initial grains. Multiple twinning in magnesium develops in two systems; a primary $\{10\bar{1}2\}<10\bar{1}1>$ and a secondary $\{10\bar{1}1\}<10\bar{1}2>$ (Kaibyshev & Sitdikov, 1994). The secondary twins occur within coarse lamellae of the primary twins, subdividing them. These crystallites can serve as nuclei and chains of recrystallized grains are evolved at the sites of former twins. This process of microstructural evolution is called twin DRX (TDRX). The second structural component comprises small areas of fine recrystallized grains formed near original boundaries and within original grains at early stages of plastic flow. These grains are smaller than twin grains. These two mechanisms operate simultaneously by further straining and contribute to the evolution of overall microstructure. The fine grains are absorbed by migrating boundaries of recrystallized twin grains, and repetitive DRX occurs within the twin grains (recrystallized grains evolved inside twins) and results in the formation of new smaller grains (Kaibyshev & Sitdikov, 1995a; Kaibyshev & Sitdikov, 1995b). This type of microstructural evolution is inherent in the cool deformation range of magnesium.

At intermediate temperatures, i.e. 300°C, deformation twinning on multiple systems results in an increase in the volume fraction of twins. Figure 1 illustrates a twin morphology developed in an AZ31 alloy after ε=0.3 rolling deformation at 300°C. The formation of secondary twins within lamellae of primary twins plays an important role in TDRX at this temperature, Figure 1. It has been proposed that TDRX mechanism comprises three

sequential stages (Sitdikov et al., 2003). Firstly, nucleation occurs by either intersection of various systems of twins or rearrangement of lattice dislocations within the twin lamellae. At the second stage, twin boundaries are changed into random high angle boundaries due to formation of orientation misfit dislocations. As a result, the nuclei are transformed into recrystallized grains, which have non-equilibrium shape close to tetragonal one. At the third stage, migration of their boundaries begins to occur. This also indicates that the size of recrystallized grains is determined by the width of twin lamellae, as also shown in Figure 1. Such a multi-stage character of the microstructure evolution is a common feature of TDRX operating over a wide range of temperatures. Regarding the second structural component, by increasing the strain, subboundaries reorient and convert into high angle boundaries. This has been seen along the original boundaries as well as near some former twin boundaries and contributes to the evolution of grain morphology (Galiyev et al., 2003). Since the growth of these grains is not limited to the width of twins, they can grow freely and, as a result, the mean grain size increases. This microstructural evolution and such an effect of strain on the recrystallized grain size usually take place in the temperature range of 250-350^{o}C, which can be regarded as the range of warm plastic deformation in magnesium.

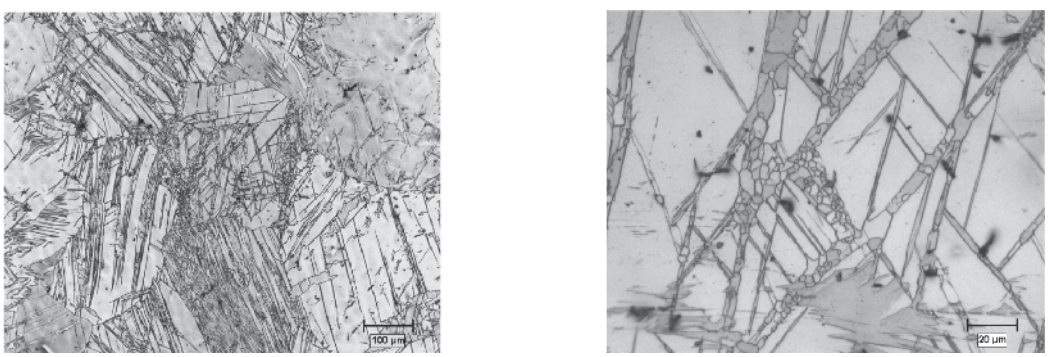

Fig. 1. Development of twins and recrystallization in an AZ31 alloy due to ε=0.3 rolling deformation at 300^{o}C. (Original structure was as-cast and twin-free.)

As the deformation temperature approaches 450^{o}C, twins become less prominent. Instead, nucleation of new grains in the vicinity of grain boundaries, so-called necklacing, plays a more important role in the evolution of microstructure, Figure 2. The formation of recrystallized grain chains evolved by continuous DRX occurs along both the initial grain boundaries and the boundaries of twin grains. However, the former begins to occur at lower strains and the rate of this process is faster than that along prior twin grain boundaries. Discontinuous DRX is also expected to contribute at large strains in this thermal regime.

In summary, there are different DRX mechanisms in magnesium; their extents of operation depend on strain and temperature. Because the growth of nuclei is affected by these DRX mechanisms, e.g. nucleation at grain boundaries and within twins, the mean grain size can increase or decrease with straining. This contradicts the normal rule of recrystallization in cubic metals, i.e. there is no strain effect on recrystallized grain size during DRX. Such dependency of grain size on temperature and strain with regard to underlying DRX mechanisms is illustrated in Figure 3 for pure magnesium (Sitdikov & Kaibyshev, 2001). It should be noted that the operation of DRX mechanisms and the evolution of grain size is also affected by alloying elements as these can change the stacking fault energy and mobility

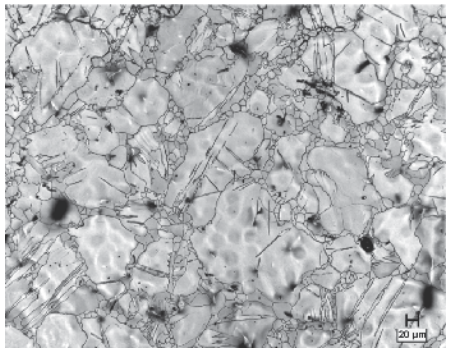

Fig. 2. Necklacing recrystallization in an AZ31 alloy due to ε=0.3 rolling deformation at 450°C. (Original structure was as-cast and twin-free.)

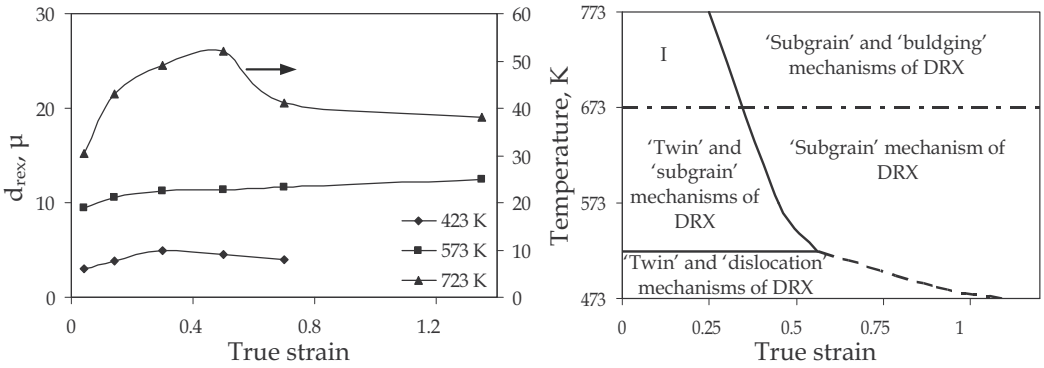

Fig. 3. Strain and temperature dependence of average recrystallized grain size in pure magnesium (left), and corresponding recrystallization mechanisms (right) (region 'I' represents the area where initial twins transform into recrystallized grains during deformation) (Sitdikov & Kaibyshev, 2001).

of boundaries. For instance, it has been shown that the final grain size after extrusion at 350°C is larger than the initial grain size in pure magnesium, but not in W0 alloy (yttrium-containing magnesium) (Cottam et al., 2006).

The fact that the dominant mechanism of DRX changes by temperature and strain suggests that there are different operating deformation and shear mechanisms; their activities depend on both temperature and strain. This is because a specific mechanism of plastic deformation can result in a certain type of DRX mechanism. The deformation mechanisms in magnesium will be explained in more detail later.

4. Formability

The lack of adequate number of slip systems to accommodate overall strain is considered as the principal reason for poor formability of magnesium. Therefore, in order to advance applications of magnesium sheet to structural components, especially in automobile and aerospace industries, enhancement of formability has been the main focus in numerous investigations. Grain refinement is proving to be an effective approach for this purpose. Moreover, prevention and retardation of basal texture development during deformation

positively affects magnesium formability, as this results in participation of more slip systems in deformation and postpones failure to larger strains. These are discussed in the following section.

4.1 Effect of grain size

Early studies on the deformation mechanisms in magnesium single crystals, which were focused on slip system analysis, revealed that deformation at room temperature occurs by slip on the basal plane in $<11\bar{2}0>$ direction. Non-basal slip was regarded as a high temperature slip system, i.e. >200°C, (Wonsiewiczs & Backofen, 1967). Later, <*a*> and <*c*+*a*> non-basal slip systems were also confirmed to be active at room temperature (Stohr & Poirier, 1972; Obara, 1973). However, the behavior of magnesium polycrystal is very different than that of the single crystal, due to the strong grain size dependency. In general, high ductility and low strain hardening rates are observed over a wide range of temperature in single crystals, whereas polycrystalline magnesium display low ductility (5-20%) and high strain hardening rates at room temperature. The restriction of magnesium to a grain size of 1 mm increases both the yield strength and the strain hardening rate by factor of >10 and $>10^3$, respectively, while reduces the fracture strain tenfold, all compared with those of single crystal (Roberts, 1964; Wonsiewiczs & Backofen, 1967). Such characteristics are very different from those in cubic metals, where single crystals and polycrystals are not greatly dissimilar. The reason for this is ascribed to the only two independent easy slip systems in magnesium, both involving the $1/3<11\bar{2}0>$ or <*a*> dislocations on the basal plane. Hence, the *hcp* structure of magnesium does not satisfy the well-known Taylor criterion requiring five independent easy slip systems for homogenous ductility of a polycrystalline aggregate (Taylor, 1938). In other words, each grain should satisfy the Taylor criterion in order to accommodate an applied strain.

However, in order to be used for the structural components, magnesium should exhibit sufficient ductility not only at static but also at dynamic strain rates, because components are often fractured by shear or tensile forces under dynamic loading. This has inspired numerous investigations on the enhancement of ductility in magnesium alloys. Figure 4 suggests that grain refinement is a promising approach to improve ductility at both quasi-static and dynamic strain rates, as shown in both pure magnesium and ZK60 (zirconium-containing magnesium) (Mukai et al., 2003). When grains are coarse, cracking along twin boundaries and grain boundaries is encouraged. Upon straining, the cracks propagate and coalesce leading to eventual failure. On the other hand, when grains are small, twins are less prominent and they are also smaller, hence, failure is delayed (Mukai et al., 2003). This example clearly denotes the importance of twins as an embrittling mechanism in magnesium. A similar improvement in ductility, even at a dynamic strain rate of $\sim 2\times10^3$ s^{-1}, was observed in WE43 alloy (magnesium alloyed with yttrium and rare earth elements) by refining the grain size (Mukai et al., 1998).

Another effect of grain refinement is on the slip systems. Although slip on basal planes is the easiest at room temperature as compared with slip on prismatic and pyramidal planes, non-basal dislocation activities and cross slip from basal to non-basal planes have been observed to take place in fine grains, e.g. 6 μm, AZ31 alloy (Koike et al., 2003). The CRSS ratio, $\tau_{prismatic}/\tau_{basal}$, estimated in this case was 1.1 which is much lower than the values (about 100) reported in single crystal magnesium. A study of the effect of grain size on

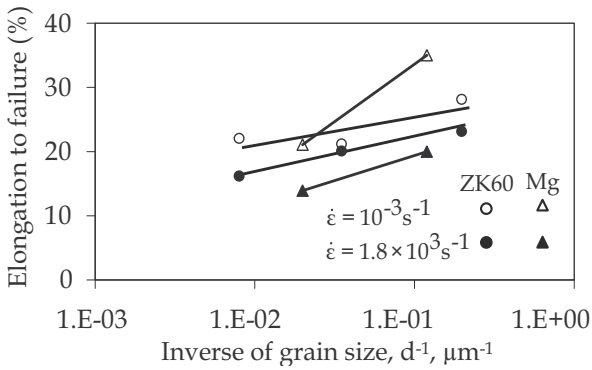

Fig. 4. Variation of elongation to failure at room temperature versus inverse of grain size in pure magnesium and ZK60 alloy (zirconium-containing magnesium) (Mukai et al., 2003).

dislocation activities at room temperature in two AZ31 alloys, one with a grain size of 50 µm and the other with 7 µm, revealed that in the coarse grain alloy, non-basal <*a*> dislocations were active near the grain boundaries while basal <*a*> dislocations were dominant in the grain interior ($\tau_{non\text{-}basal}/\tau_{basal}\approx15.4$). On the other hand, at 7 µm grain size, non-basal <*a*> dislocations were active in all regions ($\tau_{non\text{-}basal}/\tau_{basal}\approx0.88$). The density of non-basal <*a*> dislocation segments was found to be 40% of the total dislocation density (Kobayashi et al., 2003). Such activation for non-basal dislocations can be ascribed to the stresses induced to maintain grain boundary compatibility. In large grains, this effect is limited at grain boundary regions whereas it is all over grains in fine grains.

Furthermore, grain size influences twinning, the activation of which leads to distinctive features in the temperature sensitivity of yield stress. The $\{10\bar{1}2\}$ extension twin is the most common type in magnesium, and is favored when compressive stresses are applied parallel to the basal planes. This twin is also the source of the large difference between compressive and tensile behaviors of magnesium. Such anisotropy diminishes by increasing temperature and disappears at a certain temperature where tensile and compressive yield stresses coincide. It is believed that, at this temperature, the stress required to activate $\{10\bar{1}2\}$ twinning equals that required to activate second order pyramidal <*c*+*a*> slip (Barnett, 2003). These two systems are the only systems accommodating deformation along the *c*-axis direction of the *hcp* crystal. The CRSS for <*c*+*a*> slip is high at room temperature and decreases rapidly with increasing temperature, whereas that for twinning is expected to be relatively temperature insensitive. On the other hand, the twinning stress increases with decreasing grain size more rapidly than the stress required to activate slip (Meyers et al., 2001). As a result, the slope of the Hall-Petch relationship, *k*, is usually greater for twinning-dominated flow than that for slip-dominated flow. In this respect, decreasing the grain size is similar to increasing temperature in that slip is favored over twinning. As an example, Figure 5 clearly demonstrates the effect of grain size on compressive flow behavior in an AZ31 alloy. There are two classes of flow behavior. The material flows along a concave path when twins are active. This appears to be the case for grain sizes of 16µm down to 8µm, with a gradual decrease in the activity of twins by decreasing the grain size. On the other hand, the material exhibits a conventional flow behavior at grain sizes ≤4µm, where twinning is difficult. This indicates that grain refinement can be a strategy to improve

formability where twins act as an embrittling mechanism, i.e. at low temperatures. In contrast to cubic metals, Figure 5 shows that the rate of strain hardening is greater at larger grain size. This phenomenon is ascribed to the interaction between twins and dislocations, rather than to the stress required for twinning. Nevertheless, hardening due to texture development as well as softening mechanisms common in fine grain materials, e.g. recrystallization and grain boundary sliding, should also be taken into account.

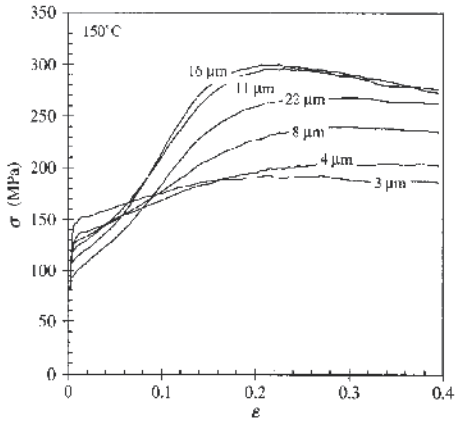

Fig. 5. Compressive true stress-strain curves obtained at 0.01 s^{-1} and 150°C at various grain sizes, AZ31 alloy, (Barnett et al., 2004).

Consequently, it is reasonable to expect a critical grain size for transition from twinning to slip dominated flow. Obviously, this grain size depends on both temperature and strain rate. Barnett et al. proposed that the correlation of such critical grain size (d_c) in AZ31 with temperature and strain rate in compression can be described as (Barnett et al., 2004);

$$d_c = \left(\frac{0.15 \ln Z - 12.2}{73 - 3.8 \ln Z} \right)^2 \tag{1}$$

where Z is the Zener-Hollomon parameter ($Z = \dot{\varepsilon} \exp(Q/RT)$), $\dot{\varepsilon}$ is strain rate, Q is deformation activation energy, R is gas constant (8.314 J/molK), and T is absolute temperature in Kelvin.

In contrast to the compression flow behavior and similar to cubic metals, the tensile flow behavior follows the Hall-Petch law in terms of the effect of grain size, Figure 6. In tension, if the direction of the applied stress is parallel to the basal planes, activation of $\{10\bar{1}2\}$ twins is difficult. Instead, the $\{10\bar{1}1\}$ contraction twin, which accommodates contractions along the *c*-axis, and the $\{10\bar{1}1\}$-$\{10\bar{1}2\}$ double twin operate in tension (Jiang, 2008). But, unlike the $\{10\bar{1}2\}$ twin, these twins do not spread over the whole microstructure even at high strains, e.g. 0.15, as they have much higher CRSS values. Nevertheless, the effect of grain size on *k* is similar to that in compression, in that decreasing the grain size lowers the strain hardening rate, Figure 6.

It is well known that high formability is usually associated with very low strain rates and high temperatures. However, it is always desirable to apply large amounts of deformation at high strain rates and low temperatures. Low strain rates limit the speed of forming

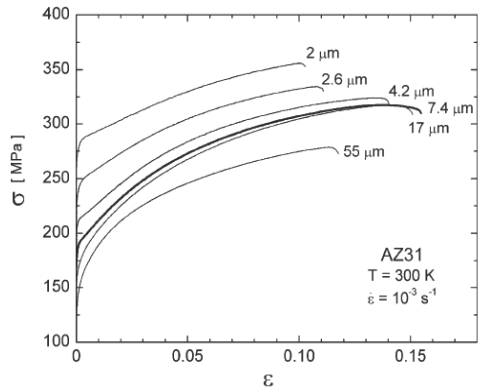

Fig. 6. Tensile true stress-strain curves of AZ31 alloy (rolled and annealed) at various grain sizes (Valle et al., 2006).

processes, and materials which do not display good formability at high strain rates tend to have inferior dynamic fracture properties, as well. Elevated temperature deformation, on the other hand, incurs increased energy costs and the possibility of surface oxidation. In addition, selective depletion of alloying elements on the surface is prevalent at high temperatures. Grain refinement has proved to be an effective strategy to alleviate these constrains. For instance, by decreasing the grain size from 10 to 2.5 μm in a ZK60 alloy, the superplastic strain rate increased by about 100 times, yet at a lower temperature (Watanabe & Mukai, 1999). This indicates that both high strain rate superplasticity and superplasticity at low temperatures in magnesium alloys can be achieved by decreasing the grain size.

It is difficult to obtain fine grain size in commercial magnesium alloys. In sheet production, the rolling temperature must be high to avoid edge and surface cracking, especially in high aluminum content alloys. Such high temperatures accelerate the growth of fine recrystallized grains. Therefore, complicated thermomechanical schedules incorporating frequent interpass reheating processes should be employed to gradually refine the grain size, which adds to the production cost. This barrier has led to investigations into the superplasticity in coarse grain alloys. In one study, an AZ61 (Mg-6wt%Al-1wt%Zn) alloy with a grain size of 16 μm displayed 950% elongation-to-fracture at strain rate of 10^{-3} s^{-1} and temperature of 400°C (Kim et al., 2001). Such a large elongation before rupture at high strain rates is noteworthy when compared with the smaller elongation of some other magnesium alloys, including AZ61 itself, with finer grains. Microstructural examination revealed cavity formation at grain boundaries and the occurrence of dynamic recrystallization followed by grain growth. However, no clear explanation has yet been offered on how dynamic recrystallization and grain growth contributes to the elongation, although the former clearly reduces applied stress and the latter reduces the stored energy. More study is required to understand the mechanisms responsible for superplasticity in coarse grain alloys.

4.2 Effect of texture

Formability of magnesium is strongly affected by orientation of the basal plane. This dependency of magnesium on crystal orientation is much more important than that of cubic metals since the former has limited number of slip systems and is very susceptible to twinning that readily orients basal planes. In addition to basal slip, which is the easiest slip

system, prismatic slip has been found to be of crucial importance during high temperature superplasticity. This was confirmed by more than 600% elongation at 300°C and 4.2×10^{-4} s^{-1} in a single crystal in which prismatic slip was the only active slip system, crystal I in Figure 7. At an orientation where prismatic slip is difficult (crystal II in Figure 7), the elongation was 430% under similar condition. Surprisingly, increasing the deformation temperature deteriorated the formability in both crystals. In this case, DRX and grain boundary cracking are the reasons for embrittlement; probably by introducing grains with different orientations where prismatic slip is difficult and regions that are susceptible to cracking, i.e. grain boundaries. Figure 7 also demonstrates that flow behavior strongly depends on crystal orientation. Crystal I strain hardens gradually during activation of a single prismatic plane and then the rate of strain hardening increases rapidly when the strain-induced crystal orientation places a second prismatic slip plane in a favored orientation and cross slip occurs. In contrast, crystal II exhibits conventional flow behavior, i.e. gradual decrease in the strain hardening rate followed by softening, in absence of the prismatic slip.

There is a similar effect in polycrystalline magnesium. Figure 8 shows the flow behavior of two textured AZ31 alloys, one pulled parallel to the basal planes and the other at an angle of ~45 degrees with the basal planes. Specimen II has a lower yield stress and exhibits a remarkable strain hardening and a large elongation at a relatively high strain rate, with a UTS almost equal to that of specimen I. In contrast, specimen I displays brittle behavior; a minor strain hardening followed by failure.

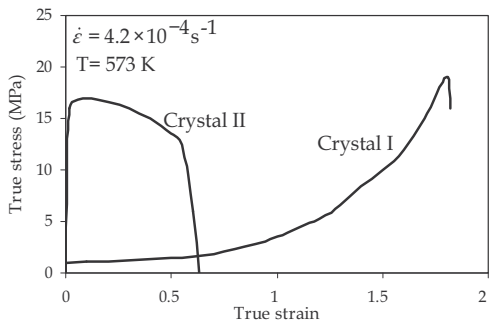

Fig. 7. Tensile deformation of magnesium single crystals; easy prismatic slip (crystal I) and difficult prismatic slip (crystal II) (Miura et al., 2005).

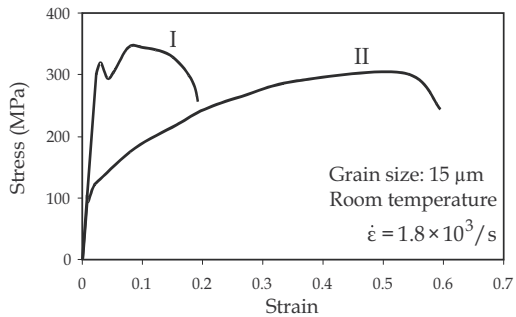

Fig. 8. Effect of crystallographic orientation on tensile flow curve in AZ31 alloy (Mukai et al., 2003). (Stress direction parallel to basal planes (I), and at 45 degrees with basal planes (II))

Generally, magnesium exhibits very poor formability when it is deformed parallel to basal planes, i.e. the direction of applied stress is perpendicular to the *c*-axis, as there are only two <*a*> non-basal independent slip systems that can be active under this condition. During sheet production, basal planes are readily oriented toward the sheet surface in early stages of rolling. This leads to the development of a basal texture parallel to the sheet surface. In the fabrication process, the sheet is stretched parallel to the basal planes and, therefore, as specimen I in Figure 8 shows, the amount of deformation it can tolerate before rupture is very limited. This suggests that alleviation of basal texture is an effective method to improve the formability of magnesium sheet. One possible strategy is to develop new alloys which are less prone to the basal texture. Alloys containing rare earth elements and yttrium have been the main focus in this respect (Senn & Agnew, 2008). However, this approach may not always be attractive economically. Furthermore, it may introduce new technical difficulties in the sheet production process, especially in the twin-roll casting. Therefore, alloys based on the AZ series constitute the main body of research in this area. Very recently, it was shown that the basal texture of AZ31 sheet, produced by twin-roll casting, can be weakened by controlled thermomechanical treatment (Masoumi et al., 2010b). The microstructure of twin-roll cast AZ31 comprises large columnar grains and densely distributed secondary-phase particles, Figure 9. Additionally, due to the rolling deformation which occurs as the solidified strip goes through the twin rolls, it exhibits a strong basal texture, as shown by the pole figure in Figure 9. When annealed at 420°C, as expected, the second phases were dissolved in the matrix and columnar grains were replaced with fine grains owing to recrystallization. But, the most important change happened in the sheet texture; the basal texture was weakened noticeably, Figure 10. The substructure in the as-twin-roll cast sheet revealed a high concentration of dislocations at the secondary-phase particles. Therefore, the texture alteration was attributed to the particle-stimulated nucleation (PSN) mechanism of recrystallization that resulted in the formation of grains with random orientations, Figure 10. A similar treatment was applied to a conventionally produced AZ31-H24 sheet and also a DC cast and cold-rolled plate. However, neither of them showed any change in its initial basal texture, Figure 11. These observations indicate the advantage of the rapid cooling associated with the twin-roll casting process; generating a large fraction and uniform distribution of fine secondary-phase particles. Preliminary evaluation of mechanical properties at room temperature also proved the beneficial effect of such texture alteration, as compared to the as-twin-roll cast AZ31 sheet (Masoumi et al., 2010a).

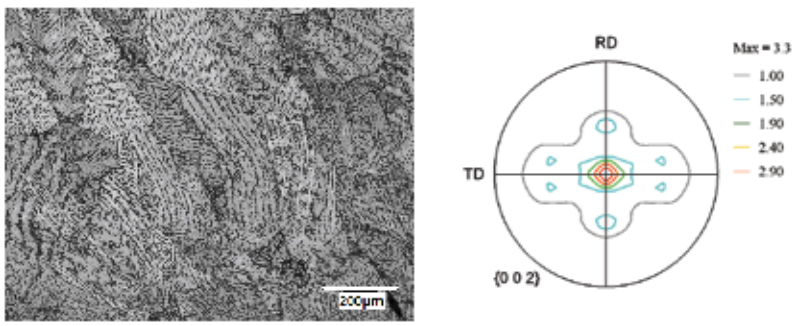

Fig. 9. Thickness microstructure of twin-roll cast AZ31 sheet and basal plane pole figure (Masoumi et al., 2010b). RD and TD are rolling and transverse directions of the sheet, respectively.

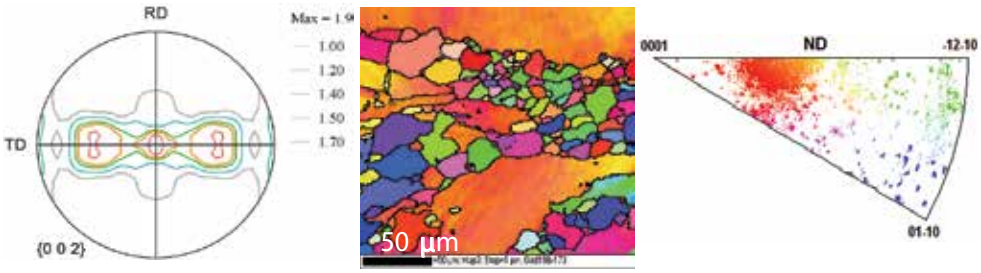

Fig. 10. Basal plane pole figure of twin-roll cast AZ31 sheet and orientation map of recrystallized grains in the plane of RD-TD, both after annealing at 420°C (Masoumi et al., 2010b). RD, TD, and ND are rolling, transverse, and normal directions of the sheet, respectively.

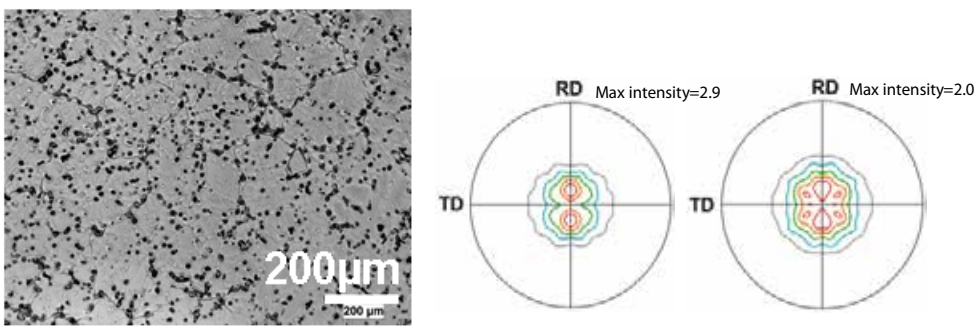

Fig. 11. DC AZ31 as-cast microstructure and {002} pole figures after 15% cold rolling (left) followed by annealing at 420°C (right). (Masoumi et al., 2010b). RD and TD are rolling and transverse directions, respectively.

5. Deformation behavior at elevated temperatures

By increasing temperatures, while the effect of twinning diminishes, concurrent operations of basal and non-basal slip systems are conducive to improved formability. On the other hand, as the deformation temperature increases, the formability becomes more dependent on the deformation rate, which often has an opposite effect to that of temperature. Since, in practice, it is desired to increase the productivity by increasing the deformation rate and, at the same time, keep the deformation temperature low for economy and surface quality, an optimum combination of temperature and strain rate is required to achieve an adequate formability in a given sheet material. This demands a thorough understanding of viable deformation mechanisms at various temperatures and strain rates, which are also affected by the alloying elements in the magnesium sheet. Essentially, this would lead to the development of constitutive models of plasticity capable of predicting flow behavior during sheet forming.

The combined additions of aluminum and zinc to magnesium yield an optimum combination of strength and ductility, in addition to increased corrosion resistance. This has promoted the AZ series alloys to the top in the list of magnesium sheet alloys. Al and Zn improve mechanical properties both by solid solution strengthening and secondary-phase

precipitation. Upon aging, the equilibrium phase $Mg_{17}Al_{12}$ precipitates from the supersaturated solid solution, affecting metal deformation and properties. At high Al contents, precipitation of coarse $Mg_{17}Al_{12}$ at grain boundaries deteriorates the formability of the alloy, especially during rolling. Hence, alloys for sheet production usually contain less than 6wt% Al. However, this may not be as much a problem with twin-roll casting where rolling deformation is limited. Manganese is also added to the AZ alloys primarily to improve corrosion resistance, and also to refine the as-cast grain size. Therefore, its possible effect on deformation behavior of the AZ series alloy, especially in the sheet form, has rarely been studied. A recent study, while reconfirming the detrimental effect of 6wt% Al to the hot rollability of AZ series magnesium sheet, showed that addition of Mn from 0.06 to 0.24wt% counteracts such effect and improves hot rollability (Zarandi et al., 2008).

Commonly, three tensile flow characteristics can be expected from the sheet of AZ series at various combinations of elevated temperature and strain rate, Figure 12. At high *Z* value, e.g. 300°C and 0.1 s^{-1}, the rate of strain hardening is initially high but decreases rapidly with strain, leading to an early onset of flow softening and a low failure strain. On the other hand, at 450°C and 0.0003 s^{-1}, where *Z* is low, the initial flow stress is very low and the material strain hardens at a low rate, but to a high fracture strain. The material exhibits an intermediate flow behavior at 400°C and 0.1 s^{-1}, but the appearance of a 'hump' makes it distinct enough to merit a separate identity. Such a flow behavior is opposite of what is usually expected when the peak stress is associated with geometric instability, i.e. necking. Instead, it is reminiscent of the steady-state region commonly observed in compression flow curves after dynamic recrystallization has taken place. This was confirmed to be the reason for the flow behaviour at 400°C and 0.1 s^{-1} in Figure 12, as well (Zarandi et al., 2008).

The different effect of Mn in each regime is also noticeable in Figure 12. It has been found that, above 400°C and below 0.001 s^{-1}, the higher Mn content results in an almost linear strain hardening behavior toward UTS. Examples of this are the flow curves at 0.0003 s^{-1} in Figure 12. Such linearity corresponds to increased strain-to-fracture (Zarandi et al., 2008). This is also consistent with the aforementioned beneficial effect of Mn on the sheet rollability. Figure 13 demonstrates a summary of how composition and strain rate can affect formability, as represented by elongation-to-fracture, in the AZ series sheets. As expected, the elongation increases with decreasing strain rate, with its maximum value at 4wt%Al at all strain rates, except at 0.0003 s^{-1} where it is slightly higher at 6wt%Al and the higher Mn content. It is interesting to note that the beneficial effect of Mn is most pronounced at the highest Al content. Even though this can partly be attributed to the grain refinement effect of Mn, Mn might have interacted with Al, reducing the density of detrimental coarse $Mg_{17}Al_{12}$ particles.

The occurrence of all these variations reflects the operation of different deformation mechanisms controlling flow behavior in different regimes. Strain-rate-change testing is commonly performed to study dominant deformation mechanisms at elevated temperatures. Typical result of such test is the plot of logarithm of strain rate versus logarithm of flow stress. This is shown in Figure 14 at three different temperatures and for two AZ61 series sheets containing two different levels of Mn.

The strain-rate sensitivity of flow stress, $m = \partial \ln \sigma / \partial \ln \dot{\varepsilon}$, is dependent upon active deformation mechanisms and, therefore, an indication of underlying deformation mechanisms. The slope of $\ln \dot{\varepsilon}$ -$\ln \sigma$ plot represents the stress exponent, *n* (or *1/m*), in the constitutive equation:

$$\dot{\varepsilon} = AD\left(\frac{b}{d}\right)^{p}\left(\frac{\sigma}{E}\right)^{n} \tag{2}$$

where $\dot{\varepsilon}$ is the true strain rate, A is a constant, $D=D_0exp(-Q/RT)$ is diffusion coefficient, b is the Burgers vector, d is the grain size, n is the stress exponent, σ is the true stress, E is the temperature-dependent Young's modulus, p is the grain size exponent, and Q is the activation energy for diffusion. As Figure 14 indicates, n is equal to 6 at high Z values, which here comprise high strain rates at all three temperatures. This high n value is often associated with dislocation slip creep where the deformation rate is controlled by dislocation climb (De La Torr et al., 1991). At low Z values; low strain rates and high temperatures, n approaches values of ≤2. In this condition, grain boundary sliding prevails as the dominant deformation mechanism (Del Valle et al., 2005). Therefore, the large elongation-to-fracture values associated with low strain rates in Figure 13 is the result of grain boundary sliding as the dominant deformation mechanism. It is also noted that the addition of Mn reduces the n value and increases the strain rate where n changes to lower values at 400°C and

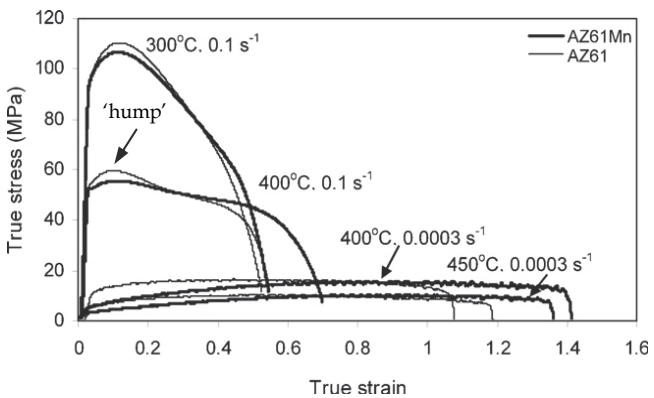

Fig. 12. Flow characteristics of two AZ61 sheets; AZ61 with 0.06wt%Mn and AZ61Mn with 0.24wt%Mn, in various conditions (Zarandi et al., 2008).

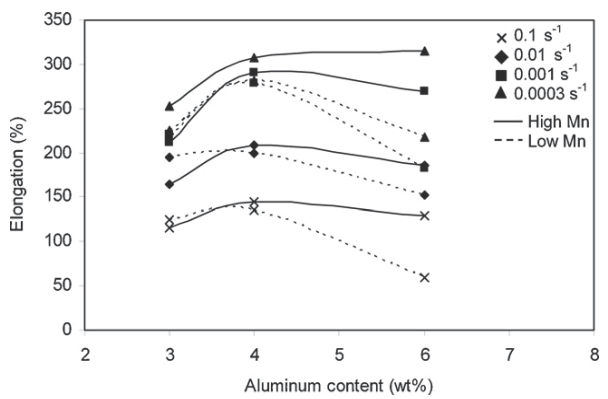

Fig. 13. Effect of Al and Mn on elongation-to-fracture at 450°C at various strain rates (Zarandi et al., 2008). Each data point is an average of four samples.

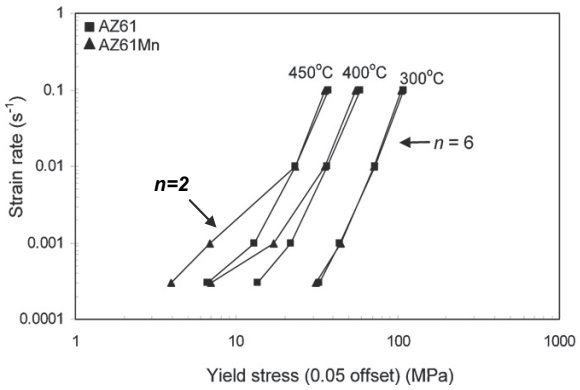

Fig. 14. Plots of strain rate versus yield stress of two AZ61 sheets; AZ61 with 0.06wt%Mn and AZ61Mn with 0.24wt%Mn (Zarandi et al., 2008).

450°C, Figure 14. In other words, Mn enhances contribution of grain boundary sliding and extends its operation to higher strain rates. Again, such an effect can be due to the grain refinement effect of Mn as this favors grain boundary sliding. This is why the alloys containing higher level of Mn tend to display larger elongations-to-fracture in Figure 13. Grain boundary sliding often leads to a uniform elongation, also known as diffuse necking, in the tested specimen. The absence of localized deformation allows the material to undergo more strain before failure. Dislocation slip creep, on the other hand, results in a localized deformation, known as necking, and an early fracture (Vespa et al., 2008).

It has been shown that grain boundary sliding in magnesium operates simultaneously with crystallographic slip (Del Valle et al., 2005). Due to low strain rates, the material resides at high temperature for a relatively long time during deformation. This, together with the stimulating effect of strain on grain boundary migration, leads to a dynamic grain growth, i.e. grain growth during deformation. The grain growth would hinder grain boundary sliding and, therefore, lattice slip takes over the deformation in large grains. It could be expected that the lattice slip would eventually trigger dynamic recrystallization in large grains, which in turn, promotes grain boundary sliding. In other words, deformation at low Z values can be a result of sequential operation of grain boundary sliding-crystallographic

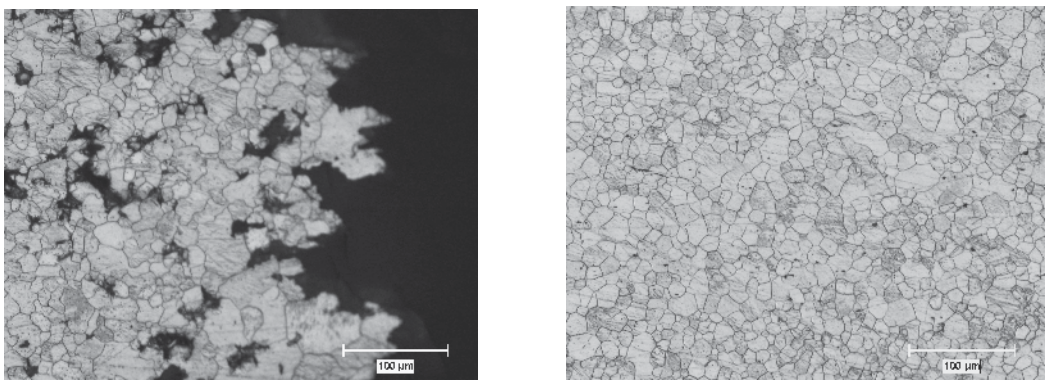

Fig. 15. Microstructures of an AZ41 alloy deformed at 400°C and 0.0003 s^{-1} (n=2); fracture tip (left) and out-of-gage region (right) (Zarandi et al., 2008).

slip-dynamic recrystallization. Eventually, the peak stress is reached and followed by a relatively shorter flow softening region, Figure 12, which is mainly a consequence of growth and coalescence of cavities at grain boundaries. A typical fractured microstructure resulting from grain boundary sliding is shown in Figure 15. For comparison, the microstructure of the out-of-gage region, i.e. unstrained microstructure, is also shown. The smaller grain size in the out-of-gage region denotes the strain-induced grain growth in the gage region.

With regard to the above discussion, it is well acknowledged that a fine grain structure is desired in sheet microstructures. To achieve this, it is required to properly design rolling schedules. Figure 16 illustrates two examples of the effect of rolling temperature. The result of rolling at 350°C is fine recrystallized grains surrounding unrecrystallized 'pancaked' material; twins are distributed throughout, and the structure is heterogeneous and 'banded'. The material rolled at 450°C, has a coarser grain size and appears to be more recrystallized, as indicated by less banding and only a few remnants of pancaked grains, although some twins are evident (it should be noted that some twins form after rolling and are the result of unloading the sheet). When tested in tension at 450°C and 0.001 s^{-1}, Figure 17, the partially recrystallized structure (rolled at 350°C) exhibited 35% larger elongation-to-fracture than the coarser grain microstructure (rolled at 450°C). By increasing the test temperature to 450°C, recrystallization by nucleation of new fine grains commences throughout in the former, while grain growth, rather than nucleation, prevails as a result of heating in the latter. Therefore, owing to the smaller grains, there is more contribution from grain boundary sliding to the accommodation of strain in the former leading to a larger elongation before failure. An opposite result is observed when the strain rate is increased to 0.1 s^{-1}; the former shows 60% smaller elongation-to-fracture than the latter, Figure 17. Examination of microstructures after fracture revealed a bimodal microstructure; large grains surrounded by small grains, in the former with cracks running along the large grains. This was suggested as the cause of ductility loss. The latter exhibited a rather uniform large grain size (Vespa et al., 2008).

A study of the effect of rolling parameters has suggested that rolling temperature and strain are of particular significance in controlling the sheet microstructure. In contrast, rolling speed and reheat time appeared less influential (Vespa et al., 2008). In that study, the maximum rolling speed was 24 m/min. However, it has been shown that increasing the rolling speed to very high rates; i.e. 2000 m/min, at 200°C leads to a very fine recrystallized

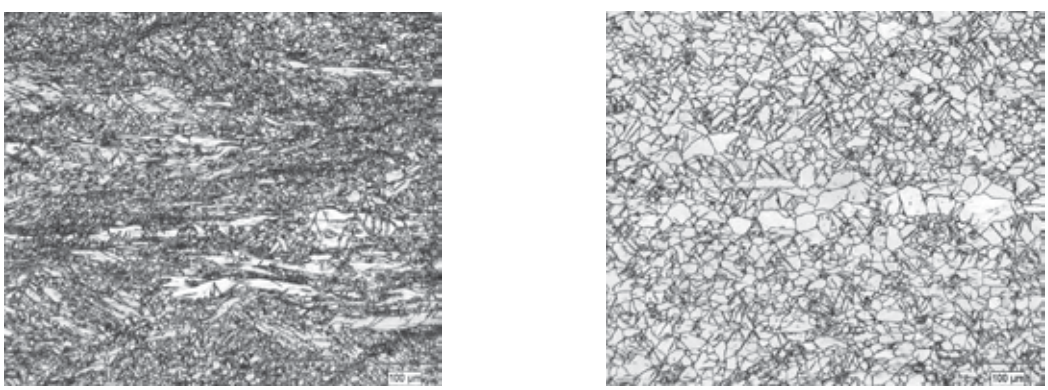

Fig. 16. As-rolled microstructures of an AZ31 sheet; rolling at 350°C (left) and 450°C (right) (Vespa et al., 2008).

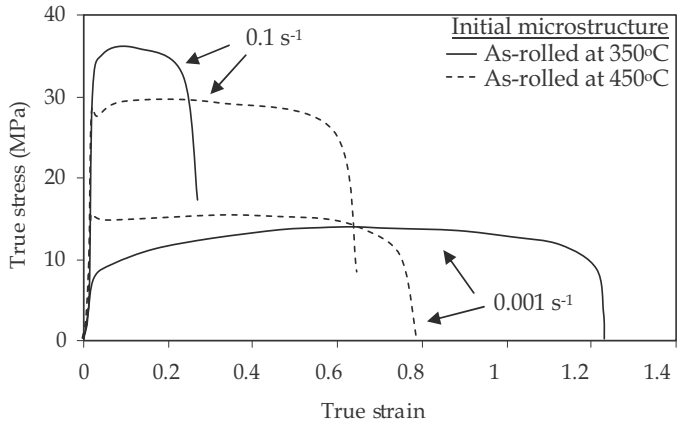

Fig. 17. Tensile deformation curves at 450°C corresponding with the microstructures in Fig. 16 (Vespa et al., 2008).

structure with an average grain size of 2.2 μm (water-quenched microstructure) (Minamiguchi et al., 2006; Sakai et al., 2006 & Utsunomiya, 2006). Such a high rolling speed also enhanced the rollability of AZ31 sheet in that 60% reduction in thickness was achieved in a single rolling pass. Since AZ31 alloy does not recrystallize at 200°C at conventional rolling speeds (Zarandi et al., 2007), the driving force and thermal energy required for recrystallization at 200°C are obviously provided by the amount of strain and very high strain rate, respectively. Although it seems difficult to implement such a high rolling speed in conventional sheet production, it introduces a new area of research to advance magnesium sheet properties. The outcome of such research would certainly help optimize rolling schedules to suit forming conditions.

6. Summary and remarks

Research into the production, deformation, and failure of magnesium alloys has provided a wealth of experimental information during the past decade. Such knowledge forms a critical basis for the development of magnesium sheet alloys. In considering the structure of magnesium and its impact on deformation and failure behavior, the grain size is more influential than it is in cubic metals, in that it also influences the relative contributions of different slip systems and deformation mechanisms to the overall flow. Strain hardening in magnesium alloys cannot be explained by the conventional models based on the Hall-Petch relationship. Solute elements and precipitates can generate anistropic characteristics by favoring one deformation mechanism or slip system over the other and affect both evolution of microstructure and mechanical properties. Moreover, orientations of basal planes have crucial impacts on the flow behavior and formability.

The absence of commercial magnesium sheet in automobile and other applications clearly indicates that more investigations and progress are still required. It is conceivable that magnesium sheets, capable of competing with commercial sheets of aluminum and steel, can be achieved through research and development in (i) sheet production technology and (ii) sheet characteristics and fabrication. In the former, the objective is to avoid intricate and multi-pass rolling schedules combined with intermediate annealing treatments. Twin-roll casting seems a promising approach toward this goal. The current research on magnesium

twin-roll casting has concentrated on producing wider and longer sheets by improving the casting and coil rolling technologies. However, development of magnesium alloys which capitalize on the twin-roll cast microstructure, i.e. supersaturated matrix with dispersion of fine particles, is urgently required. AZ series alloys with Al content higher than 3wt% as well as high Mn content alloys can be good candidates in this respect. Alloys with fine particles distributed throughout the microstructure and stable at elevated temperatures are especially important for randomizing the texture.

With regard to texture, sheet formability is the main issue, as this controls the successful fabrication of complex shapes in a timely manner. The evolution of microstructure and recrystallization are rather complicated processes in magnesium alloys. More systematic and detailed studies are required to understand underlying mechanisms. Topics such as twin-dislocation interactions, recrystallization kinetics, evolution of texture and slip systems during deformation, solute drag effect and superplasticity, superplasticity in coarse grain alloys, and effect of strain rate on formability at very fine grain sizes are among those which still need thorough investigation. Computational simulations and modeling, which have already aided progress in understanding the development of texture and slip mechanisms, should also be utilized to achieve the goal. Constitutive equations available for deformation of magnesium do not incorporate recrystallization during deformation. There is a requirement for comprehensive constitutive models that not only consider the evolution of microstructure during deformation, but also are based on multi-, rather than single, mechanism of deformation.

7. References

Alico, J. (1945). Forging, Rolling, Forming, and Extruding Magnesium Alloys, In: *Introduction to Magnesium and its Alloys*, Ziff-Davis Publication, New York.

Allen, R.V.; East, D.R.; Johnson, T.J.; Borbidge, W.E. & Liang, D. (2001). Magnesium alloy sheet produced by twin roll casting, *Proceedings of Magnesium Technology 2001*, pp. 75-79, New Orleans, Louisiana, February 11-15, 2001, The Minerals, Metals, and Materials Society, USA.

Bach, Fr.-W; Rodman, M.; Rossberg, A. & Hepke, M. (2006). Magnesium sheet production today and tomorrow, *Proceedings of Magnesium Technology in the Global Age*, pp. 255-268, Montreal, Canada, 2006, *Canadian Institute of Mining*, Metallurgy and Petroleum, Montreal, Canada.

Barnett, M.R. (2003). A Taylor model based description of the proof stress of magnesium AZ31 during hot working. *Metallurgical and Materials Transactions*, 34A, 2003, 1799-1806.

Barnett, M.R.; Keshavarz, Z.; Beer, A.G. & Atwell, D. (2004). Influence of grain size on the compressive deformation of wrought Mg-3Al-1Zn", *Acta Materialia*, 52, 2004, 5093-5103.

Cottam, R.; Robson, J. & Lorimer, G. (2006). The deformation and recrystallization of commercially pure Mg and Mg-Y alloys. *Proceedings of Magnesium Technology in the Global Age*, pp. 171-180, Montreal, Canada, October 2006, Canadian Institute of Mining, Metallurgy and Petroleum, Montreal, Canada.

CSIRO (2003). Thin magnesium sheet technology is ready to roll. *www.manufacturingtalk.com*, November 27, 2003.

De La Torr, A.; Adeva, P. & Aballe, M. (1991). Indentation creep of lead and lead-copper alloys. *Journal of Materials Science*, 26, 16, 1991, 4351-4354.

Del Valle, J.A.; Pérez-Prado, M.T. & Ruano, O.A. (2005). Deformation mechanisms responsible for the high ductility in a Mg AZ31 alloy analyzed by electron backscattered diffraction. *Metallurgical and Materials Transactions A*, 36, 6, 2005, 1427-1438.

Di, H.-S.; Li, Y.-L.; Ning, Z.-L.; Li, Z.; Liu, X. & Wang, G.-D. (2005). New processing technology of twin roll strip casting of AZ31B magnesium strip", *Materials Science Forum,* Vols. 488-489, 2005, 615-618.

Dow Chemical Company (1943). *Dowmetal Magnesium Alloys*, Dow Chemical Company, Midland, Michigan, May, 1943.

Galiyev, A.; Kaibyshev, R. & Gottstein, G. (2001). Correlation of plastic deformation and dynamic recrystallization in magnesium alloy AZ60. *Acta Materialia*, 49, 2001, 1199-1207.

Galiyev, A.; Kaibyshev, R. & Sakai, T. (2003). Continuous dynamic recrystallization in magnesium alloy. *Materials Science Forum*, Vols. 419-422, 2003, 509-514.

Ion, S.E.; Humphreys, F.G. & White, S.H. (1982). Dynamic recrystallization and the development of microstructure during the high temperature deformation of magnesium. *Acta Metallurgica*, 30, 1982, 1909-1982.

Jiang, L. (2008). Effect of twinning on texture and strain hardening in magnesium alloys subjected to different strain paths. *PhD thesis*, 2008, McGill University, Montreal, Canada.

Jung, I.-H.; Bang, W.; Kim, I.J.; Sung, H.-J.; Park, W.-J.; Choo, D. & Ahn, S. (2007). Mg Coil Production via Strip Casting and Coil Rolling Technologies, *Proceedings of Magnesium Technology 2007*, pp. 85-88, Orlando, Florida, 2007, The Minerals, Metals, and Materials Society, USA.

Kaibyshev, R.O.; Galiev, A.M. & Sokolov, B.K. (1994). Effect of grain size on the plastic deformation and dynamic recrystallization of a magnesium alloy. *Physics of Metals and Metallography*, 78, 2, 1994, 209-217.

Kaibyshev, R. & Sitdikov, O. (1994). Dynamic recrystallization of magnesium at ambient temperature. *Z. Metallkd*, 85, 10, 1994, 738-743.

Kaibyshev, R. & Sitdikov, O. (1995a). Mechanisms of plastic deformation in magnesium: I. deformation behavior of coarse-grained magnesium. *Physics of Metal and Metallography*, 80, 1995, 354-360.

Kaibyshev, R. & Sitdikov, O. (1995b). Mechanisms of plastic deformation in magnesium: II. analysis of activation processes. *Physics of Metal and Metallography*, 80, 1995, 470-475.

Kim, W.J.; Chung, S.W.; An, C.W. & Higachi, K. (2001). Superplasticity in a relatively coarse-grained AZ61 magnesium alloy. *Journal of Materials Science Letters*, 20, 2001, 1635-1637.

Kobayashi, T.; Koike, J.; Yoshida, Y.; Kamado, S.; Suzuki, M.; Maruyama, K. & Kojima, Y. (2003). Grain size dependence of active slip systems in an AZ31 magnesium alloy. *Journal of the Japan Institute of Metals*, 67, 4, 2003, 149-152.

Koike, J.; Kobayashi, T.; Mukai, T.; Watanabe, H.; Suzuki, M.; Maruyama, K. & Higachi, K. (2003). The activity of non-basal slip systems and dynamic recovery at room temperature in fine-grained AZ31B magnesium alloy. *Acta Materialia*, 51, 2003, 2055-2065.

Liang, D. & Cowley, C.B. (2004). The Twin-Roll Casting of Magnesium. *JOM*, May 2004, 26-28.

Masoumi, M.; Zarandi, F. & Pekguleryuz, M. (2010a). Microstructure and Texture Studies on Twin-Roll Cast AZ31 (Mg-3wt%Al-1wt%Zn) Alloy and the Effect of Thermomechanical Processing, *Materials Science and Engineering*, in press, 2010.

Masoumi, M.; Zarandi, F. & Pekguleryuz, M. (2010b). Alleviation of basal texture in twin-roll cast Mg-3Al-1Zn alloy. *Scripta Materialia,* 62, 2010, 823-826.

Meyers, M.A.; Vohringer, O. & Lubarda, V.A. (2001). The onset of twinning in metals: a constitutive description. *Acta Materialia*, 49, 2001, 4025-4039.

Minamiguchi, S.; Sakai, T.; Utsunomiya H. & Koh, H. (2006). Improvement of mechanical properties of AZ31B sheets by high speed rolling, *Proceedings of Magnesium Technology in the Global Age*, pp. 217-227, Montreal, Canada, October 2006, Canadian Institute of Mining, Metallurgy and Petroleum, Montreal, Canada.

Miura, H.; Sakai, T.; Nogawa, H.; Yang, X.; Watanabe, Y. & Miura S. (2005). Orientation dependence of ductility of Mg single crystals at elevated temperature. *Materials Science Forum*, Vols. 488-489, 2005, 193-196.

Mukai, T.; Mohri, T.; Mabuchi, M.; Nakamura, M; Ishikawa, K. & Higashi, K. (1998). Experimental study of a structural magnesium alloy with high absorption energy under dynamic loading. *Scripta Materialia*, 39, 9, 1998, 1249-1253.

Mukai, T.; Watanabe, H.; Ishikawa, K. & Higashi, K. (2003). Guide for enhancement of room temperature ductility in Mg alloys at high strain rates. *Materials Science Forum*, vols. 419-422, 2003, 171-176.

Nakaura, Y. & Ohori, K. (2005). Properties of AZ31 magnesium alloy sheet produced by twin roll casting. *Materials Science Forum,* Vols. 488-489, 2005, 419-426.

Obara, T.; Yoshinaga, H. & Morozumi, S. (1973). 1122 1123 slip system in Mg. *Acta Metallurgica*, 21, 7, 1973, 845-853.

Poss, R. (2003). Sheet metal production of magnesium. *Materials Science Forum*, Vols. 419-422, 2003, 327-336.

Roberts, C.S. (1964). The deformation of magnesium. *Magnesium and Its Alloys*, 81-107, John Wiley, New York.

Sakai, T. & Jonas, J.J. (1984). Dynamic recrystallization: mechanical and microstructural considerations. *Acta Metallurgica*., 32, 1984, 189-209.

Sakai, T. (2000). Microstructural development under dynamic recrystallization of polycrystalline materials. *Proceedings of Thermomechanical Processing of Steels (J.J. Jonas symposium)*, pp. 47-62, Ottawa, Canada, August 2000, Canadian Institute of Mining, Metallurgy and Petroleum, Montreal, Canada.

Sakai, T.; Utsunomiya, H.; Minamiguchi, S. & Koh, H. (2006). Single pass large draught rolling of magnesium alloy sheets by high speed rolling, *Proceedings of Magnesium Technology in the Global Age*, pp. 205-215, Montreal, Canada, October

2006, Canadian Institute of Mining, Metallurgy and Petroleum, Montreal, Canada.

Sastry, D.H.; Prasad, Y.V.R.K. & Vasu, K.I. (1969). On the stacking fault energies of some closed-packed hexagonal metals. *Scripta Metallurgica*, 3, 1969, 927-930.

Senn, J.W. & Agnew, S.R. (2008). Texture randomization of magnesium alloys containing rare earth elements. *Proceedings of Magnesium Technology 2008*, pp. 153-158, New Orleans, Louisiana, 2008, The Minerals, Metals, and Materials Society, USA.

Sitdikov, O. & Kaibyshev, R. (2001). Dynamic recrystallization in pure magnesium. *Materials Transactions*, l42, 9, 2001, 1928-1937.

Sitdikov, O.; Kaibyshev, R. & Sakai, T. (2003). Dynamic recrystallization based on twinning in coarse-grained Mg. *Materials Science Forum*, Vols. 419-422, 2003, 521-426.

Stohr, J.F. & Poirier, J.P. (1972). Electron-microscope study of pyramidal slip 1122 1123 in Mg. *Philosophical Magazine*, 25, 6, 1972, 1313-1329.

Taylor, G.I. (1938). Plastic strain in metals. *Journal of Institute of Metals*, 62, 1938, 307-324.

Uesugi, T.; Kohyama, M.; Kohzu, M. & Higashi, M. (2003). Generalized stacking fault energy and dislocation properties for various slip systems in magnesium: a first-principles study. *Materials Science Forum*, Vols. 419-422, 2003, 225-230.

Utsunomiya, H.; Sakai, T.; Minamiguchi, S. & Koh, H. (2006). High speed heavy rolling of magnesium alloy sheets, *Proceedings of Magnesium Technology 2006*, pp. 201-204, San Antonio, Texas, March 2006, The Minerals, Metals, and Materials Society, USA.

Valle, J.A. del; Carreno, F. & Ruano, O.A. (2006). Influence of texture and grain size on work hardening and ductility in magnesium-based alloys processed by ECAP and rolling. *Acta Materialia*, 54, 2006, 4247-4259.

Vespa, G.; Mackenzie, L.W.F.; Verma, R.; Zarandi, F.; Elhachmi, E. & Yue, S. (2008). The influence of the as-hot rolled microstructure on the elevated temperature mechanical properties of magnesium AZ31 sheet. *Materials Science and Engineering A*, 487, 2008, 243-250.

Watanabe, H. & Mukai, T. (1999). Superplasticity in a ZK60 magnesium alloy at low temperatures. *Scripta Materialia*, 40, 4, 1999, 477-484.

Watanabe, H.; Tsutsui, H.; Mukai, T.; Ishikawa, K.; Okanda, Y.; Kohzu, M. & Higashi, K. (2001). Grain size control of commercial wrought Mg-Al-Zn alloys utilizing dynamic recrystallization. *Materials Transactions,* 42, 2001, 1200-1205.

Wonsiewiczs, B.C. & Backofen, W.A. (1967). Plasticity of magnesium crystals. *Transactions of TMS-AIME*, 239, 1967, 1422-1431.

Yang, C.; Ding, P.; Zhang, D. & Pan, F. (2005). The Microstructure and processing in twin roll casting of magnesium alloy strip. *Materials Science Forum,* Vols. 488-489, 2005, 427-430.

Zarandi, F.; Verma, R.; Yue, S. & Essadiqi, E. (2007). Microstructure evolution during rolling of AZ31 magnesium alloy under decreasing temperature, *Proceedings of Magnesium Technology 2007*, pp. 75-80, Orlando, Florida, 2007, The Minerals, Metals, and Materials Society, USA.

Zarandi, F.; Seale, G.; Verma, R.; Essadiqi, E. & Yue, S. (2008). Effect of Al and Mn additions on rolling and deformation behavior of AZ series magnesium alloys. *Materials Science and Engineering A*, 496, 2008, 159-168.

15

Contemporary Forming Methods of the Structure and Properties of Cast Magnesium Alloys

Leszek Adam Dobrzański, Tomasz Tański, Szymon Malara,
Mariusz Król and Justyna Domagała-Dubiel
Division of Materials Processing Technology
Management and Computer Techniques in Materials Science
Institute of Engineering Materials and Biomaterials
Silesian University of Technology
ul. Konarskiego 18a, 44-100 Gliwice
Poland

1. Introduction

For the reason of growing requirements for materials made from light alloys concerning mechanical properties, corrosion resistance, manufacturing costs and the influence of the environment this efforts can be consider as very up-to-date from the scientistic view and very attractive for investigation.

The rising tendencies of magnesium alloy production, show increased need of their application in world industry and what follows the magnesium alloys become one of the most often apply construction material our century.

A contemporary technological development makes it necessary to look for new constructional solutions that aim at the improvement of the effectiveness and quality of a product, at the minimization of dimension and mass as well as the increasing of reliability and dimension stability in the operation conditions. For a dozen or so years one can observe a rising interest in the non-ferrous metals alloys including magnesium alloys which are an examination subject in many research and university centres in the country and abroad as well as in major manufacturers of mechanical engineering industry, chemical, power, textile, electronic, paper and aeronautic industries and in particular automotive, shipbuilding, aircraft, sports and even nuclear industries (Baker, 1999; Dobrzański and Tański, 2009; Fajkiel and Dudek, 2004).

Magnesium alloys which are successfully used for a long time in different industry branches are a combination of low density and high strength. The above features together with low inertia have significantly contributed to the wide use of magnesium alloys in fast moving elements, in locations where rapid velocity changes occur and in products in which lowering a final mass of a product is required. The greatest interest in magnesium alloys was shown and is still shown by an automotive industry (Figure 1) (Horst and Mordike, 2006; Kainem, 2003; Tański *et al*., 2007). For example, *General Motors* in their big cars (Savana

& Express) use 26.3 kg of magnesium cast alloys, and in smaller cars (Safari, Astro) – 165 kg, Ford F – 150 – 14.5 kg, VW Passat and Audi A4 and A6 from 13.6 to 14.5 kg, Alfa Romeo – 9.3kg. A further demand for magnesium casts is expected, of up to 50 kg per each car. It is mainly because of the fact that the magnesium casts have got a low density (1700-1900 kg/m^3), and at the same time, their mechanical properties are similar to the aluminium casting alloys.

Cylinder head cover

Wheel bands

Car inside

Casing of the minidisk

Housing of the phone

Housing of the photographic camera

Fig. 1. Elements from magnesium alloys

A desire to create as light vehicle constructions as possible and connected with it low fuel consumption have made it possible to make use of magnesium alloys as a constructional material in car wheels, engine pistons, gear box and clutch housings, skeletons of sunroofs, framing of doors, pedals, suction channels, manifolds, housings of propeller shafts, differential gears, brackets, radiators and others. Moreover, the magnesium alloys demonstrate good corrosion resistance, no aggressiveness towards the mould material and low heat of fusion what enables the use of pressure die casting ensuring good shape reproducibility (Kainem, 2003; Kiełbus *et al.*, 2006; Maltaisa *et al.*, 2004; Rzychoń and Kiełbus, 2007). Magnesium alloys have also found their application in manufacturing of mowers, saws, robots, office equipment including computer hardware, sport and medical appliances, in production of movie and video cameras, for rocket parts, space ships, and others (Dobrzański and Tański, 2009).

The increasing use of magnesium alloys is caused by the progress in the manufacturing of new reliable alloys with the addition of Zr, Ce i Cd and very light alloys are made from Li. A general tendency of a present stage of cast materials development is the increase of their plasticity together with the increase of their resistance properties (Figure 2) (Fajkiel and Dudek, 2004).

In order to effectively control microstructure development during the melting, solidification as well as further materials processing is necessary to understand all metallurgical

phenomena taking place. Knowledge of the solidification process as well as the influence of liquid and/or semi solid metal treatment on micro and macro structure characteristic is of primary importance. The simples and very effective method, which make it possible to determine a curve of the crystallization process – the cool curve $T=F(t)$,is thermal analysis. Advanced Thermal Analysis (TA) techniques monitor the temperature changes in sample as it cools through a phase transformation interval (Backuerud *et al.*, 1990; Emandi *et al.*, 2005; MacKay *et al.*, 2000). The temperature changes in the materials are recorded as a function of the heating or cooling time in such a manner that allows for the detection phase transformation. In order to increase accuracy, characteristic points on the cooling curve have been identified using the first derivative curve plotted versus time (Kasprzak *et al.*, 2008; Kierkus & Sokolowski, 1999; Patent No.: US 7,354,491 B2).

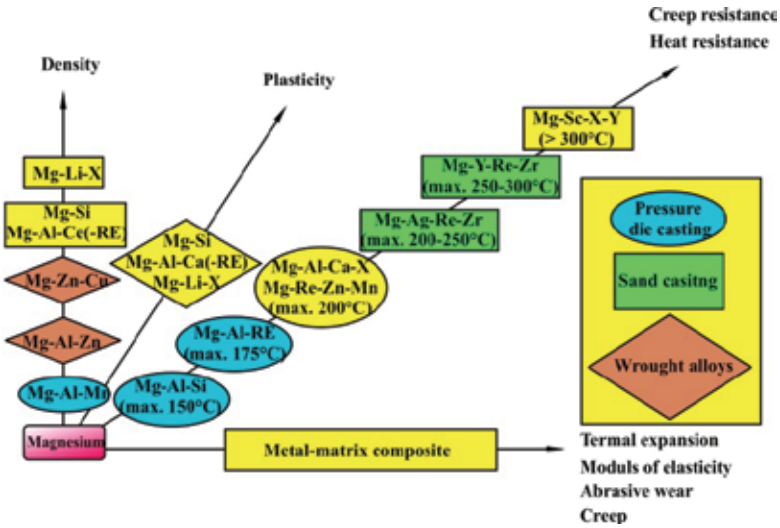

Fig. 2. Potential development directions of New magnesium alloys (Fajkiel and Dudek, 2004)

Increasing of surface layers properties can by achieved by many technologies i.e.: electroplating, anodizing, PVD, laser alloying or padding. Main advantages of laser treatment are i.e.: short time of process, flexibility or operation precision (Bachmann, 2003; Vollertsen and Partes, 2005).

Main goal of surface laser treatment is modification structure and properties. Increasing of wear resistance is creation of result of chemical homogeneous, fine-crystalline of surface layer without chemical changes. More advantageous properties can be achieved by alloying with hard particles of carbides, oxides or nitrides (Barnes *et al.*, 2003; Cao *et al.*, 2008; Dobrzański *et al.*, 2008; Dutta Majumdar *et al.*, 2003; Yadroitsev *et al.*, 2007).

Laser technologies are the most of promise and effective for assurance of continuous development of materials processing branch as a results of forecasts concerning global economic development. One considers that economies, which make use of laser technologies on a large scale, will be competitive on the global market (Bachmann, 2003; Vollertsen and Partes, 2005).

The rising tendencies of magnesium alloy production, show increased need of their application in world industry and what follows the magnesium alloys become one of the most often apply construction material our century. Therefore it is extremely important to

keep a high investigation development of a light alloy issue, furthermore performing in Institute of Material Processes and Computer Technology, Institute of Engineering Materials and Biomaterials, Silesian University of Technology.
The goal of this paper is to present of the investigation results of the casting magnesium alloy in its as-cast state and after heat and surface laser treatment.

2. Experimental procedure

2.1 Materials

The investigations have been carried out on test pieces of MCMgAl12Zn1 (Table 1, No. 1), MCMgAl9Zn (Table 1, No.2), MCMgAl6Zn (Table 1, No. 3), MCMgAl3Zn (Table 1, No. 4) magnesium alloys in as-cast and after heat treatment states. The chemical composition of the investigated materials is given in Table 1. A casting cycle of alloys has been carried out in an induction crucible furnace using a protective salt bath *Flux 12* equipped with two ceramic filters at the melting temperature of 750±10°C, suitable for the manufactured material. In order to maintain a metallurgical purity of the melting metal, a refining with a neutral gas with the industrial name of *Emgesalem Flux 12* has been carried out. To improve the quality of a metal surface a protective layer *Alkon M62* has been applied. The material has been cast in dies with betonite binder because of its excellent sorption properties and shaped into plates of 250x150x25 mm. The cast alloys have been heated in an electrical vacuum furnace *Classic 0816 Vak* in a protective argon atmosphere.

The mass concentration of main elements, %							
No.	Al	Zn	Mn	Si	Fe	Mg	Rest
1	12.1	0.62	0.17	0.047	0.013	86.96	0.0985
2	9.09	0.77	0.21	0.037	0.011	89.79	0.0915
3	5.92	0.49	0.15	0.037	0.007	93.33	0.0613
4	2.96	0.23	0.09	0.029	0.006	96.65	0.0361

Table 1. Chemical composition of investigated alloys, %

2.2 Heat treatment

The applied heat treatment was performed according to the determined scheme (Table 2)

Sing the state of heat treatment	Solution treatment			Aging treatment		
	Temperature	Time	Cooling	Temperature	Time	Cooling
0	**As-cast**					
1	430	10	air	-	-	-
2	430	10	water	-	-	-
3	430	10	furnace	-	-	-
4	430	10	water	190	15	air

Table 2. Parameters of heat treatment of investigated alloys

2.3 Thermal analysis

The thermo-derivative analysis was performed with the Mg-Al-Zn alloys using the UMSA (Universal Metallurgical Simulator and Analyzer) device (Patent No.: US 7,354,491 B2). The carrying out of the thermo analysis using the UMSA device was based on remelting, heating and cooling of the sample with a proper established cooling rate. The samples with a shape and size showed on Fig. 3 were induction heated to the temperature at 700±1°C.

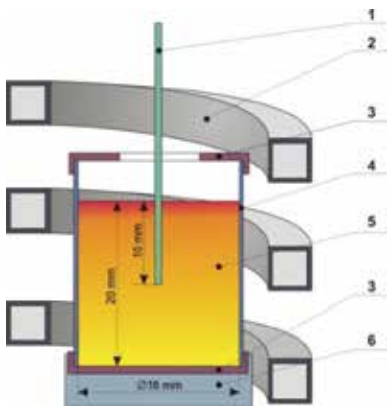

Fig. 3. Scheme of the UMSA Thermal Analysis Platform experimental set-up: 1 – low thermal mass thermocouple, 2 – heating and cooling coil, 3 – thermal insulation, 4 – steel foil, 5 – test sample, 6 – ceramic base.

For achieving of the cooling rate of:

- ≈ 0,6°C/s the sample was freely cooled,
- ≈ 1,2°C/s by a cooling system with argon using a flow rate 30 l/min,
- ≈ 2,4°C/s by a cooling system with argon using a flow rate 125 l/min.

On the basis of the ATD analysis there were determined the characteristic points describing the thermal phenomena present during the alloy crystallisation, which define the temperature and time values of the thermo-derivative analyse curves.

2.4 Laser treatment

The analysis of the surface modification influence using the high power diode laser HPDL Rofin DL 020 was performed for Mg-Al-Zn cast magnesium alloys alloyed with titanium, tungsten, vanadium, niobium and silicon carbides, as well with aluminium oxide (Table 3).

Properties	WC	TiC	VC	NbC	SiC	TaC	Al_2O_3
Density, kg/m^3	15.69	4.25	5.36	7.60	3.44	15.03	3.97
Hardness, HV	3400	1550	2850	2100	1600	1725	2300
Melting temperature, ^{o}C	2870	3140	2830	3500	1900	3880	2047
Mean grain size, μm	0.7-0.9	< 1.0		<10	<10	<10	1-5
	>5	>6.4	>1.8	<45	<75	<45	80

Table 3. Properies of ceramic powders used to laser alloying

The laser treatment of the cast magnesium alloys was performed using the permanent powder feed technique into the alloying zone area by a granulate dosage using a fluidisation feeder. The powder feeder was connected to the feeding gas cylinder as well to the powder-feeding nozzle. In the powder feeding system the feed rate of the carrier gas was set by 5 l/min. After preliminary tests the laser power for investigations was set in a range of 1.2-2.0 kW and a laser alloying rate of 0.25; 0.50; 0.75; 1.00 m/min was chosen.
The investigations has revealed that the optimal geometry of a single laser tray was achieved by an alloying rate of 0.75 m/min except the Al_2O_3 and NbC powders, where the optimal alloying rate was set like 0.50 m/min and 0.25 m/min respectively.

2.5 Specimens characterization

The observations of the investigated cast materials have been made on the light microscope LEICA MEF4A as well as on the electron scanning microscope ZEISS SUPRA 25. The X-ray qualitative and quantitative microanalysis and the analysis of a surface distribution of cast elements in the examined magnesium cast alloy specimens in as-cast and after heat, laser treatment have been made on transverse microsections on the ZEISS SUPRA 25 scanning microscope with the. Phase composition and crystallographic structure were determined by the X-ray diffraction method using the X`Pert device with a cobalt lamp, with 40 kV voltage. The measurement was performed in angle range of 2Θ: 20^o - 120^o. Hardness tests were made using Zwick ZHR 4150 TK hardness tester in the HRF scale. Compression and tensile tests were made using Zwick Z100 testing machine. Microhardness of the cross section of the laser surface melted layer was measured on Fully-Automatic Microhardness Testing System with a loading time of 15 s and the testing load of 100 g.

3. Results and discussions

3.1 Heat treatment

The results of metallographic investigations performed on light and scanning electron microscope (Figs. 4-6), confirmed also by appliance of the EDS surface analysis, quantitative EDS point wise microanalysis and X-Ray diffraction (Figs. 7-8, Table 4) it has been confirmed that the magnesium cast alloys MCMgAl12Zn1, MCMgAl9Zn1, MCMgAl6Zn1, MCMgAl3Zn1 in the cast state are characterized by a microstructure of the solid solution α constituting the alloy matrix as well as the γ – $Mg_{17}Al_{12}$ discontinuous intermetallic phase in the forms of plates located mostly at grain boundaries. Moreover, in the vicinity of the γ intermetallic phase precipitations the presence of the needle eutectics (α + γ) has been revealed.
In the structure of the examined magnesium cast alloys one can observe, apart from $Mg_{17}Al_{12}$ precipitations, turning grey phases, characterized by angular contour with smooth edges in the shape of hexahedrons (Fig. 4). Out of the chemical composition examinations with the use of the EDS dispersive radiation spectrometer (Fig. 8, Table 4) as well as literature data, one can conclude that it is the Mg_2Si compound which, when precipitating, increases the hardness of castings . There have appeared, after the process of solutioning with cooling in water and in the air, trace quantities of the γ ($Mg_{17}Al_{12}$) phase and single precipitations of a light grey phase and Mn-Al-Fe precipitation in the structure of the alloy. There have not been noticed any locations of eutectic occurrences in the structure (Fig. 5a).
However for the MCMgAl12Zn1 alloy there was found numerous areas of the γ phase – which was not dissolved in the matrix, as well some eutectics (Fig. 5b).

After the cooling bell annealing the structure of the solid solution α with many precipitations of the secondary phase γ has been revealed (locations resembling eutectics). The precipitations of the γ ($Mg_{17}Al_{12}$) phase, located at grain boundaries and the light grey phase located mostly at the phase β boundary have also been observed. The structure of this alloy is similar to the structure of the as-cast alloy (Fig. 6a). The applied ageing process after the solution heat treatment with cooling in the air has caused the release of the γ phase at grain boundaries as well as in the form of pseudo eutectic locations. There have been revealed, in the structure of the material, the parallel twinned crystals extending along the whole grain (Fig. 6b).

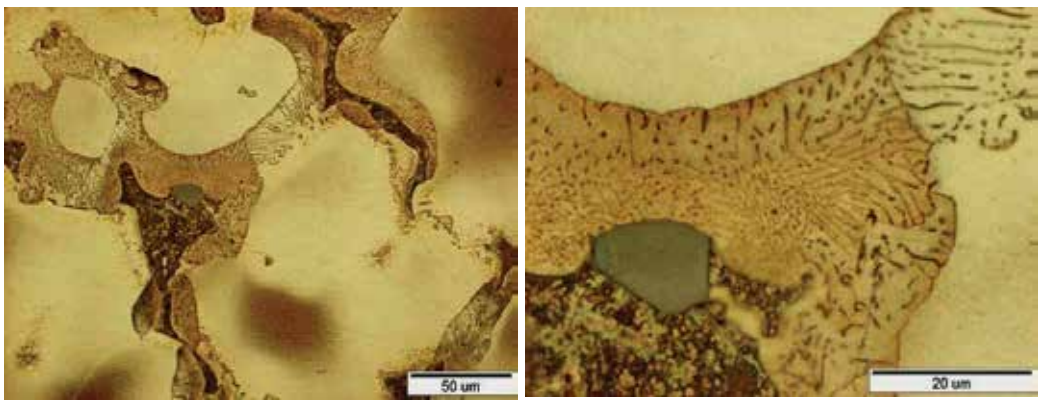

Fig. 4. Structure of the MCMgAl9Zn1 magnesium cast alloy in as- cast state

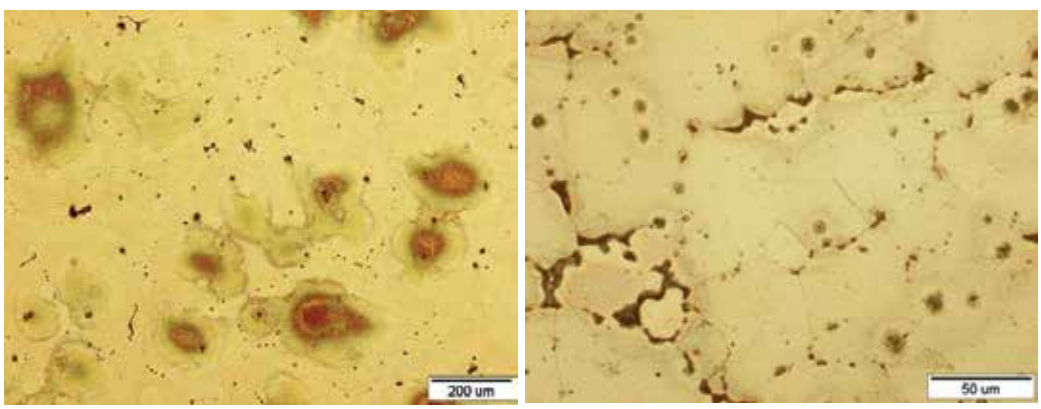

(a) (b)

Fig. 5. Structure of the magnesium cast alloy: a) MCMgAl3Zn1 after solutioning with cooling in the air; b) MCMgAl12Zn1 after solutioning with cooling in water

The chemical analysis of the surface element decomposition and the quantitative micro analysis made on the transverse microsections of the magnesium alloys using the EDS system have also confirmed the evident concentrations of magnesium, silicon, aluminium, manganese and iron what suggests the occurrence of precipitations containing Mg and Si with angular contours in the alloy structure as well as phases with high Mn and Al concentrations that are irregular with a non plain surface, often occurring in the forms of

blocks or needles(Figs. 7-8, Table 4), also information was obtained about the mass and atomic concentration of the particular elements in the point-wise investigated micro areas of the matrix and precipitates. Moreover the confirmation was achieved for alloying of Pb, Ce and Cu, identified in the γ phase area (Fig. 8, Table 4).

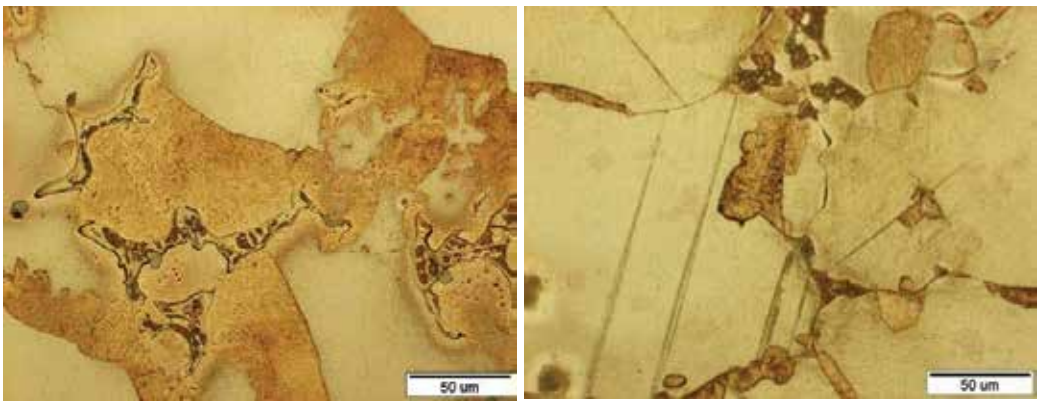

(a) (b)

Fig. 6. Structure of the magnesium cast alloy: a) MCMgAl9Zn1 after cooling with the furnace; b) MCMgAl9Zn1 after ageing treatment

A prevailing participation of magnesium and aluminium and a slight concentration of Zn has been ascertained in the alloy matrix as well as in the location of eutectics and big precipitations that arouse at phase boundaries identified as $Mg_{17}Al_{12}$ (Fig. 7).

On Figure 9 there were presented X-Ray diffraction diagrams of the investigated magnesium alloys after heat treatment. Using qualitative and quantitative X-Ray diffraction methods it was confirmed, that in the investigated materials occurs the γ ($Mg_{17}Al_{12}$) phase and α-Mg phase - the alloy matrix. The volume fraction of the γ phase precipitation in the microstructure of the MCMgAl12Zn1, MCMgAl9Zn1, MCMgAl6Zn1 alloy depends on the aluminium content as the main alloying additive, with a maximum value of 11.9% for the MCMgAl12Zn1 alloy in the state after ageing - 1.6 % for the MCMgAl9Zn1 alloys in the state after ageing and MCMgAl6Zn1 alloy in the as-cast state. A to low volume fraction of other phases occurred in the material, as well the γ –$Mg_{17}Al_{12}$ phase for alloys after solution heat treatment or with a low aluminium content: MCMgAl9Zn1, MCMgAl6Zn1, MCMgAl3Zn1 does not allow for their clearly identification using the achieved X-Ray diagrams.

As a result of thin foils examinations on the transmission electron microscope it has been stated that the structure of a newly worked out, experimental magnesium cast alloy MCMgAl12Zn1, MCMgAl9Zn1, MCMgAl6Zn1, MCMgAl3Zn1 after solutioning makes a supersaturated solid solution α – Mg with visible dislocation ranges. The analysis of thin foils after the process of ageing has validated the fact that the structure of the magnesium cast alloy consists of the solid solution α – Mg (matrix) and an intermetallic secondary phase γ – $Mg_{17}Al_{12}$ in the form of bulk precipitations (Fig. 10).

Moreover, the examinations of the thin magnesium cast alloy foils after the ageing process confirm the existence of a high density of crystal structure defects identified as a series of straight and parallel dislocations resembling a network. The ageing process has caused the precipitation of evenly distributed dispersive γ secondary phase in the needle form that has in the major performed investigations a preferred crystallographic orientation in the matrix.

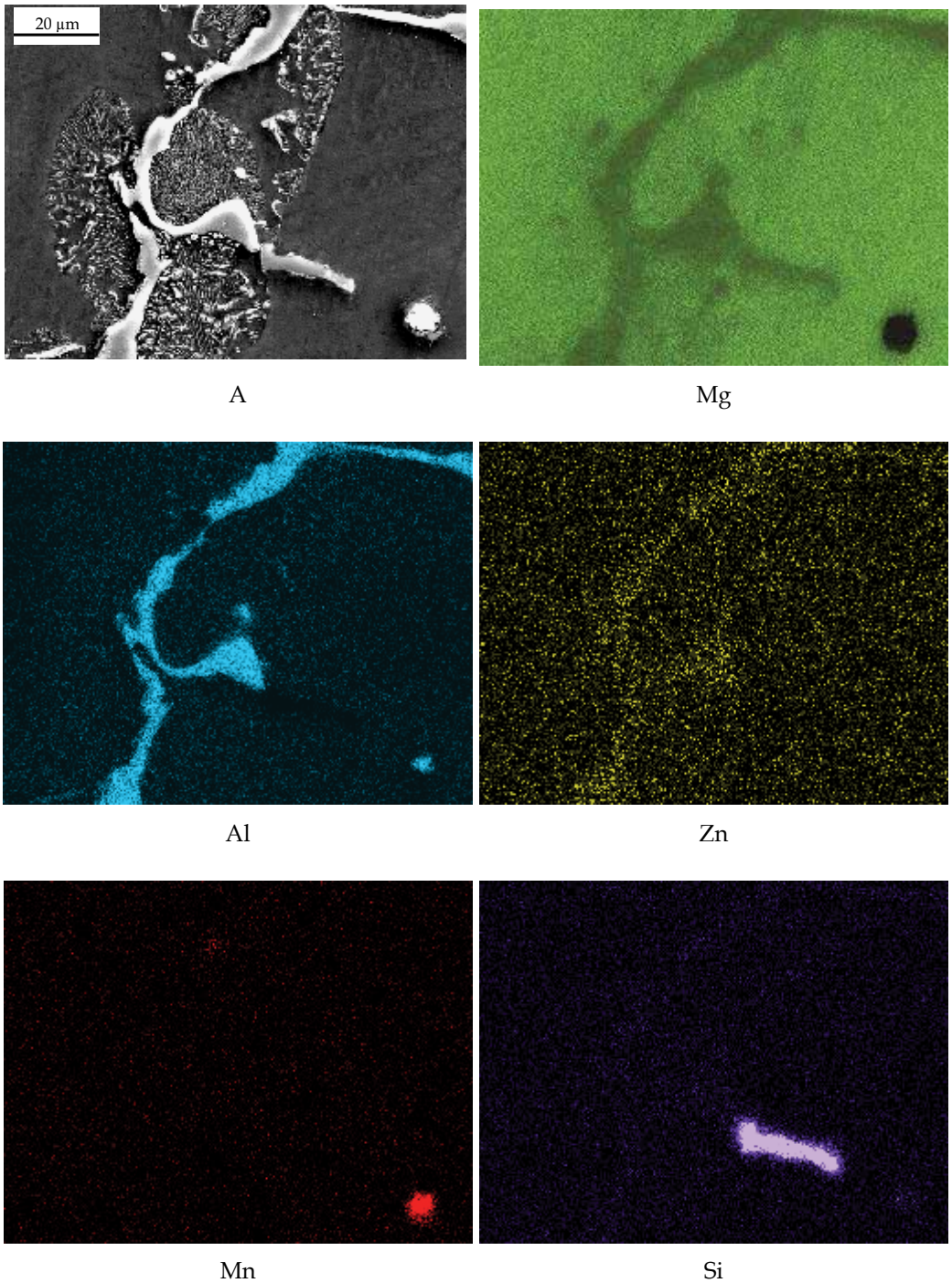

Fig. 7. The area analysis of chemical elements alloy MCMgAl6Zn1 after cooling in the furnace: image of secondary electrons (A) and maps of elements' distribution

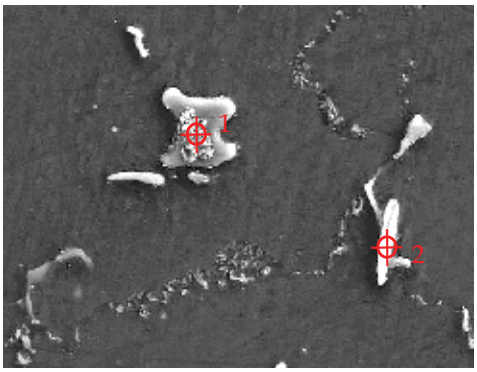

Fig. 8. Structure of the magnesium cast alloy MCMgAl6Zn1 after cooling in the furnace

Element	The mass concentration of main elements, %	
	Mass	Atomic
Analysis 1		
Mg	51.23	61.63
Al	24.36	29.25
Zn	5.54	5.23
Mn	0.11	0.06
Si	0.17	0.20
Fe	0.08	0.05
Cu	0.72	0.36
Pb	17.79	3.22
Analysis 2		
Al	50.32	60.88
Mn	37.05	34.53
Zn	0.78	0.28
Si	0.46	0.3
Fe	0.4	0.11
Cu	0.39	0.20
Pb	0.57	0.21
Ce	10.03	3.49

Table 4. Results of the quantitative analysis of chemical composition magnesium cast alloy MCMgAl6Zn1 after cooling in the furnace

According to the relations given by S. Guldberga and N. Ryuma (Guldberg and Ryum, 2000) which occured in the eutectic microstructure in the Mg alloys containing 33% Al. Some of the precipitations in the srudied magnesium alloys after solution heat treatment and ageing show an orientation, where the plains of the family {110} $Mg_{17}Al_{12}$ are rotated about 10° compared to the plains of the $\{1\bar{1}01\}$ family of the α - Mg solid solution, moreover other plains show bigger rotation value as given by S. Guldberga and N. Ryuma (Guldberg and Ryum, 2000). Precipitation of the γ - $Mg_{17}Al_{12}$ phase are mostly of the shape of roads, and the prevailing growing directions are the directions $\langle 110 \rangle$ α - Mg (Figs. 10,11).

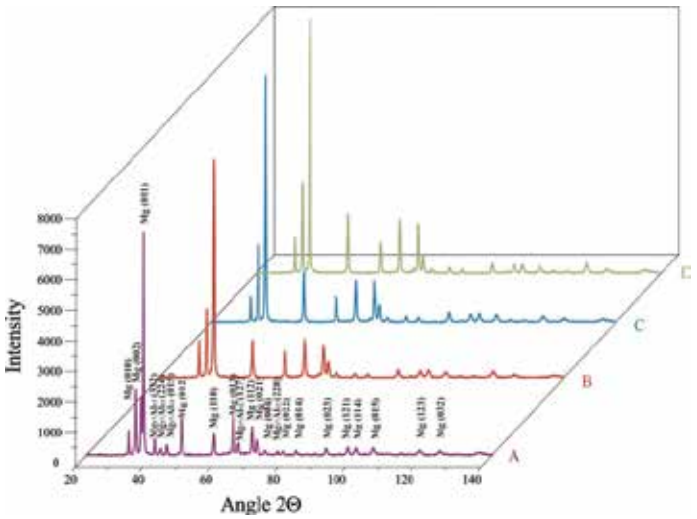

Fig. 9. X ray diffraction pattern of the magnesium cast alloys: A - MCMgAl12Zn1, B - MCMgAl9Zn1, C - MCMgAl6Zn1, D - MCMgAl3Zn1 after agening treatment

A part of them shows the following relation (Fig. 10):

$$(1\bar{1}01)\alpha\text{-Mg}||(10\bar{1})Mg_{17}Al_{12}$$
$$[11\bar{2}0]\alpha\text{-Mg}||[111]Mg_{17}Al_{12}$$

Influence of the aluminium content and heat treatment on properties of the cast magnesium alloys are presented on Fig. 12. Hardness increases together with the increase of aluminium content in the analyzed alloys from 3 to 12%. The highest hardness of 75 HRF in as cast state occurs in case of the MCMgAl12Zn1 alloy casts. This value is about two times higher compared to the MCMgAl3Zn1 alloy with a value of 30 HRF. Heat treatment applied on the material (solution heat treatment and ageing) causes a hardness increase. The MCMgAl12Zn1, MCMgAl9Zn1 and MCMgAl6Zn1 alloys have reach the highest hardness after ageing, adequately 94, 75 and 53 HRF and after solution heat treatment and cooling with furnace 85, 71 and 52 HRF. For cases after solution heat treatment hardness slightly decreases compared to the initial state. For MCMgAl3Zn1 casts the highest hardness have the samples after ageing and cooling in water - 41 HRF, for other cases the hardness values are similarly to each other.

The influence of aluminium content and heat treatment on the tensile strength of the cast magnesium alloys was showed on Figures 13 and 14. Results of the tensile strength test allows it to determine and compare the mechanical properties of the investigated cast magnesium alloys in as cast state and after heat treatment applied. On the basis of the performed investigations it was state, that the highest tensile strength in as cast state is characteristic for the MCMgAl6Zn1 and MCMgAl3Zn1 alloy - 192.1 and 191.3 MPa respectively, theses alloys have also the highest elongation value in as cast state – 11.6 and 15.2 %.

It was showed, that the increase of aluminium content from 6 to 12 % decreases the tensile strength in as cast state to the value of 170.9 MPa. Heat treatment like solution heat treatment and cooling with furnace causes increase of tensile strength (Fig. 13).

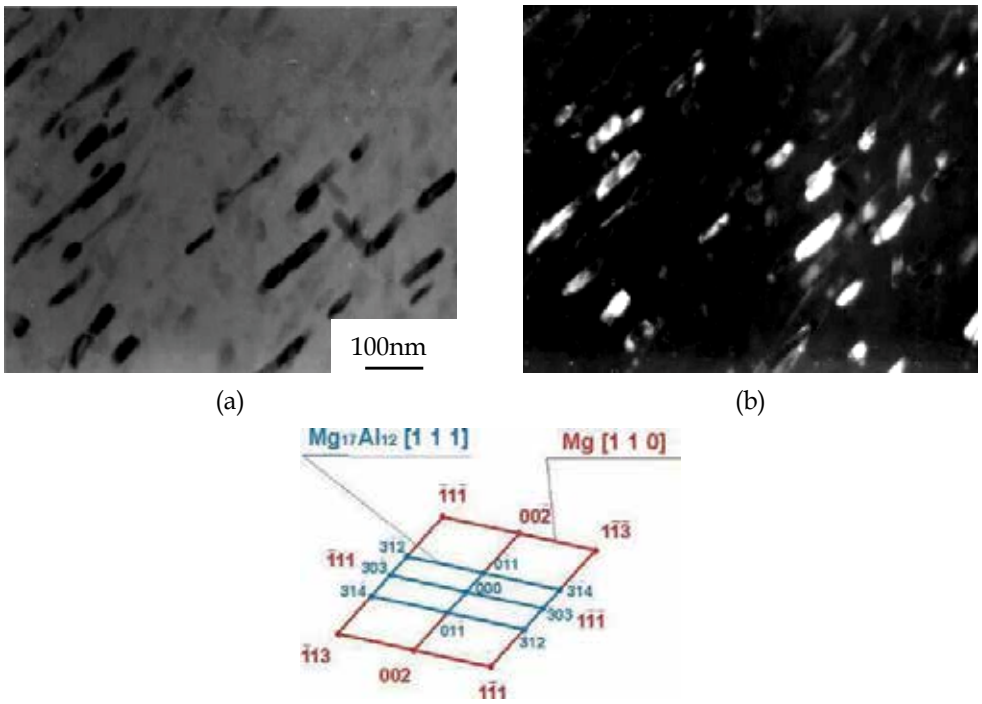

Fig. 10. a), b) Bright and dark field (with spot ($\overline{3}\overline{1}4$)) image of the MCMgAl9Zn1 alloy after aging treatment with solid solution α – Mg (matrix) and an intermetallic secondary phase γ – $Mg_{17}Al_{12}$ in the form of needle precipitations, c) diffraction pattern of area shown in a), d) part of solution for diffraction pattern shown in c

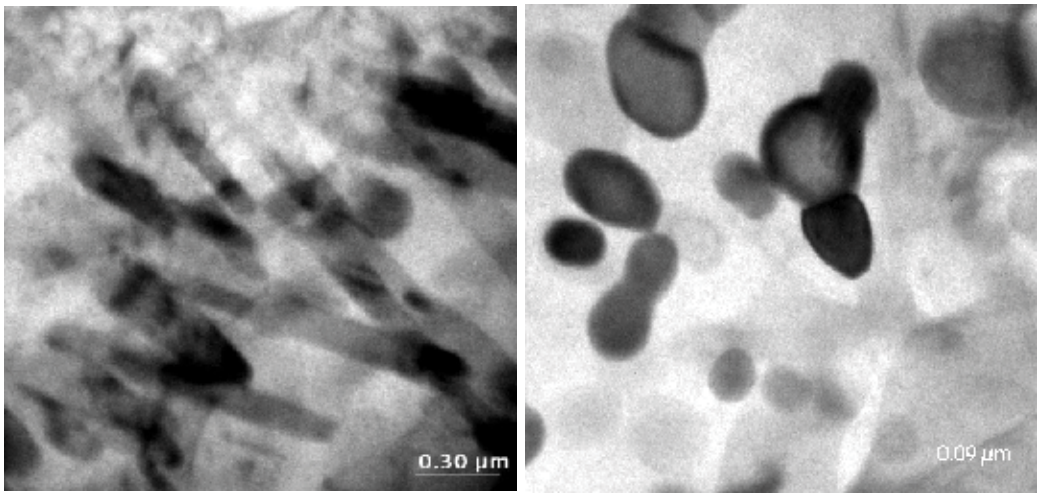

Fig. 11. TEM image examples of the intermetallic secondary phase γ – Mg17Al12 in the form of needle precipitations from the MCMgAl9Zn1 alloy after aging treatment

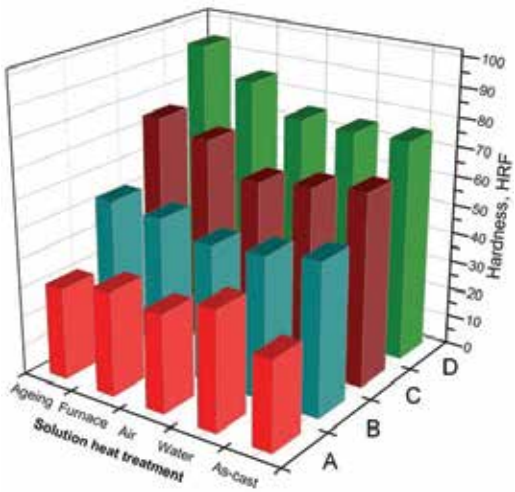

Fig. 12. Results of HRF hardness measurements of magnesium cast alloys: A –MCMgAl3Zn1, B – MCMgAl6Zn1, C – MCMgAl9Zn1, D – MCMgAl12Zn1

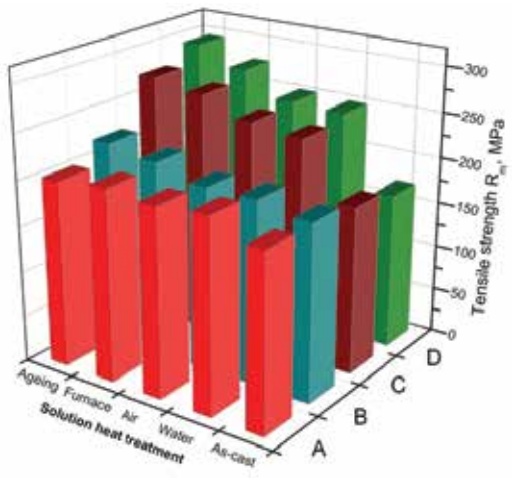

Fig. 13. Results of tensile strength Rm measurements of magnesium cast alloys: A – MCMgAl3Zn1, B – MCMgAl6Zn1, C – MCMgAl9Zn1, D – MCMgAl12Zn1

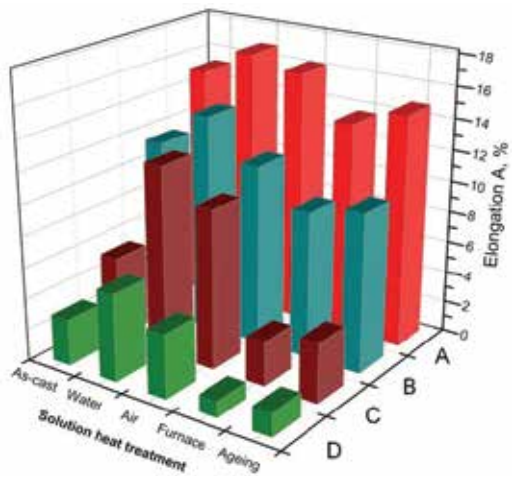

Fig. 14. Results of elongation A measurements of magnesium cast alloys: A – CMgAl3Zn1, B – MCMgAl6Zn1, C – MCMgAl9Zn1, D – MCMgAl12Zn1

3.2 Thermal analysis

An example of the cooling and crystallization curve of the Mg-Al-Zn alloy cooled with different cooling rates are presented on Figure 15. The performed crystallization process analysis on the basis of the achieved curves allows it to state, that the nucleation process of the α phase begins at the T_{DN} temperature. This effect is present on the curve in form of an inflexion in point I, as well in form of an instantaneous decrease of the cooling rate. Decrease of the crystallisation rate of the remaining liquid metal is caused by the heat provided from the α phase nuclei, which is smaller compared to the heat amount submit into the

surrounding by the solidified metal. This process ends in point II, where the crystallization temperature achieves the minimal value - T_{Dmin}, where the α phase crystals begins to growth. In this point the derivative value achieves the zero value. The cooled alloy, resulting in crystallisation heat emission, reheats the remaining liquid until the T_{DKP} (point III) temperature. The further crystal growth causes an increase of the temperature of the remaining liquid to the maximal crystallisation temperature of the α phase – T_G (point IV). Further alloy cooling causes the beginning of crystallisation of the silicon, aluminium and manganese- rich phases, which are emitting an additive heat amount present on the crystallisation curve in form of clear heat effect – described as $T_{(Mg+Si+Al+Mn)}$ and $T_{(Mg+Si+Al+Mn)f}$ (points V and VI). As a result of further alloy cooling after reaching the $T_{E(Mg+Al)N}$ temperature there occurs the nucleation of the α+γ eutectic (point VII). The cooled alloy reach the $T_{E(Mg+Al)min}$ (point VIII) temperature, as next the temperature increases until the maximum crystallisation temperature of the eutectic $T_{E(Mg+Al)G}$ (point IX). The alloy crystallisation ends in point X, where the T_{sol}. Value is reached. In Table 5 there is presented ten crystallisation temperature of the particular phases as well the solid state fraction for a chose example.

On Figure 17 there is presented the solid state fraction change as well the heat flux generated by the crystallised phases. This information is used for determination of the crystallising heat emitted by the particular phases (Table 6). On Figure 17 there is also presented the influence of the cooling rate as well the magnesium content on the temperature - T_{DN} of the *a* phase nucleation. On the basis of the performed investigation it was found that the biggest influence on the nucleation temperature has the aluminium content (it decreases the nucleation temperature of the *a* phase according to the liquidus line) as well the cooling rate (it causes an increase of the *a* phase nucleation temperature). For example for the MCMgAl3Zn1 alloy an increase of the cooling rate from 0.6 to 1.2°C/s causes an increase of the *a* phase nucleation temperature from 633.16 to 635.39°C, further increase of the cooling rate until 2.4°C/s causes a temperature growth until 640.32°C.

On Figure 18 there is presented the influence of the magnesium mass concentration as well the cooling rate on the maximal crystallisation temperature (T_G) of the *a* phase. On the basis

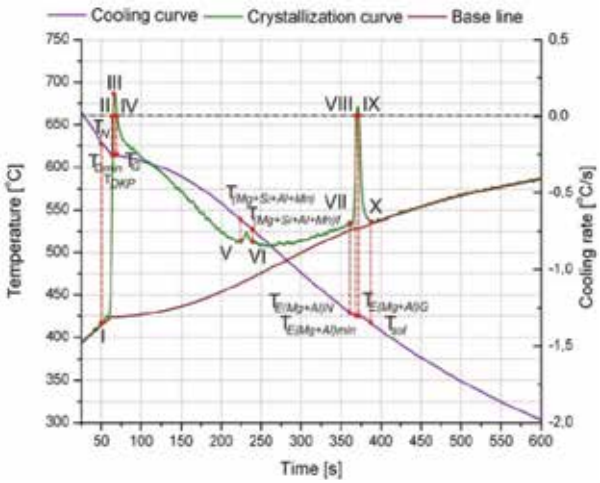

Fig. 15. Representative cooling, crystallization and calorimetric curves with characteristics points of crystallization process of MC MgAl6Zn1 alloy cooled at 0.6°C/s

Temperature, T; time, t; fraction solid, f_s	Avarage	Confidence interval		Standard deviation	Error, %
		-95%	+95%		
T_{DN}	615.88	611.66	620.09	3.40	0.55
T_{Dmin}	611.51	609.12	613.91	1.93	0.32
f_s	1.96	1.35	2.57	0.49	24.96
T_{DKP}	611.75	609.34	614.16	1.94	0.32
f_s	3.16	2.42	3.9	0.6	18.86
T_G	611.92	609.45	614.39	1.99	0.33
f_s	5.44	4.35	6.52	0.87	16.07
$T_{(Mg+Si+Al+Mn)}$	533.65	527.69	539.62	4.81	0.9
f_s	85.28	82.83	87.73	1.97	2.31
$T_{(Mg+Si+Al+Mn)f}$	520.18	513.3	527.05	5.54	1.06
f_s	88.08	85.74	90.42	1.89	2.14
$T_{E(Mg+Al)N}$	429.45	426.56	432.34	2.33	0.54
f_s	95.02	93.84	96.21	0.95	1.00
$T_{E(Mg+Al)min}$	426.59	423.81	429.36	2.23	0.52
f_s	96.03	94.72	97.34	1.05	1.10
$T_{E(Mg+Al)G}$	427.17	424.08	430.27	2.49	0.58
f_s	97.96	97.39	98.53	0.46	0.47
T_{sol}	419.47	415.42	423.52	3.26	0.78

Table 5. Thermal characteristic of MCMgAl6Zn1 alloy cooled at 0.6°C/s

Specific heat in liquid state Cp_l, J/g·°C	Specific heat in solid state Cp_s, J/g·°C		Weight, g
1.21	1.01		8.99
Reaction	Latent heat of crystallization process		Participation, %
	Per sample, J	Per 1 gram of sample, J/g	
$L \rightarrow \alpha(Mg)$	1258.22	139.96	86.31
$L \rightarrow \alpha(Mg)+Mg_2Si+(Al+Mn)$	143.63	15.98	9.85
$L \rightarrow \alpha(Mg)+\gamma(Mg_{17}Al_{12})$	55.98	6.23	3.84
Razem	1457.84	162.16	100

Table 6. Latent heat of crystallization emitted during solidification and its participation in general latent heat of MC MgAl6Zn1 cooled at 0.6 °C/s

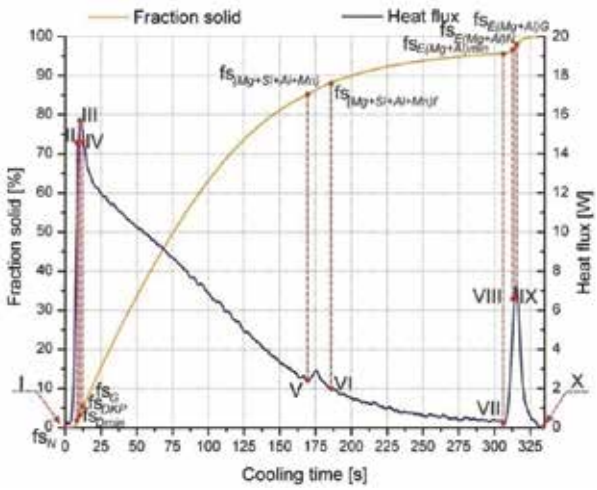

Fig. 16. Representative curves illustrate changes of heat flux and fraction solid of MCMgAl6Zn1 alloy MCMgAl6Zn1 cooled at 0.6°C/s

of the performed investigation it was found that the change of the cooling rate does not influence the maximal crystallisation temperature *(T_G)* of the *a* phase. It was also found that the T_G temperature decreases together with the increase of the aluminium content. For example for the alloys cooled with a rate of 0.6°C/s, the increase of aluminium content from 3 to 6% causes a decrease of the maximal crystallisation temperature of the *a* phase from 630.85 to 611.92°C, and a further increase of the aluminium content of 9% causes a decrease of the temperature value to 592.91°C. The lowest values of the maximal *a* phase crystallisation temperature - equal 576.03°C, was observed for the alloy with 12% aluminium content.

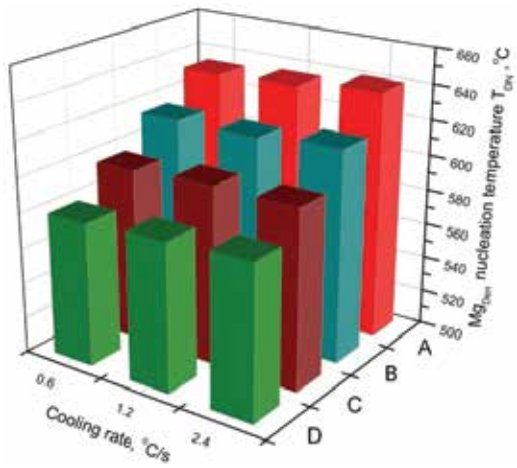

Fig. 17. Influence of cooling rate on Mg_{Den} nucleation temperature (T_{DN}):
A – MCMgAl3Zn1, B – MCMgAl6Zn1,
C – MCMgAl9Zn1, D – MCMgAl12Zn1

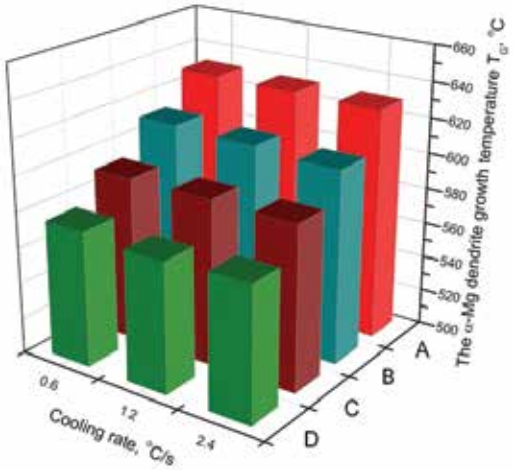

Fig. 18. Influence of cooling rate on Mg dendrite growth temperature (T_G):
A – MCMgAl3Zn1, B – MCMgAl6Zn1,
C – MCMgAl9Zn1, D – MCMgAl12Zn1

On Figure 19 there is presented the influence of cooling rate as well the influence of aluminium mass content on the heat amount emitted during the alloy crystallisation. On the basis of the performed calculations it was found, that the biggest influence on the heat (Q_c) increase generating during alloy crystallisation has the variable aluminium content. An increase of thee aluminium content in the investigated alloys causes an increase of the heat Q_c. In case of an increase of the cooling rate there was observed a small growth of the generating crystallisation heat except the MCMgAl3Zn1 alloy.

The carried out investigations revealed, that the grain size decreases together with the cooling rate increase for each of the analysed alloys. On the basis of the performed investigations it was found that the largest grain size is characteristic for the MCMgAl6Zn1 alloy (Table 7). A cooling rate change from 0.6 to 2.4°C/s causes a two times decrease of the grain size. A similar dependence was found also for other analysed alloys, which were studied in this investigation. An increase of the aluminium mass concentration causes a slightly decrease of the grain size (Fig. 20).

Figure 21 shows the influence of aluminium mass concentration as well the cooling rate on hardness of the investigated alloys. On the basis of the performed investigations it was found a linear increase of the hardness compared to the increase of the aluminium content, and also an increase of the cooling rate for the MCMgAl6Zn1, MCMgAl9Zn1 and MCMgAl12Zn1 alloy. For the MCMgAl3Zn1 alloy it was found a hardness increase up to 26 HRF by a cooling rate of 1.2°C/s. A cooling rate increase up to 2.4°C/s causes a decrease of the hardness down to 19 HRF. The highest hardness value of 74 HRF was achieved for the MCMgAl12Zn1 alloy cooled with a rate of 2.4°C/s.

Figure 22 presents the influence of aluminium mass concentration as well the cooling rate on the ultimate compressive strength. On the basis of the performed investigations it was found that the highest value of the ultimate compressive strength of 296.7 MPa has the MCMgAl6Zn1 alloy, and the lowest value of 245.9 MPa the MCMgAl3Zn1 alloy (both alloys cooled with a rate of 0.6°C/s). A change of the cooling rate of the analysed alloys causes an increase of the ultimate compressive strength. The highest increase of the R_c value in

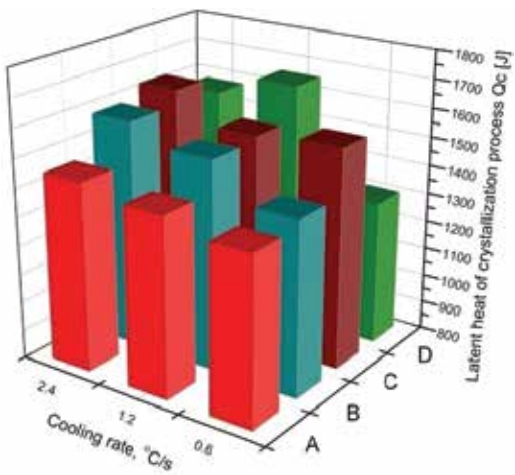

Fig. 19. Influence of cooling rate on latent heat of crystallization process:
A – MCMgAl3Zn1, B – MCMgAl6Zn1,
C – MCMgAl9Zn1, D – MCMgAl12Zn1

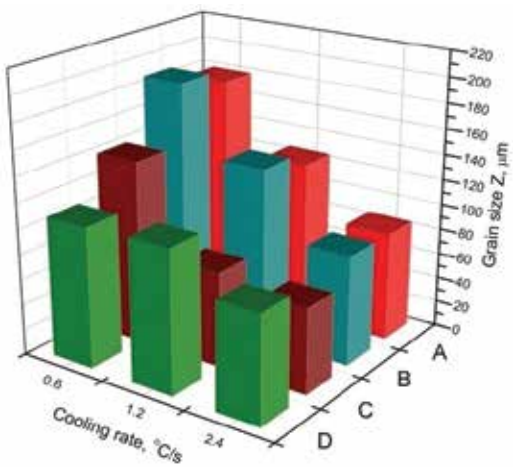

Fig. 20. Influence of cooling rate on grain size: A – MCMgAl3Zn1, B – MCMgAl6Zn1, C – MCMgAl9Zn1, D – MCMgAl12Zn1

comparison to the cooling rate increase was found in case of the MCMgAl3Zn1 and MCMgAl9Zn1 alloy. An increase of the cooling rate up to the maximum value causes an increase of the ultimate compressive strength for the MCMgAl3Zn1 and MCMgAl9Zn1 alloy up to the value of 275.8 and 316 MPa adequately, as well is ca. 10-15 MPa higher in case of the MCMgAl6Zn1 and MCMgAl12Zn1 materials.

Alloy	Cooling rate, °C/s	Grain size Z, μm	Confidence interval		Standard deviation	Error, %
			-95%	+95%		
MCMgAl3Zn1	0.6	179.26	154.38	204.14	20.04	11.18
	1.2	125.48	115.20	135.75	8.28	6.6
	2.4	85.4	77.11	93.68	6.67	7.82
MCMgAl6Zn1	0.6	190.3	177.87	202.74	10.01	5.26
	1.2	137.05	123.54	150.56	10.88	7.94
	2.4	86.28	80.27	92.29	4.84	5.61
MCMgAl9Zn1	0.6	143.53	114.83	172.24	23.12	16.11
	1.2	74.46	59.24	89.69	12.26	16.47
	2.4	66.73	52.8	80.66	11.22	16.82
MCMgAl12Zn1	0.6	110.39	83.01	137.76	22.05	19.97
	1.2	112.26	109.59	114.94	2.15	1.92
	2.4	84.58	74.73	94.44	7.94	9.39

Table 7. Grain size of MCMgAl3Zn1, MCMgAl6Zn1, MCMgAl9Zn1, MCMgAl12Zn1 cooled with different cooling rates

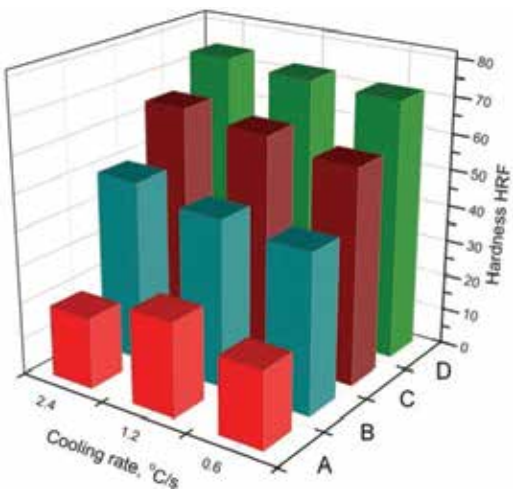

Fig. 21. Influence of coolng rate on hardness: A – MCMgAl3Zn1, B – MCMgAl6Zn1, C – MCMgAl9Zn1, D – MCMgAl12Zn1

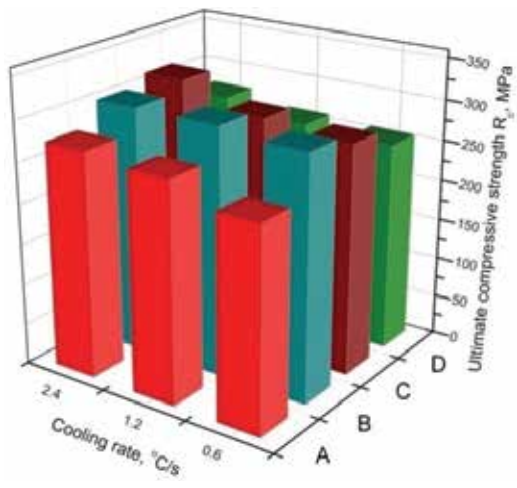

Fig. 22. Influence of coolng rate on ultimate compressive strength R_C: A – MCMgAl3Zn1, B – MCMgAl6Zn1, C – MCMgAl9Zn1, D – MCMgAl12Zn1

3.3 Laser treatment

The shape of the laser face performed on the MCMgAl3Zn1, MCMgAl6Zn1, MCMgAl9Zn1, MCMgAl12Zn1 cast magnesium alloy after laser alloying with carbides and aluminium oxide using high power diode laser HPDL is presented on Figure 23. It was found a clearly influence of the process parameters, particularly power of the laser beam as well ceramic powders used on the shape and topography of the surface. The laser face, after alloying with the TiC and WC powders using the feeder is characterised by a regular, flat surface (Fig. 23a, b). In case of vanadium carbide the laser face is characterised by a flat shape of the remelting area, however with visible discontinuities of the surface layer. The investigated material after SiC powder alloying is characterised by a clear relief of the remelting area standing over the surface level of the non remelted material (Fig. 23c). After NbC powder remelting, the surface layer of the cast magnesium alloys is characterised by very irregular surface and some break flows of the material present outside of the laser face. Where as the appliance of Al_2O_3 powder causes some small hollows in the middle of the lacer face in case of 2.0 kW laser power. On Figure 23d there is presented the laser face of the MCMgAl3Zn1 cast magnesium alloy after alloying with Al_2O_3 powder using 1.6 laser power, where the laser treatment was interrupt. Investigations reveal, that the laser power increase by a stable laser beam scanning rate influences the size of the remelting area , where some structural changes occur in the surface layer of the Mg-Al-Zn alloys. The power of the laser beam is also related

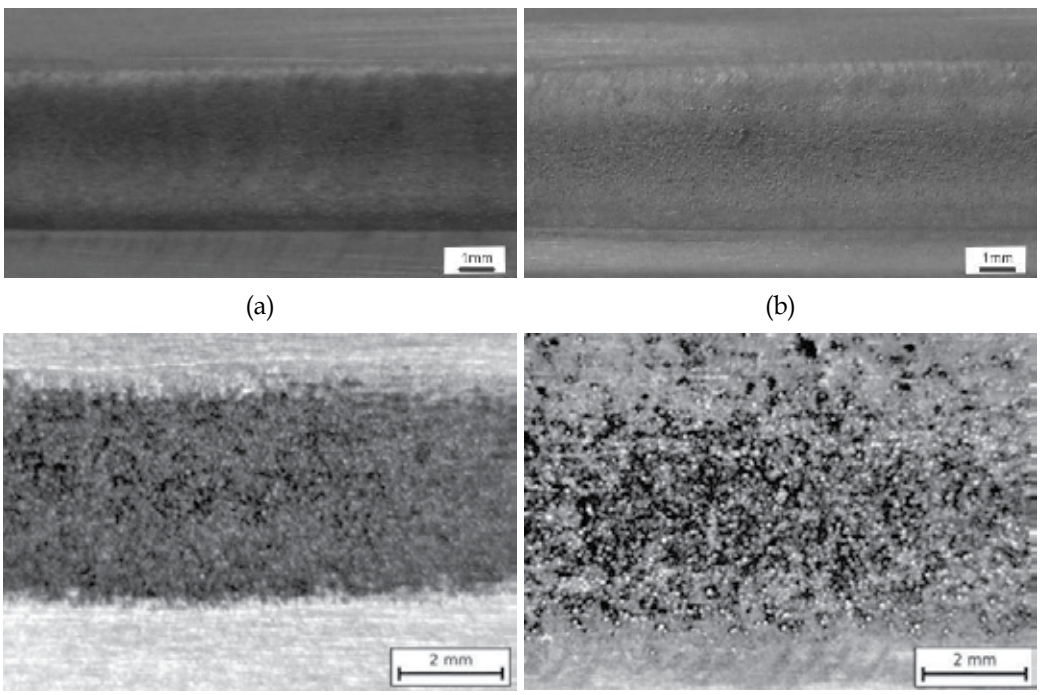

Fig. 23. Surface layer face of the magnesium cast alloy: a) MCMgAl3Zn1 alloyed with TiC, laser power 1.2 kW, alloying speed 0.75 m/min; b) MCMgAl3Zn1 alloyed with WC, laser power 1.6 kW, alloying speed 0.75 m/min; c) MCMgAl3Zn1 alloyed with SiC, laser power 1.6 kW, alloying speed 0.75 m/min; d) MCMgAl12Zn1 alloyed with Al_2O_3, laser power 2.0 kW, alloying speed 0.50 m/min

to the shape of the bottom of the remelting area as well the convexity of the laser face, which depends also on strong liquid metal movements during the remelting process.
On the basis of roughness measurements of the surface of the cast magnesium alloys after laser alloying with the titanium, tungsten, vanadium, silicon and aluminium oxide (Fig. 24) it was state, that apart from the applied ceramic powder, the roughness of the surface layers abstained by laser remelting of the Mg-Al-Zn alloys with a power in the range of 1.2 ÷ 2.0 kW increases and reach a value in the range of R_a = 6.4 – 42.5 µm.
For each type of substrate (independent of the aluminium content) the highest roughness have the samples after laser alloying by a scanning rate of 0.5 m/min with laser power of 2.0 kW. By a stable scanning rate and a not changed powder feeding, together with an increase of the laser power the surface roughens decreases. Among the investigated Mg-Al-Zn cast magnesium alloys the lowest roughness respectively 4.0 and 5.6 µm have the MCMgAl9Zn1 and MCMgAl12Zn1 materials after alloying with VC powder, by applied laser power of 2.0 kW. A maximal measured surface roughness of R_a = 42.5 µm occurs in case of the surface layer of the MCMgAl9Zn1 alloy after laser alloying with SiC powder with laser power of 1.2 kW. The investigated material after alloying with titanium carbide powder are characterised by a roughness in the range of 6.4-13.9 µm. In case of vanadium carbide powder it was found, that the highest roughness value, by a stable scanning rate of 0.75 m/min, for each type of alloy, have the samples after alloying with 1.2 kW laser power, whereas the highest roughness value has the MCMgAl3Zn1 alloy by applied laser power of 1.2 kW (25.43 µm). An increase of the irregularity of the surface after laser treatment is related to the fluctuation of the alloyed material caused by changes of the remelting material tensions as well the laser beam energy absorbed by the alloyed material.

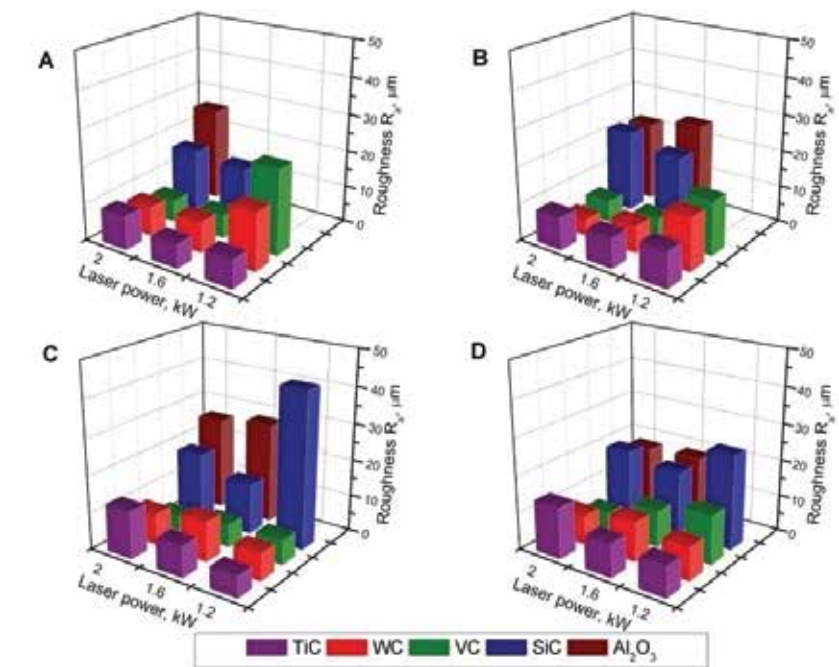

Fig. 24. Laser power and Al mass concentration influence on roughness of alloyed surface layer: A – MCMgAl3Zn1; B – MCMgAl6Zn1 ; C – MCMgAl9Zn1; D – MCMgAl12Zn1

On Figure 25 there is presented the zone placement on the cross section of the remelting laser face of the Mg-Al-Zn cast magnesium alloys. On the basis of the performed metallographic investigations it was found, that in each of the surface layer after surface laser treatment of the MCMgAl12Zn1 and MCMgAl9Zn1 cast magnesium alloys occur a remelting zone (RZ) as well a heat affected zone (HAZ). These zones, depending on the laser power as well the ceramic powder used have a different thickness and shape. In case of the TiC, WC and VC powder for the MCMgAl6Zn1 alloy it was found a very small HAZ, which increases together with the laser power applied. In case of alloying of the ceramic powder into the surface of the MCMgAl3Zn1 alloys there is present only the remelting zone as well the boundary between the remelting zone and the material substrate. On the basis of the performed investigations it is possible to state that the change of the laser power by a constant alloying rate clearly influences the thickness of both zones in the surface layer. The applied laser power influences also the shape and the convexity of the remelting zone (Fig. 25), which reach over the surface of the untreated material.

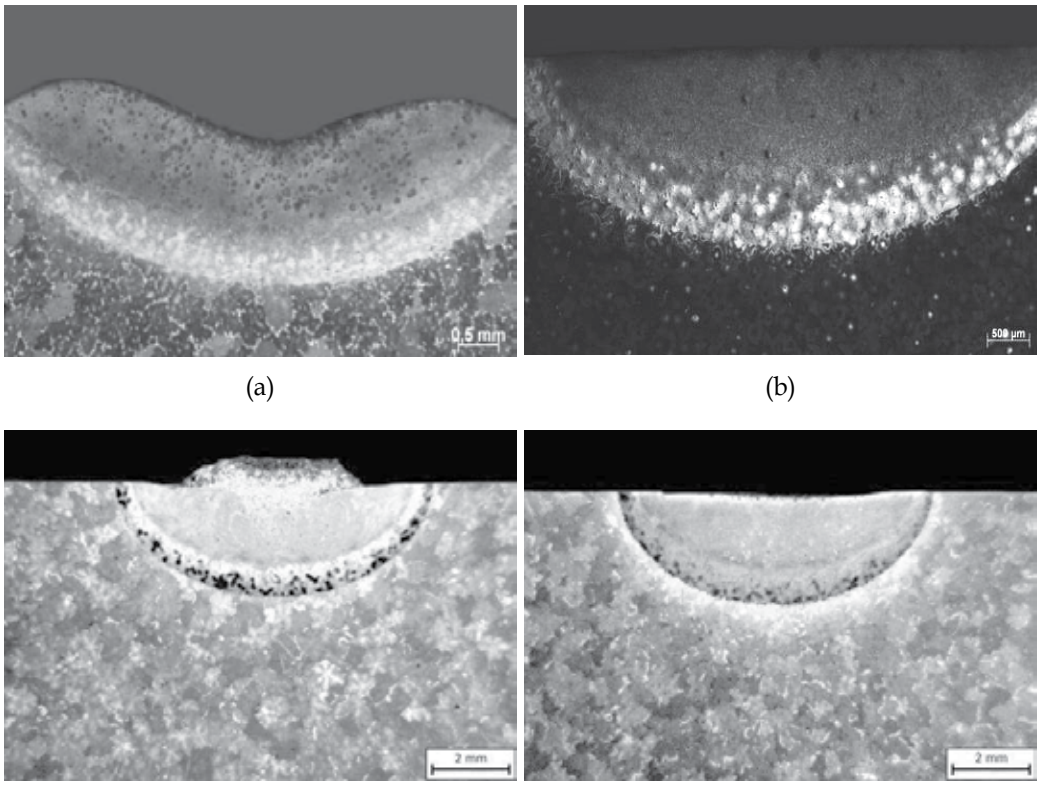

(a) (b)

(c) (d)

Fig. 25. Surface layer of the magnesium cast alloy: a) MCMgAl9Zn1 alloyed with TiC, laser power 1.2 kW, alloying speed 0.75 m/min; b) MCMgAl9Zn1 alloyed with WC, laser power 1.2 kW, alloying speed 0.75 m/min; c) MCMgAl12Zn1 alloyed with SiC, laser power 2.0 kW, alloying speed 0.75 m/min; d) MCMgAl12Zn1 alloyed with Al_2O_3, laser power 2.0 kW, alloying speed 0.50 m/min

Results of the metallographic investigations show that the structure of the solidified material after laser alloying is characterised by the occurrence of areas with different morphology connected to the crystallisation of the magnesium alloys (Fig. 26). As a result of the laser alloying a structure is achieving which is free of defects and with a clear grain refinement. The structure of the laser modified layer contains mainly dispersive particles of the applied carbide powder TiC, WC, VC, SiC, NbC or Al_2O_3 oxide placed in the matrix of the Mg-Al-Zn alloy.

Morphology of the treated area after laser alloying is mainly compound of dendrites wit plate shaped $Mg_{17}Al_{12}$ eutectic and Mg present in the interdendritic space, where the main growing axes are directed according to the heat transport directions. This can be interpret with a occurrence of a non-normal eutectic with a small amount of α-Mg in the eutectic solution. Moreover the composite structure of the area after laser treatment results from the hypo-eutectic alloy change to a hyper-eutectic one, depending from the alloyed elements distribution and the change of the process condition parameters of the laser treated surface.

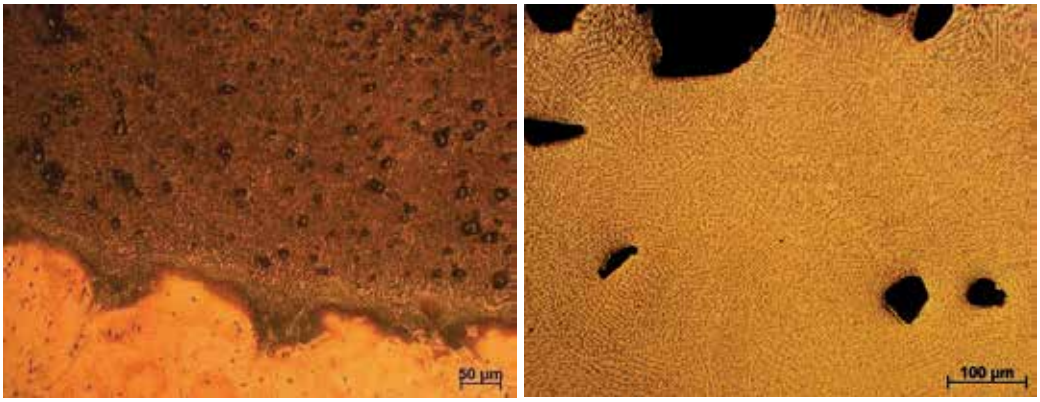

(a) (b)

Fig. 26. Microstructure of the: a) edge of remelted zone of MCMgAl6Zn1 alloyed with TiC, laser power 1.6 kW, alloing speed 0.75 m/min; b) middle of surface layer of MCMgAl3Zn1 alloyed with Al2O3, laser power 2.0 kW, alloying speed 0.50 m/min

Investigations carried out on the scanning electron microscope confirm the occurrence of the zones in the surface layer of the investigated cast magnesium alloys (Fig. 27). In the remelted zone there is present a dendritic structure build according to the heat transport directions, there are also present the alloyed powder particles of the carbides or aluminium oxide. The morphology after surface laser treatment, including the amount and distribution of the carbide particles, depends on the applied laser parameters. On the basis of the metallographic investigations of the MCMgAl3Zn1, MCMgAl6Zn1, MCMgAl9Zn1, MCMgAl12Zn1 alloys it was found a uniform distribution - on the whole remelting zone – of the used carbide particles TiC, WC and Al_2O_3. (Fig. 27a, c). In case of alloying of the SiC particles with laser power of 1.2 kW, the carbides are mainly located on the top of the surface layer. For power of 2.0 and 1.6 kW in samples of the MCMgAl12Zn1 and MCMgAl9Zn1 material, caused by a strong movement of the liquid metal in the melting area, the SiC particles are distributed over the whole area of the remelting zone. After alloying with vanadium carbide in the surface of the cast magnesium alloys there was observed only a sporadically occurrence of the carbide in the remelting area (Fig. 27b). A

similar regularity was found in case of niobium carbide, the alloyed material was not revealed in the structure of the remelting zone or was found near the top of the surface of the composite layer (Fig. 27d). In cast magnesium alloys alloyed with NbC powder there were found small cracks and breaks in the surface layer of the material.

X-Ray diffraction diagrams of Mg-Al-Zn cast magnesium alloys after laser alloying with WC, TiC, VC, SiC carbides and Al_2O_3 oxide confirm the occurrence of α – Mg phase, γ – $Mg_{17}Al_{12}$ phase, as well of picks coming from the powders using for alloying (Fig. 28).

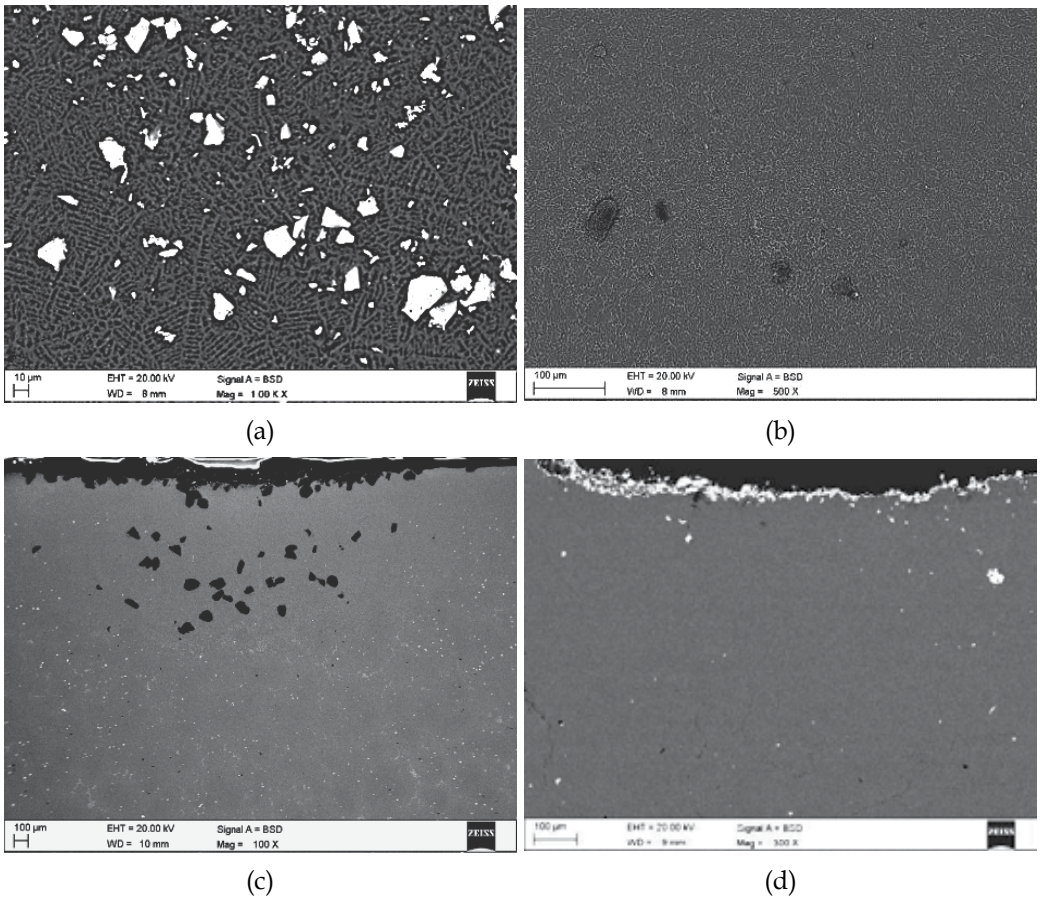

Fig. 27. Microstructure of the : a) middle of remelted zone of MCMgAl3Zn1 alloyed with TiC, laser power 1.2 kW, alloying speed 0.75 m/min; b) middle of remelted zone of MCMgAl12Zn1 alloyed with VC, laser power 1.6 kW, alloying speed 0.75 m/min; c) surface layer of MCMgAl9Zn1 alloyed with Al_2O_3, laser power 2.0 kW, alloying speed 0.50 m/min; d) surface layer of MCMgAl6Zn1 alloyed with NbC, laser power 2.0 kW, alloying speed 0.25 m/min

Line EDS analysis as well the area EDS analysis of the elements distribution on cross-section of the surface layer of laser treated Mg-Al-Zn cast magnesium alloys using TiC, WC, VC, SiC and Al_2O_3 powders confirm the occurrence of magnesium, aluminium, zinc, manganese, carbide, as well respectively titanium, tungsten, vanadium, silicon, as well

oxygen in the laser modified surface layer, the results reveal also a lack of occurrence of the alloyed particles.

On the basis of the results achieved from thin foils investigation of the cast magnesium alloys after laser alloying of TiC and WC powder it was confirmed the occurrence of the TiC (Fig. 29) and WC (Fig. 30).

The micro hardness test results performed on cross-section of the laser face measured in function of the distance from surface are presented on Figure 31. The substrate material is characterised by a hardness in the range of 50 $HV_{0,1}$ to 100 $HV_{0,1}$, whereas the remelting zone has a hardness in the range 150 to 700 $HV_{0,1.}$ The performed investigation show, that the micro hardness decreases with the distance from the top to the substrate direction, which is probably cussed by a fine grained structure in the top of the surface layer as well by the occurrence of hard carbides used for alloying. In some areas there occur some significant differences in the precision of measurements, probably caused by an irregular distribution of the hard particles.

Micro hardness of the MCMgAl6Zn1 cast magnesium alloys in the heat affected zone is similar to the micro hardness value of the substrate material after laser treatment (Fig. 31a,b), whereas in case of the MCMgAl12Zn1 and MCMgAl9Zn1 alloys there was found a decrease of the micro hardness in the heat affected zone which is below the value of the substrate material (Fig. 31c,d).

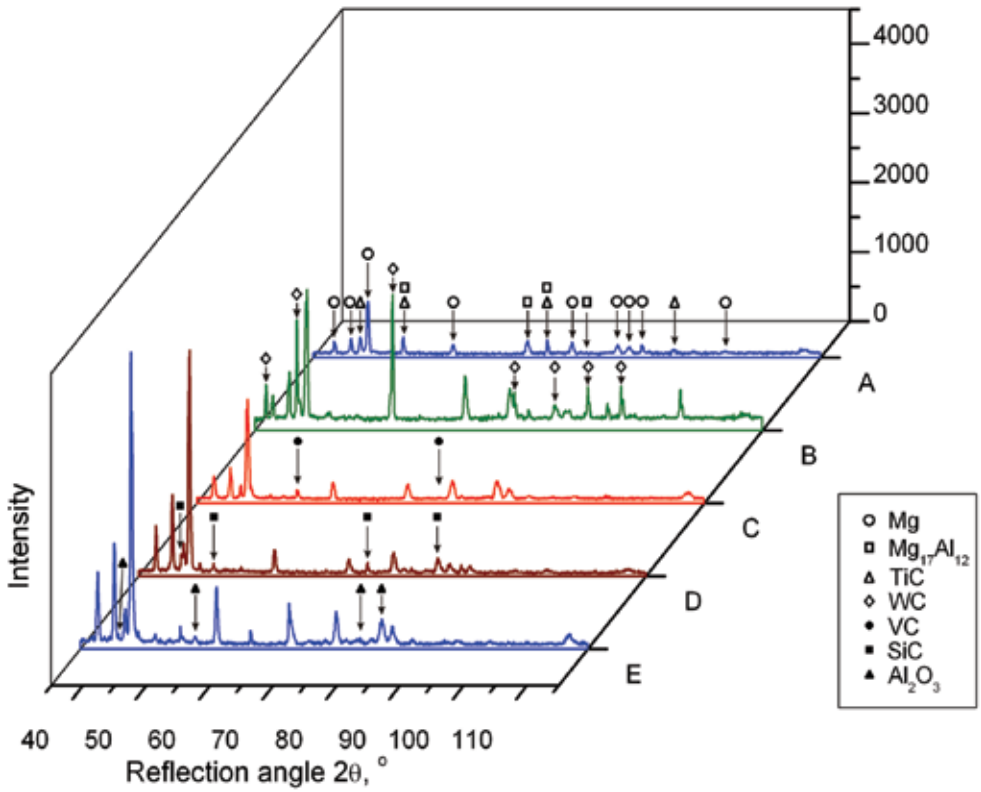

Fig. 28. X ray diffraction pattern of the magnesium cast alloy MCMgAl12Zn1 alloyed with: A – TiC; B – WC; C – VC; D – SiC; E – Al_2O_3

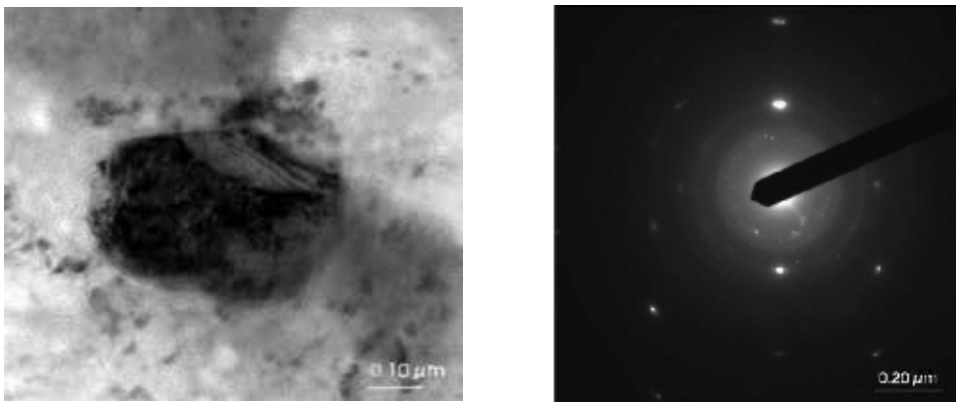

(a) (b)

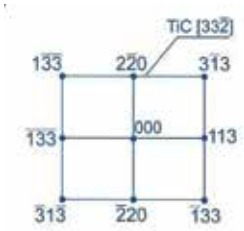

(c)

Fig. 29. TEM image of the surface layer of MCMgAl9Zn1 alloy after alloing with TiC: a) bright field; b) diffraction pattern of area shown in a), c) part of solution for diffraction pattern shown in b

7. Conclusion

The results are summarized as follows:

- The new developed experimental as-cast cast magnesium alloys MCMgAl12Zn1, MCMgAl9Zn1, MCMgAl6Zn1, MCMgAl3Zn1 are showing an α solid solution microstructure, which is the matrix, intermetallic γ – $Mg_{17}Al_{12}$ phase in a shape of plates, placed manly at grain border regions, needle shaped eutectic (α+γ) as well Mg and Si containing precipitations characterized by edged outlines, also steroidal or needle shaped phases with high Mn and Al concentration are present.
- Solution treatment wit cooling in water and in air causes solution of the γ – $Mg_{17}Al_{12}$ in the matrix and exists only in a small amount together with single phases containing silicon and manganese. Ageing with air cooling after solution treatment in water causes a precipitation of homogeny distributed $Mg_{17}Al_{12}$ in the matrix in form of needle shaped precipitations, coming into existence also in form of pseudo-eutectic areas. Dispersive precipitations in the solid solution in the aged magnesium alloys have in mostly investigated an preferred crystallographic orientation with the matrix. A part of the show a relation like:

$$(1\bar{1}01)\alpha\text{-Mg}\|(10\bar{1}1)Mg_{17}Al_{12}$$
$$[11\bar{2}0]\alpha\text{-Mg}\|[111]Mg_{17}Al_{12}$$

γ - $Mg_{17}Al_{12}$ phase precipitation have mostly a shape of rods and plates, a prevailing growing direction are the directions from the <110> family of the α-Mg phase.

- Precipitation hardening causes changes of mechanical properties. The highest hardness increase in as cast alloy and after ageing show casts from the MCMgAl12Zn1 alloy with a value of 75.4 and 94.6 HRF. The smallest average mass loss of the tribologic examined samples, connected with an increased hardened phase amount, particularly the $Mg_{17}Al_{12}$ phase and the applied heat treatment, occurs for the MCMgAl12Zn1 alloys.
- The highest strength value in as-cast state have the MCMgAl6Zn1 and MCMgAl3Zn1 alloys, which have also the highest elongation in as-cast state. It was showed , that an increase of the Al concentration from 6 to 12% decreases the strength value in as-cast state. The maximal yield strength was achieved for the MCMgAl12Zn1 alloys, slightly higher for the MCMgAl9Zn1 alloy. In as-cast state the lowest elongation show the MCMgAl12Zn1 material with 12% aluminium content, more then fife times lower compared to the elongation value of the MCMgAl3Zn1 alloy. After ageing with cooling in air the maximum strength increase of 124 1.7 MPa and a yield strength of 20 MPa was achieved for the MCMgAl12Zn1 alloy. The alloys after ageing are characterized by a slightly decreasing elongation value compared to the as-cast state.

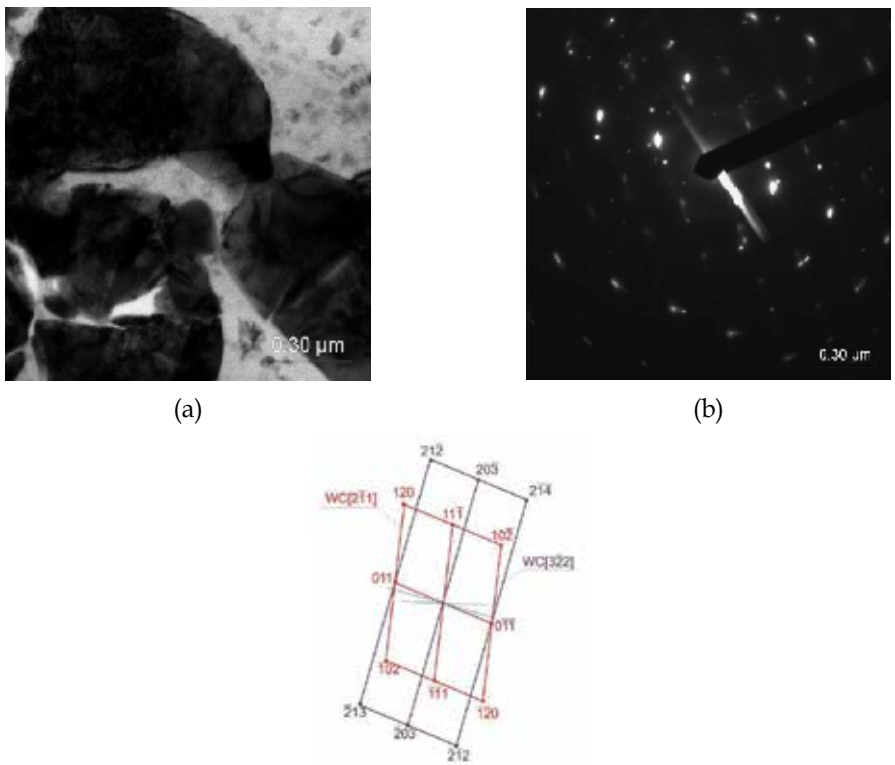

Fig. 30. TEM image of the surface layer of MCMgAl9Zn1 alloy after alloing with WC:
a) bright field; b) diffraction pattern of area shown in a), c) part of solution for diffraction pattern shown in b

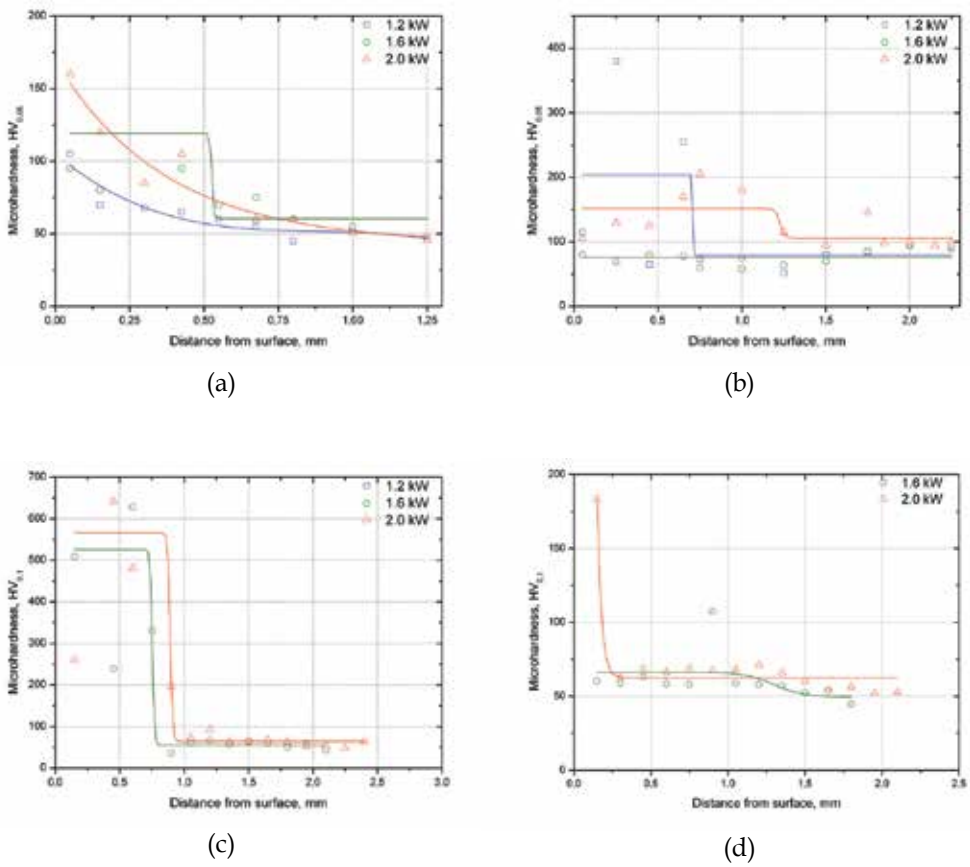

Fig. 31. Micro hardness change of the surface layer of the magnesium cast alloy: a) MCMgAl6Zn1 alloyed with WC, alloying speed: 0.75 m/min, b) MCMgAl6Zn1 alloyed with TiC, alloying speed: 0.75 m/min, c) MCMgAl12Zn1 alloying speed SiC, alloing speed: 0.75 m/min, d) MCMgAl9Zn1 alloyed with Al_2O_3, alloying speed: 0.50 m/min

- Derivative thermo-analysis performed allowed to achieve several representative cooling, crystallization and calorimetric curves with characteristics points of crystallisation process for magnesium alloys which were presented in Fig. 17, 18. Description of characteristics points obtained from thermal-derivative analysis was presented in Table 7 and made it possible to get better understanding of the thermal processes occurred during crystallization kinetics of the investigated Mg alloys.
- Solidification parameters are affected by the cooling rate. The formation temperatures of various thermal parameters are shifting with an increasing cooling rate. Increasing the cooling rate increases significantly the Mg nucleate temperature and decreases the solidus temperature simultaneously widens a solidification range.
- As expected, the results show that grain size reduces as the cooling rate increases. Increasing the cooling rate increases hardness and compressive ultimate strength of the examined magnesium alloys.

- Investigations of the surface layers carried out confirm that alloying of the surface layer of the Mg-Al-Zn casting magnesium alloys is feasible using the HPDL high power diode laser ensuring better properties compared to alloys properties after the regular heat treatment after employing the relevant process parameters. The structure of the remelted zone is mainly dendritic of primary magnesium with eutectic of phase α-Mg and intermetallic phase γ-Mg17Al12. Magnesium alloys with aluminum concentration 9 and 12 wt. % reveal heat affected zone in opposition to alloys with aluminum concentration 3 and 6 wt. %.
- Surface layers fabricated by alloying with VC, TiC, WC, SiC and Al_2O_3 the casting magnesium alloys (MCMgAl12Zn1 and MCMgAl9Zn1) demonstrate the clear effect of the alloyed material, parameters of the alloying process, and especially of the laser beam power and type of the ceramic particles on structure and mechanical properties of the surface layers. Due to laser alloying structure develops with the clear refinement of grains containing mostly the dispersive particles of the carbide and oxide used in the casting magnesium alloy matrix.
- Microhardness investigation shows that hardness increases in the alloyed zone to values from 100 to 700 HV0, 1, when hardness of substrate is in the range from 50 to 90 HV0,1. The microhardness value growth is an effect of refinement of a magnesium alloys structure and very hard carbides particles appearance within surface layer area.

8. Acknowledgements

Research was financed partially within the framework of the Polish State Committee for Scientific Research Project No. 4688/T02/2009/37 headed by Dr Tomasz Tański and the project POIG.01.01.01-00-023/08-FORSURF, headed by Prof. L.A. Dobrzański

9. References

Bachmann, F. (2003). Industrial applications of high power diode lasers in materials processing, *Applied Surface Science*, Vols. 208-209, 125-136, ISSN: 0169-4332

Backuerud, L.; Chai, G. & Tamminen, J. (1990). *Solidification characteristics of aluminum alloys Vol.2 Foundry Alloys*, AFS Skanaluminium, ISBN: 0874331196, Sweden

Baker, H. (1999). *ASM Specialty Handbook. Magnesium and Magnesium Alloys*, Avedesian (Ed.), ASM International, ISBN: 0871706571, USA

Barnes, S.; Timms, N. & Bryden, B. (2003). High power diode laser cladding, *Journal of Material Processing Technology*, Vol. 138, 411-416, ISSN: 0924-0136

Cao, X.; Jahazia, M.; Fournierb, J. & Alainb. M. (2008). Optimization of bead spacing during laser cladding of ZE41A-T5 magnesium alloy castings, *Journal of Materials Processing Technology*, Vol. 205, 322-331. ISSN: 0924-0136

Dobrzański, L.A. & Tański, T. (2009). Influence of aluminium content on behaviour of magnesium cast alloys in bentonite sand mould, *Solid State Phenomena*, Vols. 147-149, 764-769, ISSN: 1012-0394

Dobrzański, L.A.; Tański, T.; Domagała, J.; Król, M.; Malara, S. & Klimpel, A. (2008). Structure and properties of the Mg alloys in as-cast state and after heat and laser

treatment, *Journal of Achievements in Materials and Manufacturing Engineering*, Vol. 31, 123-147, ISSN: 1734-8412

Dutta Majumdar J.; Galun, R.; Mordike, B.L. & Manna, I. (2003). Effect of laser surface melting on corrosion and wear resistance of a commercial magnesium alloy, *Materials Science and Engineering: A*, Vol. 361, 119-129, ISSN: 0921-5093

Emadi, D.; Whiting, L.V.; Nafisi, S. & Ghomashchi, R. (2005). Applications of thermal analysis in quality control of solidification processes, *Journal of Thermal Analysis and Calorimetry*, Vol. 81, 235-242, ISSN: 1572-8943

MacKay, R.; Djurdjevic, M. & Sokolowski, J.H. (2000). The effect of cooling rate on the fraction solid of the metallurgical reaction in the 319 alloy, *AFS Transaction*, Vol. 108, 521-530

Fajkiel, A. & Dudek, P. (2004). High performance advanced castings. Pt 2, Examples of application of castings from non-ferrous metals alloys, *Odlewnictwo – Nauka i Praktyka*, Vol. 1, 18-22, ISSN: 1730-2250

Guldberg, S. & Ryum, N. (2000). Microstructure and crystallographic orientation relationship in directionally solidified Mg–$Mg_{17}Al_{12}$-eutectic, *Materials Science and Engineering A*, Vol. 289, 143-150, ISSN: 0921-5093

Horst, E.F. & Mordike, B.L. (2006). *Magnesium Technology. Metallurgy, Design Data, Application*, Springer-Verlag, ISBN: 978-3-540-20599-9, Berlin Heidelberg

Kainem, K.U. (2003). *Magnesium – Alloys and Technology*, Wiley-VCH Verlag GmbH & Co., ISBN: 3-527-30570-X, Weinheim, Germany

Kasprzak, W.; Sokolowski, J.H.; Sahoo, W. & Dobrzanski, L.A. (2008). Thermal and structural characteristics of the AZ50 magnesium alloy, *Journal of Achievements in Materials and Manufacturing Engineering*, Vol. 29, 179-182, ISSN: 1734-8412

Kiełbus A., Rzychoń, T. & Cibis, R. (2006). Microstructure of AM50 die casting magnesium alloy, *Journal of Achievements in Materials and Manufacturing Engineering*, Vol. 18, 135-138, ISSN: 1734-8412

Kierkus, W.T. & Sokolowski, J.H. (1999). Recent Advances in CCA:A new method of determining baseline equation, *AFS Transactions*, Vol. 66, 161-167

Maltaisa, A.; Dubé, D.; Fiseta, M.; Larochea, G. & Turgeon, S. (2004). Improvements in the metallography of as-cast AZ91 alloy, *Materials Characterization*, Vol. 52, 103-119, ISSN: 1044-5803

Rzychoń, T. & Kiełbus, A. (2007). Microstructure of WE43 casting magnesium alloys, *Journal of Achievements, in Materials and Manufacturing Engineering*, Vol. 21, 31-34, ISSN: 1734-8412

Tański, T.; Dobrzański, L.A. & Čížek, L. (2007). Influence of heat treatment on structure and properties of the cast magnesium alloys, *Journal of Advanced Materials Research*, Vol. 15-17, 491-496, ISSN: 1022-6680

Vollertsen, F.; Partes, K. & Meijer, J. (2005). State of the art of laser hardening and cladding, *Proceedings of the Third International WLT-Conference on Lasers in Manufacturing 2005*, Munich, June 2005, Munich

Yadroitsev, I.; Bertrand, P.; Laget, B. & Smurov, I. (2007). Application of laser assisted technologies for fabrication of functionally graded coatings and objects for the

International Thermonuclear Experimental Reactor components, *Journal of Nuclear Materials*, Vol. 362, Nos. 2-3, 189-196, ISSN: 0022-3115

"Method and Apparatus for Universal Metallurgical Simulation and Analysis" – *United States Patent, Patent No.: US 7,354,491 B2*, Date of Patent: Apr. 8 (2008).

16

The Recent Research on Properties of Anti-High Temperature Creep of AZ91 Magnesium Alloy

Xiulan Ai and Gaofeng Quan
School of Material Science and Engineering,
Dalian Jiaotong University,
China

1. Introduction

In all magnesium alloys, AZ91 is easy to process, i.e., easy to cast into high strength products in low cost, obtained extensive research and development, as well as industrial application (SHI., 2003; POLMEAR I J., 1994: LI et a1., 2000; KIM Ket a1., 1997; MORDIKE et al., 2001). Whereas the poor anti-high temperature (over 120°C) creep performance and the low corrosion resistance are limiting its further application.

In traditional casting Mg-Al base alloy, β-Mg $_{17}Al_{12}$ is major strengthening phase at room temperature, but the β-Mg $_{17}Al_{12}$ phase's melting point is as low as 437°C. With temperature increasing to 437°C, the atom diffusion accelerated, β-Mg $_{17}Al_{12}$ phases are easily softened and coarsened. This causes the grain boundary to be weakened obviously. So that β-Mg $_{17}Al_{12}$ phase can not pin the grain boundary thus the grain boundary sliding occurs. Currently in the most widely used AZ and AM series magnesium alloys, the microstructures are mainly composed of α-Mg solid solution (the matrix) and a little amount of β-Mg $_{17}Al_{12}$. Whereas in non-equilibrium solidification process, nearby each α-Mg grain boundary aluminium supersaturated solid solution area exists, afterwards the β-Mg $_{17}Al_{12}$ phases formed in situ. During high temperature utility, β-Mg $_{17}Al_{12}$ phases in discontinuous shape separate out of supersaturated solid solution, and become into lamellar precipitates owing to low thermal stability. This is one reason that conventional AZ and AM series alloys have poor creep performance.

The creep failure mode of Mg-Al alloys at elevated temperature is predominantly intergranular fracture. Grain boundary cracks appear at first, the process occurrs at the junctions between the hard β phases and the matrix. With the grain boundary sliding, the cracks extend gradually into cavities under the stress, the cavities expand along the grain boundaries which are vertical to the stress direction and then the cavities in the same stress state link each other. Finally the specimen breaks. On the fracture surface of AZ91 alloy analysis shows that in the grain boundary areas the connections between discontinuous precipitates β-$Mg_{17}Al_{12}$ and the matrix α-Mg are weak, so the cracks are easily generated and formed into cavities at the elevated temperature plus the stress action, then the cavities expand further and link each other and form intergranular cracks through the dislocated moving and grain boundary sliding.

This research reported that the creep of magnesium alloys mainly carried on through two ways of dislocation moving and grain boundary sliding. When the bulk alloy was stretched at room temperature, the magnesium alloy with close-packed hexagonal crystallographic structure had a sliding surface which was (0001) basal plane, and only had three slip directions (Fig.1). So its fracture mode was dominated by brittle fracture, and the grain boundary and the precipitation were main obstacles to dislocation motion. With temperature increasing, non-basal plane dislocations participated in motion, crossing-slip of dislocation, aging precipitates and primary dispersion particles became the main obstacles to dislocation motion (LIU., 2002). By transmission electron microscopy analysis, this viewpoint was confirmed objectively. During magnesium alloy breaking at room temperature, in the matrix only (0001) basal plane dislocations were active; when creep rupture at 150°C, in the matrix except for (0001) basal plane dislocation, there existed also (10$\bar{1}$11) non-basal plane dislocation, this confirms the existence of cross slip at 150°C in creep process. According to the experimental results (REGEV M.,2002; XIAO., 2001; XIAO., 2003), it can be known that despite the hcp structure of magnesium alloy slip system number is less than the fundamental requirement for continuous plastic deformation, but at high temperature it can occur that non-basal plane may slip and form cross slip as well. In addition, at elevated temperature, when loading the magnesium alloy, the atoms at grain boundary of magnesium alloy are unstable, easy to spread, and also the dislocations easy to slip so that creep accelerates. These two aspects are main reasons for weakening high temperature creep resistance property of the magnesium alloy (LIU et al., 2002).

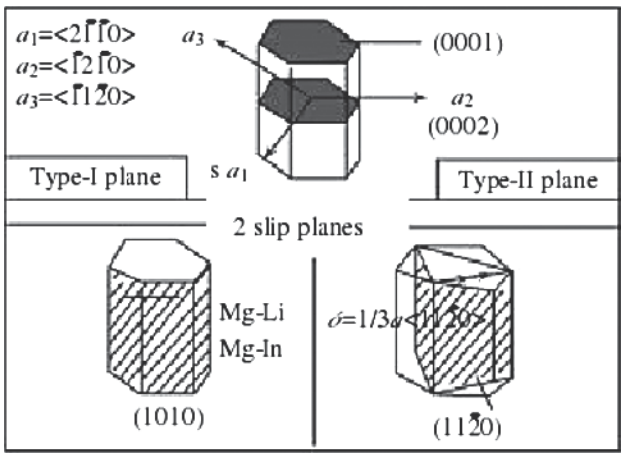

Fig. 1. Sliding system of Mg

The evaluation that resistant creep performance at high temperature of magnesium alloy is good or poor can be done by using the minimum creep rate $\dot{\varepsilon}$ to measure. The smaller the $\dot{\varepsilon}$ is, the better the creep resistance is. Minimum creep rate can be determined with following formula:

$$\dot{\varepsilon} = A\sigma^n \exp(-Q/RT) \quad (1)$$

Where A is constant, σ the stress in the alloy, and n stress coefficient, T the temperature, R gas constant, and Q surface activation energy.

One may know from the above equation that with reducing stress coefficient n, stress σ or increasing superficial activation energy Q, the minimum creep rate may be reduced and then the high temperature anti-creep ability is enhanced.

Therefore, increasing the resistance of intergranuar dislocation movement and grain boundary sliding becomes mostly useful way to improve creep resistance property (HUMBLE P., 1997; YAN et al., 2004). The concrete measures are to strengthen matix and grain boundary, as well as to develop magnesium base composite materials. The former measure is through the micro-alloying to enhance solution strengthening, precipitation strengthening and fine grain strengthening and so on. Simultaneously, small dispersion particles pinning grain boundary and hindering dislocation movement that forms a combined strengthening mechanism for magnesium alloys. Whereas micro-alloying can form the high melting point compounds to reduce or hinder the formation of β-$Mg_{17}Al_{12}$ phase. But the latter measure is through adding strengthening phases to approve anti-high temperature creep performance of the magnesium alloy.

2. AZ91 magnesium alloy micro-alloying research

The effective alloying elements to magnesium alloy should have the following characteristics:

1. The solubility degree of alloying elements in magnesium should drop sharply with temperature reducing, so that they produce precipitation hardening effect during aging or annealing treatment;
2. Alloying elements exist in precipitates in high content, so easy to obtain a large number of dispersed second-phase precipitation;
3. Alloying elements themselves should have high melting point;
4. When adding alloying elements, one should take into account the interaction with other alloying elements, so as to use multi-alloying method to increase the number of precipitates.

The alloy elements used for enhancing thermal stability of magnesium alloy mainly have the rare-earth elements, the alkali soil elements (Ca, Sr, Ba) and the IV,V Race elements (Si, Sn, Sb, Bi). Because the rare-earth element assumes trivalent electron, through strengthening Mg^{2+} interionic attraction, it may reduces atom diffusion speed. The rare earth elements can form high melting point compounds, distributes good thermal stability of intermetallic compounds with Mg, Al and other alloying element (for example, Zn, Mn, Zr) to realize dispersion strengthened, thus the heat resistance and high temperature creep properties of magnesium alloy are enhanced (GUO et al.,2002; LIU et al.,2003）.

The rare earth elements have above advantages but the price is quite high. While the alkali soil elements cost low, and simultaneously they may form high melting point intermetallic phases in the Mg-Al alloy. The intermetallic phases are not easy to decompose and can prevent grain boundary movement effectively at elevated temperature; so that they are obviously improved the high temperature mechanical properties of magnesium alloy especially the anti-creep ability (MIN et al., 2003).

The die casting manufacturability of magnesium alloy added the alkali soil elements is poor, therefore the influence of the IV,V Race element (Si, Sn, Sb, Bi) on magnesium alloy of high temperature stability becomes another research hot spot.

2.1 Rare earth elements effect on the high temperature creep properties of the AZ91 magnesium alloy

Because of unique extra atom nuclear electron distribution, in metallurgy and material fields the rare earth elements obtain widespread applications and researches. People have

obtained quite thoroughful understanding already to the function of rare earth element in magnesium alloy (LI et al., 2005; TENG et al., 2007).

Ele-ment	Atomic radius /nm	Atomic radius D-value with magnesium(%)	Electro negativity	Ele-ment	Atomic radius /nm	Atomic radius D-value with magnesium(%)	Electro negativity
Mg	0.160	0	1.31	Dy	0.175	10.8	1.22
La	0.188	17.3	1.10	Ho	0.175	10.4	1.23
Ce	0.183	14	1.12	Er	0.174	9.8	1.24
Pr	0.183	14.3	1.13	Tm	0.176	9.1	1.25
Nd	0.182	13.8	1.14	Yb	0.194	21.2	1.1
Sm	0.179	12.6	1.17	Lu	0.173	8.4	1.27
Eu	0.199	27.6	1.2	Y	0.182	12.6	1.22
Gd	0.178	12.6	1.20	Sc	0.165	2.6	1.36
Tb	0.176	11.4	1.2				

Table 1. Atomic radius and electronegativity of the magnesium and RE element

As showing in Table 1, the atomic radius and the electronnegativity of the majority of rare-earth elements are close to the magnesium's, and the atomic radius relative differential value between rare earth elements and magnesium are in about 15%, moreover the electronegativity differential value is smaller than 0.4. According to Hume-Rothery and Darken-Gurry theory, it can be obtained that the rare-earth elements have big solid solubility degree in the magnesium (showed Table 2) to realize solution strengthening and precipitation strengthening. Simultaneously they are also effective aging strengthening elements. Some rare earth elements also have dispersion strengthening effects. So the rare earth elements may enhance the alloy's room temperature intensity of the magnesium alloy as well.

RE element	Sc	Y	La	Ce	Nd	Yb	Gd	Dy
Atomic number	21	39	57	58	60	70	64	66
Eutectic temperature/°C	-	565	613	560	548	592	548	559
Max-solid solubility/wt%	25.9	12	0.79	1.6	3.6	3.3	23.5	25.8
compounds generated with magnesium	MgSc	$Mg_{24}Y_5$	$Mg_{12}La$	$Mg_{12}Ce$	$Mg_{12}Nd$	Mg_2Yb	Mg_5Gd	$Mg_{24}Dy_5$
Alloy system	peritectic	eutectic	eutectic	eutectic	eutectic	eutectic	eutectic	eutectic

Table 2. RE elements solubility degree in Mg and compounds formed with Mg

At present the rare-earth elements added into magnesium alloy are roughly divided into two categories: one is the elements with small solid solubility such as Ce, Pr element and so on, another is the elements with large solid solubility such as Y, Nd, La element etc. Many rare-earth elements by preformed alloy forming are added to the magnesium alloy (Mordike., 2002).

Generally believe that the rare earth elements with Al element form high melting point's Al-rare earth intermetallic compounds in the AZ91 alloy. The kind of compounds enhance the thermal and mechanical performance of magnesium alloy.

The primary reasons lie in following several aspects:

First, in casting solidification process, the high melting point Al- rare earth intermetallic compounds firstly separated out. These compounds become the nuclear core of α-Mg to enhance nucleation rate, or were pushed to grain boundary area to hinder α-Mg grain growing up, and refine magnesium alloy grain;

Second, because of the forming of Al-rare earth intermetallic compounds the content of Al element in the matrix alloy was dropped, the quantity of β-$Mg_{17}Al_{12}$ phase in the grain boundary place reduces. Along with the rare earth element content (within a certain range) increasing, the size of β-$Mg_{17}Al_{12}$ phase reduces gradually, and the shape of it is also changed from continual lattice gradually to spherical discrete distribution;

Third, because the Al- rare earth compounds are thermally stable phases, moreover the quantity of β-$Mg_{17}Al_{12}$ with poor thermal stability reduces and the shape of it changes, thus these all enhance the anti-high temperature creep property of magnesium alloy.

In addition, the binding capacity of rare earth elements and oxygen is greater than the binding force of magnesium and oxygen; this urges magnesium to response with hydrogen and water vapor during melting. Joining appropriate rare-earth elements into the magnesium alloy can not only remove gas, mixed, but may also increase the fluidity of solution, reduce the tendency of casting producing shrinkage porosity and enhance the density (LI., 2005).

In all the alloy elements, the rare earth elements are one of the most effective, the most direct alloy element to improve heat resistance. Due to rare earth elements have small diffusion coefficient in magnesium alloy, they slow recrystallization process, increase the recrystallization temperature, decrease grain boundary and phase boundary diffusion permeability and reduce the phase boundary aggregation. The most main are that the high melting point rare earth compounds made of the rare earth and Mg, Al or other elements (for example Zn, Mn and so on) anchor grain boundary and hinder dislocation movement for improving the high temperature strength and creep resistance. The rare earth elements form precipitation in the magnesium alloy, the precipitation process is: at 170 ~ 200°C hexagonal β "phase is generated which is superlattice structure; at 200~250°C body-centered cubic structure β′ phase appears, above 300°C face-centered cubic β phase is formed and heterogeneously distributed in grain and on grain boundary . The dispersed, thermally stable particles make magnesium alloy showing good heat resistance (GUO et al., 2002).

Rare earth element Y has the effect on the microstructure and mechanical properties of the AZ91D magnesium alloy by adding different contents in the alloy. Y element obviously refined the microstructure, formed square block $A1_6Mn_6Y$ phase and rod $A1_2Y$ phase .These two phases were high melting point phases and appeared in the liquid metal before solidification , thus became the core of non-spontaneous crystallization. So, they hindered grain growth, refined dendrites, and enabled their distribution to disseminate. Finally, the mechanical properties of the alloy were enhanced. However, the addition quantities of rare earth elements were required .The alloy with 1.5% Y had better comprehensive mechanical properties than others, while when the Y content increased above 2%, tensile strength, ductility and hardness all were decreased(WU et al.,2006).

Lu Y Z , Lu S f and so on(2000;2006) have studied the influence of the rich Ce rare earth on the microstructure and the performance of AZ91 magnesium alloy. They found that after

having added Ce into the alloy, bar $Al_{11}Ce_3$, $Al_{11}La_3$, $Al_{11}Pr_3$, $Al_{11}Nd_3$ and so on precipitated phases appeared, the quantity and the size of β-$Mg_{17}A1_{12}$ were reduced; These phases were high melting point compounds and mainly gathered at the grain boundary area, by grain boundary strengthening way to effectively improve the thermostability and the high temperature performance of AZ91 magnesium alloy. Ce content was also influential to the microstructure and the mechanical properties of AZ91 magnesium alloy. Joining 0.2%~0.8%Ce into the AZ91 alloy could obviously refine grain, made its size drop to approximately 32μm ,while before refinement the size of α-Mg grain was 108μm, and made the tensile strength to enhance 31MPa compared to the substrate(LIU.,2006).

Ce and Ce-rich series rare earth mixture have good solution strengthening effect to the magnesium alloy. Y series have remarkable aging strengthening effect and precipitation phases have low diffusion coefficient, have good contact surface union with the magnesium matrix. Therefore, the researchers joined Y together with Ce to the AZ91 magnesium alloy to observe their roles to the microstructure and the property. After have been added in alloy, with Al element, Y, Ce formed $Al_{11}Ce_3$, Al_2Y heat-stable phase respectively. These two phases separated out during solidification process firstly, and thus prevented grain growing and grain boundary sliding at high temperature. Forever, Ce ,Y and these heat-stable phases could commonly refined the grain. The interaction of solution strengthening of Y element and precipitation strengthening of $Al_{11}Ce_3$ and Al_2Y enhanced the properties of the magnesium alloy either room temperature or high temperature. The experiment proved: When joining 0.6%Ce and 0.3%Y, the room temperature tensile strength of the magnesium alloy achieved 245MPa, enhancing 64% compared to the AZ91D matrix; the yield strength achieved 213MPa, enhancing 71% compared to the AZ91D matrix(WANG et al.,2007).

The rare earth Nd added into AZ91D magnesium alloy generated new rare earth compound $Al_{11}Nd_3$, reduced the quantity and the size of β-$Mg_{17}Al_{12}$ phase, and changed the shape of the β-$Mg_{17}Al_{12}$ phase from discontinuous net to dissemination distribution. $Al_{11}Nd_3$ phase effectively hindered grain boundary sliding and fracture growing, and refined the microstructure of the alloy. Finally it enhanced the mechanical properties of the alloy. Adding different contents Nd in the die-casting AZ91D alloy, although the break way of alloy still belonged to the brittle fracture, but when the Nd content was 1%, the number of dimple in alloy fracture increased and the character of the ductile rupture was remarkable (YANG.,2007).

Through researching the influence of rare earth La on the microstructures and the properties of the AZ91 alloy, it is obtained that after having added La element, the microstructures of AZ91 alloy have some changes such as grain refinement, net shape β-$Mg_{17}Al_{12}$ separation, smaller and thinner, black spot MnAl compounds segregation obvious depletion, needle rare earth phase ($Al_{11}La_3$) appearing at grain boundary. $Al_{11}La_3$ phase made of La and Al element is high melting point and high stability phase, and it improves the distribution of the grain boundary phase and the macro hardness of cast. After solution and aging treatment, lamellar β-$Mg_{17}Al_{12}$ phase precipitates at grain boundary, and with aging time elongation the hardness of alloy increases further (PEI et al., 2005).

2.2 Alkali soil elements influence on the AZ91 magnesium alloy

Because the atom size and the negativity of rare-earth element are close to the magnesium, the rare-earth element may strengthen interatomic binding force of the magnesium alloy, forms the high melting point compound, remarkably refines the microstructure of the magnesium alloy, and enhances the room temperature mechanical properties, the high

temperature mechanical properties and the creep performance of the AZ91 magnesium alloy. But, rare-earth element's price is expensive; this has limited its widespread application. Therefore, by adding inexpensive alkali soils elements (Ca, Sr, Ba) in alloy to improve the heat-resisting performance becomes research another hot spot about the magnesium alloy.

The price of Ca element is low, the melting point low, and the density is quite close to the magnesium's; so at present it has become the most frequently using alkali soil element to enhance the magnesium alloy heat-resisting performance. Studies have shown that adding Ca element to the conventional magnesium alloy can not only enhance oxidation combustion temperature of magnesium alloy, but also refine as-cast structure so as to improve mechanical performance and high temperature creep of magnesium alloy. After Ca had been added, the hardness of the alloy was increased significantly. When the mass ratio of Ca and Al was greater than 0.8, not only the hardness of magnesium alloy was increased rapidly, but also high thermal stability $(Mg, Al)_2Ca$ phase is formed in grain boundary place. It effectively hindered grain boundary sliding during high temperature creep, thus significantly improved the heat resistance of the alloy (LIU.,2002; GUO.,2004; LI.,2005; YANG.,2005).

Another study shows that Ca added AZ91 alloy raises the eutectic reaction temperature of alloy and improves the melting point of β-$Mg_{17}Al_{12}$ phase, so it improves the weakness of stability of β-$Mg_{17}Al_{12}$ phase lower. While β-$Mg_{17}Al_{12}$ phase mostly distributes in the grain boundary, its stability enhancement can better prevent grain boundary sliding (CHEN., 2007) at elevated temperature.

Some points are worth paying attention: Microcontent Ca may refine as-cast and aging structures. Studies find that only few of Ca added in the alloy is dissolved in the matrix, massive Ca dissolutions in β-$Mg_{17}Al_{12}$.This indicates that Ca mainly salutes in the AZ91 alloy, rather than forms second phase. Because after Ca solution in β-$Mg_{17}Al_{12}$ phase it can inhibit the dissolution of β phase and improves the thermal stability of β phase, eventually enhances the room temperature and high temperature tensile property of the alloy (SUN et al, 2001).Along with the Ca content increasing, its refinement effect is also more obvious, but the tendentiousness of hot cracking of the alloy increases (TANG et al., 2004; LI et al, 2005).

The researches show: After Ca has been added in the AZ91 magnesium alloy, what phase is formed relating to the content of Ca (LI et al.,2005;MIN et al.,2002;FAN et al.,2005). When the Ca contents are lower than 1% (quality score, when similarly here and after), it mainly is saluted in β-$Mg_{17}Al_{12}$(MIN et al.,2002). Through the way of strengthening $nC^{Al\text{-}Mg_{II}}$ and $nD^{Al\text{-}Mg_{II}}$ bond which control the stability of β-$Mg_{17}A1_{12}$ phase, through the way of causing the shared electron to even assign in the principal linkage and the entire structure, Ca element enhances the melting point of β-$Mg_{17}Al_{12}$ phase and the high temperature performance of the magnesium alloy. When the Ca content is 0.8%, the Al_2Ca presents in grain boundary area of the alloy, simultaneously, β-$Mg_{17}Al_{12}$ phase reduces (see Fig.2). But the Al_2Ca worsens the tensile strength and the plasticity of the alloy (LI et al, 2005).

Generally thinks (BERKMORTEL et al., 2000; WANG et al., 2000), the reason that Ca causes the anti-thermal crack performance of the magnesium alloy dropping is because during solidification period, at grain boundary place Al_2Ca owing different cooling rate from the matrix alloy leads the stress to be created, or is because Al_2Ca gathering in the grain boundary by netted form enlarges the thermal crack tendentiousness of alloy. In addition, there is a substantial cause is: Ca promotes the divorce eutectic reaction, enhances the separation temperature, reduces the packing ability of the alloy melt. In order to eliminate

or reduce the influence of Ca element on anti-thermal crack performance of the magnesium alloy (TANG et al., 2004), many researchers are searching other microcontent alloying element to coordinates with Ca element.

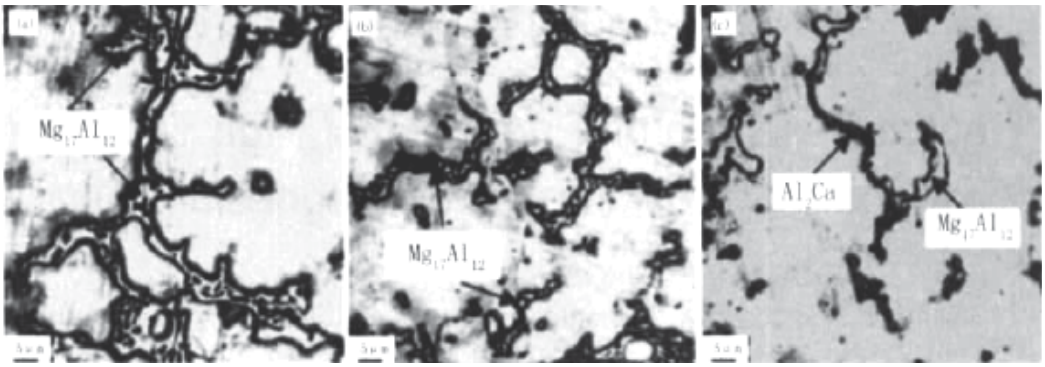

(a)0%Ca (b)0.4%Ca (c)0.8%Ca

Fig. 2. Microstructure of AZ91D alloy

Some researches indicate Ca/Sr composite addition into AZ91D alloy may make the anti-thermal crack performance of the alloy to restore to the closing AZ91D alloy level, but Sr addition will counter-balance the grain refinement effect of Ca element on the microstructure of the magnesium alloy (TANG et al., 2005). Others, because the AlSr and the Al-Ca-Sr ternary compounds were produced, the number of β-$Mg_{17}Al_{12}$ precipitations reduces as a result, simultaneously, at grain boundary place the shapes of β-$Mg_{17}Al_{12}$ and Al_2Ca have some changes, thus the embrittlement function of the Al_2Ca on the matrix is weakened (LI et al.,2004).

In AZ91- Ca magnesium alloy, joining Si or rare earth elements again, the room temperature and the high temperature mechanical properties of the alloy may obviously be improved; The high temperature creep resistance of the alloy was enhanced enormously because of producing high melting point Mg_2Si second phase or $Al_{11}RE_3$ phase (MIN et al., 2002). Simultaneously joining 1%Ca and 1%RE may make the tensile strength of the AZ91 magnesium alloy to enhance 15.9% (WU et al., 2005).

Sr can refine grains, improve the creep properties of the alloy, also is advantageous to the anticorrosion performance. Little content Sr (0.2%~0.5%) can refine as-cast structure and make the size of α-Mg grain dropping from 107μm not refinement to 60μm ; net and block shape β-$Mg_{17}Al_{12}$ phase becomes tiny dissemination. When Sr content is 0.8%, rod Al_4Sr phase appears(see Fig.3). Refinement mechanisms are that on the one hand Sr reduced the liquidus and solidus temperature of the alloy and caused the supercooling degree of alloy to reduce; on the other hand, Sr concentrated in front of the solid-liquid interface to cause α-Mg grain growing to block, thus further to refine grain(LIU et al.,2006).

Ba enhances obviously the room temperature and the high temperature tensile strength of the AZ91 alloy. It is main reason that Ba has solution strength effect on the alloy and Al_4Ba phase with high melting point and thermal stability has dispersion strengthening effect. When the content of Ba is 0.2wt%, the room temperature tensile strength of the alloy enhances 9.2%; the high temperature tensile strength enhances nearly 19%. However when the content of Ba is above 0.3%, the number of Al_4Ba phase having separated out in the crystal boundary increases and this phase gathers to group. These make Ba refinement role

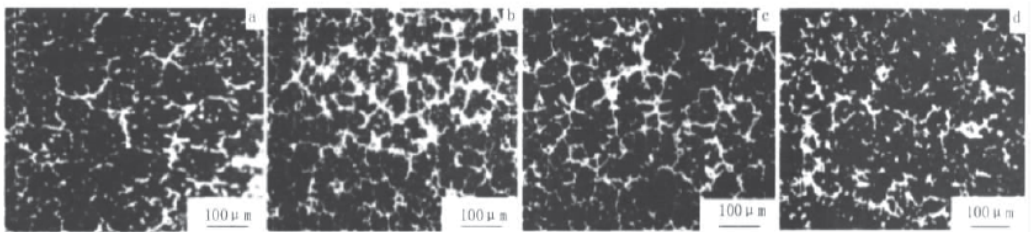

(a) 0%Sr (b) 0.2%Sr (c) 0.5%Sr (d) 0.8%Sr

Fig. 3. Effect of Sr content on the as-cast microstructure of AZ91D alloy

dropping and lead to lower grain boundary cohesion, to stress increasing. When plastic deformation occurring, the fracture easily occurs at grain boundary and the mechanical properties of the alloy decrease (LI et al., 2005).

2.3 The IV. V race element (Si, Sn, Sb, Bi,) role on AZ91 magnesium alloy

Si element added in AZ91 magnesium alloy may form an effective high-temperature strengthening phase Mg_2Si.

Magnesium alloy components	Casting mode type	Alloy element	Adding element Content (%)				Reinforcing phase	Reinforcing phase Morphology, distribution	Melting point of reinforcing phase/°C	crystal structure of reinforcing phase
			0	0.5	1	2				
			Yield strength/MPa							
Mg-9Al-0.8Zn	Metal mode	Bi	125	-	152	161	Mg_3Bi_2	Most in grainboundary, Little in grain	823	partyD_5
Mg-9Al-0.8Zn	Water-cooling metal mode	Sn	70	130	115	120	Mg_2Sn	Most in grainboundary, Little in grain	778	reverseCaF_2 structure
Mg-9Al-0.8Zn-0.2Mn	Metal mode	Sb	95	140	-	-	Mg_3Sb_2	Most in grainboundary, Little in grain	1228	hexagonal D_5 structure

Table 3. Effect of Bi, Sn, Sb addition on yield strength of magnesium alloy at 150°C

Because Si is very cheap, therefore it may become one of first choice adding elements to enhance high temperature performance of magnesium alloy .Alloy obtained can be used for the occasions that work temperature is below 150°C (LUO, 2004), The alloy production suits in using die-casting with fast solidification speed to carry on, but is not suitable with the sand casting way to produce. Because the main strengthening phase Mg_2Si in the condition of slower solidification rate will become like thick, it easily leads to stress concentration and thus seriously damages the performance of the alloy.

Sn element has refining grain function to the alloy. Table3 has listed the research results (YUAN et al., 2001). Adding Sn element has suppressed β-$Mg_{17}Al_{12}$ separation, promoted Al

atom solution in Mg and caused its solid solubility to increase. Content 0.5% Sn has expanding α-Mg region' function (TENG et al., 2007). Few Sn can enhance effectively the thermal stability of the alloy. Moreover, excessively many Sn will cause the intensity of the alloy dropping. After having added Sn into the alloy, high melting point Mg_2Sn appears in microstructure and distributes in the grain boundary. This phase may prevent effectively grain boundary slipping at the time of the high temperature stretch, so it can improve the thermal stability of the alloy. The strengthening role of Sn on the magnesium alloy will not go away along with temperature increment (Sun et al., 1999).

According to Pekguleryuz et al.(PEKGULERYUZ M O ,AVEDESIAN M M ,1992) report, it can be known that excessively high Sn content in the magnesium alloy would cause the intensity of alloy to drop, This is because the excessive Sn content easily led Mg_2Sn grain coarsening so as to cause its high temperature strengthening effect to be weaken.

添加元素及其含量（%）						拉伸性能						参考文献
						室温			高温			
Ca	Si	Sr	Bi	Sb	RE	σ_s/MPa	σ_b/MPa	δ（%）	σ_s/MPa	σ_b/MPa	δ（%）	
0.4	-	-	-	-	-	77.9	138.6	0.98	-	-	-	(LI PJ,2004)
0.4	-	0.01	-	-	-	80.3	134.0	0.94	-	-	-	
0.4	-	0.05	-	-	-	79.3	148.8	1.37	-	-	-	
0.4	-	0.10	-	-	-	76.8	173.7	1.86	-	-	-	
0.3	-	-	-	-	-	120.0	163.0	2.2	101.0	144.0	16.1	(MIN X G,2002)
0.3	0.2	-	-	-	-	160.0	200.0	4.4	111.0	154.0	11.4	
0.3	0.6	-	-	-	-	152.0	190.0	3.3	113.0	151.0	12.1	
0.3	-	-	-	-	1	140.0	175.0	4.0	110.0	142.0	16.0	
0.3	-	-	-	-	2	129.0	174.0	4.2	103.0	137.0	17.8	
-	-	-	0.5	-	-	132.0	232.0	4.7	132.0	180.0	24.3	(YANG G Y,2001)
-	-	-	1.0	-	-	166.0	250.0	4.6	134.0	180.0	21.7	
-	-	-	2.0	-	-	184.0	265.0	4.4	138.0	184.0	19.6	
-	-	-	3.0	-	-	162.0	224.0	3.2	119.0	172.0	12.1	
-	-	-	-	0.1	-	134.0	238.0	5.0	121.0	183.0	34.5	
-	-	-	-	0.4	-	177.0	264.0	4.5	138.0	185.0	34.0	
-	-	-	-	0.7	-	172.0	257.0	4.4	135.0	180.0	26.8	
-	-	-	-	1.0	-	165.0	244.0	2.7	133.0	172.0	18.9	
-	-	-	0.5	0.4	-	172.0	262.0	3.6	138.0	183.0	16.3	
-	-	-	1.0	0.4	-	178.0	269.0	3.3	140.0	187.0	14.8	

Note: In high temperature tensile properties, in literature (MIN X G, 2002) temperature is 200°C, (YANG G Y,2001) temperature is150°C; — is element not be added or performance undetected.

Table 4. Mechanical properties of AZ91 magnesium alloys microadded alloyings

The strengthening mechanism of Sb to the magnesium alloy had been studied. The research results indicated that when adding content of Sb was 0.4%, in microstructure, α-Mg was thinning, strip shape β-$Mg_{17}Al_{12}$ no longer assumed lattice and block distribution, but became thinning, short structure and dissemination distribution, and white granulated Mg_3Sb_2 was distributed in the grain and the grain boundary relatively. The tensile strength of the alloy was enhanced 20MPa comparing to the matrix. Analyzing the above reason, it is though that Sb strength effect stems from the interaction of grain refinement, the original β-$Mg_{17}Al_{12}$ morphology changing and the new particle Mg_3Sb_2 appearance (WANG et al., 2005).

Regarding Bi/Sb composite addition into AZ91D alloy ,the researches indicated that Al, Bi, Sb played solution strength role to reduce structure energy through saluting in α-Mg grain or grain boundary. In AZ91 magnesium alloy, Bi or Sb was easier than Al to gather in the grain, so suppressed Al element to gather in the grain boundary and promoted continual β-

$Mg_{17}Al_{12}$ to separate from the matrix. Thus the room temperature performance of the AZ9l magnesium alloy was improved. In the AZ91 magnesium alloy, main alloying element Al and microcontent element Bi, Sb could form big quantity, order Mg_3Sb_2 (821) or Mg_3Bi_2 (1280°C) phase in the grain boundary area. Therefore Mg_3Sb_2 or Mg_3Sb became main separation phase in the grain boundary area to hinder effectively dislocation movement during the high temperature distortion process, thus it enhanced the high temperature performance of magnesium alloy (Zhang et al., 2005; Yuan et al., 2001; Yuan et al., 2001).
Table 4 carries on the performance contrast which was obtained from the present the part micro alloy researches to the AZ91 magnesium alloy. Although existing the different of the raw material matching, the alloying element choosing, the material preparation craft and in table researcher's data, we still may see some change tendencies, namely the multi-elements coordinate effect surpassing the sole element.

3. AZ91 magnesium alloy base compound materials research

Magnesium alloy itself has some shortcomings such as high temperature strength poor (MORDIKE et al., 2001), elasticity coefficient low and anti-corrosive performance poor, therefore the people take their visions on the relatively high performance magnesium matrix composites. The researches began in the 1970s; To the beginning of the 21st century (GU et al., 2004) it has become research hot spot. Presently, the researches about magnesium matrix composites mainly concentrate in the fiber reinforcement and the particle strengthening two kinds of composites.
Early researches focused on the long fiber and whisker reinforced composites, such as adding graphite, SiC, Al_2O_3, B_4C and other fibers or whiskers into the AZ91 matrix.
Trojanová Zuzanka et al(2004) added 20vol. % δ-Al_2O_3 short fiber to the AZ91 magnesium alloy. In 20~300°C temperature period, the compressive test was carried on. The results demonstrated that the yield stress of the AZ91 magnesium alloy strengthened by δ-Al_2O_3 short fiber had remarkable enhancement comparing to not to be strengthened, while the experimental temperature continues to elevate the fiber reinforcement effect was not remarkable.
Zheng M Y et al (2003) inspected the aging behavior of squeeze cast SiCw/AZ91 magnesium matrix composite. The results showed that adding SiC whiskers changed the distribution of β-$Mg_{17}Al_{12}$ precipitation phase and made it maintaining an orientation relationship with SiC whisker priority precipitating at the interface between SiC whisker and AZ91. This kind of priority precipitation phase had consumed alloying element existing in the matrix, so the age-hardening effect of SiC/AZ91 was low compared to the alloy not to adding the SiC.
The complexity and high cost of the fiber and whisker reinforcement's process limited the marketing application. While the magnesium matrix composites reinforced with particles as reinforcements, because of these advantages such as high strength, high stiffness, good dimensional stability, excellent casting performance and property isotropic, become one of the most practical engineering materials. They have received people's attention.
Recently, the researches of magnesium matrix composite using particles as reinforcements mainly have concentrated on the selection of the particles and on the processing. At present, the particles mainly have TiC (CHEN et al., 2005; WANG et al.,2006), SiC(LEE et al.,2006), Al_2O_3 (HASSAN et al.,2006; HASSAN et al.,2005), TiB2(WANG et al.,2006) and so on.
WANG J J et al (2006) by infiltration process in situ reactive had fabricated TiC/AZ91D composites. The test results indicated that compared with the AZ91 alloy not enhanced, the

TiC/AZ91 alloy's high temperature longitudinal strength enhanced 180%; simultaneously, the break behavior of the alloy had also the change from along $Mg_{17}Al_{12}$ phases break to along the TiC/AZ91 surface break.

WANG Y et al (2006) had fabricated TiB_2 particle reinforced magnesium matrix composites by two-step processing method. TiB_2 in the AZ91 matrix was relatively uniform distribution. With the content of TiB_2 (2% to 7.5% in the period) increasing the hardness and the wear resistance properties of composites were improved, but the porosity also was increased.

Length scale of particle has a remarkable influence on microstructure and tensile properties of AZ91 magnesium alloy. Literature (HASSAN et al., 2005) demonstrated that the yield strength and tensile strength of the nano-Al_2O_3 particles reinforced AZ91 magnesium matrix composite enhanced higher than those micron-Al_2O_3 particles with higher volume fraction. Other, SUO ZY et al (2005) prepared reinforced AZ91 magnesium alloy with flow casting method. The research results showed that Ni-Nb Amorphous bond could enhance the tensile strength of AZ91 magnesium alloy, but the increasing rate decreased with increasing of volume fraction of the Ni-Nb amorphous band.

Particles reinforced magnesium matrix composites have made great progress. However, the factors such as particle uniformity, interface infiltration, reaction, and type, size, quantity of enhanced particle and so on are controlled by the nucleation and the growth kinetics, so further studies will be perfected (Aikin.,1997).

4. The research trends of AZ91 magnesium alloy on creep resistance property

In summary, in order to break through the bottleneck that AZ91 magnesium alloy high temperature creep resistance performance is poor, to meet the service requirements of high temperature applications such as automotive components, to promote its commercial application, many years, a series of researches have started in various countries and considerable progress has be made, but there are many problems and deficiencies.

1. In the creep performance of AZ91 magnesium alloy, whether alloy or composite, in the alloy side the researches mainly concentrated in the choice of elements or reinforcements; in the composite side mainly focused on the choice of process. The mechanism of the various elements or reinforcements influencing on the performance of AZ91 magnesium alloy remains to be further study.
2. Rare earth elements have active role in the creep resistance property of AZ91 magnesium alloy, but the rare earth elements, after all, are more expensive, it is also necessary to carry on the thorough discussion in the multiple element micro alloy aspect, aiming at in suppressing the adverse effects of single element aspect and developing the high performance-to-price ratio's magnesium alloy. Simultaneously, those should also become further goals to improve the mechanism of rare earth elements impacting on the heat-resistant magnesium alloys, to deeply study the influences of the alkali soil elements and the IV, V group elements on the heat-resistant property of AZ91 magnesium alloy.
3. Since fiber reinforced magnesium matrix composites have the shortcomings such as the complexity of fabricating process and the obvious anisotropy of materials. While the preparation of particle reinforced the AZ91 magnesium matrix composites has diversity and economy. Therefore, they will possibly become study focus. But it is need that to further study and improve the interface structure of AZ91 matrix composites, the

forming mechanism of the interface phase, the crystal structure and surface characteristics of the reinforced phase. Through this we can control and optimize the interface to improve the properties of AZ91 magnesium matrix composites.

5. Reference

SHI Y. (2003). Magnesium alloy industry point of no return. New Economy Weekly, 2003 (9): 66- 68.

POLMEAR I J. (1994) Magnesium alloys and applications. Materials Science and Technology, 1994 (1): 1- 16.

LI Y Z, WANG Q D, Ding W J, et a1. (2000). Fracture behavior of AZ91magnesium alloy. Materials Letters, 2000, 44 (15): 265- 268.

KIM K, HAN H N, YEO T, et a1. (1997). Analysis of surface and internal cracks in continuously cast beam blank. Iron Making and Steel Making, 1997, 24 (3): 249- 256.

MORDIKE B L, EBERT T. (2001). Magnesium: Properties-applications potential. Materials Science and Engineering, 2001, A302: 37-45.

LIU Haifeng, HOU Jun, LIU Yaohui. (2002). Status and development of study on creep problems of die cast magnesium alloys at high temperature [J]. Foundry, 2002, 51 (6):330 - 335.

XIAO X L, LUO C P. (2001). Morphology and crystallography of β-(Mg_(17)Al_(12)) precipitate in AZ91 Magnesium-Aluminum Alloy. Acta Metallrugica Sinica, 2001, 37 (1):2 - 7.

XIAO X L, LUO C P, LIU J W et al (2003). Structure of HCP/BCC interphase boundaries in AZ91 Mg-Al alloy. The Chinese Journal of Nonferrous Metals, 2003(1):15 - 19.

REGEV M, PAHUTOVA M, KUCHARAVA K et al. (2002). The role of matrix microstructure in the creep behavior of discontinuous fiber reinforced AZ91 magnesium alloys [J] .Materials Science and Engineering A, 2002, A324 (1 - 2)151 - 156.

HUMBLE P. (1997). Towards a cheap resistant magnesium alloy. Materials Forum, 1997, 21:45- 56.

YAN Y Q,ZHANG T J,DENG J et al.(2004).Research and development of heat resistant Mg Alloys. Rare Metal Materials and Engineering, 2004, 33 (6): 561- 565.

GUO X T, LI P J, LIU S X et al.(2002).Development status and prospect of heat resistant rare earth-magnesium Alloy. Foundry, 2002, 51(2):68.

LIU B, LIU S H, JIN W Z.(2003).Functions and influences of rare earths in Magnesium Alloys. Shanghai Nonferrous Metals, 2003, 24(1):27.

Min X, Sun Y, XUE F, et al. (2003).Analysis of valence electron structures(VES)of intermetallic compounds containing calcium in Mg-Al-based alloys. Mater ChemPhys, 2003(78):88.

LI J F, GENG H R, TENG X Y. (2005). Effects of Ba on microstructure and mechanical properties of AZ91 Magnesium alloy. Hot Working Technology, 2005, (7):5-8.

TENG X Y, WANG B, WANG Z M.(2007). Effects of trace Si, Ba and Sn on the As-cast microstructure of AZ91 Magnesium alloy. Special Casting & Nonferrous Alloys, 2007,27(2):83-85.

Mordike B L. (2002). Creep-resistant Magnesium Alloys[J]. Materials Science and Engineering A, 2002(324):103-112.

LI W X. (2005). Magnesium and Magnesium Alloys, Chang sha: Central South University Press, 2005:87-210.

GUO X T, LI P J, ZENG D B. (2002). Application of rare earth in heat resistant Magnesium alloy. Chinese Rare Earths, 2002, 23(2):63-67.

WU G H, LI G Q et al. (2006).Effects of element Y on the microstructure and mechanical properties of AZ91D Magnesium Alloy. Special Casting & Nonferrous Alloys, 2006, 26(5):260-263.

Lu Y Z, Wang Q D, ZENG X Q. (2000).Effects of rare earths on the microstructure, properties and fracture behavior of Mg_2Al alloys[J]. Materials Science and Engineering A，2000(278):66-76．

LIU S F, HUANG SH Y, XU P.(2006). Influence of cerium addition on As-Cast microstructure refinement of AZ91 Magnesium alloy. Acta Metallrugica Sinica, 2006,42(4):443-448.

WANG M X, ZHOU H et al.(2007). Effect of Y and Ce addition on microstructure and mechanical properties of AZ91D Magnesium alloy. Journal of Jilin University Engineering and Technology Edition, 2007,37(1):7-10.

YANG Y, LIU Y B, FANG Y.(2007). Influences of Nd on tensile and fatigue fracture mechanism of die Cast Magnesium alloys. Foundry, 2007, 56(1):41-45.

PEI L X, ZHANG J S,GAO Y B.(2005). The effect of La on microstructure and macro-hardness of AZ91 Magnesium alloy. Research Studies on Foundry Equipment, 2005, 2(1):20-22.

GUO Shijie, LE Qizhi, CUI Jianzhong.(2004).The current development of Ca addition and heat-resistant Magnesium alloy.[J] Materials Review,2004,vol18: 44 - 46.

LI EIJIE , TANG BIN ,KANDALOVA E G.(2005). Microstructure and properties of AZ91D alloy with Ca additions [J] .Materials Letters, 2005 , (59) :671 - 675.

YANG Mingbo, PAN Fusheng, ZHANG Jing.(2005). Development and application of Mg-Al based elevated temperature Magnesium alloys in automobile industry [J]. Foundry Technology, 2005, 26(4): 331 - 335.

CHEN Zhenhua.(2007). Domestic Heat Resistant Magnesium Alloy [M].Beijing: Chemical Industry Press, 2007, p134-135.

SUN Y S, ZHANG W M, MIN X G. (2001). Tensile strength and creep resistance of Mg-9Al-1Zn based alloys with calcium addition [J].ACTA Metallurgica Sinica (English Letters) , 2001, 14 (5) :330- 334.

TANG B, LI P J, ZENG D B.(2004). Effects and mechanism of Ca on hot crack resistant property of AZ91D alloy. Foundry, 2004, 53 (9): 701- 704.

LI P J, TANG B, KANDALOVA E G.(2005). Microstructure and properties of AZ91D alloy with Ca additions [J]. Materials Letters, 2005, 59:671- 675.

MIN X G, ZHU M, SUN Y S.(2002). Effect of Ca on microstructure and tensile strength of AZ91 alloys. Material Science and Technology, 2002, 10 (1): 93- 96.

FAN Y, WU G H, GAO H T et al.(2005). Effect of Calcium on microstructure, mechanical properties and corrosion resistance of Magnesium alloy. The Chinese Journal of Nonferrous Metals, 2005, 15 (2): 210- 216.

MIN X G, DU W W, XUE F, et al. (2002). Analysis of EET on Ca increasing the melting point of $Mg_{17}Al_{12}$ Phase [J]. Chinese Science Bulletin, 2002, 47 (13): 1082- 1086.

BERKMORTEL J, HENRY H, JAMES E K. (2000). Die cast ability assessment of magnesium alloys for high temperature applications: Part 1 of 2 [J]. SAE Transactions, 2000, 109: 574- 581.

WANG Q D, CHEN WZ, ZENG X Q, et al.(2000). Effects of Ca addition on the microstructure and mechanical properties of AZ91magnesiumalloy [J]. Journal of Materials Science, 2000, 36 (12): 3035 -3040.

TANG B, Li S S, WANG X S, et al.(2005). Effect of Ca/Sr composite addition into AZ91D alloy on hot-crack mechanism [J]. Scripta Materialia, 2005, 53: 1077- 1082.

LI P J, ZHENG W C, TANG B et al.(2004). Effect of Ca, Sr on structure refinement of AZ91D Mg alloy. Special Casting & Nonferrous Alloys, 2004 (3): 8- 10.

MIN X G, SUN YANG S et al.(2002). Effects of Ca, Si and RE additions on the microstructures and mechanical properties of AZ91 based alloys. Journal of Southeast University (Natural Science Edition), 2002, 32 (3):409- 414.

WU G H, FAN Y, GAO H T, et al.(2005). The effect of Ca and rare earth elements on the microstructure, mechanical properties and corrosion behavior of AZ91D [J]. Materials Science and Engineering, 2005, A 408: 255- 263.

LIU S F, WANG H Y. (2006). The influence of Sr addition on the microstructure of AZ91 magnesium alloy and its refinement mechanism. Rare Metal Materials and Engineering, 2006，35(6):971-973

LI J F, GENG H R, TENG X Y.(2005). Effects of Ba on microstructure and mechanical properties of AZ91 Magnesium alloy. Hot Working Technology, 2005, (7):5-8，

LUO A A.(2004). Recent magnesium alloy development for elevated temperature applications [J]. International Materials Reviews, 2004, 49 (1):13 - 3.

YUAN Guang-yin, SUN Yang-shan, DING Wen-jiang.(2001). Effects of bismuth and antimony additions on the microstructure and mechanical properties of AZ91 magnesium alloy (J) Materials Science and Engineering, 2001, A308:38-44

TENG X Y, WANG B, WANG Z M et al. (2007). Effects of trace Si,Ba and Sn on the As-cast microstructure of AZ91 magnesium alloy. Special Casting & Nonferrous Alloys, 2007, 27(2):83-85

SUN Y S, WENF K Z,YUAN G Y.(1999). Effects of sn addition on microstructure and mechanical properties of magnesium alloys. The Chinese Journal of Nonferrous Metals, 1999, 9(1):55-58.

PEKGULERYUZ M O, AVEDESIAN M M. (1992). Mg alloying some pole mails for alloy development [J]. Keikinzakul Journal of Japan Institute of Light Metals, 1992, 42 (12):679 - 686.

WANG Z B, LIU J, YUAN Z X. (2005). Sb on the microstructure and mechanical properties of Mg alloy. Special Casting & Nonferrous Alloys, 2005,25(9):567-569

ZhANG G Y, ZHANG H, FANG, G L et al.(2005). A study on the mechanism of the influence of Bi, Sb alloying on microstructure and properties of AZ91 magnesium alloy. Acta Physica Sinica, 2005, 54(11):5288-5291.

YUAN G Y, SUN Y S, DINGWJ. (2001). Effects of bismuth and antimony additions on the microstructure and mechanical properties of AZ91magnesium alloy [J]. Materials Science and Engineering, 2001, A308:38- 44.

YUAN G Y, SUN Y S, ZENG X Q et al. (2001). Influence of Bismuth on the aging kinetics of AZ91 Magnesium alloy. Journal of Shanghai Jiaotong University, 2001, 35 (3): 451-456.

MORDIKE B L, EBERT T. (2001). Magnesium properties-applications potential [J]. Materials Science and Engineering, 2001, A302: 37-45.

GU J H, ZHANG X N,GU M Y.(2004). The damping performance of fiber reinforcement AZ91 magnesium base compound materials. Journal of Aeronautical Materials, 2004, 24 (6): 29- 33.

Trojanová Zuzanka , G"rtnerová Viera , Luká Pavel , et al.(2004).Mechanical properties of Mg alloys composites reinforced with short saffilfibres [J]. Journal of Alloys and Compounds, 2004, 378: 19-26.

ZHENG M Y, WU K, KAMADO S, et al.(2003). Aging behavior of squeeze cast SiCw/AZ91 magnesium matrix composite [J]. Materials Science and Engineering, 2003, A348: 67- 75.

CHEN L Q, DONG Q, GUO J H et al.(2005). The behavior of TiC/AZ91D magnesium matrix composites high temperature compression deformation. Acta Metallurgica Sinica, 2005, 41 (3) : 326- 332.

WANG J J , GUO J H, CHEN L Q. TiC/AZ91D composites fabricated by in situ reactive infiltration process and its tensile deformation [J]. Transactions of Nonferrous Metals Society of China, 2006, 16 (4) : 892- 896.

LEE W B, LEE C Y, KIM M K, et al. (2006). Microstructures and wear property of friction stir welded AZ91 Mg/SiC particle reinforced composite [J]. Composites Science and Technology, 2006, 66 (11-12):1513- 1520.

HASSAN S F, GUPTA M. (2006). Effect of length scale of Al_2O_3 particulates on microstructure and tensile properties of elemental Mg [J].Materials Science and Engineering, 2006, A 425 (1- 2):22- 27.

HASSAN S F, GUPTA M. (2005). Development of high performance magnesium nano-composites using nano-Al_2O_3 as reinforcement [J].Materials Science and Engineering, 2005, A392 (1-2):163- 168.

WANG Y, WANG H Y, XIU K, et al. (2006). Fabrication of TiB_2 particulate reinforced magnesium matrix composites by two-step processing method [J]. Materials Letters, 2006, 60 (12): 1533-1537.

WANG J J, GUO J H, CHEN L Q.(2006). TiC/AZ91D composites fabricated by in situ reactive infiltration process and its tensile deformation [J]. Transactions of Nonferrous Metals Society of China, 2006, 16 (4): 892- 896.

WANG Y, WANG H Y, XIU K, et al. (2006). Fabrication of TiB_2 particle reinforced magnesium matrix composites by two-step processing method [J]. Materials Letters, 2006, 60 (12): 1533-1537.

HASSAN S F, GUPTA M. (2005). Development of high performance magnesium nano-composites using nano-Al_2O_3 as reinforcement [J].Materials Science and Engineering, 2005, A392 (1- 2): 163- 168.

SUO Z Y, QIU K Q, YU Bo et al. (2005). Flow casting fabrication Ni-Nb Amorphous bond reinforced the AZ91magnesium matrix composition. Foundry, 2005, 54 (12):1227-1230.

Aikin R M Jr. (1997).Mechanical properties of in-situ composites · JOM, 1997, 49(8): 35-39.

17

Hot Forming Characteristics of Magnesium Alloy AZ31 and Three-Dimensional FE Modeling and Simulation of the Hot Splitting Spinning Process

He Yang[1], Liang Huang and Mei Zhan
State Key Laboratory of Solidification Processing, School of Materials Science and Engineering, Northwestern Polytechnical University, P.O.Box 542, Xi'an, 710072, China

1. Introduction

As one kind of lightweight alloys in the widely applications, magnesium alloys are currently the lightest structural materials with low density, high specific strength and specific stiffness, superior damping capacity [Michael et al., 1999; Mordike & Ebert, 2001]. The superior damping capacity is provided by the lower Young's modulus-E, and the value of E is no sensitive to material microstructures. When a structural component of magnesium alloy is subject to the same impact loadings, it can perform more elastic deformation and absorb more impact energy. Besides, stress distributions inside of a structural component of magnesium alloy are more uniform, thereby high stress concentrations can be avoided. Therefore, a structural component of magnesium alloy subjected to the impact loadings can be formed. Meanwhile, as one new continuous and local plastic forming technology, splitting spinning is designed to split a revolving disk blank from the outer rectangular edge into two flanges using a roller called splitting roller with a sharp corner, and then shaping spinning is done by two or three other forming rollers [Wong et al., 2003; Wang & Liu, 1986], as shown in Fig. 1. Compared with other conventional methods combining with casting, forging and welding and then mechanical processing, splitting spinning has the remarkable advantages of high efficiency, low cost and good flexibility, and its products for aeronautics, astronautics, automobile and weapon industry meet the high quality and high precision demands and are developed at low costs in a short time [Yang et al., 2004; Song et al., 2000]. Accordingly, based on the above remarkable advantages and application foregrounds of magnesium alloy AZ31 and the above manufacturing predominance of splitting spinning, a structure component of magnesium alloy AZ31 subjected to the impact loadings and with high quality and high precision can be formed using splitting spinning, such as, a wheel hub of aero undercarriage or kinds of light whole wheels.

According to the past research on deformation property of magnesium alloy, the ductility and formability of magnesium alloy is low at room temperature due to its hexagonal close-

[1] E-mail: yanghe@nwpu.edu.cn

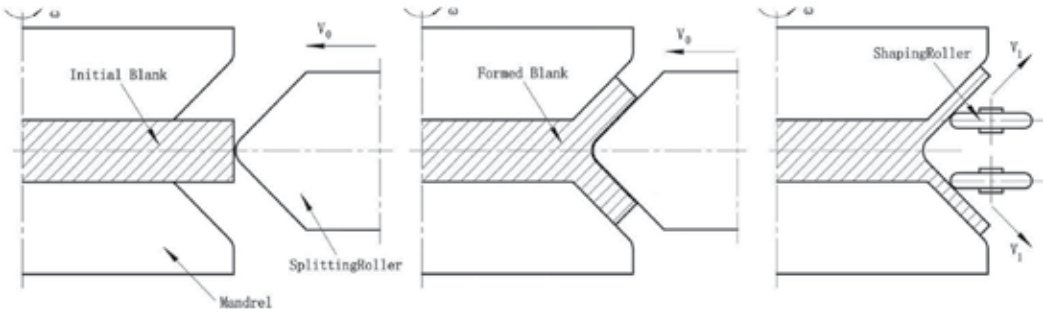

a) before forming b) during the forming process c) shaping spinning

Fig. 1. Schematic illustration of splitting spinning

packed (HCP) crystal structure, so it is difficult to be deformed. However, it shows excellent ductility and formability at elevated temperatures. Especially, magnesium alloy AZ31 is characterized by a good formability and ductility at elevated temperature [Palumbo et al., 2007]. The investigation by Ogawa et al. [Ogawa et al., 2002] indicated that the determination of appropriate forming temperature of magnesium alloy AZ31 is one of key factors, thereby the forming limit is improved and the fracture of specimen is avoided. The investigation by Doege et al. [Doege & Droder, 2001] indicated that high forming limit of magnesium alloy AZ31 could be obtained when the forming temperature exceeds 200˚C, on the contrary, forming limit reduced and forming quality of a structural component decreased when forming temperature reaches above 450˚C. Consequently, many recent research activities show that, magnesium alloy AZ31 has the features of the high plastic formability from 200˚C to 450˚C, and it can be deformed into a desired structural component.

Due to the limitation of experimental study and theoretical analysis, the investigations on the distributions of stress, strain and temperature and the influencing laws of forming parameters on forming quality are difficulties during metal forming processes. FE numerical simulation is applied increasingly and is becoming a very important tool for the research on the field distributions and forming quality of a structural component [Grass et al., 2003; Grass et al., 2006]. At present, there are only some research on the FE numerical simulations of splitting spinning. Based on the FE software DEFORM2D V5.02 and MARC/Autoforge V1.2, Hauk et al. [Hauk et al., 2000] studied the forming characteristics and rules of splitting spinning using elastic-plastic FEM, and the mechanism and laws of geometric dimensions of disk blank and friction influencing on deformation during the process are obtained under the two-dimensional space. And then experimental research are performed by means of the equipments called Tooling System, the influencing laws of different materials, different feed rates and different splitting spinning angles on splitting spinning force during the process are obtained [Schmoeckel & Hauk, 2000]. The deviation between two-dimensional simulation data and experiment data is acceptable, so the results are usable. Nevertheless, the 3D FE model reduced disk blank, simplified feeding mechanism system and ignored friction action between disk blank and supporting roller during the forming process in order to reduce computational time and improve computational efficiency. So, the above assumptions resulted in lower computational precision, such as, the splitting spinning force in simulations was less than the one in experiments, about one half. So in order to obtain more accurate simulation results, a reliable and practical 3D FE model of splitting spinning should be established.

The authors have studied the cold splitting spinning process of aluminium alloy. A reliable and practical 3D-FE model of cold splitting spinning of aluminium alloy is established, and

the variations of spinning force, stress fields and strain fields with time are obtained [Huang[1] et al., 2008]. The influencing laws of forming parameters of splitting spinning on the quality and precision of flanges are investigated based on the forming characteristics of splitting spinning combining with the behaviors of roller [Huang et al., 2009]. The influencing laws of material parameters on splitting spinning force, splitting spinning moment and forming quality of flange have been investigated [Huang[2] et al., 2008]. A reliable theoretical model established by the principal stress method is proposed for the calculation of splitting spinning force, and the influencing laws of forming parameters on splitting spinning force are investigated [Huang[3] et al., 2008]. However, the research on hot splitting spinning of magnesium alloy AZ31 is scant by now, so the above results may help study hot splitting spinning of magnesium alloy AZ31.

In this paper, according to the analysis of microstructures and deformation characteristics of magnesium alloy AZ31, the reasonable forming temperature range is obtained during the thermoplastic forming process. A three-dimentional elastic-plastic FE model of hot splitting spinning of magnesium alloy AZ31 is established based on the FEM software platform of ABAQUS/Explicit and a developed three-dimensional FE model of cold splitting spinning, and then the reliability is verified by theoretical evaluation. The modeling procedures are summarized, the comparisons of the modeling process between hot splitting spinning and traditional spinning are presented, and some key technologies are proposed. Adopting the FE model, field distributions of deformed component, including temperature fields, stress fields and strain fields, and variations of different nodal temperature are obtained, and the influencing laws of different initial temperatures of disk blank and different feed rates of splitting roller on the forming quality and precision of deformed flanges are investigated, consequently the optimal forming temperature and the optimal feed rate of splitting roller during the hot splitting spinning process of magnesium alloy AZ31 are obtained.

2. Hot forming characteristics of magnesium alloy AZ31

The deformation mechanisms of magnesium alloy mainly contain twinning and slip, and deformation texture roots in basal slips among grain boundaries [Staroselsky & Anand, 2003; Chino[1] et al., 2008; Chino[2] et al., 2008]. All these deformation mechanisms and texture characteristics affect plastic deformation behaviors, formability and mechanical property of magnesium alloy strongly. During the hot splitting spinning process, magnesium alloy AZ31 (Mg–3mass%Al–1%massZn–0.5%massMn) disk blank is mainly extruded, so microstructures of the extrusion specimen for different forming temperatures must be realized in order to obtain the optimal forming temperature range and forming parameters.

Thermal mechanical property of magnesium alloy AZ31 is quite related to processing technology, heat treatment process and so on, especially for different forming temperatures, thermal mechanical property of magnesium alloy AZ31 varies on a large scope. Therefore, according to the analysis of microstructures and deformation characteristics of magnesium alloy AZ31, hot forming characteristics are obtained. And then the forming rules during the hot splitting spinning process of magnesium alloy AZ31 under tensile stress and compressive stress simultaneously is revealed and the optimal forming parameters and forming temperature range are obtained.

According to excellent ductility and formability of magnesium alloy AZ31 at elevated temperatures and forming temperature variation from 200˚C to 450˚C, there are two kinds of specimen [Chino[2] et al., 2008], which are the extrusion magnesium alloy AZ31 processed by

extruding at 500˚C is called the sample A (above the high temperature variation) and the extrusion magnesium alloy AZ31 processed by extruding at 210˚C is called the sample B (within high temperature variation). Fig. 2 is shown as microstructure of magnesium alloy AZ31 specimen, (a) sample A and (b) sample B. Usually, the plasticity or ductility of magnesium alloy AZ31 is low at room temperature, but at elevated temperatures, plastic deformation energy is activated among grains and grain boundaries, so the plasticity and forming limit are improved. For magnesium alloy AZ31, forming temperature must be controlled from 200˚C to 450˚C. Because plastic deformation energy is inactivated among grains and grain boundaries below 200˚C, and disk blank of magnesium alloy AZ31 may brittle fracture easily, nevertheless, when temperature is above 450˚C, disk blank of magnesium alloy AZ31 may be oxide etch and grain size may become large, even phase transformation arises and plasticity decreases, as shown in Fig. 2(a). According to Fig. 2, it can be found that, microstructure of sample A shows large grain size obviously and the average grain size is 71 μm for sample A, and microstructure of sample B shows close and small grain size and the average grain size is 8 μm for sample B.

According to the above analysis of microstructures, the twin interfaces energy of magnesium alloy AZ31 is significantly large and twin nucleation decreases with decreasing grain size. The plasticity and formability of magnesium alloy AZ31 is low and the response of plastic deformation is inadequacy below 200˚C. But when magnesium alloy AZ31 is at elevated temperatures, the plastic deformation energy transforms internal energy and the forming process is done successfully and well, consequently the requirement of close and small grain size in a whole structural component is satisfied. Meanwhile, it is necessary to control the upper limit of forming temperature in order to avoid oxide etch and large grain size inside of the whole structural component of magnesium alloy AZ31, even phase transformation.

Furthermore, due to dynamic recovery (DRV) and dynamic recrystallization (DRX), deformation magnesium alloy shows distinct high temperature softening during the hot forming process. The strain softening is the typical characteristic of the elevated flow stress model of magnesium alloys, whose material response can principally be divided into two categories during the hot forming process, DRV type and DRX type. For magnesium alloy AZ31, DRX is the main characteristic of flow stress curves [Liu et al., 2008]. And also, the temperature of dynamic recrystallization (DRX) of magnesium alloy AZ31 is approximate from 533K to 593K [Liu et al., 2008].

According to the above microstructures and deformation characteristics of magnesium alloy AZ31 with the characteristics of homogeneous and isotropic elastic-plastic body, magnesium alloy AZ31 shows excellent ductility and plasticity when forming temperature ranges from 200 ˚Cto 450˚C. Therefore, plastic deformation mechanisms of magnesium alloy AZ31 and research foundations of hot splitting spinning of magnesium alloy AZ31 are obtained.

3. FE modeling process of hot splitting spinning of magnesium alloy AZ31

3.1 Establishment of FE model of hot splitting spinning of magnesium alloy AZ31

During the hot splitting spinning process of magnesium alloy AZ31, two Mandrels rotate at a rotational speed of ω, and SplittingRoller feeds at a linear speed of v in the radial

direction of Diskblank. Meanwhile, under the effects of the friction between Diskblank and SplittingRoller and the extrusions of two Mandrels, Diskblank is split into two flanges from the outer rectangular edge using SplittingRoller with a sharp corner, which come into the gaps at the joints between SplittingRoller and two Mandrels. After the forming ends, the radius of Diskblank reduces, and two flanges are produced. According to the forming characteristics of hot splitting spinning of magnesium alloy AZ31, Diskblank is defined as a 3D deformable solid body, SplittingRoller is defined as an analytical rigid body, and two Mandrels are defined as discrete rigid bodies. Each rigid body is assigned with a reference point (RP) to represent its rigid motion in all degrees of freedom. In materials Property module, the model gives the denty, Young's modulus, Poisson's ratio, constitutive equations and some thermal constants to material Diskblank which is a homogeneous and isotropic elastic-plastic body, and the model follows von Mises yield criterion and shear friction model [Yu & Chen, 1999].

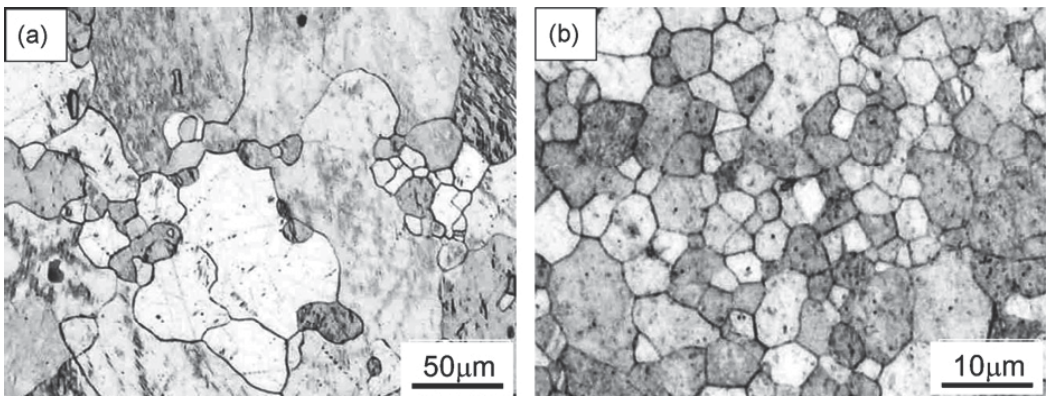

Fig. 2. Microstructure of magnesium alloy AZ31 extrusions, (a) sample A and (b) sample B[Chino[2] et al., 2008]

The heat transfer during the hot splitting spinning process of magnesium alloy AZ31 is a very complicated coupled thermo-mechanical problem. During the hot forming process, the free surface of disk blank exchanges heat with external environment by means of convection and radiation, and the contact surface conducts heat to the dies. Meanwhile, the plasticity deformation energy of disk blank is mostly converted into heat energy and internal energy. In order to define the thermal-dependent contacts among bodies and position them relative to each other in only one global coordinate system in which workpiece and dies would be identical with practical places during the hot forming process, some thermal-dependent contact surfaces and three thermal-dependent contact pairs are defined [Huang[1] et al., 2008]. The study arranges only one step called Splitting-Process in simulations, meanwhile, sets a suitable mass scaling factor in order to improve the computational efficiency. Moreover, here are the output requests, including Field output requests and History output requests, which contain stress, strain, displacement, force, temperature and energy of the whole model or special elements.

Consequently in this study, based on the FEM software platform of ABAQUS/Explicit, a three-dimentional elastic-plastic FE model of hot splitting spinning of magnesium alloy AZ31 is established, as shown in Fig. 3.

3.2 Key technologies treatments during the modeling process

3.2.1 Determination of exact forming time

During the 3D FE simulation process of hot splitting spinning of magnesium alloy AZ31, how to make sure the exact forming time is one of key factors which can exactly predict and control the hot forming process. Therefore, this study deduces a formula including velocity, displacement and time, as follows.

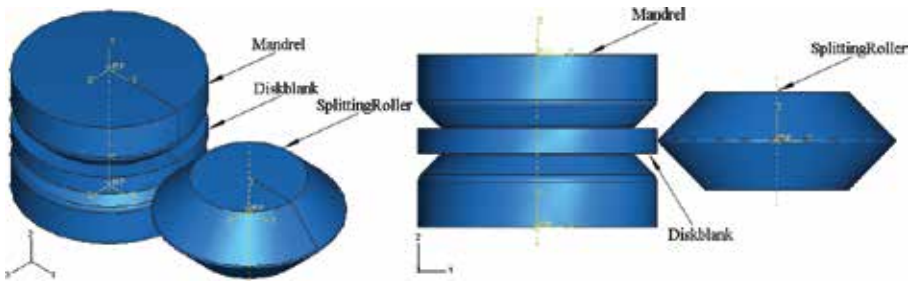

Fig. 3. Three-dimensional elastic-plastic FE model of hot splitting spinning of magnesium alloy AZ31 under ABAQUS/Explicit.

It is shown as the exact forming time calculation of splitting spinning in Fig. 4. According to Fig. 4, the ending face $\overline{A_1B_1}$ indicated by the thin broken lines before the forming translates to the ending face $\overline{A_2B_2}$ indicated by the broad real lines after the forming. Therefore, along the feeding direction of SplittingRoller, a formula is given as,

$$L_0 = V_0 T \tag{1}$$

where L_0 is the feed amount of SplittingRoller, V_0 is the feed rate of SplittingRoller, T is the forming time. Similarly, along the other feeding direction, a formula is given as,

$$L_1 = V_1 T \tag{2}$$

where L_1 is the other feed amount of SplittingRoller, V_1 is the other feed rate of SplittingRoller. Meanwhile, according to velocity vector analysis in Fig. 4, we obtain that

$$\sin\alpha = \frac{V_1}{V_0} = \frac{L_1/T}{V_0} = \frac{L - t_0/2}{V_0 T} \tag{3}$$

And the displacement L is obtained by

$$L = S_0 \cos\alpha \sin\alpha + \frac{t_0}{2}\cos\alpha \tag{4}$$

Therefore, substitution of Eqs. (4) into Eq. (3), the forming time T is expressed by

$$T = \frac{2S_0 \cos\alpha \sin\alpha + t_0 \cos\alpha - t_0}{2V_0 \sin\alpha} \tag{5}$$

Due to the round corner of SplittingRoller sticking to circumferential surface of the workpiece, the actual feed amount of SplittingRoller is less than the displacement L_0, as shown in right enlarged view of Fig. 4. So the displacement ΔL is obtained by

$$\Delta L = \frac{R}{\sin\alpha} - R \tag{6}$$

Therefore, the actual feed amount of SplittingRoller L' is expressed by

$$L' = L - \Delta L \tag{7}$$

According to Eqs. (4), (5), (6) and (7), the exact forming time of 3D FE model of splitting spinning after rearranging is given by

$$T = \frac{S_0 \cos\alpha \sin\alpha + \frac{t_0}{2}\cos\alpha + R\sin\alpha - R - \frac{t_0}{2}}{V_0 \sin\alpha} \tag{8}$$

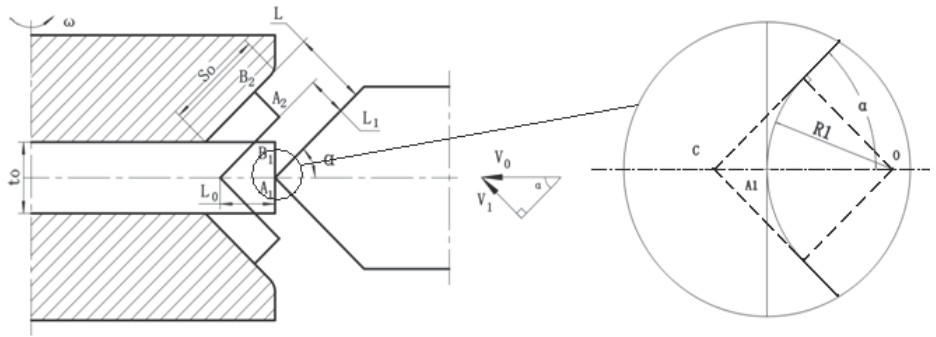

Fig. 4. Exact forming time calculation of splitting spinning

3.2.2 Determination of constitutive equations of magnesium alloy AZ31

Microstructures during the thermal plastic forming process reflects constitutive equations of thermal plastic deformation on the macroscopic view, namely, the flow stress model with the characteristics of temperature, strain rate, strain and microstructure evolution. It represents one basic variable during the hot forming process, and determines the loadings quantity and the required energy magnitude. The flow stress is affected not only by forming temperature, deformation degree, strain rate and chemical composition, but also by the microstructure evolution within deformation body.

The flow stress curves of magnesium alloy AZ31 at various strain rates is shown in Fig. 5 [Liu et al., 2008]. According to Fig. 5, the characteristics of magnesium alloy AZ31 stress-strain curves are represented as follows. (1) In the initial stage of the forming process, the stress abruptly increases to a peak due to the dominance of work hardening. (2) When the strain rate increases while the temperature is fixed, or the temperature decreases while the strain rate keeps unchanged, the overall level of the flow stress curve enhances correspondingly due to the growing work hardening. (3) When deformation exceeds the peak strain, the flow stress decreases at a rate which reduces with increasing strain as softening caused by DRX overtakes hardening caused by work hardening. (4) The flow stress shows steady-state region due to the equilibrium of work softening and work hardening finally. Consequently, a reasonable constitutive equation of magnesium alloy AZ31 which satisfies above deformation characteristics in the paper is adopted as follows [Liu et al., 2008],

$$\ln\sigma = \psi(\varepsilon - \varepsilon_p)^2 \ln\xi\varepsilon + \ln\sigma_p \tag{9}$$

where σ is plastic stress, ε is plastic strain, σ_p is the peak stress, ε_p is the peak strain, the value of parameter ξ is 0.6993, and the value of parameter ψ is 1.683 at the following deformation conditions: the temperature-T less than or equal 523 K, T less than or equal 573K and strain rate-$\dot{\varepsilon}$ greater than or equal $0.1\,s^{-1}$, T less than or equal 623 K and $\dot{\varepsilon}$ greater than or equal $1\,s^{-1}$; and the value of ψ equals to 1.28 at the other deformation conditions. The stress-strain curves of magnesium alloy AZ31 considering both macroscopic behavior and microscopic mechanism express the sensitivity of flow stress to temperature, strain rate, strain and microstructure evolution. This model of flow stress is in good agreement with the experiments data and has higher precision. The standard deviation between the model prediction values and the experiments data is approximately 2.32%. So, as far as the elevated deformation is concerned, this flow stress model can be applied to hot splitting spinning of magnesium alloy AZ31.

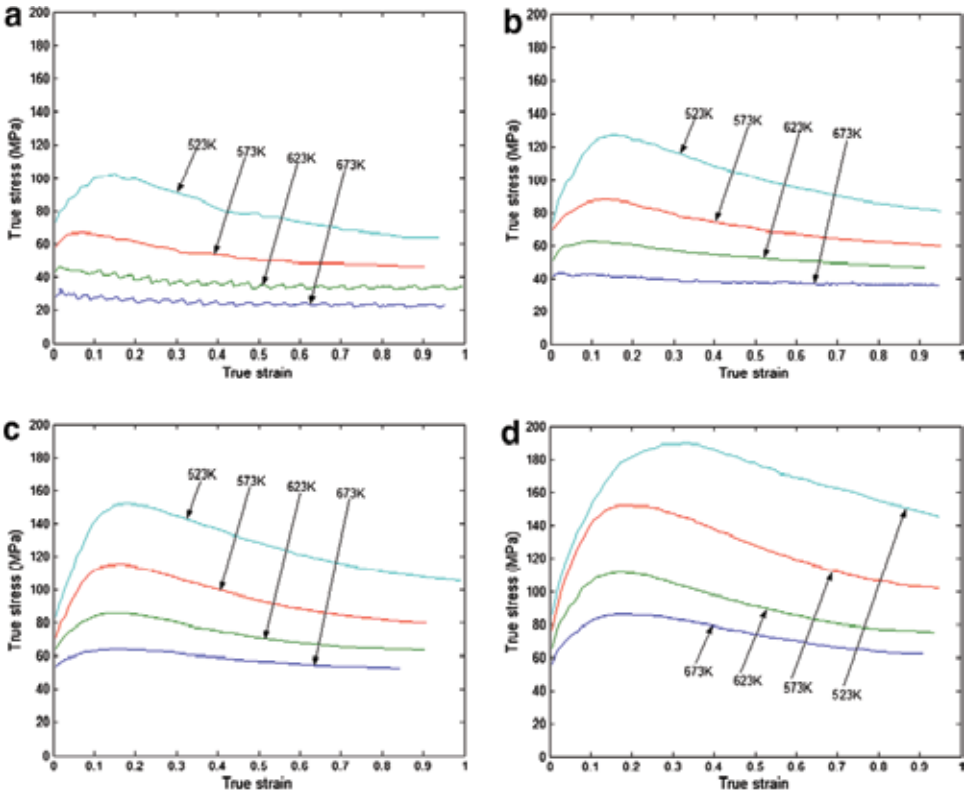

Fig. 5. Schematic of the stress-strain curves of AZ31 at various strain rates: (a) $\dot{\varepsilon} = 0.001^{-1}$, (b) $\dot{\varepsilon} = 0.01^{-1}$, (c) $\dot{\varepsilon} = 0.1^{-1}$, (d) $\dot{\varepsilon} = 1^{-1}$ [Liu et al., 2008]

3.2.3 Application of adaptive meshing technology

For one specific problem, the determinations of the number of elements, element shapes and element types are very important in order to get more precise results based on reasonable

computational fees. During the 3D FE modeling process of hot splitting spinning of magnesium alloy AZ31, elements must own not only appreciable rigidity called anti-distorting ability, but also appreciable flexibility called good forming ability [ABAQUS (version 6.4), 2004]. Therefore, adaptive meshing technology is used to avoid the element distortion and large deformation.

Adaptive meshing technology is a tool makes it possible to maintain a high-quality mesh throughout the analysis, even when large deformation or loss of material occurs, by allowing the mesh to move independently of material. According to a comparison between distorted elements without adaptive meshing technology and normal elements with adaptive meshing technology, practical deformation can be simulated by using adaptive mesh technology [Huang[1] et al., 2008]. Adaptive meshing technology in ABAQUS does not change the topology of the mesh, and combines the features of pure Lagrangian analysis and pure Eulerian analysis. This type of adaptive meshing is named Arbitrary Lagrangian Eulerian (ALE) analysis.

Therefore, the FE model makes use of adaptive meshing technology in order to reduce element distortion and maintain good element aspect ratios. The domain using adaptive meshing technology is defined as Diskblank, and then the definition of the boundary smoothing region is followed that: initial feather angle is 30˚, transition feather angle is also 30°, and mesh constraint angle is 60°. These settings can guarantee high computational efficiency in simulation computation. Meanwhile, in the settings of adaptive meshing technology, different remeshing frequencies may bring to different simulation results. For instance, there is almost no significant for the spinning force at different remeshing frequencies, but there is a significant deviation for the maximum equivalent plastic strain rate at different remeshing frequencies. Thus, in order to eliminate the impact on simulation results at different remeshing frequencies, the model uses remeshing sweeps after everyone increment, and define a suitable remeshing frequency.

3.2.4 Definition of frictional type and constraint type

The hot splitting spinning process of magnesium alloy AZ31 belongs to a continuous local plastic forming process, and the plastic forming area focuses on a small circumferential area of Diskblank. Friction behaviors during the hot forming process have particular characteristics: (1) friction between SplittingRoller and Diskblank is a main force driving the plastic forming, companying with material plastic movement, and (2) friction between flanges and exteriors of SplittingRoller or surfaces of mandrels produces along with the hot forming process, which holds back presentation of flanges and influences surface roughness of flanges. Therefore, based on the above frictional characteristics, the FE model calculates friction force by using the shear friction mode.

Constraint between mandrels and Diskblank cannot cause the plastic deformation, but may cause the elastic deformation at the beginning of the hot splitting spinning process of magnesium alloy AZ31. Diskblank rotates with mandrels, and deforms with SplittingRoller feedings. In ABAQUS, the types of constraints contain tie, rigid body, display body, coupling, shell-tosolid coupling, embedded region and equation [ABAQUS (version 6.4), 2004]. Therefore, based on above forming characteristics, one constraint called Tie is adopted to link Diskblank with mandrels due to the fact that Diskblank must rotate with mandrels. Tie can integrate mandrels with Diskblank as a whole, and provide them with different meshing methods, especially three-dimensional meshing.

3.3 Verification of FE model of hot splitting spinning of magnesium alloy AZ31

The FE model is reliable and reasonable based on the validation of the past research [Huang[1] et al., 2008]. Due to joining the thermal analysis procedure, it is necessary for hot splitting spinning of magnesium alloy AZ31 to carry out the theoretical evaluation [ABAQUS (version 6.4), 2004]. In order to indicate the FE simulation results being a receivable quasi-static solution, there are two main criteria, (1) when kinetic energy of deformation materials don't exceed approximately 5% to 10% of internal energy during the mostly simulation time, the adoptive mass scaling factor is reasonable, and (2) in order to obtain smooth solutions, it is necessary to validate whether the curve of kinetic energy is adequately smooth.

The relative values between Kinetic energy (ALLKE) and Internal energy (ALLIE) for whole model is shown in Fig. 6. According to Fig. 6, at the steady forming stage, the relative values between Kinetic energy and Internal energy is less than 5% obviously, so the curve satisfies the first criterion. The variations of Kinetic energy for whole model are shown in Fig. 7. According to Fig. 7, the Kinetic energy reaches a peak value in a short time, and then keeps steady state all the time, so the curve satisfies the second criterion. Therefore, the 3D elastic-plastic coupled thermo-mechanical FE model of hot splitting spinning of magnesium alloy AZ31 is reliable, steady and usable.

3.4 Characteristics of FE model

The comparisons of the modeling process between hot splitting spinning of magnesium alloy AZ31 and traditional spinning are as follows in this paper.

1. As Diskblank is extruded into the deformation zone step by step and then departs from the deformation zone after the flanges are manufactured, elastic-plastic FE method is adopted to control the elastic recovery of Diskblank in the modeling process of hot splitting spinning of magnesium alloy AZ31. But the rigid-plastic FE method is usually adopted in the modeling process of traditional spinning.
2. In the choice of FE arithmetic, a dynamic explicit algorithm in simulation of hot splitting spinning of magnesium alloy AZ31 is the same as the one in simulation of traditional spinning. The choice can avoid the characteristic of not-constringency by using a dynamic implicit algorithm.
3. In the definition of boundary conditions, since the angle between roller and blank is an important processing parameter and the roller-traces are variable, displacement boundary conditions are adopted in the definition of mechanics conditions of traditional spinning. But the angle between SplittingRoller and Diskblank is 0˚ and the roller-trace is unique during the hot splitting spinning process of magnesium alloy AZ31. Therefore, the velocity boundary conditions are adopted in the definition of mechanics conditions of hot splitting spinning of magnesium alloy AZ31.
4. In the element choice and meshing, triangle shell elements are usually adopted to study numerical simulations of traditional spinning, and the meshing are random. Only one element is modeled in the thickness. In this paper, due to hot splitting spinning belongs to the bulk deformation, hexahedral brick elements are adopted, which are the temperature-dependent quadratic reduced-integration elements (C3D8RT). These elements are not susceptible to locking, even when subjected to complicated states of stress. Therefore, these elements are also generally the best choice for the most general temperature-stress-displacement simulations. In meshing, concentric circle meshing mode is adopted in order to avoid hourglass modes. Furthermore, in the generation of flanges along axial direction, meshing is symmetrical.

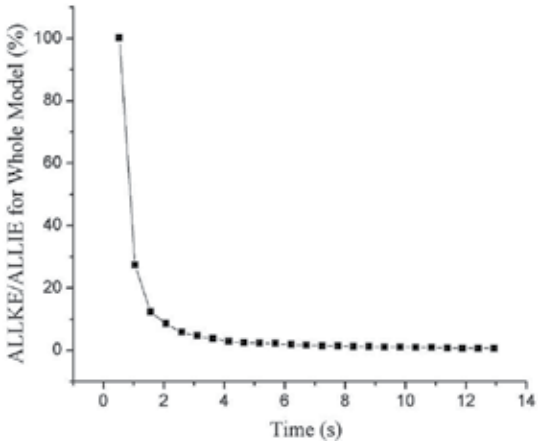

Fig. 6. The relative values between Kinetic energy and Internal energy for whole model

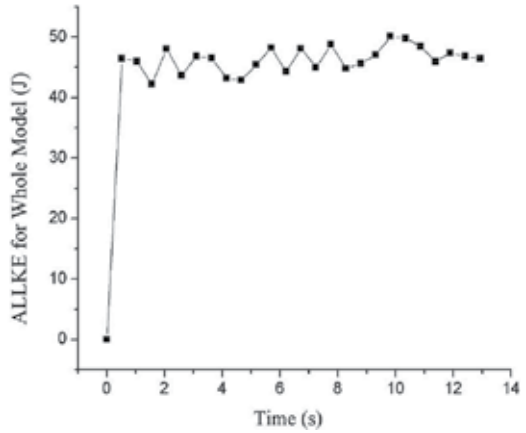

Fig. 7. The variations of Kinetic energy for whole model

4. Simulation results and discussion of hot splitting spinning of magnesium alloy AZ31

Based on the above established reliable, steady and usable 3D FE model of hot splitting spinning of magnesium alloy AZ31, this study adopts the temperature-dependent thermal conductivity, thermal expansion coefficient, Young's modulus and specific heat for magnesium alloy AZ31 (density: 1780 kg/m^3, Poisson ratio: 0.33) listed in Table 1-4 [Chen, 2005; Zhang & Zhang, 2004] and processing parameters of hot splitting spinning listed in Table 5 to numerical simulate. The field distributions of deformed component, including temperature fields, stress fields and strain fields, and the variation of different nodal temperature are obtained, and the influencing laws of different initial temperatures of disk blank and different feed rates of splitting roller on the quality and precision of deformed flanges are investigated, consequently the optimal forming temperature and the optimal feed rate of splitting roller during the hot splitting spinning process of magnesium alloy AZ31 are determined.

Temperature, ˚C	Thermal conductivity, W/(m·˚C)
96.4	25
101	100
105	200
109	300
113	400

Table 1. Thermal conductivity of magnesium alloy AZ31

Temperature,˚C	Expansion coefficient,˚C $^{-1}$
100	2.64E-005
200	2.7E-005
300	2.79E-005

Table 2. Thermal expansion coefficient of magnesium alloy AZ31

Temperature,˚C	Young's modulus, GPa
20	40.2
75	37.3
100	34.3
125	30.9
150	30.4
200	29.4
250	27.5

Table 3. Young's modulus of magnesium alloy AZ31

Temperature,˚C	Specific Heat, J/(kg·˚C)
20	1050
100	1130
200	1170
300	1210
350	1260

Table 4. Specific Heat of magnesium alloy AZ31

Initial diameter of Diskblank, mm	100.0
Initial thickness of Diskblank, mm	10.0
Diameter of SplittingRoller, mm	99.17
Splitting angle of SplittingRoller, degree	45.0
Radius of corner of SplittingRoller, mm	1.0
Feed rate of SplittingRoller, mm/s	1.0
Rotational speed of Mandrels, rpm	98.0
Dimension of Mandrels, mm	100.0
Friction coefficient between Diskblank and SplittingRoller	0.15
Friction coefficient between Diskblank and Mandrels	0.15
Temperature of environment, ˚C	20
Temperature of dies, ˚C	200
Initial temperature of Diskblank, ˚C	300
Heat transfer coefficient (Diskblank-dies), W/(m²˚C·)	2000
Heat transfer coefficient (Diskblank-environment), W/(m²˚C·)	20

Table 5. Processing parameters of hot splitting spinning

4.1 Temperature fields

During the hot splitting spinning process of magnesium alloy AZ31, because of the heat exchange between Diskblank and the external environment or the heat loss and the uneven interior heat source caused by the inhomogeneous deformation of Diskblank, the inner temperature gradient of deformed Diskblank are very large. Temperature field distributions of Diskblank during the process are shown in Fig. 8. According to Fig. 8, temperature field distributions of Diskblank are very uneven, and the temperature of deformed section of Diskblank is much higher than that of undeformed section. The temperature of inner section of Diskblank contacting with roller is higher than that of bilaterally symmetrical sections of Diskblank contacting with mandrels. The former temperature reaches about 270˚C and the latter temperature is just about 220˚C, as shown in Fig. 8(a), and the former temperature reaches about 250˚C and the latter temperature is just about 210˚C, as shown in Fig. 8(b). It is because friction and plastic deformation produce heat during the process, but the type of contact is surface contact and the temperature difference between dies and Diskblank is relatively large, so as to appear the large temperature gradients.

4.2 Nodal temperatures

In order to study the variations of different nodal temperatures for the whole disk blank, the location of trace points, including point A, point B and point C in the middle layer of disk blank and point D, point E and point F in the upper layer of disk blank, are shown in Fig. 9. The variations of temperatures with time at different trace points during the process are

shown in Fig. 10. From Fig. 10, the temperature variations between point A and point D is similar, so do point B and point E as well as point C and point F. Point A and point D are both the trace points of outer circumferential surface of disk blank, but point A contacting with roller in the middle layer belongs to local plastic deformation zone and point D contacting with mandrels in the upper layer belongs to deformed flanges zone. Although the curves between point A and point D are similar, the temperature of point A reaches one extremum at intervals at the ending stage of the process and the extremum is a little more than that of point D. Because at the ending stage of the process, the deformation heat leads to ascend at intervals at point A after the temperature of point A goes down to about 240˚C. Besides, point A obtains the contact heat, radiation and friction heat, so that the temperature of point A is more than that of point D. Because of higher temperature of Diskblank, heat exchange exists between dies and environment. There is no enough time to exchange heat with the outside at the beginning of simulation, but as the simulation going on, external temperature of Diskblank descends, so there is a temperature gradient between inside and outside of Diskblank leading to the heat is transferred to the outside of Diskblank.

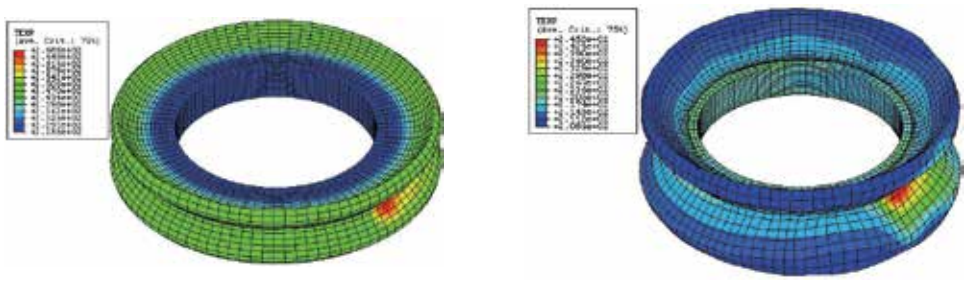

(a)step=12,time=6.206s. (b)step=25,time=12.93s.

Fig. 8. Temperature field distributions of Diskblank

The curve of point B is extremely similar to the curve of point E and the curve of point C is also extremely similar to the curve of point F, but the temperature of point B is a little more than that of point E and the temperature of point C is a little more than that of point F. The point in the middle layer of disk blank lies on the local plastic deformation zone, so more deformation heat is obtained. For the temperature distributions in the same layer of disk blank, the temperature of point A is more than that of point B and the temperature of point B is more than that of point C, and meanwhile the temperature of point D is more than that of point E and the temperature of point E is more than that of point F. The reasons are that, the deformation of outside circumferential zone is larger, and meanwhile the deformation energy and friction heat is larger than heat transferred from the surface to the environment. So, the temperature of point A and that of point D are relatively higher.

4.3 Strain fields

The logarithmic strain vector distributions at the ending stage of deformation are shown in Fig. 11. The logarithmic strain can reflect the accumulative effects of plastic deformation and metal flow directions. Therefore, the upper surface of deformed flanges contacting with mandrels and the under surface of deformed flanges contacting with roller both perform the tensile stress during the hot splitting spinning process of magnesium alloy AZ31, including

section A and section C, as shown in Fig. 11. This state leads to the increase of deformed flanges steadily. But Diskblank in section A and section C will fracture on condition that larger tensile stress. The middle part of deformed flanges performs the compressive stress during the process, including section B, as shown in Fig. 11. This state leads to deformed flanges being more regular figures and higher quality and precision. But Diskblank in section B will wrinkle on condition that larger compressive stress.

The variations of equivalent plastic strain fields with time during the hot splitting spinning process of magnesium alloy AZ31 are shown in Fig. 12. Compared with the past research on cold splitting spinning [Huang[1] et al., 2008], the temperature of two flanges is higher than that of local plastic deformation zone of flanges during the process due to deformed flanges

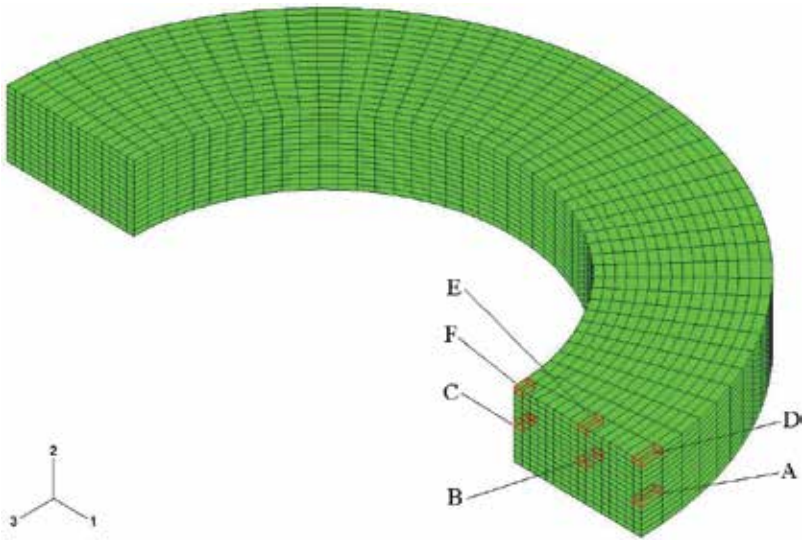

Fig. 9. Location of trace points

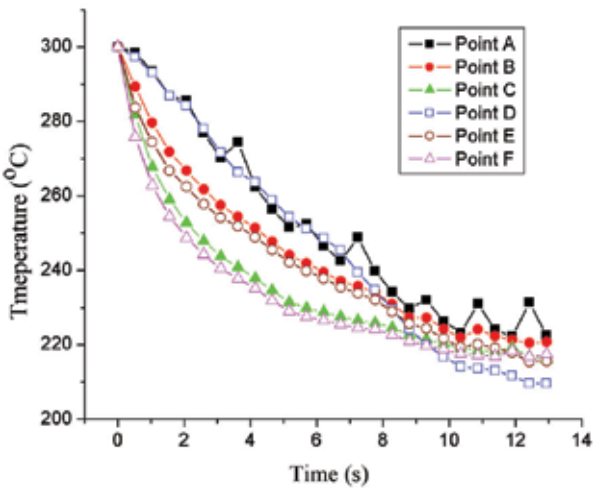

Fig. 10. Variations of temperatures with time at different trace points

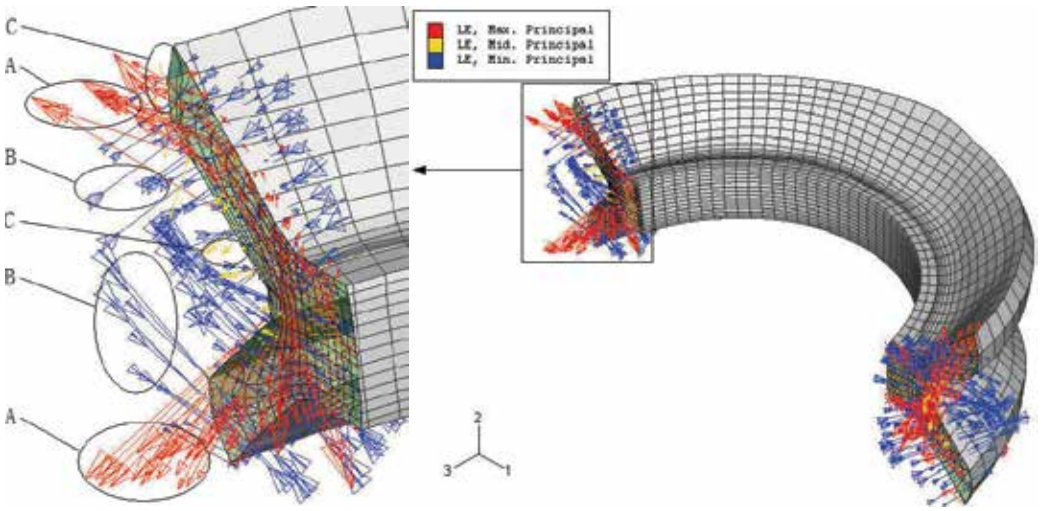

Fig. 11. Logarithmic strain vector distributions at the ending stage of deformation: A-Red, B-Blue, C-Yellow

contacting with both roller and mandrels. Consequently, there are two symmetrical belts in which equivalent strain distributions are uniform and even, as shown in Fig. 12(b). Furthermore, due to the thermal plastic deformation, the maximum equivalent plastic strain of hot splitting spinning is more than the maximum equivalent plastic strain of cold splitting spinning.

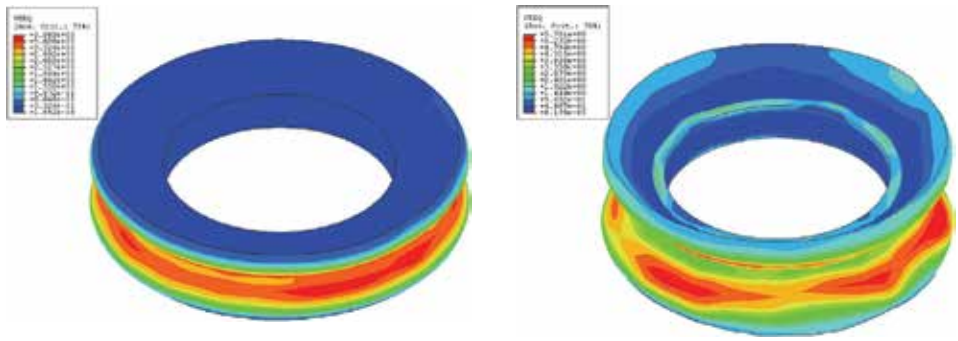

(a)step=12,time=6.206s. (b)step=25,time=12.93s.

Fig. 12. The variations of equivalent plastic strain fields with time

4.4 Stress fields

The variations of equivalent stress fields with time during the hot splitting spinning process of magnesium alloy AZ31 are shown in Fig. 13. From Fig.13, compared with the past research on cold splitting spinning [Huang[1] et al., 2008], stress concentration are not presented in the local plastic deformation zone contacting with roller due to the existence of softening process from DRX. There are enough heat for DRX in the upper surface of disk blank, therefore stress concentration are presented in the zone contacting with mandrels. Furthermore, the figure of stress concentration zone isn't like a belt, only a corresponding section contacting with local plastic deformation zone.

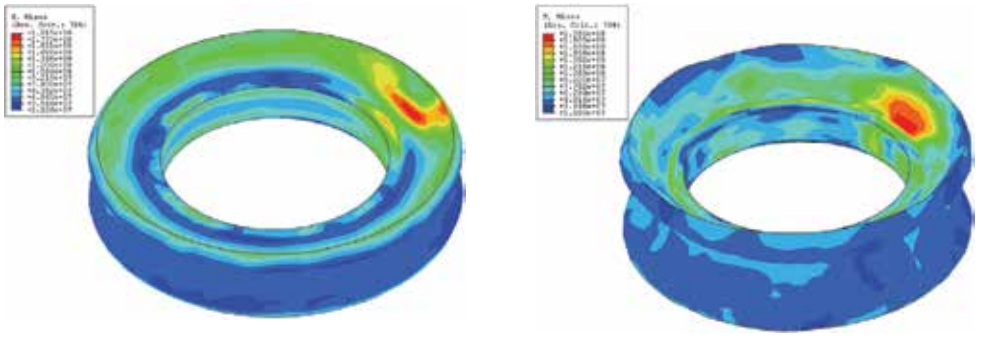

(a)step=12,time=6.206s. (b)step=25,time=12.93s.

Fig. 13. The variations of equivalent stress fields with time

4.5 Forming quality of deformed flanges

Due to the existence of softening process from DRX, different initial temperatures of disk blank and different feed rates of splitting roller have the important effects on the forming quality and precision of deformed flanges, so the corresponding influencing laws must be investigated. To study of the influencing laws of different initial temperatures of disk blank and different feed rates of splitting roller on the forming quality and precision of deformed flanges, the quantitative evaluations of deformed flanges are as following [Huang et al., 2009], including thickness deviation of flanges - δ_t and angle deviation of inner-face/outer-face - δ_1 / δ_2 . The definition of the responding geometries of roller and disk blank is shown in Fig. 14. The thickness deviation of flanges - δ_t is expressed by

$$\delta_t = \frac{t - t_0}{t_0} \times 100\% \tag{10}$$

where t is the thickness of simulation results and t_0 is the standard thickness. The angle deviation of inner-face - δ_1 , which contacts with the surfaces of roller, is expressed by

$$\delta_1 = \frac{\alpha_1 - \alpha_0}{\alpha_0} \times 100\% \tag{11}$$

where α_1 is the angle of inner-face of flanges and α_0 is the standard angle. The angle deviation of outer-face - δ_2 , which contacts with the surfaces of mandrels, is expressed by

$$\delta_2 = \frac{\alpha_2 - \alpha_0}{\alpha_0} \times 100\% \tag{12}$$

where α_2 is the angle of outer-face of flanges.

The influencing laws of initial temperature of Diskblank on thickness deviation of deformed flanges are shown in Fig. 15. From Fig. 15, in the defined scope of initial temperature of Diskblank, thickness deviation of deformed flanges decreases distinctly at the beginning stage, and then is close to approximately zero when temperature is 300˚C, and increases gradually with the increase of forming temperature, and finally reaches about 2%.

The influencing laws of initial temperature of Diskblank on angle deviation of deformed flanges are shown in Fig. 16. From Fig. 16, in the defined scope of initial temperature of Diskblank, the angle deviation of outer-face is a little more than that of inner-face, and they remain with the similar curves. The curves decrease distinctly at the beginning stage, and then increase gradually with the increase of forming temperature. When temperature is 300˚C, both angle deviations of deformed flanges are close to approximately zero simultaneously.

The influencing laws of feed rate of splitting roller on thickness deviation of deformed flanges are shown in Fig. 17. From Fig. 17, in the defined scope of feed rate of splitting roller, there are three phases for the changing curve. When $v < 1$ mm/s, thickness deviation of deformed flanges increases distinctly and is negative. When $1 \le v \le 3$ mm/s, thickness deviation holds approximately zero. When $v > 3$ mm/s, thickness deviation increases gradually and are positive, and the value is more than 4%.

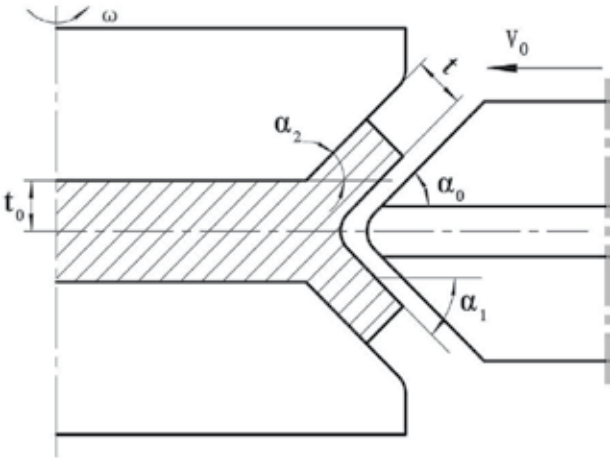

Fig. 14. The definition of the responding geometries of roller and disk blank

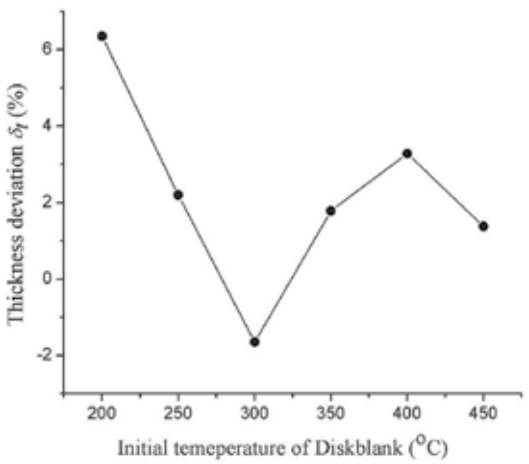

Fig. 15. The influencing laws of initial temperature of Diskblank on thickness deviation

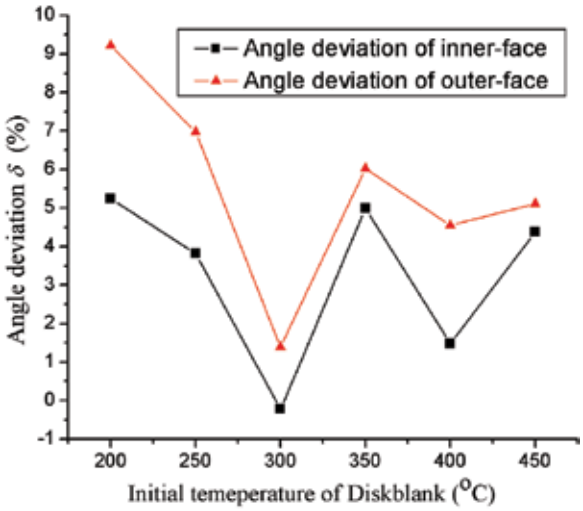

Fig. 16. The influencing laws of initial temperature of Diskblank on angle deviation

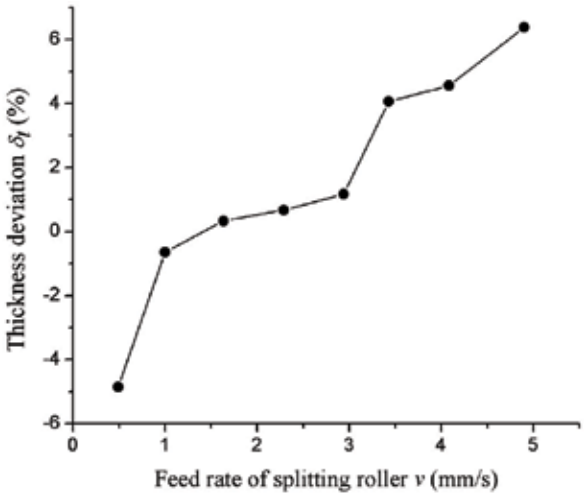

Fig. 17. The influencing laws of feed rate of splitting roller on thickness deviation

The influencing laws of feed rate of splitting roller on angle deviation of deformed flanges are shown in Fig. 18. From Fig. 18, in the defined scope of feed rate of splitting roller, when $v < 1$ mm/s, angle deviation of deformed flanges increases suddenly and are negative, and the values are less than –8%; when $1 \le v \le 3$ mm/s, angle deviation hold approximately from 0 to 2%; when $v > 3$ mm/s, angle deviation increases gradually, and angle deviation of inner-face reaches above 2% and angle deviation of outer-face reaches above 4%.

The above two quantitative evaluations of deformed flanges are relatively larger values when temperature is about 200˚C, namely, for initial temperature of Diskblank, thickness deviation is more than 6%, angle deviation of inner-face is more than 9% and angle deviation of outer-face is more 5%, and meanwhile for feed rate of splitting roller, thickness deviation is less than –5%, angle deviation of inner-face and outer-face are both less than

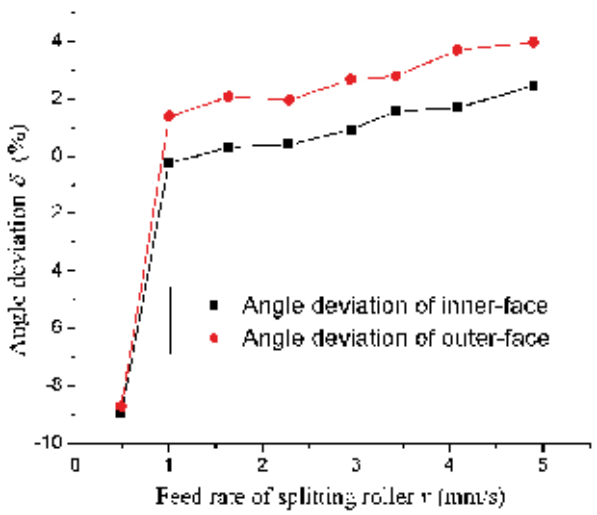

Fig. 18. The influencing laws of feed rate of splitting roller on angle deviation

–9%. And when temperature is about 450˚C, the above two quantitative evaluations of deformed flanges become even and steady, but larger values, namely, for initial temperature of Diskblank, thickness deviation is more than 4%, angle deviation of inner-face is more than 6% and angle deviation of outer-face is more 5%, and meanwhile for feed rate of splitting roller, thickness deviation is more than 6%, angle deviation of inner-face and outer-face are both less than 4%. Only when forming temperature is about 300˚C, the above two quantitative evaluations of deformed flanges are close to zero. The reasons are that, strain hardening and softening from DRX keeps an appropriate balance during the hot splitting spinning process of magnesium alloy AZ31 when temperature is about 300˚C, so here thickness deviation is minor and angle deviation is close to zero, and forming quality and precision are highest. In the same way, when the feed rate of splitting roller is defined from 1 to 3mm/s, forming quality and precision are also highest during the hot splitting spinning process of magnesium alloy AZ31. Consequently, the optimal forming temperature is approximate 300˚C and the optimal feed rate of splitting roller ranges from 1 to 3mm/s during the hot splitting spinning process of magnesium alloy AZ31.

5. Conclusions

In this paper, hot forming characteristics of magnesium alloy AZ31 are analyzed and a reasonable deformation temperature range is obtained during the thermoplastic forming process. Based on the FEM software platform of ABAQUS/Explicit and a developed three-dimensional FE model of cold splitting spinning, a three-dimensional elastic-plastic FE model of hot splitting spinning of magnesium alloy AZ31 is established, and the forming characteristics and laws are as follows.

1. During the hot splitting spinning process of magnesium alloy AZ31, temperature field distributions of Diskblank are very uneven, and the temperature of inner section of Diskblank contacting with roller is higher than that of bilaterally symmetrical sections of Diskblank contacting with mandrels, so there is a temperature gradient between inside and outside of Diskblank.

2. During the process, section A and section C (Fig. 11) perform the tensile stress, and this state leads to the increase of deformed flanges steadily; section B (Fig. 11) performs the compressive stress, and this state leads to deformed flanges being more regular figures and higher quality and precision. There are two symmetrical uniform belts in the equivalent strain distributions, and the stress concentration is presented in only one section contacting with mandrels.
3. The optimal forming temperature is approximate 300˚C and the optimal feed rate of splitting roller ranges from 1 to 3mm/s during the hot splitting spinning process of magnesium alloy AZ31.

6. Acknowledgements

The authors would like to thank the National Natural Science Foundation of China (Nos. 50405039 and 50575186), the National Science Found of China for Distinguished Young Scholars (No. 50225518), the National "863" Project of China (No. 2008AA04Z122) and the Foundation of NWPU (No. W018104) for the support given to this research.

7. References

ABAQUS (version 6.4) (2004). ABAQUS Analysis User's Manual, Inc.

Chen Zhenhua (2005). *Deformation Magnesium Alloys*, Chemical Industry Press, Beijing (in Chinese)

Chino[1] Yasumasa, Kimura Katsuya, Hakamada Masataka & Mabuchi Mamoru (2008).Mechanical anisotropy due to twinning in an extruded AZ31 Mg alloy, *Mater. Sci. Eng. A*, 485, 311–317

Chino[2] Yasumasa, Kimura Katsuya & Mabuchi Mamoru (2008) Twinning behavior and deformation mechanisms of extruded AZ31 Mg alloy, *Mater. Sci. Eng. A*, 486, 481–488

Doege E. & Droder K. (2001). Sheet metal forming of magnesium wrought alloys — formability and process technology, *J. Mater. Process. Technol.*, 115, 14–19

Grass H., Krempaszky C., Reip T. & Werner E. (2003). 3-D Simulation of hot forming and microstructure evolution, *Comput. Mater. Sci.*, 28, 469–477

Grass H., Krempaszky C. & Werner E. (2006). 3-D FEM-simulation of hot forming processes for the production of a connecting rod, *Comput. Mater. Sci.*, 36, 480–489

Hauk Stefan, Vazquez Victor H. & Altan Taylan (2000). Finite element simulation of the Flow-Splitting-Process, *J. Mater. Process. Technol.*, 98,70–80

Huang[1] Liang, Yang He & Zhan Mei (2008). 3D-FE modeling method of splitting spinning, *Comput. Mater. Sci.*, 42, 643–652

Huang[2] Liang, Yang He, Zhan Mei & Hu Li-jin (2008). Numerical simulation of influence of material parameters on splitting spinning of aluminum alloy, *Trans. Nonferrous Met. Soc. China*, 18, 674–681

Huang[3] Liang, Yang He, Zhan Mei & Yuli Liu (2008). Analysis of splitting spinning force by the principal stress method, *J. Mater. Process. Technol.*, 201, 267–272

Huang Liang, Yang He, Zhan Mei & Lijin Hu (2009). Forming characteristics of splitting spinning based on the behaviors of roller, *Comput. Mater. Sci.*, 45, 449–461

Liu Juan, Cui Zhenshan & Li Congxing (2008). Modelling of flow stress characterizing dynamic recrystallization for magnesium alloy AZ31B, *Comput. Mater. Sci.* 41, 375–382

Michael M. , Avedesian & Baker, Hugh (1999). *Magnesium and Magnesium Alloys*, ASM Specialty Handbook, USA

Mordike B. L. & Ebert T. (2001). Magnesium Properties — applications — potential, *Mater. Sci. Eng. A*, 302, 37–45

Ogawa N., Shiomi M. & Osakada K. (2002). Forming limit of magnesium alloy at elevated temperatures for precision forging, *Int. J. Mach. Tools Manuf.*, 42, 607–614.

Palumbo G., Sorgente D., Tricarico L., Zhang S. H. & Zheng W. T. (2007). Numerical and experimental investigations on the effect of the heating strategy and the punch speed on the warm deep drawing of magnesium alloy AZ31, *J. Mater. Process. Technol.*, 191, 342–346

Schmoeckel Dieter & Hauk Stefan (2000). Tooling and process control for splitting of disk blanks, *J. Mater. Process. Technol.*, 98, 65–69

Song Y. H., Zhang K. F., Wang Z. R. & Diao F. X. (2000). 3-D FEM analysis of the temperature field and the thermal stress for plastics thermalforming, *J. Mater. Process. Technol.*, 97, 35–43

Staroselsky A. & Anand L. (2003). A constitutive model for hcp materials deforming by slip and twinning: application to magnesium alloy AZ31B, *Int. J. Plast.*, 19, 1843–1864

Wang Chenghe & Liu Kezhang (1986). *Spinning Technology*, China Machine Press, Beijing (in Chinese)

Wong C. C., Dean T. A. & Lin J. (2003). A review of spinning, shear forming and flow forming process, *Int. J. Mach. Tools Manuf.*, 43, 1419–1435

Yang H., Zhan M., Liu Y. L., Xian F. J., Sun Z. C., Lin Y. & Zhang X. G. (2004). Some advanced plastic processing technologies and their numerical simulation, *J. Mater. Process. Technol.*, 151, 63–69

Yu Hanqing & Chen Jinde (1999). *The principle of metal plastic forming*, China Machine Press, Beijing (in Chinese)

Zhang Jin & Zhang Zonghe (2004). *Magnesium Alloy and Its Application*, Chemical Industry Press, Beijing (in Chinese)

18

Study on Thixotropic Plastic Forming of Wrought Magnesium Alloy

Hong Yan
Nanchang University
China

1. Introduction

Semi-sold material (SSM) forming was proposed by Flemings et al. from Massachusetts Institute of Technology (MIT) in 1972. SSM forming is one of the near-net-shape-forming processes which manufacture the final part by loading the materials at a temperature between liquidus and solidus. This way of forming difficult-to-machine materials is useful because there is much less strain resistance compared with conventional forging processes. Furthermore, energy savings and compact forming machinery become possible because of forming at smaller loads. Therefore, SSM forming is taken for one of the near-net-shape-forming having the best future in the 21th century (Kang et al., 1999).

Compared with casting magnesium alloys, wrought magnesium alloys have higher mechanical strength, better ductility and more varied mechanical properties. But the magnesium element is so lively that it is liable to be oxidated or burned during smelting and working. Simultaneously, the lower strength under high temperature and creep properties restrict the application of magnesium alloys in high temperature occasion. In addition, influenced by the microstructure, magnesium alloys have low deforming property and poor plasticity. Start from pursuing to the net forming technology and lighter production, the semi-solid thixo-forming technology becomes a preferred hot forming technique for wrought magnesium alloys (Flemings, 1991; Yan & Xia, 2005).

At high solid volume fraction (≥50%~60%), the behaviour of semi-solid material mechanics in the thixotropic plastic deformation process can be solved only when the relationship between stress and strain is obtained. Recently there have been a lot of studies on this field. A stress-strain relationship was investigated through considering the separate coefficient for semi-solid materials (Kang et al., 1998). The mathematical models of yield criterion and constitutive equations of mushy/semi-solid alloys were proposed (Kiuchi et al., 1998). The viscoplastic constitutive equations of SSM were presented by analyzing viscoplastic behaviour of material (Martin et al., 1997). On the basis of analysis of the thixotropic plastic deformation behaviour of semi-solid wrought magnesium alloy in compression process (Yan & Zhou, 2006), its constitutive model was established (Yan & Zhou, 2006).

Semi-solid processing technology is a new metal working technology in recent years, in which the alloys in semi-solid state have the excellent thixotropic and rheological properties. The deformation resistance in semi-solid state is influenced by not only solid volume

fraction and shear rate but also time, it's difficult to simulate semi-solid metal processing. Many researchers had carried out many investigations to simulations of semi-solid metal processing. The filling behaviours of semi-solid materials were described by computer simulation (Tims et al., 1996). Three-dimensional filling analyses with considering flow phenomena and solidification as a function of viscosity were performed (Lipinski & Flender, 1998). The numerical simulations on thixotropic as well as rheological forming focused mainly on the treatment of slurry or description of flow filling process. The few numerical simulations on the thixotropic forge in high solid volume fraction were reported.

The three main procedures in semi-solid metal processing are blank-making (Yan et al., 2005), reheating (Yan et al., 2006) and thixoforming (Yan et al., 2008). Thixo-forming is the last procedure, which benefits the quality of workpiece. Therefore the technological parameters in wrought magnesium alloy thixoforming process are well understood, analyzed, controlled and optimized using numerical simulation and experimental methods.

2. Thixotropic deformation behaviours of wrought magnesium alloy

2.1 Expermental

The experimental materials were the semi-solid wrought magnesium alloy (AZ61) and the conventional as-casted. In this study the chemical compositions of AZ61 magnesium alloy were listed in Table 1.

Element	Al	Mn	Zn	Si	Cu	Ni	Fe	others	Mg
Weight(%)	5.8%～7.2%	>0.15%	0.40%～1.5%	0.10%	0.05%	0.05%	0.005%	0.30%	Balance

Table 1. Chemical compositions of AZ61 magnesium alloy used in the experiment

The experiments were carried out in the Gleeble-1500 dynamic material testing machine. The sample was heated with the electric resistance method, whose temperature was measured by thermocouples. The graphite slices were placed between the specimen and the compression heads for reducing the influence of friction on experiment.

The solidus of AZ61 magnesium alloy was 525^{o}C, the liquidus was 620^{o}C. Therefore, the semi-solid deformation temperature period was 525^{o}C -620^{o}C. In order to study and master the characteristics of semi-solid magnesium alloy mechanics at high solid volume fraction, the deformation temperatures were taken as 528^{o}C, 538^{o}C, 550^{o}C and 560^{o}C respectively. According to the heating procedure shown in Fig.1, the initial heating rate was 10^{o}C/s; when the sample's temperature reached 500^{o}C, the temperature rate was down to 1^{o}C/s. The above scheduled temperatures reached with holding time 10mins. Then the semi-solid compression experiments were done under the strain rates of 0.1s^{-1}, 0.5s^{-1}, 5s^{-1} and 10s^{-1} respectively, in which the total strain was 0.8. At the same time, the compression of as-casted specimen was carried out with its temperature heated 522^{o}C and strain rate $\dot{\varepsilon} = 0.1s^{-1}$. The sample was taken immediately out for water quenching. Then the specimen was made to metallurgical phase sample and corrupted with 4% nitric and liquor, its microstructure changes were observed under the optical microscope.

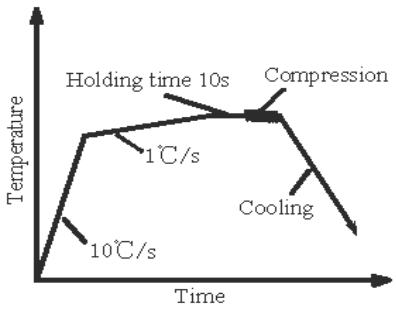

Fig. 1. Experimental heating procedure

2.2 The deformed and undeformed microstructures of wrought magnesium alloy

The undeformed microstructure of AZ61 magnesium alloy was composed of the branched grains that had a few large branched grains shown in Fig.2a. An ideal semisolid non-branched grain microstructure was obtained with prior compressive deformation 22%, heat treatment temperature 595°C and holding time 40min (Fig.2b) (Yan et al., 2005). Then the deformed microstructure of semi-solid AZ61 alloy was gained in thixotropic compression process.

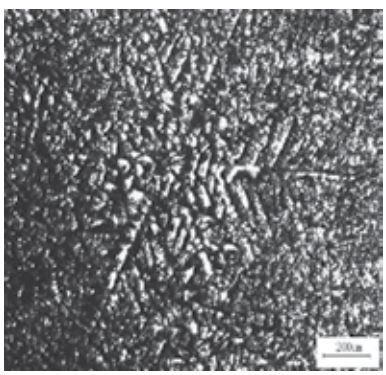

(a) Microstructure of conventional as-casted

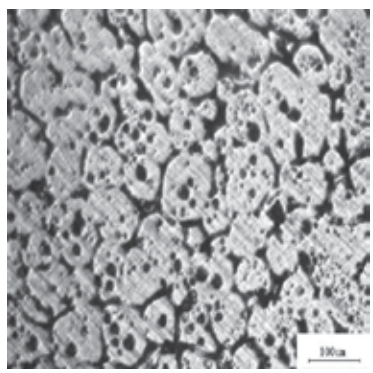

(b) Microstructure of semi-solid sample

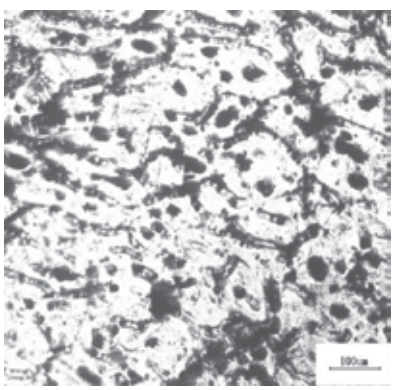

(c) Thixotropic deformed microstructure at free deformation zone

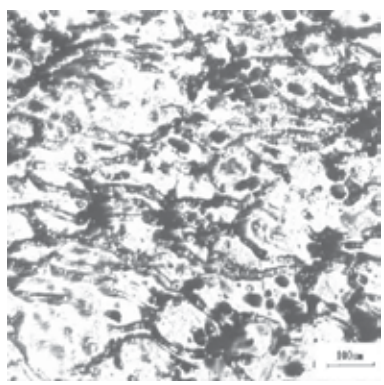

(d) Thixotropic deformed microstructure at large deformation zone

Fig. 2. The undeformed and deformed microstructures of AZ61 magnesium alloy

After the semi-solid AZ61 alloy was pressed by the large plastic deformation, its structure was changed obviously. The regular globular grains were flatted, having the unregular shape. Few liquid phases in the semi-solid material run basically off, the eutectic phase was deformed accordingly. As shown in Fig.2c, Fig.2d, the deformation degree of semi-solid globular grains was associated with the position of deformation zone in sample. The deformation degree in the centre zone (large deformation zone) was larger than one in brim zone (free deformation zone). In the whole thixotropic compression deformation process of semi-solid AZ61 magnesium alloy, the four deformation mechanisms exist such as liquid/flow; flow of liquid incorporating solid particles; sliding between solid particles and plastic deformation of solid particles mechanisms. Because of high solid volume fraction in the thixotropic compression deformation process, the sliding between solid particles and plastic deformation of solid particles mechanisms dominated in the centre of sample, the mix mechanisms ruled in the brim.

2.3 The relationships between stress and strain in thixotropic compression processes

The true stress-strain curves of thixotropic compression at the different temperatures for strain rate $\dot{\varepsilon} = 5s^{-1}$ were shown in Fig.3a, whose developing trends resembled basically. At the beginning of compression deformation, the strain value increased from 0 to 0.1. The stress increased rapidly with the strain increasing. When the stress reached the peak value, its strain value was around 0.1. After the stress reached up peak value, the stress held a little time with the strain increasing, the skeleton composed by solid particle slid and deformed gradually until it was destroyed thoroughly under pressure. When the stress peak value platform was passed, the stress descended slowly with the strain increasing, the softening phenomenon took place. As shown in Fig.3a, the stress peak values at temperatures of 550°C, 538°C and 522°C were 20.60MPa, 26.4MPa and 37.63MPa respectively. When the semi-solid temperature decreased from 550°C to 538°C, the stress peak value increased 5.81MPa, its growth rate was 25%. However, when the semi-solid temperature decreased from 538°C to 522°C, the stress peak value increased 11.22MPa, its growth rate was 43%. It was shown hat the deformation resistance of semi-solid AZ61 magnesium alloy was obviously smaller than one of conventional as-casted sample.

As shown in the Fig.3a and Fig.3b, under the same strain rate condition, the higher deformation temperature, the lower deformation resistance, and deformation resistance decreased obviously with the deformation temperature increasing. This was because the higher deformation temperature, the thicker thin film of liquid phase in grain boundary, and then the grain shape neared to spheroid, which made it slip and turn easily, the deformation resistance decreased. In the thixotropic compression deformation process of semi-solid AZ61 magnesium alloy, the deformed mechanisms were four major mechanisms: liquid/flow; flow of liquid incorporating solid particles; sliding between solid particles and plastic deformation of solid particles mechanisms.

However, which deformed mechanism was predominant? The increase or decrease of deformation resistance was decided by the solid volume fraction. When the solid volume fraction was lower, the solid particles were surrounded by liquid phase, and the deformation took place with liquid flow. The deformation force was thus very small, which was only required to overcome liquid resistance. When the solid volume fraction was higher, the liquid was few, the solid particles contacted with each other. The deformation force was required to overcome the friction generated from the sliding between solid

particles, and also to overcome the restriction of the solid particle movement due to the spatial constraint imposed by the surrounding particles. Therefore, in the beginning of compression process, the liquid/flow mechanism is unimportant, the other three mechanisms (namely flow of liquid incorporating solid particles, sliding between solid particles and plastic deformation of solid particles) are dominant. The original stress value was large, because the solid particles contacted with each other in very short time, taking place plastic deformation and finally leading the true stress rapidly increasing. At the same time, the higher the strain rate, the smaller the function of liquid/flow and flow of liquid

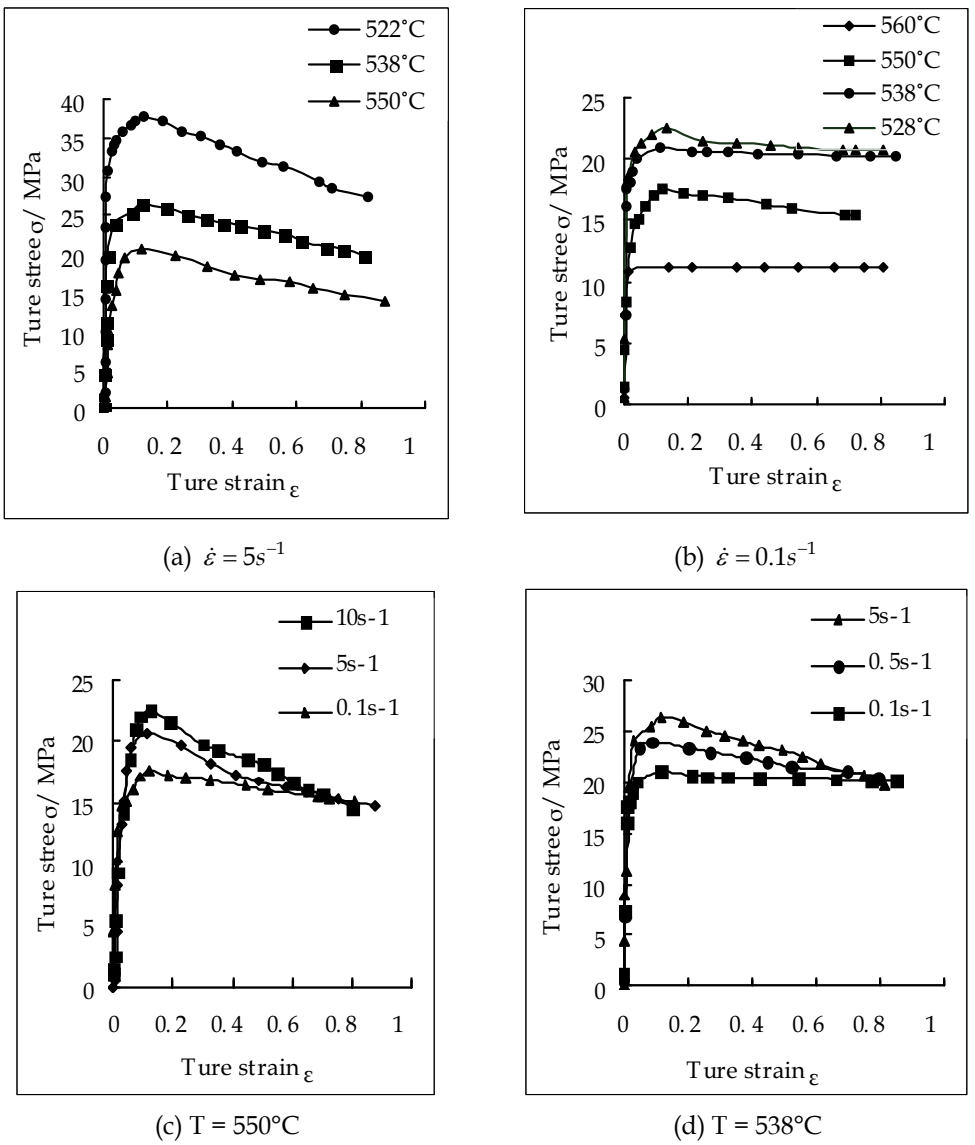

(a) $\dot{\varepsilon} = 5s^{-1}$ (b) $\dot{\varepsilon} = 0.1s^{-1}$

(c) T = 550°C (d) T = 538°C

Fig. 3. Relationships between true strain and stress in thixotropic compression deformation process

incorporating solid particles mechanisms in the same deformation temperature, in which the sliding between solid particles and the plastic deformation of solid particles mechanisms were dominant. The corresponding stress was larger.

3. Constitutive model of thixotropic plastic forming

3.1 Establishment of constitutive model

The relationship among processing parameters (strain rate, strain, temperature, liquid volume fraction) and stress was studied for semi-solid material at high solid volume fraction (Yan & Xia, 2002; Yan & Zhou, 2006). The relationship among variables was nonlinear. The relationship among stress σ, strain rate $\dot{\varepsilon}_z$ and strain ε_z was power function. The relationship among stress σ, temperature T and liquid volume fraction f_L was exponential function. So the relationship among stress σ, strain rate $\dot{\varepsilon}_z$, strain ε_z, temperature T and liquid volume fraction f_L was supposed as follows:

$$\sigma = \alpha_0 \cdot \exp(\alpha_1 T) \cdot \dot{\varepsilon}_z^{\alpha_2} \cdot \varepsilon_z^{\alpha_3} \cdot [1 - \beta f_L]^{a_4} \tag{1}$$

Where σ was stress, ε_z strain, $\dot{\varepsilon}_z$ strain rate, T temperature, β geometric constant (=1.5), α_0, α_1, α_2, α_3 and α_4 were material constants, f_L liquid fraction. $f_L = (\frac{T_M - T_L}{T_M - T})^{\frac{1}{1-K}}$, T_M the melting point of material, T_L liquidus temperature, k the distribution ratio of equilibrium.

The parameters in proposed constitutive model were determined by the multiple nonlinear regression method. Experimental dates were obtained in the unilateral compression processes. The nonlinear equation was transformed into linear one using logarithms for Eq. (1).

$$\ln\sigma = \ln\alpha_0 + \alpha_1 / T + a_2 \ln\dot{\varepsilon}_z + a_3 \ln\varepsilon_z + a_4 \ln[1 - \beta f_L] \tag{2}$$

Where $y = \ln\sigma$, $A_0 = \ln a_0$, $A_1 = a_1$, $A_2 = a_2$, $A_3 = a_3$, $A_4 = a_4$, $X_1 = 1/T$, $X_2 = \ln\dot{\varepsilon}_z$, $X_3 = \ln\varepsilon_z$, $X_4 = \ln(1 - \beta f_L)$.

Eq. (2) was changed as follow:

$$y = A_0 + A_1 X_1 + A_2 X_2 + A_3 X_3 + A_4 X_4 \tag{3}$$

The regression calculation and analysis of above equation were done by SPSS (Statistical Package for the Social Sciences). The usual statistics values were listed in Table 2 where the correlation coefficient R = 0.951, determination coefficient R^2 = 0.904, adjusted determination coefficient $\overline{R}^2$ =0.899, the Std. Error of the Estimate S=0.071, Durbin-Watson=0.343. Those showed that the representativeness of proposed constitutive model was strong.

R	R^2	$\overline{R}^2$	S	Durbin-Watson
0.951	0.904	0.899	0.07101259	0.343

Table 2. Model Summary

The analysis of variance was listed in Table 3 where the statistics values F=206.805, the concomitant probability value p<0.001. The relationship between independent variable x and dependent variable y was linear. In addition, Sum of Squares regression was 4.167, the residual error sum of squares 0.443, the total sum of squares 4.610, d.f. was degree of freedom.

	Sum of Squares	d. f.	Mean Square	F	Sig.
Regression	4.167	4	1.042	206.805	0.000
Residual	0.443	88	0.005		
Total	4.610	92			

Table 3. ANOVA

The analysis results of regression coefficients were listed in Table 4 where t was the inspection & statistics value of regression coefficient, Sig. was the concomitant probability value. It can be seen that the constant term A_0=25.000; regression coefficients A_1= -11560.385, A_2=0.026, A_3=-0.09, A_4=7.655; the inspection & statistics value of regression coefficient t= 6.443, -5.651, 5.761, -10.671, 8.220; the concomitant probability value p<0.001. Those indicated that the constitutive model had significance meaning.

$$y = 25 - 11560X_{1x} + 0.026X_2 - 0.09X_3 + 7.655X_4 \tag{4}$$

So Esq. (1) became

$$\sigma = \exp(25 - 11560/T) \cdot \dot{\varepsilon}_Z^{\,0.026} \cdot \varepsilon_Z^{\,-0.09} \cdot (1 - \beta f_L)^{7.655} \tag{5}$$

Eq.(5) was the nonlinear constitutive relationship of semi-solid AZ61.

	Unstandardized Coefficients		Standardized Coefficients	t	Sig.
	B	Std. error			
A_0	25.000	3.881		6.443	0.000
A_1	-11560.385	2045.703	-1.815	-5.651	0.000
A_2	0.026	0.005	0.217	5.761	0.000
A_3	-0.09	0.012	-0.356	-10.671	0.000
A_4	7.655	0.931	2.618	8.220	0.000

Table 4. Coefficients

3.2 Analytical results and discussion

Comparisons between the predicted and experimental results in thixotropic compression processes were shown in Fig.4 The true stress-strain curves of thixotropic compression at the different temperatures for strain rate $\dot{\varepsilon}_z$ = 0.1s-1 were shown in Fig.4a, whose developing trends resembled basically. At the beginning of compression deformation, the strain value

increased from 0 to 0.1. The stress increased rapidly with the strain increasing. When the stress reached the peak value, its strain value was around 0.1. After the stress reached up peak value, the stress held a little time with the strain increasing, the skeleton composed by solid particle slid and deformed gradually until it was destroyed thoroughly under pressure. When the stress peak value platform was passed, the stress descended slowly with the strain increasing, the softening phenomenon took place. Under the same strain rate condition, the higher the deformation temperature, the lower the deformation resistance, and the deformation resistance decreased obviously with the deformation temperature increasing. The true stress-strain curves of thixotropic plastic compression at the different strain rate under the same deformation temperature were shown in Fig.4b. It is seen that under the same deformation temperature, the lower the strain rate, the lower the deformation resistance and the peak value.

Fig.4 showed that the results calculated by multiple nonlinear regression method were good agreement with experimental ones. So, the proposed constitutive model had the higher forecast precision and practice meaning.

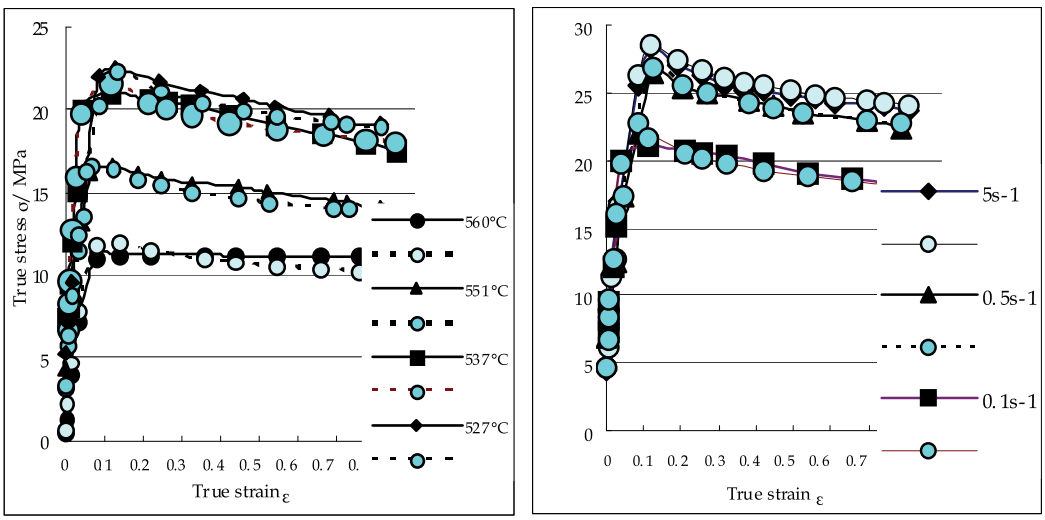

(a) $\dot{\varepsilon} = 0.1s^{-1}$ (b) T = 538°C

Fig. 4. Comparisons between predicted and experimental results in thixotropic plastic compression processes

4. Numerical simulation of thixotropic plastic forming

To investigate thixoforming process with numerical simulation method, which was a nonlinear system, some assumptions were taken as follows: (1) The semi-solid metal was assumed as a continuous and incompressible metal fluid. (2) The solid grains in semi-solid metal were uniformly distributed in liquid phase, and because of the large deformation in forming, the semi-solid material was considered as an isotropy uniform medium.

The material adopted in this paper was AZ61 wrought magnesium alloy, and the simulations were performed in traditional forging/extrusion and thixo-forging/thixo-

extrusion processes. The flow stress model of AZ61 wrought magnesium alloy in traditional forging/extrusion processes was presented as follows (Zhou et al., 2004):

$$\sigma = A_5 \cdot \varepsilon^n \cdot \dot{\varepsilon}^m \cdot \exp(s\varepsilon - \frac{Q}{RT}) \tag{6}$$

Where A_5 is constant; n is exponent; m is strain-rate sensitivity; s is exponent for the strain softening influence, negative; Q is activation energy; R is gas constant (8.31kJ/mol).
The flow stress model of AZ61 wrought magnesium alloy in thixo-forging/thixo-extrusion processes was expressed as follows (Yan & Zhou, 2006)

$$\sigma = \exp(25 - 11560 / T) \cdot \dot{\varepsilon}_Z^{\,0.026} \cdot \varepsilon_Z^{\,-0.09} \cdot (1 - \beta f_L)^{7.655} \tag{7}$$

Where σ is the stress; ε_z the strain; $\dot{\varepsilon}_z$ the strain rate; T temperature; β constant; f_L liquid volume fraction.

4.1 Finite element analysis of thixo-forging

In this study, the magnesium alloy workpiece is formed by the close-forge method. The experiment set-up was shown in Fig.5. Fig.6 shows the workpiece, whose structure and flow character are complicated. Comparisons between forging and thixoforming of the workpiece will be done and predicted in advance using numerical simulation. This is an effective method to instruct application of semi-solid forming technology into its practice production. The same simulated parameters are used to analyze the differences of mechanics properties, flow rule and temperature between forging and thixoforming processes. The materials are normal and semi-solid AZ61 magnesium alloy respectively.
Fig.7 shows the load-stroke curves at 559°C in forging and thixoforming. In the two forming processes, the loads in the initial stage varied gently. When the stroke reached 12.3mm, the rest of the load increased evidently, resulted from forming of claw. When the stroke reached

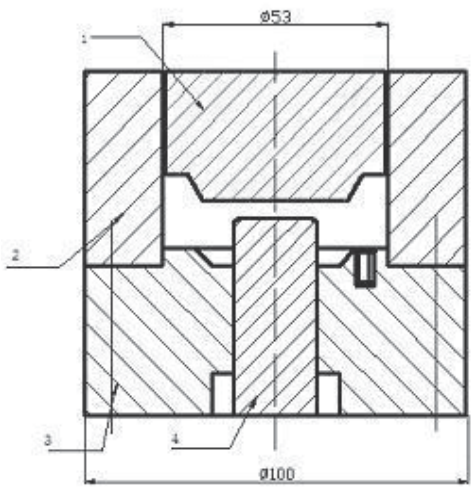

Fig. 5. Experiment set-up

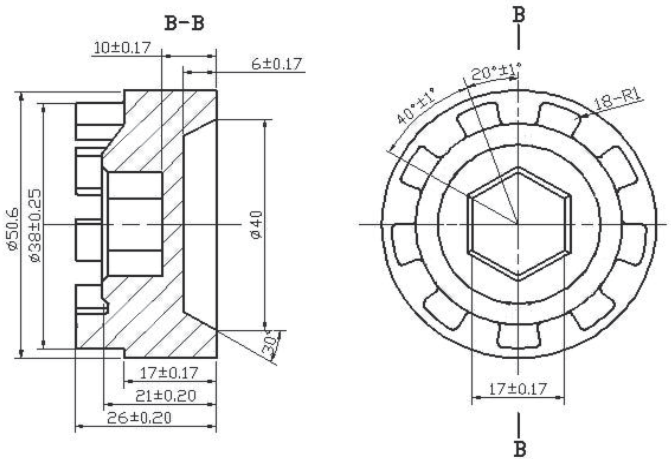

Fig. 6. AZ61 alloy workpiece

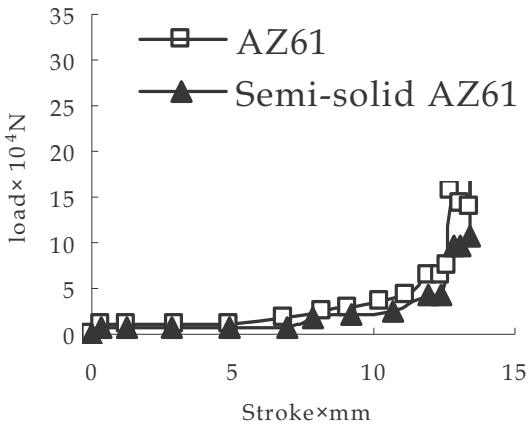

Fig. 7. Load-stroke curve at 559℃

12.8mm, the load had the trend of decreasing. And in the last stage of filling, the load rose sharply. From Fig.7 we can get that at 12.88mm, the load of forging is much larger than that of thixoforming, and it can be illustrated that the deformation resistance in semi-solid forming process was smaller than that in forging process, in which the former filling property was superior to the latter. The maximum simulated load in forging was 0.29MN, The maximum simulated load in thixo-forging was 0.19MN. The results presented that in the same conditions, the deformation resistance in thixo-forging was about 1/3 less than that in forging, which show a very good agreement with those observed in the experiment. But they were less than the experimental results. The friction coefficient was invariability, and interference fit was used in the simulation model, in which the material can't be squeezed into the gap between dies. The workpiece margin was formed in the experiment, which resulted that experimental loads were higher than simulation ones.

Fig.8 showed the effective stress distributions before completed fill in both forging and thixo-forging at 559°C.The effective stress distribution existed unevenly in forging, whose value (the final 92.4Mpa) was so big that the residual stress could be resulted in workpiece.

That needed to add another working procedure for treating. Effective stress distribution in thixoforming was uniform and its value (the final 30.8Mpa) was small, which was contributed from the excellent fluidity of semi-solid metal.

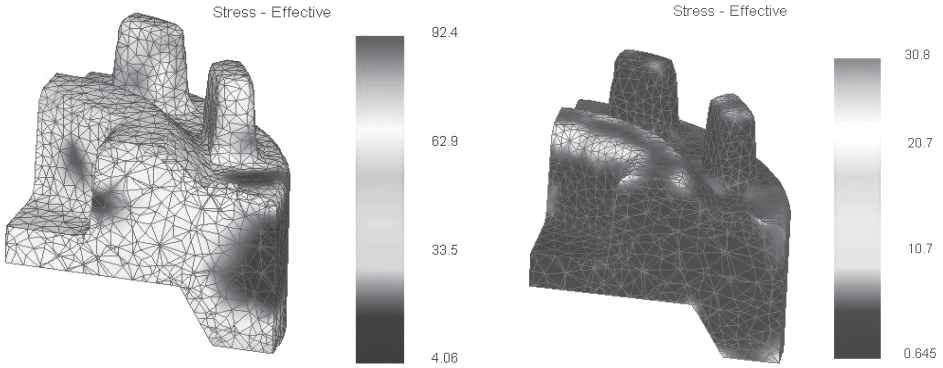

(a) Traditional forging (b) Thixo-forging

Fig. 8. Effective stress distributions of wrought magnesium alloy in traditional forging and thixo-forging processes

Fig.9 and Fig.10 gave the effective strain simulated results in forging and thixo-forging respectively. In the initial stage, the hexagon hole in central section of workpiece was extruded and the rest moved in the rigid motion. In this stage, the strain distributions had few differences between forging and thixo-forging. As the stroke increased, metal deformation entered into the second stage, in which metal flowed from central to around in the extrusion pressure, and the central protruded and bottom platforms were formed. In the second stage, the strain distributions in the two kind of forming processes had a great of differences. Effective strain of the claw root in thixo-forging reached 2.0, and the most of semi-solid metal except outermost layer were in the big strain zone. Effective strain of the claw root in forging reached only 1.1, and most of metal had smaller effective strain, which resulted in material flowing difficulty. In the last stage of metal forming, semi-solid material, due to its prior good strain distribution, could fill up claw easily, and the effective strain in the claw root reached 3.0, and the stress decreased to 30.8MPa. Whereas, effective strain in forging was smaller than that in thixo-forging, and its maximum effective strain in the claw root was only 1.91, and the stress reached 92.4MPa. Therefore, forging was more difficult in filling cavity than thixo-forging. That coincides with the experimental results.

Fig.11 showed the traditional forging and thixo-forging workpieces of magnesium alloy. The thixo-forging had better fill effect and surface finish quality than traditional forging, which could achieve near-end deforming with high workpiece quality. The maximum load was 0.35MN in traditional forging, and 0.24 MN in thixo-forging, which showed that the deforming force of semi-solid material was one third of that of traditional material in same conditions. The reason was that the branched grains formed continuous net framework structure in traditional forging. It had better support stress ability, higher deforming resistance and worse filling effect. In thixo-forging, the deformation force was required mainly to overcome particle sliding and particle plastic deformation, in which the sliding between solid particles and plastic deformation of solid particles mechanisms were dominant. The deformation resistance decreased obviously with deformation temperature increasing.

Fig. 9. Effective strain distribution of wrought magnesium alloy in thixo-forging process

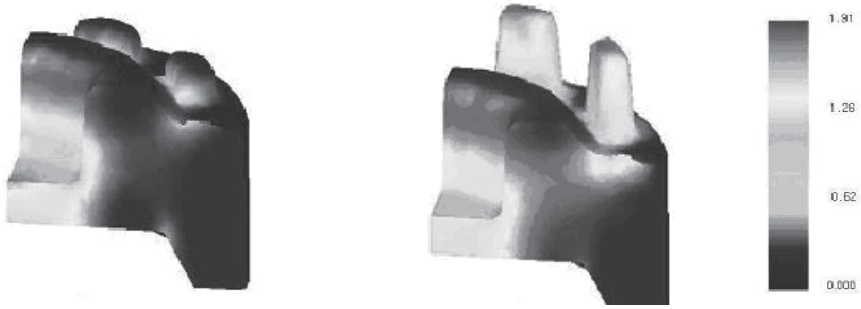

Fig. 10. Effective strain distribution of wrought magnesium alloy in traditional forging process

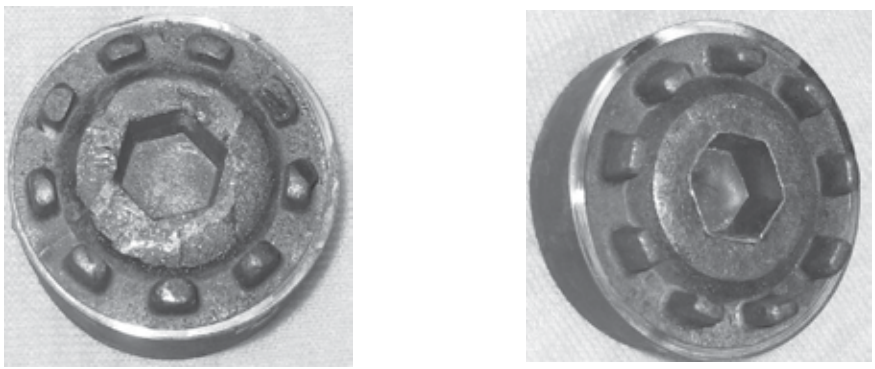

(a) Traditional forging workpiece (b) Thixo-forging workpiece

Fig. 11. Traditional forging and thixo-forging workpieces of wrought magnesium alloy

4.2 Finite element analysis of thixo- extrusion

The same simulated parameters were used to analyze the differences of mechanics properties, flow rule and temperature between traditional extrusion and thixo-extrusion processes. The extrusion set-up was shown in Fig.12. The materials were normal and semi-solid AZ61 wrought magnesium alloy respectively. Environment temperature was 20°C, the warm-up temperature of die was 300°C. The friction model was constant shearing stress model, whose friction factor was 0.65. Extrusion ratio was 4. Extrusion speeds were 100mm/s and 200mm/min respectively.

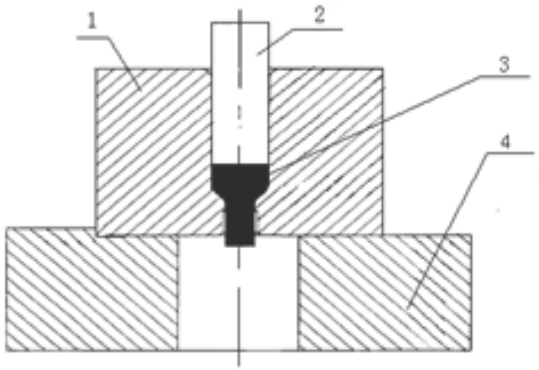

Fig. 12. Extrusion set-up （1.die 2.punch 3.billet 4.base seat）

Fig.13 and Fig.14 gave the effective strain distributions simulated results in extrusion and thixo-extrusion processes respectively. The strain distributions had few differences between extrusion and thixo-extrusion processes.

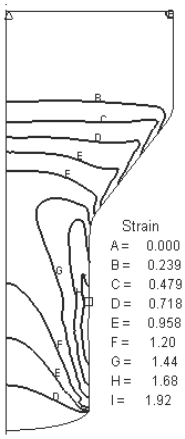

(a) step 18

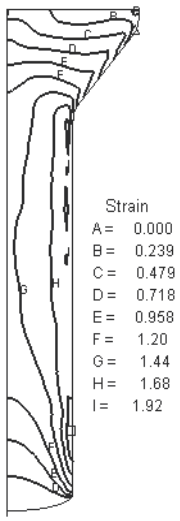

(b) step30

Fig. 13. Effective strain distributions in extrusion

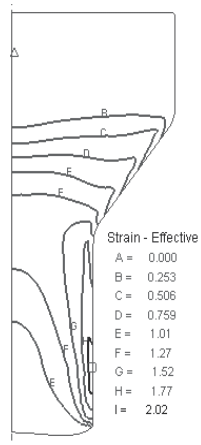

(a) step 18

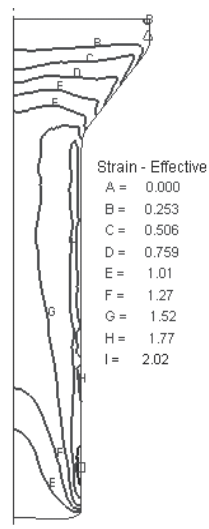

(b) step30

Fig. 14. Effective strain distributions in thixo-extrusion

Fig.15 showed the effective stress distributions before finished in extrusion and thixo-extrusion processes. From Fig.4a we could know that effective stress distribution existed unevenly in extrusion process, whose value was so big (100MPa) that the residual stress could be resulted in workpiece. That needed to add another working procedure for treating. The effective stress distribution in thixo-extrusion process was uniform and its value was small (30MPa), which was contributed from the excellent fluidity of semi-solid metal.

Distribution of temperature influenced the stress distribution of workpiece, which affected the local deformation resistance, and also influenced the distribution of strain and deformation fluidity. Fig.16 showed the temperature distributions in both extrusion and

thixo-extrusion processes. It could be gained that the temperature grads in extrusion process was larger than that in thixo-extrusion process, the former distribution was worse than the latter.

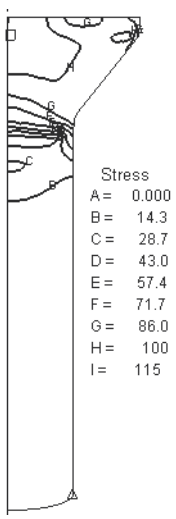

(a) extrusion

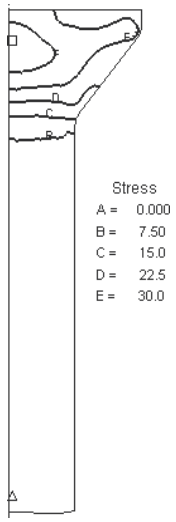

(b) thixo-extrusion

Fig. 15. Effective stress distributions

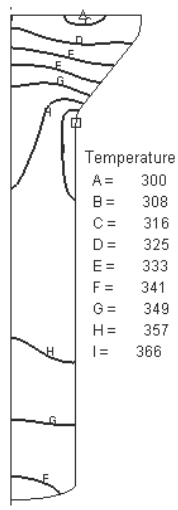

(a) extrusion

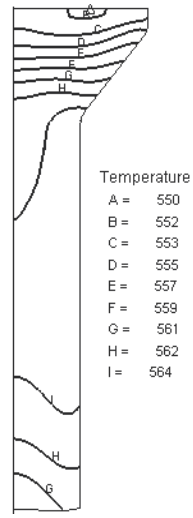

(b) thixo-extrusion

Fig. 16. Temperature distributions

The load-stroke curves between thixo-extrusion and conventional extrusion processes were shown in Fig.17(a) and Fig.17(b), in which the real line stood for extrusion speed 100mm/min and the broken line stood for extrusion speed 200mm/min. The deformation resistance in thixo-extrusion process was about 1/3 less than that in conventional extrusion process. The deformation resistance in conventional extrusion process was higher because a conventional dendritic structure formed the continuous mesh skeleton and the withstanding stress ability was stronger. The deformation resistance in thixo-extrusion process was lower, which was resulted from overcoming the grains' gliding and plastic deformation, because the liquid phase existed. The liquid phase increased with the temperature increasing, its resistance descended largely. Fig.17 (b) showed the thixo-extrusion load-stroke curves with different velocities and temperatures. The deformation resistance decreased with the increasing of temperature at the same velocity, in which the decreasing trend was obvious at the higher temperature. This reason was that the liquid membrane in the grain boundary was thicker and the grain' shape was close to spherical, made the grain turning and gliding more easy. The deformation resistance increased with the increasing of velocity at the same temperature. The maximum load in conventional extrusion process was 75KN at 300°C, which was 4 times larger than that in thixo-extrusion process. Simulation results were good agreement with experimental ones.

Fig.18 showed the samples resulted in thixo-extrusion process at different temperatures (590°C, 580°C, 570°C, 550°C, 530°C), in which the sample's surface was perfect with no crack when the temperature was lower than 570°C (Fig.18c-18e). The sample's surface had the micro crack above 580°C (Fig.18b), which become serious when the temperature reached 590°C (Fig.18a).

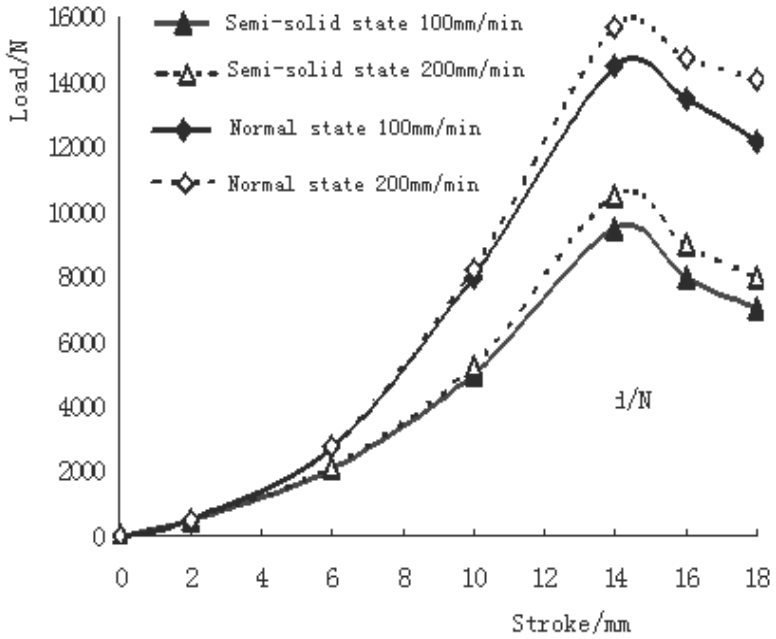

(a) Conventional extrusion and thixo-extrusion

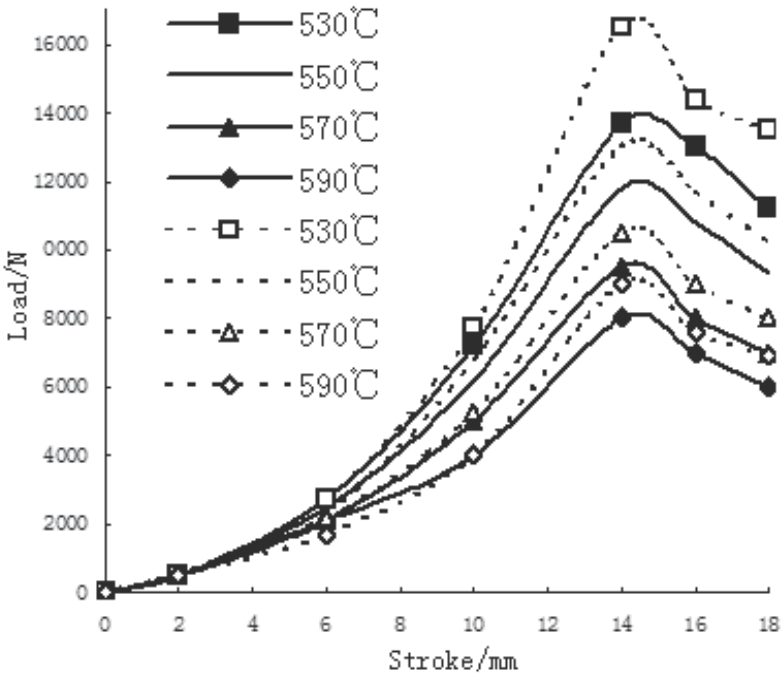

(b) Thixo-extrusion

Fig. 17. Load-stroke curves (speed: real line-100mm/min; broken line-200mm/min)

(a) 590°C

(b) 580°C

(c) 570°C

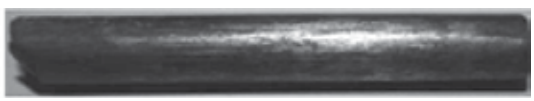

(d) 550°C

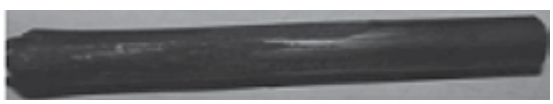

(e) 530°C

Fig. 18. Samples resulted in thixo-extrusion processes

5. Conclusion

Thixotropic deformation behaviours of semi-solid wrought magnesium alloy during compression process were obtained as follows: (1) The deformation force was required mainly to overcome particle sliding and particle plastic deformation in thixotropic compression process of high solid volume fraction for semi-solid AZ61 magnesium alloy, in which the sliding between solid particles and plastic deformation of solid particles mechanisms were dominant. (2) The deformation resistance decreased obviously with deformation temperature increasing under the same strain rate condition in thixotropic plastic compression processes for semi-solid AZ61 magnesium alloy.(3) The true stress peak value increased with the strain rate increasing under the same deformation temperature.(4) The deformation resistance of semi-solid AZ61 magnesium alloy was obviously smaller than one of conventional as-casted.

The proposed constitutive equation of semi-solid AZ61 was followed by

$$\sigma = \exp(25 - 11560 / T) \cdot \dot{\varepsilon}_Z^{\,0.026} \cdot \varepsilon_Z^{\,-0.09} \cdot (1 - \beta f_L)^{7.655}$$

The calculated results were good agreement with the experimental ones.

The flow stress models of AZ61 alloy for traditional forging/extrusion and thixoforming (thixo-forging and thixo-extrusion) were adopted to simulate the magnesium thixoforming process. The differences between the two forming processes were analyzed, and the following results have been obtained: (1) The deformation resistance in thixoforming was smaller than that in traditional forging/extrusion, in which the maximum load was about 1/3 less than that in traditional forging/extrusion. (2) The effective stress of workpiece in thixoforming was well distributed, whereas the stress concentration was liable to occur in traditional forging/extrusion, and in order to erase it more procedures should be supplemented. The effective strain of workpiece in thixoforming was distributed uniformly, its flow property and filling ability exceeded that in traditional forging/extrusion, so the complicated workpiece can be done once. (3) Simulation results were in good agreement with experimental ones. Numerical simulation can provide a help for the analysis of comparison between traditional forging/extrusion and thixoforming, and metal flow rule and plastic behavior accorded with practice can be obtained, which provide for the practice production as theory bases. (4) The semi-solid thixoforming technology has taken priority of the traditional processing.

6. Acknowledgement

This research was supported jointly by grant # 50465003 and # 50765005 from the National Natural Science Foundation of China, Innovative Group of Science and Technology of College of Jiangxi Province and the Jiangxi Province Education Commission Foundation.

7. References

Kang, C. G., Choi, J. S., Kim, K. H. (1999). The effect of strain rate on macroscopic behavior in the compression forming of semi-solid aluminum alloy. *Materials Processing Technology*, Vol.88, No.1-3: 159-168

Flemings, M. C. (1991). Behavior of metal alloy in the semi-solid state. *Metall Trans A,* Vol.22, No.5: 957-981

Yan, H., Xia, J. C. (2005). Theoretical analysis of plastic forming process for semi-solid material. *Materials Science Forum*, Vol.488-489, 389-392

Kang, C. G., Kang, B.S., Kim, J. I. (1998). An investigation of the mushy state forging process by the finite element method. *Mater. Pro. Tech*. Vol.80-81, 444-449.

Kiuchi, M., Yanagimtom, J., Yokobayashi, H. (2001). Flow stress, yield criterion and constitutive equation of mushy/semi -solid alloys, *Annals of the CIRP*, Vol. 50, 157-160.

Martin, C L., Favier, D., Suery, M. (1997). Viscoplastic behaviour of porous metallic materials saturated with liquid part I: Constitutive equations. *Int. J. Plast*., Vol.13, No.3, 215-235.

Yan, H., Zhou, B. F. (2006). Thixotrpic deformation behavior of semi-solid AZ61 magnesium alloy during compression process, *Materials Science and Engineering B*, Vol.132, No.1-2, 179-182.

Yan, H., Zhou, B. F. (2006). Constitutive model of thixotropic plastic forming for semi-solid AZ61 magnesium alloy. *Solid State Phenomena*, Vol.116-117, 577-682.

Tims, M. L., Xu, J., Nickodemus, G. (1996). Numerical simulation on thixoforming of wrought magnesium alloy. *Proceedings of Fourth International conference on Semi-solid Processing of Alloys and composites*, 120-124, UK, Sheffield.

Lipinski, D. M., Flender, E. (1998). Numerical simulation of flow and heat phenomena for semi-solid processing of complex casting, *Proceedings of the Fifth International Conference on Semi-solid Processing of Alloys and composites*, 273-277, USA, Colorado.

Yan, H., Zhang, F. Y. (2005). Structure evolution of AZ61 magnesium alloy in SIMA process. *Transactions of Nonferrous Metals Society of China*, Vol.15, No.3, 560-564.

Yan, H., Zhang, F. Y. (2006). Microstructural evolution of semi-solid AZ61 magnesium alloy during reheating process. *Solid State Phenomena*, Vol.116-117, 275-278.

Yan, H., Zhou, B. F. (2008). Study on thixo-forging of AZ61 wrought magnesium alloy. *Solid State Phenomena*, Vol.141-143, 577-682

Zhou, H. T., Zeng, X. Q., Wang, Q. D. and Ding, W. J. (2004). A flow stress model for AZ61 magnesium alloy. *Acta Metallurgic Sinica*, Vol.17, No.2, 155-160.

19

Study on Semi-solid Magnesium Alloys Slurry Preparation and Continuous Roll-casting Process

Shuisheng Xie, Youfeng He and Xujun Mi
State Key Laboratory of Nonferrous Metals and Processes
General Research Institute for Non-ferrous Metals
China

1. Introduction

Magnesium and its alloys, as the lightest functional and structural materials, have great increasingly application in the automobile, electronic and aeronautical industries due to their low density, high specific stiffness and strength, good heat conductivity, high electromagnetic interference shielding and damping capabilities, etc. However, at present the major problem to the application of magnesium alloys is still lack of suitable forming process.

As a new type of metal forming method, Semi-solid metal (SSM) processing technology has attracted close attention all over the world, since M.C Flemings in MIT firstly introduced this concept in 1970s (Spencer et al., 1972), (Flemings, 1991). Compared with the conventional processes, SSM process has many advantages: higher viscosity than fully liquid, leading to laminar flow and even filling of a die; low solidification shrinkage, leading to more precise dimension product; lower casting temperature and less latent heat resulting in less thermal shock to the die. Compared with solid forming processed, SSM process needs lower loads and can fill more complicated shapes and thinner sections (Xie, 2002). The mechanical properties of SSM product are close to the forged product. So, it is significant to combine the semi-solid process techniques with continuous roll-casting techniques to produce the high quality magnesium alloy strip with non-dendritic structure. However, the key of SSM process is to prepare non-dendritic structure semi-solid magnesium slurry with rosette or globular microstructure or billets with non-dendritic structure. Usually, the non-dendritic structure can be obtained by continuous stirring or controlling nucleation and growth processes during the early stages of solidification.

In recent years, many new method of the semi-solid slurry preparation have been developed. These include UBE's new rheocasting (NRC) process (Hall et al., 2000) and the Cooling Slope method (Haga & Suzuki, 2000; Haga et al, 2004; He et al, 2009); the SLC (sub-liquids casting) process (Jorstad et al, 2002); the "Continuous Rheoconversion Process" (CRP) (WPI, 2002), the SIMA (Strain-Induced Melt Activation) Process, the SEED (Swirled Enthalpy Equilibration Device) Process; the SCR (Shear-Cooling Roll) process and etc. In essence, all of the above-mentioned processes utilize the same fundamental concept: nucleation and dispersion of the nuclei to achieve the semi-solid structure as the alloy melt is cooled below the liquidus temperature.

In this chapter, a new process named "Damper Cooling Tube (DCT) method" for preparing semi-solid magnesium alloy slurry was introduced (Xie et al, 2004 and 2007; Yang et al, 2007), which absorbs the characteristics of "new MIT method" and "Cooling Slope method". Numerical simulation and experiment on the preparation process of semi-solid AZ91D slurry using DCT method was carried out based on CFD software Flow 3D. The distribution of the flow field, shearing rate and solid fraction were obtained. The effects of processing parameters such as the position and dimension of the wedge block, fall head and gap size on the slurry properties were investigated in detail, which provides effective guidelines for DCT structure design and optimization of processing parameters. According to the numerical simulation results, the actual experiment for preparing semi-solid AZ91D slurry using DCT method was done. In addition, numerical simulation on semi-solid continuous roll-casting process of magnesium AZ91D alloy using a two-dimensional incompressible non-Newtonian flow model was studied for getting the optimizing processing parameters. According to the simulation results, semi-solid continuous roll-casting process (CRP) experiment for AZ91D was investigated.

2. The damper cooling tube method

The DCT device consists of five basic functional units: a pouring system, a cooling system, a heating system, a stirring system and a second temperature adjusting system, as shown in Fig.1 (Xie et al, 2004). The pouring system is designed to pour molten alloy at the predetermined temperature into a container, and need to keep stated height of molten alloy. The cooling system is a cooling tube and can effectively adjust the cooling rate of the molten alloy passing through the cooling tube and therefore it is convenient to adjust the velocity of nucleation as required. The stirring system is introduced to stir the molten alloy uniformly while it flows through the cooling tube. The heating system is to clear the alloy solidified in the inner wall of the cooling tube when the system appears some problems. The second temperature system is designed to adjust the temperature of the slurry from the cooling tube, which can accurately control the solid fraction of semi-solid slurry.

Firstly, the molten alloy is poured into the container from the holding furnace and at the same time some protection gas is inlet the container so as to separate the molten alloy with high temperature from air and thus avoid the oxidation or inflammation of molten alloy. When the molten alloy (several degrees above the liquidus temperature) in the container is poured into the damper cooling tube, due to the cooling system around the tube outer wall, the copious fine nucleation of primary particles are produced and adhere to inner wall of the cooling tube. Crystal nucleuses grow up quickly and then are divorced from the tube wall into molten alloy because of the impact of molten alloy. The molten alloy is stirred by the stirring system and uniform semi-solid slurry is obtained. Finally, the slurry flow into the nether container and under gas protection the semi-solid slurry is adjusted to an expected solid fraction. It can be directly rheo-casted or rheo-formed into work pieces.

Because the height (fall head) of the molten alloy in the container is a driving force to flow, the flow velocity of molten alloy passing through cooling tube is mainly dependent on the height of molten alloy. Therefore, the height of molten alloy in the container needs to be kept steady and it should be determined by experiment. So, in this chapter the semi-solid slurry preparation process by DCT method was simulated based on the *FLOW3D* software. Effects of the position of wedge block, the gap size between wedge block and the inner wall of cooling tube and height of wedge block on the slurry flow and stirring were investigated.

In addition, the processing parameters were optimized by numerical simulation, which provides theoretical guide for the preparation of semi-solid slurry by DCT method.

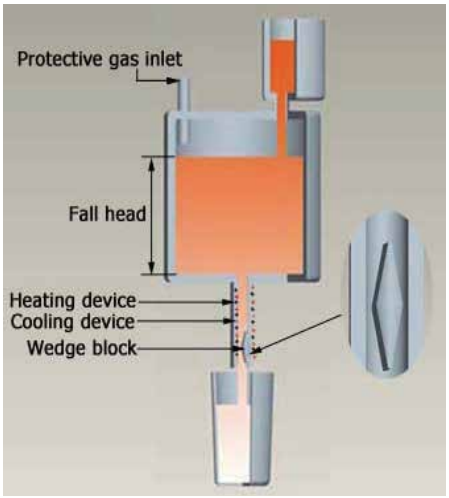

Fig. 1. The DCT with sphenoid damper

3. Numerical simulation and experiment on DCT method

3.1 Mathematical modeling

Three-dimensional incompressible non-Newtonian flow with heat transfer was considered, which was described by the continuity equation, the Navier-Stokes equation and the energy equation. These equations were solved by the *FLOW3D* software for a steady-state solution. Due to the velocity fluctuation of flow field of DCT, the turbulent model of *FLOW3D* was selected in this paper. For momentum transport, the turbulent kinetic energy k and its dissipation ε were employed (k – ε model). The k – ε double equation model introduces a turbulent dissipation ratio ε based on single equation model, which was firstly presented by Launder and Spalding in 1972 (Launder & Spalding, 1972).

Turbulent kinetic energy k equation is:

$$\frac{\partial k}{\partial t}+\frac{\partial(\overline{u_j}k)}{\partial x_j}=\frac{1}{\rho}\frac{\partial}{\partial x_j}\left[\left[\mu+\frac{\mu_t}{\sigma_k}\right]\frac{\partial k}{\partial x_j}\right]+\frac{\mu_t}{\rho}\left[\frac{\partial\overline{u_i}}{\partial x_j}+\frac{\partial\overline{u_j}}{\partial x_i}\right]\frac{\partial U_j}{\partial x_i}-\varepsilon \tag{1}$$

Turbulent dissipation ratio ε equation is:

$$\frac{\partial \varepsilon}{\partial t}+\frac{\partial(\overline{u_j}\varepsilon)}{\partial x_j}=\frac{1}{\rho}\frac{\partial}{\partial x_j}\left[\left[\mu+\frac{\mu_t}{\sigma_\varepsilon}\right]\frac{\partial \varepsilon}{\partial x_j}\right]+\frac{c_1\mu_t\varepsilon}{k}\left[\frac{\partial\overline{u_i}}{\partial x_j}+\frac{\partial\overline{u_j}}{\partial x_i}\right]\frac{\partial U_j}{\partial x_i}-\frac{c_2\varepsilon^2}{k} \tag{2}$$

Turbulent viscosity coefficient μ_t is:

$$\mu_t=c_\mu\rho k^2/\varepsilon \tag{3}$$

where, k is turbulent kinetic energy, ε is turbulent kinetic dissipation ratio, μ_t is dynamic flow viscosity coefficient; c_p is die material specific heat, $\rho\overline{u_i}\overline{T}$ is turbulent heat flux; c_1, c_2, c_μ, σ_k, σ_ε are turbulent empirical parameters, which provided by Launder & Spalding now as shown in Table 1.

Parameters	c_1	c_2	c_μ	σ_k	σ_ε
Value	1.44	4.92	0.09	1.00	1.30

Table 1. The empirical coefficient about k – ε model

The dynamic viscosity used in the mass and momentum equations was the sum of molecular viscosity and turbulent viscosity. The viscosity of semi-solid material has drastically changed in the mushy state that the liquid phase and the globular solid phase coexist in the semi-solid forming region. The dependency of viscosity on shear rate must be recognized to establish the rheology model of semi-solid material. The viscosity decreases as shear rate increases in semi-solid region. The rheological model in *FLOW3D* is Carreau model as follows:

$$\eta = \eta_\infty + (\eta_0 - \eta_\infty)(1 + (\lambda\dot{\gamma})^2)^{(n-1)/2} \tag{4}$$

where η_0 is low shear rate viscosity (zero shear rate viscosity, g.s/cm), η_∞ is the high shear rate viscosity (g.s/cm), λ is the time constant and n is the sensitivity exponent of material. If the exponent n is 1, this equation becomes Newtonian flow model.

3.2 Geometric model and initial parameters

Due to vertical (i.e. left-right) and horizontal (i.e. front-back) mid-plane symmetry, only a quarter of the DCT was modelled as the computation. The geometric model and mesh is shown in Fig.2. The fall head is kept no variable, and the pressure of the inlet is kept a constant at initial condition. The AZ91D magnesium alloy was performed in this simulation, and its thermo-physical properties are presented in Table 2.

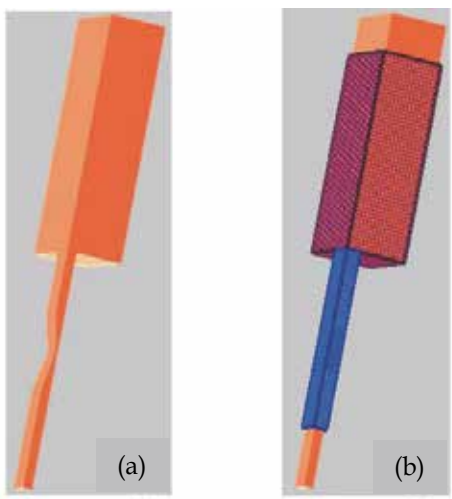

(a) geometry (b) mesh

Fig. 2. Geometry and mesh of the DCT

Parameters	Unit	Values
Temperature at Liquidus	*K*	868
Temperature at Solidus	*K*	743
Specific heat	*KJ/Kg.K*	1050
Density	Kg/m^3	1810
Latent heat	*KJ/Kg*	373
Heat transfer coefficient	$W/m^2.K$	104

Table 2. The thermal-physical properties for AZ91D magnesium alloy

3.3 Boundary conditions

There are four boundaries specified in this DCT model. One boundary is the inlet surface which the molten alloy is poured into the container. The molten alloy temperature is 880K above several degrees of the liquidus. The second boundary is the interface between the stationary wall of the container and the liquid alloy. The molten alloy temperature in the container is kept no variable, so the wall temperature of the container equal to the molten alloy temperature. The third boundary is the interface between the wall of the cooling tube and the molten alloy. The wall temperature of the cooling tube is room temperature 300K. The fourth boundary is the outlet boundary in the bottom.

3.4 Numerical simulation results and discussion

Fig.3 shows that the distribution of temperature, dynamic viscosity, shearing rate, velocity and solid fraction when the wedge block located in the middle of the cooling tube. It was found when the molten alloy passed through the wedge block, its temperature decreased highly from 880*K* to 842*K* under the cooling process of the tube and the stirring of wedge block; its dynamic viscosity increased quickly from 0.24 to 8.66*P*; its shearing rate increased from 0 to 1840 s^{-1}; the velocity of molten alloy increased from 1.29 to 12*m/s*; and the solid volume fraction increased from 0 to 5%.

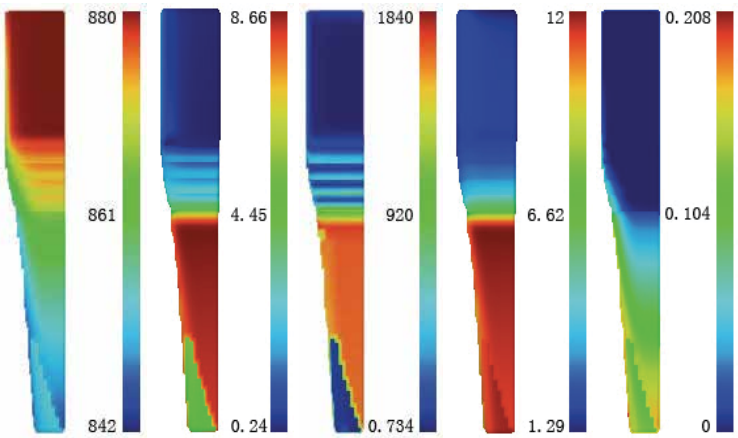

(a) temperature (*K*); (b)dynamic viscosity (*P*); (c) shearing rate (s^{-1}); (d) velocity (*m/s*); (e) solid fraction

Fig. 3. Simulation results when wedge block in the middle of the damper tube

In addition, the fluid velocity near the outlet has a local variation because the tube wall cools continually, as shown in Fig.3 (d). It can also be seen that the flow field distribution is non-uniform at outlet. After the molten alloy flow passes the wedge block, it is still cooled by the tube but have no stirring. That is the reason that solid fraction is non-uniform at outlet and the slurry is not uniform at outlet.

Base on the above simulation results, we change the position of wedge block from middle to the outlet of the cooling tube while other parameters are the same. The simulation results are shown in Fig.4, it can be seen that the distribution of temperature, dynamic viscosity, shearing rate, velocity and solid fraction is more uniform. The shearing rate is up to the biggest value about 1860s^{-1} at the gap. It shows that the wedge block has the perfect stirring in the process. The solid volume fraction of slurry is about 10% at outlet. The mixture of the semi-solid slurry is more homogeneous, which indicates that the wedge block plays good role in stirring the slurry. So, the wedge block should be located near outlet of the damper tube.

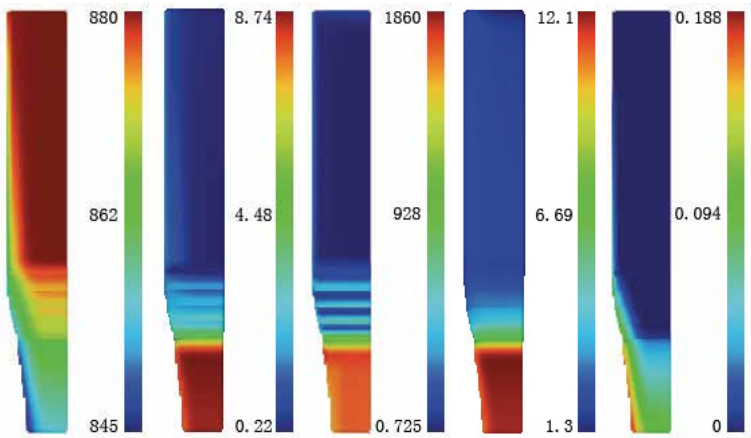

(a) temperature (K); (b) dynamic viscosity(P); (c) shearing rate (s^{-1}); (d) velocity (m/s); (e) solid fraction

Fig. 4. Simulation results when wedge block at outlet of the damper tube

Fig.5 shows the temperature distribution at different gap size between the wedge block and the inner wall of cooling tube. It can be seen that the temperature distribution below the gap size is more uniform gradually with increasing the gap size from 2mm to 10mm. The molten alloy flow per unit time through the gap increases with increasing the gap size, so mean cooling intensity of the cooling tube to the molten alloy decreases, which leads to the uniform temperature distribution below the wedge block. In addition, with increasing the gap size, the temperature gradient at the inclined surface of wedge block clearly increases for the friction between the molten alloy and inclined surface of the wedge block.

Fig.6 shows the dynamic viscosity distribution for different gap size from 2mm to 10mm. It can be seen that the dynamic viscosity in a local area at the cooling tube outlet is higher when the gap size is 2 and 4mm. When the gap size is greater than 8mm, the dynamic viscosity at the side surface of the cooling tube is higher than the center. Only when the gap size is 6mm, the dynamic viscosity below the gap size is more uniform. The variation of mean dynamic viscosity is shown in Fig.7. It can be seen that with increasing the gap size, the mean dynamic viscosity first gradually increases and then decreases. When the gap size is 6mm, the dynamic viscosity is up to maximum about 9.86P.

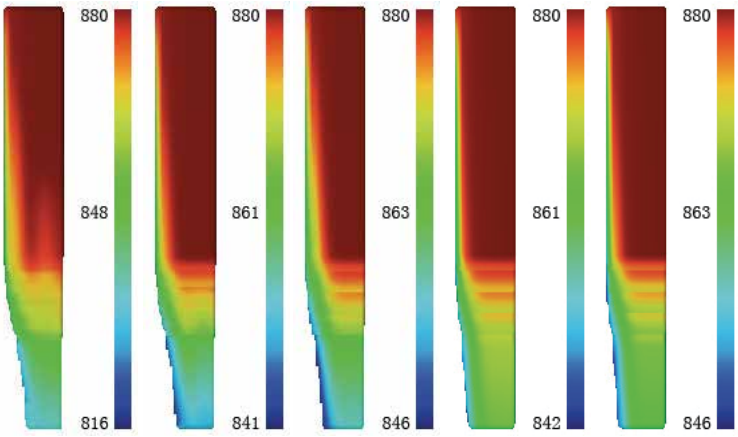

(a) 2*mm* (b) 4*mm* (c) 6*mm* (d) 8*mm* (e) 10*mm*

Fig. 5. Temperature distribution for different gap size (*K*)

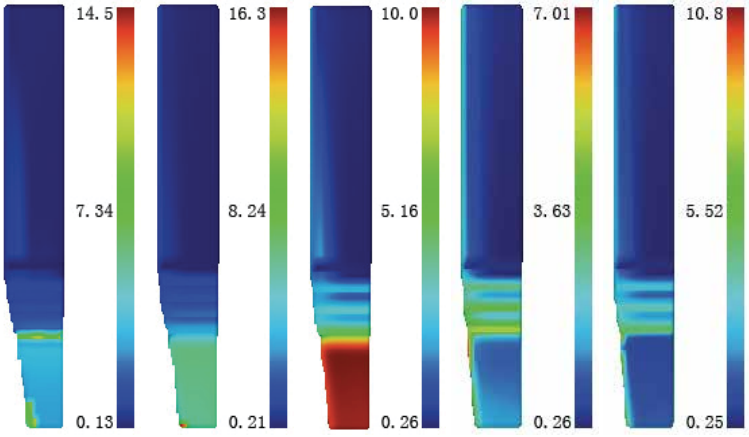

(a) 2*mm* (b) 4*mm* (c) 6*mm* (d) 8*mm* (e) 10*mm*

Fig. 6. Dynamic viscosity distribution for different gap size (*P*)

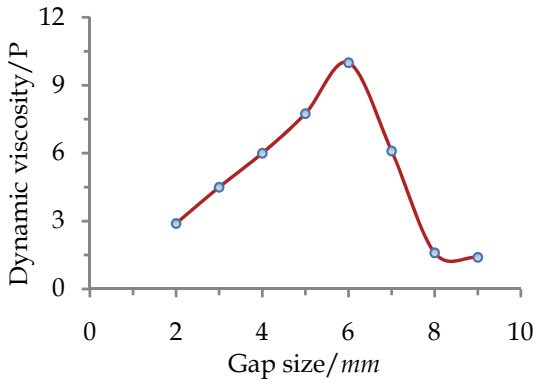

Fig. 7. Variation of dynamic viscosity for different gap size

Fig.8 and Fig.9 shows the distribution and variation of shearing rate in the cooling tube for different gap size. It can be seen that the gap size has great influence on the shearing rate distribution, too small or too large gap size will lead to lower shearing rate below the gap and almost close to zero. Only when the gap size ranges from 4 and 6*mm*, the shearing rate is higher about 1550s^{-1}, which indicates that the optimum gap size should be between 4*mm* and 6*mm*.

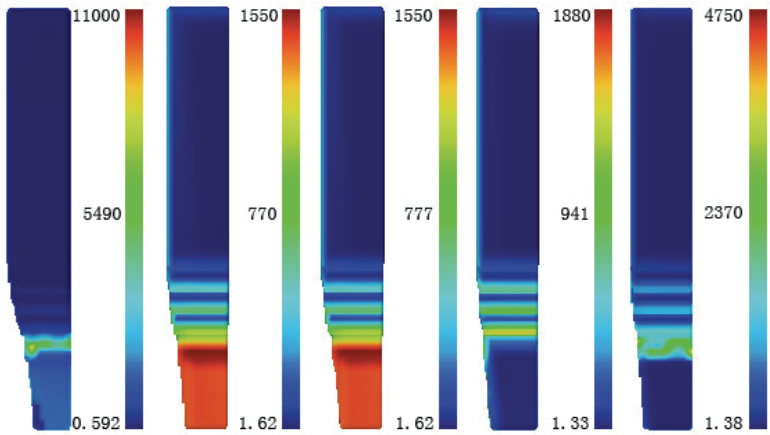

(a) 2*mm* (b) 4*mm* (c) 6*mm* (d) 8*mm* (e) 10*mm*

Fig. 8. Shearing rate distribution for different gap size (s^{-1})

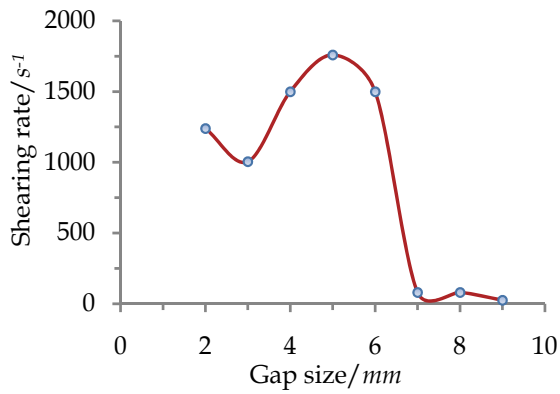

Fig. 9. Variation of shearing rate for different gap size

The velocity distribution for different gap size is shown in Fig.10. It can be seen that the local metal flow velocity below the gap in cooling tube is non-uniform when the gap size is too large and too small. When the gap size increases from 4 to 8*mm*, the metal flow velocity distribution is more uniform and little difference each other, about 1.18*m/s*.

Fig.11 and Fig.12 shows the distribution and variation of solid fraction for different gap size. It can be seen that with increasing the gap size, the solid fraction distribution is more non-uniform, and the solid fraction gradually decreases, which indicates the gap size has great effect on the solid fraction. When the gap size is beyond 7*mm*, the solid fraction of the molten alloy in then cooling tube is close to zero as show in Fig.12. So, the gap size must be less than 7*mm*.

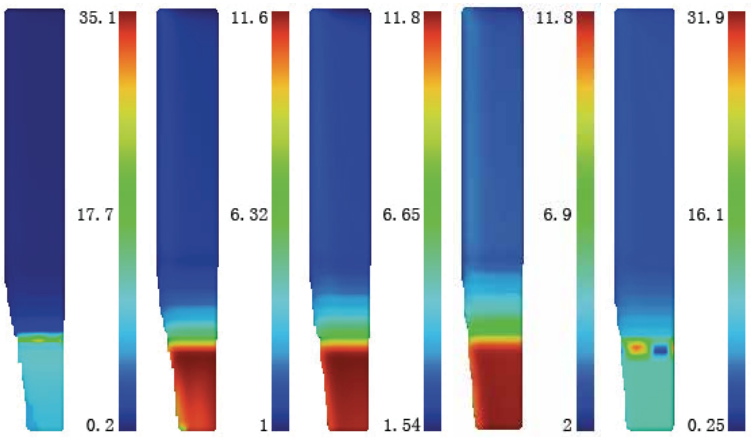

(a) 2*mm* (b) 4*mm* (c) 6*mm* (d) 8*mm* (e) 10*mm*

Fig. 10. Velocity distribution for different gap size (*m/s*)

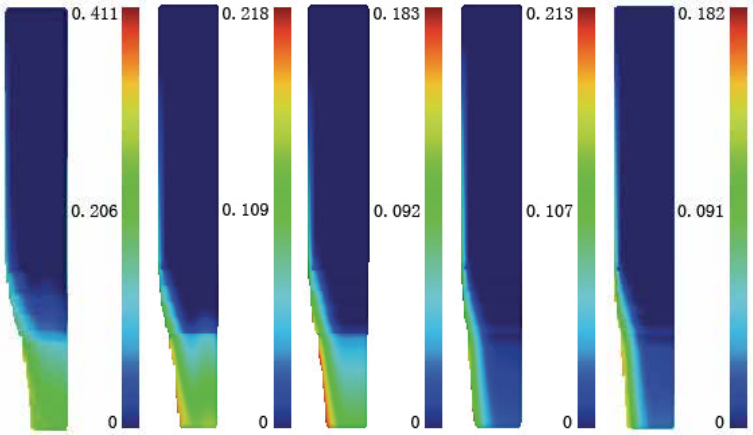

(a) 2*mm* (b) 4*mm* (c) 6*mm* (d) 8*mm* (e) 10*mm*

Fig. 11. Solid fraction distribution for different gap size

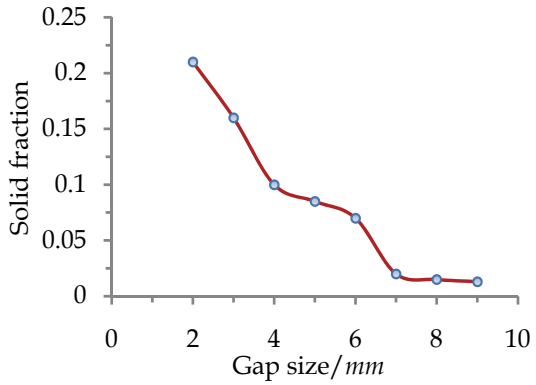

Fig. 12. Variation of solid fraction for different gap size

Because the fall head of the molten alloy in the container is the driving force of the flowing of molten alloy, the fall head is an important factor in the process, the effect of fall head is analyzed. The varieties of the temperature and shearing rate with fall head from 50*mm* to 700*mm* are shown in Fig.13 and Fig.14. Fig.13 shows that the fall head have a little effect on the temperature distribution. Fig.14 shows that the shearing rate is non-uniform when the fall heat was below 300*mm*. But when the fall head is higher than 500*mm*, the distribution of shearing rate is uniform and has little change. So the fall head must be higher than 500*mm* to get the better stirring function.

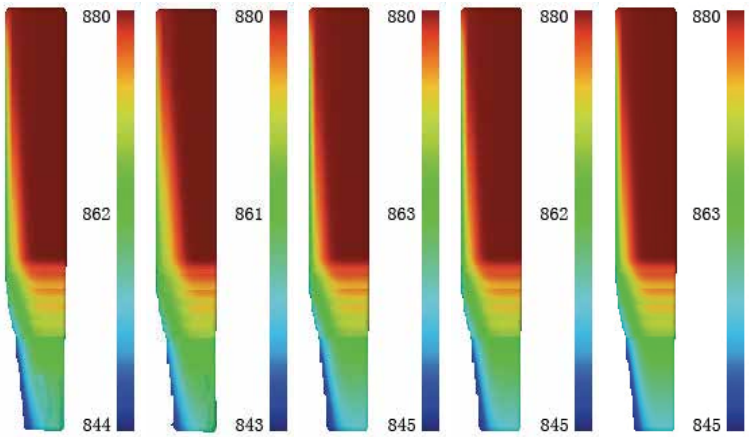

(a) 50*mm* (b) 100*mm* (c) 300*mm* (d) 500*mm* (e) 700*mm*

Fig. 13. Temperature distribution for different fall height (*K*)

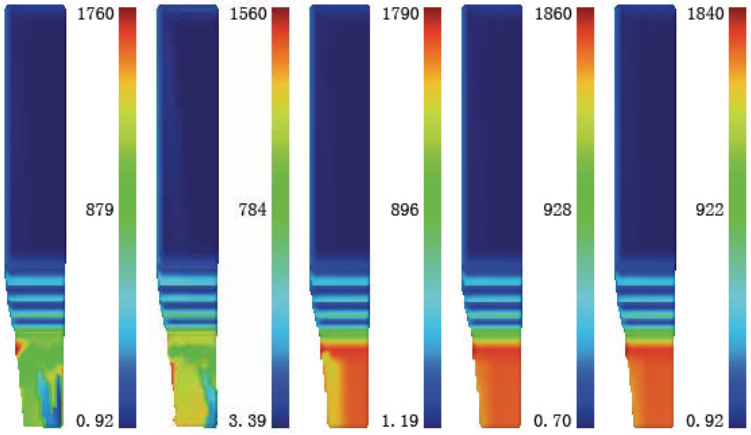

(a) 50*mm* (b) 100*mm* (c) 300*mm* (d) 500*mm* (e) 700*mm*

Fig. 14. Shearing rate distribution for different fall height (s^{-1})

The temperature distribution at different height of wedge block from 60*mm* to 140*mm* (the fall head is 500*mm*) are shown in Fig.15. It was shown that the height of wedge block has little effect on the temperature distribution. The temperature at outlet is about 855*K*. The temperature of the left tube wall is lower, about 845*K*. So, it can be concluded that the height of wedge block has little influence on the temperature distribution.

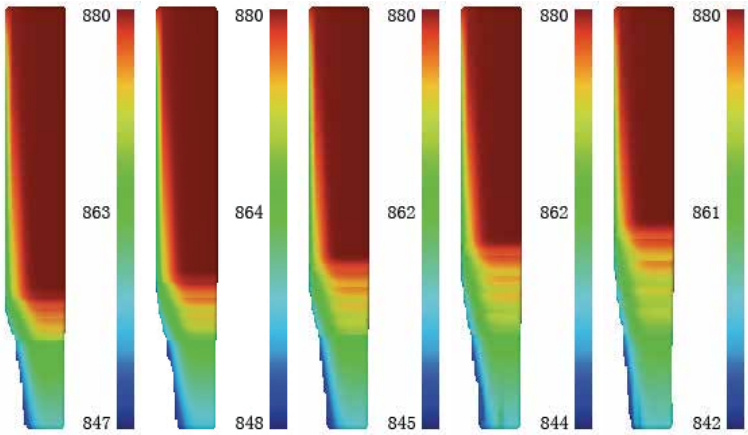

(a) 60*mm* (b) 80*mm* (c) 100*mm* (d) 120*mm* (e) 140*mm*

Fig. 13. Temperature distribution for different height of wedge block (*K*)

3.5 Experimental research on DCT

The experimental device of DCT for preparing the semi-solid magnesium alloys slurry was designed and fabricated as shown in Fig.14. According the numerical simulation results, the wedge block was set near the outlet of cooling tube; the height of wedge block was 100*mm*. The fall head was 300, 500 and 700 *mm* respectively.

Fig. 14. Experimental device of DCT

AZ91D magnesium was used in this experiment. The smelting device was an electric resistance furnace with controllable silicon power (20*KW*). Other relative devices contained a controllable silicon power, a set of thermo detector and recording instrument, a set of casting device, a group of stainless steel mould and ten groups of sand moulds. And the smelting process was protected using Argon gas. Detailed experimental condition was shown in Table 3.

Material	AZ91D magnesium alloy
Casting temperature/*K*	880
Smelting device	20*Kg* Electric resistance furnace
Shielding gas	Argon
Casting mould	Stainless steel mould
DCT device	Designed by oneself
The location of wedge block	Outlet of cooling tube
The height of wedge block/*mm*	100
The height of fall head/*mm*	300, 500, 700

Table 3. The experimental condition

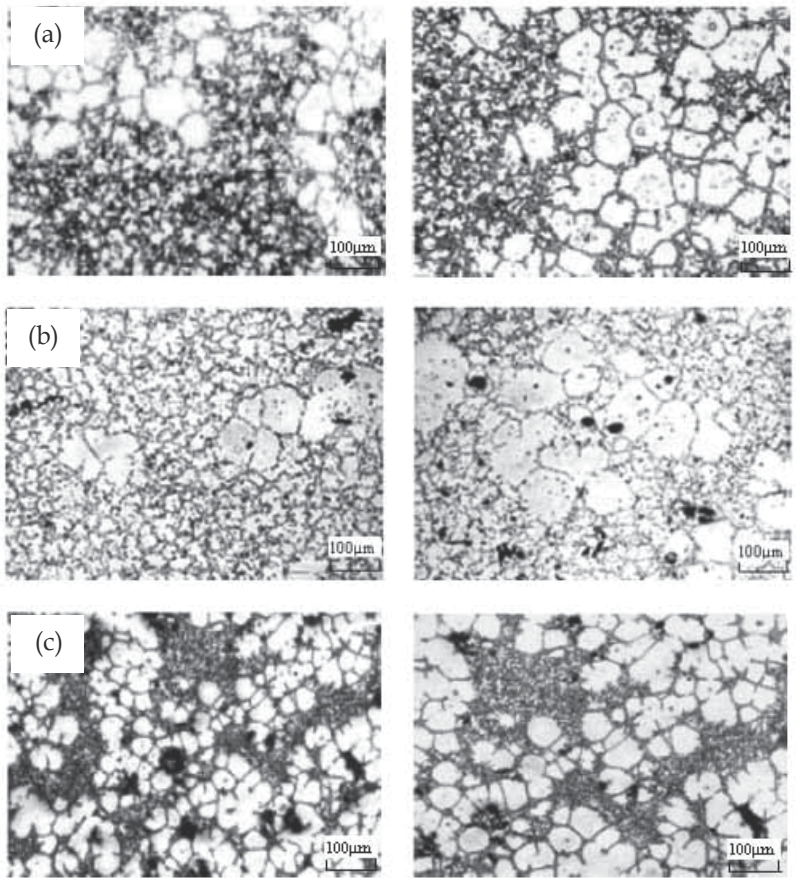

a) edge b) centre

Fig. 15. The microstructure with the different fall head (a) 300*mm*; (b) 500*mm*; (c) 700*mm*

The edge and centre microstructure of billets using the DCT device are shown in Fig.15. It is shown that the microstructure is non-uniform when the fall head is 300*mm* in Fig.15 (a). When the fall head is 500*mm*, the microstructure is better than the 300*mm*, but there are many big grains in the centre of the billets as shown in Fig.15 (b). Fig.15 (c) shows that the

microstructure is more uniform and thinner when the fall head is 700*mm*. From the experiment it can be concluded that the height of wedge block should be located near outlet of the damper tube and it was not the main influence factor to the temperature distribution. The fall head must be higher than 500*mm* to get the better stirring function. The fall head must be higher than 500*mm* for getting better microstructure, which is in accord with the numerical simulation results.

4. Semi-solid continuous roll-casting processing

In semi-solid continuous roll-casting process of magnesium alloy, several processing parameters such as the solid fraction of semi-solid slurry, the heat transfer between rollers and molten alloy, the roll-casting speed, the position of solidification final point have great influence on the quality of final strips (Xie et al, 2005, 2006, 2007and 2008; Zhang et al, 2008). So, in this section numerical simulation on semi-solid continuous roll-casting process of magnesium alloy using a two-dimensional incompressible non-Newtonian flow model was studied for getting the optimizing processing parameters. Based on the simulation results, semi-solid continuous roll-casting process experiment for AZ91D magnesium alloy were investigated.

4.1 Mathematical modeling

1. Governing equations

The continuity equation is:

$$\frac{\partial \rho}{\partial t} + \frac{\partial (\rho u_i)}{\partial x_i} = 0 \tag{5}$$

The Navier-Stokes equation is:

$$\frac{\partial (\rho u_i)}{\partial t} + \frac{\partial}{\partial x_j}(\rho u_j u_i + P\delta_{ij} - \sigma_{ij}) = \rho g_i \tag{6}$$

The energy equation is:

$$\rho c \frac{\partial T}{\partial t} - \lambda \frac{\partial^2 T}{\partial x_i^2} - q(x) = 0 \tag{7}$$

where ρ is the density, u_i is the velocity of element i, x_i is the displacement of element i, P is the pressure, δ_{ij} is the Kronecker delta function, σ_{ij} is the viscosity tension between element i and j, g_i is the gravity acceleration of element i, c is the specific heat, T is the temperature, λ is the thermal conductivity coefficient and $q(x)$ is the thermal source.

These equations were solved by the *FLOW3D* software for a steady-state solution. In *FLOW3D*, the above equations are formulated with the Fractional Area/Volume Obstacle Representation *(FAVOR)* method. In addition, the non-Newtonian viscosity model is used by eq.(4).

2. Solidification latent heat

The solidification process of semi-solid continuous roll-casting processing is an unsteady state heat transfer process with phase transformation. Semi-solid slurry can release mass crystallization latent heat from solid-liquid mixing to pure solid phase. At present, there are many methods, such as temperature compensation method, effective specific heat method,

heat content method, assumption heat flow method and so on, for dealing with the crystallization latent heat. The heat content method was used in this chapter, namely, the crystallization latent heat was defined as follow:

$$H = \int \rho C_p(T) dT \tag{8}$$

where, H is material heat content, ρ is material density; C_p is material specific heat capacity, which is the function of temperature T.

3. Geometry and parameters

Applying simple geometric mode was a good way to get some progress in study. So, some assumption condition was made before establishing the analysis model: 1) steady-state roll-casting process; 2) no relative slip between semi-solid slurry and semi-solid magnesium strips and rollers; 3) well contact between strips and rollers, thus ignoring thermal resistance between them. In semi-solid continuous roll-casting process, the molten pool was enclosed by two water cooling rollers and side plate. The width of water slot was nearly equal to the roller width and thermal insulation device and heated side plate was used, so the edge effect of casting strips can be ignored. The two-dimensional geometric model and mesh was built after simplifying the semi-solid continuous roll-casting process as shown in Fig.16. The detailed calculation parameters in numerical simulation were shown in Table 4.

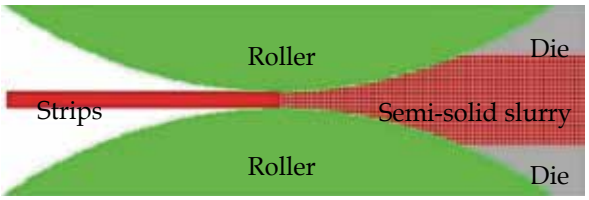

Fig.16. The 2D model and mesh of semi-solid continuous roll-casting process

Roll-casting speed	Roll diameter	Pool depth	Roll gap	Inlet temperature
0.6-1.2 *m/min*	210 *mm*	30-50 *mm*	4 *mm*	840-860 *K*
V	D	h	δ	T_0

Table 4. The detailed calculation parameters in numerical simulation

4. Boundary condition

The governing equations must satisfy every surface's boundary condition in calculation zone, which mainly contains velocity and thermal boundary condition. The boundary condition descriptions in this study are as follows:

Inlet zone:

$$V_x = V_{in}\ ,\ V_y = 0\ ,\ T = T_0$$

where V_x is the node velocity at x direction in the inlet position of molten pools, V_y is the node velocity at y direction in the inlet position of molten pools, V_{in} is the velocity of molten alloy in the let position, T_0 is the casting temperature.

Free surface:

$$V_y = 0\ ,\ \frac{\partial V_x}{\partial y} = 0\ ,\ \frac{\partial V_z}{\partial y} = 0$$

The contact surface between molten alloy and roller:
In continuous roll-casting process, the viscosity force near the roller surface zone plays important role in transportation, so the velocity of element nodes contacted with the roller surface is defined as the linear velocity of roller, namely, the element node velocity is:

$$V_x = VCos\theta \ , V_y = VSin\theta \ , z=0$$

where, V is the linear velocity of rollers surface, θ is the angle from the line between node and axis line of rollers to x-z plate.

4.2 Numerical simulation results and analysis

At beginning continuous roll-casting process the inlet velocity of slurry V_0 is 0.05m/min; the roll gap δ is 4mm; pool depth h is 20mm; the roll-casting velocity is 1m/min. The AZ91D semi-solid slurry firstly was poured into the right molten pool in the simulation, at this time, the effect of rollers temperature was ignored. When the flow field of roll-casting zone was up to steady state, the boundary condition of roller temperature was set, thus, the semi-solid slurry started to solidify under the rollers cooling. Lastly, the distribution of temperature and solid fraction at continuous casting zone was obtained.

4.2.1 The distribution of temperature and solid fraction at roll-casting zone

Based on the experience and experiment, the solid fraction of initial semi-solid slurry has been selected 10~20% in CRP. It is known that the solid fraction of semi-solid slurry corresponding to the temperature, thus the temperature of semi-solid slurry has been selected from 840 K to 860 K. In this study, the inlet temperature of molten alloys T_0 is 855 K. Fig.17 shows the changing of the temperature and solid fraction at roll-casting zone, when the rollers cooling time is 0.5, 1.0, 1.5, 2.0, 2.5s, respectively.
When the cooling time was 0.5s, the temperature of molten alloy near the rollers dropped down about 800K rapidly due to the high temperature difference between the molten alloy and the water cooled rollers. Here, the solid fraction of the molten alloy at the rollers surface increased by 70%, but no solidification layer. As shown in Fig.17 when the cooling time was 1.0s, the temperature of molten alloy near the rollers continuously down to about 742K, and the solid fraction also increased. At this time the thin solidified layer formed at rollers surface contacted with the molten alloy, and the thickness of the solidified layer was about 0.2mm at minimum roll gap. When the cooling time was 1.5s, the temperature of molten alloy decreased about 700K and the thickness of solidified layer was about 0.5mm. The solidified layers, however, were not jointed together due to the roll gap was 4mm. So, the thickness must be up to 2mm, two solidified layers can contact and press together. With the decreasing the temperature of molten alloy, the thickness of solidified layers increased and the two layers had contacted each other when the cooling time was 2.0s. When the cooling time was 2.5s, the temperature of molten alloy near rollers surface had decreased into about 650K as shown in Fig.10, the thickness of solidified layer had grown to more than 2 mm at the roll tip where two solidified layers contacted and welded together. From the solid fraction distribution, it was observed that the solidified layers welded to each other about 5 mm at the right of the roll tip which was the position of solidification final point. Therefore, the solidification in the roll gap was completed and ready for the following rolling operation. At this moment the solidified strip was withdrawn from the roll tip and had been rolled. According to the numerical simulation results, the roll-casting speed must be

controlled strictly and the contact time between the rollers and strips must exceed 2.5*s*. It means that only when the roll-casting speed is lower than 1*m/min*, the roll-casting strip can be solidification at roll gap and CRP can be finished successfully.

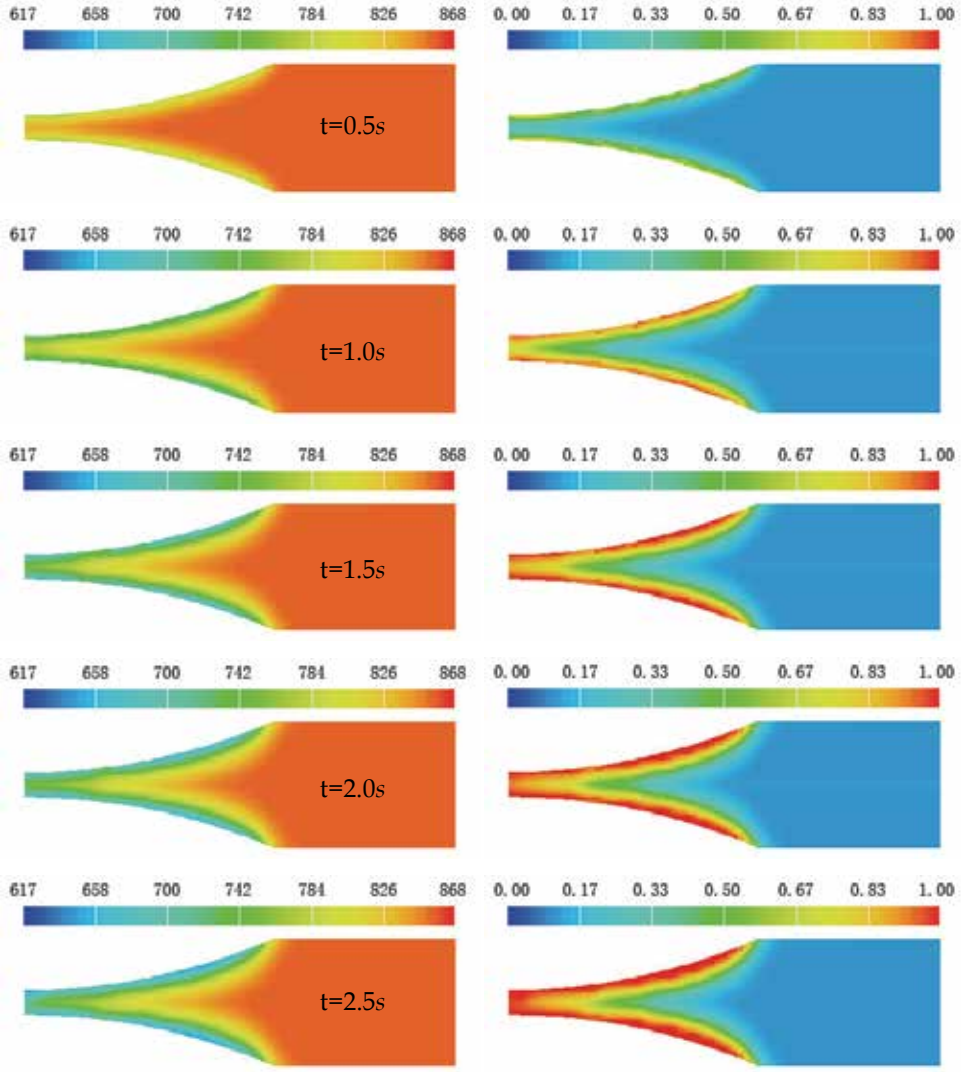

(a) Temperature (b) Solid fraction

Fig. 17. Distribution of temperature and solid fraction at different roller cooling time

4.2.2 Effect of pouring temperature on the CRP processing

It is known that different pouring temperature of semi-solid slurry correspond to different solid volume fraction with unchanging other parameters, while the solid volume fraction can affect the flow and heat transfer ability of semi-solid slurry. Thus, the pouring temperature has great influence on the metal flow and heat transfer in molten pool. In this

study, the temperature and solid volume fraction is assumed to be linear. Fig.18 shows the relation between the pouring temperature and solid fraction of semi-solid AZ91D alloy.

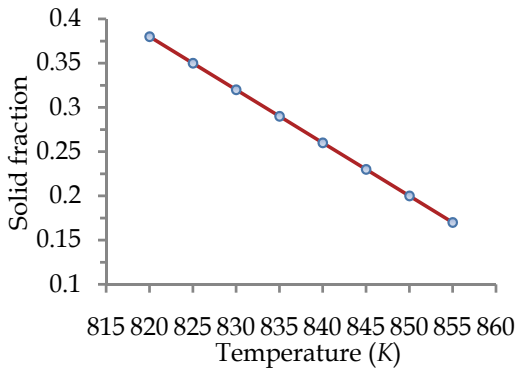

Fig. 18. Relation between pouring temperature and solid fraction of semi-solid AZ91D alloy

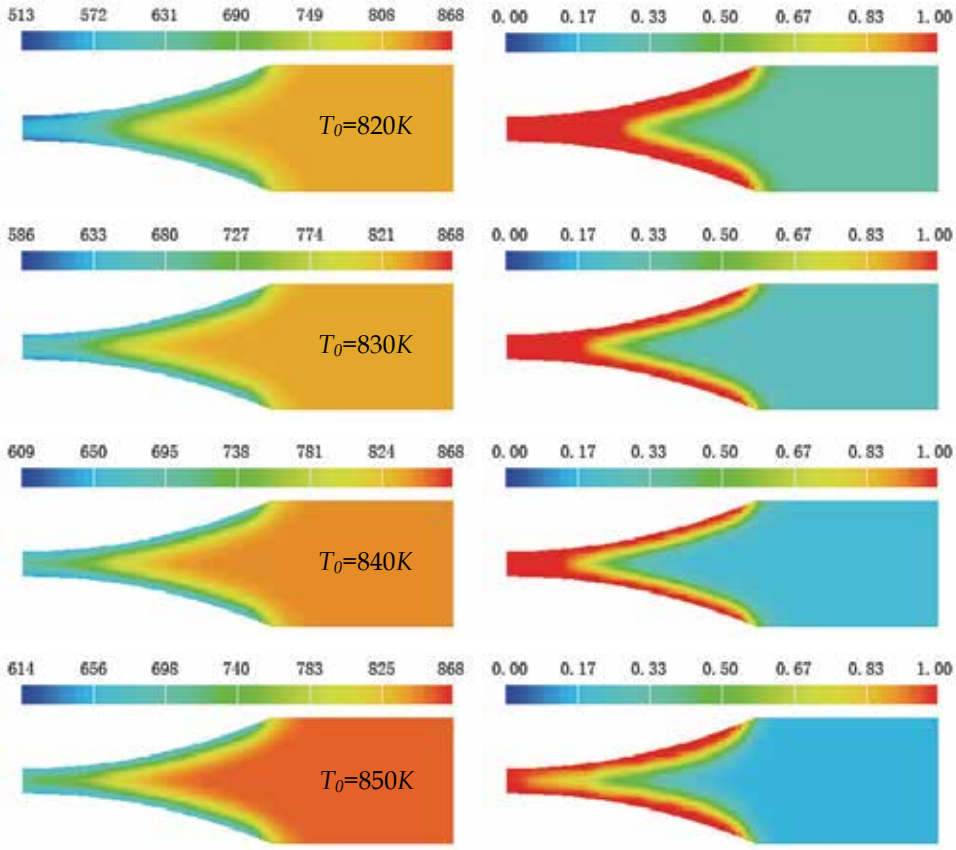

(a) Temperature (b) Solid fraction

Fig. 19. Distribution of temperature and solid fraction at different pouring temperature

Fig.19 shows the distribution of temperature and solid fraction in molten pool at different pouring temperature 820, 830, 840, 850*K*, respectively. It is shown that when the pouring temperature is 820*K*, the position of solidification final point is near the right side for lower pouring temperature, and the length of rolling zone is about 21*mm*, which cause higher roll-casting load and is not benefit to CRP process. With increasing the pouring temperature, the length of rolling zone decreases continuously, the solidification final point move towards to the outlet of strips. As T_0 is 850*K*, the length of rolling zone is about 3*mm*.
It can be conclude that the pouring temperature has great influence on the temperature and solid fraction in molten pool and the solidification final point. With increasing the pouring temperature, the length of rolling zone decreases. Also the pouring temperature can affect the flow filed in molten pool. Lower pouring temperature increases the viscosity of slurry, which leads to bad flowing ability. In addition, lower pouring temperature easily results in higher roll-casting load. However, higher temperature makes short position of rolling zone, which leads to breaking of CRP for incompletely solidification of strips.

4.2.3 Effect of roll-casting velocity on the CRP processing

Roll-casting velocity plays important role in the CRP processing, rational velocity can keep the CRP stability. Higher roll-casting velocity will lead to insufficient solidification of molten alloy; Lower roll-casting velocity will lead to longer standing time of the molten alloy in roll-casting zone for excessive cooling, which makes the molten alloy solidify at casting lip and breaks the semi-solid continuous roll-casting process. In this part, different roll-casting velocities 0.6, 0.8, 1.0, 1.2 *m/min*, respectively were studied when the depth of molten pool was 20*mm*, pouring temperature T_0 was 855*K*.
Fig.20 shows the distribution of temperature and solid fraction at different roll-casting velocities. It is shown that when the velocity *V* is 0.6*m/min*, the solidification final point is far from the outlet of strips, the length of rolling zone is about 17*mm*.With increasing the roll-casting velocity, the length of rolling zone decreases gradually. When the velocity is 1.2*mm/s*, the length of rolling zone is only about 1*mm*. So, in practical roll-casting process, the proper velocity should be chosen according the specific condition, in order to guarantee the quality of strips.

5. Experimental researches on the semi-solid CRP of magnesium alloy

Semi-solid continuous roll-casting device was designed with the combination of semi-solid metal processing and horizontal double roll-casting technology. The CRP experiment of AZ91D and AZ31B (Zhang et al, 2007) was investigated for verifying the numerical simulation model and results of CRP. In addition, the further processability of semi-solid AZ91D and AZ31B strips by hot rolling, cold rolling and punching experiment was studied.

5.1 Experimental procedures

AZ91D and AZ31B alloy were melted in electrical resistance furnace, and modified at 1013*K*. Molten alloy was stirred below 868*K* in the range of between liquid and solid phase, semi-solid metal slurry was obtained, and then poured into the roll-casting machine. Fig.21 shows experimental equipment of the horizontal double roll-casting. Liquidus and solidus temperature of AZ91D alloy is 868*K* and 743*K* respectively. Chemical composition of AZ91D and AZ31B alloy are shown in Table 5.

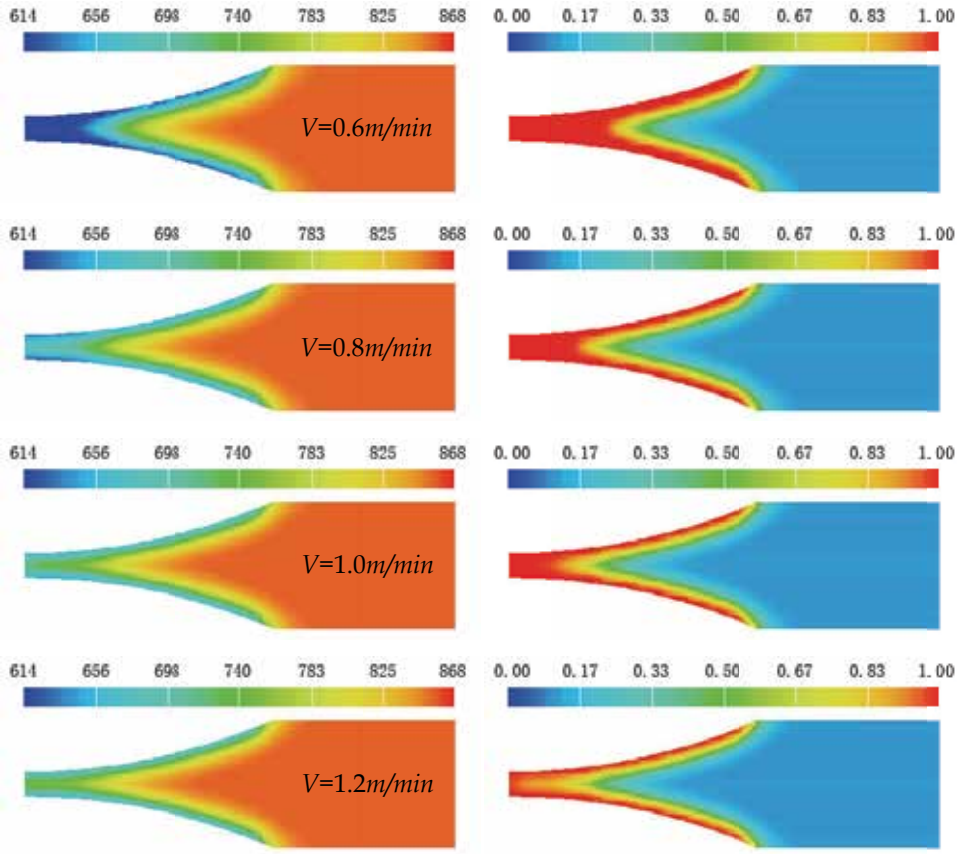

(a) Temperature (b) Solid fraction

Fig. 20. Distribution of temperature and solid fraction at different roll-casting velocity

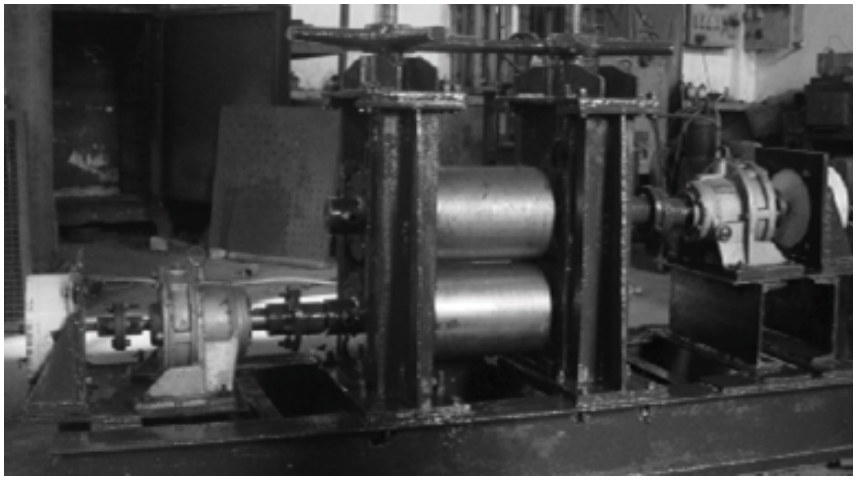

Fig. 21. The experimental equipment of horizontal double roll-casting

Alloy	Al	Zn	Mn	Be	Si	Cu	Fe	Ni	Mg
AZ91D	8.3-9.7	0.35-1.0	0.15-0.2	0.0014	0.031	0.0049	0.0011	0.002	Balance
AZ31B	2.946	0.992	0.3003	0.0014	0.0049	0.0028	0.0016	0.0003	Balance

Table 5. Chemical composition of AZ91D and AZ31B magnesium alloy ($wt\%$)

5.2 Experimental results and discussion

One sample of before roll-casting and other sample of after roll-casting have been taken respectively. All samples were polished and etched by 5% hydrochloric acid reagent. And then its microstructure has been analyzed by the method of metallographic analysis, the microstructure compare of pre and pro roll-casting strip are shown in Fig.22. Here, the temperature of semi-solid metal slurry is 842*K*, 838*K*, 833*K* respectively, the stirring speed is 516*rpm/min* and stirring time is 5 *min*. It can be seen that there is obvious diversity in the microstructure of before and after roll-casting strips, the microstructure of before roll-casting is clear polygonal primary crystal, but the microstructure of after roll-casting is globular and closely resembles globular crystal; and the roll-casting temperature has little influence on the final structure. So, higher semi-solid slurry temperature can be adopted in practical production, which is of great benefit to the distributary of the molten alloy.

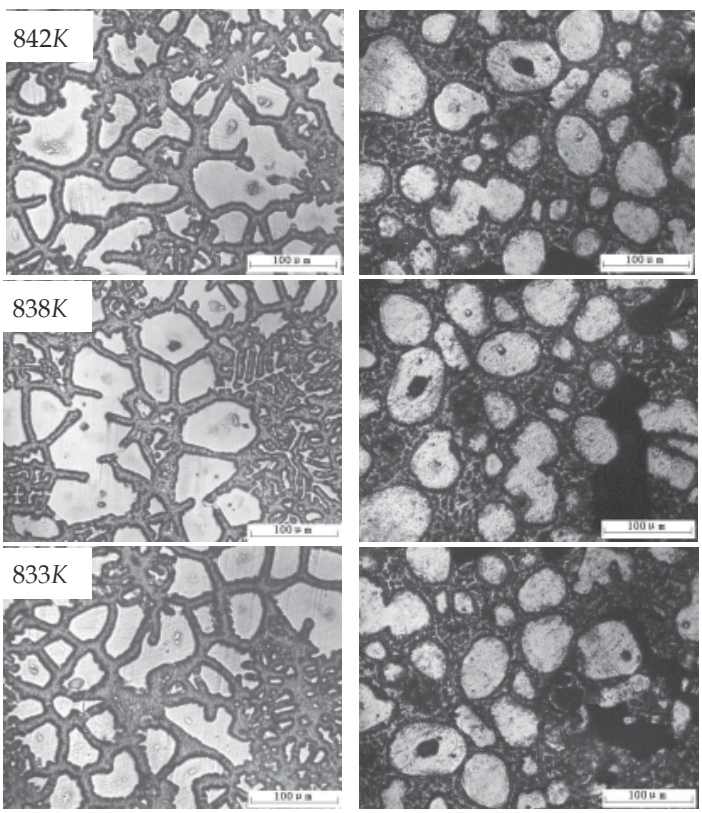

(a) Before roll-casting (b) After roll-casting

Fig. 22. The microstructure contrast of before and after roll-casting at different temperature

The semi-solid magnesium roll-casting strips were obtained when the roll-casting temperature is 842*K*, stirring velocity is 516*rpm/min* and stirring time is 5 *min*. Fig.23 shows the microstructure of top surface, inner and bottom surface of the thick strips. It can be seen that surface microstructure is fine equiaxed grain for quickly cooling of rollers surface and the grain size of the surface is smaller than it of the inner. When the height of roll gap decreases and other processing parameters are invariable, the difference of primary solid particles in inner and surface also decreases. However, when the height of roll gap increases the difference of primary solid particles in inner and surface also increases.

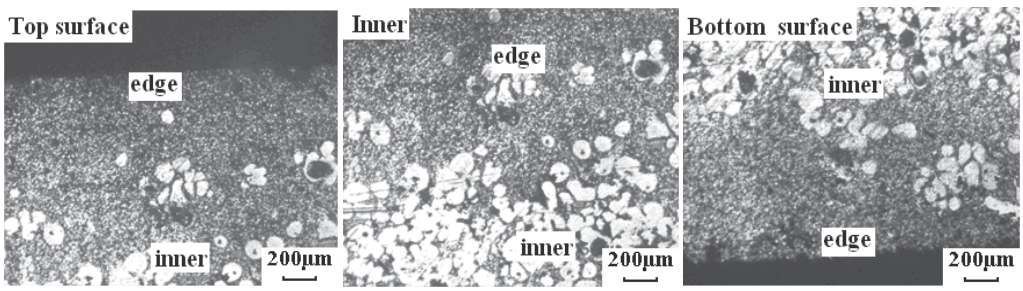

Fig. 23. Microstructure of top surface, inner and bottom surface of the thick strips

5.3 Processing property test of semi-solid strips

In order to examine the processing property of semi-solid AZ91D magnesium strips by CRP, hot-rolling and cold-rolling experiments were carried out respectively. The semi-solid roll-casting strips were tested under hot-rolling and cold-rolling, and the results were shown in Table 6. It can be seen that semi-solid roll-casting AZ91D strips have significant plasticity. The largest deformation of AZ91D strips is by cold rolling can reach as high as 18% and by hot rolling can reach 21% with one-pass roller. In addition, the total deformation of cold rolling and hot rolling can be up to 28% and 47% respectively with three-pass. The largest deformation of AZ31 strips can reach as high as 57% after two-pass. The samples are shown in Fig.24. It can be seen that the surface and edges of the samples are well and only little crack in the edges.

No.		1	2	3
Material		AZ91D	AZ91D	AZ31B
Deformation condition		Cold rolling	Hot rolling	Hot rolling
Temperature/*K*		RT	613	623
Original Thickness/*mm*		3.2	3.3	2.3
First pass	Thickness/*mm*	2.6	2.6	1.6
	ψ/%	18	21	30
Second pass	Thickness/*mm*	2.3	2.12	1.0
	ψ/%	11	18	37.5
Third pass	Thickness/*mm*		1.75	
	ψ/%		17	
Total deformation ψ/%		28	47	57

Table 6. The experimental results of semi-solid roll-casing strips by hot and cold rolling

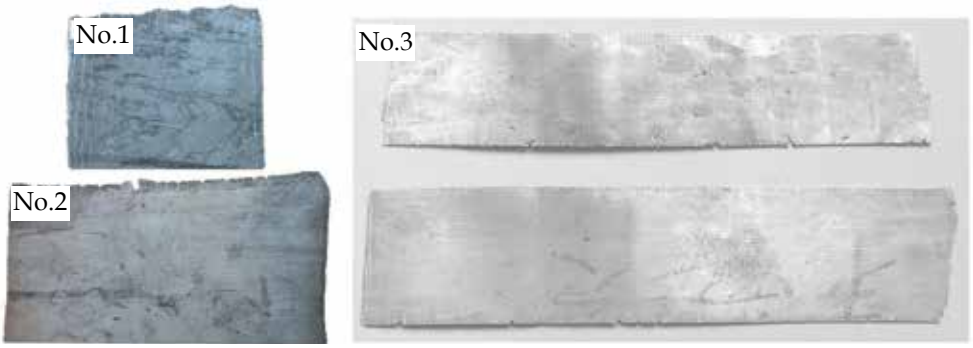

Fig. 24. Samples by hot and cold rolling: (No.1) AZ91D; (No.2) AZ91D; (No.3) AZ31B

The microstructure of cross and lengthwise section by hot rolling are shown in Fig.25. Compared Fig.25 with Fig.22, there are many changes in the microstructure before and after hot rolling. The grains have been crushed. And there are difference of the microstructure on cross and lengthwise section; the grains in cross section are crushed due to the reduction of roller, and the grains in lengthwise section are lengthened along roll direction.

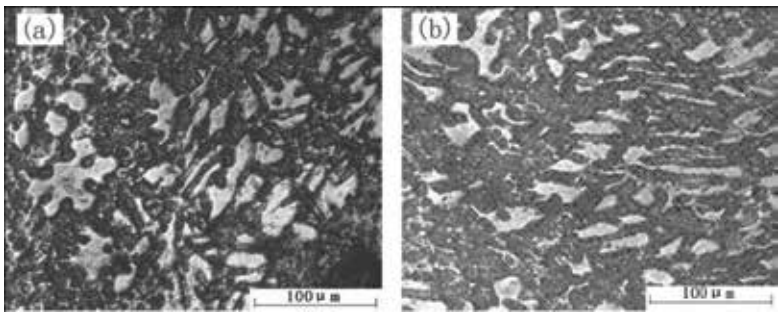

Fig. 25. Microstructure of samples after hot rolling: (a) cross section (b) lengthwise section

5.4 Punching process test of strips

The punching experiment was made for further examining the forming property of the semi-solid strips after hot rolling as shown in Fig.26. The testing results indicate that the AZ31B strips through further hot rolling still have better forming property.

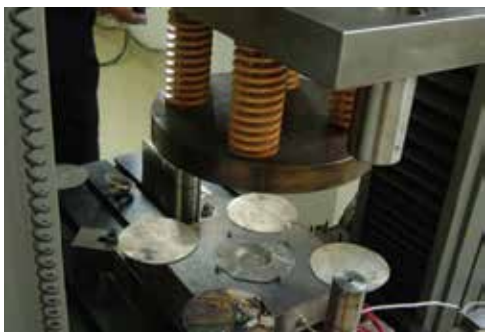

Fig. 26. The punching processing test device

6. Acknowledgement

The authors greatly acknowledge the sponsor of the National Natural Science Foundation of China (NSFC), Sponsor No. 51075006, 50374014, 50674017.

7. Conclusion

Semi-solid magnesium alloys slurry preparation by DCT method and continuous roll-casting process were studied based on numerical simulation and experiment in this chapter. The main research results are as follow:

1. The position of wedge block, gap size, fall head and the height of wedge block have great influence on the molten alloy flow in damper cooling tube based on the numerical simulation.
2. The position of wedge block has great effect on the cooling tube, when the wedge block is located at the outlet of tube, the mixture of the semi-solid slurry is more homogeneous; gap size plays important role in the cooling and stirring ability of tube and the optimum gap size is 4-6*mm* for getting better stirring and cooling; the height of fall head must be higher than 500*mm* and the wedge block height should be less than 100mm.
3. The AZ91D magnesium alloy billets with thin and homogeneous microstructure prepared by the DCT method were obtained when the fall head is 700*mm*, which indicates that the numerical simulation results is accorded with the experimental results and the DCT method is an effective way for preparing the semi-solid slurry.
4. Numerical simulation of semi-solid magnesium roll-casting process was studied using FLOW3D. It was found that the pouring temperature has great influence on the temperature and solid fraction in molten pool and the final point of solidification. With decreasing the pouring temperature, the length of rolling zone and roll-casting load increase. So, the proper velocity should be chosen according the specific condition, in order to guarantee the quality of strips.
5. The semi-solid AZ91D roll-casting strips were obtained by horizontal double rollers roll-casting device. The microstructure of before roll-casting is clear polygonal primary crystal, but the after roll-casting is globular and closely resembles globular crystal. And the strips had good processability and plasticity.
6. The largest deformation of AZ91D strips is by cold rolling can reach as high as 18% and by hot rolling can reach 21% with one-pass roller. In addition, the total deformation of cold rolling and hot rolling can be up to 28% and 47% respectively. The largest deformation of AZ31 strips by hot rolling can reach as high as 57%

8. References

Spencer, D.B.; Mehrabian, R. & Flemings, M.C. (1972). Rheological behavior of Sn-15Pb in the crystallization range. *Metallurgical Transactions*, Vol. 3, pp. 1925-1932.

Flemings, M.C. (1991). Behavior of metal alloys in the semisolid state. *Metallurgical Transactions*, Vol. 22B, pp. 269-293.

Xie, S.S. (2002) The Overview of Study and Application of Semi-solid Metals Processing Technology. *Journal of Plasticity Engineering*, Vol. 9, pp. 1-16.

Hall, K.; Kaufmann, R.H., et al. (2000) Detailed processing and cost considerations for new-rheocasting of light metal alloys. *Proceedings of the 6th International Conference of Semi-solid Processing of Alloy and Composites*, pp.23-28, Turin Italy.

Haga, T.; Suzuki, S. (2001) Casting of Aluminum Alloy Ingots for Thixoforming Using A Cooling Slope. *Journal of materials processing technology*, Vol. 118, pp. 169-172.

Haga, T.; Tkahashi, K.; Ikawa, M. et al (2004) Twin roll casting of aluminum alloy strips. *Journal of Materials Processing Technology*, Vol. 153-154, pp. 42-47.

He, Y.F.; Xing, S.M., et al. (2009) Semi-solid Casting of High Speed Steel Ingots Using Inclined Slope Pre-crystallization Method. *Journal of Wuhan University of Technology-Mater. Sci. Ed*, Vol. 24, pp. 750-752.

Jorstad, J.; Thieman, M. & Kamm, R. (2002). SLC- The newest and most economical approach to semi-solid metal casting. *Proceedings of the 7th International Conference on Semi-solid Processing of Alloys and Composites*, pp. 701-706, Tsukuba Japan.

Xie, S.S.; Yang, H.Q., et al. (2004) Damper cooling tube method to manufacture semi-solid slurry of magnesium alloy. *Proceedings of the 8th International Conference of Semi-solid Processing of Alloy and Composites*, Limassol, Cyprus.

Xie, S.S.; Yang, H.Q., et al. (2006) Numerical Simulation and Parameters Optimization of Preparation of AZ91D Magnesium Alloy Semi-solid Slurry by Damper Cooling Tube Method. *The Chinese Journal of Nonferrous Metals*, Vol. 16, pp. 488-493.

Xie, S.S.; Huang, G.J., et al. (2007) Study on Numerical Simulation and Experiment of Fabrication Magnesium Semisolid Slurry by Damper Cooling Tube Method. *The 10th International Conference on Numerical Methods in Industrial Forming Processes*, Faculty of Engineering, University of Porto，Portugal.

Yang, H.Q.; Xie, S.S., et al. (2007) Numerical Simulation of the Preparation of Semi-solid Metal Slurry with Damper Cooling Tube Method. *Journal of University of Science and Technology Beijing*, Vol.14, pp. 443-448.

Launder, B.E.; Spalding, D.B. (1972). *Lectures in Mathematical Models of Turbulence*. Academic Press, London.

Xie, S.S.; Geng, M.P., et al. (2005) A New Technique of Casting-rolling Strips for Semi-solid Magnesium Alloys [J]. *Material Science and Technology*, Vol. 21, pp. 785-787.

Xie, S.S.; Yang, H.Q., et al. (2006) Numerical simulation of semi-solid Magnesium alloy in continuous roll-casting process. *International Conference on Semi-Solid Processing of Alloys and Composites*, Trans Tech Publications, Switzerland, Solid State Phenomena, Vol. 116-117, pp. 583-586.

Xie, S.S.; Yang, H.Q., et al. (2007) Numerical Simulation of Semi-solid Magnesium Alloy in Continuous Casting Process. Journal of Plasticity Engineering, Vol. 14, pp. 80-88.

Xie, S.S.; He, Y.F., et al. (2008) Study on Semi-solid Continuous Roll-casting Strips of AZ91D Magnesium Alloy. *Proceedings of the 10th International Conference of Semi-solid Processing of Alloy and Composites*, Solid State Phenomena, Vol. 141-143, pp. 469-473.

Zhang, Y.; Geng, M.P., et al. (2008) Influence of Processing Parameters on Microstructure of Casting Rolling Semi-solid AZ91D Magnesium Alloy. *Proceedings of the 10th International Conference of Semi-solid Processing of Alloy and Composites*, Solid State Phenomena, Vol. 141-143, pp. 535-538.

Zhang, Y.; Xu, J.H., et al. (2007) Study on Rheocasting-rolling of Semi-solid AZ31B Magnesium Alloy. Trans. Nonferrous Met. Soc. China, Vol. 17, pp. s814-s817.

20

Design and Development of High-Performance Eco-Mg Alloys

Shae K. Kim
Korea Institute of Industrial Technology
Korea

1. Introduction

The importance of Mg alloy can be clearly expressed by the never ending request for weight reduction to decrease fuel consumption and emission in the transportaion industry. The importance of Mg alloy is also acknowledged in terms of designer's choice due to the unique properties not found in other materials. On the contrary, we can expect the gloomy future of Mg alloy because aluminum, steel, and plastic industries take great effort to keep and/or win back their territory, which in turn suggests that cost plays more and more important role on this situation. As far as I am concerned, I believe that Mg and Al alloys do synergetic effect on the transportation industry in the balance of weight, quality, and cost.
We can approach Mg alloy in this way - considering the questions of 'what is the secret of sustainability?' 'what is the best material for that?' and 'what should we do for Mg alloy?' Mg alloy is the lightest metallic structural material in the world. The resource of Mg alloy is not abundant but unlimited. Mg alloy is inherently recyclable. These 3 points of Mg alloy show fundamentally qualification criteria as the best material for sustainability. However, the need for using SF6 gas or other protective gases and adding toxic Beryllium (Be) and the safety issue of machined chips and products have been the obstacles of Mg alloy for the best sustainable material.
The environmental benefits provided by lightweight, unlimited, and recyclable Mg alloy have the potential to grow significantly in the future if the global Mg members are working together to demonstrate its stewardship by eliminating global warming SF6 or other protective gases and Be addition as well as by ensuring safety during manufacturing and application. It should be done without sacrificing process ability and mechanical property and increasing the life-cycle cost of Mg alloy. This is what Eco-Mg (Environment COnscious magnesium) is all about.
The simple and plain approach of Eco-Mg alloy is to introduce CaO particles in the range of 0.3wt% to 0.7wt% as an ingredient into conventional cast and wrought Mg alloys for (1) non-SF6 process, (2) Be elimination, (3) improved melt cleanliness, (4) ensured original process adjustability for casting, forming, joining as well as surface treatment, (5) improved mechanical property by grain refinement and internal soundness, (6) ensured safety during manufacturing and application by raising oxidation and ignition resistances of machined chips and products, and (7) improved recyclability. CaO of over 0.5~0.7wt% can be introduced for special purposes to develop creep-resistant, fire-retardant or fire-proof,

damping, bio-degradable, desulphurizing Mg alloys. The R&BD fields of Eco-Mg alloy are well illustrated in Figure 1.

There are 2 things to be clearly demonstrated. One thing, indicated in Figure 2, is that Eco-Mg alloy is not only related to CaO. The approach of Eco-Mg alloy promotes alkaline metal oxides such as NaO and KO, alkaline earth metal oxides such as CaO and SrO, and calcium compounds such as CaO, Ca(OH)2, CaC2, CaCN2, CaCO3 and CaSO4 according to the purpose. For commercial applications, CaO, Ca(OH)2, SrO and CaCN2 are now mainly considered.

As illustrated in Figure 3, the other thing is that CaO does not exist as CaO itself in the solidified state. By the reactive phase formation, Mg2Ca phase (C14) in pure Mg and Al2Ca (C15) and/or (Mg, Al)2Ca (C36) phases in Al-bearing Mg alloys are formed. The exceptional difference between Ca and CaO addition is Ca content in α-phase (solid solution phase). It is clear in pure Mg. Although Ca has the strong segregation tendency, Ca added pure Mg solidifies first as α-phase with Ca solid solution and then as divorce eutectic phase of Mg and Mg2Ca, according to Ca content and process condition. On the contrary, CaO added pure Mg alloy solidifies together as α-phase with almost no Ca solid solution and as divorce eutectic phase, regardless of CaO content and process condition. The same phenomena can be obtained with SrO, CaC2 additions in pure Mg and Mg alloys. For example, SrO added Mg alloys generate together α-phase with almost no Sr solid solution and Al4Sr.

This paper will not cover all the aspects of Eco-Mg alloy. Focused only on CaO addition, the general issues of non-SF6 process, process adjustabilities, oxidation and ignition behaviors, and recyclability will be addressed.

2. Non-SF6 process

It is needless to say how important it is not to use SF6 gas during Mg process in terms of global warming potential. There have been 2 approaches for non-SF6 process of Mg melting and casting processes – alternative gas development and alloy development that can be processed without SF6 gas.

There are several alternative gases which have been already developed and actually in the stage of application. The development of alternative gas at current situation is more realistic than alloy development. However, the apporach of alternative gas can not answer the safety of melt cleanliness, machined chips and products, and recyclability.

The research to add metallic Ca into Mg alloy has been carried out for non-SF6 process. It has been revealed to be very useful in terms of non-SF6 process. However, non-SF6 process with Ca added Mg alloy causes another problems such as fluidity decrease, die soldering, and Ca subtraction during recycling. The most serious problem is the change of material property and process condition.

By Non-SF6 process with Eco-Mg alloy, we can simultaneously improve melt quality and fluidity, maintain at least process ajdustability and mechanical property, ensure the safety of machined chips and products, and improve recyclability.

Figure 4 clearly demonstrates the effect of small amount of CaO on non-SF6 casting for pure Mg; and AZ31, AM50, AM60, and AZ91 Mg alloys (Kim et al., 2009; Kim, 2009; Lee, et al., 2007; Lee & Kim, 2008). Figure 4(a) shows the surface changes of pure Mg during casting and solidification under ambient atmosphere without any protective gas. Severe oxidation began and tarnished surface appeared in 10 seconds just after being poured. Severe burning started in 10 seconds and continued even with white flame to the point when all the melt

was consumed by burning. The similar phenomena occurred in AZ31 (Figure 4(c)), AM50 (Figure 4(e)), AM60 (Figure 4(h)), and AZ91 (Figure 4(l)) Mg alloys. It is well known that the continuous oxidation and resultant burning of Mg alloy occur, at high temperature over 500 ^{o}C, due to the porous surface nature of MgO films that do not act as protective layer to prevent further oxidation and burning. The effect of alloying elements on the oxidation and burning resistances is not clear. However, based on the results of Figure 4, the oxidation and burning resistances increase with increasing Al content during casting and solidification, although Al addition cause the decrease of the liquidus and solidus temperatures of Mg alloy. It should be pointed out that the results of Figure 4 are totally different from the oxidation and buring resistances of Mg alloy during oxidation and ignition tests of Mg parts, which will be addressed in chapter 3.1.

Figure 4(b) shows the surface changes of 0.3wt% CaO added pure Mg during casting and solidification under ambient atmosphere without any protective gas. No burning appeared and shiny surfaces were maintained after the solidification was completely stopped. The similar phenomena occurred in AZ31-0.27wt%CaO (Figure 4(d)), AM50-0.27wt%CaO (Figure 4(g)), AM60-0.3wt%CaO (Figure 4(j)), and AZ91-0.27wt%CaO (Figure 4(n)) Mg alloys. The experiments with AM50-0.1wt%CaO (Figure 4(f)), AM60-0.1wt%CaO (Figure 4(i)), and AZ91-0.1wt%CaO (Figure 4(m) Mg alloys were carried out to investigate the minimum amount of CaO for non-SF6 process. The results show that 0.1wt% CaO addition into Mg alloy is not enough to be cast in ambient atmosphere without any protective gas. The further research should be taken to verify the minimum amount of CaO about non-SF6 process for the case of melting and long holding in the furnace, with an emphais on the effect of alloying elements and on various protective conditions such as dry air or nitrogen atmosphere.

Figure 5 shows the as-cast microstructures of pure Mg and AZ31, AM50, AM60, and AZ91 Mg alloys without and with CaO. One thing to be obtained with Eco-Mg alloy is not to sacrifice the original mechanical property of Mg alloy without CaO. Therefore, what is expected by CaO addition is no change in the microstructure, except the grain refinement due to grain-boundary pinning and the internal soundness related to melt cleanliness. The typical microstructures of Mg alloy without CaO under non-equilibrium solidification are the coarse primary α-phase dendrites and bulk skeletal β-phase (Mg17Al12) in the divorced eutectics. The microstructures of Mg alloy with CaO are similar to those without CaO, as mentioned before, except the grain refinement. This is because the grain-boundary consists of β-phase and C15 (Al2Ca), which can be confirmed by the results in Figures 6 and 7 (Lee, et al., 2007; Kim, 2009). The mass fraction of CaO was deduced from Ca mass fraction detected by ICP-mass.

3. Process adjustabilities

3.1 Strip casting adjustability

Figure 8 clearly demonstrates the effect of small amount of CaO on non-SF6 strip casting of AZ31 Mg alloy (Jang, et al., 2008; Kim et al., 2009). Figure 8(a) shows the surface condition of AZ31 Mg alloy strip castings without SF6 gas. The surface was blackened because molten AZ31 Mg alloy reacted with oxygen in the air when the strip left the rolls. Figure 8(b) shows the surface condition of AZ31 Mg alloy strip castings with SF6 gas. In the used prototype strip casting machine, SF6 gas protection was not enough to prevent strip castings from being oxidized. Furthermore, cracks were observed on the surface of the strip castings due

to the adulteration of impurities, which were made by oxidation and burring during strip casting even with SF6 protection. Figure 8(c) shows the surface condition of 0.1wt%CaO added AZ31 Mg alloy strip castings without SF6 gas. Compared with the effect of CaO on gravity casting of AZ31 Mg alloy, 0.1wt%CaO addition was enough for non-SF6 process during strip casting due to the faster cooling rate, that is, the shorter solidification time.
Figure 9 shows the hardness values of the strip castings of AZ31 Mg alloy without and with CaO on the surface area and in the middle section. As planned and expected, the Vickers hardness values of CaO added AZ31 Mg strip castings are similar to those of AZ31 Mg alloy strip castings. The Vickers hardness values are uniform in all the sections.
Figure 10 shows the tensile properties of the strip castings of AZ31 Mg alloy without and with CaO in the as-received condition. The yield strength (YS), ultimate tensile strength (UTS), and elongation (EL) of AZ31 Mg alloy strip castings are 52.0MPa, 161.0MPa and 14.5%, respectively. The YS, UTS and EL of AZ31-0.1wt%CaO Mg alloy strip castings are 87.6MPa, 140.7MPa and 11.7%, respectively. The YS, UTS and EL of AZ31-0.2wt%CaO AZ31 Mg alloy strip castings are 74.9MPa, 175.9MPa and 18.0%, respectively. Not only for non-SF6 process but also for strip casting process optimization, the further research is necessary to verify the optimum amount of CaO and the effect of alloying elements.

3.2 Diecasting adjustability

Figure 11 shows the non-SF6 diecasting process of 0.3wt%CaO added AZ91D Mg alloy under nitrogen atmosphere without SF6 gas (Kim, 2009). Figure 11(b) shows the clean surface of 0.3wt%CaO added AZ91D Mg alloy melt in the open condition of the furnace. The result showed that 0.3wt%CaO was enough for melting, holding, and casting AZ91D Mg alloy only under nitrogen atmosphere wihtout SF6 gas. Figure 11(c) and 11(d) show hot chamber diecasting process for the cellular phone case and mechanical specimens, respectively. Diecasting was performed by using Frech 250-ton hot chamber machine. Figure 12(a) shows the mechanical test specimen of AZ91D Mg alloy diecast under SF_6 and CO_2 atmospheres (Kim, 2009). Figure 12(b) shows the mechanical test specimen of 0.3wt%CaO added AZ91D Mg alloy diecast under nitrogen atmospheres without SF6 gas. Figures 12(c) and 12(d) show the resultanct microstructures of Figures 12(a) and 12(b), respctively. The microstructure of AZ91D Mg alloy consists of porosity and coarse grain, while the grain-refined microstructure of 0.3wt%CaO added AZ91D Mg alloy is obtained with little porosity. Figure 13 shows the hardness values of the mechanical property specimens of Figures 12(a) and 12(b), respectively. The Rockwell hardness values of AZ91D and 0.3wt%CaO added AZ91D Mg alloys are 61.2 and 64.5, respectively. The Rockwell hardness value of 0.3wt%CaO added AZ91D Mg alloy is little higher than that of AZ91D Mg alloy, due to the grain refinement and diespersion stregnthening of Al2Ca phase. Figure 14 shows the tensile properties of AZ91D and 0.3wt%CaO added AZ91D Mg alloys prepared by the process indicated in Figure 12. The yield strengths of AZ91D and 0.3wt%CaO added AZ91D Mg alloys are 151 MPa and 162 MPa, respectively. The yield strength of 0.3wt%CaO added AZ91D Mg alloy is little higher than that of AZ91D Mg alloy, due to the grain refinement and dispersion strengthening of Al2Ca phase. The tensile strengths of AZ91D and 0.3wt%CaO added AZ91D Mg alloys are 242 MPa and 257 MPa, respectively. The improvement of the tensile strength of 0.3wt%CaO added AZ91D Mg alloy is due to the increased yield strength plus the work hardening by the increased elongation. The elongation values of AZ91D and 0.3wt%CaO added AZ91D Mg alloys are 2.96 % and 8 %, respectively. The elongation of 0.3wt%CaO added AZ91D Mg alloy is much higher than

that of AZ91D Mg alloy, due to the soundness of specimem by decreased defects such as oxides, inclusion, and porosity and grain refinement as shown in Figure 12.

Figure 15 shows the non-SF6 cold chamber diecasting process for CaO added AM60 under nitrogen atmosphere without SF6 gas. The diecasting was performed for AM60-(0.25~0.65)wt%CaO Mg alloys by using a Buhler 1,450-ton cold chamber machine as shown in Figure 15(a). Figures 15(b) through 15(d) show the billet preheating system, the clean surface of molten 0.65wt%CaO added AM60 Mg alloy, and oil pan diecasting process. 1-ton of molten AM60 Mg alloy was prepared in a steel crucible heated to 720°C in an electric resistance furnace and then 5kg ingot of 1.2wt%CaO added AM60 Mg alloy was added repeatedly into the furnace. Therefore, the oil pan diecastings with varying CaO content up to 0.65wt% could be diecast. The samples for chemical analysis were prepared at 30-minute interval and the chemical composition was detected by ICP-mass spectrometer. It should be noted that the mechanical test specimens were prepared directly by diecasting even at the end of the product as shown at Figure 16(a). The tensile test specimen has a gauge length of 30mm and a diameter of 6 mm as shown in Figure 16(b).

Figure 17 shows the tensile properties of AM60-(0.25~0.65)wt%CaO Mg alloys prepared by the process indicated in Figure 15. The yield strength, as shown in Figure 17(a), increases linearly with increasing CaO content up to 0.5wt%CaO addition. Over 0.5~0.6wt%CaO addition, the yield strength can be said to be maintained. The highest yield strength at 0.4~0.5wt%CaO addition is 160 MPa and much higher compared with that of AM60 Mg alloy without CaO. The ultimate strength, as shown in Figure 17(b), also increases linearly with increasing content up to 0.5 wt%CaO addition. The highest ultimate strength is 260 MPa at 0.4~0.5 wt%CaO addition. Figure 17(c) shows that the elongation also increases in proportion to CaO content up to 0.4~0.6 wt%CaO addition. The highest elongation value is 16 % at 0.4~0.5wt%CaO addition. Over 0.5~0.6wt%CaO addition, the elongtation can be said to decease due to the higher amount of strengthening phase, Al2Ca.

The yield strength, tensile strength, and elongation of 0.65wt%CaO added AM60 Mg alloy at room temperature are 164 MPa, 260 MPa, and 12 %, respectively. The tensile properties of 0.65wt%CaO added AM60 Mg alloy at 150°C by the cross-head speed of 1mm/min. are 152 MPa, 225 MPa, and 13 %, respectively, as shown in Figure 18. The excellent tensile properties of CaO added AM60 Mg alloy even at 150°C should be carefully revieved by tensile test in diffent cross-head velocity and by creep resistance test.

Figure 19 summarizes the proportional relationship between the strength and elongation of CaO added AM60 Mg alloys, unlike those of AM and AE series Mg alloys. It is common that the optimization of one property by alloying comes at the expense of one or more other properties. A typical example is the relationship of yield strength and ductility. In order to increase yield strength significantly, some ductility has to be sacrificed. The tensile properties of CaO added AM60 Mg alloy at room temperature are greatly improved due to the grain refinement, Al2Ca dispersion strengthening, and increased soundness without oxides, inclusion, and porosity. This can lead to a conclusion that, for a given Al content, controlled CaO addition to AM60 Mg alloy improves both the strength and ductility.

Figure 20 shows the typical microstructures of as-diecast AM60 Mg alloys with (0.2~0.6)wt%CaO. The microstructures are continuously refined with increasing CaO content. The fracture surfaces in Figure 21 also demonstrates that the dimples are demarcated by the intensive slips at grain boundaries in as-diecast AM60 Mg alloys with (0.2~0.6)wt%CaO, unlike the cleavage planes prominently observed in the brittle Mg alloys.

3.3 Extrusion and rolling adjustabilities

The goal of extrusion and rolling adjustabilities for Eco-Mg alloy is to find out minimum amount of CaO that can be processed without SF6 gas during continuous casting and subsequent forming and heat treatment, to apply the same forming conditions, and to maintain mechanical properties of Mg alloy. Figure 22(a) shows the extruded bars of AZ31 Mg alloy without and with CaO (Lee, et al., 2006; Kim, 2007; Kim et al., 2009). The extrusion experiments were done at 350 °C with the extrusion ratio 20:1 without SF6 gas. The surfaces of all extruded bars are clear. Figure 22(b) shows the relationship between surface roughness and CaO content. The values of surface roughness slightly decrease with increasing CaO content. The surface roughness of AZ31-0.45wt%CaO Mg alloy is flatter than those of AZ31 and AZ31-0.07wt%CaO Mg alloys in part due to the temperature response change. As planned and expected, the Rockwell hardness and tensile properties of the extruded bars of CaO added AZ31 Mg alloy are almost uniform and similar with those of AZ31 Mg alloy extruded bar.

Figure 23 shows the mechanical properties of hot-rolled AZ31 and AZ31-0.3wt%CaO Mg alloys sheets in the as-received condition just after 15-pass hot-rolling without any post heat-treatment. The Rockwell hardness (*F*-scale) values are the same in the both cases, as planned and expected. The hot-rolling experiments were carried out by using a prototype rolling machine. The specimen was preheated at 400 °C for 20 minutes and the temperature of the rolls was 150 °C. The reduction ratio per pass was 30% and 15 passes were totally performed.

3.4 Joining adjustability

Friction stir welding was carried out for AZ31 Mg alloy without and with CaO. Butt and laser welding experiments will be expected to be carried out (Ha, et al., 2007; Kim, et al., 2009). Generally, the stir zone of friction stir welded metals is characterized by dynamic recrystallization. As shown in Figures 24(a) and 24(b), the stir zone of AZ31-0.25wt%CaO added AZ31 alloy shows the significantly refined grains compared with that of AZ31 alloy, while the other TMAZ, HAZ, and base metal zone show the similar microstructures for the both cases. It seems that the stir zone of AZ31-0.25wt%CaO Mg alloy was refined in part due to heterogeneous nucleation or grain growth pinning by C15 along the grain-boundary during dynamic recrystallization. The hardness profiles of friction stir welded AZ31 and AZ31-0.25wt%CaO Mg alloys sheets are given in Figure 24(c). There is not a visible difference between AZ31 and AZ31-0.25wt%CaO Mg alloys in TMAZ, HAZ and base metal zone, while, in SZ, the hardness values of AZ31-0.25wt%CaO Mg alloy is much higher than those of AZ31 Mg alloy.

4. Oxidation and ignition behaviors

4.1 Oxidation behavior

Figure 25 shows the weight gain of Mg-Al alloys during oxidation test under dry air atmosphere at 500°C for 7 hours, according to Al content. Pure Mg shows the stable oxidation resistance compared with AZ31 and AM60 Mg alloys. AZ91 Mg alloy shows the poor oxidation resistance. The oxidation resistances of Mg-Al alloys decrease with increasing Al content at 500°C. The effect of Al element on the oxidation resistance of Mg

alloys seems to be attributed to the decrease of the solidus temperature of the alloys. As mentioned in chapter 2, the oxidation resistances of Mg-Al alloys during oxidation test are totally different from the oxidation and burrning resistances during casting and solidification.

Figure 26(a) shows the weight gain of pure Mg and CaO added pure Mg as a function of oxidation time at 500°C for 7 hours (Ha, et al., 2008; Kim, et al., 2009). The results indicate that pure Mg show the parabolic law due to the loose and porous structure of MgO. On the contrary, in CaO added pure Mg, the oxidation rate is reduced with respect to CaO content at the same temperature. Figures 24(b) through 24(e) show the weight gain behaviors of AZ31, AM50, AM60 and AZ91 without and with CaO addition, respectively (Kim, et al., 2005; Kim, et al., 2009; Lee, et al., 2009; Lee & Kim, 2009). As seen in the Figures, the poor oxidation resistances of Mg alloys are exhibited in proportion to the reaction time. The results indicate that Mg alloys show the parabolic law due to the loose and porous structure of MgO. On the contrary, 0.3wt%CaO added AZ31, AM50 and AM60 Mg alloys show the stable oxidation resistances at 500°C, except 0.3wt%CaO added AZ91 Mg alloy with high Al content.

Figure 27 shows the AES depth profiles sputtered form the surface of pure Mg, AM60 and AZ91 without and with CaO. In pure Mg as shown in Figure 27(a), there is the thick MgO layer on the surface because the concentration of Mg and O are constant for sputtering time. In CaO added pure Mg, as shown in Figure 27(b), there is the thin oxide layer mixed with MgO and CaO. The oxidation resistance of CaO added Mg is similar to those of Ca added Mg alloys studied by B. S. You et al (You, 2000). As indicated in Figures 27(c), 27(d), 27(e), and 27(f), the AES depth profiles sputtered from the surfaces of AM60, AM60-0.45wt%CaO, AZ91, and AZ91-0.7wt%CaO Mg alloys after oxidation at 500°C for 7 hours show the similar behaviors like the results of pure Mg and CaO added pure Mg. Generally, MgO layer on the surface of Mg alloys exhibits protective behavior below about 450°C, while the weight gain by oxidation is accelerated with respect to temperature above 450°C, because of the porous naute of MgO surface film at high temperature. It can be explained by Pilling-Bedworth ratio, the ratio of oxide volume to metal volume. Because the Pilling-Bedworth ratio for pure Mg is 0.83, MgO film on the surface of pure Mg can not act as a protective barrier to prevent continuous oxidation. Although it can not be explained by Pilling-Bedworth ratio (Pilling & Bedworth, 1923), it has been reported that the oxidations of Ca added Mg alloys are suppressed due to the dense film mixed with MgO and CaO (0.78).

4.2 Ignition behavior

While the oxidation resistance is related to product performance and durability, the ignition resistance is to the safety and the fear to impede practical application. For the ignition resistance of Mg alloy, the quantitative data is prerequisite. For the quantitative data, the definition and standard test method of the ignition resistance of Mg alloy should be decided.

There are 2 goals for ignition experiments of Eco-Mg alloy. One is to increase the ignition resistance as high as possible with CaO addition for the safety of machined chips and products. The result can be understood with that of non-SF6 process and improved oxidation resistance. The other is to investigate the effect of test method, test environment, and specimen shape on the resistance for obtaining quantitative data. In terms of accuracy,

DTA is the best method. The furnace chip test is useful to verify the safety of machined chips while the torch test is for the safety of products. For the furnace chip test, the thickness of chips, that is, the used tool kinds, the amount of chips, and the degree of compaction should be stated for quantification. The heating rate for DTA test, the furnace temperature for the furnace test, and the flame temperature for the torch test should also be stated.

Figure 28 shows the results of DTA ignition tests of Mg-Al alloys under dry air atmosphere. The ignition temperatures of AZ31, AM60, and AZ91 Mg alloys are 590°C, 560°C, and 559°C, respectively. The ignition temperatures decrease with increasing Al content due to the decrease of the liquidus and solidus temperatures. The similar phenomena are obtained in the oxidation results of Mg-Al Mg alloy as shown in Figure 25.

Figure 29 shows the results of DTA for AZ31, AM60, and AZ91 Mg alloys without and with CaO under dry air atmosphere (Lee, et al., 2007; Lee & Kim, 2008; Lee & Kim, 2009). The ignition temperatures of CaO added Mg alloys increase almost linearly with increasing CaO content. The ignition temperatures of AZ31, 0.32wt%CaO added AZ31, 0.82wt%CaO added AZ31 and 1.22wt%CaO added AZ31 Mg alloys are 590°C, 691°C, 806°C, and 1,177°C, respectively. From the results of DTA for 1.22wt%CaO added AZ31 Mg alloy, it should be noted that fire-proof performance can be controlled by CaO addition. Figures 44(b) and 44(c) show the similar behaviors of CaO added AM60 and AZ91 Mg alloys, respectively.

Figure 30 compares the results of DTA for AZ31, AM60, and AZ91 Mg alloys without CaO and with 1wt% CaO as a function of Al content under dry air atmosphere. The ignition temperatures decrease with increasing Al content without and with CaO. The ignition temperatures of 1wt%CaO added Mg-Al Mg alloys increase by about 300°C in all Mg-Al alloys without CaO. As mentioned before, the effect of Al content can be understood by the liquidus and solidus temperature drops regardless of CaO. The fact that the ignition temperatures increase with increasing CaO content can be understood by the combined effect of the increased oxidation resistance and the decreased Al content to Al2Ca formation in CaO added Mg-Al alloys. Figure 36 clearly demonstrates the changes of solidus and liquidus temperatures with respect to Al and CaO contents in Mg-Al alloys.

Figure 31 shows the results of DTA for commercial high temperature Mg alloys and CaO added Mg-Al Mg alloys under dry air atmosphere. The ignition temperatures of AS21, AE44, MRI153, MRI230, 1.22wt%CaO added AZ31, 1.65wt%CaO added AM60, and 1.5wt%CaO added AZ91 Mg alloys are 591°C, 602°C, 1,057°C, 1,165°C, 1,177°C, 1,161°C, and 1,142°C, respectively. The ignition temperatures of CaO added Mg-Al and MRI230 are over 1,100°C. The ignitions of MRI and CaO added Mg-Al Mg alloys occurred over the liquidus temperatures while AS and AE series Mg alloys ignited below the liquidus temperatures.

Figure 32 shows the chip ignition results of Mg-Al Mg alloys under an ambient atmosphere in the furnace at 800°C. The chip ignition temperatures also decrease with increasing Al content. The chip ignition temperatures of pure Mg, AZ31, AM60, and AZ91 Mg alloys are 602°C, 583°C, 583°C, and 567°C, respectively. Figure 33 shows the effect of CaO on the chip ignition temperatures of pure Mg, AZ31, AM60, and AZ91 Mg alloys under an ambient atmosphere in the furnace at 800°C (Lee, et al., 2007; Lee & Kim, 2008; Lee & Kim, 2009). Figure 33(a) shows the effect of CaO on the chip ignition temperatures of pure Mg. With increasing CaO content, the ignition temperatures of pure Mg increase linearly, as planned and expected. The effect of CaO on the ignition temperatures of AZ31, AM60, and AZ91 Mg

alloys are shown in Figures 33(b), 33(c), and 33(d), respectively. The results say 2 things; one is the possibility to control the ignition temperatures of Mg machined chips and the other is the difficulty to improve much higher the ignition temperatures of Mg alloys in the state of machined chips unlike products. The difference of test atmosphere should be also considered: DTA under dry air atmosphere and furnace chip test under an ambient atmosphere.

Figure 34 shows the chip ignition results of commercial high temperature Mg alloys and CaO added Mg-Al Mg alloys under an ambient atmosphere (Lee & Kim, 2010). The ignition temperatures of AS21, AE44, MRI153, MRI230, 1.22wt%CaO added AZ31, 1.65wt%CaO added AM60, and 1.5wt%CaO added AZ91 Mg alloys are 569°C, 568°C, 584°C, 627°C, 653°C, 638°C, and 604°C, respectively. The ignition temperatures of 1.22wt%CaO added AZ31 and 1.65wt%CaO added AM60 Mg alloys are much higher than those of the other high temperature Mg alloys. The ignition temperatures of MRI230 and CaO added AZ31 and AM60 Mg alloys are only over the liquidus temperatures.

Figure 35 shows the results of torch ignition test for AZ91 and 0.3wt%CaO added AZ91 Mg alloys under an ambient atmosphere (Lee & Kim, 2009). The diecast product was continuously heated by the torch until the ignition occurred. The ignition time was defined at the time when the diecast product was ignited. The ignition times of AZ91 and 0.3wt%CaO added AZ91 Mg alloys are 70 seconds and 210 seconds, respectively. This result might indicate that small CaO addition is of interest for fire-retardant Mg products when they are exposed to fire or spark under an ambient atmosphere. The important point is that the fire of 0.3wt%CaO added AZ91 Mg alloy was extinguished when the torch was turned-off even after the ignition. However, the fire of AZ91 Mg alloy continuously propagated by self-heating. The behavior of the torch ignition results can be discussed from the AES depth profile results. Figure 36 shows the AES depth profiles sputtered from the surface of as-received diecastings. In AZ91 Mg alloy diecastings, there is the thick MgO layer on the surface because the concentration of Mg and O were constant for sputtering time. In 0.3wt%CaO added AZ91 Mg alloy diecastings, on the contrary, there is the thin oxide layers mixed with MgO and CaO.

Figure 37 shows the results of torch ignition test for CaO added Mg-Al alloys and high temperature Mg alloys under an ambient atmosphere (Lee & Kim, 2010). The cast product was continuously heated by the torch until the ignition occurred. The ignition times of 1.13wt%CaO added AZ31, 1wt%CaO added AM60, and 1.02wt%CaO added AZ91 Mg alloys are 200 seconds, 120 seconds, and 120 seconds, respectively. The ignition times of AS21, AE44, MRI153, and MRI230 are 100 seconds, 110 seconds, 100 seconds and 110 seconds, respectively. When the torch was turned-off even after the ignition, the fire of 1.13wt%CaO added AZ31, 1wt%CaO added AM60, 1.02wt%CaO added AZ91, MRI 153, and MRI230 Mg alloys were extinguished. However, the fire of AS21 and AE44 Mg alloys continuously propagated by self-heating.

5. Recyclability

It is well known that Ca in Mg alloys disappears during recycling due to the reaction of Ca with the fluxes. The Ca addition to Mg alloys forms α-phase with Ca solid solution and C14 or C15 phase. As mentioned earlier, CaO addition to Mg alloys forms only C14 or C15 phase as far as Ca is concerned. The goal of flux recycling experiments for Eco-Mg alloy is to verify

separately the reaction of α-phase with Ca solid solution and C14 or C15 phase with each flux. It was confirmed that the flux change could minimize the reduction of Ca content during flux recycling even for Ca added Mg alloys. The suitable fluxes for Mg alloys with C14 and C15 phases are KCl and NaCl without Ca loss.

Figure 38 shows the microstructures of as-cast CaO and Ca added AZ31 Mg alloys. The typical microstructure of as-cast AZ31-0.3wt%Ca Mg alloy is obviously α-phase and irregular β-phase along grain boundaries (Lee & Kim, 2009). The microstructure of as-cast AZ31-0.3wt%CaO Mg alloy is α-phase, irregular β-phase and C15 phase along grain boundaries. Figures 38(b), 38(c), 38(d), 38(e), 38(g), 38(h), 38(i), and 38(j) show the as-recycled microstructures of CaO and Ca added AZ31 Mg alloys after flux recycling by MgCl2, KCl, NaCl, and MnCl2. Table 1 gives the ICP results before and after the recycling of each flux.

The reaction between α-phase with Ca solid solution and MgCl2 is described as $MgCl_2(s) + Ca(s) = CaCl_2(s) + Mg(\ell)$, ΔG_f = -159.943 kJ/mol at 700°C, which explains that the solid solution Ca in AZ31-0.3wt%Ca Mg alloy disappears during recycling because ΔG_f of the reaction is -159.943 kJ/mol. The reactions at 700°C between α-phase and KCl, NaCl, and MnCl2 are described as $2KCl(s) + Ca(s) = CaCl_2(s) + 2K(\ell)$, ΔG_f = +41.401 kJ/mol, $2NaCl(s) + Ca(s) = CaCl_2(s) + 2Na(\ell)$, ΔG_f = -3.773 kJ/mol, and $MnCl_2(s) + Ca(s) = CaCl_2(s) + 2Mn(s)$, ΔG_f = -289.719 kJ/mol. The microstructures, the ICP results, and the thermodynamic equations for the reactions of α-phase with the fluxes indicate the well known fact that the solid solution Ca in Mg alloys disappears during flux recycling.

The reaction of C15 phase with MgCl2 at 700°C is described as $MgCl_2(s) + Al_2Ca(s) = CaCl_2(s) + Mg(\ell) + 2Al(\ell)$, ΔG_f = +45.711 kJ/mol, which explains that C15 phase in AZ31-0.3wt%CaO and AZ31-0.3wt%Ca Mg alloys can be maintained during recycling because ΔG_f of the reaction is +45.711 kJ/mol. The reactions at 700°C between C15 phase and KCl, NaCl, and MnCl2 are described as $2KCl(s) + Al_2Ca(s) = CaCl_2(s) + 2K(\ell) + 2Al(\ell)$, ΔG_f = +247.055 kJ/mol, $2NaCl(s) + Al_2Ca(s) = CaCl_2(s) + 2Na(\ell) + 2Al(\ell)$, ΔG_f = +201.881 kJ/mol, and $MnCl_2(s) + Al_2Ca(s) = CaCl_2(s) + 2Al(\ell) + Mn(s)$, ΔG_f = -84.065 kJ/mol. The microstructures, the ICP results, and the thermodynamic equations for the reactions of C15 with the fluxes well indicate that Ca in the form of C15 phase is not consumed all during conventional flux recycling. With high temperature Mg alloys, Ca in the form of solid solution disappears but Ca in the form of C15 phase could be maintained if the fluxes were selected appropriately. The result clearly demonstrates the superiority of CaO over Ca even for recyclability.

6. Conclusion

We believe that the environmental benefits provided by lightweight, unlimited, and recyclable Mg alloy have the potential to grow significantly in the future by Eco-Mg approach. This paper, regarding CaO as ingredient, described non-SF6 process, process adjustabilities of strip casting, diecasting, extrusion, rolling, and joining, oxidation and ignition resistances, and recyclability of Eco-Mg alloy.

Compared with what have been already accomplished, what will be achieved is much bigger and greater for Eco-Mg alloy. For international cooperation not only for R&D and but also for commercial applications should be carried out.

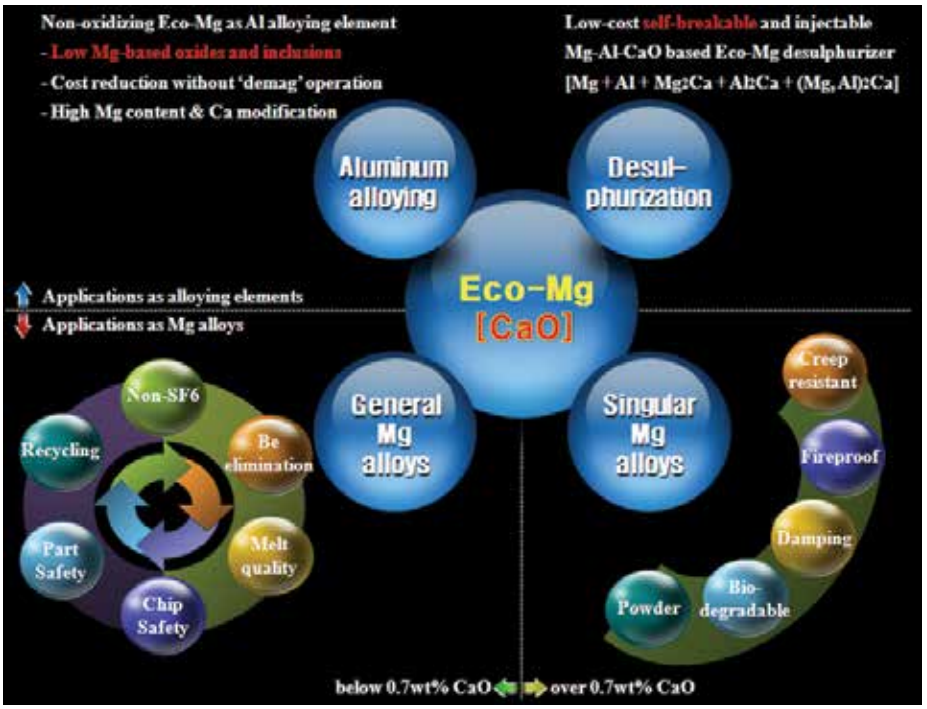

Fig. 1. R&BD fields covered by Eco-Mg utilizing CaO.

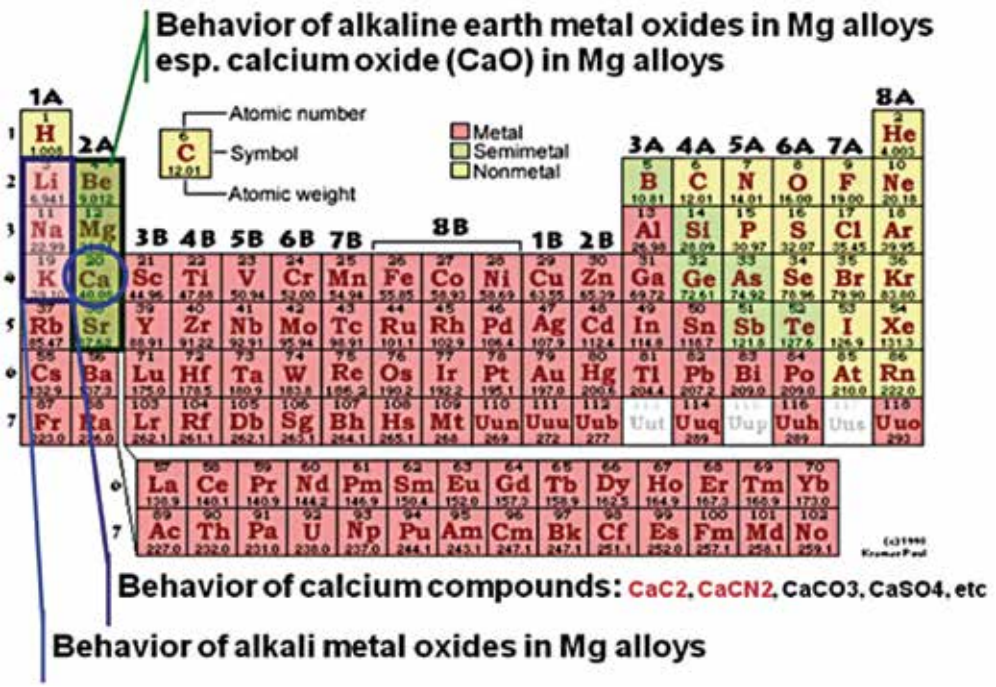

Fig. 2. Research areas covered by Eco-Mg approach.

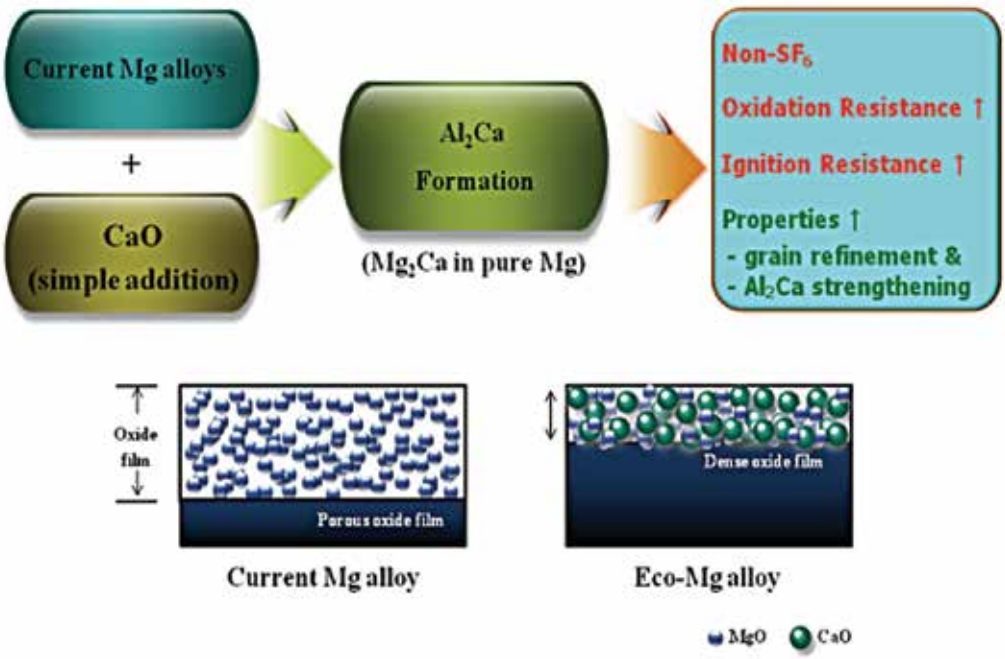

Fig. 3. General introduction, phase formation, surface structure, and resultant effects of CaO added Eco-Mg alloys.

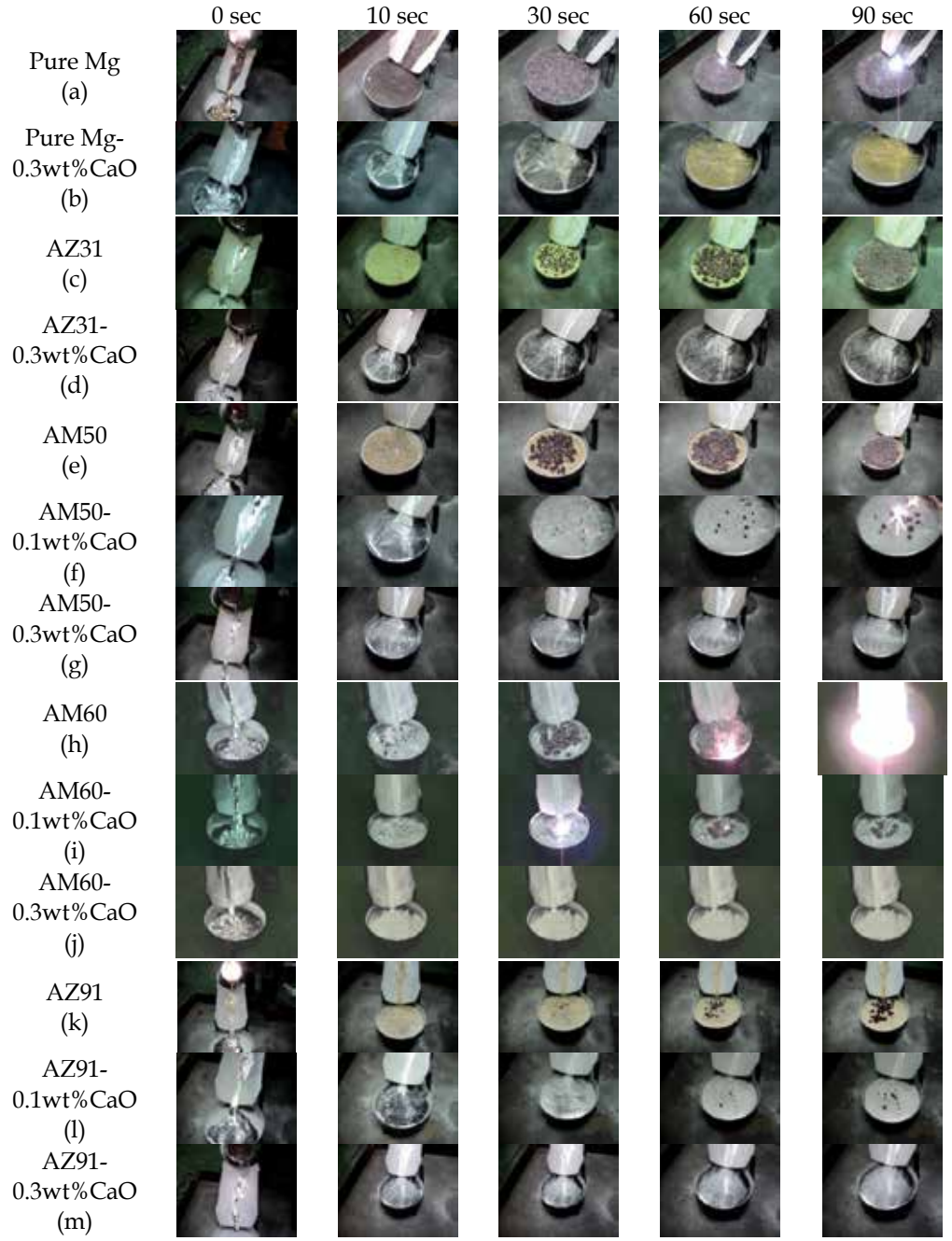

Fig. 4. Surface changes of the (a) pure Mg, (b) pure Mg-0.3wt%CaO, (c) AZ31, (d) AZ31-0.3wt%CaO, (e) AM50, (f) AM50-0.1wt%CaO, (g) AM50-0.3wt%CaO, (h) AM60, (i) AM60-0.1wt%CaO, (j) AM60-0.3wt%CaO, (k) AZ91, (l) AZ91-0.1wt%CaO, and (m) AZ91-0.3wt%CaO during casting and solidification (Kim et al., 2009; Kim, 2009; Lee, et al., 2007; Lee & Kim, 2008).

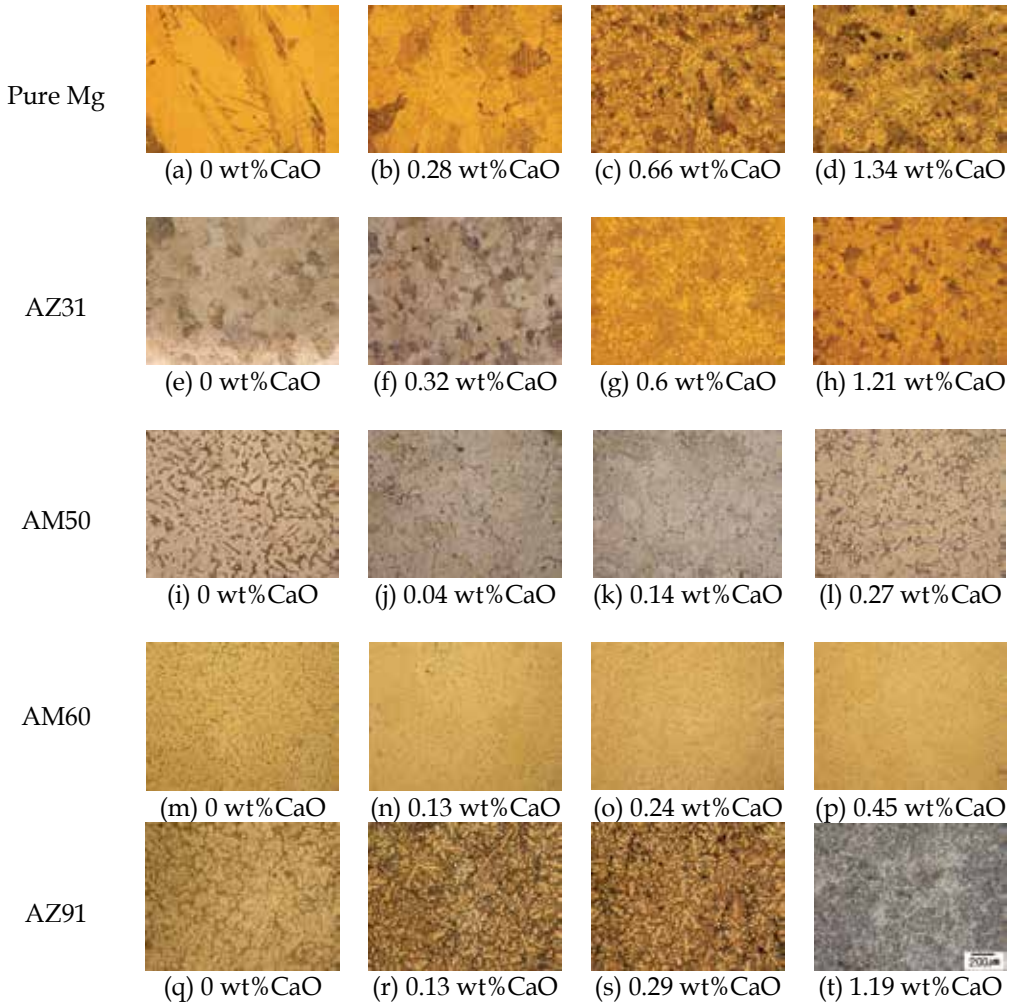

Fig. 5. Microstructures of the (a) pure Mg, (b) pure Mg-0.28wt%CaO, (c) pure Mg-0.66wt%CaO, (d) pure Mg-1.34wt%CaO, (e) AZ31, (f) AZ31-0.32wt%CaO , (g) AZ31-0.6wt%CaO , (h) AZ31-1.21wt%CaO, (i) AM50, (j) AM50-0.04wt%CaO, (k) AM50-0.14wt%CaO, (l) AM50-0.27wt%CaO, (m) AM60, (n) AM60-0.13wt%CaO, (o) AM60-0.24wt%CaO, (p)AM60-0.45wt%CaO, (q) AZ91, (r) AZ91-0.13wt%CaO, (s) AZ91-0.29wt%CaO, and (t) AZ91-1.19wt%CaO (Kim, 2005; Lee, et al., 2007; Ha et al., 2008; Kim et al., 2009).

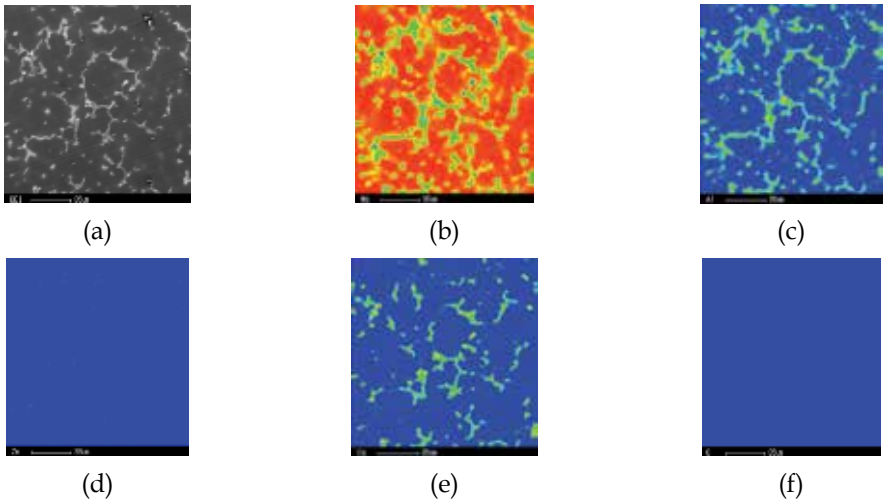

Fig. 6. EPMA mapping results of AZ91-0.29wt%CaO; (a) BE image, (b) Mg, (c) Al, (d) Zn, (e) Ca, and (f) O (Lee, et al., 2007).

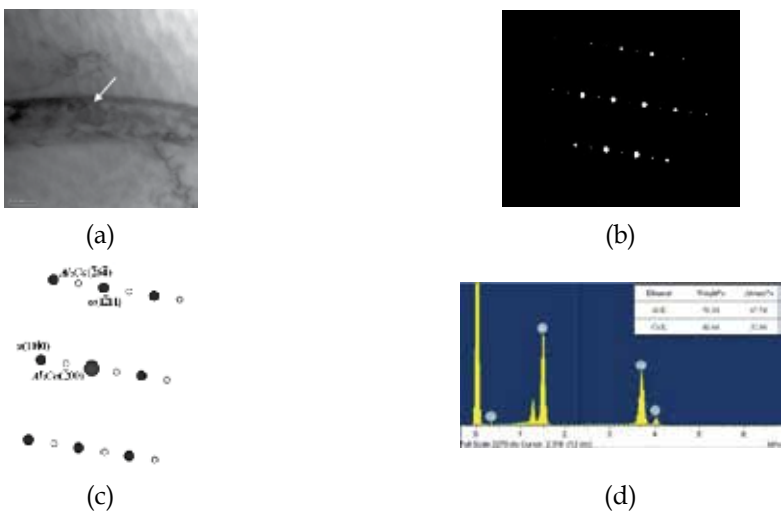

Fig. 7. TEM results of AM50-0.58wt%CaO; (a) BFI, (b) SASD pattern ($Z=[\bar{1}\,2\,\bar{1}\,6]_{\alpha\text{-Mg}}$, $[023]_{Al2Ca}$), (c) the schematic illustration for the SAD pattern, and (d) quantitative elemental analysis (Kim et al., 2009).

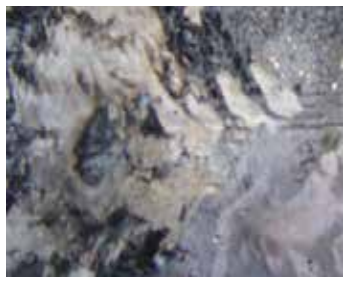

(a)

(b)

(c)

Fig. 8. Surface conditions of as-strip cast (a) AZ31 without SF6 gas, (b) AZ31 with SF6 gas, and (c) AZ31-0.1wt%CaO without SF6 gas (Jang, et al., 2008).

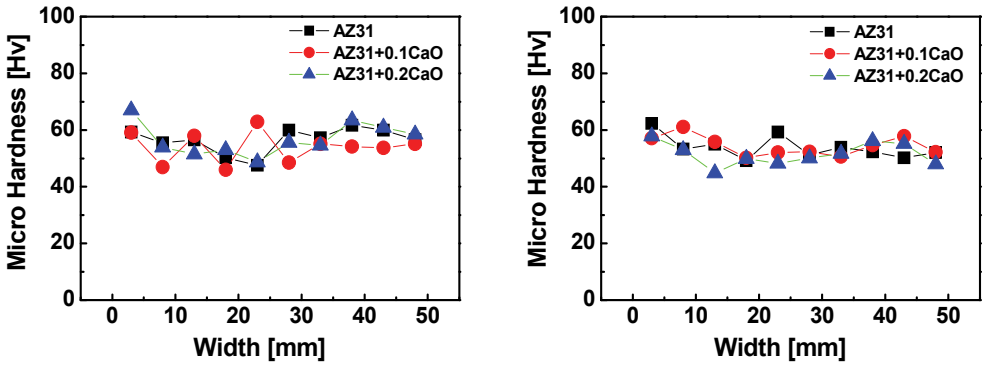

Fig. 9. Hardness values of AZ31, AZ31-0.1wt%CaO and AZ31-0.2wt%CaO strip castings; (a) surface area and (b) middle section of strip castings (Jang, et al., 2008).

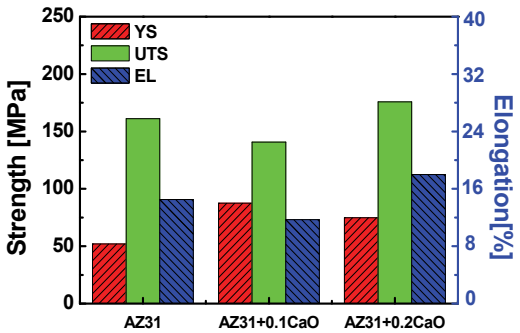

Fig. 10. Mechanical properties of AZ31, AZ31-0.1wt%CaO and AZ31-0.2wt%CaO strip castings (Jang, et al., 2008).

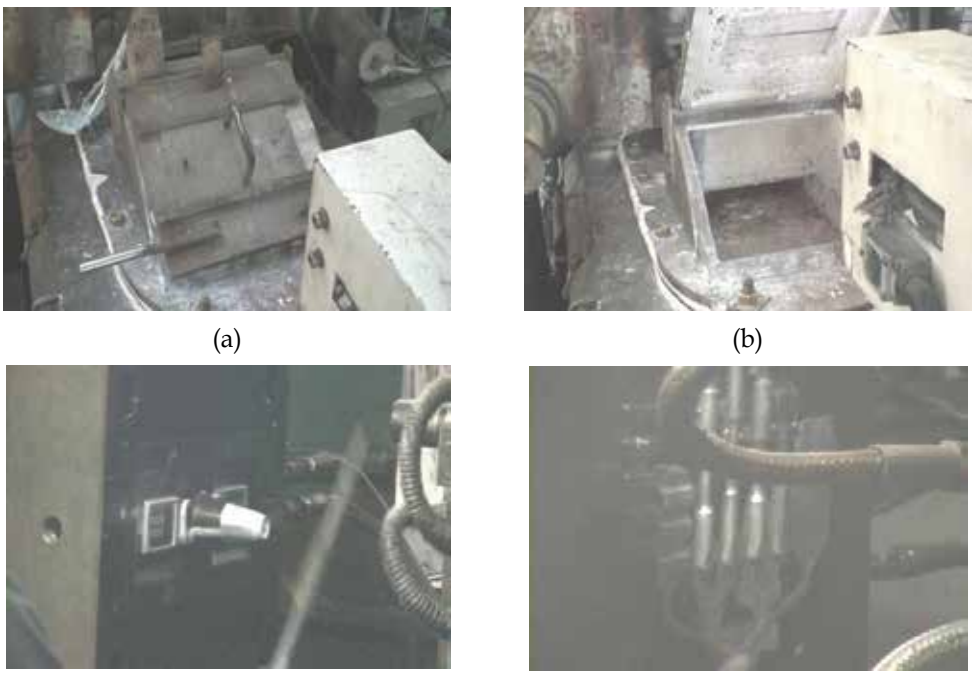

Fig. 11. Non-SF6 diecasting process of AZ91D-0.3wt%CaO under nitrogen atmosphere without any protective gas; (a) close furnace condition, (b) open furnace condition, (c) diecasting of cellular phone case, and (d) diecasting of mechanical test specimen (Kim, 2009).

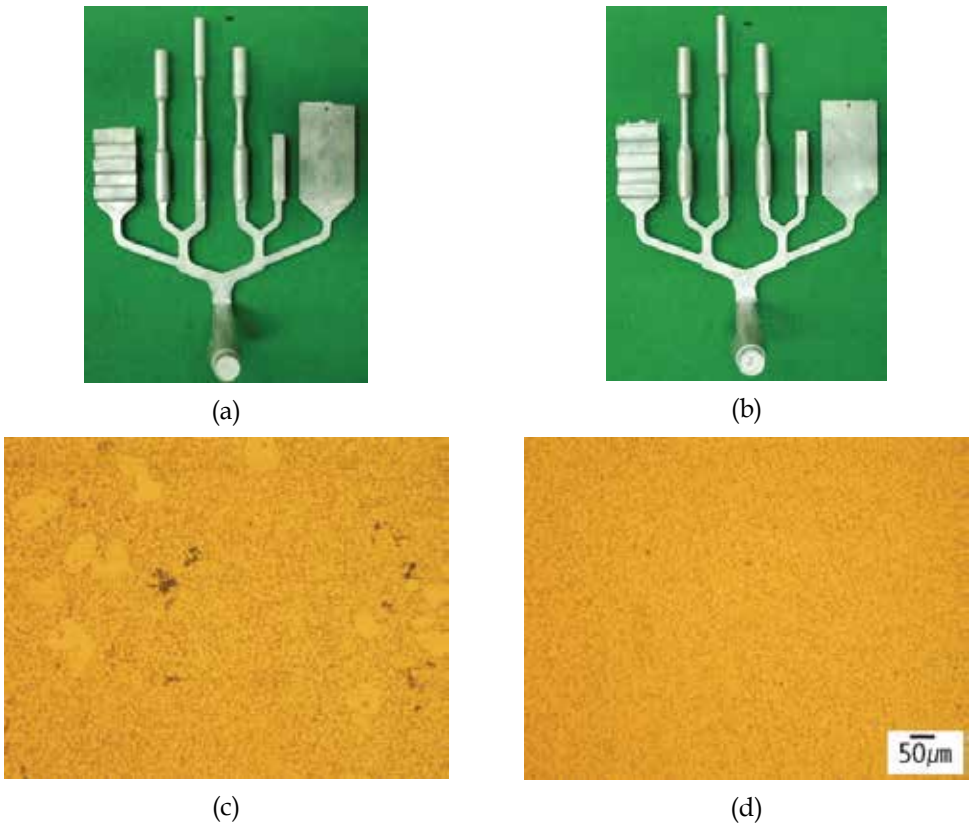

Fig. 12. Photographs of the mechanical test specimens produced by hot chamber diecasting of (a) AZ91D and (b) AZ91D-0.3wt%CaO and the related microstructures of (c) AZ91D and (d) AZ91D-0.3wt%CaO (Kim, 2009).

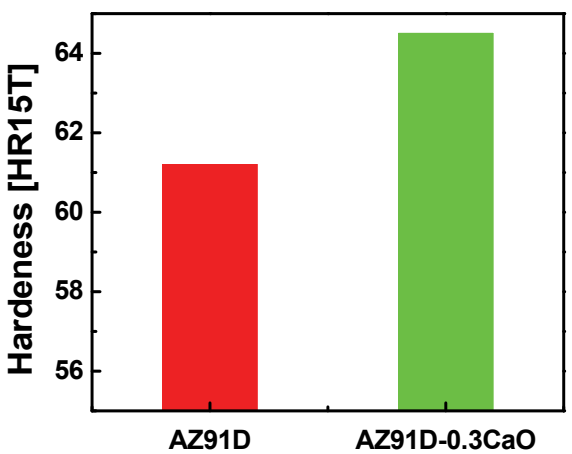

Fig. 13. Rockwell hardness values of the mechanical test specimens produced by hot chamber diecasting of AZ91D and AZ91D-0.3wt%CaO (Kim, 2009).

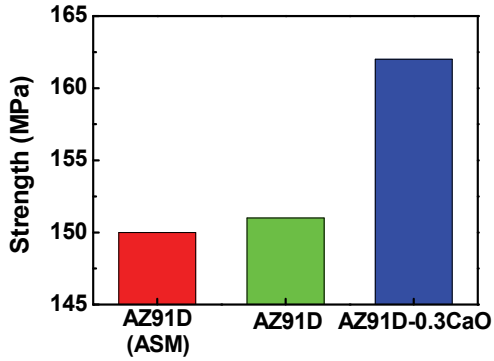

(a)

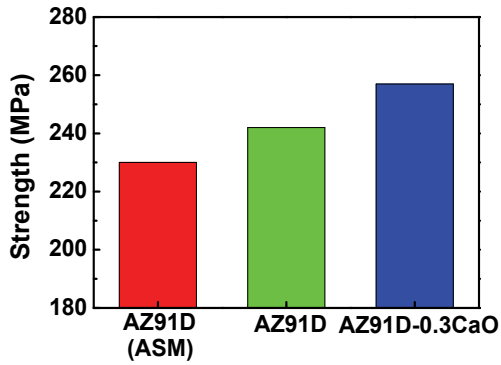

(b)

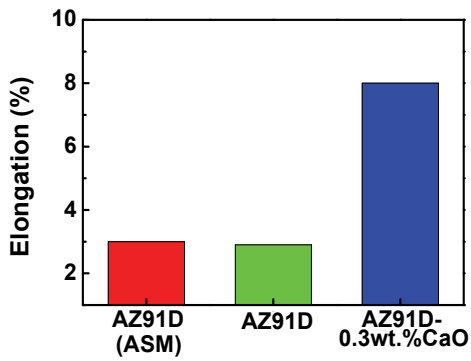

(c)

Fig. 14. Mechanical properties of the mechanical test specimens produced by hot chamber diecasting of AZ91D and AZ91D-0.3wt%CaO with the ASM reference; (a) yield strength, (b) tensile strength, (c) elongation (Kim, 2009).

(a) (b)

(c) (d)

Fig. 15. Non-SF6 cold chamber diecasting process for CaO added AM60 Eco-Mg alloys under nitrogen atmosphere without protective gas.

(a) (b)

Fig. 16. Photograph of oil pan produced by cold chamber diecasting of (a) AM60 Eco-Mg and (b) mechanical test specimens.

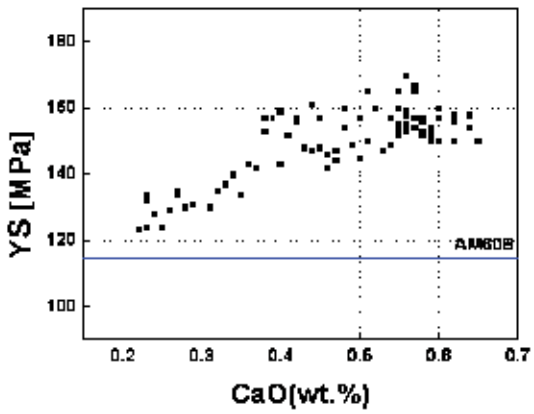

(a)

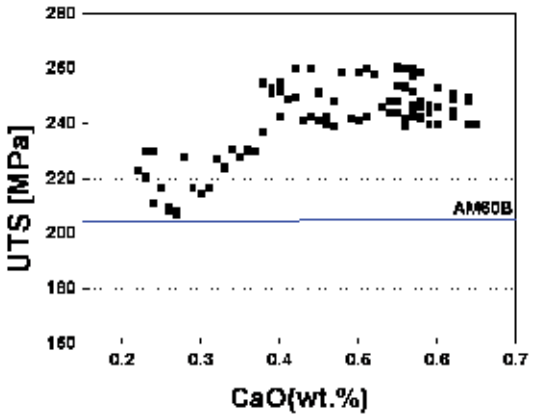

(b)

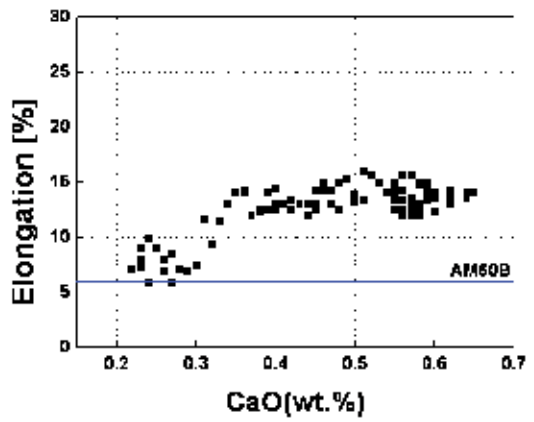

(c)

Fig. 17. Mechanical properties of mechanical test specimen produced by cold chamber diecasting of AM60 and AM60 Eco-Mg alloys at room temperature; (a) yield strength, (b) tensile strength, (c) elongation.

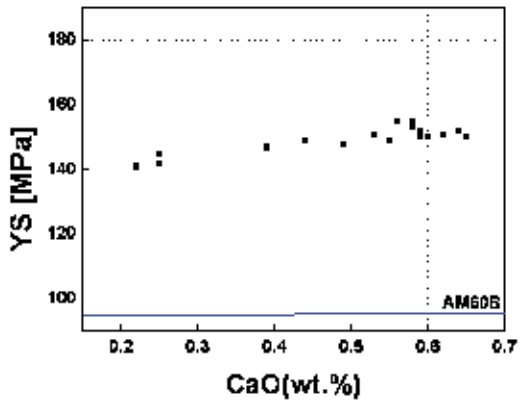

(a)

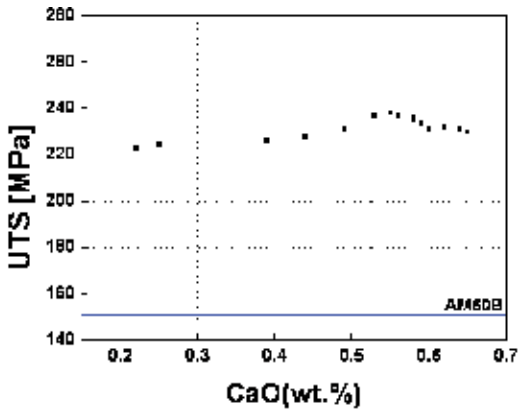

(b)

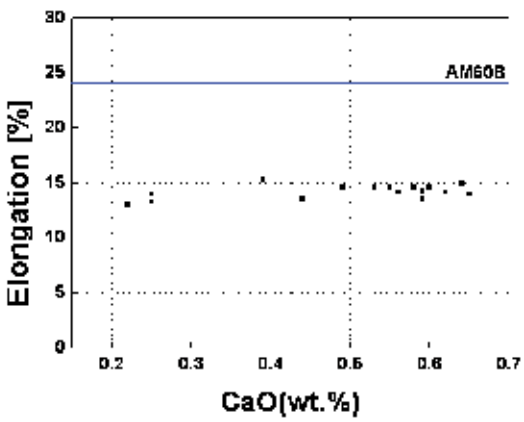

(c)

Fig. 18. Mechanical properties of mechanical test specimen produced by cold chamber diecasting of AM60 and AM60 Eco-Mg alloys at 150°C; (a) yield strength, (b) tensile strength, (c) elongation.

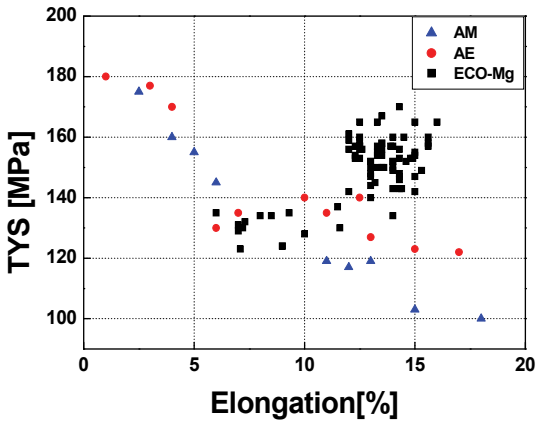

Fig. 19. Proportional strength and elongation relationship of AM60 Eco-Mg alloys.

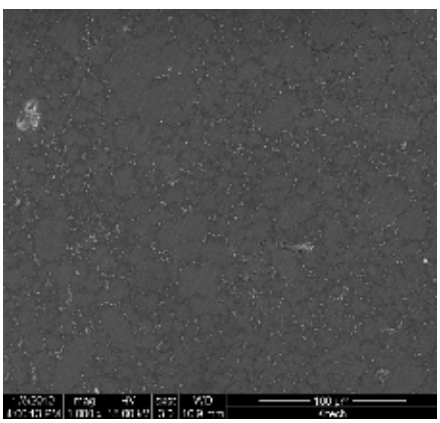

(a) 0.2wt%CaO

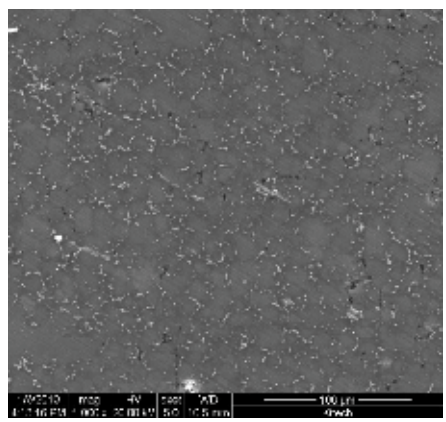

(b) 0.3wt%CaO

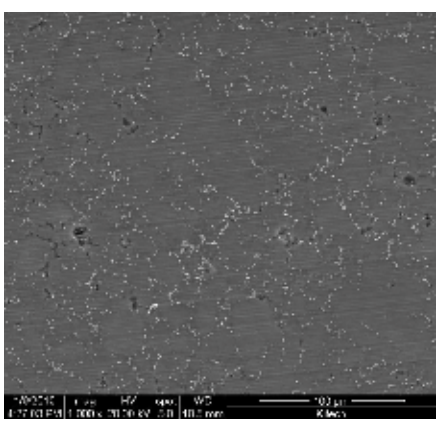

(c) 0.5wt%CaO

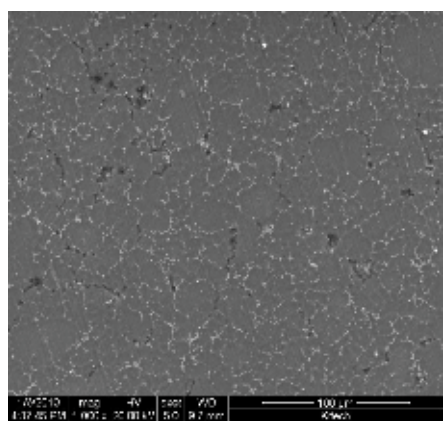

(d) 0.6wt%CaO

Fig. 20. Microstructures of (a) AM60-0.2wt%CaO, (b) AM60-0.3wt%CaO, (c) AM60-0.5wt%CaO and (d) AM60-0.6wt%CaO produced by cold chamber diecasting.

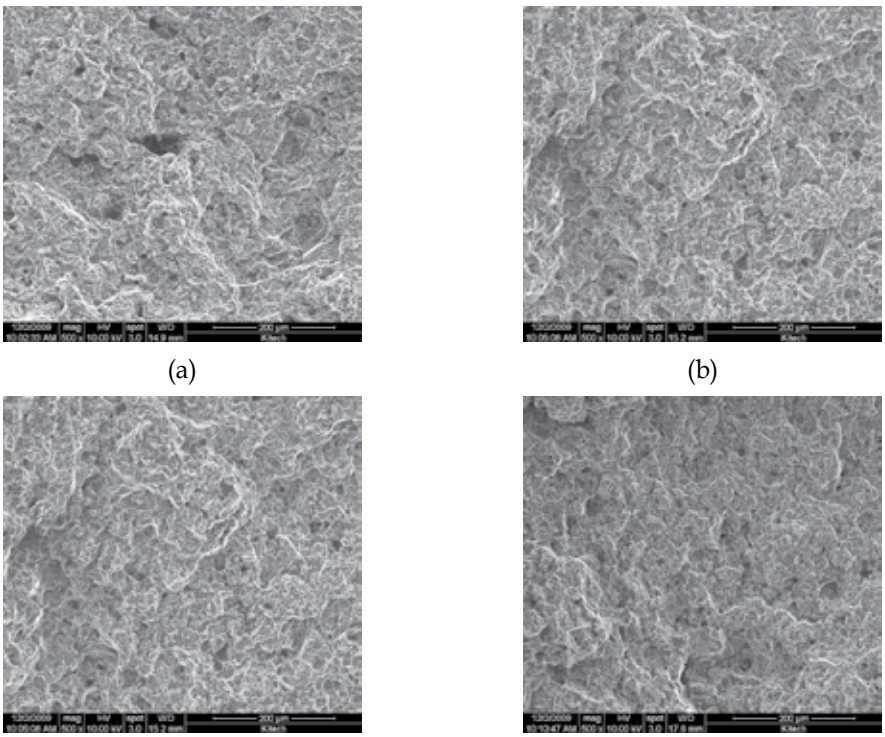

(a) (b)

(c) (d)

Fig. 21. SEM images of the fracture surface of tensile test specimens; (a) AM60-0.2wt%CaO, (b) AM60-0.3wt%CaO, (c) AM60-0.5wt%CaO and (d) AM60-0.6wt%CaO produced by cold chamber diecasting.

(a)

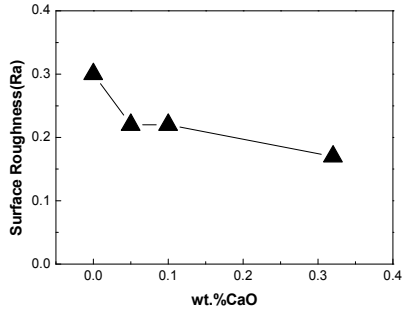

(b)

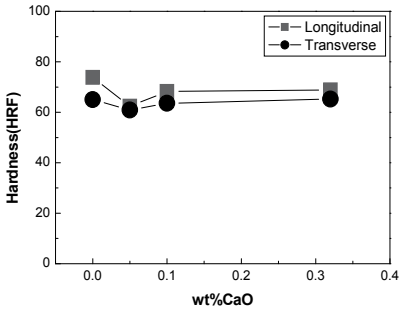

(c)

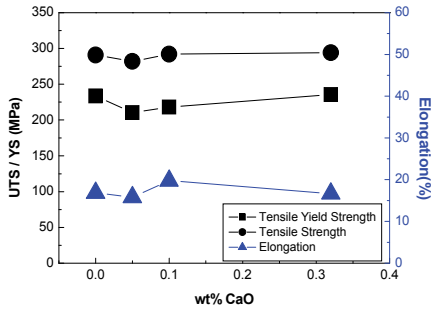

(d)

Fig. 22. (a) photographs showing the extruded bars of AZ31 and CaO added AZ31 Mg alloys and (b) surface roughness values, (c) hardness values, and (d) mechanical properties of the extruded bars (Lee, et al., 2006; Kim, 2007).

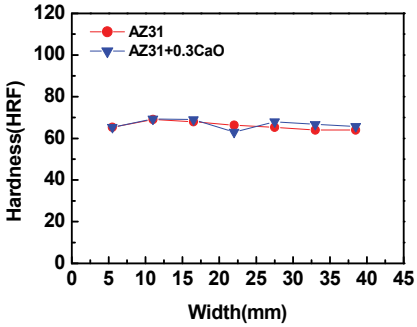

(a)

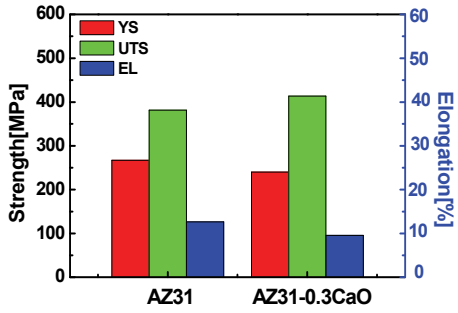

(b)

Fig. 23. (a) hardness values and (b) mechanical properties of hot-rolled AZ31 and AZ31-0.3wt%CaO Mg alloy sheets in the as-received condition (Jang, et al., 2007).

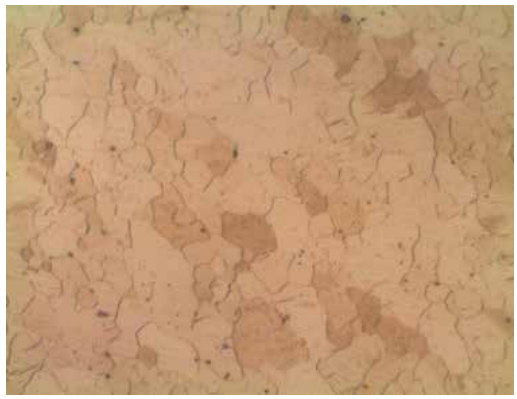

(a)

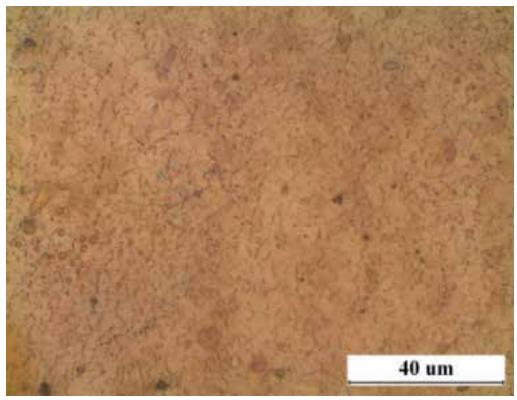

(b)

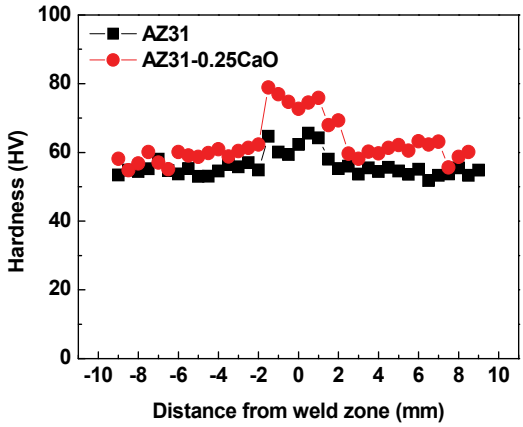

(c)

Fig. 24. Microstructures of the stir zone in (a) AZ31 and (b) AZ31-0.25wt%CaO Mg alloys and (c) hardness distribution of friction stir welded AZ31 and AZ31-0.25wt%CaO Mg alloys (Ha, et al., 2007).

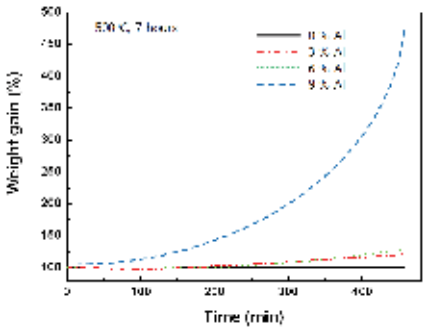

Fig. 25. Dependence of weight gain on Al content of Mg-Al Mg alloys under dry air atmosphere at 500°C for 7 hours.

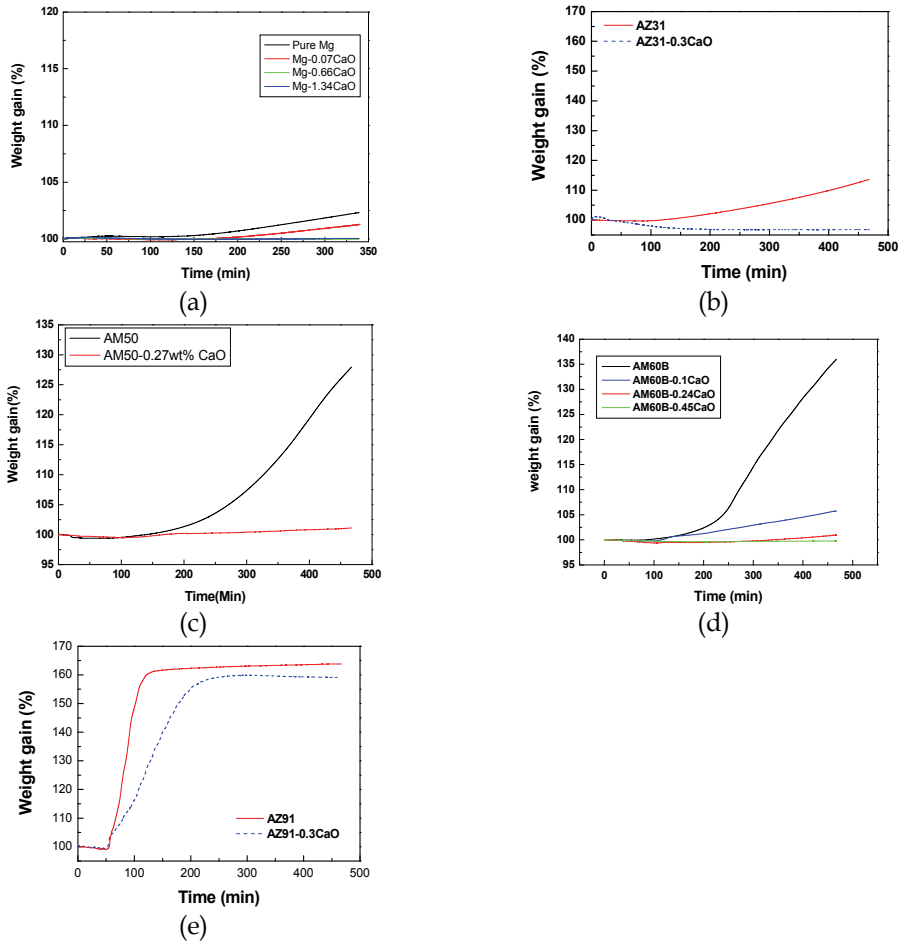

Fig. 26. Weight gain curves of (a) pure Mg, Mg-0.07wt%CaO, Mg-0.66wt%CaO, and 1.34wt%CaO, (b) AZ31 and AZ31-0.13wt%CaO, (c) AM50 and AM50-0.27wt%CaO, (d) AM60, AM60-0.1CaO, AM60-0.24wt%CaO, and AM60-0.45wt%CaO, (e) AZ91 and AZ91-0.29wt%CaO alloys (Kim, et al., 2005; Ha, et al., 2008; Lee & Kim, 2009).

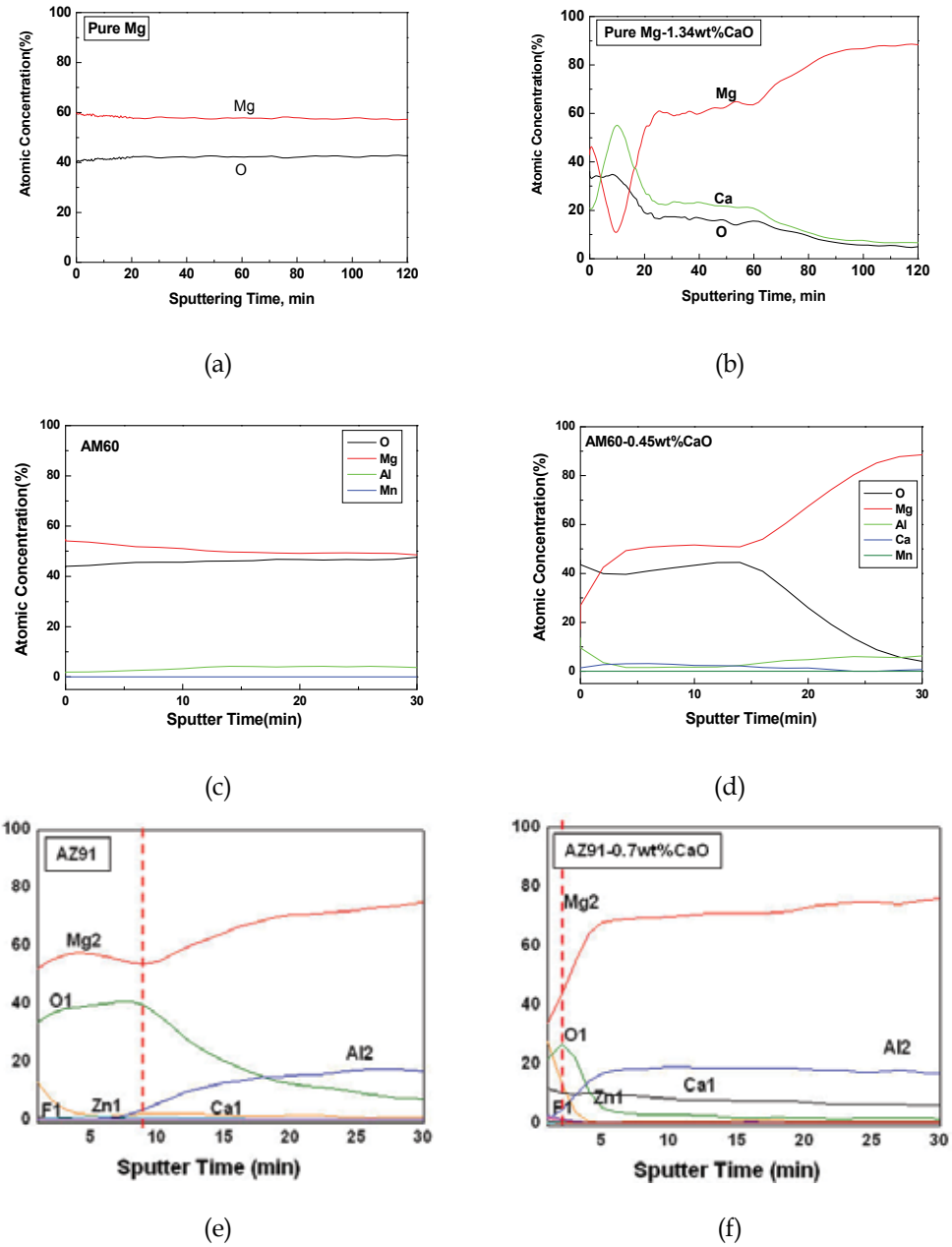

Fig. 27. AES depth profiles sputtered from the surface of (a) pure Mg, (b) Mg-1.34wt%CaO, (c) AM60, (d) AM60-0.45wt%CaO, (e) AZ91, and (f) AZ91-0.7wt%CaO alloys oxidized during TGA at 500°C for 7hours (Ha, et al., 2008; Kim, et al., 2009).

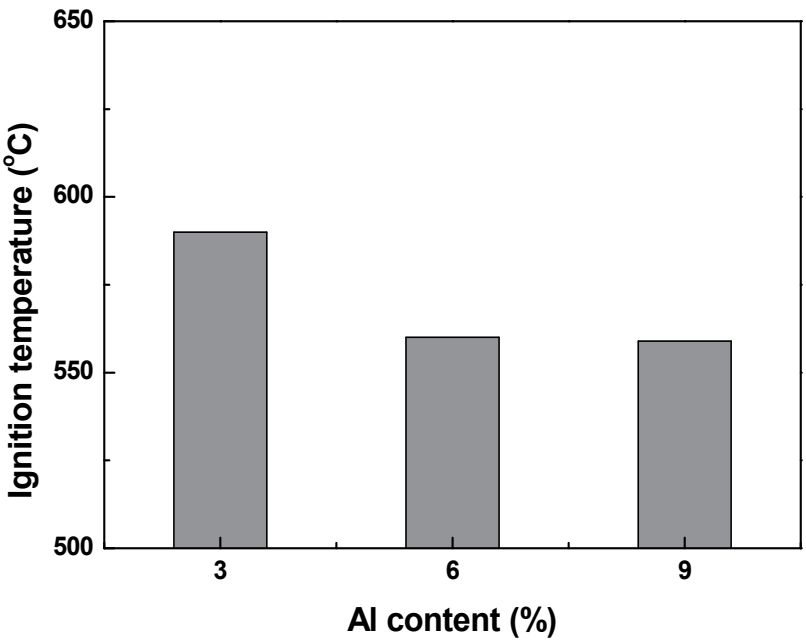

Fig. 28. Dependence of ignition temperature on Al content of Mg-Al alloys under dry air atmosphere by DTA.

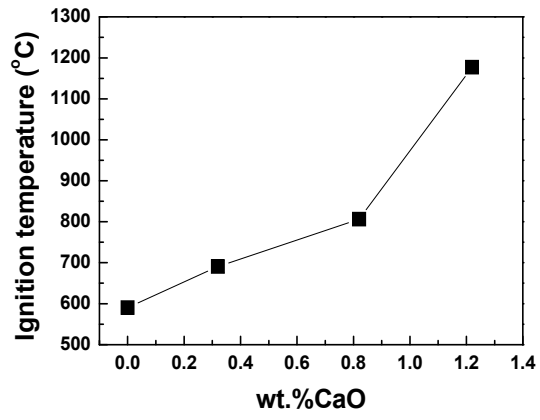

(a)

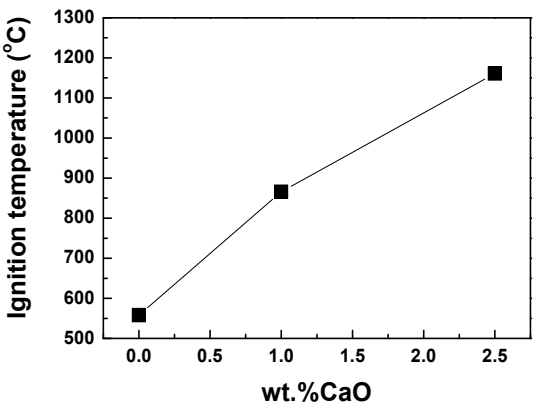

(b)

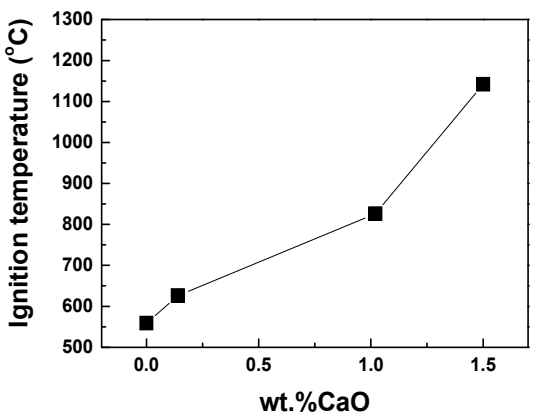

(c)

Fig. 29. Dependence of ignition temperature on CaO amount of CaO added (a) AZ31, (b) AM60, and (c) AZ91 Mg alloys under dry air atmosphere by DTA (Lee & Kim, 2009).

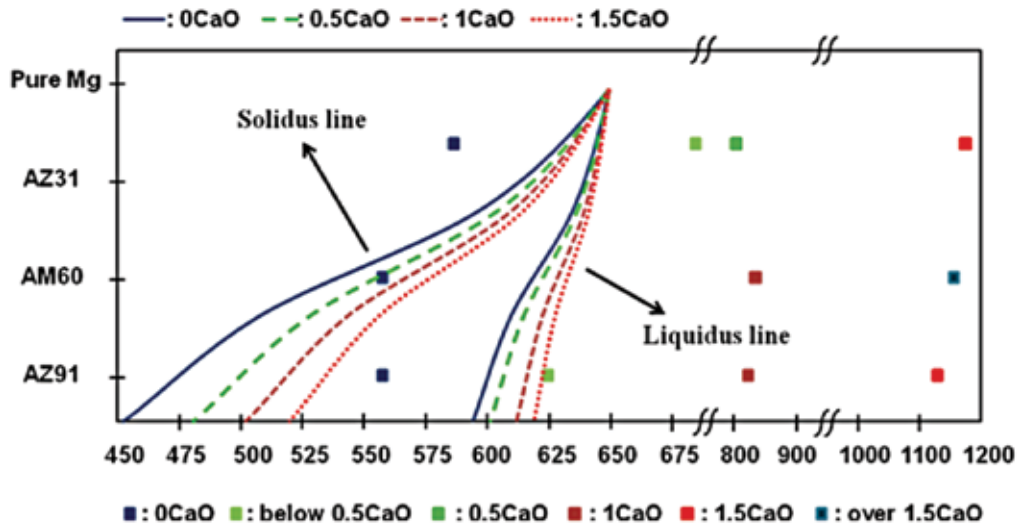

Fig. 30. Ignition temperatures for CaO added AZ31, CaO added AM60 and CaO added AZ91 Mg alloys on the solidus and liquidus lines by DTA.

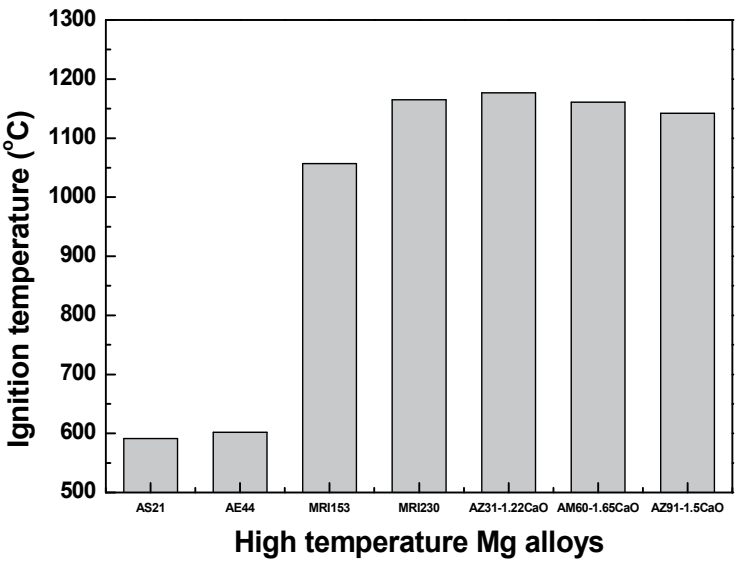

Fig. 31. Dependence of ignition temperature for AS21, AE44, MRI153, MRI230, 1.22wt%CaO added AZ31, 1.65wt%CaO added AM60, and 1.5wt%CaO added AZ91 Mg alloys under dry air atmosphere by DTA (Lee & Kim, 2009).

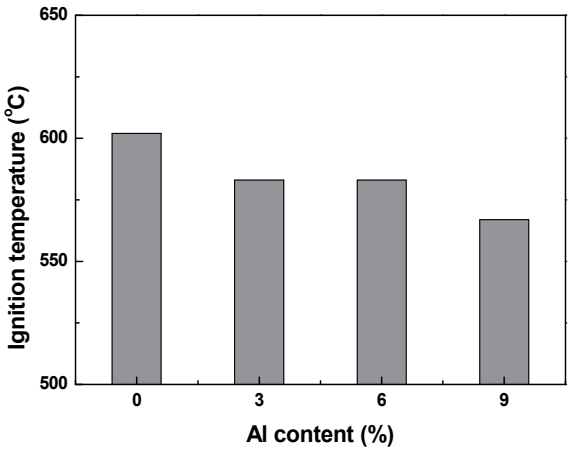

Fig. 32. Dependence of chip ignition temperatures on Al content of Mg-Al Mg alloys under an ambient atmosphere.

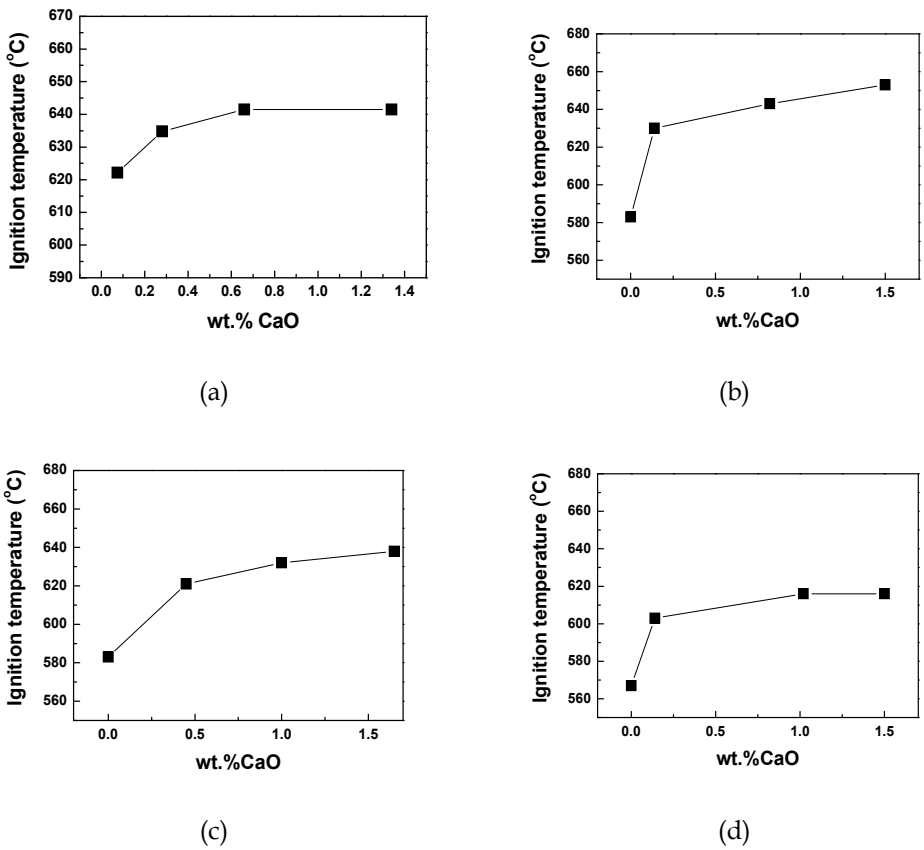

Fig. 33. Dependence of chip ignition temperatures for CaO added (a) Pure Mg, (b) AZ31, (c) AM60, and (d) AZ91 Mg alloys under an ambient atmosphere (Lee & Kim, 2009).

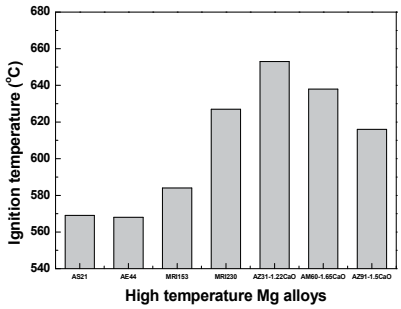

Fig. 34. Dependence of chip ignition temperatures for AS21, AE44, MRI153, MRI230, 1.22wt%CaO added AZ31, 1.65wt%CaO added AM60, 1.5wt%CaO added AZ91 Mg alloys under an ambient atmosphere (Lee & Kim, 2009).

(a) 0 sec.

(b) 30 sec.

(c) 60 sec.

(d) 90 sec.

(e) 120 sec.

(f) 150 sec.

(g) 180 sec.

(h) 210 sec.

Fig. 35. Results of torch ignition test of AZ91D and 0.3wt%CaO added AZ91 Mg alloys produced by hot-chamber diecasting (Lee & Kim, 2009).

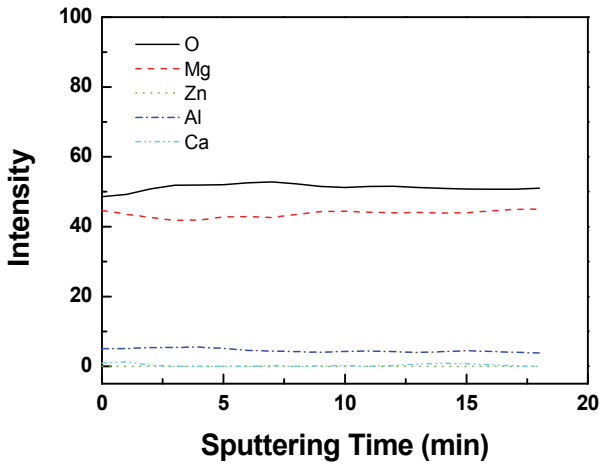

(a)

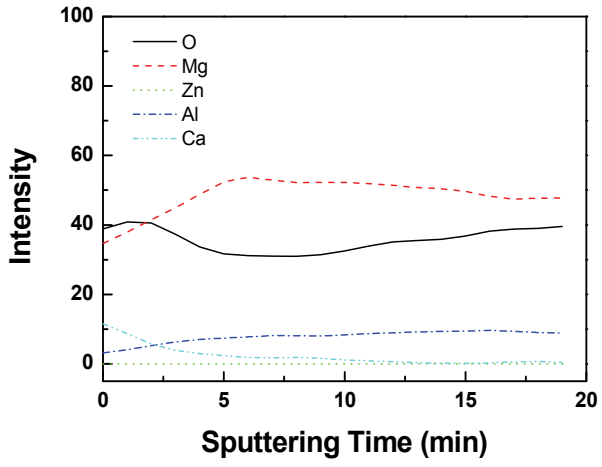

(b)

Fig. 36. AES depth profiles sputtered from the surface of (a) AZ91 and (b) 0.3wt%CaO added AZ91 Mg alloys (Lee & Kim, 2009).

Fig. 37. Results of torch ignition test of AZ31-1.13wt%CaO, AM60-1wt%CaO, AZ91-1.02wt%CaO, AS21, AE44, MRI153, and MRI230 (Lee & Kim, 2009; Lee & Kim, 2010).

	before	after flux recycling			
AZ31 -CaO					
	(a)	(b) MgCl2	(c) KCl	(d) NaCl	(e) MnCl2
AZ31 -Ca					
	(f)	(g) MgCl2	(h) KCl	(i) NaCl	(j) MnCl2

Fig. 38. As-cast microstructures of (a) AZ31-0.3wt%CaO and (f) AZ31-0.3wt%Ca and as-recycled microstructures of (b) AZ31-0.15wt%CaO after MgCl2 recycling, (c) AZ31-0.29wt%CaO after KCl recycling, (d) AZ31-0.21wt%CaO after NaCl recycling, (e) AZ31-0.10wt%CaO after MnCl2 recycling, (g) AZ31-0.12wt%Ca after MgCl2 recycling, (h) AZ31-0.25wt%Ca after KCl recycling, (i) AZ31-0.21wt%Ca after NaCl recycling, and (j) AZ31-0.10wt%Ca after MnCl2 recycling (Lee & Kim, 2009).

Alloy type	As-cast (ICP, wt%)	Flux	After recycling (ICP, wt%)	Ca loss (wt% / %)
AZ31 -0.3wt%CaO	0.29	$MgCl_2$	0.15	0.14 / 48.3
	0.30	KCl	0.29	0.01 / 3.3
	0.27	NaCl	0.21	0.06 / 22.2
	0.29	$MnCl_2$	0.10	0.19 / 65.5
AZ31 -0.3wt%Ca	0.3	$MgCl_2$	0.12	0.18 / 60.0
	0.28	KCl	0.25	0.03 / 10.7
	0.31	NaCl	0.21	0.10 / 32.3
	0.31	$MnCl_2$	0.10	0.21 / 67.7

Table 1. ICP results of CaO and Ca added AZ31 Mg alloys before and after flux recycling (Lee & Kim, 2009).

7. References

Ha, S. H.; Lee, J. K.; Yoon, Y. O.; Lee, C. Y.; Jung, S. B. & Kim, Shae K. (2007). Effect of CaO on joint properties of AZ31 alloy sheet during friction stir welding. *Proceedings of 6th International Conference on Materials Processing for Properties and Performance (MP3-2007)*, Beijing, September 2007, MP3, China

Ha, S. H.; Lee, J. K. & Kim, Shae K. (2008). Effect of CaO on oxidation resistance and microstructure of pure Mg. *Materials Transactions*, Vol. 49, No. 5 (March 2008) pp.1081-1083, ISSN 1345-9678

Jang, D. I.; Yoon, Y. O.; Kim, D. U.; Jung, S. B. & Kim, Shae K. (2007). Behavior of CaO in hot-rolled AZ31 Mg alloys. *Proceedings of 6th International Conference on Materials Processing for Properties and Performance (MP3-2007)*, Beijing, September 2007, MP3, China

Jang, D. I.; Yoon, Y. O.; Jung, S. B. & Kim, Shae K. (2008). Effect of CaO on AZ31 Mg strip castings. *Materials Transactions*, Vol. 49, No. 5 (April 2008) pp.976-979, ISSN 1345-9678

Kim, Shae K.; Lee, J. K.; Cho, H.; Jo, H. H.; Ha, W. & Kim, Y. J. (2005). The behavior of CaO in magnesium alloys. *Magnesium Technology 2005* (TMS-2005), Neale R. N., pp. 285-289, ISBN 0-87339-582-4, San Francisco, February 2005, USA

Kim, Shae K.; Lee, J. K.; Yoon, Y. O.; & Jo, H. H. (2007). Development of AZ31 Mg alloy wrought process route without protective gas. *Journal of Materials Processing Technology*, Vol. 187-188, pp. 757-760, ISSN 0924-0136

Kim, Shae K.; Lee, J. K.; Jang D. I.; Yoon, Y. O.; Ha, S. H.; Yoo, H. J.; Park, S. M.; Lee, C. H. & Kim, Y. J (2009). Eco-Mg for magnesium future. *Proceedings of 66th Annual World Magnesium Conference (IMA-2009)*, San Francisco, May 2009, IMA, USA

Kim, Shae K. (2009). Non-SF6 diecasting process of 0.3wt%CaO added AZ91D Mg alloy. *Proceedings of 18th International Conference on Processing and Fabrication and Advanced Materials (PFAM18-2009)*, Sendai, December 2009, PFAM18, Japan

Kim, Shae K. (2009). Effect of Al content on phase formation of CaO added Mg alloy. *Proceedings of 18th International Conference on Processing and Fabrication and Advanced Materials (PFAM18-2009)*, Sendai, December 2009, PFAM18, Japan

Lee, J. K.; Yoon, Y. O. & Kim, Shae K. (2006). Development of CaO added wrought Mg alloy for cleaner production. *Magnesium Technology 2006* (TMS-2006), Neale R. N., pp. 517-521, ISBN 978-0-87339-620-2, San Antonio, March 2006, USA

Lee, J. K.; Ha, S. H.; Kim, Y. J.; Jo, H. H. & Kim, Shae K. (2007). Melt protection property and ignition resistance property of CaO added AZ91D Mg alloy. *Journal of the Korean Foundrymen's Society*, Vol. 27, No. 3, pp. 131-134, ISSN 1598-706X

Lee, J. K. & Kim, Shae K. (2008). Development of novel environment-friendly magnesium alloys. *Advanced Materials Research*, Vol.47-50, pp. 940-943, ISSN 1022-6680

Lee, J. K. & Kim, Shae K. (2009). Thermodynamic consideration of CaO added Mg alloys in recycling process. *Materials Science Forum*, Vol. 620-622, (January 2009) pp. 615-618

Lee, J. K. & Kim, Shae K. (2009). Flame resistance behaviors of AS, AE, MRI and AO series Mg alloys. *Magnesium Technology 2009* (TMS-2009), Eric A. N., pp. 155-159, ISBN 978-0-87339-730-8, San Francisco, February 2009, USA

Lee, J. K. & Kim, Shae K. (2009). Flame resistance of 0.3wt%CaO added AZ91D Mg alloy manufactured by diecasting process. *Proceedings of 18th International Conference on Processing and Fabrication and Advanced Materials (PFAM18-2009)*, Sendai, December 2009, PFAM18, Japan

Lee, J. K. & Kim, Shae K. (2009). Oxidation resistance behaviour of CaO added Mg-Al alloys. *Proceedings of 18th International Conference on Processing and Fabrication and Advanced Materials (PFAM18-2009)*, Sendai, December 2009, PFAM18, Japan

Lee, J. K. & Kim, Shae K. (2010). Fire-proof evaluation of CaO added Mg-3Al, Mg-6Al, and Mg-9Al Mg cast products. *Magnesium Technology 2010* (TMS-2010), Sean R. A, pp. 121-128, ISBN 978-0-87339-746-9, Seattle, February 2010, USA

Pilling, N. B. & Bedworth, R. E. (1923). The oxidation of metals in high temperature. Journal of Institute of Metals, Vol. 29, pp. 529-582

You, B. S.; Park, W. W. & Chung, I. S. (2000). The effect of calcium additions on the oxidation behaviour in magnesium alloys. Scripta Materialia, Vol. 42, pp. 1089-1094, ISSN 1359-6462

21

Welding and Joining of Magnesium Alloys

Frank Czerwinski
Bolton, Ontario
Canada

1. Introduction

Welding and joining of magnesium alloys exert a profound effect on magnesium application expansion, especially in ground and air transportations where large-size, complex components are required. This applies to joints between different grades of cast and wrought magnesium alloys and to dissimilar joints with other materials, most frequently with aluminum and steel.

Due to specific physical properties of magnesium, its welding requires low and well controlled power input. Moreover, very high affinity of magnesium alloys to oxygen requires shielding gases which protect the liquid weld from an environment. To magnify complexity, also solid state reaction with oxygen, which forms a thermodynamically stable natural oxide layer on magnesium surface, is an inherent deficiency of joining (Czerwinski, 2008). Both the conventional and novel welding techniques were adapted to satisfy these requirements, including arc welding, resistance spot welding, electromagnetic welding, friction stir welding, electron beam and laser welding. Since fusion welding has a tendency to generate porosities and part distortion, many alternative joining practices were implemented. These include soldering, brazing, adhesive bonding and mechanical fastening. However, also the latter techniques have disadvantages associated, for example, with stress induced by drilling holes during mechanical fastening, preheating during clinching or extensive surface preparation in adhesive bonding. Hence, experiments are in progress with completely novel ideas of magnesium joining.

An application of magnesium is often in multi-material structures, requiring dissimilar joints, involving magnesium alloys as one side where on another end there are alloys with drastically different properties. How to weld dissimilar materials is one of the most difficult problems in welding. A difference in physicochemical properties of dissimilar joint components creates challenges for mechanically bolted assemblies as well. Due to its very low electronegative potential, magnesium is susceptible to galvanic corrosion thus affecting performance of mechanical joints in conductive environments.

This chapter covers key aspects of magnesium welding and joining along with engineering applications, challenges and still existing limitations. For each technique, the typical joint characteristics and possible defects are outlined with particular attention paid to weld metallurgy and its relationship with weld strength, ductility and corrosion resistance. Although fundamentals for each technique are provided, the primary focus is on recent global activities.

2. Arc welding

There are two basic methods of arc welding. In an inert gas tungsten arc welding (TIG), an arc is generated between a non-consumable tungsten electrode and the welded metal. The electrode and welded metal are shielded with an inert gas, typically argon. In general, weld can be made with or without filler. In case the filler is used, it has a form of wire, provided to the weld. For magnesium alloys, filler rods may be of the same chemistry as welded part or lower melting range. The latter allows the weld to remain liquid until other parts of the weld are solid, thus reducing the probability of cracking. During an inert gas metal arc welding (MIG), the arc is formed between the consumable electrode and the part to be welded. The electrode is continuously provided from the spool. Both the welded area and the arc zone are protected by a gas shield.

The specific heat of magnesium is around 1 $Jg^{-1}{}^{o}C^{-1}$ but due to lower density of magnesium, its heat capacity is lower than aluminum or steel (Table 1). Due to similar melting ranges of Mg and Al alloys and the lower latent heat of fusion of magnesium alloys the heat required to melt magnesium is two third of that required for melting the same volume of aluminum alloys. Relatively high coefficient of thermal expansion of magnesium alloys of 26 $\mu m\ m^{-1}\ {}^{o}C^{-1}$ and high thermal conductivity of 51 $Wm^{-1}K^{-1}$ make it susceptible to distortion during welding.

Property	Units	AZ91	A6061	ZA12	Steel 304
Melting range	^{o}C	470-595	582-652	377-432	1400-1455
Density	$g\ cm^{-3}$	1.8	2.7	6.0	8.0
Modulus of elasticity	GPa	45	68.9	83	200
Thermal conductivity (20 ^{o}C)	$Wm^{-1}K^{-1}$	51	180	116	16.2
Coefficient of thermal expansion (20-100 ^{o}C)	$\mu m\ m^{-1}\ {}^{o}C^{-1}$	26.0	23.6	24.1	17.2
Specific heat (20 ^{o}C)	$J\ g^{-1}\ {}^{o}C^{-1}$	0.8	0.896	0.450	0.5
Latent heat of fusion pure base metals	J/g	368	398	272	113
Electrical resistivity	μΩm	0.0000143	0.00000360	0.00000610	0.0000720

Table 1. Selected properties of AZ91 magnesium alloy, A6061 aluminum alloy, ZA12 zinc alloy and AISI 304 stainless steel (Avedesian, 1999), (ASM, 1990)

For transition metal alloys, a technique exists of flux-assisted gas tungsten arc welding (FA-TIG) when the welding path is coated with chemical fluxes. In general, fluxes allow full penetration welding at greater rates using relatively inexpensive gas tungsten arc as the heat source. Using argon shielding and chloride fluxes, magnesium alloy welding tests showed an increase in weld penetration as much as one hundred percent (Marya and Edwards, 2002). The deeper weld penetration was accompanied by higher heat input. Among several chlorides, including LiCl, $CaCl_2$, $CdCl_2$, $PbCl_2$ and $CeCl_3$, cadmium chloride was the most effective. Images of arc area during welding revealed that the heat flux from the arc appeared more concentrated towards the center of the pool with chloride additions.

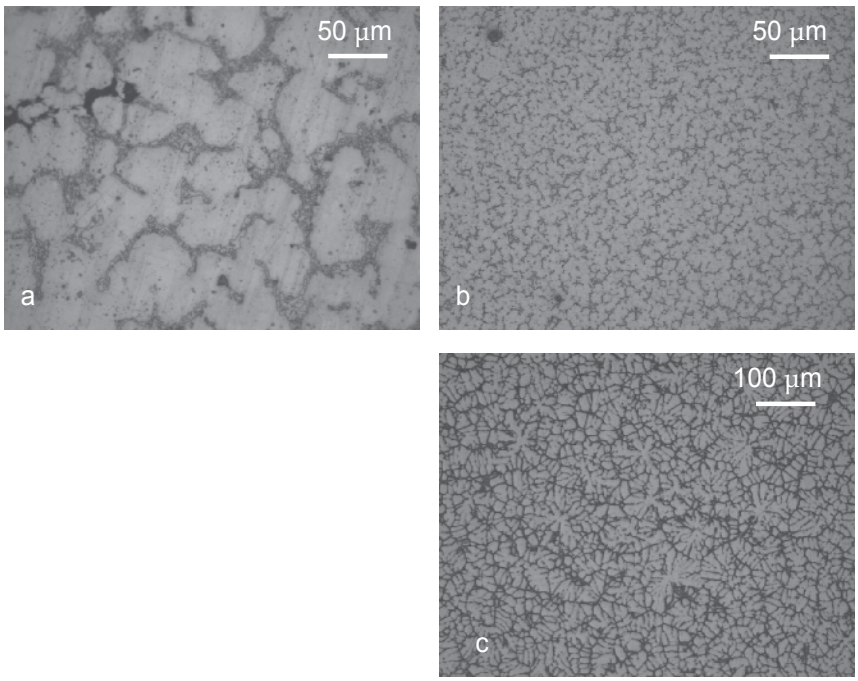

Fig. 1. Effect of cooling rate during solidification on microstructure of magnesium and aluminum alloys: (a) AZ91 slow cooling; (b) AZ91 rapid cooling; (c) A356 rapid cooling.

2.1 Weld microstructure

The solidification microstructure of the weld is controlled by constitutional undercooling, depending on the thermal gradient and growth rate (Fig. 1). The microstructure of MIG welded AZ91D alloy with AZ61 as welding wire consisted of solid solution of α-Mg and intermetallic compound of $Mg_{17}Al_{12}$ (Sun et al., 2008). The weld contained roughly 7% of Al. In HAZ near the fusion line, subjected to temperatures between solidus and liquidus, a part of α-Mg solid solution and eutectics, distributed at grain boundaries, experienced melting. Thus, after subsequent solidification the boundary regions formed islands of eutectic solid solution of α-Mg surrounded by $Mg_{17}Al_{12}$ precipitates. The chloride fluxes during welding using FA-TIG technique affected the weld microstructure (Marya and Edwards, 2002). It appears that alloying from fluxes did not drastically affect the solute partitioning during solidification. The AZ21 fusion zone, obtained with cadmium chloride fluxes, was significantly more dendritic than the zone of the alloy identically welded without fluxes. It is believed that differences in microstructure between welds with and without chloride fluxes are caused by thermal gradient. During welding with cadmium chloride, the arc temperature was significantly higher and the liquid weld experienced higher constitutional undercooling.

2.2 Weld cracking

In addition to extensive porosity, as shown in Fig. 2, hot cracking is considered the major problem of magnesium welding. This is especially true for a repair practice where thick plates are welded using the metal inert gas technique. During MIG welding of 10 mm thick

plates of AZ91D, two types of hot cracking occurred: solidification cracking of weld and liquation cracking in HAZ (Sun, et al., 2008). In general, solidification cracking takes place within a specific temperature range when a liquid film appears between dendrites. Solidification cracking occurerd within the crater at the weld end and was caused by the high segregation of Mn, Al and Zn accompanied by high tensile stress. A frequency of both types of cracks increased at low welding speeds and was associated with high heat input and tensile stress. The experimental observations indicate that for MIG welding of magnesium alloys a reduction in the heat input reduces the frequency of cracks in weld and HAZ.

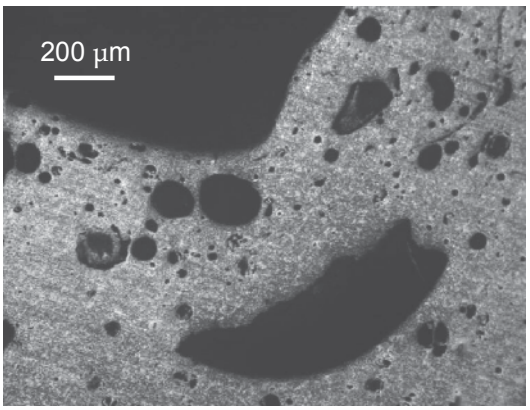

Fig. 2. Gas porosity in a weld of magnesium alloy Mg-8%Al.

3. Laser beam welding

The term laser is an acronym for "Light Amplification by Stimulated Emission of Radiation". The solid or gaseous media are stimulated to emit a monochromatic, coherent source of light which is then focused to a point source and delivered to the workplace. A delivery by hard optics explores mirrors and lenses for laser deflection and focusing. A limitation of hard optics is the short distance between the laser source and welded part. The use of fiber optics cable allows for a longer separation of laser source. The latter is also more suitable for manipulation by robotics. There are two major types of lasers, commonly used in industrial applications. The laser of Nd:YAD – Neodymium-doped Yttrium-Aluminum-Garnet explores a crystalline rod and emits light in the ultraviolet range with a wavelength of 1.06 μm. The CO_2 laser is based on gaseous media and has a wavelength of 10.6 μm.

3.1 Process and its advantages

During welding the laser fires many pulses per second (Fig. 3). The light is absorbed by the metal, causing the "keyhole" effect since the beam drills, melts and vaporizes some metal volume. When the pulse ends, the molten metal around the "keyhole" flows back, and after solidification forms a spot weld. A shielding gas is used to protect the molten metal. Welds may be created with a filler metal or without it. As major benefits of laser beam welding there are quoted: high travel speeds, minimal amount of heat added during welding, resulting in a small heat affected zone, low part distortion, no slag or spatter and great flexibility in tooling design.

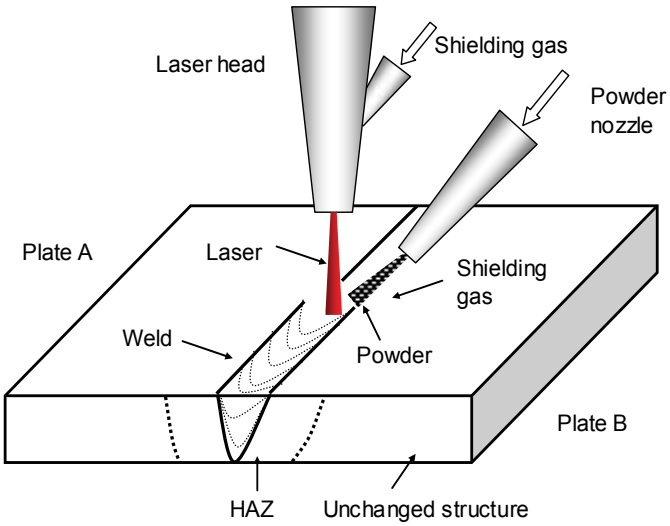

Fig. 3. Schematic of laser beam welding process

3.2 Weld structure, defects, process modeling

The AM60 alloy, welded with a continuous wave CO_2 laser, formed a weld with the narrow heat affected zone and no obvious grain coarsening (Quan et al., 2008). The fusion zone was fine-grained with high density of $Mg_{17}Al_{12}$ precipitates. The redistribution of elements occurred during welding with lower Mg and higher Al content in weld than in the base alloy. A hardness of the fusion zone reached the higher level than of the base alloy.

The mechanism of porosity formation during continuous-wave Nd-YAG laser beam welding of AM60B cast alloy revealed a significant increase in fusion-zone porosity for most of welding conditions (Zhao and DebRoy, 2001). The pre-existing pores, their coalescence and expansion were seen as the cause of porosity increase. The keyhole was found more stable than during welding of Al alloys but its stability did not substantially affect the overall porosity. During CO_2 laser welding of AZ31 wrought alloy, pores were found in welds mainly around the fusion boundary (Zhou et al., 2005). Since in wrought alloy the level of initial porosity is relatively low, pore formation during welding is attributed to the surface contamination and hydrogen rejection from the solid phase during solidification. It appears that porosity is created due to a collapse of the keyhole and turbulent flow in the weld. An example of welding speed effect on porosity is shown in Fig. 4.

In recent attempt, an analytical thermal model for welding the magnesium alloy WE43 was developed (Abderrazak et al., 2008). Since laser welding is controlled by many parameters including power, beam characteristics, welding speed, focal position, gas flow and material characteristics, finding the optimum is a complex task. The model allows determining the penetration depth and the bead width as a function of both the incident laser power and the welding speed. Modeling along with experimental verification were also used to study the keyhole formation and the geometry of weld profiles during welding of ZE41A-T5 alloy with Nd-YAG laser (Al-Kazzaz et al., 2008). Generally, the weld width and fusion area decrease with increasing welding speed. It was found that the excessive reduction in laser power resulted in lower surface power density and change of the welding mode through partially penetrated keyhole to the conduction mode. There was no significant effect of the filler wire feed rate on the coupling and melting efficiency.

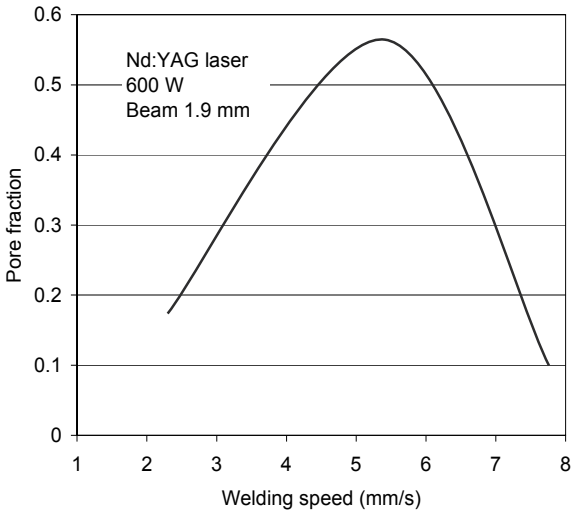

Fig. 4. Effect of welding speed on the pore fraction in AZ91 alloy weld (Marya and Edwards, 2000)

3.3 Hybrid laser beam welding

Hybrid laser beam technologies are defined as a combination of a laser beam source with an additional secondary beam source or another joining technique. A hybrid laser-TIG welding (LATIG) of AZ31 alloy, achieved higher welding speed than in laser or TIG welding (Liu et al., 2004). The penetration depth was twice of that for TIG and four times of that for laser welding. The same combination of laser beam and TIG was used to weld AZ31B magnesium alloy with a mild steel, applying a nickel interlayer (Qui and Song, 2010). As a result, semi-metallurgical bonding was achieved. Along the Mg – Ni interlayer the Mg_2Ni phase with solid solution of Ni in Fe formed. However, at the interface of molten pool and steel, the fusion zone did not interact with solid solution, suggesting mechanical bonding.

A new method of hybrid joining, called laser continuous weld bonding, was developed as an alternative to laser welding and adhesive bonding (Liu et al., 2007a). The technique was successful in joining of AZ31B magnesium and A6061 aluminum alloys by reducing a volume of brittle intermetallic compounds of Al_3Mg_2 and $Mg_{17}Al_{12}$ phases which are formed in the fusion zone, reducing the joint strength. The intermetallic phase formation was reduced due to the fluid generated by the gasification of adhesives. It appears that rising of adhesive vapor slows down the downward movement of liquid Mg, thus reducing its content in the weld. Hence, the weld is composed of two-phase mixture with less intermetallic compound and more solid solution.

4. Resistance spot welding

Resistance spot welding represents the localized joining of two or more metal parts together by an application of heat and pressure. The weld is formed due to the heat generated by the resistance to the electrical current passage between copper electrodes, being also the source of pressure. As a result, at the interface of welded materials a liquid pool (weld nugget) is formed. For high electrical conductivity of magnesium and low heat generation in the weld,

high welding currents are required. The process is used mainly in assembly lines to weld products made of thin gauge metals and it has potentials for joining sheets of magnesium alloys.

4.1 Weld microstructure

The joint obtained with a technique of resistance spot welding consists of the weld nugget and the heat affected zone. For AZ31 alloy the weld nugget contained the cellular dendritic structure at nugget edge, accompanied by equiaxed dendritic structure within its center (Sun et al., 2007). The boundary melting and coarsening was observed in the heat affected zone. It was revealed that the weld nuggets show a tendency to hot cracking. The joint strength and cracking susceptibility are influenced by the welding current. While the higher current increases strength it also increases the nugget tendency to cracking.

4.2 Effect of welding parameters on joint properties

The influence of selected process parameters on joint properties is shown in Fig. 5 (Shi, et al., 2010). For a constant electrode force, an increase in current reduces weld integrity as seen through porosity level (Fig. 5, left). An increase in the electrode force reduces the role of current and at sufficiently high electrode force the effect of current disappears. To improve heat generation at the connection, cover plates made of cold rolled steel were implemented. The plates allowed obtaining joints with larger weld nuggets and higher strength by applying the reduced current. As was the case without steel plates, the reduction in pore formation was achieved by increasing the electrode force and extending the holding time after current shut-off. The relative importance of holding time after current shut-off depended on welding current.

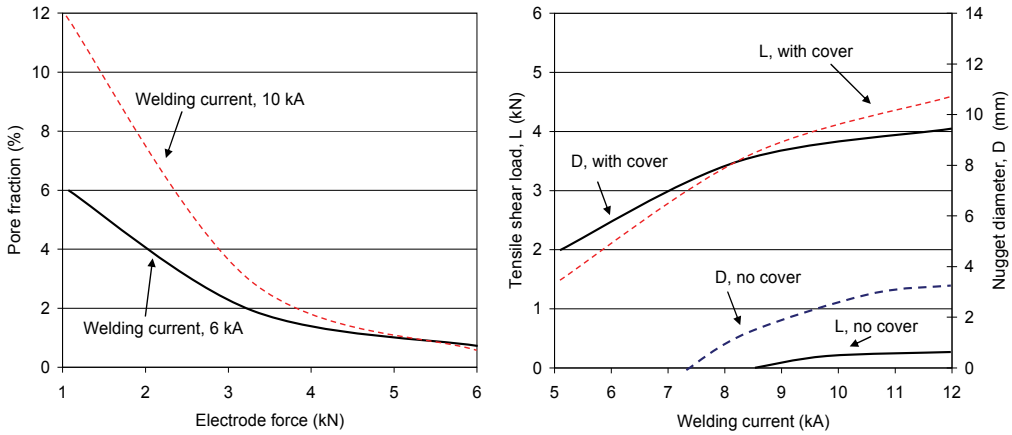

Fig. 5. Resistance spot welding of AZ31B alloy without and with steel cover plates: (left) pore fraction versus electrode force; (right) tensile shear load and nugget diameter as a function of welding current (Shi et al., 2010)

5. Friction stir welding

Friction stir welding is a relatively new joining technique and was invented in 1991 by The Welding Institute, England (TWI). It uses a rotating, non-consumable, cylindrical-

shouldered tool to deform the surrounding material without melting. Thus, the joint is essentially formed in a solid state. The concept is depicted in Fig. 6. Due to frictional contact of the tool and welded parts the heat generated plasticizes metal. As the tool moves forward, its special profile forces the plasticized material to the back and due to substantial forging force consolidates material so the joint is formed. The process is accompanied by severe plastic deformation, involving dynamic recrystallization of the base metal (Kumbhar and Bhanumurthy, 2008).

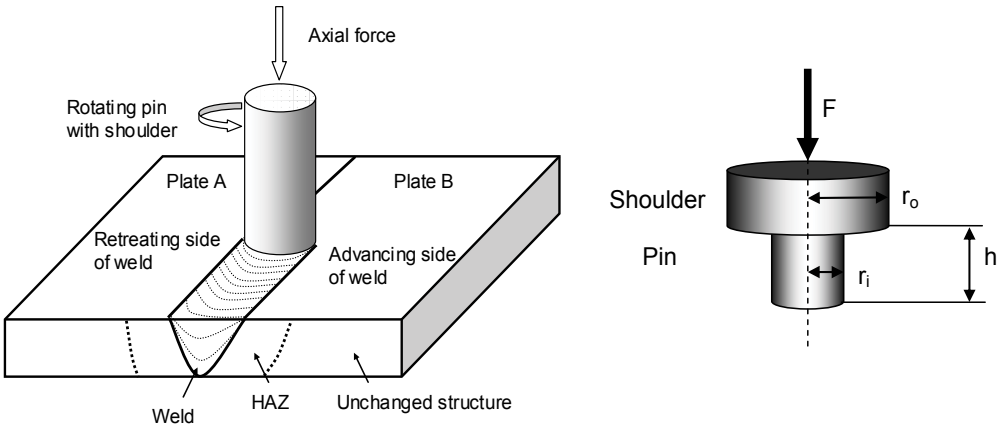

Fig. 6. Schematics of friction stir welding process and tool geometry

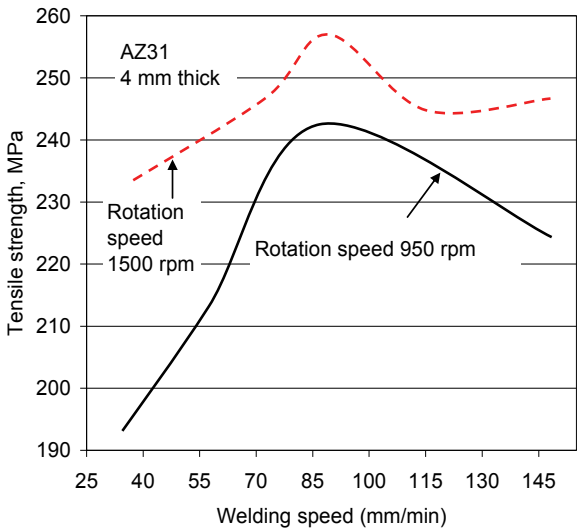

Fig. 7. Influence of welding speed and rotation speed on tensile strength of friction stir weld of AZ31 magnesium alloy plates with a thickness of 4 mm. The tool pin diameter is 4 mm and the shoulder diameter is 12 mm (Wang and Wang, 2006)

The total energy generated per unit length of the weld E equals the energy due to friction between the tool and the work piece E_f and the energy generated due to the plastic deformation of the work piece E_p (Emam and Domiaty, 2009):

$$E = E_f + sE_p \tag{1}$$

where: s is the scaling factor introduced in order to control the effect of the energy due to plastic deformation. The friction component E_f is expressed by:

$$E_f = 2\mu F\left(\frac{1}{3}r_o + \frac{r_i^2}{r_o^2}h\right)\frac{\omega}{\upsilon_o} \tag{2}$$

Where: r_o is the radius of the shoulder, r_i is the radius of the pin, h is the height of the pin (Fig. 6), ω is the pin angular speed, μ is the friction coefficient, F is the compressive force. The component E_p, associated with the plastic deformation, is defined as follows:

$$E_p = K\varepsilon^{n+1}\left(2r_i h\right)\exp\left(\frac{mQ}{R_G T}\right) \tag{3}$$

where: K is the strength coefficient, n is the strain hardening exponent, m is the strain rate sensitivity, Q is the apparent activation energy, R_G is a constant equals 8.32 $J^{-1}K^{-1}$, T is the absolute temperature. The heat due to the plastic deformation has a significant effect on final temperature, especially at low energy levels.

There are many benefits associated with friction stir welding. A low heat input and bonding below the melting point result in higher joint properties and lower distortion. The severe plastic deformation, introduced by the tool action, generates the fine-grained microstructure. The process is energy efficient and environmentally friendly with no fumes or UV radiation. Since there is no weld gravity issue, various welding positions are possible as orbital, vertical or overhead. As likely drawbacks of friction stir welding the large force and system stiffness requirements are quoted. Another drawback was a fixed pin capable handling of only one material thickness. However, modern solutions offer pins which can retract or expand within material thus allowing welding components with varying thickness.

5.1 Application to magnesium joints

Friction stir welding is extensively applied for magnesium alloys and for dissimilar joints with a magnesium component (Fig. 7).

The development of weld microstructure is controlled by shear deformation and thermal effects. In weld of wrought AZ61 alloy the crystallographic texture develops with a strong concentration of {0001} basal planes, being heterogeneously distributed in stir zone (Park et al., 2003). It was suggested that texture develops due to shear deformation caused by the rotating pin. Deformation of magnesium with hexagonal close packed structure is controlled by a slip along {0001} basal plane. Therefore, formation of this type of texture during welding affects the mechanical properties of weld. During friction stir welding of two AZ61 plates with a thickness of 6.3 mm both the transition and stir regions developed similar grain size, much finer than in the base alloy (Park et al., 2003a).

The technique of friction stir welding was applied to join magnesium with steel. During welding of AZ31 alloy and stainless steel 400, the rotation speed and pin axis orientation affected the microstructure and strength of the joint (Watanabe et al., 2006). The maximum strength of a butt type joint achieved approximately 70% of the strength measured for pure magnesium. The effect of tool geometry on microstructure and mechanical properties of Mg-steel welding was also studied (Chen and Nakata, 2009). For brushed finished steel joints,

the strength increased significantly with the probe length. Also microstructure was found to be sensitive to the probe length. The longer probe resulted in diffusion bonding while the shorter probe provided only the mechanical bond. The different observations were recorded for zinc coated steel where the probe length did not improve the joint strength. In that case, the short probe contributed to the defect-free joint.

Alloy	Weld/parent	Tensile strength, MPa	Yield stress, MPa	Elongation, %	Literature
AZ31	weld	201	125	3.7	1
	parent	255	200	12	2
AZ91	weld	183	153	1.5	1
	parent	250	160	3	2
	weld	200	150	2	4
AZ61	weld	280	120	17	3
	parent	310	230	25	2
AM50	weld	164	110	4	1
	parent	230	125	15	2
	weld	150	100	3	4

Table 2. A comparison of tensile properties of selected magnesium alloys after friction stir welding with properties of parent alloys. References: (1) (Johnson and Threadgill, 2003); (2)(Avedesian, 1999); (3) (Park, et al., 2003a); (4) (Skar et al., 2004)

6. Electromagnetic welding

Electromagnetic welding explores a phenomenon that current carrying conductors exert a force on each other (Fig. 8). The force depends on the current direction and is repulsive for opposite direction flow and attractive for the same flow direction. In practice, the electric current in the coil creates an eddy current within the work piece which generates forces between the coil and the material placed within it. During the welding process, these forces cause the outer work piece to plastically deform after it accelerates towards the inner work piece, thus creating a solid state weld. There are several modifications of magnetic welding which were successfully applied for magnesium. Similar concept of electromagnetic compression forming was used for processing of hollow profiles of magnesium alloys (Psyk et al., 2006).

Magnetic pulse welding is a solid state joining process and has a modification called pressure seam welding (Lee et al., 2007). Very high currents are generated by discharging a set of charged capacitors rapidly through the coil which surrounds the component to be welded. The eddy currents oppose the magnetic field in the coil and a repulsive force is created which drives the parts together at very high force speed and creates an explosive or impact type of weld. The eddy current i is expressed by the following equation (Aizawa et al., 2007):

$$\nabla \times i = -\kappa \left(\frac{\partial B}{\partial t} \right) \tag{4}$$

where: κ and B are electrical conductivity and magnetic flux density, respectively.

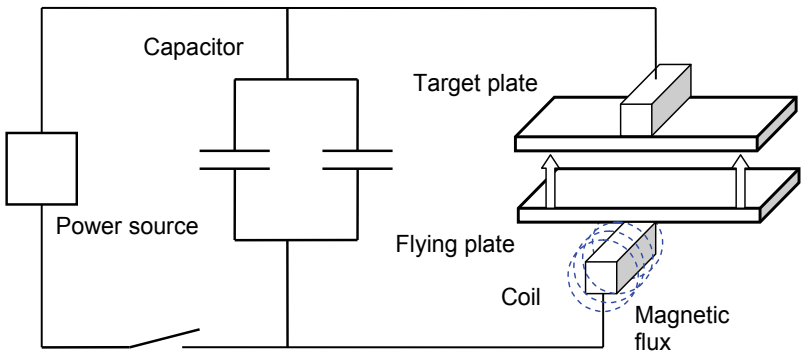

Fig. 8. Schematic diagram of electromagnetic pulse welding

The magnetic pressure p generated is given as follows:

$$p = \left(B_o^2 - B_i^2\right) / 2\mu = \left(\frac{B_o^2}{2\mu}\right)\left(1 - e^{-2x/\delta}\right) \tag{5}$$

Where: B_o^2 and B_i^2 are magnetic flux densities at lower and upper surfaces of welded sheet, μ is magnetic permeability, δ is the depth skin effect, given by the following:

$$\delta = \sqrt{2 / \omega\kappa\mu} \tag{6}$$

Where: ω is the angular frequency of changing field.

The technique provided satisfactory results for Al- AZ91 magnesium alloy. The sheets with a thickness of 0.5 to 1 mm were seam welded, producing a weld having the width of 5 mm. The weld thickness was 10% less than the original sheet thickness (Aizawa and Kashani, 2010). It is believed that the weld zone is formed as a combined effect of heating by eddy currents and the strong impulse electromagnetic force (magnetic pressure). No clear fusion boundary in the joint interface was microscopically detected. The transition layer had the characteristic wavy shape without any significant heat affected zone.

The same concept, called electromagnetic impact welding, was used for 0.6 mm sheet of AZ31 magnesium alloy and 1 mm thick A3003 aluminum alloy (Kore et al., 2009). The difference in electrical conductivities of Al and Mg led to the skin depth of 0.7 mm in Al and 0.6 mm in Mg alloys. The weld microscopy revealed a wavy interface and complete metal continuity without weld defects. Both x-ray diffraction and electron microscopy did not detect the intermetallic phase at the interface, suggesting a lack of melting. When welding was conducted at optimum conditions, failure during tensile testing occurred beyond the weld, in the base metal.

The electromagnetic compression of tubular profiles with high electrical conductivity is an innovative joining process for lightweight materials. The components are joined using pulsed magnetic fields which apply radial pressures of up to 200 MPa to the material causing a symmetric reduction of the diameter with typical strain of about 10^{-4} s^{-1} (Barreiro et al., 2008). Since there is no contact between components to be joined and the joining machine, there is not possible damage of the welded parts. The method was tested for aluminum alloys and has potentials for magnesium.

7. Electron beam welding

Electron beam welding (EBW) is a fusion welding which employs a dense stream of high velocity electrons to bombard, heat and melt the materials being joined. The electron beam is generated by electron gun composed of a cathode made of tungsten and an anode placed in high-vacuum. When the electron beam moves forward, the melted and evaporated alloy flows from the front to the back of the keyhole. It was developed in 1950's and first applied in nuclear industry. It is suitable for difficult welding where high repeatibility is required. When compared to arc welding, EBW creates the narrower weld and heat affected zone. The present drawbacks include high equipment cost, work piece size limitations, or X-ray generation during the electron bombardment.

During 3-dimensional modeling of thermal effect during welding of AZ61 alloy it was found that the welding heat source of electron beam produces two special thermal effects: deep-penetration thermal effect and surface thermal effect of metal vapor (Luo et al., 2010a). The experimental data for AZ61 alloy showed that the key parameters affecting the keyhole thermal effect are the welding heat input and focus coil current, which has also an impact on the weld shape.

A range of welding parameters of electron beam welding was analyzed to assess their importance on weld quality of AZ-series of magnesium alloys (Chi et al., 2008). The following ranking, in order of decreasing influence, was established: beam oscillation, focal position, stress relief, material difference, beam current, welding speed, and accelerating voltage. The best choices were a non-oscillating beam, a focus at the bottom and no stress relief. Of a number of alloys tested, the weldability, as determined by defects and precipitates distribution, follows the order of AZ61, AZ91, and AZ31 with AZ61 being the best.

During electron beam welding of 11 mm thick AZ31B plates with a power of 3000 W to 5000 W the effect of various process parameters was examined (Chi and Chao, 2007). The factors reducing the weld strength were: deviations of weld geometry, porosity and grain coarsening. In general, the weld strength reached over 90% of that for the base alloy.

8. Diffusion bonding

Diffusion bonding represents a solid state joining, achieved where two materials are brought into close contact at elevated temperatures of less than 0.7 T_m under moderate pressure, thus the atomic migration is not accompanied by macro-deformation. Since temperature does not exceed melting, it allows to eliminate many problems associated with fusion welding. The process is typically conducted in a press, heated by conventional methods or induction units. Microwave sources are also explored for this purpose. To obtain high bonding, the surface should be clean and flat. There are three major stages of the bonding progress. First, a contact between materials occurs through the mating surfaces (Poddar, 2009). During the second stage, diffusion within grain boundaries predominates, thus eliminating pores and ensuring arrangements of grain boundaries. During the third stage, the volume diffusion dominates and process is completed.

8.1 Joints between magnesium alloys

Diffusion bonding was found applicable for pure magnesium and its alloys. For pure magnesium rolled sheet, tests were carried out at the pressure range of 2-20 MPa, temperature range from 300 ^oC to 400 ^oC and time periods up to 72 h (Somekawa et al.,

2001). The maximum lap shear strength was 0.888 at a bonding pressure of 20 MPa, temperature 400 °C and for time of 1 h. A ductile fracture was revealed after the compression lap shear test.

During manufacturing of complex sheet structures, diffusion bonding is often combined with superplastic forming. The combination allows to reduce weight and fabrication cost, as compared with mechanically fastened structures (Gilmore et al., 1991). The technology was successfully implemented for superplastic magnesium alloy AZ31 with a grain size of approximately 17 μm (Fig. 9) (Somekawa, et al., 2003a). The maximum of lap shear strength was 0.85 at a bonding pressure of 3 MPa and a bonding temperature of 400 °C and time of 3 h. No bond line was revealed during microscopic observations, indicating the extensive diffusion. A successful diffusion bonding was also achieved for a superplastic alloy AZ31 hot rolled at 250 °C (Somekawa et al., 2003b). Having a grain size of 8.5 μm, the alloy behaved in a superplastic manner within the temperature range of 250-300 °C. Both phenomena, the diffusion bonding and superplasticity are grain size dependant, thus structures with finer grains will have lower bonding temperature. The effect is related to the bonding mechanism where diffusion controls the joint formation. The numerous voids, initially present at the interface between joined metals will disappear due to the plastic flow and diffusion towards the void surface. For finer grains the boundary diffusion has the higher contribution because more grain boundaries intersect with voids.

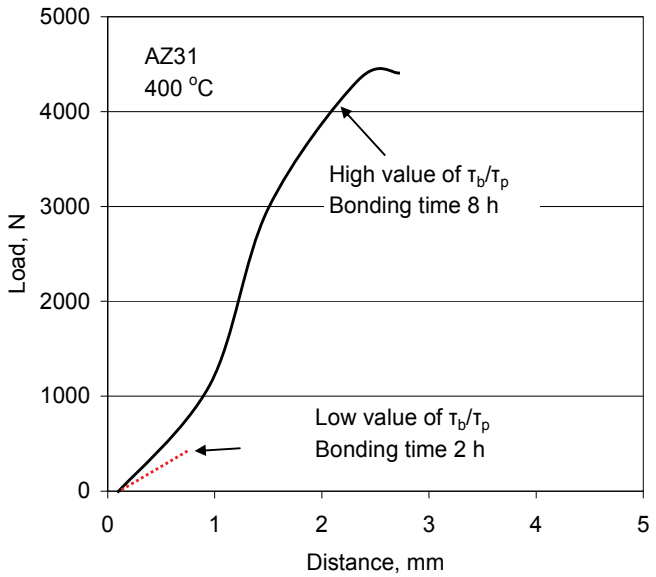

Fig. 9. Load versus distance measured during the compression lap test of diffusion bonded AZ31 magnesium alloy (Somekawa et al., 2003a)

8.2 Dissimilar joints formed by diffusion bonding

For dissimilar joints of Mg alloys, of special importance is Al. This is due to the substitution of Al with Mg in automotive industry, which requires Mg-Al joints. An example is the Mg/Al joint made using vacuum bonding at 460-480 °C, time of 40-60 min and a pressure of 0.08-0.10 MPa (Li et al., 2008). Hence, the diffusion zone was formed with two different transition regions on both sides. At the interface with Al, various Mg_xAl_y phases, such as

MgAl, Mg_3Al_2 and Mg_2Al_3 were formed. On the Mg side in addition to Mg grains, Mg_3Al_2 phase was formed. The latter has fcc structure as opposed to hcp of magnesium. It is claimed that Mg_3Al_2 phase has the positive effect on cracking resistance of the joint.
The major obstacle during welding of Mg and Al is a formation at the interface between both alloys brittle compounds of Mg-Al, causing cracking during service. Thus eliminating or improving that interlayer is the critical factor in producing strong joints. One of possible solutions is to introduce an interlayer between Al and Mg. For AZ31B andA6061 alloys, Zn interlayer was found to be effective (Zhao and Zhang, 2008). The Zn layer with a thickness of 60 μm was deposited on Al surface by hot dipping. The bonding was conducted at 360 °C for 3 s.
Diffusion bonding was proved effective for joining Mg with alloys having substantially higher melting ranges, such as Cu alloys. Joints made at the bonding temperature of 450 °C, pressure of 12 MPa and time of 30 min exhibited shear strength of 66 MPa and bonding strength of 81 MPa (Mahendran et al., 2010).

8.3 Experimental joining techniques

The new technique of in-situ joint formation of magnesium cast and wrought components, without necessity of welding, was recently proposed (Papis, et al., 2010). The focus of this technique is on eliminating the natural oxide layer present on magnesium and replacing it with metallic $Zn/MgZn_2$ layer by a sequence of chemical, electrochemical and heat treatments. The objective is to change the surface reactivity and increase surface wettability to create Mg-Mg compound. The process verification, performed on AZ31 substrate, joined with AJ62 cast alloy and pure Mg, revealed an area-wide metallurgic in nature and defect free interface between both couples. The coating material dissolved into the bulk metal during casting. The issue of formation of shrinkage cavities at the interface can be solved by selecting appropriate solidification intervals (Fig. 10).

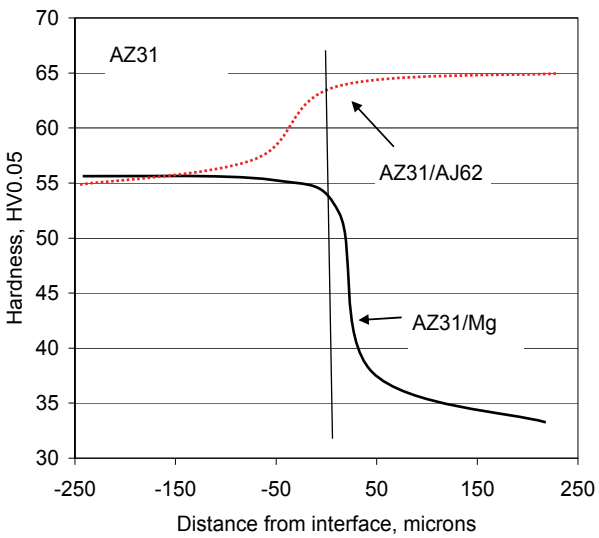

Fig. 10. Microhardness versus distance from interface for AZ31/AJ62 and AZ31/Mg connections using continuously metallurgic joining (Papis et al., 2010)

9. Other techniques of magnesium joining

This section describes joining techniques where diffusion is negligible or does not occur at all. Although no evident metallurgical bond is created, techniques satisfy many applications where other solutions are not viable due to technical or economical reasons.

9.1 Soldering

Soldering is a joining process where a filler metal with a melting temperature below 450 °C fills the joint by capillary action between closely fitting parts. Generally, magnesium is considered "unsolderable" by conventional means. There are, however, attempts to overcome this obstacle. Already in 1980's, magnesium soldering flux, acetamid with a melting point of 82 °C, was developed which was able to dissolve magnesium oxide. As a solder, indium-tin with a melting point of 120 °C was proposed (Humpston and Jacobson, 2004).

Recently, high frequency induction soldering was found to be effective for joining magnesium alloy AZ31 (Ma et al., 2010). The process was conducted with a high frequency induction heating device using 80.8%Zn-19.2%Al filler metal and argon gas shielding. A wide temperature range and time of 120 s were applied. As a result of AZ31 alloy solution and transfer to soldering region, the solder chemistry changed during the process to 84.0%Zn-12.7%Al. In the soldering region, the α-Mg solid solution and α-Mg + Mg-Zn eutectoid were formed. The zinc solid solution and aluminum solid solution in the original filler metal disappeared completely. The joint achieved a shear strength of 19 MPa and fractured in the intercrystalline mode originating from the eutectoid structure.

There is a development in progress to find the suitable filler metals for magnesium. Several chemistries of Al-Zn-Mg alloys were proposed for soldering temperatures from 390 °C to 450 °C (Liu and Wu, 2010). For 25% of Al, range of Zn was of 25-95% and Mg of 2-72%.The role of Mg was to minimize a contact corrosion with the base metal, Zn due to the same crystal structure and electrode potential as Mg. The role of Al was to provide the joint strength. As a result, the Zn-enriched phases disappeared and α-Mg with dendritic morphology existed in the joint. The increased solidification rate by applying water cooling led to the formation of equiaxed fine dendrites and increasing their number by 40-50 times.

9.2 Brazing

Brazing is a joining process where a filler metal is placed at or between parts to be joined and the temperature is raised to melt the filler metal but not the work piece. The filler metal for brazing has the melting range above 450 °C.

Diffusion brazing methods are used to join advanced alloys and offer an alternative for dissimilar joints. A double stage process was applied to join stainless steel 316L to magnesium alloy AZ31 (Elthalabawy and Khan, 2010). In the first stage, thin nickel foil was diffusion bonded to stainless steel at 900 °C for 15 min and a pressure of 2 MPa. Then, the 316L/Ni was bonded in a vacuum chamber at 510 °C, a pressure 0.2 MPa and for time interval of 20 min. The possible phases between Ni and Mg may be deduced from Fig. 11.

A technique of brazing, called contact reaction brazing (CRB), is flux-free and benefits from low melting liquid phase formed by the eutectic reaction of dissimilar metals (Liu et al., 2008). A Zn interlayer with a thickness of up to 30 μm provided solution in brazing of Mg with Al alloys. In particular case of AZ31 magnesium and A6061 aluminum alloys, the best shear strength was achieved by joints made with a 3 μm thick Zn layer at 360 °C, 5 MPa

pressure and bonding times from 10 min to 30 min. Additions of Zn-based brazing alloy inhibited the formation of Mg-Al brittle phases. The Al substrate is bonded to the brazing alloy by a thin Al-Zn transition layer with no brittle phases. On the other side, the Mg plate is bonded to the brazing alloy by the reaction zone with low fraction of Mg-Zn intermetallics. At the interface between the reaction zone and the remnant brazing alloy, some pores were created, affecting a location of the failure zone (Liu et al., 2007b).

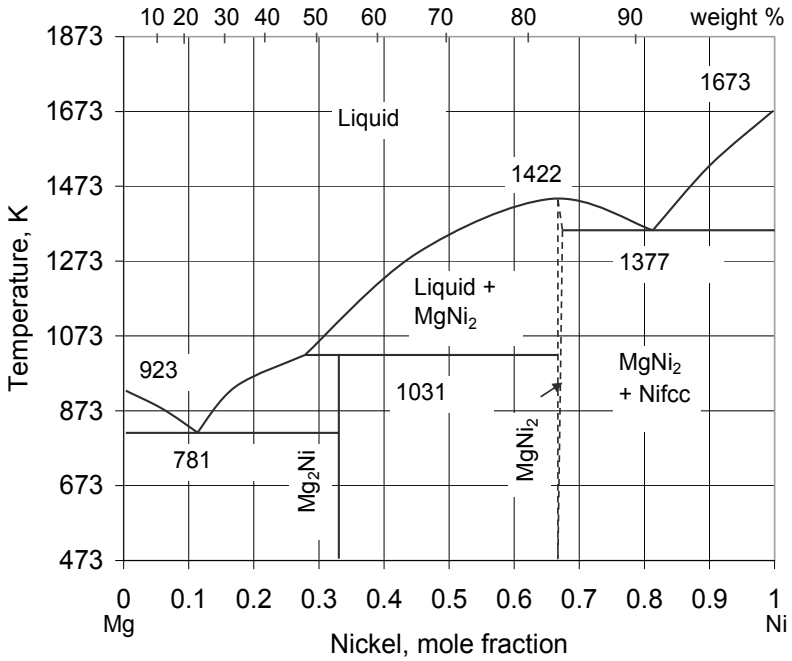

Fig. 11. Equilibrium phase diagram of Mg-Ni (Islam and Medraj, 2005; Zeng, 1999)

9.3 Adhesive bonding

Adhesive bonding is defined as joining using a non-metallic substance (adhesive) which undergoes hardening due to physical or chemical reaction. As a result, parts are joined together through surface adherence (adhesion) and internal strength (cohesion).

During adhesive bonding of magnesium alloys and polypropylene, satisfactory joint strength was achieved only after chemical pretreatment of both components (Liu and Xie, 2007b). An addition of 1% of SiO_2 particles into the adhesive increased the joint strength. The mechanism of bonding between polypropylene and the adhesive is based on diffusion and mechanical interaction. The bonding between magnesium alloy and adhesive is controlled by the coordinative bond forces.

10. Mechanical fastening of magnesium

10.1 Threaded fasteners

The galvanic corrosion of magnesium caused by fasteners is the key concern of mechanical joints. Although negligible corrosion occurs for 6000 series of aluminum alloys, for some applications the steel fasteners are required. A technique of Al plating of steel fasteners does

not present viable solution. A better compatibility in salt water environment exhibit steel fasteners with zinc or tin-zinc coatings, however they also experience corrosion due to the coating porosity. During performance simulation of mild steel fastener to AZ91 cast alloy in 5% NaCl solution, two corrosion mechanisms active in area from 1 to 2 cm from the interface were identified: galvanic corrosion and self corrosion (Jia et al., 2005). It was confirmed that the microgalvanic cells exist on the surface of AZ91D alloy which have potential differences of the order of 100 mV between alloy phases: matrix of α-Mg and $Mg_{17}Al_{12}$ intermetallics. This heterogeneous composition fuels both the galvanic and general corrosion. In addition to galvanic corrosion, steel fasteners have large difference in thermal expansion coefficient (Table 1) causing creep and preload loss if joint is subjected to thermal cycling, as is the case in an automotive engine.
Fasteners made of 6000 series of aluminum alloys, containing less than 1% of copper do not require additional surface treatment and their corrosion resistance does not change through their service life (Westphal et al., 2005). A comparison of clamp load of AlSi9Cu3 fasteners on AZ91 and AS21 cast alloys shows substantial lost of the preload after 200 h at 150 °C. At 120 °C the moderate lost of preload took place after 100 h of thermal exposure. At both temperatures there was no influence of magnesium alloy grade on the preload change.

10.2 Riveting

Riveting belongs to mechanical fastening methods which employs auxiliary joining elements. In self-piercing riveting the formation of holes, necessary in conventional process, is replaced by a combined cutting-riveting stage. Industrial applications include two processes based on half-hollow or solid type of rivets used. Self-piercing riveting is a high speed fastening for point joining of sheet materials with benefits shown in Fig. 12.

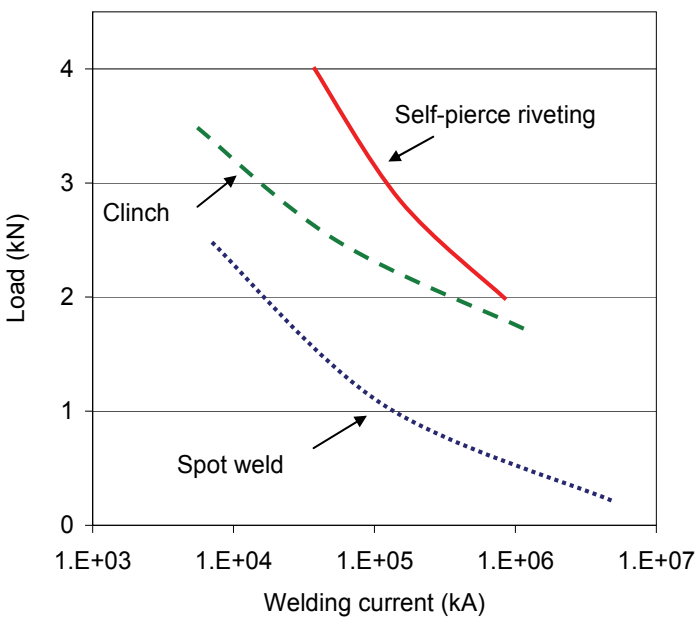

Fig. 12. Comparison of fatigue behaviour of joints obtained by spot-welding, clinching and self-pierce riveting (Cai et al., 2005)

A method of attaching a magnesium panel via self-piercing rivet was invented recently (Luo and Sachdev, 2010). The magnesium panel is spot heated and then the self-piercing steel rivet is punched through the steel panel and only partly through the magnesium panel, to displace the magnesium panel into the cavity. The purpose of heating is to improve formability of magnesium and prevent cracking. The invention proposes also solution to potential corrosion by concealing the interface between the steel rivet and the magnesium panel between the aluminum panel and magnesium panel. To prevent cracking, it is required to heat the magnesium panel in the region of the die cavity to a temperature of about 200 ^{o}C. The joint shows good combination of lap shear and cross-tension strength.

10.3 Clinching

Clinching represents a direct joining of materials using the forming technology where a local deformation of components with a rigid punch creates a form of locked joint. The wide variation of tools allows for a selection of the optimum joint geometry. Applicability of clinching for magnesium is limited by the low formability of magnesium at room temperature, causing cracking. To improve it, parts are heated up to 220 ^{o}C to increase an alloy formability. Two heating options are used in practice: heating of the entire part in a furnace or localized heating of the joint area using, for example, an induction method. Another option is to heat the die or punch to much higher temperature of almost 400 ^{o}C.
During conventional clinching the components are deformed together with a clinching punch in a contoured die, having a shape that controls the component interlocking. In a new solution, called dieless clinching, the contoured die is replaced by a flat anvil (Neugbauer et al., 2008). The benefit of the flat anvil as a counter tool is a possibility to decrease the heating time to 1 s instead of 3-6 s with the conventional clinching method. The heat is applied to the flat counter tool. A hybrid solution, combining clinching with adhesive bonding, was not successful since the adhesive layer was displaced during the first stage of clinching. Also experiments, combining a conventional clinching with contoured dies and adhesive bonding, cause problems due to inclusions of adhesive in the neck areas of the joint.

11. Summary

During last decade, a substantial progress was made in welding and joining of magnesium alloys. In addition to improvement in conventional fusion welding techniques, novel methods and their hybrids were developed. They allow producing commercially viable joints of different grades of cast and wrought magnesium alloys. Although there is a substantial progress on fusion welding, its application to dissimilar joints, which involve a number of materials with drastically different properties, is still limited. Also, alternative joining technologies, which require local deformation, are not fully successful due to limited formability of magnesium. To compensate low formability a preheating up to over 200 ^{o}C is required which diminishes the process economy. Low temperature processes, such as soldering and brazing, require improvement in joint strength by better control of interface phenomena. Novel ideas, aimed at eliminating the detrimental effect of natural oxides on magnesium surface seem to represent a step in correct direction. They may require complex surface engineering solutions but preliminary tests are promising. It is obvious, therefore, that there is a search for alternative methods of joining magnesium alloys, especially with dissimilar alloys.

12. References

Abderrazak, K., Salem, W. B., Mhiri, H., Lapalec, G. and Autric, M. (2008) Modeling of CeO2 laser welding of magnesium alloys, *Optics and Laser Technology*, 40, 581-588

Aizawa, T. and Kashani, M. (2010) Magnetic pulse welding (MPW) method for dissimilar sheet metal joints, *www. irjp.jp*,

Aizawa, T., Kashani, M. and Okagawa, K. (2007) Application of magnetic pulse welding for aluminum alloys and SPCC steel sheet joints, *Welding Research*, 86, 119-124

Al-Kazzaz, H., Medraj, M., Cao, X. and Jahazi, M. (2008) Nd:YAG laser welding of aerospace grade ZE41A magnesium alloy: Modeling and experimental investigations, *Materials Chemistry and Physics*, 109, 61-76

ASM (1990) *Metals Handbook*, ASM International, Materials Park, Ohio

Avedesian, M. M. (1999) *Magnesium and Magnesium Alloys*, ASM International, Materials Park, Ohio

Barreiro, P., Schulze, V. and Loehe, D. (2008) Influence of process parameters on structure and mechanical properties of joints produced by electromagnetic forming and friction stir welding, *Advanced Materials Research*, 43, 47-56

Cai, W., Wang, P. C. and Yang, W. (2005) Assembly dimensional prediction for self-piercing riveted aluminum panenls, *Inter. Journal of Machine Tools Manufacturing*, 45, 695-704

Chen, Y. C. and Nakata, K. (2009) Effect of tool geometry on microstructure and mechanical properties of friction stir lap welded magnesium alloy and steel, *Materials and Design*, 30, 3913-3919

Chi, C., T., Chao, C. G., Liu, T. F. and Wang, C. C. (2008) Relational analysis between parameters and defects for electron beam welding of AZ-series of magnesium alloys, *Vacuum*, 82, 1177-1182

Chi, C. T. and Chao, C. G. (2007) Characterization on electron beam welds and parameters for AZ31B-F extrusive plates, *Journal of Materials Processing Technology*, 182, 369-373

Czerwinski, F. (2008) *Magnesium Injection Molding*, Springer Verlag, New York

Elthalabawy, W. M. and Khan, T. I. (2010) Microstructural development of diffusion brazed austenitic stainless steel to magnesium using nickel interlayer, *Materials Characterization*, 61, 703-712

Emam, S. A. and Domiaty, A. E. (2009) A refined energy-based model for friction-stir welding, *World Academy of Science, Engineering and Technology*, 53, 1016-1022

Gilmore, C. J., Dunfold, D. V. and Parteidge, P. G. (1991) *Journal of Materials Science*, 26, 3119-3124

Humpston, G. and Jacobson, D. M. (2004) *Principles of Soldering*, ASM International, Materials Park, Ohio

Islam, F. and Medraj, M. (2005) The phase equilibria in the Mg-Ni-Ca system, Calphad, 29, 289-302.

Jia, J. X., Atrens, A., Song, G. and Muster, T. H. (2005) Simulation of galvanic corrosion of magnesium coupled to a steel fastener in NaCl solutiion, *Materials and Corrosion*, 56, 7, 468-474

Johnson, R. and Threadgill, P., Friction stir welding of magnesium alloys, Magnesium Technology 2003, 2003, TMS

Kore, S. D., Imbert, J., Worswick, M. J. and Zhou, Y. (2009) Electromagnetic impact welding of Mg to Al sheets, *Science and Technology of Welding and Joining*, 14, 6, 549-553

Kumbhar, N. T. and Bhanumurthy, K. (2008) Friction stir welding of Al6061 alloy, *Asian Journal of Experimental Science*, 22, 2, 63-74

Lee, K. J., Kumai, S., Arai, T. and Aizawa, T. (2007) Interfacial microstructure and strength of steel/aluminum alloy lap joint fabricated by magnetic pressure seam welding, *Materials Science and Engineering A*, 471, 95-101

Li, Y., Liu, P., Wang, J. and Ma, H. (2008) XRD and SEM analysis near the diffusion bonding interface of Mg/Al dissimilar materials, *Vacuum*, 82, 15-19

Liu, L., Tan, J. and Liu, X. (2007b) Reactive brazing of Al alloy to Mg alloy using zinc-based brazing alloy, *Materials Letters*, 61, 2373-2377

Liu, L., Wang, J. and Song, G. (2004) Hybrid laser-TIG welding, laser beam welding and gas tungsted arc welding of AZ31B magnesium alloy, *Materials Science and Engineering A*, 381, 129-133

Liu, L. and Xie, L. (2007b) Adhesive bonding between Mg alloys and polypropylene, *Materials Technology: Advanced Performance Materials*, 22, 2, 76-80

Liu, L. M., Tan, J. H., Zhao, L. M. and Liu, X. J. (2008) The relationship between microstructure and properties of Mg/Al brazed joints using Zn filler metal, *Materials Characterization*, 59, 479-483

Liu, L. M., Wang, H. Y. and Zhang, Z. D. (2007a) The analysis of laser weld bonding of Al alloy to Mg alloy, *Scripta Materialia*, 56, 473-476

Liu, L. M. and Wu, Z. (2010) Microstructure and interfacial reactions of soldering magnesium alloy AZ31B, *Materials Characterization*, 61, 1, 13-18

Luo, A. A. and Sachdev, K. (2010) Method for attaching magnesium panels using self-piercing rivet, *US 2010/0083481*, April 8, 2010,

Luo, Y., You, G., Ye, H. and Liu, J. (2010a) Simulation on welding thermal effect of AZ61 magnesium alloy based on three-dimensional modeling of vacuum electron beam welding heat source, *Vacuum*, 84, 890-895

Ma, L., He, D. Y., Li, X. Y. and Jiang, J. M. (2010) High frequency soldering of magnesium alloy AZ31B using Zn-Al filler metal, *Materials Letters*, 64, 5, 596-598

Mahendran, G., Balasuramanian, V. and Senthilvelan, T. (2010) Influence of diffusion bonding process parameters on bond characteristics of Mg-, *Transactions of Nonferrous Metals Society of China*, 20, 6, 997-1005

Marya, M. and Edwards, G. R. (2002) Chloride contribution in flux-assisted GTA welding of magnesium alloys, *Welding Journal*, 12, 291-298

Marya, M. and Edwards, G. R. (2000) The laser welding of magnesium alloy AZ91D, *Welding World*, 44, 2, 31-37

Neugbauer, R., Kraus, C. and Dietrich, S. (2008) Advances in mechanical joining of magnesium, *CIRP Annals - Manufacturing Technology*, 57, 283-286

Papis, K. J. M., Loffler, J. F. and Uggowitzer, P. J. (2010) Interface formation between liquid and solid Mg alloys - An approach to continuously metallurgic joining of magnesium parts, *Materials Science and Engineering A*, 527, 2274-2279

Park, S. H. C., Sato, Y. S. and Kokawa, H. (2003) *Metallurgical and Materials Transactions A*, 34, 987

Park, S. W. C., Sato, Y. S. and Kokawa, H. (2003a) Effect of micro-texture on fracture location in friction stir weld of Mg allloy AZ61 during tensile test, *Scripta Materialia*, 49, 161-166

Poddar, D. (2009) Solid-state diffusion bonding of commercially pure titanium and precipitation hardening stainless steel, *International Journal of Recent Trends in Engineering*, 1, 5, 93-99

Psyk, V., Beerwald, C., Klaus, A. and Kleiner, M. (2006) Characterization of extruded magnesium profiles for electromagnetic joining, *Journal of Materials Processing Technology*, 177, 266-269

Quan, Y., Chen, Z., Yu, Z., Gong, X. and Li, M. (2008) Characteristics of laser welded wrought Mg-Al-Mn alloy, *Materials Characterization*, 59, 1799-1804

Qui, X. and Song, G. (2010) Interfacial structure of the joints between magnesium alloy and mild steel with nickel as interlayer by hybrid laser-TIG welding, *Materials and Design*, 31, 605-609

Shi, H., Qiu, R., Zhu, J., Zhang, K., Yu, H. and Ding, G. (2010) Effects of welding parameters on the characterestics of magnesium alloy joint welded by resistance spot welding with cover plates, *Materials and Design*, 31, 4853-4857

Skar, J. I., Gjestland, H., Oosterkamp, L. and Albright, D. L., Friction stir welding of magnesium die castings, Magnesium Technology 2004, 2004, TMS, Warrendale

Somekawa, H., Hosokawa, H., Watanabe, H. and Higashi, K. (2001) Experimental study of diffusion bonding in pure magnesium, *Materials Transactions*, 42, 10, 2075-2078

Somekawa, H., Hosokawa, H., Watanabe, H. and Higashi, K. (2003a) Diffusion bonding in superplastic magnesium alloys, *Materials Science and Engineering A*, 339, 328-333

Somekawa, H., Watanabe, H., Mukai, T. and Higashi, K. (2003b) Low temperature diffusion bonding in a superplastic AZ31 magnesium alloy, *Scripta Materialia*, 48, 1249-1254

Sun, D. Q., Lang, B., Sun, D. X. and Li, J. B. (2007) Microstructure and mechanical properties of resistance spot welded magnesium alloy joints, *Materials Science and Engineering A*, 460, 461, 494-498

Sun, D. X., Sun, D. Q., Gu, X. Y. and Xuan, Z. Z. (2008) Hot cracking of metal inert gas arc welded magnesium, *ISIJ International*, 49, 2, 270-274

Wang, X. and Wang, K. (2006) Microstructure and properties of friction stir butt-welded AZ31 magnesium alloy, *Materials Science and Engineering A*, 431, 114-117

Watanabe, T., Kagiya, K., Yanagisawa, W. and Tanabe, H. (2006) Solid state welding of steel and magnesium alloy using a rotating pin, *Quart. Journal of Japanese Welding Society*, 24, 108-123

Westphal, K., Mulherkar, T. and Schneiding, W. (2005) Joining of magnesium components using Al fasteners, *Light Metal Age*, 4, 2-3

Zeng, K. (1999) Thermodynamic analysis of the hydriding process of Mg-Ni alloys, *Journal of Alloys and Compounds*, 283, 213-224

Zhao, H. and DebRoy, T. (2001) Pore formation during laser beam welding of die-cast magnesium alloy AM60B - mechanism and remedy, *Welding Research Supplement*, 8, 204-209

Zhao, L. M. and Zhang, Z. D. (2008) Effect of Zn alloy interlayer on interface microstructure and strength of diffusion-bonded Mg-Al joints, *Scripta Materialia*, 58, 283-286

Zhou, J., Li, L. and Liu, Z. (2005) CO2 and diode laser welding of AZ31 magnesium alloy, *Applied Surface Science*, 247, 300-306

22

High Strength Magnesium Matrix Composites Reinforced with Carbon Nanotube

Yasuo Shimizu
Shinshu University
Japan

1. Introduction

It has been increasingly important to develop lightweight and high-strength materials for improving energy-efficiency through the weight reduction of transportation carriers. Magnesium alloys have attracted lots of attentions[1-3], since the density of magnesium is approximately two thirds of that of aluminum and one fifth of steel. As a result, magnesium alloys offer a very high specific strength among conventional engineering alloys. In addition, magnesium alloys posses good damping capacity, excellent castability, and superior machinability. However, compared to other structural metals, magnesium alloys have a relatively low mechanical strength, especially at elevated temperature. The need for high-performance and lightweight materials for some demanding applications has led to extensive efforts in the development of magnesium matrix composites and cost-effective fabrication technologies. They are proved to have good mechanical properties through an incorporation of structural filler (e.g., ceramic whiskers such as silicon carbide whisker and others, aluminum oxide, graphite and other particles, carbon fibers and carbon nanotubes: CNTs) [4-7]. Within this context, the dimensionally nano-sized, mechanically strong CNTs [8-11], considered as the ideal reinforcing filler in various composite systems [12-15], have been incorporated into magnesium matrix [16-19]. This chapter put the spotlight into the very attractive new magnesium alloy matrix composites reinforced with CNTs.

2. Processing techniques for fabricate the metal matrix composite (MMC) with CNTs

The reinforcing phases such as powders, fibers and whiskers are generally incorporated into the metal matrices mostly by two typical techniques of liquid state fabrication and solid state fabrication [3,20]. The key techniques in the processing of MMC are how to realize the homogeneous distribution of reinforcement phases and to achieve a defect-free microstructure.

2.1 Liquid state fabrication of MMC

Liquid state fabrication of MMC involves incorporation of dispersed reinforcing phase into a molten matrix metal, followed by its solidification. There are many liquid state fabrication

methods such as stir casting, rheocasting, infiltration, gas pressure infiltration, squeeze casting infiltration, pressure die infiltration, etc., however, a few methods are applied for fabricating MMC with CNTs. Their features are written below. In order to provide high level of mechanical properties of the MMC, good interfacial bonding (procuring the wetting reaction) between CNTs and matrix should be obtained. Wetting improvement may be usually achieved by coating the reinforcing phases [21]. Unfortunately, proper coating for CNTs has not yet established.

2.1.1 Stir casting

Stir Casting is the simplest and the most cost effective method of liquid state fabrication. A dispersed phase (ceramic particles, short fibers) is mixed with a molten matrix metal by means of mechanical stirring. Liquid state composite material is then cast by conventional casting methods and may also be processed by conventional metal forming technologies. When CNTs are selected as a reinforcing phase, uniform distribution of CNTs in the matrix structure should be obtained since the CNT exhibits inherent deficiency of wetting for molten magnesium and magnesium alloy matrices.

2.1.2 Rheocasting

Rheocasting is a modified method using stirring metal composite materials in semi-solid state. Distribution of dispersed phase may be improved because the high viscosity of the semi-solid matrix material enables better mixing of the dispersed phase.

2.2 Solid state fabrication of MMC

Typical solid state fabrication method in which MMC is formed as a result of bonding matrix metal and dispersed phase due to mutual diffusion occurring between them. Raw powders of the matrix metal are mixed with the dispersed phase in form of particles or short fibers for subsequent compacting and sintering. Sintering involves consolidation of powder grains by heating the "green" compact part to the elevated temperature below melting point.

Relatively low process temperature as compared to Liquid state fabrication is expected to depress undesirable reaction generating fragile phase such as carbide on the boundary between the matrix and dispersed phase when carbon fiber or CNT are used as the reinforcing phase.

3. Microstructure of the composite with CNTs

3.1 Characteristics of the CNTs introduced into matrix

Kroto *et al*. discovered fullerene (C60) in 1985 [22] and won Nobel Prize in Chemistry in 1996. After their discovery, Iijima found that carbon nanotube (CNT) generated on the electrode of the generation device of C60 in 1991and opened the beginning to the CNT generation [23]. As it should be noted that CNTs are sorted into two main groups by their structure and size. Fig.1 shows the illustration sorting the carbon fiber and CNTs [24]. The first group of CNTs is single-layered carbon nanotube (SWCNT) having wondrous strength such as 1 TPa in Young's modulus and 140 GPa in Yield strength [25]. However, SWCNT is too expensive for normal industrial application. The second CNT group is multilayered

carbon nanotube (MWCNT). Table 1 presents the characteristics of an example of MWCNT called as a vapor grown carbon fiber (VGCF)[26] made by SHOWA DENKO K.K. in Japan. In late years mass production of MWCNT has been achieved and enabled to use it with relatively low cost.

Density	(kg/m^3)	2000
Bulk density	(kg/m^3)	40
Fiber diameter	(nm)	150
Fiber length	(μm)	10~20
Aspect ratio		10~500
Elastic modulus [28]	(GPa)	100~700
Tensile strength [28]	(GPa)	0.5~2.2
Thermal conductivity	(W/mK)	1260

Table 1. Characteristics of the MWCNT(VGCF) [26]

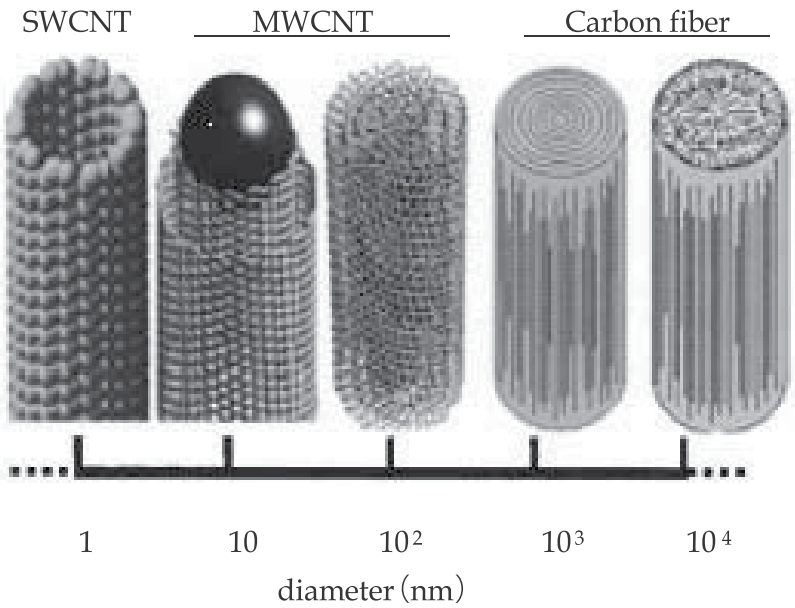

Fig. 1. Illustration sorting carbon fiber and CNTs[24]

3.2 Distribution of CNTs in the matrix

Scanning electron microscopies of the composite showing distribution state are presented for instance in Fig.3(a) and (b). These microstructure were observed on the tensile fracture surface of the test specimens prepared by the following powder metallurgical process[27], i.e. at first, AZ91D magnesium alloy powders of 100 μm or less in diameter were prepared by tri-axial ball

milling process from lathe cutting chips of AZ91D raw ingot. Then, the AZ91D powders and MWCNTs were physically blended with zirconia balls (diameter = 1 mm) in a container using the same ball miller in argon atmosphere. The absence of the aggregated MWCNTs for the magnesium alloy powder containing 1 mass% MWCNTs indicates that the short MWCNTs are homogeneously impinged on the near surface of magnesium alloy particles

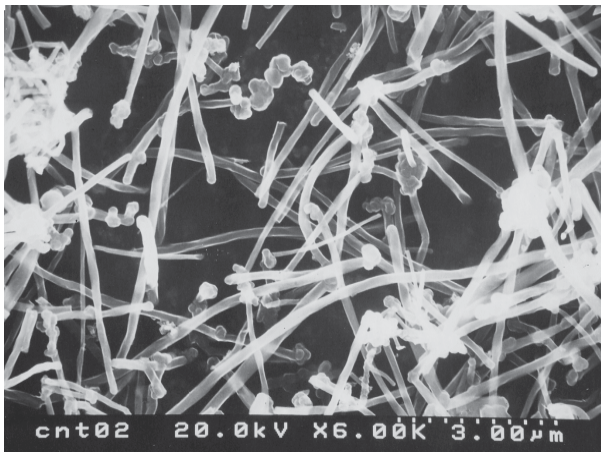

Fig. 2. Scanning microscopy of MWCNTs

(Fig.4(a)). In the case of the powders containing 5 % MWCNTs, aggregated MWCNTs were indicative of non-homogeneous distribution (Fig.4(b)). Next, the magnesium powders containing 0.5 to 5mass % MWCNTs were hot-pressed in a molder to form precursor at 823 K for 5 hrs by applying a pressure of 25.5 MPa in a vacuum below 10 Pa. Then finally composites obtained in a form of rod (Fig.4(c)) (diameter = 6 mm, length = 120 mm) by extruding precursors at 723 K with an extrusion ratio of 9. There was no distinctive defect in appearance.

3.3 Chemical reaction between the alloy matrix and CNTs

It should be noted that the interfacial state between magnesium alloy matrix and CNTs because the formation of carbide (Al_2MgC_2) was reported when the temperature was above 773 K and the aluminum level in magnesium alloy compositions was above 0.6 % and below 19 % [25]. Therefore, TEM (JEOL, JEM-2100F) observations and EDS mappings for the samples, prepared by ion milling technique, were carried out. As shown in elemental mappings in Figure 5, magnesium alloys containing homogeneously distributed aluminum elements occupied around carbon elements. Also, it is confirmed that there are the absence of void (Fig.5(e)) and new phase (Fig.5(f)) between MWCNT and magnesium alloys. From the viewpoint of bonding nature for the samples, it is rational to say that magnesium alloys have high capability to move on the outer surface of MWCNTs, and they don't have chemical reactivity to form new products like carbides.

4. Mechanical properties of the composites

Mechanical properties such as Young's modulus, yield strength, tensile strength and fatigue elongation are usually the major attraction for the composite materials. Very small particles (less than 0.25 micron in diameter) finely distributed in the matrix impede movement of

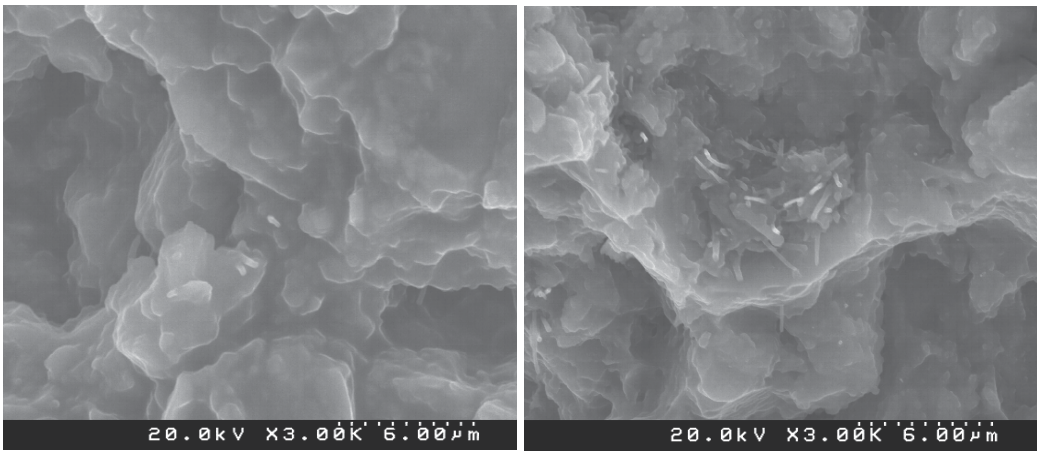

(a) (b)

Fig. 3. Scanning microstructure of the tensile fracture surface observed on the composite specimens. (a)AZ91D-1mass%MWCNT, (b) AZ91D-5mass%MWCNT, in which the aggregation of MWCNTs was observed.

dislocations and deformation of the material. Such strengthening effect is similar to the precipitation hardening. In contrast to the precipitation hardening, which disappears at elevated temperatures when the precipitated particles dissolve in the matrix, dispersed phase of MWCNT and/or particulate composites (ceramic particles) is usually stable at high temperatures, so the strengthening effect is expected to be retained.

Remarkable studies on the mechanical properties of the composites reinforced with any of MWCNTs and other fillers are reviewed in Table 2.

Magnesium matrix composites investigated by S. F. Hassen *et al*. [29] and C. S. Goh *et al*. [18] are strengthened with fine particles or MWCNTs as well as magnesium alloy matrix composites. However, it is interesting phenomenon that the breaking elongation is also increased. It was explained that the MWCNT fillers act as an obstacle to prevent cleavage fracture and increase fracture energy.

Mechanical properties of the magnesium alloy composites are similarly improved by reinforcing fillers of MWCNTs or various ceramic materials, on the contrary to the magnesium matrix composite, the breaking elongation decreases due to the peculiar brittleness of reinforcing fillers. K. Osada *et al*. [31] developed the AZ91D alloy composite reinforced with 14.8 vol.% SiC particles reaching highest tensile strength of 485MPa, whereas breaking elongation decreased less than 1 %. T. Honma *et al*. [33] recently reported that the AZ91D alloy composite with 7.5 mass % MWCNTs improved its wettability by surface coating of Si was gained 470MPa in tensile strength and breaking elongation of 2%.

By the way, when the additive amount of MWCNT was increased too much, MWCNT could not be uniformly distributed and partially aggregated. The aggregation of MWCNTs act like a cave defect, consequently the performance of the Composite are degraded.

Technological development to improve the limit of an effective MWCNT additive amount is important. Recently, author *et al*. [34] fabricated new AZ91D alloy composite with simultaneous additions of 2mass%MWCNTs and 1mass% graphite particles by means of the

ball milling method. This new method resulted higher properties of 51GPa in elastic modulus, 464MPa in tensile strength, 420MPa in 0.2% proof stress and 4% in breaking elongation respectively. These results were explained by the Hall Petch effect related to crystal grain refining.

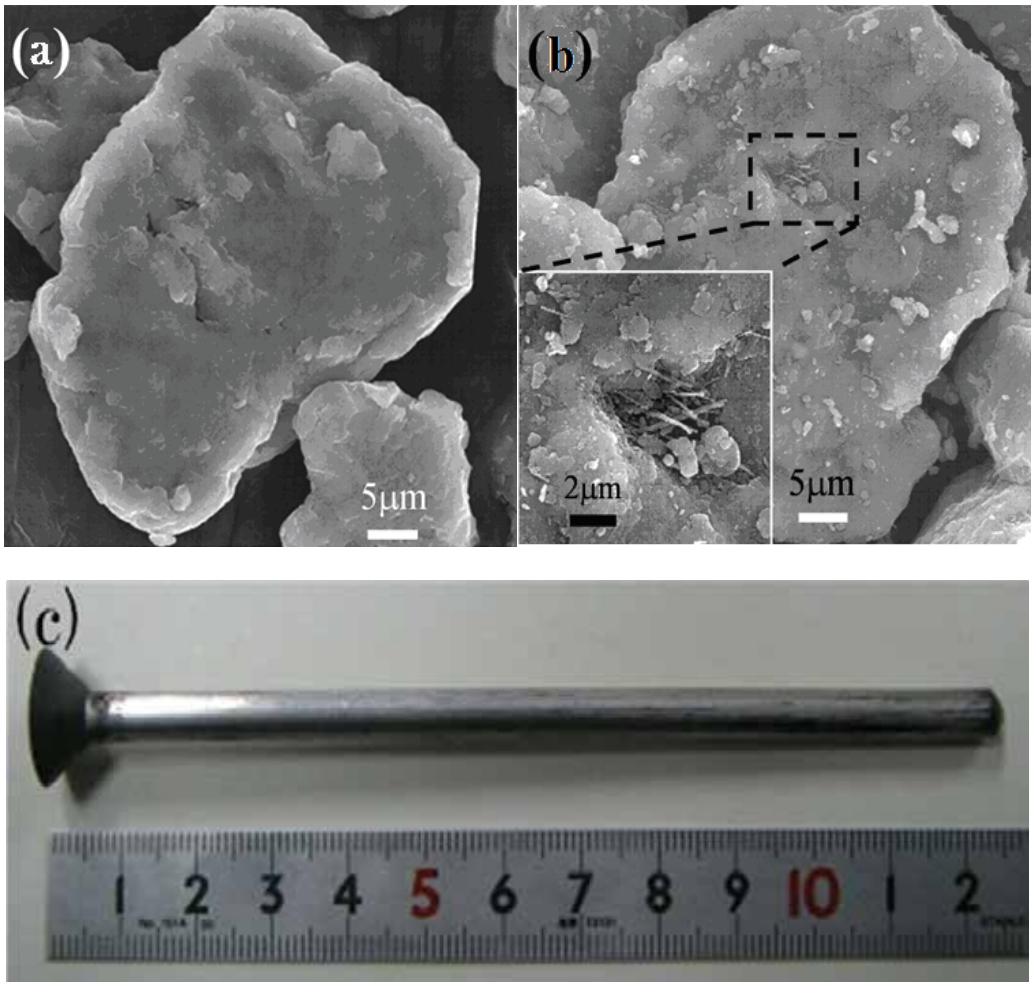

Fig. 4. SEM images (a, b) mechanically mixed magnesium powders containing 1 mass % and 5 mass % MWCNTs, respectively. Note that the aggregated MWCNTs were observed in magnesium powders containing 5 mass% of MWCNTs (inset is a magnified SEM image). (c) Photo of carbon nanotube-reinforced magnesium composite-based rod exhibiting clean appearance without any macro-morphological defects).

5. Application and problem of the composites

Promising developments are carried out, however, few applications using CNT reinforced magnesium and magnesium alloy matrix composite materials has been realized. Mechanical

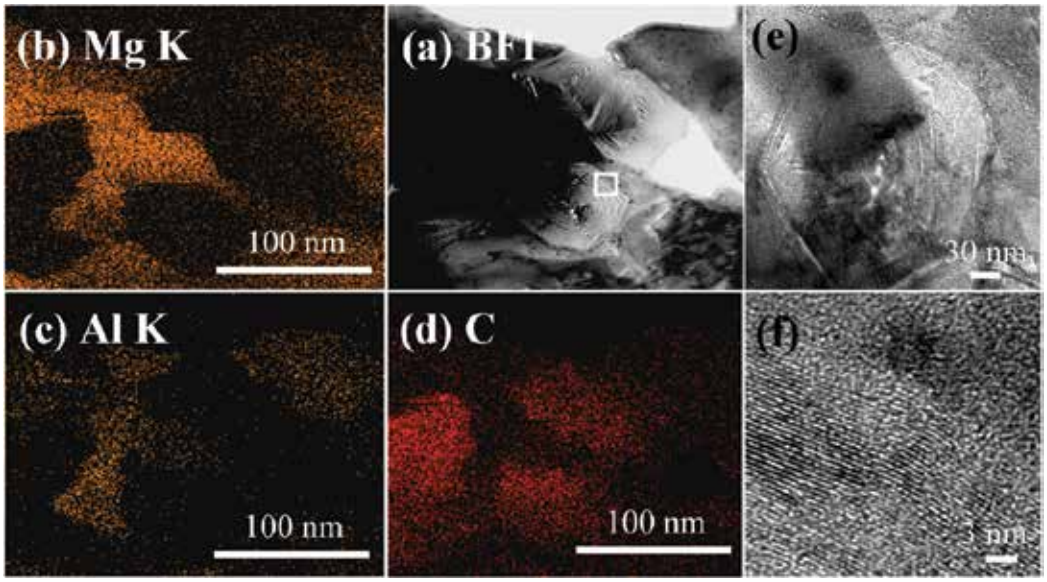

Fig. 5. TEM image of 1mass% MWCNT-reinforced AZ91D-type magnesium alloy composite; (a) bright field image, (b) elemental Mg mapping (in yellow) , (c) elemental Al mapping (in light yellow) , (d) elemental C mapping (in light red). TEM images showing the characteristic facetted cross sectional MWCNT (e) and linear lattices (f) contacted with magnesium alloy matrix, revealing that there was the absence of void and new phase between MWCNT and magnesium alloy matrix.

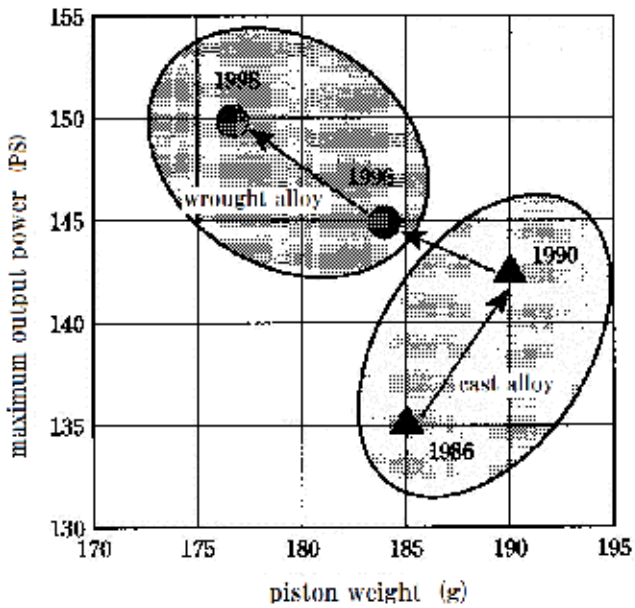

Fig. 6. Historical review of the relation between maximum output power and aluminum alloy piston weight for 1,000cm^3 engine[35)]

Composite system (mass%, vol%)	Fabrication Method (r:extrusion ratio)	Heat treatment	Elastic Modulus (GPa)	0.2%Proof Stress (MPa)	Tensile Strength (MPa)	Fracture Elongation (%)
Mg(≧98.59 mass%)[29]	Powder Metallurgy + Hot Extrusion (extrusion ratio: r=20.25)	None	41.2	132±7	193±2	4.2 ±0.1
Mg-2.5mass% Al_2O_3(p)[29]	Powder Metallurgy + Hot Extrusion (r=20.25)	None	44.5	194±5	250±3	6.9±1.0
Mg (99.9mass%)[18]	DMD※ + Hot Extrusion (r=20.25)	None	—	126±7	192±5	8.0±1.6
Mg-1.3mass %MWCNT[18]	DMD※ + Hot Extrusion (r=20.25)	None	—	140±2	210±4	13.5±2.7
AZ91A[30]	DMD※ + Hot Extrusion (r=20.25)	T6	43±3	263±12	358±5	7±4
AZ91A-15.54%Cu(p)[30]	DMD※ + Hot Extrusion (r=20.25)	T6	54±1	299±5	382±6	6±1
AD91D[31]	Melt Stiring + High Pressure casting + Hot Extrusion (r=54)	T6	—	240	370	12
AD91D-14.8vol%SiC(p)[31]	Melt Stiring + High Pressure casting + Hot Extrusion (r=54)	T6	—	449	485	1
AZ91D-11vol%Al_2O_3(f)[32]	Squeeze casting	T6	—	—	260	1
AZ91D[27]	Powder Metallurgy + Hot Extrusion (r=9)	T6	40±2	225±4	320±4	17±3
AD91D-1.0%MWCNT[27]	Powder Metallurgy + Hot Extrusion (r=9)	T6	49±3	288±5	395±4	6±1
AD91D-5.0%MWCNT[27]	Powder Metallurgy + Hot Extrusion (r=9)	T6	51±4	267±6	305±8	1.6±0.4
AZ91D[33]	Rheocastig + Hot Extrusion (r=25)	None	—	250	340	12
AD91D-7.5mass%Si-MWCT[33]	Rheocastig + Hot Extrusion (r=25)	None	—	416	470	2
AD91D-2mass%Graphite (P)+1mass%MW CNT[34]	Powder Metallurgy + Hot Extrusion (r=9)	None	51	420	464	4

※DMD: Disintegrated Melt Deposition Method

Table 2. Remarkable results on the mechanical properties of the magnesium and magnesium alloy matrix composites reinforced with any of MWCNTs and other fillers.

strength of magnesium alloy composites with MWCNTs is highly improved today and comparable to that of the generally utilized mild steel in automobiles. Fig.6 shows the historical review of the relation between maximum output power and aluminum alloy piston weight for 1,000cm^3 engine [35]. Although the magnesium alloy has not been applied, it is clearly suggests that the effort to reduce the piston weight is very effective to enhance the engine performance, therefore the magnesium alloy composite with MWCNTs will be increasingly promising material.

The lying problems on the magnesium and magnesium alloy matrix composites with CNTs should be overcome is not only to promote the performance advantages but also to develop the cost-effective processing technologies.

6. Acknowledgement

This Work was supported by Regional Innovation Cluster Program of Nagano, granted by MEXT, Japan.

7. References

[1] K.U. Kainer: Magnesium Alloys and Their Applications, Willey-VCH, 2000.
[2] W.L.E. Wong, M. Gupta: J. Mater. Sci. 40 (2005) 2875.
[3] H.Z. Ye, X.Y. Liu: J. Mater. Sci. 39 (2004) 6153.
[4] M. Zheng, K. Wu, C. Yao: Mater. Sci. Eng. A 318 (2001) 50.
[5] F. Wu, J. Zhu, Y. Chen, G. Zhang: Mater. Sci. Eng. A 277 (2000) 143.
[6] J.C. Viala, P. Fortier, G. Claveyrolas, H. Vincent, J. Bouix : J. Mater. Sci. 26 (1991) 4977.
[7] Y. Kagawa, E. Nakata: J. Mater. Sci. 11 (1992) 176.
[8] A. Oberlin, M. Endo, T. Koyama: J. Crys. Grow. 32 (1976) 335.
[9] M. Treacy, T.W. Ebbesen, J.M. Gibson: Nature 381 (1996) 678.
[10] H. Dai, E.W. Wong, C.M. Lieber, Science 272 (1996) 523.
[11] T.W. Ebbesen, H.J. Lezec, H. Hiura, J.W. Bennett, H.F. Ghaemi, T. Thio: Nature 382 (1996) 54.
[12] P.M. Ajayan, L.S. Schadler, C. Giannaris, A. Rubio: Adv. Mater. 12 (2000) 750.
[13] R.H. Baughman, A.A. Zakhidov, W.A. De Heer: Science 297 (2002) 787.
[14] E.T. Thostenson, Z. Ren, T.W. Chou: Composites Science and Technology 61 (2001)1899.
[15] Y.A. Kim, T. Hayashi, M. Endo, Y. Gotoh, N. Wada: J. Seiyama, Scripta Materialia 54 (2006) 31.
[16] J. Yang, R. Schaller: Mater. Sci. Eng. A 370 (2004) 512.
[17] E. Carreno-Morelli, J. Yang, E. Couteau, K. Hernadi, J.W. Seo, C. Bonjour, L. Forro, R. Schaller: Phys. Stat. Sol. 201 (2004) R53.
[18] C.S. Goh, J. Wei, L.C. Lee, M. Gupta: Mater. Sci. Eng. A 423 (2006) 153.
[19] C.S. Goh, J. Wei, L.C. Lee, M. Gupta: Nanotechnology 17 (2006) 7.
[20] William D Callister Jr: Materials Science and Engineering, An Introduction, John Wiley & sons, Inc. (2006) 577.
[21] Z. L. Pei, K. Li, J. Gong, N. L. Shi, E. Elangovan, C. Sun: J of Mater. Sci, 44 (2009) 4124.
[22] H. W. Kroto, J. R・Heath, S. C. 0'Brien, R. F. Curl, R. E. Smaley: Nature，318 (1985) 362.
[23] S. Iijima: Nature, 354 (1991) 56.
[24] M. Endo: SEN'I GAKKAISHI, 59 (2003) 412 (in Japanese).

[25] K.M. Liew *et al*.: Acta Materialia, 52 (2004) 2521.
[26] http://www.sdk.co.jp/html/products/finecarbon/vgcf.html
[27] Y. Shimizu *et al*.: Scripta Materialia, 58 (2008) 267.
[28] M. Endo, Y.A.Kim, T. Hayashi, K. Nishimura, T. Matusita, K. Miyashita, M.S. Dresselhaus, Carbon, 39 (2001) 1287.
[29] S.F. Hassan *et al*.: Materials Science and Engineering A392 (2005) 163.
[30] K. F. Ho, M. Gupta: Materials Science Forum, 437 (2003) 153.
[31] K. Osada *et al*.: Technical Report of Aichi Industrial Technology Institute, (2005) 30, (in Japanese).
[32] M. Nakagawa *et al*.: KEIKINZOKU (The J. of Japan Institute of Light Metals), 45 (2005) 31 (in Japanese).
[33] T. Honma, S. Kamado: KINZOKU (Materials Sci. & Tech.), 80 (2010) 643 (in Japanese).
[34] Y.Shimizu *et al*.: Japanese Open Patent No. 2010-159445.
[35] H. Yamamoto, T. Koike: KEIKINZOKU (The J. of Japan Institute of Light Metals), 49 (1999) 178 (in Japanese).

23

Magnesium Alloys Based Composites

Zuzanka Trojanová[1], Zoltán Száraz[2],
Peter Palček[3] and Mária Chalupová[3]
[1]*Charles University, Prague*
[2]*Joint Research Centre, European Commission, Petten*
[3]*University of Žilina*
[1]*Czech Republic*
[2]*The Netherlands*
[3]*Slovak Republic*

1. Introduction

Metal matrix composites offer a wide range of opportunities for many structure applications because of their improved mechanical properties in comparison with their monolithic metal counterparts. Light alloys reinforced with short fibres or particles allow adapting more exactly the work piece material properties to requirements. There is an increasing trend in the automotive industry to use these materials for various components. Advanced properties of metal matrix composites are:

- increased apparent limit of elasticity, stiffness, tensile and fatigue strength,
- improved creep resistance and high temperature properties,
- improved material damping,
- increased wear resistance,
- decreased thermal expansion.

Metal matrix composites (MMCs) based on magnesium alloys are excellent candidates for engineering light structure materials, and have great potential in automotive, high performance defence and aerospace applications. In spite of relatively high number of papers dealing with microstructure and mechanical properties of MMCs based on Mg alloys, the deformation mechanisms and other physical properties of these materials are not known enough. It has already been shown that the reinforcing fibres and/or particles improve mechanical and creep properties of magnesium based MMCs compared to their monolithic counterparts. But also the disadvantage of higher production costs due to more complicated manufacturing processes has to be taken into account (Dieringa et al., 2005). Only the use of cheap materials - both the alloy and the reinforcement – in relation to cost effective production processes for manufacturing of magnesium based MMCs can introduce this class of low density materials into the market. The objective of this chapter – following from this fact – is to reveal influence of various reinforcement types on the mechanical and physical behaviour of composites in which various magnesium alloys were reinforced with short alumina (Saffil®) fibres and/or SiC and Si particles. Different routs for magnesium based MMCs preparation were used:

i. Squeeze casting – the melt is infiltrated into the prefabricated perform (fibres and/or particles with some binder). The preform is preheated to 800–1000 °C in order to avoid

solidification during the infiltration process. The melt (in the case of Mg alloys) is superheated to a temperature between 700 and 720 °C and poured over the preform. The vertical stamp squeezes the melt under a pressure of about 60 MPa into the preform and the solidification takes approximately one minute. After the infiltration, the solidification process occurs under the pressure which leads to the fine microstructure without porosity and residual gases.

ii. Gas pressure infiltration – similarly as in the case of the squeeze casting the melt is infiltrated into the perform and the pressure is applied using the inert gas (argon).

iii. Powder metallurgy - Gas atomised alloy powder and SiC particles were mixed in an asymmetrically moved mixer with subsequent milling in a ball mill. In order to obtain an optimum dispersion of reinforcement in the matrix it is necessary to assure a certain particle/matrix powder size ratio. The maximum powder size was fixed at 63 μm. The powder was encapsulated in magnesium containers and extruded at 400 °C using a 400 t horizontal extrusion press.

A commercially available AZ91 magnesium alloy with the nominal composition Mg – 9%Al; 1%Zn; 0.3%Mn, in weight percent was reinforced by various reinforcement: 20 vol % of short Al_2O_3 (Saffil®) fibres (AZ91f), 15 vol.% of short Saffil fibres and 5 vol.% of SiC particles (AZ91h), further samples contained 10% SiC particles and an addition of 3wt.% Si (AZ91p). Composites were prepared by the squeeze casting method. The preforms consisted Al_2O_3 short fibres showing a planar isotropic fibre distribution and a binder system (containing Al_2O_3 and starch). Thermal treatment T6 was used (homogenisation for 18 h at 413 °C, then precipitation for 8 h at 168 °C). Samples of AZ91f were cut from the bulk with two orientations with respect to the fibre plane: the sample with the fibre plane parallel to the stress axis (AZ91f$\parallel$) and perpendicular to the stress axis (AZ91f$\perp$). The mean Saffil fibre length and fibre diameter measured after squeeze casting were 78 and about 3 μm, respectively. The sharply shaped SiC particles in the AZ91h composite had a size of about 10 μm. The size of the SiC particles in the AZ91p composite was about 20 μm. Figure 1 shows the microstructure of undeformed AZ91f composite. It can be seen that many fibres are broken as a consequence of the squeeze casting procedure. The cut has been performed perpendicular to the fibres plane; 2D random distribution of fibres is well visible. Typical features of the microstructure are a solid solution of Al in Mg (δ-phase) and the γ-phase ($Mg_{17}Al_{12}$) intermetallic compound. Figure 2 shows the structure of AZ91h hybrid composite. The observed microstructure consists from δ-phase, electron compound $Al_{12}Mg_{17}$ (γ-phase) and discontinuous precipitate (lamellae of γ+δ phase). From the micrograph it can be seen that SiC particles are distributed non-uniformly. A representative view of the AZ91p composite with the addition of 3%Si and 10vol.% of SiCp is shown in Figure 3. The microstructure of AZ91 matrix (see Fig.3) consists of the δ-phase, the γ-phase and the discontinuous precipitate (lamellae of γ+δ phase). The addition of 3%Si gives rise to the Mg_2Si phase formed as eutectic Chinese script type particles, or primary Mg_2Si coarse dendrites. The Mg_2Si phase is present usually in the interior of δ-phase grains, and often islands of the entrapped δ-phase are present in some Mg_2Si coarse dendrites. The γ-phase is distributed mainly around grain boundaries and lamellae discontinuous precipitate was often adjacent to the γ-phase or grain boundaries. A typical feature of the microstructure of AZ91p composite is a small grain size of about 3 μm. Sharply shaped SiC particles with a size of about 9 μm are not uniformly distributed.

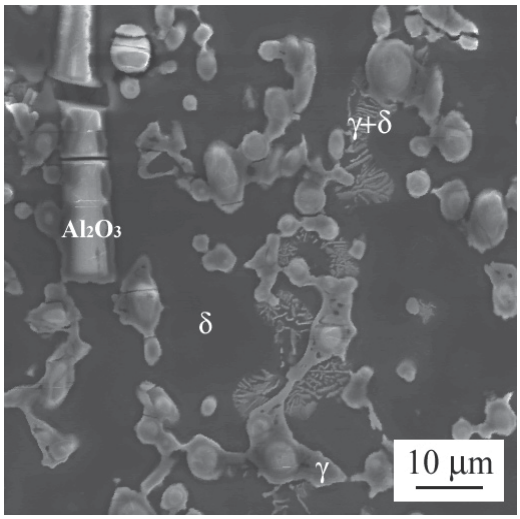

Fig. 1. Scanning electron micrograph of AZ91f MMC.

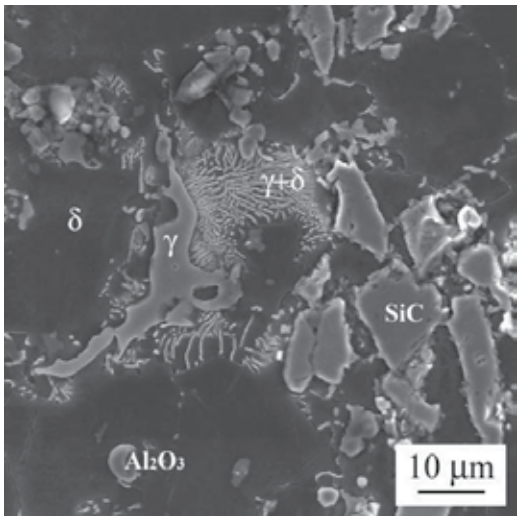

Fig. 2. Scanning electron micrograph of AZ91h MMC.

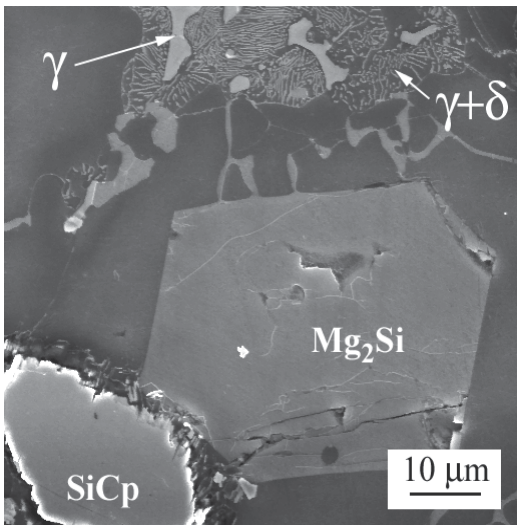

Fig. 3. Scanning electron micrograph of AZ91p MMC.

The microstructure of AZ91 matrix (see Fig.3) consists of the δ-phase, the γ-phase and the discontinuous precipitate (lamellae of γ+δ phase). The addition of 3%Si gives rise to the Mg_2Si phase formed as eutectic Chinese script type particles, or primary Mg_2Si coarse dendrites. The Mg_2Si phase is present usually in the interior of δ-phase grains, and often islands of the entrapped δ phase are present in some Mg_2Si coarse dendrites. The γ phase is distributed mainly around grain boundaries and lamellae discontinuous precipitate was often adjacent to the γ-phase or grain boundaries. A typical feature of the microstructure of AZ91pm composite is a small grain size of about 3 μm. Sharply shaped SiC particles with a size of about 9 μm are not uniformly distributed.

Commercial AS21 (2.2Al-1Si-0.1Mn-balance Mg-in wt%) alloy was used as the matrix material for composites with 30 vol.% short fibres of δ-Al_2O_3 (Saffil®) (hereafter AS21(f)) and hybrid composite with 5 vol.% of Saffil short fibres and 15 vol.% of SiC particles (AS21h). Composites were prepared using squeeze casting. The light micrograph of the AS21f composite is introduced in Fig. 4a.b. Planar random orientation is well visible in micrographs taken from two perpendicular sample surfaces. Characteristic feature of the composite microstructure is MgSi phase having a form of the dendritic crystals or characteristic Chinese-script. Microstructure of the AS21h hybrid composite consists of Saffil fibres. SiC particles and Mg_2Si particles.

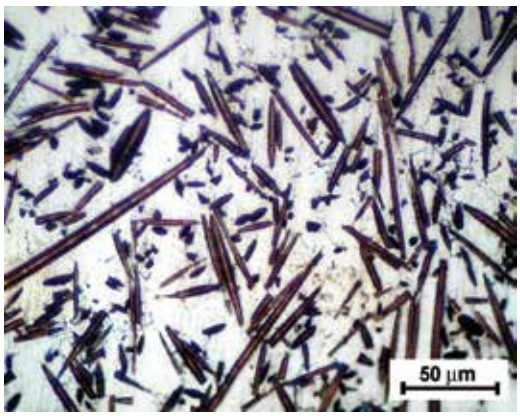

Fig. 4a. Light micrograph of AS21f MMC.

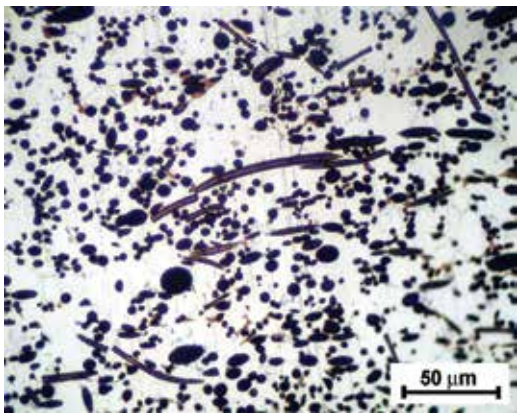

Fig. 4b. Micrograph from the perpendicular surface plane of the same sample as in Fig. 4a.

AX41 alloy (Mg – 4 wt.% Al – 1 wt.% Ca) reinforced with 13% Saffil fibres (AX41f) was prepared by squeeze casting technology. A typical feature of the AX41 alloy consists from solid solution of Al in Mg, α-Mg grains decorated by particles. SEM showed $Mg_{17}Al_{12}$ intermetallic phase surrounded with smaller particles of Al_2Ca. The microstructure of the composite is more complicated as it can be seen in Fig. 5.

Light Mg-Li alloys are attractive candidates for reinforcement with ceramic fibres or particles. Pure Mg has hcp structure. The density of Mg-Li alloy decreases with an increase of lithium content. The addition of Li increases ductility. The Mg-Li phase diagram shows that Li is soluble in hcp α phase up to 4 wt.%, while Mg alloyed with greater than 12 wt% Li has a bcc structure. Mechanical properties of the hcp α phase are worse in comparison with the *bcc* alloys, which are very good machinable and weldable. Disadvantages of Mg-Li alloys with *bcc* structure are a high chemical activity and poor corrosion resistivity. Some compromise would be an alloy with 8 wt% of Li (a mixture of phases α+β), which might exhibit both improved mechanical properties as well as a good corrosion resistance. Further improvement of mechanical properties is possible if the alloy is reinforced with the ceramic fibres or particles. Mg-xLif composites reinforced with Saffil fibres were produced by the gas pressure infiltration of evacuated fibrous preform with metallic melt in the autoclave. The mean fibre length and fibre diameter after infiltration was ~100 μm and ~3 μm, respectively. Microstructure of the as prepared Mg-4Lif sample is shown in Fig. 6. The structure of as-cast Mg-8Lif alloys under consideration consists essentially of *hcp*

magnesium-based α-phase (lighter) and *bcc* lithium-based β-one (darker). Accordingly, interpenetrated (α+β) matrix structure with dominating α-phase is characteristic of short δ-Al_2O_3 fibre reinforced Mg-8Lif composites wherein the fibres are planar randomly distributed within α and β matrix regions (Fig.7).

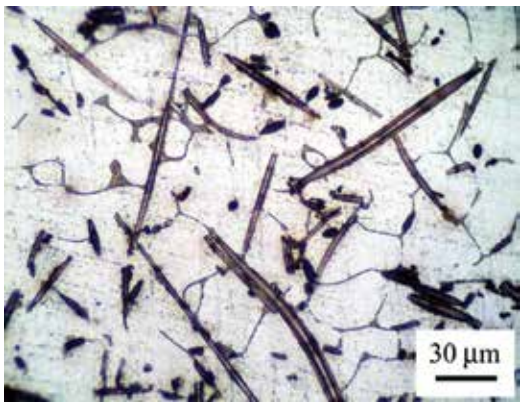

Fig. 5. Light micrograph of AX41f MMC.

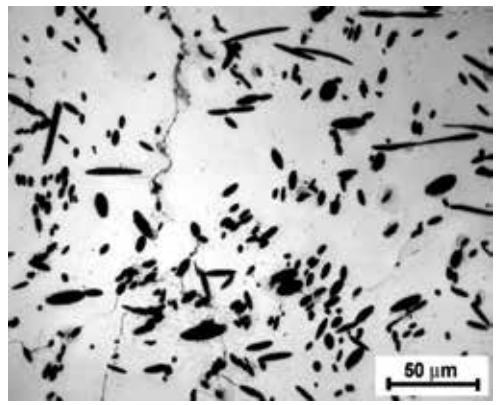

Fig. 6. Light micrograph of Mg-4Lif MMC.

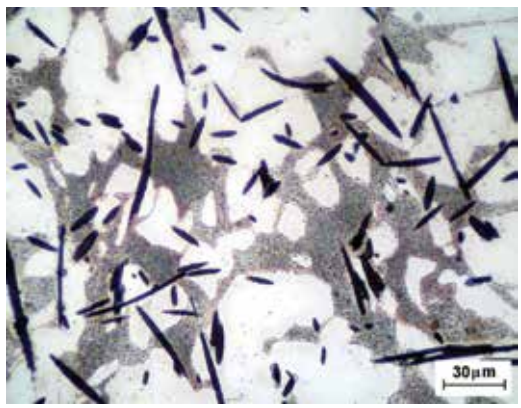

Fig. 7. Light micrograph of Mg-8Lif MMC.

An example of the microstructure of the composite reinforced with particles, prepared by a powder metalurgy method is introduced in Fig. 8. The WE54 alloy (Mg–5%Y–4%RE) was reinforced by 13vol.% SiC particles. The micrograph in Fig. 8 was taken perpendicularly to the extrusion direction. SiC particles are non-uniformly distributed in the matrix; they form in many cases small clusters. The typical feature of the powder metallurgic composites is the small grain size, smaller than the size of the reinforcing particles. The size of sharp bounded more or less uniaxial particles is in this case approximately 9 µm and the grain size in the matrix about 3-4 µm. Light micrographs and scanning electron micrographs showed no pores in the composite and the binding between SiC particles and the matrix was perfect. No defects were found in the vicinity of SiC particles and no chemical reaction at the interface matrix/SiC particles was observed. The same method was used for preparing of the composite based in Mg-8Li alloy with 7 vol. % of SiC. From the micrograph taken from

the cross section, shown in Fig. 9, it is obvious that the matrix microstructure has two phases. The light *a* phase (hcp solid solution of Li in Mg) and the dark β phase (bcc solution with the higher content of Li). The X–ray analysis revealed the relation between both phases as α : β = 55 : 45. As the grain size the mean value of 5±2 μm was taken from both phases. The size of sharp bounded more or less equiaxial SiC particles was approximately 9 μm. The distribution of particles is not uniform; small clusters of SiC particles are present similarly as in the case of other composites prepared in this way.

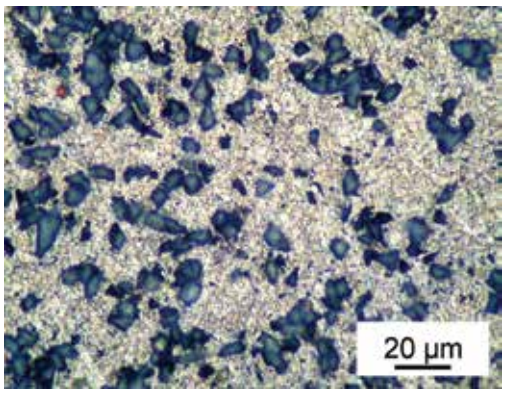

Fig. 8. Light micrograph of WE54/ SiC.

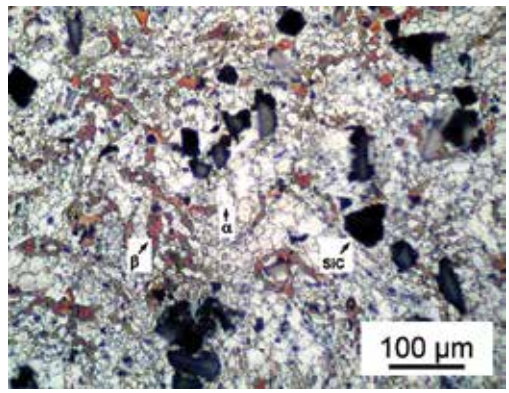

Fig. 9. Light micrograph of Mg-8Li/ SiC.

2. Mechanical properties

Physical properties of composites are affected by properties of individual constituents, by properties of the matrix and the reinforcing phase. The volume fraction, geometry and distribution of reinforcement influence dislocation behaviour and the mechanical properties of composites. Reinforcement may also influence other material properties as the wear resistance or damping capacity. Mechanical properties of composites are determinate not only by properties of matrix and the reinforcing phase, but also with their interaction. It is well established that the microstructure and the mechanical properties of MMCs are strongly affected by the nature of the interfaces between the matrix and the reinforcement. Generally, week bonding between them worsen their properties. Another important factor is the preparation method (powder metallurgy, squeeze casting, etc.).

Composites are inhomogeneous in both elastic as well as plastic properties. While the reinforcing phase remains usually only elastically deformed due to mechanical loading of composites, the plastic deformation occurs in the matrix. Geometry and distribution of the reinforcement have a great influence on the localization of the deformation during straining. Ductility of the composites decreases rapidly with increasing volume fraction of the reinforcement and significantly reduced compared to unreinforced alloys (Lloyd, 1994). The addition of the reinforcing phase increases the yield stress and strength of composite materials. Strengthening in metals and alloys reinforced by fibres or particles were analysed in many papers with the aim to find the correlation between mechanical properties and microstructural characteristics of composites. In spite of many attempts there is no generally accepted model for MMC strengthening. It is probably due to very complex character of the

problem. Many factors and mechanisms play role and synergetic operation of these mechanisms has been not sufficiently studied.
It is not straightforward to propose theoretical model including all deformation mechanisms predicting mechanical properties of given composite. Individual models take into account only some mechanisms and influence of other mechanisms is neglected. However, we can estimate contribution of various factors and to establish the most important mechanism (-s).
Flow stress, necessary for deformation of the composite is affected with different processes and is a superposition off different contributions:

- load transfer from matrix to fibres;
- enhanced dislocation density due to different elasto-plastic and thermal properties; of the matrix and the reinforcing phase;
- Orowan strengthening;
- residual thermal stresses in the matrix;
- grain boundary hardening. Discontinuously reinforced composites usually have finer grains than the unreinforced alloy.

2.1 Hardening mechanisms

Load transfer

For interpretation of the strengthening effect of long fibres embedded homogeneously in a continuous weak matrix and aligned parallel to the stress axis the shear-lag theory was proposed by Cox (Clyne & Withers, 1993). This theory assumes that if no slip occurs on the matrix-fibre interfaces, transfer of the applied load from the matrix to the fibres occurs by the shear stresses acting on the fibre/matrix interface. The presence of the fibre redistributes the stresses and strains within the composite material. The harder reinforcement carries greater part of the stress, while the soft matrix tends to take the greater part of the deformation. This model gives prediction of the axial tensile stress in fibres and the shear stresses at the fibre-matrix interface during axial straining. The shear lag model is based on the simplifying assumption of uniform matrix deformation and, therefore, it yields a very simplified expression for stiffness and strength contribution. Except for the stress transfer from the matrix to the fibres, the shear lag model does not account for the contributions from effects, which are associated with the anisotropic matrix behaviour, resulting in enhanced dislocation density and residual thermal stresses. In the original model of Cox, the load transferred from the matrix to the end faces of the fibre is ignored. However, for short fibre lengths the tensile transfer of load cannot be neglected because the aspect ratio significantly affects the predicted composite strength. In order to overcome this shortcoming of the original model, modifications of the original model have been made by several authors. The contribution of the load transfer when the fibres are aligned parallel to the applied stress is then done by the following equation (Aikin & Christodoulou, 1991):

$$\Delta\sigma_{LT} = \sigma_y\left(\frac{(L+t)A}{4L}\right)f \tag{1}$$

where σ_y is the stress in the matrix, L the fibre length in the stress direction, t the fibre diameter, A the fibres aspect ratio A = L/t, and *f* is the volume fraction of reinforcing fibres in the matrix. From the Eq. (1), it follows that possible influence of particles (with the same

volume fraction) may be weaker due to low value of the aspect ratio A. For equiaxial particles, an increase in the deformation stress due to load transfer may be given by:

$$\Delta\sigma_{LT} = 0.5\sigma_y f \tag{2}$$

Enhanced dislocation density due to thermal mismatch

In MMCs higher dislocation density was observed than in the unreinforced alloy (Arsenault & Fisher, 1983). The thermoelastic properties are different for reinforcement and matrix and therefore temperature changes will cause misfit between them. Typically, the coefficient of thermal expansion (CTE) of the metallic matrix is higher than CTE of the ceramic reinforcement. When the metal matrix composite is cooled from a higher temperature to room temperature, misfit strains occur because of differential thermal contraction at the matrix-reinforcement interface. These strains induce thermal stresses that may be higher than the yield stress of the matrix. Thermal stresses arising from the cooling of the composites from the processing temperature can be partially released by plastic relaxation, i.e. by dislocation generation in the vicinity of the interface. This leads to the formation of a high dislocation density in the matrix, hence to higher yield strength. The density of newly formed dislocations, near reinforcement can be calculated as (Arsenault & Shi, 1986):

$$\Delta\rho_T = \frac{Bf\Delta\alpha\Delta T}{b(1-f)}\frac{1}{t'} \tag{3}$$

where B is a geometrical constant (B = 10 for fibres and B = 12 for particles), b is the magnitude of the Burgers vector of the newly created dislocations, t' is a minimum size of the reinforcing phase particles or fibres, $\Delta\alpha$ is the difference between the two thermal expansion coefficients and ΔT the temperature variation.

When the thermal stresses achieve the yield stress, plastic zones can be formed in the matrix near the interfaces, especially, in the vicinity of fibre ends.

With addition of the reinforcing phase, the geometrically necessary dislocations are generated to accommodate the mismatch of plastic deformation in the matrix. The density of the geometrically necessary dislocations may be expressed as (Ashby, 1993):

$$\Delta\rho_G = \frac{f8\varepsilon_p}{bt'} \tag{4}$$

where ε_p is the plastic strain. The influence of the geometrically necessary dislocations increases with increasing strain.

The strengthening in the matrix is attributed to the deformation resistance induced by the reinforcing phase. According to Taylor relation, the contribution to the total stress due to the presence of dislocations in the matrix may be written:

$$\Delta\sigma_D = \alpha_1\Psi Gb(\Delta\rho_T + \Delta\rho_G)^{1/2} \tag{5}$$

where α_1 is a constant, ψ is the Taylor factor and G is the shear modulus. This higher dislocation density as well as the reinforcement/matrix interfaces can provide high diffusivity paths in a composite. The higher dislocation density would also affect the precipitation kinetics in a precipitation hardenable matrix.

Orowan strengthening

The yield stress is characterized by the state when the matrix plastic flow is developed. Reinforcements (fibres, particles) in the matrix are obstacles for dislocation motion. Therefore, the stress necessary for motion of dislocations in the composite is higher than in the matrix without reinforcement. We consider a similar mechanism as in the case of strengthening by incoherent particles, i.e. Orowan strengthening. The gliding dislocation bows out between inclusions, and then bypasses them leaving a loop around them. The reinforcements also accumulating dislocations during deformation, thus internal stress is generating. Aside from reinforcements, dislocations may overcome these stress fields from dislocation pile-ups. Increase in the yield stress caused by this mechanism, in the first approximation, can be expressed as (Lilholt, 1991):

$$\Delta\sigma_{OR} = \frac{Gb}{\Lambda} + \frac{5}{2\pi} Gf\varepsilon_P , \tag{6}$$

where Λ is the inclusion spacing and ε_p is the plastic deformation.

Grain size refinement

Grain boundaries play important role in strengthening of polycrystalline metals. At low temperatures grain boundaries impede dislocation motion, thus strengthening the material. Impeding dislocation movement increases the stress required to continue the deformation process from grain to grain and hence increase the yield strength of the material. When the deformation rate and grain size are constant during the deformation than the effect of grain boundaries on strengthening is constant. The relation between yield stress and grain size is described by the Hall-Petch equation. Decreasing grain size increases the yield stress. Discontinuously reinforced composites usually have very fine grains, smaller than their unreinforced matrices (Trojanová et al., 2007). The contribution to the yield stress can then be estimated using the relation:

$$\Delta\sigma_{GS} = K_y \left(d_2^{-1/2} - d_1^{-1/2} \right) \tag{7}$$

Residual thermal stresses

At higher temperatures, internal stresses can achieve the yield stress and the composite is plastically deformed only owing to the temperature cycling. Thermal stresses directly in the matrix/fibre interface may be calculated in the simple approximation as (Carreño-Morelli et al., 2000):

$$\sigma_{TS} = \frac{E_f E_m}{(E_f f + E_m (1-f))} f\Delta\alpha\Delta T \tag{8}$$

where E_f and E_m are Young's moduli of the reinforcing phase (fibres or particles) and the matrix, respectively. In a certain distance r from the fibre the thermal stress is lower because it decreases with the distance as $1/r^3$. Thermal stresses arising at higher temperatures can be partially accommodated inducing new dislocations. Residual thermal stresses exist also at ambient temperature and relax very slowly (Miller & Humphreys, 1991). These stresses in the matrix are tensile ones; they may increase the stress necessary for compressive deformation of the composite. Volume-averaged stresses can be estimated by averaging the

local stresses predicted in a representative volume element. Volume-averaged residual stresses in the matrix reach their maximum value (Delannay, 2000):

$$\langle \sigma_m \rangle_{max} = \frac{2}{3}\sigma_y \ln\left(\frac{1}{f}\right)\frac{f}{1-f} \tag{9}$$

Combination of strengthening terms

Several schemes have been proposed for addition of the various strengthening terms. The most commonly accepted are those reviewed by Lilholt (Clyne & Withers, 1993), who differentiates between the range of magnitude of the strengthening mechanisms and their relative strength. In principle, computer models are required to sample statistically the different contributions. Clearly, stress contributions, which act more or less uniformly throughout the matrix must be superimposed linearly, whereas mechanisms of similar strengthening ability, which act unevenly throughout the matrix, are most suitably combined as the root of the sum of the squares.

2.2 Experimental results

Composites based on AS21, AX41, AX61, AZ91, Mg-4Li, Mg-8Li, and WE54 perspective magnesium alloys were investigated. AS21f, AX41f, AX61f and AZ91f alloys were reinforced with short δ-Al_2O_3 (Saffil) fibres. In case of AX41 alloy also Sigrafil C40 short fibres were used as reinforcement. AZ91p, Mg-8Lip and WE54p alloys were reinforced with equiaxed SiC particles. The hybrid composites AS21h and AZ91h were reinforced with short fibres and SiC particles. The type and the volume fraction of the reinforcement are introduced in the Table 1. Specimens for the compression test had cylindrical or rectangular shape. Specimens of composites, reinforced with Saffile fibres, were cut from the bulk with two orientations with respect to the fibre plane: the sample with the fibre plane parallel (||) to the stress axis and perpendicular to the stress axis (⊥).

Alloy	Volume fraction of reinforcement. %			Notation
	Saffil	SiC	Sigrafil	
AS21	30	–	–	AS21f
AS21	5	15	–	AS21h
AX41	13	–	–	AX41f
AX41	–	–	25	AX41S
AX61	26	–	–	AX61f
Mg-4Li	10	-	-	Mg-4Lif
AZ91	20	–	–	AZ91f
AZ91	15	5	–	AZ91h
AZ91	–	10	–	AZ91p
Mg-8Li	–	7	–	Mg-8Lip
WE54	–	13	–	WE54p

Table 1. Volume fraction of reinforcements in composites investigated.

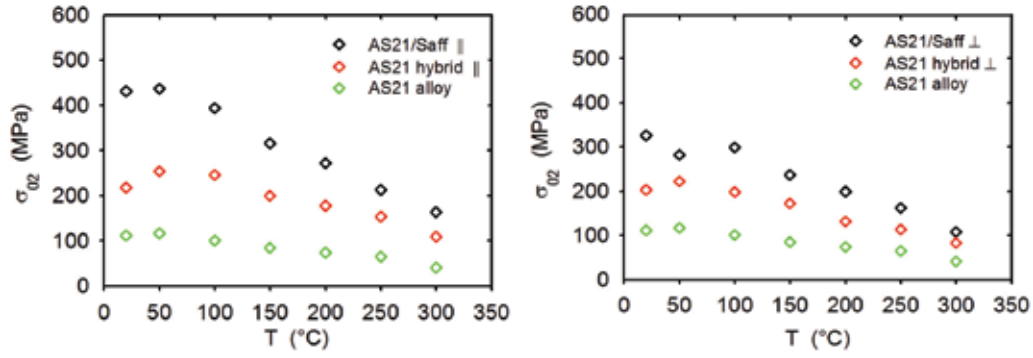

(a) (b)

Fig. 10. Comparison of the yield stress σ_{02} for AS21f, AS21h MMCs and the matrix alloy AS21 in parallel orientation (a) and perpendicular orientation (b)

Ceramics fibres and particles significantly influence the mechanical properties of composites. The flow stress and the maximum stress are higher for composites than those for unreinforced alloy. The influence of the reinforcing phase on the yield stress is well apparent from figure 10 and for the maximum stress in figure 11 where the characteristic stresses for AS21h, AS21f and unreinforced AS21 alloy are introduced depending on temperature. Anisotropy in the mechanical properties of fibre reinforced composites was found. Parallel orientation of the fibres plane in composites markedly increases characteristic stresses. This fibres impact decreases with increasing temperature. It can be seen the major effect of fibres in comparison with particles. For composites reinforced with equiaxial particles the load transfer plays marginal role. Anisotropy of the hybrid composite is lower but not negligible.

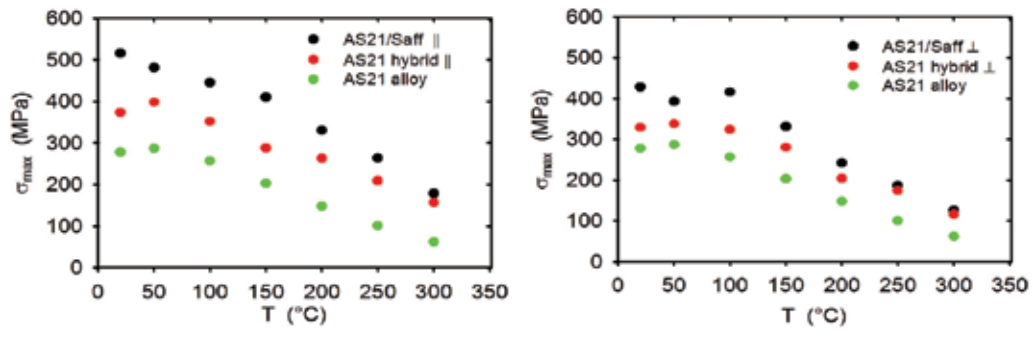

(a) (b)

Fig. 11. Comparison of the maximum stress σ_m for AS21f, AS21h MMCs and the matrix alloy AS21 in parallel orientation (a) and perpendicular orientation (b)

The main disadvantage in the mechanical properties of MMCs is their limited ductility. The elongation decreases rapidly with the addition of reinforcing phase. The quality of the interface between the particles and the matrix, the particle size, distribution and volume

fraction influence the composite ductility. Higher ductility for a given volume fraction of the particles is possible to achieve with (Lloyd, 1994):

- uniform particle distribution;
- using fine (<10 μm) particles;
- high interfacial strength;
- controlling the particle shape;
- using of ductile matrix.

Various strengthening mechanisms which can operate in MMCs were described in section 2.1. Individual contributions to the strengthening for composites AS21f, AX41f, Mg-4Lif, AX41S, AX61f, AZ91f, AZ91h, AZ91p, Mg-8Lip a WE54p, calculated using constants introduced in Table 2 and 3, are summarized in Table 4. Contributions were evaluated at room temperature in the vicinity of the yield stress (plastic strain ε_p = 0.002). The combination of individual strengthening terms gives the increase in the yield stress with addition of the reinforcing phase into the matrix. In case of fibre reinforced end hybrid composites the contributions were calculated for parallel fibre orientation. Difference between two orientations is in the load transfer. For fibres oriented perpendicular to the compression axis the transfer of the load from the matrix to the fibres is not effective.

From Table 4 it follows that the load transfer ($\Delta\sigma_{LT}$), in which the part of the external load within the matrix is transferred to reinforcement, is important strengthening mechanism in the composites reinforced by short fibres (see also Trojanová et al., 2007, 2008). On the other hand, this mechanism is in the particle reinforced composites marginal. From the Eq. (1), it follows that possible influence of particles (with the same volume fraction) may be weaker due to low value of the aspect ratio A. Enhanced dislocation density may also significantly increase the yield stress in the composites reinforced with short fibres.

AS21	AX41	AX61	AZ91	Mg-4Li	Mg-8Li	WE54	Saffil	SiC
26	25	25	26	26	30	26	26	6.6

Table 2. Linear thermal expansion coefficients $\alpha \times 10^6$ in K^{-1} used for calculations of values in Table 4.

K_y (*hcp*) ($MPam^{-3/2}$)	K_y (bcc) ($MPam^{-3/2}$)	b (m)	G (GPa)	Taylor factor	α_1
0.28	0.2	3.2×10^{-10}	17	6	0.35

Table 3. Constants used for calculations of values in Table 4.

The higher dislocation density is a consequence of the difference between the thermal expansion coefficients of both phases. Enhanced dislocation density was a common feature for all non-deformed composites. Fig. 12 is showing high dislocation density in as-received composites AS21f and WE54p. As it follows form the Table 4, the Orowan mechanism play only marginal role for the composites strengthening. Orowan strengthening for reinforcing particles is not significant for the selected composites, because the particles are coarse and the inter-particle spacing exhibits several μm (see also Száraz et al., 2007).

The main hardening mechanism seems to be the small grain size of the materials prepared by the powder metallurgical route. Smaller matrix grain size also reduces twinning which is important deformation mode in the coarse grained hcp materials. The grain size refinement does not play important role in the strengthening of fibre reinforced composites where the load transfer mechanism plays the significant role.
Thermal stresses arising due to a high difference between the thermal expansion coefficients can be partially accommodated by dislocation generation in the matrix. Residual stresses exist also at ambient temperature and they relax very slowly. Residual thermal stresses have at ambient temperature tensile character and they may increase the stress necessary for compressive deformation of the composite. Maximum values of the volume-averaged residual stresses in the matrix are introduced in Table 4. The increase in the composite yield strength was estimated as a linear combination of individual strengthening terms. Comparison with the experimental result shows that the theoretically predicted values of σ_{02} introduced in table 4 are in very good agreement wit the experimental measured values.

Composite	$\sigma_{02alloy}$ (MPa)	$\Delta\sigma_{LT}$ (MPa)	$\Delta\sigma_{D}$ (MPa)	$\Delta\sigma_{OR}$ (MPa)	$\Delta\sigma_{GS}$ (MPa)	$\langle\sigma_m\rangle_{max}$ (MPa)	σ_{total} (MPa)	$\sigma_{02exp.}$ (MPa)
AS21f	112	136	84	8	12	39	391	432
AX41f	68	36	51	2	15	14	186	168
AX41/S	83.5	51.5	57.3	2	17	25.7	237	248
AX61f	84	89	79	7	23	27	309	322
Mg-4Lif	69	36	48	3	17	12	185	251
AZ91f	116	94	55	5	25	31	326	324
AZ91h	116	32	38.4	5	15	31	237.4	267
AZ91p	116	9	24	0	96	26	271	222.5
Mg-8Lip	85	3	17	0	101	13	219	198
WE54p	140	11	28	4	52	28	263	246

Table 4. Contributions of various strengthening mechanisms to the yield stress of the selected composites at room temperature.

It is well established that the microstructures and the mechanical properties of MMCs are strongly affected by the nature of the interfaces between the matrix and the reinforcement. (Models are constructed for perfect bonding between the reinforcement and the matrix.) Moreover, individual models take into account only some strengthening mechanisms and influence of other mechanisms are neglected. Nevertheless, we can estimate contribution of various factors and establish the most important mechanism.

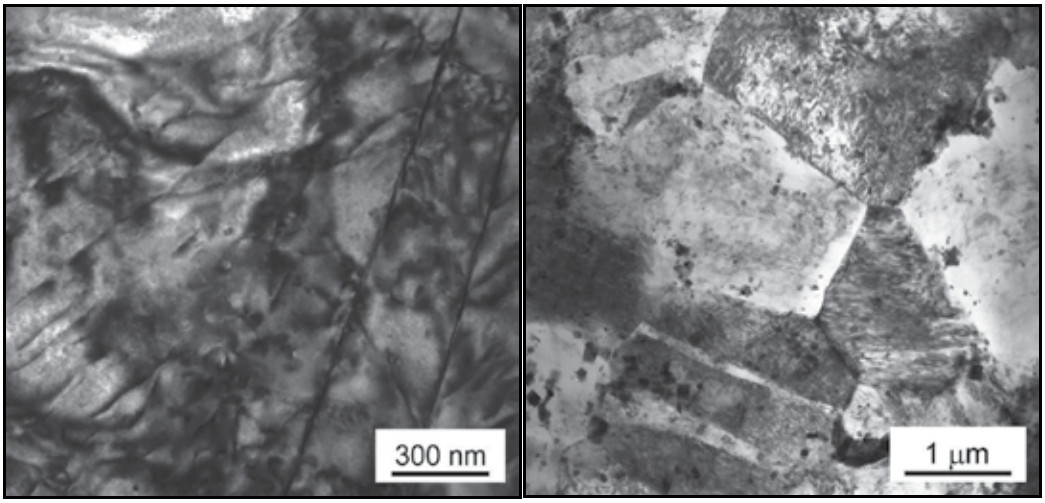

(a) (b)

Fig. 12. TEM micrographs showing high dislocation density in non deformed AS21f (a) and WE54p (b) samples.

Concluding remarks

Ceramics fibres and particles significantly influence the mechanical properties of composites. The flow stress and the maximum stress are higher for composites than those for unreinforced alloy.

Investigations revealed that the high dislocation density is a common feature for both non-deformed and deformed composites. Dislocations in the matrix of the non-deformed composites were induced during the fabrication process due to the large difference in the CTE of the matrix and ceramic reinforcement.

The main hardening mechanism in the composites strengthened with short fibres is the load transfer in which the part of the external load within the matrix is transferred to reinforcement. An increase in the dislocation density plays also important role.

High strength of the composites prepared by powder metallurgy may be attributed to the small grain size. Smaller matrix grain size also reduces twinning which is important deformation mode in the Mg alloys.

Thermal stresses arising due to a big difference between the thermal expansion coefficients may be partially accommodated by dislocation generation in the matrix. Tensile residual stresses exist also at ambient temperature. They have tensile character and in compression test increase the stress necessary for the plastic deformation. Other possible mechanisms play in strengthening only a marginal role.

3.2 High temperature properties

From Figs. 10 and 11 it can be seen that the strength of composites decreases with increasing temperature. The difference between the yield stress and the maximum stress decreases with increasing temperature. The stress-strain curves are very flat and the work-hardening rate $\vartheta = (d\sigma/d\varepsilon)$ exhibits small values. Physical processes responsible for plastic flow are similar to those occurring in creep.

Strain hardening in the matrix

The deformation behaviour of the composite can be explained under assumption that the macroscopic work-hardening rate is a result of two microscopic effects: storage and annihilation of dislocations. We should consider processes of storage of dislocations at both dislocation forest and non-dislocation obstacles (e.g. incoherent second phase particles, dispersoids, fibres). Assuming that the particle size and the spatial distribution of particles remain unchanged during deformation process we may consider two hardening and two softening processes. Lukáč and Balík formulated a constitutive model (Lukáč & Balík, 1994) giving the stress dependence of work hardening rate in the form

$$\vartheta = d\sigma / d\varepsilon = A/(\sigma - \sigma_y) + B - C(\sigma - \sigma_y) - D(\sigma - \sigma_y)^3 \quad (10)$$

where σ_y is the yield stress, A and B are parameters determined by impenetrable obstacles and forest dislocations, respectively, C and D express the dislocation annihilation due to cross slip and dislocation climb. While parameters A and B are virtually independent of temperature, C and D parameters are strongly temperature and strain rate dependent; increasing with increasing temperature and/or decreasing strain rate. The observed stress-strain curves can be correlated with Eq. (10). The analysis was performed for ZE41 alloy reinforced with 20 vol.% of Saffil fibres (Trojanová et al. 2004). Estimated parameters are shown in Table 5.

Temperature	A (MPa^2)	B (MPa)	C	D (MPa^{-2})	σ_y (MPa)	σ_{02} (MPa)	R^2
RT	114439	3078	33.12	4.43e-10	253	254	0.988
50 °C	164641	3984	42.07	6.28e-6	243	236	0.974
100 °C	143212	1106	22.67	1.85e-4	237	241	0.992
150 °C	334442	1164	93	9.18e-3	163	210	0.998

Table 5. Fit parameters in the equation (10).

From Table 5 it follows that the main dislocation obstacles are the impenetrable obstacles. The development of the dislocation density increases the storage probability of dislocations. With increasing temperature the storage probability should decrease. This could cause a decrease in the parameter B with temperature, which is indeed observed. The parameter C increases with temperature, which indicates that cross slip becomes a significant recovery process at higher temperatures. The parameter D increases with increasing temperature, which is expected in the case of climb. Similar results were found also in the case of other magnesium composites prepared by squeeze casting and gas pressure infiltration. Changes in the forest dislocation density (the density of dislocations in non-basal planes) can be expected with increasing temperature.

Cross slip recovery process

The variation of the flow stresses with increasing temperature may be accounted for by increasing activity of cross slip of dislocations. The values of the maximum stress could be, therefore, considered as characteristics of the cross slip activity. The maximum stress should then decrease with increasing temperature in similar way as the stress necessary for cross slip, i.e. the temperature dependence may be expressed by the following equation:

$$\ln \sigma_{max} = K_0 - K(\gamma, \dot{\varepsilon})\, T \tag{11}$$

where K_0 is a constant and $K(\gamma, \dot{\varepsilon})$ is a function of the stacking fault energy γ and the strain rate $\dot{\varepsilon}$. Schematic representation of this mechanism is shown in Fig. 13a. Screw dislocations may cross slip from one basal plane through a non-basal plane (prismatic or pyramidal) and continue the movement in the parallel slip basal plane. The cross-slipped dislocations may eventually annihilate with the dislocations having the opposite sign.

(a) (b)

Fig. 13. Schematic diagram of cross slip of dislocation in the vicinity of a fibre (a) and dislocation reaction and climb of dislocations (b).

Local climb of dislocations

The moving dislocations cannot cut the fibres (or particles). The dislocations may pass the fibres leaving loops around the fibres. This athermal passing mechanism is similar to the Orowan mechanism. Dislocation pile-ups at the fibres can act as stress concentrators. Screw dislocation components locally cross slip forming superjogs having a height of about fibre diameter and at higher temperatures, edge components are able to climb. Both may then annihilate in neighbouring slip planes. Annihilation of dislocations may also be supported by diffusion of vacancies in the thin layer at the matrix-fibre interface. On the other hand, dislocations in the basal and pyramidal planes may interact forming the sessile dislocation according to reaction

$$\frac{1}{3}\left\langle 2\bar{1}\bar{1}3\right\rangle_{(2\bar{1}\bar{1}2)} + \frac{1}{3}\left\langle \bar{2}110\right\rangle_{(0001)} \rightarrow \left\langle 0001\right\rangle . \tag{12}$$

The resulting dislocation is not able to glide in the basal as well as pyramidal plane. Such dislocations may climb along the fibres as it is illustrated in Figure 13b. Local climb of dislocations may reduce the work hardening in the matrix and is very probably an important recovery process. With increasing temperature, the plastic strain rate is also increasing (diffusion increases with temperature exponentially). Accordingly, this mechanism influences the deformation behaviour of the composite.

3. Stres relaxation tests

Internal stress in the matrix

In alloys, the applied stress σ necessary for deformation of any polycrystalline material can be divided into two components: the internal (athermal) stress σ_i and the effective stress σ* i.e. one can write

$$\sigma = \sigma_i + \sigma^*. \tag{13}$$

In a composite the athermal component includes the stress which is necessary for deformation due to the load transfer σ_{LT} and σ_i^D the stress necessary for generation of dislocations, their movement and storage. The flow stress σ_{LT} necessary for composite deformation due to the load transfer which is done by the equation (1). The internal stress σ_i^D resulting from long-range internal stresses impeding the plastic flow is done as

$$\sigma_i^D = \alpha_1 G b \rho_t^{1/2}, \tag{14}$$

where α_1 is a constant describing interaction between dislocations and ρ_t is the total dislocation density. The effective shear stress, σ^*, acts on dislocations during their thermally activated motion when they overcome short range obstacles.

The internal stress increases due to dislocation storage in the matrix, $\sigma_i^D \propto \rho_t^{1/2}$, because the total dislocation density ρ_t increases due to two reasons: (a) generation of thermal dislocations and (b) the presence of dislocations geometrically necessary.

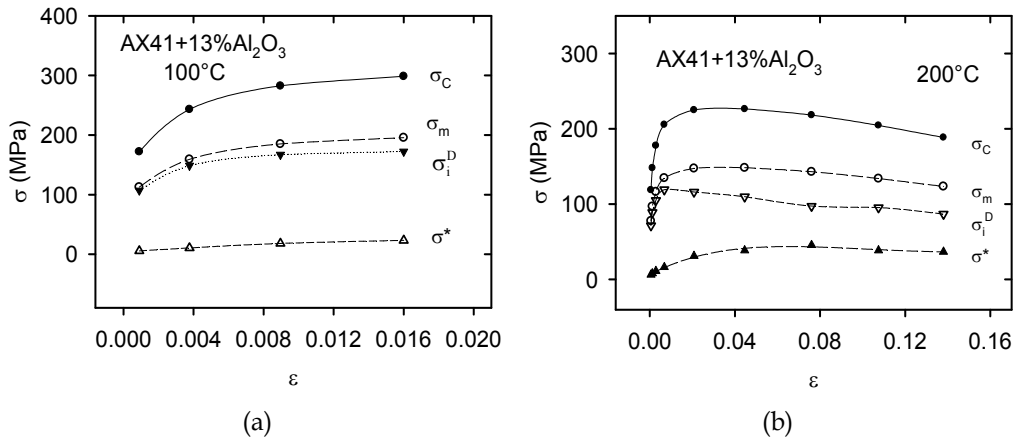

Fig. 14. Part of the true stress-true strain curves obtained at 100 °C (a) and 200 °C (b). Points indicate the stresses at which the SR tests were performed.

The stress relaxation technique is very useful method to estimate the internal stress component and parameters of the thermally activated processes. In a stress relaxation (SR) test, the specimen is deformed to a certain stress σ_0 and then the machine is stopped and the stress is allowed to relax. The stress decreases with the time t. The specimen can be again reloaded to a higher stress (load) and the SR test may be repeated. The time derivative $\dot{\sigma} = d\sigma/dt$ is the stress relaxation rate and $\sigma = \sigma(t)$ is the flow stress at time t during the SR. The stress components (σ_i^D,σ^*) were estimated from the stress relaxation curves using the Li equation (Li, 1967). The SR curves were fitted to the power law function in the form: $\sigma - \sigma_i = [a(m-1)]^{\frac{1}{1-m}} (t + t_0)^{\frac{1}{1-m}}$, where a, t_0 and m are fitting parameters. A part of the stress strain-curve for AX41+13%specimens deformed at 100 °C is shown in Fig. 14a. Full circles depict points at the stress-strain curve where the stress relaxation tests were performed.

Blank circles indicate the matrix stress and full and blank triangles designate the internal stress, σ_i^D, and the effective stress, σ^*, respectively. It is obvious that the internal stress, σ_i^D, is a substantial contribution to the matrix stress, σ_m. A similar analysis was performed at 200 °C and introduced in Fig. 14b. As it follows form Fig. 14b the internal stress increases with strain only in the very beginning of deformation; for strains higher than about 2%, it decreases with strain while the effective stress increases continuously up to a true strain of 8%. For higher strains, the effective stress remains constant, while the applied stress is decreasing. Comparison of the internal stress estimated for the AX41 alloy and that for the composite with the AX41 matrix reinforced with the 13% of Saffil fibres is introduced in Fig. 15. Subtracting the value of the load transfer, it can be seen that the internal stress level in the composite is higher than that in the unreinforced alloy. The difference exhibiting 64.5 MPa is due to a higher density of thermal dislocations (ρ_T=1.78x10^{13} m^{-2}) and dislocations geometrically necessary (ρ_G=1.4x10^{13}m^{-2}). Corresponding stress $\Delta\sigma_\rho = \alpha\psi Gb(\Delta\rho)^{1/2}$= 64.4 MPa.

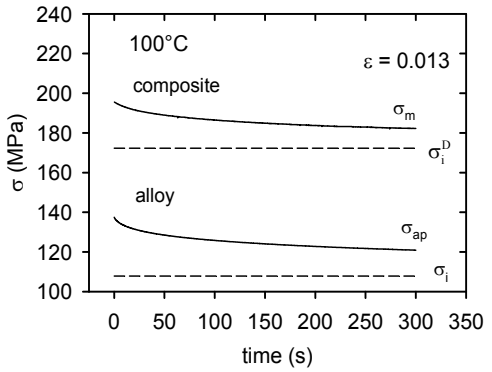

Fig. 15. A comparison of the dislocation internal stress estimated at 100 °C and at a strain of 0.013 for the composite and the monolithic alloy.

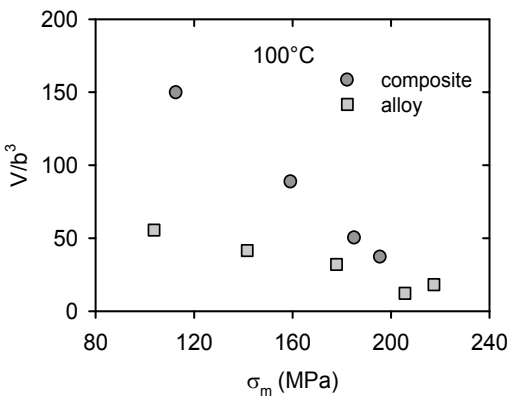

Fig. 16. Activation v volume in b^3 depending on the stress in the matrix estimated for the composite and the monolithic alloy.

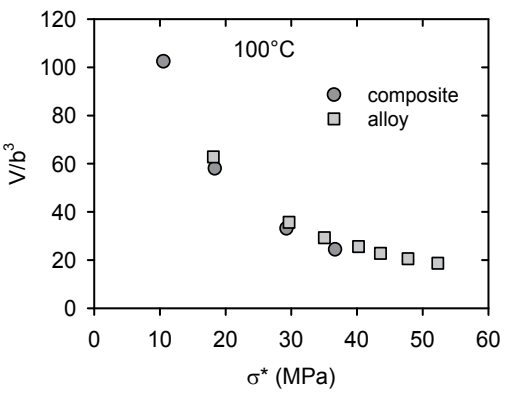

Fig. 17 The plot of the activation volume in b^3 against the effective stress estimated at 100 °C for the composite and the monolithic alloy.

Thermal activation

The stress decrease with the time during the SR test can be described by the well known Feltham equation (Feltham 1963):

$$\Delta\sigma(t) = \sigma_0 - \sigma(t) = \alpha\ln(\beta t+1), \tag{15}$$

where α and β are parameters. The dislocation activation volume V is given as $V=kT/\alpha$. The values of the apparent activation volume V_{app} were estimated according Eq.15 using stress decrease in the matrix $\sigma_m = \sigma_{app} - \Delta\sigma_{LT}$. As usual, the values of the activation volume were divided by b^3.

The values for samples deformed at 100 °C are plotted against the matrix stress σ_m in Fig. 16. For comparison, the values of the activation volume (divided by b^3) estimated for unreinforced alloy at temperature of 100 °C are also introduced. If the same values of the activation volume are plotted against the effective (thermal) stress σ^* all data lies on one line - "master curve" (Fig. 17). Kocks et al. (Kocks et al. 1975) suggested an empirical equation between the Gibbs enthalpy ΔG and the effective stress σ^* in the following form:

$$\Delta G = \Delta G_0\left[1-\left(\frac{\sigma^*}{\sigma_0^*}\right)^p\right]^q \tag{16}$$

where ΔG_0 and σ_0^* are Gibbs enthalpy and the effective stress without thermal activation, p and q are phenomenological parameters reflecting the shape of a resistance obstacle profile. The possible ranges of values p and q are limited by the conditions $0 < p \leq 1$ and $1 \leq q \leq 2$. Ono (Ono, 1968) and Kapoor (Kapoor et al. 2002), suggested that Eq (16) with $p = 1/2$, $q = 3/2$ describes a barrier shape profile that fits many predicted barrier shapes. Thermodynamics generally defines the activation volume as a derivative of the Gibbs potential with respect to the effective stress, i.e. $V= -(d\Delta G/d\sigma^*)_T$, then the equation (16) ca be rewritten as

$$V = \frac{\Delta G_0 pq}{\sigma_0^*}\left[1-\left(\frac{\sigma^*}{\sigma_0^*}\right)^p\right]^{q-1}\left(\frac{\sigma^*}{\sigma_0^*}\right)^{p-1}. \tag{17}$$

The values of the activation volume lie at the curve given by Eq (17), as it is obvious from Fig. 17. The activation enthalpy $\Delta H = \Delta G - T\Delta S$ (ΔS is the entropy) is done by $\Delta H = -TV(d\sigma/dT)$. The differential coefficient $d\sigma/dT$ was estimated from the temperature dependence of the yield stress in the temperature range from at 200 °C to be 0.159 MPa/K. The activation enthalpy calculated for 200 °C gives (0.95 ± 0.05) eV. Similar value of 0.96 eV has been reported for AX41 alloy (Trojanová et al. 2007). A rapid decrease of the flow stress at elevated temperatures indicates the possible occurrence of recovery process(-es) that is usually thermally activated. The values of the activation volume and the activation enthalpy may help to identify this thermally activated process. The activation of the prismatic slip and subsequent annihilation of the dislocation segments with the opposite sign have been found as the main reason for the observed internal stress decrease. The double cross slip and the thermally activated glide of the <c+a> dislocations in pyramidal planes should be taken into account. Because the values of the activation volume and activation energy are very

similar to that estimated for monolithic AX41 alloy, we can conclude that the thermally activated processes are the same.

4. Fracture properties

The observation of fracture surfaces may help to identify operating fracture mechanism (-s) of constituents at different temperatures and the bonding abilities of their interfaces. The fracture properties were studied on three materials: AZ91f (20vol.% Saffil), AZ91h (5% Saffil, 15% SiC, 3%Si) and AZ91p (10%SiC, 3% Si). The investigation was concentrated on the U-notch side of the fracture surface, where bending stresses are assumed to be generated during the impact testing. Specimens were fractured predominantly in a brittle manner even at 300 °C. The measured fracture energies were almost identical for all temperatures tested (about 1-2 J). This implies that on one hand the composite fibres/particles interfaces contribute to the stiffness, and on the other hand they serve as the crack initiators.

4.1 Fracture surfaces

AZ91f samples were slowly loaded in the three points bending with the aim to see the stable crack opening. The fracture mechanism is well seen in the scanning electron micrographs shown in Fig. 18a,b. The fibres plane is oriented perpendicular to the fracture surface. Fibres were pulled out on the fracture surface while in the side plane secondary cracks are visible. They cut the fibres lying perpendicular to the fracture surface and go around the other. The matrix (γ phase) is plastically deformed. The dimple morphology of the matrix is shown in Fig. 19a together with the bended fibres pulled out from the matrix. The similar dimple morphology of the fracture surface remained also after bending at 100 °C as it is demonstrated in Fig. 19b.

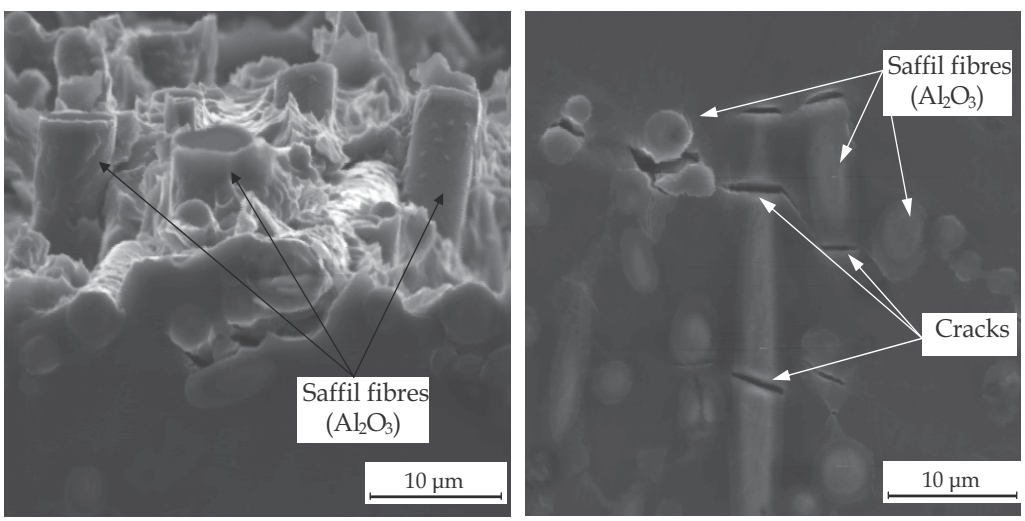

(a) (b)

Fig. 18. Detail of the fracture surface of AZ91f sample (a) and the secondary cracks at the side plane (b).

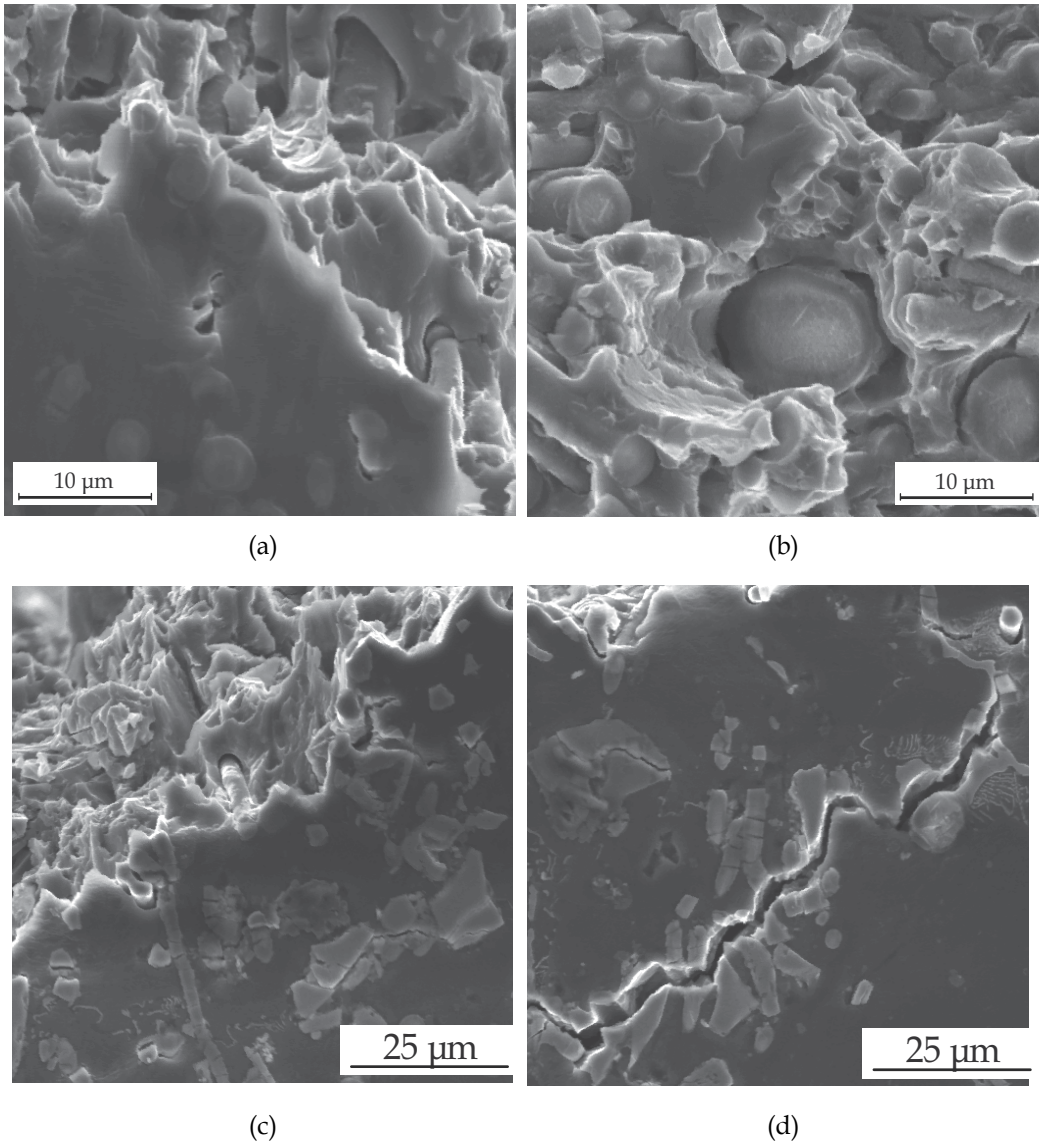

Fig. 19. Dimple morphology of the fracture surface of AZ91f sample (a) and fine dimples observed after bending at 100 °C (b). The crack formation in AZ91h sample (c). Reinforcing particles and fibres are the preferential places for the crack formation (d).

The formation of the fracture profile in the slowly bended AZ91h sample at ambient temperature is shown in Fig. 19c. Secondary cracks are created remote of the fracture surface in the vicinity of SiC particles and partially also Saffil fibres. The preferential places for the cracks formation are clusters of the reinforcing phase particles/fibres. Wang et al. studying the fracture properties of AZ91/SiC particles prepared by stir casting found that interface and particle segregation within the intergranular regions have their significant effect on thefracture behaviour of AZ91/ SiCp composite (Wang et al., 2007).

The matrix is deformed only slightly as it is demonstrated in Fig. 19d. Character of fracture surfaces and breakage of phases were almost identical for both composites AZ91f and AZ91h in the whole temperature range from 25 to 300 °C. During crack propagation, reinforcements serve as inhibitor of plastic deformation in the matrix. Moreover, the reinforcements are a source for formation of dimples and give originate to cracks. Separation at the matrix/reinforcement interface indicates weak bonding in the investigated temperature range (25-300 °C).
In addition, cleavage fracture of reinforcements was observed at lower temperatures (at RT and 100 °C). An increase of temperature causes also increase of plastic strain, which is responsible for debonding of reinforcements. The main features of the fracture surfaces of AZ91p samples in the investigated temperature range were similar: brittle fracture of SiCp and Mg_2Si phases (see Figs. 20) and slightly ductile fracture of the δ phase. Cracks were mostly initiated at the Mg_2Si phase (Fig.20).

4.2 Fracture mechanisms

Fracture of the γ phase in the AZ91f composite is transcrystalline ductile with dimples morphology with plastically transformed walls. The shape of walls depends on the orientation of Saffil fibres on fracture surface. At and above 200 °C slip bands were observed on the walls - depicted in Fig. 21 with the arrow, which correspond with the activity of non-basal dislocation glide. The γ phase is fractured by the transcrystalline cleavage mechanism (Fig. 22). Fine secondary microcracks were observed at temperatures between RT and 300 °C. Secondary microcracks are a result of the multiaxial plastic deformation in the matrix. Additionally, at and above 200 °C, complement fracture mechanism of γ phase arises simultaneously with transcrystalline cleavage mechanism; debonding at the interface γ phase/δ phase as well as γ phase/discontinuous precipitates occur and indicate interphase cleavage fracture. On the contrary, discontinuous precipitates were failed by the transcrystalline ductile fracture with the fine dimples morphology in the whole investigated temperature range.
In the AZ91p samples, coarse dendritic crystals and Chinese script particles failed by the transcrystalline cleavage fracture at all temperatures tested. The interface between the γ phase and the Mg_2Si is unlikely to be coherent since the lattice constants and the crystal structures are different. In spite of this, the bonding strength of the matrix/Mg_2Si interface is high as documented in Fig. 20a by comparison of the opposite surfaces of the fractured specimen. It appears that the development of crack within Mg_2Si coarse dendrites is easier than the debonding at the interface. The strong bonding between matrix and Mg_2Si may be a result of an "in situ" formation. Plastic deformation of the matrix and/or high velocity of main crack propagation may result in a large number of secondary cracks in the Mg_2Si coarse dendritic crystals as observed in Fig. 20. The second main contribution to the crack propagation comes from SiC particles. Fracture mechanisms did not change throughout the temperature range RT to 300 °C. In comparison with Mg_2Si, SiC particles cracks are developed mainly by the delamination of interfaces with the Mg matrix. However, trancrystalline cleavage fracture was observed as well.
Minor contributions to the crack propagation are from the γ phase, the γ phase and the discontinuous precipitates (Fig. 23). The transcrystalline cleavage of the γ phase with secondary microcracks and the transcrystalline ductile fracture with the fine dimples morphology of the discontinuous precipitates (γ+δ) were observed in the entire investigated

temperature range. The nature of γ phase fracture varied with temperature (Fig.23a,b) but this change was not significant; generally the higher the temperature the more plastic fracture surface, which corresponds with anticipated activity of other slip systems at higher temperatures (~ 200 °C).

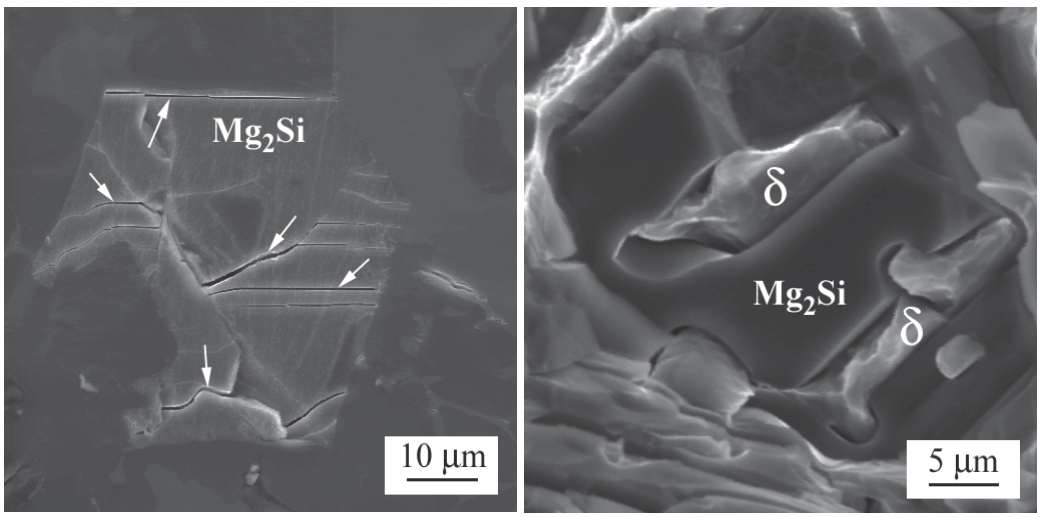

(a) (b)

Fig. 20. Microcracks (arrows) between matrix and SiC particles near the fracture surface in AZ91p sample after impact test at RT (a), brittle fracture of SiCp after test at 300 °C (b).

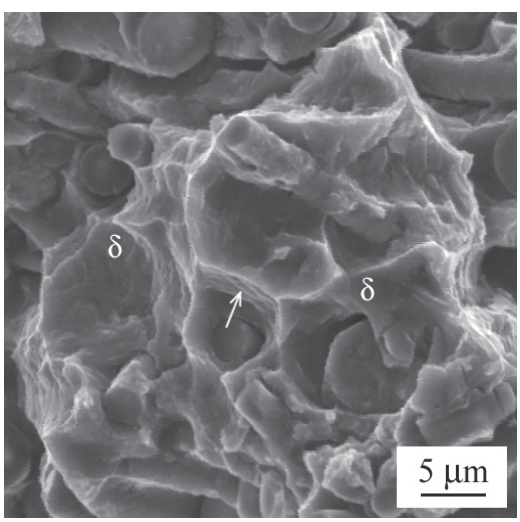

Fig. 21. Fracture surface of AZ91f after impact test at 300 °C.

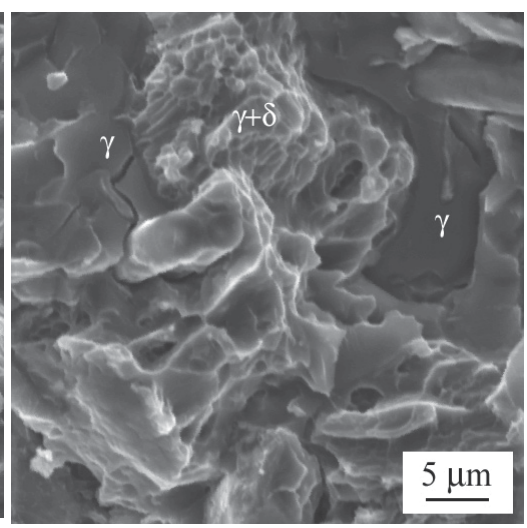

Fig. 22. Fracture surface of AZ91h sample after impact test at 200 °C.

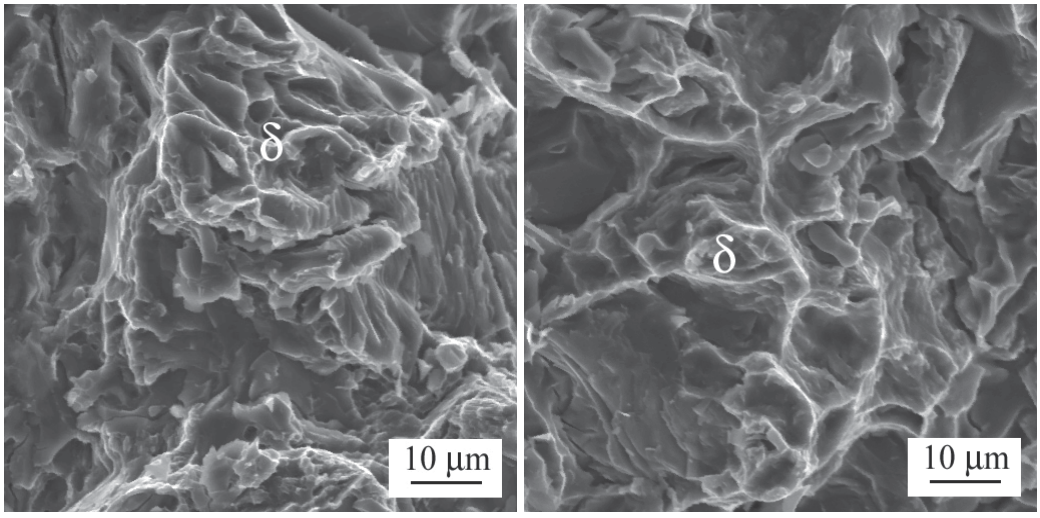

(a) (b)

Fig. 23. Comparison of γ phase breakage at RT (a) and 300 °C (b), mechanism for both is transcrystalline ductile fracture with plastically transformed walls.

The fracture mechanism was identified as transcrystalline ductile with dimples morphology accompanied by plastically transformed walls. As temperature increased the walls become higher and the dimples spread out. However, in comparison with AZ91f and AZ91h samples the plasticity of walls with temperature change is not as significant as in the case of AZ92f and AZ91h composites. Furthermore, slip bands were not observed on the walls at higher temperatures. The most probable reason for such behaviour is that brittle components present in considerable amount impede the plastic straining of the relatively ductile matrix. The increased plasticity of the matrix with temperature rise is in agreement with the deformation behaviour.

Concluding remarks

The Mg alloys based composites studied is very brittle at all temperatures as proved by impact tests. The fracture mechanism of Mg-MMCs was controlled by fiber/matrix interface and fiber breakage (see also Hu et al., 2010). The Mg matrix exhibits a slightly plastically deformed fracture surface at and above 200 °C.

5. Acknowledgements

The authors dedicate this paper to Prof. RNDr. František Chmelík, CSc, on the occasion of his 50th birthday. This work received a support from the Ministry of Education, Youth and Sports of the Czech Republic by the project MSM 0021620834.

6. References

Aikin, Jr. R.M. & Christodoulou, L. (1991). The role of equiaxed particles on the yield stress of composites. *Scripta Metall. Mater.*, 25, 1991, 9-14. ISSN: 1359-6462.

Arsenault, R.J. & Fisher, R. (1983). Microstructure of fiber and particulate SiC in 6061 Al composites. *Scripta Metall.*, *17*, 67-71, ISSN: 1359-6462

Arsenault, R.J. & Shi, N. (1986). Dislocation generation due to differences between the coefficients of thermal expansion. *Mater. Sci. Eng.*, *81*, 175-187. ISSN: 0254-0584.

Ashby, M.F. (1993). Criteria for selecting the components of composites. *Acta Metall. Mater.*, *41*, 1313-325. ISSN: 1359-6454.

Carreño-Morelli, E.; Urreta, S.E. & Schaller, R. (2000). Mechanical spectroscopy of thermal stress relaxation at metal–ceramic interfaces in aluminium-based composites. *Acta Mater.*, *48,* 4725-4733. ISSN: 1359-6454.

Clyne, T.W. & Withers, P.J. (1993). *An Introduction to Metal Matrix Composites*, Cambridge Univ. Press, Cambridge. ISBN 0-521-41808-9.

Delannay, F. (2000). *Thermal stresses and thermal expansion in MMCs*. pp. 341-369. In: Clyne T.W. Ed.. Comprehensive composite materials, Vol. 3. Amsterdam, Elsevier 341. ISBN:903761-04-2.

Dieringa, H.; Hort, H. & Kainer, K.U. (2005) The "AZo Journal of Materials Online"*AZojomo* 1 1–10; DOI:10.2240/azojomo0117.
http://www.azom.com/details.asp?ArticleID=2984,

Feltham, P. (1963) Stress relaxation in magnesium at low temperatures. *Phys. Stat. Sol.* 3. 1340–1346. ISSN: 1862-6300.

Kapoor, R.; Wadekar, S.L. & Chakravartty, J.K. (2002). Deformation in Zr-1Nb-1Sn-0.1 Fe using stress relaxation technice. *Mater. Sci. Eng. A,* 328, 324–333. ISSN: 0921-5093.

Kocks, U.F.; Argon, A.S. & Ashby, M.F. (1975). Thermodynamics and kinetics of slip. *Progr. Mater. Sci.*, 19, 1–288. ISSN: 0079-6425.

Lilholt, H. (1991). Aspects of deformation of metal matrix composites. *Mater. Sci. Eng. A*, 161-171. ISSN: 0921-5093.

Lloyd, D.J. (1994). Particle-reinforced aluminum and magnesium matrix composites. *Int. Mater. Rev. 39* 1-23. ISSN: 0950-6608.

Li, J.M.C. (1967) Dislocation dynamics in deformation and recovery *Canad. J. Appl. Phys.* 45 493–509. ISSN : 0008-4204..

Miller, W.S. & Humphreys, F.J. (1991). Strengthening mechanism in particulate metal matrix composites. *Scripta Metall. Mater.,* 25, 33-38. ISSN: 1359-6462.

Ono, K. (1968). Temperature dependence of dispersed barrier hardening. *J. Appl. Phys.* 39, 1803–1806. ISSN: 0021-8979.

Z. Száraz, Z. Trojanová, M Cabbibo, M. & Evangelista, E. (2007). Strengthening in a WE54 magnesium alloy containing SiC particles. *Mater. Sci. Eng. A, 462*, 225-229. ISSN: 0921-5093.

Lukáč, P. & Balík, J. (1994). Kinetics of plastic deformation. *Key Engn. Mater*., 97-98, 307-322. ISBN: 0-87849-687-4.

Trojanová, Z.; Drozd, Z.; Kúdela, S.; Száraz, Z. & Lukáč, P. (2007). Strengthening in Mg-Li matrix composites. *Comp. Sci. Tech.,* 67, 1965-1973. ISSN: 0266-3538 .

Trojanová, Z.; Gärtnerová, V.; Drozd, Z.; Száraz, Z. & Lukáč, P. (2008). Short fibres and particles impact on compressive behaviour of an AZ91 alloy. *Int. Foundry Res*., 60, 44-52. ISSN: 0046-5933.

Trojanová, Z.; Gärtnerová, V.; Lukáč, P. & Drozd, Z. (2004). Mechanical properties of Mg alloys composites reinforced with short Saffil fibres. *J. Alloys Comp.* 378, 19-26. ISSN: 0266-3538.

Trojanová, Z., Lukáč, P. & Kainer, K.U. (2007) Stress relaxation in AX41 magnesium alloy studied at elevated temperatures. *Advanced Engn. Mater*. 9, 370-374. ISSN: 1438-1656.

Wang, X.J.; Wu, K.; Huang, W.X.; Zhang, H.F.; Zheng, M.Y. & Peng D.L. (2007).. Study on fracture behavior of particulate reinforced magnesium matrix composite using in situ SEM. *Comp. Sci. Tech.* 67 2253–2260. ISSN: 0266-3538.

Hu, B.; Peng, L.; Powell, B.R.; Balough, M.P.; Kubic, R.C. & Sachdev, A.K. (2010). Interfacial and fracture behavior of short-fibers reinforced AE44 based magnesium matrix composites. *J. Alloys Comp.* 504, 527-534. ISSN: 0925-8388.

Edited by Frank Czerwinski

Scientists and engineers for decades searched to utilize magnesium, known of its low density, for light-weighting in many industrial sectors. This book provides a broad review of recent global developments in theory and practice of modern magnesium alloys. It covers fundamental aspects of alloy strengthening, recrystallization, details of microstructure and a unique role of grain refinement. The theory is linked with elements of alloy design and specific properties, including fatigue and creep resistance. Also technologies of alloy formation and processing, such as sheet rolling, semi-solid forming, welding and joining are considered. An opportunity of creation the metal matrix composite based on magnesium matrix is described along with carbon nanotubes as an effective reinforcement. A mixture of science and technology makes this book very useful for professionals from academia and industry.

ISBN 978-953-51-4527-1

Photo by alex grichenko / iStock

IntechOpen